Transactions of the ASME, Journal of Heat Transfer (ISSN 0022-1481) is published monthly by The American Society of Mechanical Engineers, Three Park Avenue, New York, NY 10016. Periodicals postage paid at New York, NY and additional mailing offices. POSTMASTER: Send address changes to Transactions of the ASME, Journal of Heat Transfer, c/o THE AMERICAN SOCIETY OF MECHANICAL ENGINEERS, 22 Law Drive, Box 2300, Fairfield, NJ 07007-2300. **CHANGES OF ADDRESS** must be received at Society headquarters seven weeks before they are to be effective. Please send old label and new address. **STATEMENT from By-Laws.** The Society shall not be responsible for statements or opinions advanced in papers or ... printed in its publications (B7.1, Para. 3).

Journal of Heat Transfer

Published Monthly by ASME

VOLUME 130 • NUMBER 9 • SEPTEMBER 2008

RESEARCH PAPERS

(Contents continued on inside back cover)

This journal is printed on acid-free paper, which exceeds the ANSI Z39.48-1992 specification for permanence of paper and library materials. ♾™
♻ 85% recycled content, including 10% post-consumer fibers.

Journal of Heat Transfer Volume 130, Number 9 SEPTEMBER 2008

The ASME Journal of Heat Transfer is abstracted and indexed in the following:

Applied Science and Technology Index, Chemical Abstracts, Chemical Engineering and Biotechnology Abstracts (Electronic equivalent of Process and Chemical Engineering), Civil Engineering Abstracts, Compendex (The electronic equivalent of Engineering Index), Corrosion Abstracts, Current Contents, E & P Health, Safety, and Environment, Ei EncompassLit, Engineered Materials Abstracts, Engineering Index, Enviroline (The electronic equivalent of Environment Abstracts), Environment Abstracts, Environmental Engineering Abstracts, Environmental Science and Pollution Management, Fluidex, Fuel and Energy Abstracts, Index to Scientific Reviews, INSPEC, International Building Services Abstracts, Mechanical & Transportation Engineering Abstracts, Mechanical Engineering Abstracts, METADEX (The electronic equivalent of Metals Abstracts and Alloys Index), Petroleum Abstracts, Process and Chemical Engineering, Referativnyi Zhurnal, Science Citation Index, SciSearch (The electronic equivalent of Science Citation Index), Theoretical Chemical Engineering

Developments in Blood Perfusion Measurements Using the Forced Convection Approach

Christopher P. B. Nicholson
e-mail: chris.nicholson@gmail.com

Darina B. Murray
e-mail: dmurray@tcd.ie

Department of Mechanical and Manufacturing Engineering,
Trinity College Dublin,
Dublin 2, Ireland

This paper reports on an investigation into the relationship between blood perfusion in the tissues of the limbs and thermal measurements at the skin surface during cooling under an array of impinging air jets. The technique is known as the forced convection approach. The objective was to address a number of the simplifying assumptions made in previous studies in order to establish the feasibility of measuring perfusion using this technique. The study is concerned with investigating the thermal aspects rather than the physiological reasons for a given perfusion measurement. Advances from previous studies are made in the area of modeling where magnetic resonance imaging scans of the test subject's leg are used to develop more physiologically realistic models. A new technique is then outlined to simultaneously assess skin and muscle perfusion from one noninvasive test at the skin surface. It is established that the sensitivity of the forced convection approach, when based on surface temperature measurements, is not high enough to allow an accurate determination of perfusion. Future work will use nonbiological mock-ups to investigate the capabilities of the method proposed for measuring skin and muscle perfusion simultaneously. If this testing is successful, a study will be conducted on the application of this approach to other thermal perfusion measurement techniques.
[DOI: 10.1115/1.2944251]

Keywords: blood perfusion, forced convection, bioheat transfer

1 Background of Perfusion Measurement

Blood perfusion (ω) is defined as the volumetric flow rate of blood through a given volume of tissue. Li et al. [1] noted that, despite its clinical significance, there is still no ideal method of measurement. Blood perfusion is an important medical parameter in a wide variety of clinical conditions, such as peripheral vascular disease, diabetic arthropathy, Raynaud's syndrome, and Buerger's disease. It is also useful in the diagnosis and treatment of cancer, as an aid to decision making in surgery, in the transdermal administration of drugs, and in the evaluation of statin treatments.

There is a range of methods in existence for measuring perfusion including those based on laser Doppler devices, plethysmographic equipment, and even radioactive tracers. However, all of these methods have associated disadvantages such as high cost, impracticality, or an inability to deliver absolute measurements. In addition to this, there are potential thermal methods, which offer the possibility of low cost and greater accuracy. This category includes techniques which either heat or cool the skin. Anderson et al. [2] and Newman et al. [3] investigated the thermal diffusion method, which requires a heated thermistor to be inserted into the skin. The rate of heat dissipation is then related to perfusion. Liu et al. [4] investigated applying a sinusoidally varying heat source to the skin; the phase shift between the skin temperature and the applied heating signal is then related to perfusion. The disadvantage of heating methods is that there is a risk of damaging the tissue if too much heat is applied. There are also methods based on cooling, which use either constant temperature cooling devices, as studied by Wilson and Spence [5], or apply a constant cooling water or air flow rate as investigated by a number of researchers at Virginia Polytechnic Institute and State University (Virginia Tech), namely, Michener et al. [6], O'Reilly et al. [7], and Scott et al. [8,9]. These are known variously as the induced cooling method and the forced convection approach. The forced convection approach allows for greater control over the degree of cooling through simple alteration of the cooling air flow rate. O'Reilly et al. [7] noted it to be inherently safe, easy to operate, and no more restrictive to a patient than a standard electrode.

1.1 Objectives. The objective of this work was to investigate the capabilities of the forced convection approach as a practical perfusion measurement tool by improving the measurement and modeling methodologies and building on the work of previous researchers. Perfusion depends on a variety of factors, such as heart rate, skin temperature, blood pressure, hormonal levels, and demands from other organs. It is not the aim of this study to ascribe the measured perfusion level to any particular factor as listed above (other than ambient temperature). Testing was conducted on healthy candidates and physiological variation was minimized as much as practically possible. The only variable that is deliberately altered to provoke a change in the perfusion level is the ambient temperature as this is well known to have a significant and predictable effect.

1.2 Forced Convection Approach to Blood Perfusion Measurement. Much of the research done to date on the forced convection approach to perfusion measurement has been conducted at Virginia Tech. Michener et al. [6] developed a "perfusion probe" to apply a localized cooling load to the skin of the forearm. The perfusion probe was developed over the course of further studies by O'Reilly et al. [7] and Scott et al. [8,9]. The cooling load applied to the arm results in a drop in temperature of the underlying tissues. A numerical model of the process is used to estimate the value of perfusion. This is achieved by varying the level of perfusion in the numerical model until the numerical and experimental heat fluxes and temperature responses matched those from the experimental test. Values of heat flux were used as the primary diagnostic index. Fundamental to this approach is the requirement to accurately model the heat transfer processes in the tissue. The model chosen was Pennes 1948 [10] bioheat equation,

Contributed by the Heat Transfer Division of ASME for publication in the JOURNAL OF HEAT TRANSFER. Manuscript received May 31, 2007; final manuscript received December 21, 2007; published online July 14, 2008. Review conducted by Bengt Sunden.

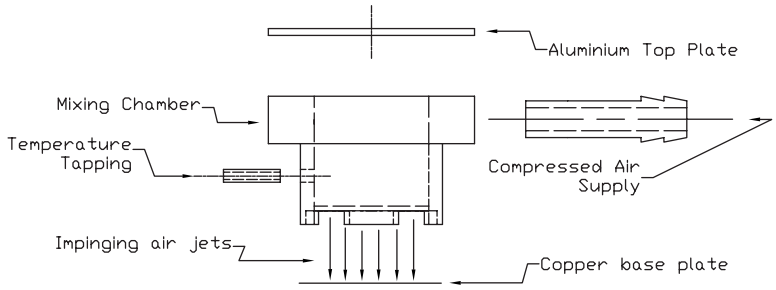

Fig. 1 Exploded view of compressed air probe

described in more details in the next section. The work carried out in Virginia Tech showed the level of perfusion in the tissue to affect the rate of temperature decay, i.e., the greater the perfusion level, the less rapid the decay in temperature on cooling of the skin surface by the perfusion probe.

1.3 Pennes Bioheat Equation. To date, Pennes [10] bioheat equation is the most established and widely used bioheat model

$$(\rho C)_t \frac{\partial T_t}{\partial t} = k_t \nabla^2 T + (\rho C \omega)_b (T_a - T_v) + \dot{q}_{\text{meta}} \tag{1}$$

where T is the temperature, ρ the density, C the specific heat, k the thermal conductivity, and ω the blood perfusion. Subscripts t, b, a, and v refer, respectively, to the tissue, the blood, the arterial blood, and the venous blood. This equation represents an energy balance within the tissue. The left hand term accounts for the rate of change in the thermal energy of the tissue; the terms on the right account for the heat transfer due to conduction through the tissue, convective heat transfer due to perfusion, and internal heat generation due to metabolism, respectively. Since Pennes' [10] paper was published, a number of the assumptions made in the derivation of the bioheat equation have been shown to be incorrect. Two areas, which have received particular criticism, are the assumptions that the capillaries are the principal sites for thermal equilibrating of the warm arterial blood with tissue temperature and that the blood in the venous system is at the tissue temperature. Chen and Holmes [11] analyzed the length required for blood in vessels of different calibers to reach equilibrium with tissue temperature. From this, they concluded that the arterial blood equilibrates with tissue temperature in vessels with diameters ranging from 0.2 mm to 0.5 mm. However, as these vessels are still relatively numerous, the use of an isotropic perfusion term is reasonable.

Mitchell and Myers [12] and Keller and Seiler [13] showed that the venous blood is rewarmed by countercurrently running arterial vessels. These realizations led to the development of a number of more physiologically realistic models by a series of researchers including Roemer and Dutton [14], Chen and Holmes [11], and Weinbaum et al. [15]. However, these models either require large amounts of anatomical data, which are not generally applicable, or their complicated formulations make them intractable. This encouraged a trend for the development of simpler bioheat formulations, which use Pennes' equation while incorporating a correction factor to account for countercurrent rewarming of blood in the venous system. Brink and Werner [16,17] and Weinbaum et al. [18] are among those who have proposed such models. In fact, Pennes [10] included such a correction factor (k_{pen}) in his original formulation to account for incomplete heat exchange between the blood vessels and tissue. This can be seen in Eq. (2). However, he assumed this term to be equal to zero and so it is not included in the standard expression, represented by Eq. (1)

$$\dot{q}_{\text{per}} = (\rho C \omega)_t (k - 1)(T_v - T_a) \tag{2}$$

1.4 Focus of Present Study. Although the choice of Pennes [10] model for bioheat transfer is appropriate, a number of the simplifications made in the application of the model warrant attention. Thus, previous studies have not accounted for countercurrent rewarming of the blood in the venous system and have assumed the perfusion levels and thermal properties of the various tissues to be isotropic. In addition, a modeling plane running longitudinally along the arm has been used; this requires the application of an internal temperature boundary condition, which is impossible to specify accurately using surface temperature measurements. These are clearly significant issues and must be addressed in order to determine whether the forced convection method may be used for perfusion estimation in the limbs.

The focus of the present work has three complementary strands:

1. Optimization of test procedure
   - to address some practical issues with regard to the design of the perfusion measurement device
   - testing on the leg rather than the arm
2. Improvement in numerical modeling
   - Modeling on a transverse cross section to remove the uncertainty associated with the estimation of the internal boundary temperature
   - the application of finite element techniques in conjunction with the use of magnetic resonance imaging (MRI) scans of a test subject's limb to develop a geometrically realistic model with the various tissues represented (see Fig. 2)
3. Investigation of a method for determination of muscle and skin perfusion from surface thermal measurements

2 Experimental Testing

This section addresses the refinement of the experimental procedure, together with a description of the experimental setup and an outline of the experimental procedures.

2.1 Advances in the Experimental Test Procedure. Unlike previous studies, testing was conducted on the lower leg rather than the forearm. One reason for this is the natural test orientation for the limb. Thus, the most natural mode of testing on the leg is from a seated position with the lower leg vertical, whereas the forearm is generally supported in a horizontal position. The significance of this is that the horizontal orientation necessitates the inclusion of a circumferentially varying convective boundary condition in the numerical model. In contrast, the vertically supported leg has uniform convective boundary conditions.

2.2 Experimental Setup. A perfusion measurement device identical in operating principle and similar in design to the probe used by O'Reilly et al. [7] was designed and manufactured. This is shown in Fig. 1.

Compressed air enters a mixing chamber before passing through an array of holes in the bottom of the chamber; this gives rise to a series of jets, which are directed at the skin surface. To ensure uniform cooling of the skin, the probe was designed with a greater open flow area than previous probe designs. Thus, there are 45 jets of 0.4 mm diameter spaced at 3.13 mm intervals in a rectangular matrix. The ratio of plate spacing to jet diameter was fixed at 6.5, which extends just past the potential core length and was shown by Ashforth-Frost and Jambunathan [19] to yield the maximum convective cooling effect. An initial probe design for this study used a copper base plate onto which the heat flux sensor was mounted. When using the plate, there is significant contact resistance between the sensor and the skin due to inconsistent plate pressure. Therefore, an alternative approach was used where the heat flux and temperature sensors were attached to the skin surface using double sided tape. As the sensors were held firmly against the surface, the contact resistance was minimal and constant over the cooling area. The total insulating effect due to the contact resistance and thermal resistance of the adhesive tape and sensors was reflected in a slight drop in the measured convective heat transfer coefficient that could be offset by increasing slightly the cooling air flow rate.

A National Instruments 16 bit data acquisition card is used in conjunction with a LABVIEW program to record the surface heat flux, skin temperature, ambient temperature, and cooling air temperature. An RdF microfoil heat flux sensor (27036-3) was employed with an amplification factor of 1000. Betatherm thermistors (10K3A1B) were used for all the temperature measurements. All sensors used were calibrated to ASME standards. The precision uncertainty associated with the thermistors was found to be $\pm 0.1\,^{\circ}\mathrm{C}$. Full calibration details are included in Nicholson [20].

2.3 Test Procedure. The experimental testing contains two parts, a free convection test to record parameters before cooling, followed by the forced convection part of the test. The test procedure is as follows. First, the test location, on the lateral side of the leg, at a defined height up from the ankle and at a specific circumferential location, must be marked accurately so as to correlate well with the geometry in the numerical model. Before a test begins, the candidate sits at rest for a period of 15 min with the leg uncovered. This is to allow it to equilibrate with the ambient environment in order to give a true steady state temperature measurement. After this time, double sided tape is placed over the entire measurement area. The heat flux sensor and thermistor are then attached to the outer surface of the tape. (The heat flux sensor is used to calculate a value for the convective heat transfer coefficient during testing.) The thermistor is placed alongside the heat flux sensor, in the center of the cooling region. The LABVIEW program is started and begins acquiring and logging the surface heat flux, skin temperature, ambient temperature, and cooling air temperature. Once it has been established that steady state conditions prevail, the forced convection part of the test may begin.

The probe, with a preset air flow rate specifically designed to give a desired heat transfer coefficient, is then held against the leg for the allotted time period, after which time the probe is removed and measurement of heat flux and temperatures ceases.

3 Numerical Solution Method

Previous studies [6,7] used a finite difference model with a mesh running longitudinally down the limb, requiring a constant boundary temperature to be estimated at the bottom of the mesh, i.e., at the center of the limb. The approach used here is to model on a plane perpendicular to the central axis of the limb as it removes the uncertainty associated with estimation of the internal arm temperature. The finite element package COMSOL MULTIPHYSICS was chosen because it incorporates a specific module for the bioheat equation and because it can handle complex geometries. The first step was to generate a geometrically realistic representation of the test site using MRI scans of the test subject's leg. This was done by importing the MRI scans to AUTOCAD where a "tracing" was made, such as that shown in Fig. 2. As the MRI scans were of high quality, it was possible to generate an accurate model of the tissue distribution.

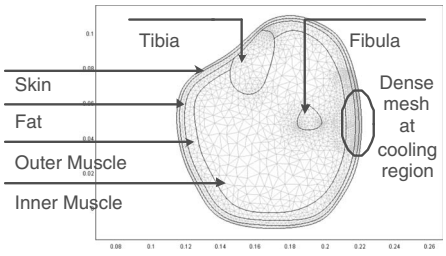

Fig. 2 Screenshot of meshed tracing of MRI image in COMSOL including various tissue regions and location of cooling region

This model is then imported into COMSOL MULTIPHYSICS where the relevant tissue properties (as shown in Table 1) and the experimentally determined boundary conditions are applied.

As testing was conducted with the candidate at rest, basal metabolic rates were used. The muscle domain is divided into inner and outer regions to allow application of Brink and Werner's [16] correction factor, which accounts for countercurrent heat transfer between the arterial and venous vessels in the muscle layer. The correction factor is a function of both perfusion rate and radial location. When considering the radial variation, Brink and Werner [16] established that it is sufficient to divide the tissue region into two areas. They noted that for the skin tissue Pennes equation does not need correction.

Often during testing, there were minor variations in cooling jet temperature or air flow rate. These variations are included as time varying parameters in the model for each test under investigation. As described in Sec. 2.2, the thermistor and heat flux sensor were attached to the leg using double sided tape. As the contact resistance was constant over the cooling area, it was not explicitly modeled. Its presence was manifested as a slight drop in the convective heat transfer coefficient during testing. Therefore, the effect of the contact resistance is included in the model through inclusion of the actual time varying convective heat transfer coefficient during testing.

Before starting the test program, a 3D model was developed to investigate the accuracy of the 2D representation. Both models were run for a range of cooling times and convective heat transfer coefficients. The 2D assumption was found to break down after long cooling times (>500 s, $h=100\ \mathrm{W/m^2\,K}$) or at shorter times for higher values of the convective heat transfer coefficient (300 s, $h=250\ \mathrm{W/m^2\,K}$). Under these conditions, the 2D model overestimates the cooling as it does not account for extra heat flowing in the z direction (along the limb). It is not possible to define a complete table of maximum cooling times for 2D modeling as the

Table 1 Thermal constant values for various tissue types from Fiala et al. [21] and maximum range of values from literature review

	k (W/m K)	ρ (kg/m^3)	c (J/kg K)	q_m (W/m^3)
Bone	0.75	1357	1700	0
	(0.5–2.21)	(1357–1418)	(1700–2094)	
Muscle	0.42	1085	3768	684
	(0.38–0.54)	(1010–1085)	(3600–3800)	(684–800)
Fat	0.16	850	2300	58
	(0.16–0.2)	(850–940)	(2200–2400)	(5–58)
Skin	0.47	1085	3680	368
		(1085–1200)	(3680–3800)	
Blood		1069	3650	

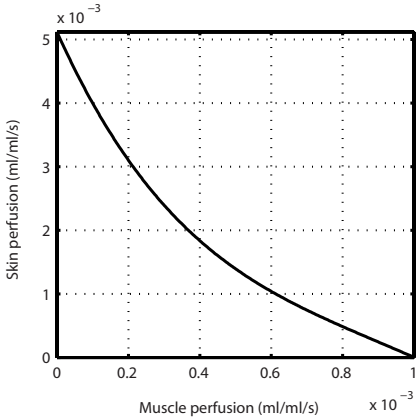

Fig. 3 Conceptual PPV curve: showing the possible combinations of skin and muscle perfusion for a human limb at a given steady state temperature

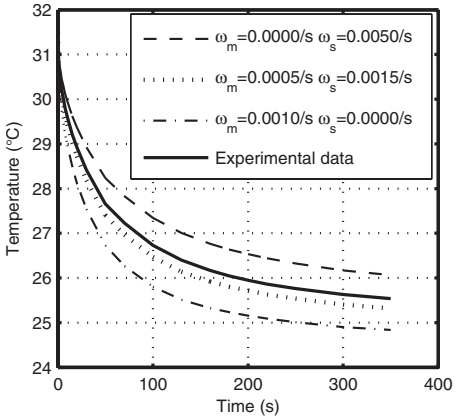

Fig. 4 Illustrative comparison of experimental and numerical temperature profiles for a range of values from the PPV curve shown in Fig. 3

problem is multifactorial. However, for the test conditions used in the present investigation the 2D assumption held true.

4 Simultaneous Estimation of Skin and Muscle Perfusion

It is well known that the factors driving muscle and skin perfusion differ significantly. Skin perfusion is driven mainly by thermoregulatory factors while muscle perfusion is mainly a function of the exertion of the muscle. (Wilson and Spence [5] noted that the thermal contribution of perfusion to the fatty tissue is negligible.) Previous studies assigned a global perfusion value to all tissues. This is not a realistic representation. Now that a geometrically realistic model that represents the various tissues has been developed, it is possible to assign different perfusion values to skin and muscle. This new modeling capability is embedded in the Possible Perfusion Value (PPV) concept, which allows for more realistic perfusion modeling and is applicable to virtually all thermal methods of perfusion estimation. The theoretical concept and the associated modelling steps are explained next using theoretically generated data.

4.1 Possible Perfusion Values Concept. The basic premise of the PPV concept is that a given value of skin temperature, under steady state free convection conditions, can only be produced by certain combinations of skin and muscle perfusion, e.g., a high value of skin perfusion and a low value of muscle perfusion or vice versa. These possible skin and muscle perfusion combinations are determined from a curve, which we define here as the PPV curve (Fig. 3).

The method for finding the combinations of skin and muscle perfusion giving the same steady state surface temperature as measured under free convection conditions in the experimental tests is as follows. The model is run for a large range of possible skin and muscle perfusion combinations. This is achieved by running the steady state model inside two loops, one to iterate the muscle perfusion and one to iterate the skin perfusion. These loops are implemented in MATLAB, an interface for which is supplied with COMSOL MULTIPHYSICS. For a given value of muscle perfusion, the value of skin perfusion, which correlates to the experimental temperature value, is determined. This procedure continues until the maximum value of muscle perfusion has been reached (which can take up to 60 separate runs).

Although this curve identifies all the possible combinations of skin and muscle perfusion that will give the measured steady state temperature under the test conditions, it is impossible from a single surface temperature reading to deduce which particular combination of perfusion values from the PPV curve is applicable. Thus, it is also necessary to run a forced convection test, with the expectation that when the model is run for a range of perfusion combinations identified from the PPV curve only one resulting temperature response will match the experimental data from the forced convection test. This concept is illustrated in Fig. 4. As Curve "B" (which corresponds to a muscle perfusion value of 0.0005/s and a skin perfusion value of 0.0015/s) most closely matches the form of the experimental temperature decay, this is taken to be the combination of perfusion values that is actually occurring.

The modeling procedure for the forced convection part of the test is as follows. Possible muscle and skin perfusion combinations are chosen from the PPV curve and the convective heat transfer coefficient and air temperature measured during the forced convection test are applied as boundary conditions to the model. The MATLAB interface is used again to run the model for the various combinations of perfusion levels. For each combination of perfusion levels chosen, the steady state model is run once more so that the initial condition for the transient model is generated. The transient model is then run for the allotted time and the numerical results are automatically compared to those from the experimental test. The final decision on the best fit between experimental and numerical curves is carried out by the tester using visual inspection.

This PPV concept is the basis for refinement of the perfusion estimation procedure and allows both the skin and muscle perfusion to be established from a two stage noninvasive surface test. The free convection part (Stage 1) is used to generate the PPV curve and the forced convection part (Stage 2) to identify the specific point on the PPV curve. This approach links surface temperatures to individualized tissue perfusion levels and, as a result, is considered to be more rigorous and physiologically realistic than previous thermal methods of estimating blood perfusion.

5 Results and Discussion

The previous section used theoretically generated data to explain the PPV concept. The experimental and numerical improvements in conjunction with the PPV concept are now implemented in an actual perfusion estimation test. A PPV curve is first derived, as shown in Fig. 6 (using the boundary conditions and test location shown in Fig. 5). Next, the forced convection part of the test is modeled. The comparison between experimental and numerical results is shown in Fig. 8 (using the boundary conditions and test location shown in Fig. 7). From Fig. 8, a significant problem with this methodology for estimation of tissue perfusion emerges. Thus, there is only a small difference in predicted skin temperature (0.4°C) over the entire range of possible perfusion combinations, which implies that the results are quite insensitive to perfusion levels. Considering that the experimental error associated

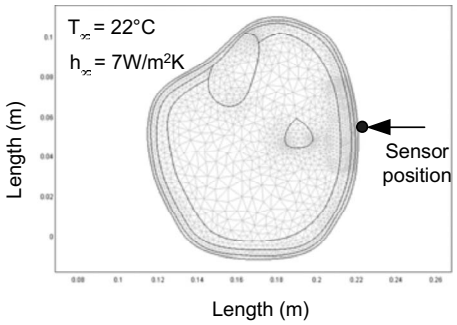

Fig. 5 Test conditions and measurement location for free convection part of the test

with the thermistors is $\pm 0.1\,^{\circ}\mathrm{C}$, this temperature range is clearly not large enough to allow accurate determination of perfusion.

From these results, the insensitivity of skin temperature to tissue perfusion levels needs to be explained. As described in Sec. 4.1, there are various combinations of muscle and skin perfusion that give the same surface temperature for specified free convection conditions. This implies that the heat flow from the surface of the limb is also constant, i.e., the sum of the heat generated by skin perfusion and the heat conducted into the skin tissue from the muscle tissue is equivalent for various combinations of skin and muscle perfusion. During the forced convection part of a test, this is also substantially true, explaining the limited divergence between the predicted skin temperature variations. What divergence there is can be explained as follows. As the skin tissue temperature starts to drop during forced convection testing, the rate of heat generation due to skin perfusion increases, as this rate is

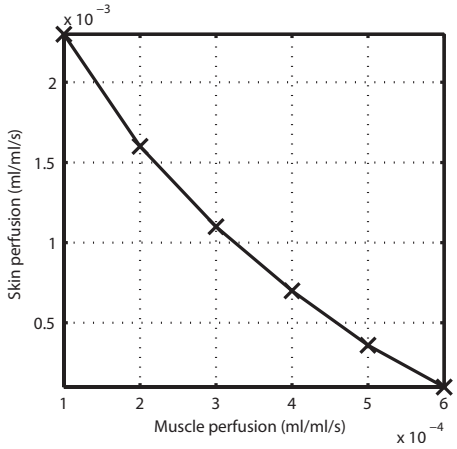

Fig. 6 PPV curve for test data generated from free convection part of the test

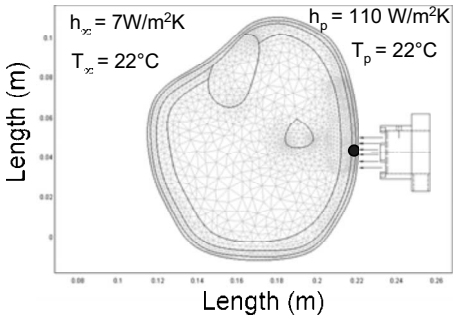

Fig. 7 Test conditions and measurement location for forced convection part of test

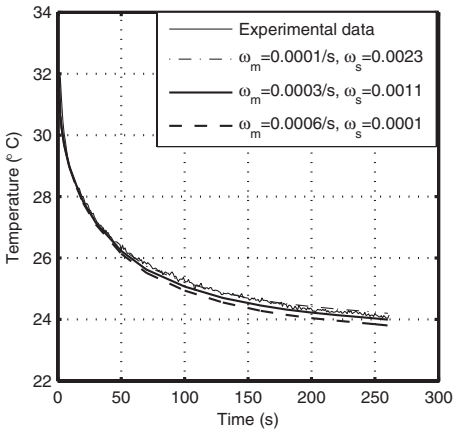

Fig. 8 Comparison between experimental and numerical results for forced convection part of test

proportional to the temperature difference between the arterial and local tissue temperatures. This prevents the skin temperature from falling very rapidly in cases where skin perfusion is high. In contrast, the temperature drop of the insulated muscle tissue under forced cooling is not as rapid, and so the increase in heat generation from muscle perfusion is less significant. Thus, the skin temperature drops more rapidly when skin perfusion is low and muscle perfusion is high, accounting for the small difference in predicted skin temperature shown in Fig. 8.

In order to increase the sensitivity of the method, an optimization procedure for the forced convection test parameters was conducted using the numerical model. For the conditions of the present investigation, the optimum value of convective heat transfer coefficient is $75\ \mathrm{W/m^2\,K}$ (as shown in Fig. 9) and the maximum temperature difference between the different perfusion combinations occurs at 500 s into the test.

The sensitivity is low initially; it then increases to a maximum (at $75\ \mathrm{W/m^2\,K}$) before decreasing once again. Although this optimization process leads to an increase in skin temperature sensitivity to perfusion, the temperature range for different perfusion combinations is still only $0.65\,^{\circ}\mathrm{C}$. This lack of sensitivity was observed over a range of tests under various ambient conditions.

6 Conclusions

This paper reports on an investigation into the relationship between blood perfusion in the tissues of the limbs and thermal measurements at the skin surface during forced cooling by impinging air jets. An initial study of this forced convection approach identified issues to be addressed before the technique could be used for perfusion measurement. In particular, the actual

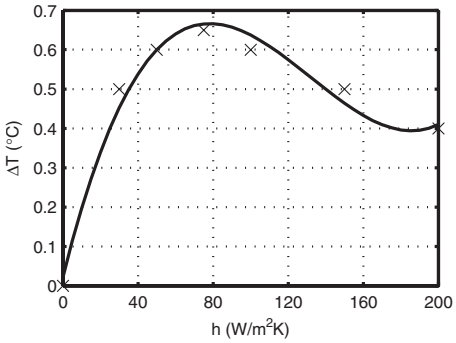

Fig. 9 Results of optimization procedure for increasing the maximum temperature difference over the range of perfusion values from the PPV curve

thermal properties and distribution of the various tissues in the limbs needed to be accounted for. This was achieved using actual MRI scans of the test subject's limb. The concept of the PPV curve was then developed in order to identify the possible combinations of skin and muscle perfusion. It was postulated that a forced convection test would be able to subsequently isolate the specific combinations of skin and muscle perfusion occurring. However, the difference in the cooling temperature profiles for different perfusion combinations was found not to be significant enough to allow an accurate determination of perfusion. An optimization procedure was carried out to increase the sensitivity of the method. This established that, even at the optimum convective heat transfer coefficient and cooling time, the temperature range was still not great enough. Thus, the conclusion is that the skin surface temperature profiles generated from the forced convection approach do not allow accurate estimation of perfusion. However, application of the PPV methodology might be of benefit when applied to other thermal techniques as it is the only way to account for the difference in skin and muscle perfusion values when using noninvasive thermal measurements for perfusion estimation. Future work will focus on learning more about the fundamental underlying heat transfer problem by testing on a mock-up of the limb. A simple comparison can be made between the derived and the actual controlled flow rate into the arm in order to clarify the feasibility of the method in the absence of physiological variation. If testing here is successful, then the techniques can again be extended to testing on live subjects where it is hoped that it will make a valuable contribution to perfusion measurement by thermal methods.

Nomenclature

c = specific heat capacity, J/kg K
h = convective heat transfer coefficient, W/m^2 K
k = thermal conductivity, W/m K
k_{pen} = Pennes correction factor,
$\dot{q}$ = volumetric heat generation, W/m^3
q'' = heat flux, W/m^2
t = time, s
T = temperature, °C
X_e = equilibrium length, m

Greek Letters

ρ = density, kg/m^3
ω = blood perfusion, ml/ml/s

Subscripts

a = artery
amb = ambient
b = blood
meta = metabolic
p = probe
per = perfusion
s = skin
t = tissue
v = vein
∞ = freestream conditions

References

[1] Li, H. J., Zhang, X. X., and Yi, Y. F., 2002, "Measurement of Blood Perfusion Using the Temperature Response to Constant Surface Flux Heating," Int. J. Thermophys., **23**(6), pp. 1631–1644.
[2] Anderson, G. T., Valvano, J. W., and Santos, R. R., 1992, "Self-Heated Thermistor Measurements of Perfusion," IEEE Trans. Biomed. Eng., **39**, pp. 877–885.
[3] Newman, W. H., Bowman, H. F., Orgill, D. P., and Klar, E., 1995, "A Methodology for In Vivo Measurement of Blood Flow in Small Tissue Volumes," *Advances in Heat and Mass Transfer in Biotechnology*, ASME, New York, HTD-Vol. 322/BED-Vol. 32, pp. 99–105.
[4] Liu, J., and Xu, L. X., 1999, "Estimation of Blood Perfusion Using Phase Shift in Temperature Response to Sinusoidal Heating at the Skin Surface," IEEE Trans. Biomed. Eng., **46**(9), pp. 1037–1043.
[5] Wilson, S. B., and Spence, V. A., 1988, "A Tissue Heat Transfer Model for Relating Dynamic Skin Temperature Changes to Physiological Parameters," Phys. Med. Biol., **33**(8), pp. 895–912.
[6] Michener, M., Hager, J. M., Tarrell, J. P., Veit, H., and Diller, T. E., 1991, "Non-Invasive Blood Perfusion Measurement With a Heat Flux Microsensor," *Advances in Heat and Mass Transfer in Biotechnology*, ASME, New York, HTD-Vol. 189/BED-Vol. 18, pp. 1—8.
[7] O'Reilly, T. B., Diller, T. E., and Gonzales, T. L., 1996, "Development of a Non-Invasive Blood Perfusion Probe," *Advances in Heat and Mass Transfer in Biotechnology*, ASME, New York, HTD-Vol. 337/BED-Vol. 34, pp. 67–73.
[8] Scott, E. P., Robinson, P., and Diller, T. E., 1997, "Estimation of Blood Perfusion Using a Minimally Invasive Blood Perfusion Probe," *Advances in Heat and Mass Transfer in Biotechnology*, ASME, New York, HTD-Vol. 355/BED-Vol. 37, pp. 205–212.
[9] Scott, E. P., Robinson, P. S., and Diller, T. E., 1998, "Development of Methodologies for the Estimation of Blood Perfusion Using a Minimally Invasive Thermal Probe," Meas. Sci. Technol., **9**, pp. 888–897.
[10] Pennes, H. H., 1948, "Analysis of Tissue and Arterial Blood Temperatures in the Resting Human Forearm," J. Appl. Physiol., **1**(2), pp. 93–122.
[11] Chen, M. M., and Holmes, K. K., 1980, "Microvascular Contributions to Tissue Heat Transfer," Ann. N.Y. Acad. Sci., **335**, pp. 137–150.
[12] Mitchell, J. W., and Myers, G. E., 1968, "An Analytical Model of the Countercurrent Heat Exchange Phenomena," Biophys. J., **8**, pp. 897–911.
[13] Keller, K. H., and Seiler, L., 1971, "An Analysis of Peripheral Heat Transfer in Man," J. Appl. Physiol., **30**, pp. 779–786.
[14] Roemer, R. B., and Dutton, A. W., 1998, "A Generic Tissue Convective Energy Balance Equation: Part 1—Theory and Derivation," ASME J. Biomech. Eng., **120**, pp. 395–404.
[15] Weinbaum, S., and Jiji, L. M., 1998, "A New Simplified Bio-Heat Equation for the Effect of Blood Flow on Local Average Tissue Temperature," ASME J. Biomech. Eng., **107**, pp. 131–139.
[16] Brinck, H., and Werner, J., 1994, "Efficiency Function: Improvement of Classical Bio-Heat Approach," J. Appl. Physiol., **77**(4), pp. 1617–1622.
[17] Brinck, H., and Werner, J., 1994, "Estimation of the Thermal Effect of Blood Flow in a Branching Countercurrent Network Using a Three-Dimensional Vascular Model," ASME J. Biomech. Eng., **116**, pp. 324–330.
[18] Weinbaum, S., Xu, L. X., Zhu, L., Ekpene, A., 1997, "A New Fundamental Bio-Heat Equation for Muscle Tissue: Part I—Blood Perfusion Term," ASME J. Biomech. Eng., **119**, pp. 278–288.
[19] Ashforth-Frost, S., and Jambunathan, K., 1996, "Effect of Nozzle Geometry and Semi-Confinement on the Potential Core of a Turbulent Axisymmetric Free Jet," Int. Commun. Heat Mass Transfer, **23**, pp. 155–162.
[20] Nicholson, C. P. B., 2006, "The Relationship Between Blood Perfusion and Thermal Measurements at the Skin Surface," Ph.D. thesis, Trinity College Dublin, Dublin.
[21] Fiala, D., Lomas, K. J., and Stohrer, M., 1999, "A Computer Model of Human Thermoregulation for a Wide Range of Environmental Conditions: The Passive System," J. Appl. Physiol., **87**(5), pp. 1957–1972.

L. Thiery
e-mail: laurent.thiery@univ-fcomte.fr

S. Toullier

D. Teyssieux

FEMTO-ST (CNRS UMR 6174),
32 avenue de l'Observatoire,
25030 Besancon Cedex, France

D. Briand
Institute of Microtechnology,
rue Jaquet-Droz 1,
P.O. Box 526,
CH-2002 Neuchâtel, Switzerland

Thermal Contact Calibration Between a Thermocouple Probe and a Microhotplate

Since local thermal probing has become a major tool for studying transport phenomena at micro- and nanoscale levels, the fundamental aspect of the interaction between the tip of the probe and the sample has remained the key point on which any quantitative measurement relies. In this paper, we present results on thermal resistances involved in the contact mechanism of a microthermocouple cantilever probe that is used to scan the surface of a microhotplate at different levels of temperature. We point out the potential of such an active microsystem as an efficient calibration tool for near-field thermal probes. [DOI: 10.1115/1.2943306]

Keywords: contact resistance, thermal probes, calibration, thermocouple, microhotplate

1 Introduction

Nowadays, the accurate measurement of the temperature at the surface of microsystems remains challenging. This is not only the case for the detection of hotspots in nanoelectronic devices or for the thermal characterization of one-dimensional nanostructures, but also for the simple thermal analysis of microelectromechanical systems (MEMSs). Indeed, improvements in the performance of many microthermal devices are depending on the modeling abilities and subsequently the experimental techniques from which models are corrected. Microhotplates are a thermal microsystems for which many investigations have been performed to model their thermal behavior. The key element of these microsystems is an isolated area, which is generally a dielectric suspended membrane that can be heated by means of an embedded resistor whose temperature can be precisely adjusted and controlled. They are widely used as thermal flow sensors, microbolometers, Joule heating igniters, infrared sources, gas sensors, etc. [1–4].

However, the experimental conditions make it rather difficult to achieve precise temperature measurements on such devices. The thermally involved area exceeds naturally the heater itself at the center of the suspended membrane. Thus, a precise analysis requires extracting the complete temperature distribution of a surface that could exceed 1 mm^2, with an acceptable resolution. Thermal gradients are important since the hottest part at the center of the membrane can reach temperatures up to 1000 K, whereas the frame of the device remains near the ambient temperature. The optical properties of the hotplate membrane (silicon nitride or oxide) are generally problematic for any infrared or optical techniques [5]. As a consequence, only a few measurement points are taken on the metals or the (poly)silicon forming the components of the active heated area. Among the possible techniques, Raman scattering has been recently improved to decrease the spatial resolution but remains complicated and also depends on the sample material [6–8]. In these conditions, the techniques based on the contact of the surface remain an attractive method to determine the surface temperature of such devices, eliminating the problems related to the calibration of the emissivity of the materials, even if the problem of surface thermal disturbance has not been completely resolved for those techniques.

Today, thermal probing has high potential for improving near-field imaging techniques and developing a new tool to investigate heat transfer mechanisms at micro- and nanoscale. Different techniques have been proposed to fabricate a temperature sensor at the tip of a microprobe. They consist generally to enhance the capabilities of atomic force microscope (AFM) tips on silicon oxide or nitride cantilevers on which a diode or a thermocouple junction is fabricated. A complete overview of the technology of scanning thermal probes and the problematic of thermal contact has been published by Majumdar [9]. However, only a very few laboratories are involved in these developments and their availability is rather limited. Moreover, the thermal response of these probes depends strongly on both the sample materials and the external thermal conditions, and they cannot operate at temperatures above 500 K typically. For such an application, a thin wire thermoelectric sensor remains the most simple and practical technique. However, a specific calibration procedure is necessary to quantify the measurement error due to the contact of the sensor with the surface.

In this paper, by focusing on this calibration procedure, complete measurement of the thermal resistances involved in the use of microthermocouples is obtained. An analysis of the probe thermal behavior is presented. The extension of the use of a microhotplate for calibrating temperature sensors is proposed.

2 Experimental Methods

2.1 Microhotplate Characteristics. The microhotplate designs developed at the Institute of Microtechnology have been previously reported in the literature [10,11]. They consist in a membrane (0.75 or 1.0 μm thick) made of two low-stress low pressure chemical vapor deposition (LPCVD) silicon nitride films. A platinum film heater with a tantalum adhesion layer is embedded in the suspended membrane and is therefore thermally isolated from the chip frame. Platinum electrodes are then patterned onto the membrane. When the microhotplate is used as a gas sensor, these electrodes are used to detect a variation of resistivity of the gas sensitive material (not present in this study). The membrane is released using backside micromachining of the silicon wafer (Fig. 1).

By supplying an electrical current to the heater, the membrane temperature is increased. The design of the heater is optimized for ensuring a surface temperature distribution as homogeneous as possible. The heater resistance, whose value is near 100 Ω at room temperature, is increasing with temperature, following a quasilinear relation. A precise control of both voltage and current is then possible with a resolution of less than 1 μW. Conse-

Contributed by the Heat Transfer Division of ASME for publication in the JOURNAL OF HEAT TRANSFER. Manuscript received March 26, 2007; final manuscript received November 13, 2007; published online July 3, 2008. Review conducted by Yutaka Asako.

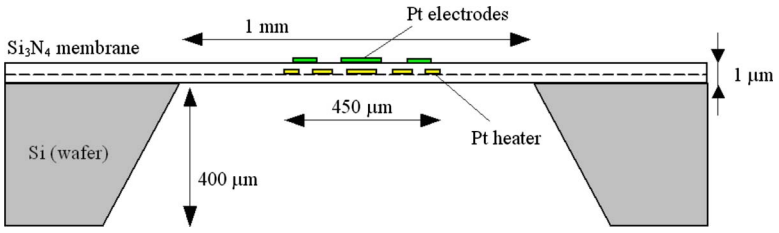

Fig. 1 Schematic cross section of the microhotplate

quently, any change in the power dissipated by the heater that can be induced by a probe in contact with the membrane of the device is precisely measurable.

2.2 Thermal Probes. The thermocouple probes are obtained by welding two Wollaston wires (Pt and Pt-10%Rh), with a diameter of 1.3 μm. The silver cladding (diameter of 75 μm) is removed by means of a chemical (nitrid acid) or electrochemical etching process [12]. These wires are commonly used as thermal resistors for hot-wire anemometry and commercial scanning thermal microscope (SThM ®Topometrix), techniques for which the relation between the measured signal and the surface or contact temperature is hard to derive. In the case of our thermocouple composed of thin wires, this drawback is avoided by manufacturing a thermoelectric microjunction.

We have extensively used our micrometric thermocouples in different applications [12–14]. The principle of a cantilevered microthermocouple for near-field applications has already been demonstrated [15]. However, lately we have reduced the available size of these wire sensors and verified that the resulting thermoelectromotive force has remained similar to the standard S type thermocouples. An improvement of our wire preparation and welding technique has led to the so called "cantilever" shape probes. This shape provides a lateral flexibility to the thermocouple and allows its operation in a near-field operation mode similar to AFM (Fig. 2). The resulting stiffness of such a spring is ideal to provide a controlled contact strain without any risk to damage the membrane.

The main reason that such probes are not widely used in laboratories is due to the difficulty to fabricate them reproducibly. However, this remains a reliable tool for temperature mapping of microsystems especially for intermediate levels of temperature and conditions for which optical techniques are not suitable.

2.3 Thermal Modeling and Calibration Procedures

2.3.1 Contact Model. The main problem when measuring the contact temperature is to correctly evaluate the effect of this contact on the actual surface temperature. This effect is approached by the expression of the thermal response τ. This quantity is defined as a ratio between the temperature of the probe T_p (elevation from ambient T_a) and the actual surface temperature T_s (before any contact). This can be considered as an error of estimation due to the thermal contact of the probe, then

$$\tau = \frac{T_p - T_a}{T_s - T_a} \tag{1}$$

However, this does not characterize the probe only, but the couple probe-surface together. This is due to the thermal transfers involved in the system, which relate the sample surface nature, the probe, and the environment media. As a result, one single probe thermal response may usually vary in a range of one order of magnitude when changing the sample nature [16]. The same consequence could result of a change in the operating conditions from ambient to vacuum [17].

The thermal contact between a probe and a surface remains an open question especially in submicron thermal analysis [9]. Furthermore, the specific case of a thin membrane differs slightly from massive object. Let us consider first T_s as the actual surface temperature without any probe contact. As soon as the probe is put on the object, T_s is lowered. This is related to the constriction of the flux lines inside the object. It is known that both the thermal conductivity of the surface and the contact area of the probe are involved in this phenomenon [9,18]. Then, the surface temperature becomes T_m, a modified surface temperature, and for semi-infinite solid, T_s remains unchanged at a sufficient depth below the

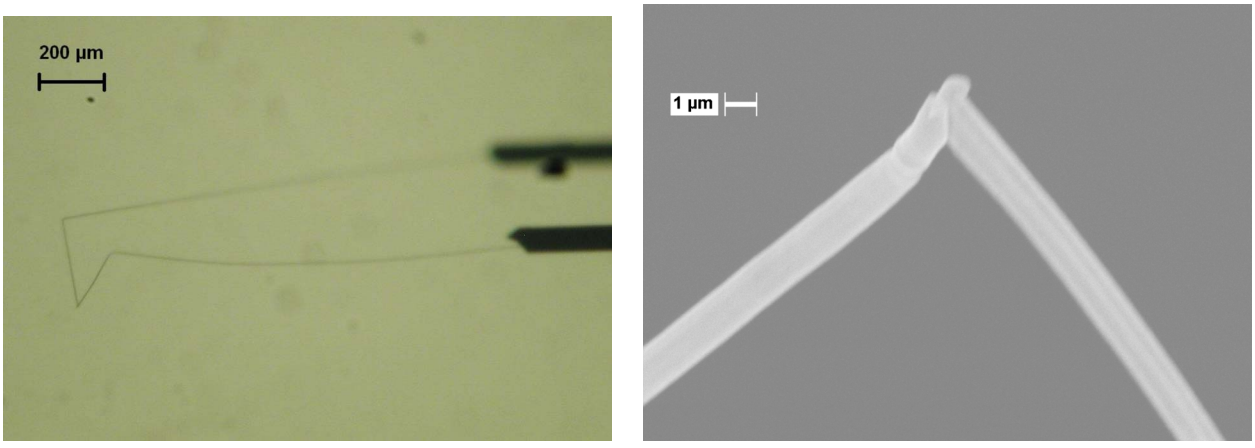

(*a*) (*b*)

Fig. 2 Pt-PtRh (S type) thermocouple cantilever probe used for contact temperature measurements. Wire diameter: 1.3 μm. Optical image of the cantilever and scanning electron microscope view of the junction tip.

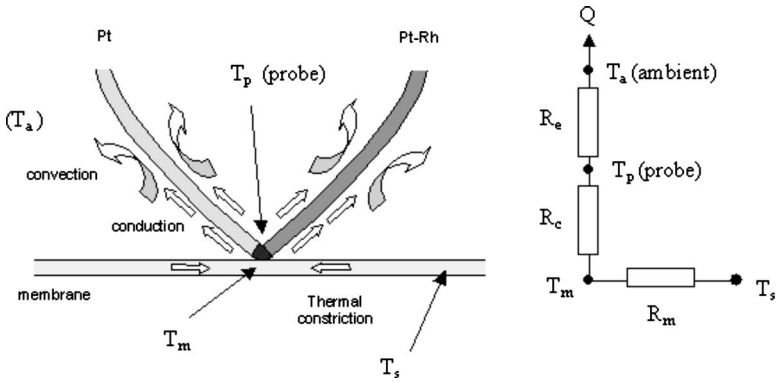

Fig. 3 Schematic thermal configuration of the thermocouple junction on the hotplate membrane

surface. Thin solids, such as the membrane of a hotplate at homogeneous temperature, are, however, subjected to similar effects except that T_s remains unchanged at a lateral distance in the membrane, as shown in Fig. 3. Therefore, the definition of a thermal resistance between T_s and T_m can still be applied.

Second, the contact between the probe and the surface exhibits a finite thermal conductance. Inversely, the resulting thermal resistance cannot be nil. Then, the probe temperature never equals the surface temperature T_m but always indicates its own value, called T_p. Finally, the probe itself is thermally connected to ambient and dissipates heat as a fin. The thermal power that is dissipated from the hottest temperature to the ambient value flows through three resistances:

(a) thermal flux constriction resistance R_m, between T_s and T_m
(b) thermal contact resistance R_c, between T_m and T_p
(c) an external dissipation resistance of the probe R_e, between T_p and T_a

This thermal power is then written as

$$Q = \frac{T_s - T_m}{R_m} = \frac{T_m - T_p}{R_c} = \frac{T_p - T_a}{R_e} \tag{2}$$

leading to another expression of the sensor thermal response:

$$\tau = \frac{R_e}{R_e + R_c + R_m} \tag{3}$$

2.3.2 Contact Procedures. First, it was verified that the thermoelectric response of the probe corresponds strictly to the S type thermoelectric couple for which usual tolerance standard is applicable. This step is of great importance and cannot be avoided when developing new temperature probes. Then, the two remaining procedures are necessary to extract R_e, R_m, and R_c. This is due to the lack of temperature sensor embedded in the membrane, or the lack of any other methods to access to the local T_s or T_m at any time.

The first procedure consists in the measurement of a surface temperature of a massive solid for which the surface temperature is easily controlled. This is achieved by using a 70 μm diameter platinum wire whose temperature is set by adjusting a self-heating current. A thermocouple junction has been welded on its surface by means of a capacitive discharge. Measuring its floating thermoelectric voltage provides a first temperature called T_{p1}. This thermocouple is strictly identical to the probe to be used in contact mode whose measurement is called T_{p2} (Fig. 4).

Let us consider that the contact thermal resistance (R_c) of the welded probe is negligible. As a result, the modified surface temperature (T_m) equals the probe one (T_{p1}). Now, the second probe that is put on the wire surface provides its own temperature (T_{p2}), which differs from T_m due to the contact resistance. As an extension of relation (2), we can express the heat power that crosses from the wire to the ambient through this probe with

$$\frac{T_s - T_m}{R_m} = \frac{T_m - T_{p2}}{R_c} = \frac{T_{p2} - T_a}{R_e} \tag{4}$$

T_s being the surface temperature of the wire before contact.

Since the welded probe ensures that $T_m = T_{p1}$, the previous equality gives

$$\frac{T_{p1} - T_{p2}}{R_c} = \frac{T_{p2} - T_a}{R_e} \tag{5}$$

defining a ratio

$$\phi = \frac{T_{p1} - T_{p2}}{T_{p2} - T_a} = \frac{R_c}{R_e} \tag{6}$$

This ratio characterizes the contact of a probe for given conditions of temperature and the contact strength that will be reproduced in the following procedure.

The second procedure is performed on the tested microhotplates in order to extract the remaining parameters. For this, we lean on

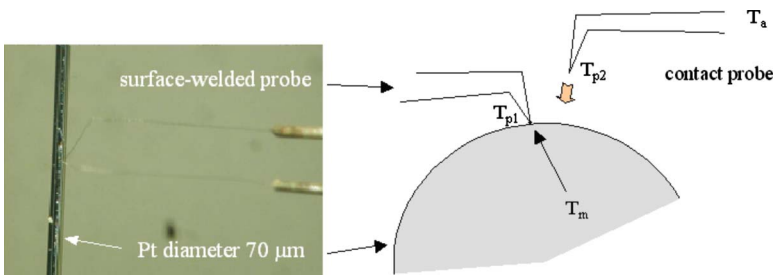

Fig. 4 Principle of thermal contact resistance calibration

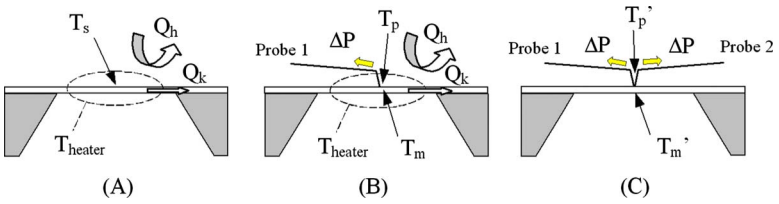

Fig. 5 Contact probe calibration procedure on a microhotplate. (*a*) initial thermal balance, (*b*) contact perturbation compensated to maintain T_{heater} as unchanged, and (*c*) double contact allowing to measure the local temperature drop.

the hotplate capabilities to precisely control the power consumption and the global thermal balance, especially for estimating the heat excess involved by the contact probe. The design of the heater ensures a thermal homogeneity of an area centered on the membrane and that represents a quarter of its total area. The electrical resistance of this heater directly relates on its average temperature (T_{heater}), and results from the global thermal balance of the membrane in which only conduction (Q_k) and convection-radiation (Q_h) dissipation terms occur prior to any probe contact (Fig. 5(*a*)). After the contact of a probe, measuring the power dissipated by the probe alone is possible if the initial dissipation terms (Q_k and Q_h) remain unchanged. Therefore, if we assume that the probe contact introduces only a weak perturbation located at the center point, then the condition of a constant average heater temperature (T_{heater}) is enough to consider these terms (Q_k and Q_h) as identical. Consequently, the supplied electrical power is adjusted to maintain the heater resistance at a constant value. The power difference ΔP then corresponds to the power dissipated by the probe (Fig. 5(*b*)). Finally, since the membrane is not equipped with any local temperature sensor, a second identical probe is used to measure the decrease of temperature due to the contact of one probe with the surface. This second probe is put in contact with the membrane as close as possible to the first probe (Fig. 5(*c*)).

According to these assumptions, the initial heat balance of the hotplate is

$$P_0 = Q_k + Q_h = u_0 \,.\, i_0 \tag{7}$$

and

$$u_0/i_0 = R_{\text{heater}} \propto T_{\text{heater}} \tag{8}$$

where P_0 is the electrical supplied power, Q_k and Q_h are the heat powers dissipated by conduction and convection-radiation, respectively. After the first probe has been put in contact with the membrane, the supplied power is adjusted to keep the average temperature of the heater (R_{heater}) at the same value. Then, the thermal balance becomes

$$P_1 = Q_k + Q_h + \Delta P = (u_0 + \Delta u) \,.\, (i_0 + \Delta i) \tag{9}$$

with

$$\frac{u_0 + \Delta u}{i_0 + \Delta i} = \frac{u_0}{i_0} = R_{\text{heater}} \tag{10}$$

and

$$\Delta P = P_1 - P_0 \tag{11}$$

This measured value ΔP corresponds to the heat dissipated by the probe in contact with the hotplate. Then, the thermal resistance that characterizes the probe R_e is quantified with

$$R_e = \frac{T_p - T_a}{\Delta P} \tag{12}$$

where T_p and T_a are, respectively, the probe and ambient temperatures.

Subsequently, the contact resistance is accessible using Eq. (6):

$$R_c = \phi R_e \tag{13}$$

After contacting a second probe, the measured temperature T_p becomes T_p'. At the surface point of contact, temperature varies from T_m to T_m' and the initial definition of the constriction extracted from Eq. (2)

$$T_s - T_m = R_m \Delta P \tag{14}$$

is also written as

$$T_s - T_m' = 2R_m \Delta P \tag{15}$$

since the second probe is strictly identical to the first one. Subtracting Eqs. (14) and (15) gives

$$T_m - T_m' = R_m \Delta P \tag{16}$$

If we consider now the first contact temperature drop, Eq. (2) also gives

$$T_m - T_p = R_c \Delta P \tag{17}$$

After the second contact, the subsequent temperature drop is written as

$$T_m' - T_p' = R_c \Delta P \tag{18}$$

Subtracting these two last relations leads to

$$T_m - T_m' + T_p' - T_p = 0 \tag{19}$$

in which Eq. (16) introduces the thermal resistance R_m such that

$$R_m = \frac{T_p - T_p'}{\Delta P} \tag{20}$$

The global thermal response τ can be deduced from Eq. (3) and the actual surface temperature of the microhotplate T_s with

$$T_s = T_a + \frac{T_p - T_a}{\tau} \tag{21}$$

3 Results and Discussion

3.1 Calibration Results. Series of measurements have been performed to extract values of ϕ from Eq. (4) as a function of the contact temperature measured on the Pt wire surface (T_{p2}). Results are shown in Fig. 6. These measurements have been performed under standard atmospheric conditions (laboratory air) during which the contact force of the probe was kept in the range of 20–30 nN by maintaining a constant flexion of the wires whose respective Young's moduli are known. However, no changes have been noticed on the temperature when adjusting the value of the contact force.

The influence of a possible water film between the junction and the surface seems to be confirmed in the results of Fig. 6. Values decrease below the liquid-vapor transition temperature, in accordance with previous work that demonstrated that a water meniscus at the contact point could mainly contribute to reduce the thermal

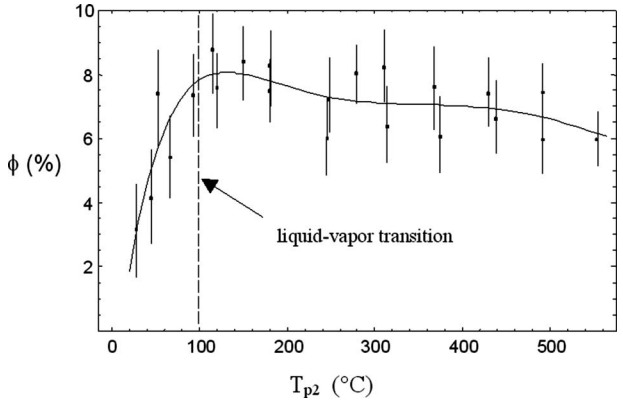

Fig. 6 Probe thermal contact parameter ϕ on platinum heated wire versus contact temperature.

contact resistance R_c [9,16–18]. Above this limit, this contribution vanishes and the thermal contact remains only related to air conduction, convection, radiation, and solid-solid contact.

In the second procedure, calibrations have been performed by means of two identical microhotplates except their membrane thickness: 0.75 μm and 1.0 μm thick, respectively. The interest lies in the possibility to point out the influence of the membrane thickness on the constriction resistance (R_m). Three different temperature levels have been tested. Electrical power levels have been adjusted so as to approximately reach the same surface temperature (T_p) at the center of the membrane, for both membrane thicknesses. These values correspond to usual operating temperature for this kind of devices at which the center part of the membrane is typically between 200°C, and 500°C. Results obtained have been synthesized in Table 1 in which uncertainties are mainly derived from the temperature (1.5°C typically) and the current variation for the calculation of ΔP (about 5%). Then, thermal resistances are subjected to a relative tolerance of 7%.

These results indicate that both membranes have different thermal behaviors. Due to a lower membrane conductance but identical external dissipation, the thinner membrane requires less power to reach the same temperature than the thinner one. Values obtained for ΔP are proportional to the surface temperature and then practically identical for both hotplates.

3.2 Thermal Constriction Resistance R_m. Since R_m expresses a cooling effect due to the limited thermal mass of the membrane, values obtained in Table 1 clearly indicate two distinct values independent of the temperature, around 3.36×10^4 K W^{-1} for the thin membrane and 2.45×10^4 K W^{-1} for the thick one.

However, in the theoretical treatments of the thermal constriction effect of a spherical contact, only the surface nature and the contact area are considered, so that the constriction resistance is expressed as [18]

$$R_m = \frac{1}{2\pi k b} \tag{22}$$

where b is the radius of the probe-to-surface contact area that depends on the contact force, and k is the thermal conductivity of the surface. One can remark that the thermal conduction is mainly in the plane of the membrane and that the thermal conductance of the membrane is proportional to its thickness. Thus, the membrane thickness difference could explain a large part of the increase of the resistance values, whereas the alteration of the contact radius cannot. Further measurements, using different probes, and a reliable knowledge of surface thermal conductivities could help to correct Eq. (22) that is derived from a semi-infinite model.

By assuming a membrane apparent thermal conductivity in the range of 4–8 W m^{-1} K^{-1}, a calculation of the contact radius b using this relation gives about 1 μm. This is quite large but remains possible.

3.3 Thermal Contact Resistance R_c. The dependence of the external and the contact thermal resistances (R_e and R_c) versus temperature is not established. Values of R_c are directly related to the first contact calibration (ϕ) and then to the probe thermal resistance R_e. The analysis of R_c is difficult in our case since it requires to control the vertical position and contact strength. We can, however, deduce from the temperature level that the liquid meniscus cannot contribute to enhance the heat transfer, and from the dimension of the hot surface that the gas conduction and convection provide the main contribution to the contact conductance. In such a condition, the spatial resolution of the probe may extend up to several junction diameters.

Our values are consistent with the results obtained by Shi and Majumdar [8,15] or Lefevre et al. [18]. The tip-to-surface contact of a curved resistive Wollaston wire (whose diameter is 5 μm) exhibits a value of R_c in the range of 0.25×10^5–10^5 K W^{-1} [18]. The case of the SThM probe developed by Shi [19] is quite different due to the tip dimension and the geometry of the cantilever. In this particular case, measurements and calculations have led to values ranging from 3×10^7 K W^{-1} to 4×10^7 K W^{-1} [16]. In the present results, we have obtained intermediate values between 1.3×10^5 K W^{-1} and 1.7×10^5 K W^{-1}, that are easily explainable if we simply compare the size of the probe tips in these three different cases.

3.4 Probe Thermal Resistance R_e. It is possible to estimate the external thermal resistance R_e by means of fin theory. For this, let us consider a thin "Wollaston" platinum or platinum-rhodium wire thermally connected to a hot wall (temperature T_p) that dissipates heat in a surrounding gas at temperature T_g. Its boundary corresponds to the wires silver cladding of diameter 75 μm (see Fig. 2) whose temperature is assumed to be the ambient temperature (T_a) due to the thermal conductivity of this metal (Dirichlet condition).

In such a configuration, the thermal resistance of a wire is expressed as

Table 1 Results of the calibration procedures for both 0.75 and 1.0 μm thick micro-hotplate membranes.

Membrane thickness	T_p-T_a (K)	ϕ (%)	P (mW)	ΔP (μW)	R_e (10^6 K W^{-1})	R_c (10^5 K W^{-1})	R_m (10^4 K W^{-1})	T_s-T_a (K)	τ
0.75 μm	227.3	7.2	28.5	98	2.32	1.66	3.47	246.6	0.920
	362.1	7	49.6	163	2.22	1.54	3.31	392.7	0.922
	483.3	6.4	71.5	190	2.54	1.62	3.31	520.4	0.929
1 μm	227.7	7.2	30	102	2.23	1.6	2.45	246.6	0.923
	354.4	7	50.9	165	2.15	1.49	2.42	383.1	0.925
	481.5	6.4	75.1	225	2.14	1.37	2.49	517.8	0.930

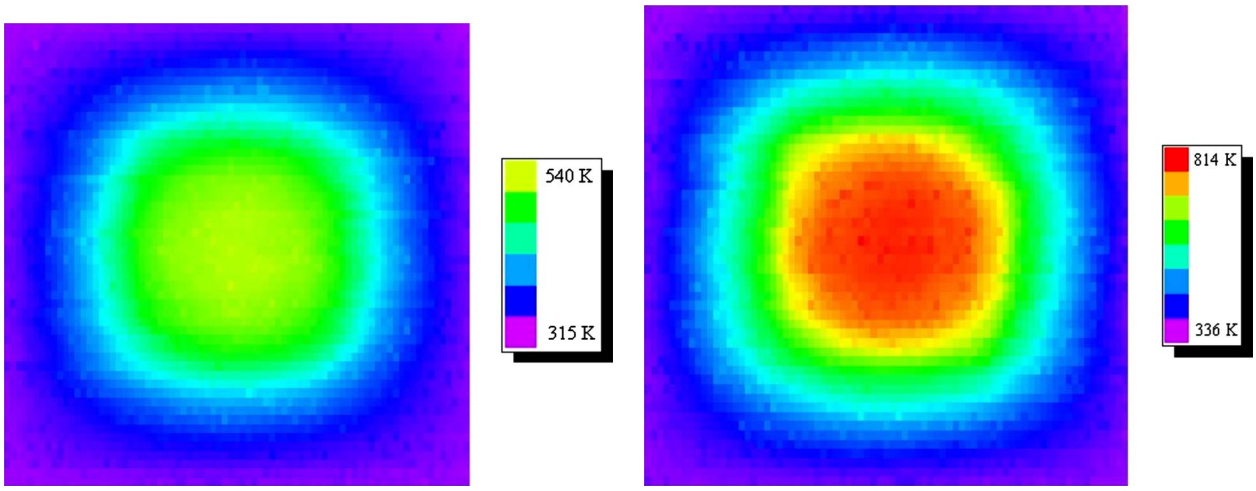

(*a*) (*b*)

Fig. 7 Temperature distribution of the thin (0.75 μm) microhotplate membrane (1 mm^2) at 30 mW (left) and 75 mW (right)

$$R_w = \frac{T_p - T_a}{kS} \frac{\sinh[mL]}{m(T_p - T_g)\cosh[mL] - m(T_a - T_g)} \quad \text{and } m = \sqrt{\frac{hp}{kS}} \tag{23}$$

where h is the external convection coefficient (W m^{-2} K^{-1}), k is the thermal conductivity of the wire (W m^{-1} K^{-1}), p is the perimeter (m) of the wire (diameter d), S its cross section (m^2), and L its length (m). Taking into account of both thermocouple wires leads to divide this expression by a factor 2, then $R_e = R_w/2$.

It is significant to notice that an upper limit of this thermal resistance can be determined when the convection coefficient h tends to zero. Then, Eq. (23) is reduced to

$$R_e^0 = \lim_{h \to 0} it(R_w) = \frac{L}{2kS} \tag{24}$$

This corresponds to the classical thermal resistance of a wall. To calculate these thermal resistances, we have fixed constant values to $d = 1.3 \times 10^{-6}$ m, $k = 75$ W m^{-1} K^{-1}, and $L = 0.8 \times 10^{-3}$ m. Equation (24) gives 4.02×10^6 K W^{-1}, which is almost twice the Table 1 results whose mean value is 2.27×10^6 K W^{-1}.

Then, Eq. (23) could help to estimate the actual values of the convection coefficient around the probe wires that is always difficult to evaluate. In the present case, wires are subjected to a thermal gradient between the measured surface temperature (T_p) and the ambient temperature (T_a). Besides, the thermal boundary layer above the membrane center has been measured to be 1 mm thick using the same probe. This distance represents typically the length of the probe wires. As an example, at a distance of 200 μm above the surface at 400°C, the air is still at 200°C. Therefore, we can simplify Eq. (23) by considering T_g as a mean value between its both limits, so that $T_g = (T_p + T_a)/2$ leads to

$$R_e = \frac{1}{2kS} \frac{\sinh[mL]}{m(1 + \cosh[mL])} \tag{25}$$

Since this expression is not temperature dependent, we can obtain an estimation of a mean value of the convection coefficient h, around $410 \times$ W m^{-2} K^{-1}. However, this value may significantly increase with the gas temperature. The thermal behavior of a probe also depends on the thermally implied area. For instance, by reducing the size of the heated object, the gas temperature can be assumed to be equal to ambient $T_g = T_a$. If the h coefficient is unchanged, the value of R_e decreases to 1.22×10^6 W K^{-1}. According to Eq. (6), this will also affect the value of the contact thermal resistance R_c. As a result, this point out that a direct comparison between different thermal probes remains difficult since it must be performed under similar thermal configurations.

3.5 Surface Temperature Scanning of Microhotplates. To illustrate the capabilities of the thermocouple probe and the thermal behavior of the microhotplate, we have scanned the thinner membrane surface, whereas the heater was supplied with two different powers, 30 mW and 75 mW. The duration of the scanning is rather important since the area is 1 mm^2. The number of pixels is about 4000 and only two points are captured per second. The distance between two points is of about 12 μm, which slightly exceeds the spatial resolution of the probe. The temperatures of each measurement point have been corrected with the help of the calibration factors presented in Table 1. The resulting images are presented in Fig. 7 for which the central part of the membrane exhibits a homogeneous temperature distribution for the temperature levels tested in this study, near 540 K and 814 K, respectively, at 30 mW and 75 mW.

4 Conclusion

We have calibrated a thermocouple cantilever in a real situation of contact measurement on a microhotplate. A complementary procedure performed with a platinum wire was necessary to extract thermal resistances and the actual surface temperature. It was also shown that an effect of conductance through a possible water film around the thermocouple junction was measurable at lower temperatures. This observation, however, requires further specific studies to be confirmed. Furthermore, we have focused on the interest of using the microhotplate to thermally calibrate any other kinds of thermal probes. The example reported here is a first step in our approach. Indeed, during this calibration, a double contact procedure was necessary due to a lack of measuring the actual surface temperature at the probe contact point. Two ways are possible to avoid this drawback. The first consists to embed a thin-film thermoelectric sensor on the membrane of the microhotplate, and the second requires improving or developing new optical techniques for the measurement of temperature.

Finally, an example of temperature measurements on a microhotplate has been presented, showing the potential of miniaturized wire thermocouples to perform thermal measurements on microscale object.

Acknowledgment

The authors thank the French-Swiss Associated European Laboratory (LEA) in Microtechnology for financial supports of this work.

References

[1] Sarro, P. M., Van Herwaarden, A. W., and Van der Vlist, W., 1994, "Silicon-Silicon Nitride Membrane Fabrication Process for Smart Thermal Sensors," Sens. Actuators, A, **42**, pp. 666–671.

[2] Simon, I., Barsan, N., Bauer, M., and Weimar, U., 2001, "Micromachined Metal Oxide Gas Sensors: Opportunities to Improve Sensor Performance," Sens. Actuators B, **73**, pp. 1–26.

[3] Rossi, C., Briand, D., Dumonteuil, M., Camps, T., Pham, P. Q., and De Rooij, N. F., 2006, "Matrix of 10×10 Addressed Solid Propellant Microthrusters: Review of the Technologies," Sens. Actuators, A, **126**, pp. 241–252.

[4] Konz, W., Hildenbrand, J., Bauersfeld, M., Hartwig, S., Lambrecht, A., Lehmann, V., and Wöllenstein, J., 2005, "Micromachined IR Source With Excellent Blackbody Like Behaviour," Proc. SPIE, **5836**, pp. 540–548.

[5] Altet, J., Dilhaire, S., Volz, S., Rampnoux, J. M., Rubio, A., Grauby, S., Patino Lopez, L. D., Claeys, W., and Saulnier, J. B., 2002, "Four Different Approaches for the Measurement of IC Surface Temperature: Application to Thermal Testing," Microelectron. J., **33**, pp. 689–696.

[6] Serrano, J. R., Phinney, L. M., and Kearney, S. P., 2006, "Micro-Raman Thermometry of Thermal Flexure Actuators," J. Micromech. Microeng., **16**, pp. 1128–1134.

[7] Jungen, A., Stampfer, C., and Hierold, C., 2006, "Thermography on a Suspended Microbridge Using Confocal Raman Scattering," Appl. Phys. Lett., **88**, 191901–3.

[8] Abel, M. R., and Graham, S., 2007, "Raman Thermometry of Polysilicon Microelectro-Mechanical Systems in the Presence of an Evolving Stress," ASME J. Heat Transfer, **129**, pp. 329–334.

[9] Majumdar, A., 1999, "Scanning Thermal Microscopy," Annu. Rev. Mater. Sci., **29**, pp. 505–585.

[10] Briand, D., Krauss, A., van der Schoot, B., Weimar, U., Barsan, N., Göpel, W., and de Rooij, N. F., 2000, "Design and Fabrication of High Temperature Micro-Hotplates for Drop-Coated Gas Sensors," Sens. Actuators B, **68**, pp. 223–233.

[11] Briand, D., Heimgartner, S., Gretillat, M. A., Van Der Schoot, B., and De Rooij, N. F., 2002, "Thermal Optimization of Micro-Hotplates That Have a Silicon Island," J. Micromech. Microeng., **12**, pp. 971–978.

[12] Voisin, P., Thiery, L., and Bröm, G., 1999, "Exploration of the Atmospheric Lower Layer Thermal Turbulences by Means of Microthermocouples," Eur. Phys. J.: Appl. Phys., **7**(2), pp. 177–187.

[13] Thiery, L., Porcar, R., and Prenel, J. P., 1994, "Performance Limits of Microthermocouples as Opto-Thermal Sensors," Opt. Commun., **107**, pp. 309–317.

[14] Thiery, L., Marini, N., Prenel, J. P., Spajer, M., Bainier, C., and Courjon, D., 2000, "Temperature Profile Measurements of Near-Field Optical Microscopy Fiber Tips by Means of Sub-Micronic Thermocouple," Int. J. Therm. Sci., **39**, pp. 519–525.

[15] Majumdar, A., Carrejo, J. P., and Lai, J., 1993,"Thermal Imaging Using the Atomic Force Microscope," Appl. Phys. Lett., **62**(20), pp. 2501–2503.

[16] Shi, L., and Majumdar, A., 2002, "Thermal Transport Mechanisms at Nanoscale Point Contacts," ASME J. Heat Transfer, **124**, pp. 329–332.

[17] Gomes, S., Trannoy, N., and Grossel, P., 1999, "DC Thermal Microscopy: Study of the Thermal Exchange Between a Probe and a Sample," Meas. Sci. Technol., **10**, pp. 805–811.

[18] Lefevre, S., Volz, S., and Chapuis, P. O., 2006, "Nanoscale Heat Transfer at Contact Between a Hot Tip and a Substrate," Int. J. Heat Mass Transfer, **49**, pp. 251–258.

[19] Shi, L., Kwon, O., Miner, A., and Majumdar, A., 2001, "Design and Batch Fabrication of Probes for Sub-100 nm Scanning Thermal Microscopy," J. Microelectromech. Syst., **10**, pp. 370–378.

An Analytical Model of External Streaming and Heat Transfer for a Levitated Flattened Liquid Drop

Sungho Lee
Research and Development Division,
Hyundai Motor Company,
Yongin 446-912, Korea

S. S. Sadhal[1]
e-mail: sadhal@usc.edu

Alexei Ye. Rednikov

Aerospace and Mechanical Engineering,
University of Southern California,
Los Angeles, CA 90089-1453

We present here the heat-transfer and fluid flow analysis of an acoustically levitated flattened disk-shaped liquid drop. The interest in this work arises from the noncontact measurement of the thermophysical properties of liquids. Such techniques have application to liquids in the undercooled state, i.e., the situation when a liquid stays in a fluidic state even when the temperature falls below the normal freezing point. This can happen when, for example, a liquid sample is held in a levitated state. Since such states are easily disrupted by measurement probes, noncontact methods are needed. We have employed a technique involving the use of acoustically levitated samples of the liquid. A thermal stimulus in the form of laser heating causes thermocapillary motion with flow characteristics depending on the thermophysical properties of the liquid. In a gravity field, buoyancy is disruptive to this thermocapillary flow, masking it with the dominant natural convection. As one approach to minimizing the effects of buoyancy, the drop was flattened (by intense acoustic pressure) in the form of a horizontal disk, about 0.5 mm thick. As a result, with very little gravitational potential, and with most of the buoyant flow suppressed, thermocapillary flow remained the dominant form of fluid motion within the drop. This flow field is visualizable and subsequent analysis for the inverse problem of the thermal property can be conducted. This calls for numerical calculations involving a heat-transfer model for the flattened drop. With the presence of an acoustic field, the heat-transfer analysis requires information about the corresponding Biot number. In the presence of a high-frequency acoustic field, the steady streaming originates in a thin shear-wave layer, known as the Stokes layer, at a surface of the drop. The streaming develops into the main fluid, and is referred to as the outer streaming. Since the Stokes layer is asymptotically thin in comparison to the length scale of the problem, the outer streaming can be formally described by an effective slip velocity at the boundary. The presence of the thin Stokes layer, and the slip condition at the interface, changes the character of the heat-transfer mechanism, which is inherently different from the traditional boundary layer. The current analysis consists of a detailed semianalytical calculation of the flow field and the heat-transfer characteristics of a levitated drop in the presence of an acoustic field. [DOI: 10.1115/1.2943305]

Keywords: acoustic streaming, slip velocity, Stokes layer, levitation, noncontact measurement

1 Introduction

The measurement of the thermophysical properties of undercooled liquids is a considerable scientific challenge because of the inherent instability of liquids in such states. We refer to the undercooled state as the situation when a liquid stays in a fluidic state even when the temperature falls below the normal freezing point. Such states are attainable when a liquid is held without a container such as with an acoustic levitator. From the standpoint of understanding fundamentals, there is presently interest in the measurement of the thermophysical properties of liquids in the undercooled state. Conventional measurement techniques involving containers are not applicable to undercooled liquids simply because bulk liquids seldom attain significant undercooling before solidification takes place at one of the numerous solid nucleating sites, including the container walls. Measurement devices involving probes on an undercooled liquid sample would quite likely disrupt the state by initiating solidification. It has been known that levitation of a small liquid sample is an effective way to attain a large degree of undercooling because the small sample volume reduces the number of the potential nucleation sites and the self-contained sample is free from the possibility of nucleation at the container walls [1,2]. The interest in levitation has come from various applications involving containerless processing, and acoustic methods have led to some several experimental and theoretical investigations with interesting results [3–11]. As for noncontact measurement of thermophysical properties, several investigators have conducted experiments in the past ten years (see, e.g., Refs. [12–21]).

Noncontact diagnostic techniques are required for property measurements of undercooled liquids because any contact with the liquids may initiate solidification. The thermophysical properties that have been measured on levitated undercooled liquid drops include the density [1], surface tension [2,12], viscosity [12], heat capacity [13], and electrical resistivity [14]. In an earlier paper [15], we presented a technique that allowed us to determine the thermal diffusivity coefficient of levitated liquids. We employed an acoustic levitator for levitation and an infrared (IR) camera as a diagnostic device. We used glycerin drops, whose thermal diffusivity coefficient is well known, as a model liquid to demonstrate the feasibility of the technique. By laser-heating a

[1]Corresponding author.

Contributed by the Heat Transfer Division of ASME for publication in the JOURNAL OF HEAT TRANSFER. Manuscript received June 21, 2007; final manuscript received November 5, 2007; published online July 10, 2008. Review conducted by Sung Jin Kim. Paper presented at the 2007 ASME-JSME Thermal Engineering Conference and Summer Heat Transfer Conference (HT2007), Vancouver, BC, Canada, July 8–12, 2007.

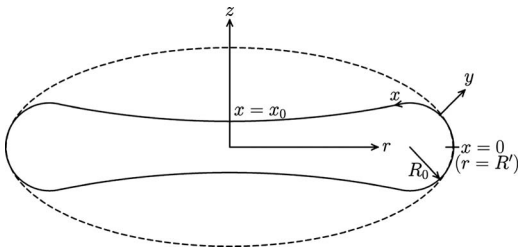

Fig. 1 Coordinate system for the Stokes layer on the dimpled drop. The broken line indicates an oblate spheroid with an equivalent edge curvature.

spot on the liquid drop of glycerin, a thermal stimulus was provided to instigate thermocapillary flow whose character depends on the thermophysical properties of the liquid. Of course, in a gravity field, there would also be buoyancy-driven flow that would dominate the overall thermally driven flow. In order to minimize the effects of buoyancy, the drop was flattened (by intense acoustic pressure) in the form of a horizontal disk, about 0.5 mm thick. As a result, there was very little gravitational potential in the system, and most of the buoyant flow was suppressed, leaving the thermocapillary flow to be the dominant form of fluid motion within the drop (see also Refs. [16,17]). With the measurement of the flow field and the temperature distribution, the thermal diffusivity was calculated. The numerical calculations involved in doing the inverse problem called for the development of a heat-transfer model for the flattened drop in the presence of an acoustic field, in particular, the gas-phase heat transfer to obtain a Biot number.

It is well known that if an object is in the presence of a high-frequency acoustic field, there exists a thin shear-wave layer (Stokes layer), which has vorticity due to interaction with the boundary of the object. It is in this Stokes layer that steady streaming originates, and the oscillatory vorticity is confined to this region in the high-frequency limit (see, e.g., Riley [22] and Rayleigh [23]). The streaming itself cannot be confined to the Stokes layer (the inner streaming), but develops into the main fluid, air (the outer streaming). In case of oscillatory fluid flow, the nonlinear terms in the momentum equation produce a higher order trigonometric forms (such as $\cos^2 \Omega t$), which we know have nonzero mean values. This means the phase difference in these velocities gives rise to a nonzero average over one cycle and allows a net momentum transfer. Mathematically, as the Stokes layer is asymptotically thin as compared with the length scale of the problem, the outer streaming formally appears to be caused by an effective slip velocity at the boundary. Rednikov and Sadhal [6] calculated the steady streaming from an oblate spheroid due to vibrations along its axis. The presence of the thin Stokes layer and the slip condition at the interface and change the character of the heat-transfer mechanism, which is inherently different from the traditional boundary layer. The heat-transfer aspects in connection with acoustic streaming in a two-dimensional rectangular enclosure have, in fact, been studied by Aktas et al.[24] and for the exterior of a sphere by Gopinath and Mills [25]. The current problem involves heat transfer from a flattened drop for which a schematic of the shape profile is shown in Fig. 1. The streaming flow calculation for this shape is a very difficult problem and, therefore, the oblate spheroid solution [6] is used as an approximation. The flow field is taken to be in the laminar range, and instabilities, such as those observed for magnetically levitated for molten metals [26], are not considered. This assumption is justifiable because we are restricting our work to highly viscous liquids such as glycerin, and, additionally, the flattening limits the liquid-phase internal flow considerably. The equivalent spheroid is taken to be one for which the radius of curvature R_0 at the outermost edge of the disk is the same as that for the spheroid's edge. This is a reasonable approximation because, as seen by Rednikov and Sadhal [6], the streaming flow is dominant around the edge. We use the slip-velocity calculation from that mode and apply it to the dimpled drop to obtain a suitable Biot number for the inverse problem [15]. The main work here is the setup of a streaming flow model for a flattened glycerin drop and obtaining an expression for the Biot number function that may be applied to such a system. This result has been effectively used in Ref. [15].

2 Slip-Velocity Calculation

The oblate spheroidal coordinates are used to solve the problem, and the modified coordinates are used, denoted as $\{\mu', \lambda', \phi'\}$. In terms of the cylindrical coordinates $\{z, r, \phi\}$, they are expressed [6] as follows:

$$z = c\lambda'\mu' \tag{1a}$$

$$r = c(1+\lambda'^2)^{1/2}(1-\mu'^2)^{1/2} \tag{1b}$$

where r is the distance from its center, z is the upward normal distance to r, and c is the focal radius.

Along the surface line, x is defined as the distance from maximum r (farthest edge of the dimpled drop) and y is the normal to its surface. The coordinate surface, $\lambda' = \text{constant}$, forms a confocal oblate spheroid. The effective slip velocity on the body surface is given [6] as

$$v^s = \frac{A^2}{4c^3}\left[3\frac{\mu'(1-\mu'^2)^{3/2}}{(\lambda_0^2+\mu'^2)^{5/2}} + 5\frac{\mu'(1-\mu'^2)^{1/2}}{(\lambda_0^2+\mu'^2)^{3/2}}\right]$$

where

$$A = \frac{c}{(1+\lambda_0^2)\text{arccot}(\lambda_0) - \lambda_0} \tag{2}$$

To determine the variables in the slip-velocity equation for a dimpled drop, the maximum radius of the drop is equated to the equatorial length of oblate spheroid, and the curvatures at the equatorial points are the same. At the equatorial point ($x=0$), r becomes maximum and $\mu'=0$. Let us set $r|_{x=0} = R'$ and $\lambda' = \lambda_0$ corresponding to the physical oblate spheroid surface. Then,

$$R' = c(1+\lambda_0)^{1/2} \tag{3a}$$

and

$$\frac{z^2}{c^2\lambda_0^2} + \frac{r^2}{c^2(1+\lambda_0^2)} = 1 \tag{3b}$$

where R' is the maximum radius of the dimpled drop. For the same curvatures,

$$-\left.\frac{d^2r}{dz^2}\right|_{z=0} = \frac{1}{R_0} \tag{4}$$

where R_0 is the radius of curvature of the dimpled drop at its circumference, and the left hand side is the curvature function of the oblate spheroid. Here, the dimpled drop surface is defined by two curves: one for the dimpled region and another for the rounded edge. The two curves meet tangentially with the same slope at $r=1$ (see Fig. 2). The dimpled region is described by the parabola

$$z = 0.01r^2 + 0.1 \quad \text{for } 0 \le r \le 1 \tag{5a}$$

while the rounded edge is given by the circular segment

$$z = \sqrt{0.11^2 - (1.002 - r)^2} \quad \text{for } 1 \le r \le 1.1122 \tag{5b}$$

with a radius of curvature

$$R_0 = 0.11 \tag{5c}$$

Then, from Eqs. (3*a*), (3*b*), and (4), we obtain

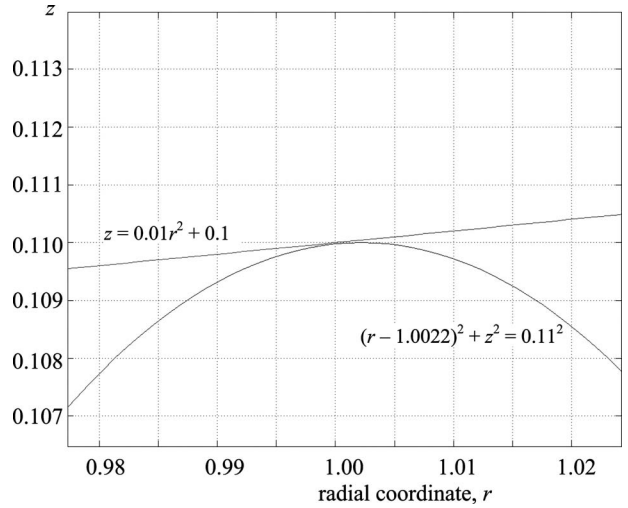

Fig. 2 Contact point of two curves on the dimpled drop surface. The nearly straight line is a parabola curve describing the dimpled region while the other curve is the circular edge.

$$\lambda_0 = \sqrt{\frac{R_0}{(R'^2 - R_0)}} \tag{6}$$

and

$$c = \sqrt{R'(R' - R_0)} \tag{7}$$

From Eqs. (1*a*) and (1*b*), μ' can be determined on every point on the surface using

$$\mu' = \frac{z}{c\lambda} \tag{8a}$$

where λ' on the surface is given by

$$\lambda' = \left\{ \frac{1}{2c^2}[-(c^2 - z^2 - r^2) + \sqrt{(c^2 - z^2 - r^2)^2 + 4c^2z^2}] \right\}^{1/2} \tag{8b}$$

The slip-velocity distribution on the surface is presented from the equator towards the pole in Fig. 3.

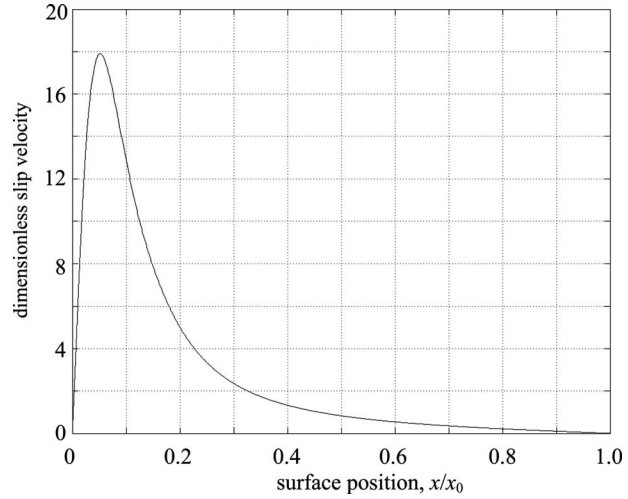

Fig. 3 Dimensionless slip-velocity distribution on the dimpled drop surface. The point x_0 corresponds to the end of the *x*-coordinate at the center of the top surface.

3 External Streaming

The Stokes layer plays the role of a slip velocity in driving the outer flow and is directed from the equatorial plane to the polar axes. For this outer streaming, the boundary layer equation based on the above x, y-coordinate system is

$$u\frac{\partial u}{\partial x} + v\frac{\partial v}{\partial y} = \frac{\partial^2 u}{\partial y^2}$$

where the following scaling is used:

$$y = \frac{y'}{\sqrt{\mathrm{Re}}} \quad \text{and} \quad v = \frac{v'}{\sqrt{\mathrm{Re}}} \tag{9}$$

The continuity equation is

$$\frac{1}{r(x)}\frac{\partial (ru)}{\partial x} + \frac{\partial v}{\partial y} = 0 \tag{10}$$

and the energy equation is

$$u\frac{\partial T}{\partial x} + v\frac{\partial T}{\partial y} = \frac{1}{\mathrm{Pr}_{\mathrm{air}}}\frac{\partial^2 T}{\partial y^2} \tag{11a}$$

Here, the temperature scaling

$$T = \frac{T^* - T_\infty}{T_{\max} - T_\infty} \tag{11b}$$

is used and also the scaled coordinates given in Eq. (9) apply. The boundary conditions are

$$u = u(x), \quad v = 0, \quad T = T(x) \quad \text{at } y = 0 \tag{12a}$$

$$u = 0, \quad \frac{\partial v}{\partial y} = 0, \quad T = 0 \quad \text{as } y \to \infty \tag{12b}$$

$$u = 0, \quad \frac{\partial v}{\partial y} = 0, \quad \frac{\partial T}{\partial x} = 0 \quad \text{at } x = 0 \tag{12c}$$

Here, $u(x)$ is used from the slip-velocity calculations for the oblate spheroid in Ref. [6], and boundary temperature is taken as $T(x) = 1$.

The coupled sets of nonlinear partial differential equations are solved using an implicit finite-difference scheme with marching from equator to pole ($x=0$ to $x=1$). The symmetry in the problem about the stagnation plane $x=0$ is utilized in carrying out the solution procedure over only the upper half of the drop.

(1) *Momentum equation*. Derivatives with respect to both x and y are approximated by central differences based on the halfway point in the x-direction, $(i+1/2, j)$.

$$\left.\frac{\partial u}{\partial x}\right|_{i+1/2,j} = \frac{u_{i+1,j} - u_{i,j}}{\Delta x} \tag{13a}$$

$$\left.\frac{\partial u}{\partial y}\right|_{i+1/2,j} = \frac{1}{2}\left(\frac{u_{i,j+1} - u_{i,j-1}}{2\Delta y} + \frac{u_{i+1,j+1} - u_{i+1,j-1}}{2\Delta y}\right) \tag{13b}$$

$$\left.\frac{\partial^2 u}{\partial y^2}\right|_{i+1/2,j} = \frac{1}{2}\left(\frac{u_{i,j+1} - 2u_{i,j} + u_{i,j-1}}{\Delta y^2} + \frac{u_{i+1,j+1} - 2u_{i+1,j} + u_{i+1,j-1}}{\Delta y^2}\right) \tag{13c}$$

For convergence of the nonlinear term, Eq. (13*a*) is written as

$$\left.\frac{\partial u}{\partial x}\right|_{i+1/2,j} = \frac{u_{i+1,j}^{n+1} - u_{i,j}^{n}}{\Delta x} \equiv \frac{2u_{i+1,j}^{n+1} - u_{i+1,j}^{n} - u_{i,j}^{n}}{\Delta x} \tag{13d}$$

Then, the momentum equation can be represented in the familiar tridiagonal form as

$$au_{i+1,j-1}^{n+1} + bu_{i+1,j}^{n+1} + cu_{i+1,j+1}^{n+1} = d \tag{14}$$

where

$$a = -\frac{v_{i+1/2,j}^{n}}{4\Delta y} - \frac{1}{2\Delta y^2} \tag{15a}$$

$$b = \frac{1}{\Delta x}(u_{i,j}^{n} + u_{i+1,j}^{n}) + \frac{1}{\Delta y^2} \tag{15b}$$

$$c = \frac{v_{i+1/2,j}^{n}}{4\Delta y} - \frac{1}{2\Delta y^2} \tag{15c}$$

and

$$d = \frac{1}{2\Delta x}(u_{i+1,j}^{n} + u_{i,j}^{n})(u_{i+1,j}^{n} + u_{i,j}^{n}) - \frac{v_{i+1/2,j}}{4\Delta y}(u_{i,j+1}^{n} - u_{i,j-1}^{n}) + \frac{u_{i,j+1}^{n} - 2u_{i,j}^{n} + u_{i,j-1}^{n}}{2\Delta y^2} \tag{15d}$$

(2) *Continuity equation*. By numerical integration of the continuity equation, $v_{i+1/2,j+1}^{n}$ is obtained as

$$v_{i+1/2,j+1}^{n} = v_{i+1/2,j}^{n} - \frac{1}{2}\frac{1}{r_i}\frac{\Delta y}{\Delta x}[r_{i+1}(u_{i+1,j+1}^{n} + u_{i+1,j}^{n}) - r_i(u_{i,j+1}^{n} + u_{i,j}^{n})] \tag{16}$$

(3) *Energy equation*. As the discretization procedure of momentum equation, the differentiated quantities in the energy equation are as follows:

$$\left.u\frac{\partial T}{\partial x}\right|_{i+1/2,j} = \frac{1}{2}(u_{i,j} + u_{i+1,j})\frac{T_{i+1,j} - T_{i,j}}{\Delta x} \tag{17a}$$

$$\left.v\frac{\partial T}{\partial y}\right|_{i+1/2,j} = v_{i+1/2,j}\frac{1}{2}\left(\frac{T_{i,j+1} - T_{i,j-1}}{2\Delta y} + \frac{T_{i+1,j+1} - T_{i+1,j-1}}{2\Delta y}\right) \tag{17b}$$

$$\left.\frac{1}{\mathrm{Pr}_{\mathrm{air}}}\frac{\partial^2 T}{\partial y^2}\right|_{i+1/2,j} = \frac{1}{\mathrm{Pr}_{\mathrm{air}}}\frac{1}{2}\left(\frac{T_{i,j+1} - 2T_{i,j} + T_{i,j-1}}{\Delta y^2} + \frac{T_{i+1,j+1} - 2T_{i+1,j} + T_{i+1,j-1}}{2\Delta y^2}\right) \tag{17c}$$

With the above terms, the energy equation can be represented in the familiar tridiagonal form as

$$aT_{i+1,j-1}^{n+1} + bT_{i+1,j}^{n+1} + cT_{i+1,j+1}^{n+1} = d \tag{18}$$

where

$$a = -\frac{v_{i+1/2,j}^{n}}{4\Delta y} - \frac{1}{2\Delta y^2}\frac{1}{\mathrm{Pr}_{\mathrm{air}}} \tag{19a}$$

$$b = \frac{1}{2\Delta x}(u_{i,j}^{n} + u_{i+1,j}^{n}) + \frac{1}{\Delta y^2}\frac{1}{\mathrm{Pr}_{\mathrm{air}}} \tag{19b}$$

$$c = \frac{v_{i+1/2,j}^{n}}{4\Delta y} - \frac{1}{2\Delta y^2}\frac{1}{\mathrm{Pr}_{\mathrm{air}}} \tag{19c}$$

$$d = \frac{1}{2\Delta x}(u_{i+1,j}^{n} + u_{i,j}^{n})T_{i,j}^{n} - \frac{v_{i+1/2,j}}{4\Delta y}(T_{i,j+1}^{n} - T_{i,j-1}^{n}) + \frac{T_{i,j+1}^{n} - 2T_{i,j}^{n} + T_{i,j-1}^{n}}{2\Delta y^2 \mathrm{Pr}_{\mathrm{air}}} \tag{19d}$$

4 Convective Heat Transfer From a Sphere

To confirm that the governing equations and the model predictions are correct, the known solution for streaming and convective transport from a sphere [25] is used as a reference. For symmetric conditions, the first quadrant ($0 \le \theta \le \pi/2$) is considered. The dimensionless slip velocity due to the Stokes layer around the sphere is known as [22,25]

$$v_\theta = \tfrac{45}{16}\sin\theta\cos\theta \tag{20}$$

At the beginning of the calculations, v and T are assumed to be symmetric at the equator ($i=1$). The process is repeated until it satisfies the boundary condition and that the sum of absolute differences between the current and previous iterates at all y locations falls down below a certain prescribed tolerance.

The computation results for this steady flow field are represented by the boundary layer velocity profiles in Fig. 4 showing the radial variation of u at different angular locations along the periphery of the sphere. The appropriate boundary conditions specified at the surface ($j=1$) and in the far field ($j=ny$) for the energy equation are

$$T_{i,1} = 1, \quad T_{i,ny} = 0 \quad \text{for } 1 \le i \le nx \tag{21}$$

A plot of the boundary layer temperature profiles for air ($\mathrm{Pr}_{\mathrm{air}} = 0.7$) is presented in Fig. 5, and the dimensionless heat flux is given in Fig. 6. These results show very good agreement with Gopinath and Mills [25] for both the velocity and the temperature profiles. These investigators [25] characterized the total heat transfer between the sphere and the fluid by the average Nusselt number, which can be expressed as

$$\frac{\mathrm{Nu}}{\sqrt{\mathrm{Re}_s}} = -2\int_0^1 \left(\frac{\partial T}{\partial y}\right)_{y=0} dx \tag{22}$$

The derivative in the integrand, representing the temperature gradient at the surface of the sphere, is approximated from the numerical results for the temperature field to second-order accuracy, i.e.,

$$\left.\frac{\partial T}{\partial y}\right|_{y=0} = (2T_{i,2} - 1.5T_{i,1} - 0.5T_{i,3})/\Delta y + \mathrm{O}(\Delta y^2) \tag{23}$$

With $\mathrm{Pr}_{\mathrm{air}} = 0.7$, their [25] average Nusselt number is 1.1022 while in the present study it is calculated as 1.1060.

5 Convective Heat Transfer From the Dimpled Drop

With uniform temperature on a dimpled drop surface, the velocity profile and the temperature profile are similar to the sphere case. The heat transfer from the surface to the air is calculated by Eq. (22). Figure 7 shows its temperature gradient at the surface on a logarithmic scale as the surface temperature is 1. For an arbitrary temperature profile on the surface, the corresponding heat flux could be calculated in the same way.

The convective heat transfer from each of the grid points to the external flow is considered as a boundary condition for the energy balance of dimpled glycerin drop. However, the iterative method by which the boundary condition is applied at every step takes an enormous amount of computational time. To save CPU time, Legendre polynomials are employed to replace the iteration. The surface temperature profile along the x-coordinate can be expressed in terms of Legendre polynomials as

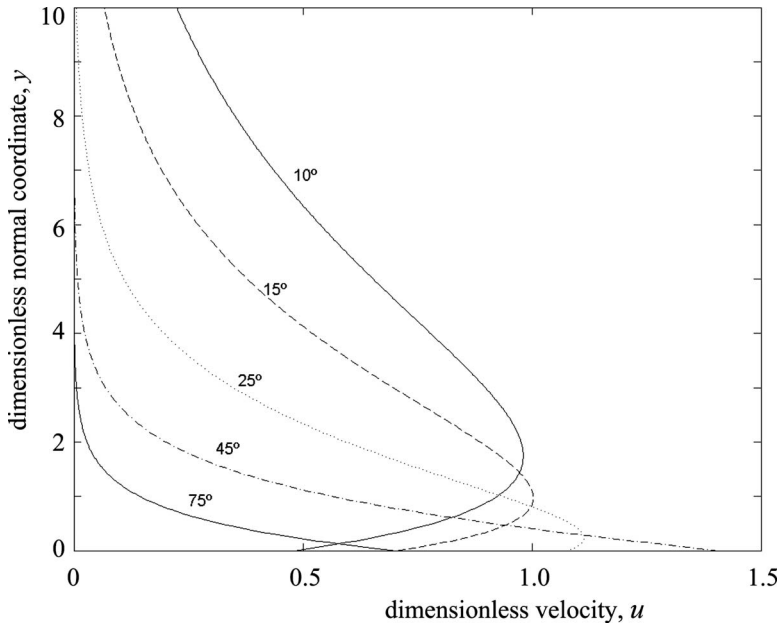

Fig. 4 Boundary layer velocity profiles for the outer streaming flow on a sphere. The corresponding angular locations, θ, in degrees are shown.

$$T_s(\mu') = \sum_{n=0}^{\infty} C_n P_n(\mu') \tag{24a}$$

where

$$C_n = (2n+1)\int_0^1 T_s(\mu') P_n(\mu') d\mu' \tag{24b}$$

and

$$0 \leqslant \mu' \leqslant 1 \tag{24c}$$

represents the oblate spheroidal coordinate starting with $x=0$. When each Legendre polynomial $P_n(\mu')$ is taken as a surface temperature and the iterative method is used, the corresponding heat flux $Q_n(\mu')$ is obtained. Then, the convective heat flux per unit area is

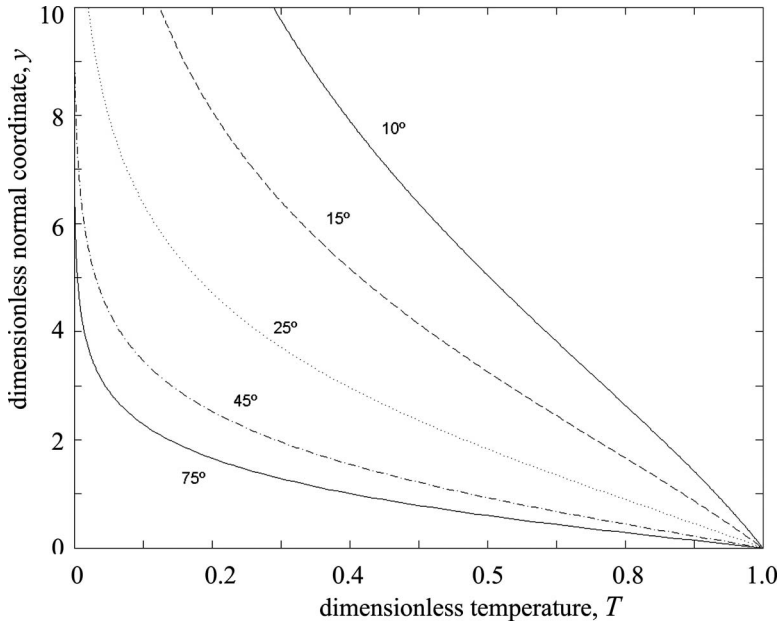

Fig. 5 Boundary layer temperature profiles ($Pr_{air}=0.7$) for the outer streaming flow on a sphere. The corresponding angular locations, θ, in degrees are shown.

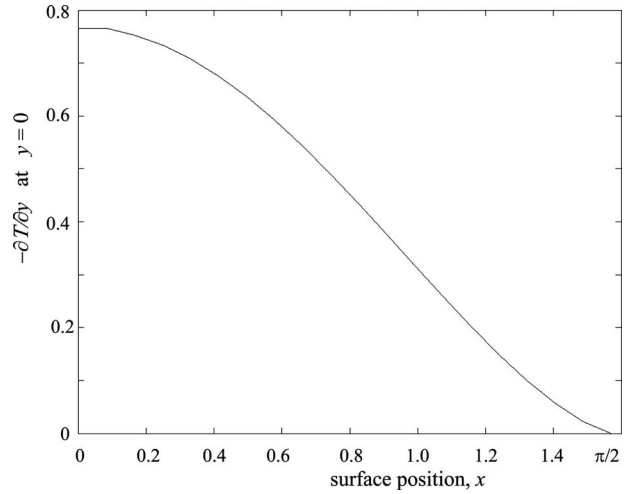

Fig. 6 Temperature gradient at the surface of a sphere with uniform temperature. The *x*-coordinate is along a meridian from the equator to the top pole.

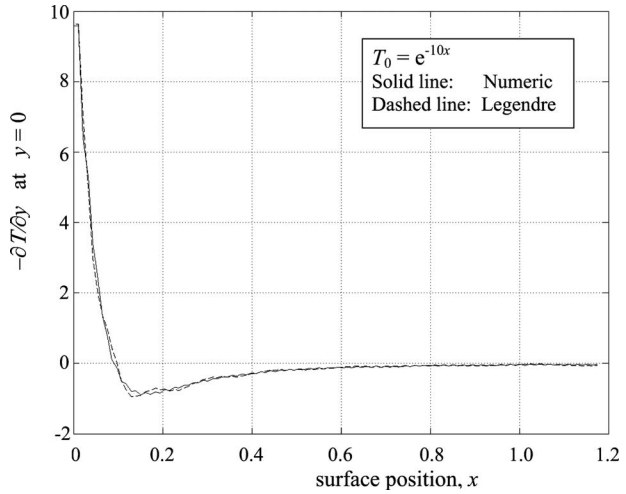

Fig. 8 Comparison of the results from an iterative procedure and a Legendre polynomial expansion

$$q_s(\mu') = \sum_{n=0}^{\infty} C_n Q_n(\mu') \tag{25}$$

For the symmetry condition at $x=0$, n can be only even numbers (0, 2, 4, 6, 8,…). As the number of points in the x-grid is 100 and n is taken up to 30, the coefficient $Q_n(\mu)$ becomes a 100×16 matrix. This matrix can be expressed in a much simpler form by using Legendre polynomials as follows:

$$Q_n(\mu') = \sum_{m=0}^{\infty} B_{mn} P_m(\mu') \tag{26a}$$

where

$$B_{mn} = (2m+1)\int_0^1 Q_n(\mu') P_m(\mu') d\mu' \tag{26b}$$

The set of coefficients B_{mn} is a 16×16 square matrix shown in Table 1. For any arbitrary surface temperature profile on a dimpled shape drop, the convective heat transfer can be calculated from this 16×16 matrix with Legendre polynomials. The iterative result and polynomial result are compared in Fig. 8. Its sample surface temperature profile is taken as

$$T_s = e^{-10x} \tag{27}$$

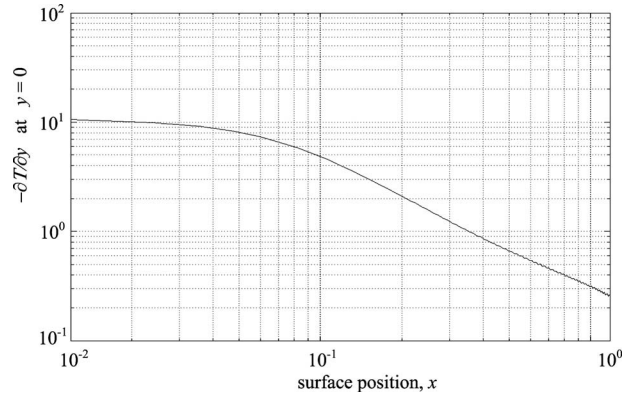

Fig. 7 Temperature gradient on a dimpled drop surface with a uniform temperature

6 Results: Convective Boundary Conditions for Internal Flow and Biot Number Calculation

The heat flux on the droplet surface is scaled in terms of a Biot number in the energy balance equation of internal flow. In terms of normal temperature gradient, the Biot number takes the form

Table 1 The coefficient matrix of Legendre polynomials

−3.21	5.60	−4.83	3.68	−2.55	1.70	−1.09	0.70	−0.45	0.29	−0.19	0.12	−0.08	0.05	−0.04	0.03
0.30	−3.29	3.64	−2.56	1.89	−1.22	0.85	−0.53	0.35	−0.19	0.12	−0.06	0.06	−0.05	0.05	−0.04
0.09	−0.13	−3.48	3.72	−2.40	1.77	−1.09	0.75	−0.41	0.24	−0.09	0.05	−0.01	0.02	−0.01	0.01
−0.17	0.52	−0.44	−3.93	4.17	−2.61	1.90	−1.13	0.77	−0.40	0.26	−0.11	0.09	−0.05	0.07	−0.04
0.14	−0.61	0.89	−0.59	−4.39	4.61	−2.79	1.97	−1.11	0.75	−0.37	0.24	−0.08	0.05	0.01	0.01
−0.12	0.41	−0.92	1.10	−0.63	−4.85	5.04	−2.99	2.11	−1.21	0.84	−0.44	0.29	−0.11	0.08	−0.02
0.09	−0.34	0.64	−1.20	1.34	−0.75	−5.19	5.39	−3.18	2.24	−1.25	0.85	−0.41	0.24	−0.05	0.03
−0.06	0.19	−0.49	0.84	−1.45	1.54	−0.79	−5.61	5.83	−3.44	2.41	−1.35	0.91	−0.45	0.29	−0.10
0.03	−0.15	0.32	−0.72	1.10	−1.72	1.72	−0.83	−5.97	6.18	−3.59	2.48	−1.35	0.91	−0.42	0.27
−0.01	0.05	−0.24	0.47	−0.91	1.27	−1.87	1.80	−0.80	−6.36	6.56	−3.82	2.65	−1.46	1.00	−0.49
−0.01	−0.03	0.13	−0.38	0.62	−1.06	1.42	−2.02	1.93	−0.83	−6.69	6.91	−4.02	2.79	−1.54	1.04
0.00	0.02	−0.12	0.24	−0.51	0.76	−1.24	1.60	−2.22	2.09	−0.87	−6.98	7.21	−4.18	2.86	−1.54
0.00	−0.01	0.03	−0.15	0.28	−0.58	0.85	−1.35	1.72	−2.33	2.13	−0.82	−7.35	7.59	−4.40	3.02
−0.01	0.00	−0.03	0.05	−0.20	0.36	−0.70	0.98	−1.49	1.84	−2.44	2.21	−0.81	−7.66	7.91	−4.58
0.00	−0.01	0.00	−0.04	0.09	−0.29	0.46	−0.81	1.07	−1.59	1.94	−2.55	2.30	−0.81	−7.96	8.22
−0.01	0.01	−0.03	0.03	−0.12	0.18	−0.39	0.56	−0.93	1.20	−1.73	2.09	−2.71	2.42	−0.84	−8.22

$$\mathrm{Bi} = \frac{\varepsilon\sqrt{\mathrm{Re}_{\mathrm{ext}}}}{T}\frac{K_{\mathrm{air}}}{K_{\mathrm{gly}}}\left.\frac{\partial T}{\partial y}\right|_{y=0} \tag{28}$$

where the values for $\partial T/\partial y|_{y=0}$ are given in Figs. 7 and 8 for constant temperature and an exponential behavior [Eq. (27)] at the surface. Here, the temperature difference T in the denominator is with reference to a zero far field (see Eq. (11*b*)). The parameter $\varepsilon = H/R'$ is an aspect ratio based on the minimum half-thickness H of the drop (at the center) and the drop radius (see Ref. [15]). Thus, for other types of surface conditions, an appropriate normal directional temperature gradient, $\partial T/\partial y|_{y=0}$, can be obtained from the external flow model, and the thermal conductivities are given by tables. In an iteration cycle, the previous temperatures are used for the Biot number calculation. For the Reynolds number corresponding to external flow, the velocity is calculated from the paper by Lee et al. [27]. They have two plots of the acoustic Bond number versus dimensionless equatorial radius for drops of size $\alpha = 0.74$ and $\alpha = 0.58$ with α defined as a scaled drop radius given by the product of a wavenumber and the equatorial radius of the drop. The equatorial radius R is scaled by the spherical drop radius R_{eq} to become

$$R^* = R/R_{\mathrm{eq}} = \frac{0.325 \times 1.1\ \mathrm{cm}}{0.186\ \mathrm{cm}} = 1.922 \tag{29}$$

When the wave number is 4.25 cm^{-1} for 23 kHz, and the equivalent spherical drop radius is 0.186 cm,

$$\alpha = 4.25\ \mathrm{cm}^{-1} \times 0.186\ \mathrm{cm} = 0.791 \tag{30}$$

With the above R^* and α, the acoustic Bond number B_a is 1.71. From the Bond number definition, the velocity amplitude of the acoustic wave is

$$U_a = \sqrt{\frac{B_a\sigma}{\rho_{\mathrm{air}}R_{\mathrm{eq}}}} = \sqrt{\frac{1.71 \times 0.0633\ \mathrm{kg/s}^2}{1.1614\ \mathrm{kg/m}^3 \times 0.00186\ \mathrm{m}}} = 7.0787\ \mathrm{m/s} \tag{31}$$

and the streaming velocity amplitude (at 23 kHz) is

$$A = \frac{U_a^2}{\omega d} = \frac{7.0787^2}{2\pi \times 23000 \times 0.0065} = 0.05334\ \mathrm{m/s} \tag{32}$$

Then, the Reynolds number of external streaming is

$$\mathrm{Re}_{\mathrm{ext}} = \frac{\mathrm{AR}}{\nu} = \frac{0.05334 \times 0.00325}{15.89 \times 10^{-6}} = 10.91 \tag{33}$$

This completely defines the parameters necessary to obtain a Biot number for the flattened drop under convective transport from acoustic streaming. Therefore, Eq. (28) can be used as a boundary condition for internal flow energy balance.

7 Conclusions

Acoustic streaming about a heated body causes convective heat transfer that has an inherently different character from the conventional heat transfer. This is so particular because the streaming velocity distribution is characterized by a very thin Stokes layer at the interface, effectively equivalent to a slip velocity. In the present analysis, the case of an acoustically flattened disk-shaped drop was considered, and the acoustic streaming together with the associated slip velocity was approximated by the available results for an oblate spheroid. The flow field was considered in the laminar range. With the application of the slip velocity on the surface of the drop, together with the application of a temperature distribution on the drop surface, the corresponding heat-transfer rates and, hence, the Biot number (spatially variable) were calculated for application to other more complicated spot-heating cases [15].

Acknowledgment

The authors are grateful to NASA for the support of this work (Grant No. NAG8-1663).

Nomenclature

A = streaming amplitude, slip-velocity coefficient
a,b,c = coefficients of coordinate transformation
a,b,c,d = coefficients of tridiagonal matrix form
Bi = Biot number
B_{mn} = Legendre polynomial coefficients for $Q_n(\mu')$
C_n = Legendre polynomial coefficients for surface temperature, $T_s(\mu')$.
B_a = acoustic Bond number
i, j = discretization parameters
K = thermal conductivity
Nu = Nusselt number
Pr = Prandtl number
$P_n(\mu')$ = Legendre polynomials
$q_s(\mu')$ = surface heat flux
$Q_n(\mu')$ = expansion function for heat flux
r = radial coordinate (cylindrical)
R' = Maximum radius of dimpled drop
R_0 = radius of curvature of the edge of the dimpled drop
R_{eq} = spherical equivalent radius
R^* = scaled radius R_0/R_{eq}
Re = Reynolds number
$\mathrm{Re}_{\mathrm{ext}}$ = external flow Reynolds number
Re_s = streaming Reynolds number
T = temperature
T_s = surface temperature
U_a = streaming velocity amplitude
u = velocity in the x-direction
v = velocity in the y-direction
v^s = slip velocity
x = coordinate along the surface (Fig. 1)
y = coordinate perpendicular to the surface
z = axial coordinate (cylindrical)
α = scaled drop size (radius × wavelength)
ε = drop aspect ratio
(λ', μ', ϕ') = oblate spheroidal coordinates

References

[1] Chung, S. K., Thiessen, D. B., and Rhim, W. K., 1990, "A Noncontact Measurement Technique for the Density and Thermal Expansion Coefficient of Solid and Liquid Materials," Rev. Sci. Instrum., **67**, pp. 3175–3181
[2] Trinh, E. H., Marston, P. L., and Robey, J. L., 1988, "Acoustic Measurement of the Surface Tension of Levitated Drops," J. Colloid Interface Sci., **124**, pp. 95–103
[3] Chung, S. K., and Trinh, E. H., 1998, "Containerless Protein Crystal Growth in Rotating Levitated Drops," J. Cryst. Growth, **194**, pp. 384–397.
[4] Rednikov, A. Y., Riley, N., and Sadhal, S. S., 2003, "The Behaviour of a Particle in Orthogonal Acoustic Fields," J. Fluid Mech., **486**, pp. 1–20.
[5] Rednikov, A. Y., and Riley, N., 2002, "A Simulation of Streaming Flows Associated With Acoustic Levitators," Phys. Fluids, **14**(4), pp. 1502–1510.
[6] Rednikov, A., and Sadhal, S. S., 2004, "Steady Streaming From an Oblate Spheroid Due to Vibrations Along Its Axis," J. Fluid Mech., **499**, pp. 345–380.
[7] Sadhal, S. S., Rednikov, A. Y., and Ohsaka, K., 2004, "Shape Relaxation of a Liquid Drop in a Microgravity Environment," Ann. N.Y. Acad. Sci., **1027**, pp. 447–463.
[8] Rednikov, A. Y., Zhao, H., Sadhal, S. S., and Trinh, E. H., 2006, "Steady Streaming Around a Spherical Drop Displaced From the Velocity Antinode in an Acoustic Levitation Field," Q. J. Mech. Appl. Math., **59**, pp. 377–397.
[9] Hyers, R. W., Matson, D. M., Kelton, K. F., and Rogers, J. R., 2004, "Convection in Containerless Processing," Ann. N.Y. Acad. Sci., **1027**, pp. 474–494.
[10] Li, B. Q., and Song, S. P., 1998, "Thermal and Fluid Flow Aspects of Electromagnetic and Electrostatic Levitation—A Comparative Modeling Study," Microgravity Sci. Technol., **11**, pp. 134–143.
[11] Matson, D. M., Fair, D. J., Hyers, R. W., and Rogers, J. R., 2004, "Contrasting Electrostatic and Electromagnetic Levitation Experimental Results for Transformation Kinetics of Steel Alloys," Ann. N.Y. Acad. Sci., **1027**, pp. 435–446.
[12] Rhim, W. K., Ohsaka, K., Paradis, P.-F., and Spjut, R. E., 1999, "Noncontact Technique for Measuring Surface Tension and Viscosity of Molten Materials Using High Temperature Electrostatic Levitation," Rev. Sci. Instrum., **70**, pp. 2796–2801.
[13] Rulison, A. A., and Rhim, W. K., 1994, "A Noncontact Measurement Technique for the Specific Heat and Total Hemispherical Emissivity of Under-

cooled Refractory Materials," Rev. Sci. Instrum., **65**, pp. 695–700.
[14] Rhim, W. K., and Ishikawa, T, 1998, "Noncontact Electrical Resistivity Measurement Technique for Molten Metals," Rev. Sci. Instrum., **69**, pp. 3628–3633.
[15] Lee, S. H., Ohsaka, K., Rednikov, A. Y., and Sadhal, S. S., 2006, "Noncontact Thermophysical Property Measurement by Levitation of a Thin Liquid Disk," Ann. N.Y. Acad. Sci., **1077**, pp. 75–95.
[16] Ohsaka, K., Sadhal, S. S., and Rednikov, A., 2002, "Thermocapillary Flow Induced by Laser-Heating of an Acoustically Levitated Flattened Glycerin Drop," ASME J. Heat Transfer, **124**, p. 599.
[17] Ohsaka, K., Rednikov, A., and Sadhal, S. S., 2003, "Noncontact Technique for Determining the Thermal Diffusivity Coefficient on Acoustically Levitated Liquid Drops," Rev. Sci. Instrum., **74**, pp. 1107–1112.
[18] Li, B. Q., 2006, "Effect of Convection on the Measurement of Thermophysical Properties Using Levitated Droplets," Ann. N.Y. Acad. Sci., **1077**, pp. 1–32.
[19] Shen, F., Khodadadi, J. M., Woods, M. C., Weber, J. K. R., and Li, B. Q., 1997, "Containerless Thermal Diffusivity Determination of High-Temperature Levitated Spherical Specimen by Extended Flash Methods: Theory and Experimental Validation," ASME J. Heat Transfer, **119**, pp. 210–219.
[20] Rhim, W. K., Chung, S. K., Rulison, A. J., and Spjut, R. E., 1997, "Measurements of Thermophysical Properties of Molten Silicon by a High-Temperature Electrostatic Levitator," Int. J. Thermophys., **18**, pp. 459–469.
[21] Ohsaka, K., Rednikov, A., Sadhal, S. S., and Trinh, E. H., 2002, "Noncontact Technique for Determining Viscosity From the Shape Relaxation of Ultrasonically Levitated and Initially Elongated Drops," Rev. Sci. Instrum., **73**, pp. 2091–2096.
[22] Riley, N., 1966, "On a Sphere Oscillating in a Viscous Fluid," Q. J. Mech. Appl. Math., **19**, pp. 462–472.
[23] Rayleigh, L., 1883, "On the Circulation of air Observed in Kundt's Tubes and Some Allied Acoustical Problems," Philos. Trans. R. Soc. London, **175**, pp. 1–21.
[24] Aktas, M. K., Farouk, B., and Lin, Y., 2005, "Heat Transfer Enhancement by Acoustic Streaming in an Enclosure," ASME J. Heat Transfer, **127**, pp. 1313–1327.
[25] Gopinath, A., and Mills, A. F., 1993, "Convective Heat Transfer From a Sphere Due to Acoustic Streaming," ASME J. Heat Transfer, **115**, pp. 332–341.
[26] Bullard, C., Hyers, R. W., and Abedian, B., 2005, "Spin-Up Instability of a Levitated Molten Drop in Magnetohydrodynamic-Flow Transition to Turbulence," IEEE Trans. Magn., **41**(7), pp. 2230–2236.
[27] Lee, C. P., Anilkumar, A. V., and Wang, T. G., 1994, "Static Shape of an Acoustically Levitated Drop With Wave-Drop Interaction," Phys. Fluids, **6**(11), pp. 3554–3566.

Power Law Velocity and Temperature Profiles in a Fully Developed Turbulent Channel Flow

Abu Seena
Department of Mechanical Engineering,
Korea Advanced Institute of Science and Technology,
Daejeon 305-701, Korea
e-mail: abuseena@kaist.ac.kr

Noor Afzal
Faculty of Engineering,
Aligarh Muslim University,
Aligarh 202002, India
e-mail: noor.afzal@yahoo.com

The power law temperature distribution in a fully developed turbulent channel flow for large Peclet numbers has been proposed in the present work. The analysis of the power law velocity profile in a fully developed mean turbulent channel flow would be used for carrying out the analysis of the power law temperature profile. The Reynolds mean thermal energy equation in a fully developed mean turbulent channel flow has been analyzed. The mean turbulent thermal flow is divided in the inner and outer thermal layers that have been matched by Izakson–Millikan–Kolmogorov hypothesis to get the power law temperature profiles and the power law heat transfer law in the overlap region, in addition to traditional log laws for temperature profiles and heat transfer. It has been shown that the envelope of the heat transfer power law gives the heat transfer log law. Further, it is shown that the temperature power law index and prefactor are functions of the friction Peclet number, as well as function of an alternate variable, the nondimensional friction temperature. It is shown that for large Peclet numbers the power law temperature profile is equivalent to the log law temperature profile. The direct numerical simulation velocity profile data of fully developed turbulent flow provide good support for the power law temperature profile theory. [DOI: 10.1115/1.2944239]

1 Introduction

The convective heat transfer from surfaces beneath a flowing turbulent fluid is especially important in a large number of technological applications as the rate of this heat transfer is significantly augmented relative to the laminar flow condition [1,2]. Despite the importance of the Reynolds shear stress and Reynolds heat flux relative to momentum and energy transport, the proper scaling remains an open question [3–7]. Challenges limiting progress relate to the scarcity of high quality data sets that also span a useful Reynolds number range. Interestingly, neither inner nor outer normalizations are successful in the vicinity of the peak in the Reynolds stress and Reynolds heat flux profiles. The present effort explicitly addresses this issue.

Nikuradse [8] proposed the power law velocity distribution $u_+ = Cy_1^\alpha$ from his data in a fully developed turbulent pipe flow, and found that the power law index α and power law prefactor C are Reynolds number dependent (Ref. [6]). The power law constants α and C as functions of Reynolds number were estimated by Nikuradse [8] from his own data. Narasimha [9] has pointed out that the recent analysis of relation between power law and log law velocity profiles of Barenblatt and co-workers, reviving an issue raised already in Ref. [12], call for accurate experimental data at a high Reynolds number. Further, the pipe flow velocity profile exhibits a very weak defect layer, so a more severe test for power law velocity profile would be a high Reynolds number turbulent boundary layer (where the overlap would not constitute what Barenblatt and co-workers called "main body of flow"). The correlations for the power law constants proposed by various workers and shown in Refs. [10,11,13–17]. It has been shown that the envelope of the friction factor gives the friction factor log law. The matching of the velocity profile u by the Izakson–Millikan–Kolmogorov hypothesis gives an open functional equation and its solution, as shown by Afzal et al. [16,17], lead to power law velocity profiles in addition to log laws. Further, it has also been described that the power law index α and prefactor C are functions of the friction Reynolds number, as well as function of an alternate variable, the nondimensional friction velocity ϵ. An interesting review of the research work on the power law velocity profile has been reported by Buschmann and Gad-el-Hal [18].

The present work deals with the power law temperature distribution in a fully developed turbulent channel flow for large Peclet numbers. The velocity profile analysis in a fully developed mean turbulent channel flow would be used for carrying out the analysis of the temperature profile. The Reynolds mean thermal energy equations in a fully developed mean turbulent channel flow have been analyzed. The mean turbulent thermal flow is divided in the inner and outer thermal layers that have been matched by the Izakson–Millikan–Kolmogorov hypothesis to get the power law temperature profiles and the power law heat transfer law in the overlap region, in addition to traditional log laws. It has been shown that the envelope of the heat transfer power law gives the heat transfer log law. Further, it has also been described that the power law temperature index α_t and prefactor C_t are functions of the friction Peclet number, as well as function of an alternate variable, the nondimensional friction temperature ϵ_t. It is shown that for large Peclet numbers, the power law temperature profile is equivalent to the log law temperature profile. The velocity profile in a fully developed turbulent flow in a channel from direct numerical simulation (DNS) by Iwamoto et al. [19] is for $R_\tau = 109.4$, 150.5, 297.9, 395.8, and 642.5. Abe et al. [20], Abe and Kawamura [21], and Abe et al. [22] for $R_\tau = 180$, 395, 640, and 1020, Hoyas and Jimenez [23] for $R_\tau = 2000$, and experimental data of Zanoun [24] provided good support for the power law velocity profile theory. The DNS temperature profile data of a fully developed turbulent flow in a channel given by Abe and Kawamura [20] and Abe et al. [21] for $R_\tau = 180$, 395, and 640 provide good support for the power law temperature profile theory.

Contributed by the Heat Transfer Division of ASME for publication in the JOURNAL OF HEAT TRANSFER. Manuscript received April 14, 2007; final manuscript received November 7, 2007; published online July 3, 2008. Review conducted by Yogesh Jaluria.

2 Velocity Profile in Turbulent Channel Flow

The turbulent channel flow momentum equation in standard notations [1,2] is

$$\nu\frac{\partial^2 u}{\partial y^2}+\frac{1}{\rho}\frac{\partial \tau}{\partial y}=\frac{1}{\rho}\frac{\partial p}{\partial x} \tag{1}$$

Here, $u(y)$ is the axial velocity, y is the normal coordinate, $\tau=-\rho\langle u'v'\rangle$ is the appropriate Reynolds shear stress, $u_\tau=\sqrt{\tau_w/\rho}$ is the friction velocity, τ_w is the skin friction, ρ is the fluid density, and ν is the molecular kinematic viscosity of fluid. The boundary conditions on the wall and axis of symmetry are $y=0$, $u=\tau=0$ and $y=\delta$, and $u-U_c=\tau=0$ where δ is the half channel depth or pipe radius as appropriate and U_c is the center line velocity. The overall description of turbulent shear flow has been in terms of two separate length scales (inner wall layer and outer wake layer) at large Reynolds numbers. The inner variables and inner layer Reynolds equation become

$$u=u_\tau u_+(y_+,R_\tau),\quad \tau=\rho u_\tau^2\tau_+(y_+,R_\tau),\quad y_+=\frac{yu_\tau}{\nu} \tag{2}$$

$$\frac{du_+}{dy_+}+\tau=1-\mathrm{R}_\tau^{-1}y_+ \tag{3}$$

The outer variables and outer layer Reynolds equation become

$$u=U_c-u_\tau F(Y,R_\tau),\quad \tau=\rho u_\tau^2 G(Y,R_\tau),\quad Y=\frac{y}{\delta} \tag{4}$$

$$G=1-Y+R_\tau^{-1}\frac{dF}{dY} \tag{5}$$

Here, $R_\tau=u_\tau\delta/\nu$ is the friction Reynolds number and $\mathrm{Re}=U_b d/\nu$ is the Reynolds number based on channel depth 2δ and average velocity U_b.

By assuming that for sufficiently large Reynolds numbers, there exist an overlap domain where the inner and outer layer solutions must match with the Izakson–Millikan–Kolmogorov hypothesis as

$$u_+(y_+)=U_{c+}(R_\tau)-F(Y),\quad U_{c+}\equiv\frac{U_c}{u_\tau} \tag{6}$$

The matching relation (6) for the first and second derivatives become

$$y_+\frac{\partial u_+}{\partial y_+}=R_\tau\frac{\partial U_{c+}}{\partial R_\tau} \tag{7a}$$

$$y_+^2\frac{\partial^2 u_+}{\partial y_+^2}=R_\tau^2\frac{\partial^2 U_{c+}}{\partial R_\tau^2} \tag{7b}$$

The mean turbulent flow is divided in the inner and outer layers that have been matched by the Izakson–Millikan–Kolmogorov hypothesis [25–28] to get the traditional log laws [26,27] as well as the power law velocity profile [16,17].

2.1 Power Law Velocity Profile From Matching. The alternate functional equation described here gives the power law velocity profile. The functional Eq. (7*b*) may be divided by the functional relation (7*a*), which gives an alternate functional equation

$$y_+\frac{\partial^2 u_+/\partial y_+^2}{\partial u_+/\partial y_+}=R_\tau\frac{\partial^2 U_{c+}/\partial R_\tau^2}{\partial U_{c+}/\partial R_\tau} \tag{8}$$

and its functional solution may be expressed, in the variable separable form, as

$$y_+\frac{\partial^2 u_+/\partial y_+^2}{\partial u_+/\partial y_+}=\alpha-1 \tag{9a}$$

$$R_\tau\frac{\partial^2 U_{c+}/\partial R_\tau^2}{\partial U_{c+}/\partial R_\tau}=\alpha-1 \tag{9b}$$

where constant α is independent of y_+ and R_τ. The integral of these equations give

$$\frac{\partial u_+}{\partial y_+}=Jy_+^{\alpha-1} \tag{10a}$$

$$\frac{\partial U_{c+}}{\partial R_\tau}=JR_\tau^{\alpha-1} \tag{10b}$$

where J is a constant of integration. The two cases $\alpha=0$ and $\alpha\neq 0$ would arise during further integration leading to the log law and the power law. In the second case $\alpha\neq 0$, the integration on each side of Eqs. (10*a*) and (10*b*) gives the power law relations. The solution is

$$u_+(y_+)=Cy_+^\alpha \tag{11a}$$

$$u_+=C_1Y^\alpha \tag{11b}$$

$$\frac{U_c}{u_\tau}=CR_\tau^\alpha+E \tag{11c}$$

Here, $C=J/\alpha$, $C_1=CR_\tau^\alpha$, and E is a constant of integration. The uniformly valid solution for the velocity profile and skin friction power law become

$$\frac{u}{u_\tau}=Cy_+^\alpha+E\Omega(Y) \tag{12a}$$

$$\frac{u}{u_\tau}=C_1Y^\alpha+E\Omega(Y) \tag{12b}$$

$$\frac{U_c-u}{u_\tau}=C_1(-Y^\alpha+1)+E[1-\Omega(Y)] \tag{12c}$$

Here, $\Omega(Y)$ is the power law wake function subjected to the boundary conditions $\Omega(0)=0$ and $\Omega(1)=1$. The average velocity u_b from the integration of the power law velocity profile (12*a*) over the cross section of the channel becomes

$$\frac{U_b}{u_\tau}=\frac{C}{1+\alpha}R_\tau^\alpha+E_b \tag{13}$$

The friction factor λ becomes

$$\lambda=8m\mathrm{Re}^{-n}\left[1+E_b m^{(1+\alpha)/2}\mathrm{Re}^{-\alpha}\left(\frac{8}{\lambda}\right)^{\alpha/2}\right]^{-2/(1+\alpha)} \tag{14}$$

where $\mathrm{Re}=2\delta U_b/\nu$, $m=(2^\alpha(1+\alpha)/C)^{2/(1+\alpha)}$, and $n=2\alpha/(1+\alpha)$. The Reynolds shear stress is

$$\frac{\tau}{\tau_w}=1-C\alpha y_+^{\alpha-1}-\frac{y_+}{R_\tau}-\frac{E}{R_\tau}\frac{d\Omega}{dY},\qquad \frac{\tau}{\tau_w}=1-Y-\frac{1}{R_\tau}C_1\alpha Y^{\alpha-1}-\frac{E}{R_\tau}\frac{d\Omega}{dY} \tag{15}$$

The location of the maxima in Reynolds stress y_{+m} and its maximum value τ_{+m} become

$$y_{+m}=(C\alpha(1-\alpha)R_\tau)^{1/(2-\alpha)} \tag{16a}$$

$$\tau_{+m}=1-\frac{2-\alpha}{1-\alpha}(C\alpha(1-\alpha))^{1/(2-\alpha)}R_\tau^{-(1-\alpha)/(2-\alpha)} \tag{16b}$$

The envelope of the skin friction power law with $C=a\alpha^{-1}+b$ provides $(a+b\alpha)\ \alpha\ln R_\tau=a$ and the skin friction log law

$$\frac{U_c}{u_\tau}=\frac{1}{k}\ln R_\tau+B+E \tag{17}$$

$$k^{-1} = \frac{a}{\Gamma}\exp(\Gamma) \tag{18a}$$

$$B = b\exp(\Gamma) \tag{18b}$$

where k is the Karman constant and B is the intercept of the log law, which as shown later, depends on the Reynolds number through function Γ. The power law index α and prefactor C yield

$$\alpha = \frac{\Gamma}{\ln R_\tau} \tag{19a}$$

$$C = \left(\frac{\Gamma}{k\alpha} + B\right)\exp(-\Gamma) \tag{19b}$$

$$C = \left(\frac{1}{k}\ln R_\tau + B\right)\exp(-\Gamma) \tag{19c}$$

The power law constants α and C may also be expressed in terms of the friction velocity ϵ, by eliminating the $\ln R_\tau$ term from Eq. (17) as

$$\alpha = k^{-1}\frac{\epsilon}{1 - E\epsilon} \tag{20a}$$

$$C = \left(\frac{1}{\epsilon} - E\right)\exp(-\Gamma) \tag{20b}$$

$$\epsilon = \frac{u_\tau}{U_c} \tag{20c}$$

The constant Γ, which is based on expressions (19*a*)–(19*c*) and (20*a*)–(20*c*) yield,

$$\Gamma = \left(1 + \frac{kB}{\ln R_\tau}\right)^{-1} \tag{21a}$$

$$\Gamma = \frac{1 - (B + E)\epsilon}{1 - E\epsilon} \tag{21b}$$

2.2 Log Law Velocity Profiles From Matching. The uniformly valid solution for the velocity profile becomes

$$\frac{u}{u_\tau} = \frac{1}{k}\ln y_+ + B + DW(Y) \tag{22a}$$

$$\frac{U_c - u}{u_\tau} = -\frac{1}{k}\ln Y + D[1 - W(Y)] \tag{22b}$$

Here, $W(Y)$ is the Coles [29] wake function subjected to the boundary conditions $W(0)=0$ and $W(1)=1$. The average velocity u_b from integration of velocity profile (22*a*) over the cross section of the channel gives friction factor as

$$\lambda = 8\left(\frac{u_b}{u_\tau}\right)^2 = 8\left[\frac{1}{k}\ln\left(\mathrm{Re}\sqrt{\frac{\lambda}{8}}\right) + B + D - \frac{1}{k}\right]^{-2} \tag{23}$$

The Reynolds shear stress relations are

$$\frac{\tau}{\tau_w} = 1 - \frac{1}{ky_+} - \frac{y_+}{R_\tau} - \frac{D}{R_\tau}\frac{dW}{dY}, \quad \frac{\tau}{\tau_w} = 1 - Y - \frac{1}{R_\tau kY} - \frac{D}{R_\tau}\frac{dW}{dY} \tag{24}$$

The location of the maxima in Reynolds stress y_{+m} and its maximum value τ_{+m} become

$$y_{+m} = \sqrt{\frac{R_\tau}{k}} \tag{25a}$$

$$\tau_{+m} = 1 - \frac{2}{\sqrt{kR_\tau}} \tag{25b}$$

3 Temperature Profiles in a Turbulent Channel Flow

The thermal Reynolds equation of temperature profile in a fully developed channel is [1,2]

$$u\frac{\partial T}{\partial x} = \frac{\nu}{\sigma}\frac{\partial^2 T}{\partial y^2} + \frac{\partial \tau_t}{\rho C_p \partial y} \tag{26}$$

Here, $T(y)$ is the temperature, y is the normal coordinate, $\tau_t = -\rho C_p\langle v't'\rangle$ is the appropriate thermal Reynolds stress, σ is molecular Prandtl number, $T_\tau = -q_w/(\rho C_p u_\tau)$ is the friction temperature, and q_w is the wall heat flux. The boundary conditions on the wall and axis of symmetry are $y=0$, $T - T_w = \tau_t = 0$ and $y=\delta$, $T - T_c = \tau_t = 0$, where T_w is the wall temperature and T_c is the centerline temperature. The wall heat transfer rate $q_w/(\rho C_p) = -\nu\sigma^{-1}(dT/dy)_w$ and Stanton number $\mathrm{St} = u_\tau T_\tau/|U_c(T_c - T_w)|$. An integral of thermal Eq. (26) for y between 0 and δ yields $\partial T/\partial x = q_w/(\rho c_p \delta U_b) = -u_\tau T_\tau/(\delta U_b)$. The thermal Reynolds equation of temperature profile (26) in a fully developed channel becomes

$$\frac{\nu}{\sigma}\frac{dT}{dy} + \frac{\tau_t}{\rho C_p} = u_\tau T_\tau\left(1 - \frac{1}{\delta}\int_0^y \frac{u}{U_b}dy\right) \tag{27}$$

Two layer theory of turbulent heat transfer. The overall description of turbulent shear flow has been in terms of two separate layers (inner wall variable $\eta = \sigma y_+$ and outer wall variable $Y = y/\delta$) at large Reynolds numbers as described below.

Inner wall layer:

$$T - T_w = T_\tau t_+(\eta, P_\tau), \quad \tau_t = \rho C_p u_\tau T_\tau \tau_t(\eta, P_\tau), \quad \eta = \sigma y_+ \tag{28}$$

$$\frac{dt_+}{d\eta} + \tau_t = 1 - P_\tau^{-1}\frac{u_\tau}{U_b}\int_0^\eta u_+ d\eta \tag{29}$$

Outer defect layer:

$$T - T_c = T_\tau F_t(Y, P_\tau), \quad \tau_t = \rho C_p u_\tau T_\tau G_t(Y, P_\tau), \quad Y = \frac{y}{\delta} \tag{30}$$

$$G_t = 1 - \frac{U_c}{U_b}Y - \frac{u_\tau}{U_b}\int_0^Y F dY + P_\tau^{-1}\frac{dF_t}{dY} \tag{31}$$

The matching of the inner and outer layers would have overlap regions and the appropriate parameter is the friction Peclet number $P_\tau = \sigma R_\tau$. In the overlap region, the matching is carried out for large Peclet numbers $P_\tau \to \infty$ through the Izakson–Millikan–Kolmogorov hypothesis.

The temperature profile expansion (28) in the inner layer and Eq. (30) in the outer layer are matched in the overlap region by functional equation

$$t_+(\eta) = T_{c+}(T_\tau) - F_t(Y) \tag{32}$$

where $T_{c+}(P_\tau) = (T_c - T_w)/T_\tau$. The first and the second differentials become

$$\eta\frac{dt_+}{d\eta} = P_\tau\frac{dT_{c+}}{dP_\tau} \tag{33a}$$

$$\eta\frac{d^2 t_+}{d\eta^2} = P_\tau\frac{d^2 T_{c+}}{dP_\tau^2} \tag{33b}$$

3.1 Power Law Temperature Profile From Matching. The alternate functional equation described here gives the power law temperature profile. The functional Eq. (33*b*) may be divided by the functional relation (33*a*), which gives an alternate functional equation

$$\eta \frac{\partial^2 t_+/\partial \eta^2}{\partial t_+/\partial \eta} = P_\tau \frac{\partial^2 T_{c+}/\partial P_\tau^2}{\partial T_{c+}/\partial P_\tau} \tag{34}$$

and its functional solution may be expressed, in the variable separable form, as

$$\eta \frac{\partial^2 t_+/\partial \eta^2}{\partial t_+/\partial \eta} = \alpha_t - 1 \tag{35a}$$

$$P_\tau \frac{\partial^2 T_{c+}/\partial P_\tau^2}{\partial T_{c+}/\partial P_\tau} = \alpha_t - 1 \tag{35b}$$

where constant α_t is independent of η and P_τ. The integral of these equations gives

$$\frac{\partial t_+}{\partial \eta} = J_t \eta^{\alpha_t - 1} \tag{36a}$$

$$\frac{\partial T_{c+}}{\partial R_\tau} = J_t P_\tau^{\alpha_t - 1} \tag{36b}$$

where J_t is a constant of integration. The two cases $\alpha_t = 0$ and $\alpha_t \neq 0$, would arise during further integration leading to the log law and the power law. In the second case, $\alpha_t \neq 0$, the integration of the relations (36*a*) and (36*b*) give the following power law relations:

Wall power law

$$t_+(y_+) = C_t(\sigma y_+)^{\alpha_t} \tag{37a}$$

$$t_+(Y) = C_{t1} Y^{\alpha_t} \tag{37b}$$

Heat transfer power law

$$\frac{T_c - T_w}{T_\tau} = C_t(\sigma R_\tau)^{\alpha_t} + E_t \tag{38}$$

Here, $C_t = J_t/\alpha_t$, $C_{t1} = C_t(\sigma R_\tau)^{\alpha_t}$, and E_t is a constant of integration. Uniformly valid solutions for velocity profile and skin friction power law become

$$\frac{T - T_w}{T_\tau} = C_t(\sigma y_+)^{\alpha_t} + E_t \Omega_t(Y) \tag{39a}$$

$$\frac{T - T_w}{T_\tau} = C_{t1} Y_t^{\alpha} + E_t \Omega_t(Y) \tag{39b}$$

$$\frac{T_c - T}{T_\tau} = C_{t1}(-Y_t^{\alpha} + 1) + E_t[1 - \Omega_t(Y)] \tag{40}$$

Here, $\Omega(Y)$ is the power law thermal wake function subjected to the boundary conditions $\Omega_t(0) = 0$ and $\Omega_t(1) = 1$. The heat transfer power law (38) and the friction factor power law are combined as

$$\frac{\mathrm{St}^{-1} C_f/2 - \epsilon E_t}{1 + \epsilon E} = \frac{C_t \sigma^{\alpha_t}}{C} \mathrm{Re}_\tau^{\alpha_t - \alpha} \tag{41}$$

For Prandtl number $\sigma = 1$, the thermal and momentum equations imply $C = C_t$, $\alpha = \alpha_t$, and $E = E_t$, and we get $2\mathrm{St}/C_f = 1$, the Reynolds analogy between momentum and heat transfer in a channel. The average temperature T_b from the integration of the temperature profile (39*a*) over the cross section of the channel becomes

$$\frac{T_b - T_w}{T_\tau} = \frac{C_t}{1 + \alpha}(\sigma R_\tau)^{\alpha_t} + E_{tb} \tag{42}$$

In terms of Stanton number St_b, it becomes

$$\mathrm{St}_b^{-1} = \frac{C_t}{2^{\alpha_t}(1 + \alpha_t)} \left[\frac{C}{2^{\alpha}(1 + \alpha)} \right]^{(1 - \alpha_t)/(1 + \alpha)} \sigma^{\alpha_t} \mathrm{Re}^{(\alpha_t + \alpha)/(1 + \alpha)} + E_{tb} \left[\frac{C}{2^{\alpha}(1 + \alpha)} \right]^{(1 - \alpha_t)/(1 + \alpha)} \mathrm{Re}^{\alpha_t/(1 + \alpha)} \tag{43}$$

The Reynolds heat flux in the overlap region becomes

$$\frac{\tau_t}{q_w} = 1 - C_t \alpha_t \eta^{\alpha_t - 1} - \mathrm{Pr}^{-1} \frac{u_\tau}{U_b} \sigma \frac{C}{1 + \alpha} y_+^{1 + \alpha} \tag{44}$$

$$\frac{\tau_t}{q_w} = 1 - \frac{1}{P_\tau} C_{1t} \alpha_t Y^{\alpha_t - 1} - \frac{u_\tau}{U_b} \frac{C_1}{1 + \alpha} Y^{1 + \alpha} \tag{45}$$

The location of maxima of Reynolds heat flux y_{tm+} and maxima value τ_{tm+} become

$$y_{tm+} = \left(\frac{C_t}{C} \frac{\alpha_t U_b}{u_t} (1 - \alpha_t) \sigma^{\alpha_t - 1} R_\tau \right)^{1/(2 + \alpha - \alpha_t)} \tag{46a}$$

$$\tau_{tm+} = 1 - 2 \frac{u_t}{U_b} \frac{C}{1 + \alpha} \left(\frac{C_t}{C} \frac{\alpha_t U_b}{u_t} (1 - \alpha_t) \sigma^{\alpha_t - 1} \right)^{(1 + \alpha)/(2 + \alpha - \alpha_t)} \times R_\tau^{-(1 - \alpha_t)/(2 + \alpha - \alpha_t)} \tag{46b}$$

Envelope of heat transfer power law. The power law prefactor $C_t = J_t/\alpha_t$, where constant J_t is of order unity. Let $J_t = a_t + b_t \alpha_t$ so that for $\alpha_t \to 0$ as $R_\tau \to \infty$, and power law prefactor becomes

$$C_t = \frac{a_t}{\alpha_t} + b_t + \cdots \tag{47}$$

where a_t and b_t are constants. The heat transfer power law (38), in view of relation (47), becomes

$$T_{c+} = \left(\frac{a_t}{\alpha_t} + b_t \right) \exp(\alpha_t \ln P_\tau) + E_t, \quad T_{c+} \equiv \frac{T_c - T_w}{T_\tau} \tag{48}$$

which forms a family of curves in the $(T_{c+}, \ln P_\tau)$-plane, where α_t is the parameter of the family. The family has an envelope, which satisfies both Eq. (48) and the equation $\partial T_{c+}/\partial \alpha_t = 0$. The derivative of Eq. (48) with respect to α gives

$$\frac{\partial T_{c+}}{\partial \alpha_t} = R_\tau^{\alpha} \left[\left(b_t + \frac{a_t}{\alpha_t} \right) \ln P_\tau - \frac{a_t}{\alpha_t^2} \right] = 0 \tag{49}$$

which may be simplified as

$$(a_t + b_t \alpha_t) \alpha_t \ln P_\tau = a \tag{50}$$

Relation (50) is a quadratic equation in power index α_t and its solution is given as

$$\alpha_t = \frac{\Gamma_t}{\ln(\sigma R_\tau)} \tag{51a}$$

$$\Gamma_t = \frac{a_t}{2 b_t} \ln(\sigma R_\tau) \left[\left(1 + \frac{4 b_t}{a_t \ln(\sigma R_\tau)} \right)^{1/2} - 1 \right] \tag{51b}$$

The heat transfer power law (48), after elimination of the power index α_t from relation (51*a*), yields the heat transfer log law

$$\frac{T_c - T_w}{T_\tau} = \frac{1}{k_t} \ln(\sigma R_\tau) + B_t + E_t \tag{52}$$

$$k_t^{-1} = \frac{a_t}{\Gamma_t} \exp(\Gamma_t) \tag{53a}$$

$$B_t = b_t \exp(\Gamma_t) \tag{53b}$$

where k_t is the Karman constant and B_t is the intercept of the log law, as shown later, which depends on the Reynolds number through function Γ_t. The results show that the envelope of the heat transfer power law (48) gives the heat transfer log law (52). The power law temperature profile solution is equivalent to the log law

solution, provided that the log law constants k_t and B_t predicted by relations (53*a*) and (53*b*) based on relations (51*a*) and (51*b*) are adopted as functions of the friction Peclet number. The classical privileged log law solution, where log law constants k_t and B_t are universal numbers (independent of Reynolds number), is also equivalent to the power law solution, in the limiting situation of very large Reynolds numbers R_τ (or $R_\theta = U_\infty \delta/\nu$ the momentum Reynolds number). The power law prefactor C_t after the elimination of a_t and b_t from relations (51*a*) and (51*b*) give

$$\alpha_t = \frac{\Gamma_t}{\ln(\sigma R_\tau)} \tag{54a}$$

$$C_t = \left(\frac{\Gamma_t}{k_t \alpha_t} + B_t\right)\exp(-\Gamma_t) \tag{54b}$$

$$C_t = \left(\frac{1}{k_t}\ln(\sigma R_\tau) + B_t\right)\exp(-\Gamma_t) \tag{54c}$$

and constant $C_{t1} = C_t \exp(\Gamma_t)$. The power law constants α_t and C_t may also be expressed in terms of the friction velocity, by eliminating the $\ln R_\tau$ term by using relations (54*a*)–(54*c*) to obtain

$$\alpha_t = k_t^{-1}\frac{\epsilon_t}{1 - E\epsilon_t} \tag{55a}$$

$$C_t = \left(\frac{1}{\epsilon_t} - E_t\right)\exp(-\Gamma_t) \tag{55b}$$

$$\epsilon_t = \frac{T_\tau}{T_w - T_c} = \frac{\mathrm{St}}{\epsilon} \tag{55c}$$

The constant Γ_t, which is based on expressions (54*a*)–(54*c*) and (55*a*)–(55*c*), yield

$$\Gamma_t = \left(1 + \frac{k_t B_t}{\ln(\sigma R_\tau)}\right)^{-1} \tag{56a}$$

$$\Gamma_t = \frac{1 - (B_t + E_t)\epsilon_t}{1 - E_t \epsilon_t} \tag{56b}$$

3.2 Log Law Temperature Profile From Matching. The uniformly valid solution for the temperature profile becomes

$$\frac{T - T_w}{T_\tau} = \frac{1}{k_t}\ln(\sigma y_+) + B_t + D_t W_t(Y) \tag{57}$$

$$\frac{T_c - T}{T_\tau} = -\frac{1}{k_t}\ln Y + D_t[1 - W_t(Y)] \tag{58}$$

Here, $W_t(Y)$ is the thermal wake function subjected to the boundary conditions $W_t(0) = 0$ and $W_1(1) = 1$. Heat transfer log law is

$$\frac{T_c - T_w}{T_\tau} = \frac{1}{k_t}\ln(\sigma R_\tau) + B_t + D_t \tag{59}$$

The elimination of $\ln R_\tau$ term from relations (23) and (59) gives an alternate relation

$$\frac{2\mathrm{St}}{C_f} = \frac{k_t}{k}\left[1 + \left\{(B_t + D_t + k_t^{-1}\ln\sigma)\frac{k_t}{k} - (B + D)\right\}\sqrt{\frac{C_f}{2}}\right]^{-1} \tag{60}$$

where St is the Stanton number and C_f is the skin friction coefficient. For large Reynolds numbers, relation (60) yields $2\mathrm{St}/C_f = k_t/k$. If Prandtl number $\sigma = 1$, the solution implies $k_t = k$, and we get $2\mathrm{St}/C_f = 1$, the Reynolds analogy between the momentum and heat transfer in a turbulent channel flow.

The Reynolds shear stress in the inner variables is

$$\frac{\tau_t}{q_w} = 1 - \frac{1}{k_t \sigma y_+} - \frac{u_\tau}{u_b} I_1, \quad I_1 = \frac{\sigma}{k}(y_+ - y_+ \ln y_+) + B\sigma y_+ \tag{61}$$

and in the outer variables is

$$\frac{\tau_t}{q_w} = 1 - \frac{1}{k_t \sigma R_\tau Y} - \frac{U_c}{u_b} Y + \frac{u_\tau}{u_b} I_2, \quad I_2 = \frac{1}{k}(Y - Y\ln Y) - DY \tag{62}$$

The location of maxima of Reynolds heat flux y_{tm+} and maxima value τ_{tm+} become

$$y_{tm+} = \sqrt{\frac{U_b}{U_c}}\sqrt{\frac{R_\tau}{\sigma k_t}} \tag{63a}$$

$$\tau_{tm+} = 1 - \frac{2}{\sqrt{\sigma k_t R_\tau}}\sqrt{\frac{U_c}{U_b}} \tag{63b}$$

4 Results and Discussion

The DNS data of a fully developed turbulent flow in a channel given by Iwamoto et al. [19] are for $R_\tau = 109.4$, 150.5, 297.9, 395.8, and 642.5. Abe et al. [20], Abe and Kawamura [21], and Abe et al. [22] for $R_\tau = 180$, 395, 640, and 1020, and Hoyas and Jimenez [23] for $R_\tau = 2000$ have been considered. The flow is simulated as a fully developed 2D turbulent flow between two parallel walls. The flow is homogeneous, both in the streamwise and spanwise directions, and the statistics are dependent only on the distance from the wall. The data presented are nondimensionalized by the wall variables u_τ and ν. The flow condition is defined by the pressure gradient imposed (or the friction velocity) and the distance between the walls (channel height).

Log law velocity profile from DNS data. The inner and outer velocity profiles have been matched in the overlap domain to present the logarithmic behavior, considering the flows in the inner wall region (where the variable is y_+) and the outer wake region (where the variable is Y). For this, the turbulent channel flow DNS data of Iwamoto et al. [19], Abe et al. [20–22], and Hoyas and Jimenez [23] and the experimental data of Zanoun [24] are shown in the three figures marked (*a*) in Fig. 1 on a semilog scale, respectively. The substantial log region is observed from the data beyond $y_+ > 30$. The extent of this log region increases toward the outer layer as R_τ increases. For large values of y_+, the data depart from the logarithmic region due to outer wake layer effects. The same data are also shown in the three figures marked (*b*) in Fig. 1 on the velocity defect coordinates $[(U_c - u)/u_\tau, Y]$. The plots of velocity defect $(U_c - u)/u_\tau$ versus Y show that the DNS data follow log law behavior only in the outer region: $0.1 < Y < 1$, whereas, at small values of Y, the data depart from the logarithmic behavior due to the influence of the wall sublayer. The predictions of the location of the Reynolds stress (25*a*) and its magnitude ma (25*b*) compare very well with the DNS data [19–23] and experimental data [24] (see Fig. 4 of [30]). Here the scale of the thermal layer (63) has been analogous with the scale of the momentum layer (25*b*) as the inverse square root of friction Reynolds number, in contrast to Wei et al. [31] as described on p. 031701-2 of Seena and Afazal [30].

Power law velocity profile from DNS data. The mean turbulent velocity profiles from the DNS data of Iwamoto et al. [19], Abe et al. [20–22], Hoyas and Jimenez [23] and experimental data of Zanoun [24] for the same ranges of Reynolds number described earlier are shown in the three figures marked (*a*) as a log-log plot in Fig. 2 in the inner variables (u_+, y_+). The plots of the data show a linear region, indicating the existence of the power law velocity profile in the overlap domain. The data collapse for all Reynolds numbers in a narrow band and show the dependence of power law prefactor C and index α on the Reynolds number. The same data for the outer wall variables (u_+, Y) are shown in the three figures marked (*b*) in Fig. 2 on the log-log plot.

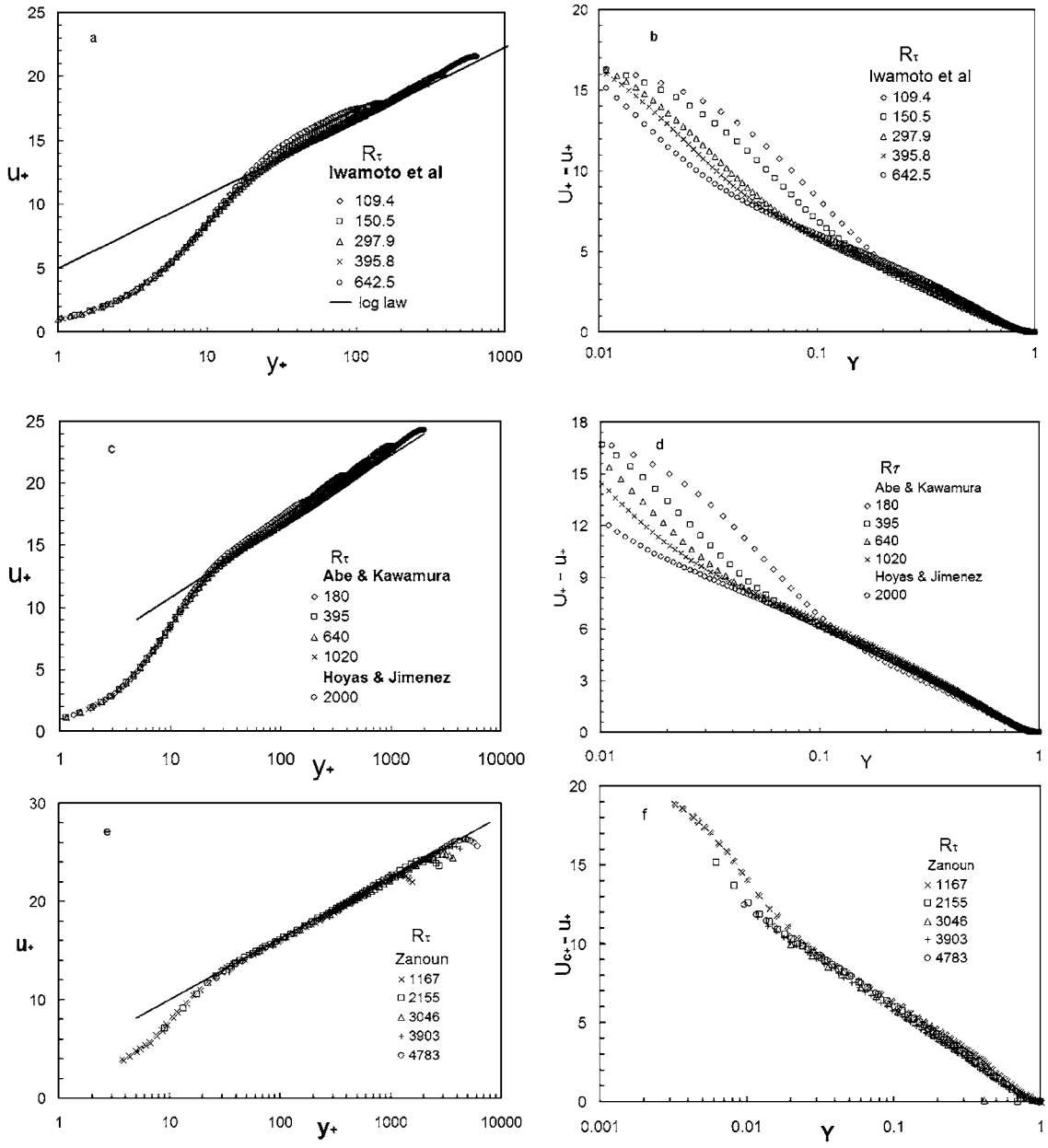

Fig. 1 ***Log law*. The velocity profiles for fully developed channel flow in the inner and outer layers' variables in the semilog plot from the DNS data of Iwamoto et al., Abe et al., and Hoyas and Jimenez, and experimental data of Zanoun for various values of Reynolds numbers**

The power law prefactor C and the power law index α for each friction Reynolds number R_τ has been estimated for the velocity profile data of Iwamoto et al., Abe et al., and Hoyas et al. This power law prefactor C is plotted against α^{-1}, the inverse of the power law index, as shown in Fig. 3(*a*). All the data for the power law prefactor C are correlated with the power law index α as follows

$$C = \frac{0.87}{\alpha} + 2.5 \tag{64}$$

which is supported by our prediction (19*b*). The power law index α has been exhibited against R_τ from the DNS data of Iwamoto et al. [19], Abe et al. [20–22], Hoyas and Jimenez [23], and experimental data of Zanoun [24] for the fully developed turbulent channel flow, as shown in Fig. 3(*b*). The data fit to correlation

$$\alpha = \frac{1.1}{\ln R_\tau} \tag{65}$$

is predicted by relation (19*a*). The power law prefactor C also depends on the friction Reynolds number R_τ

$$C = 0.79 \ln R_\tau + 2.5 \tag{66}$$

which is shown in Fig. 3(*c*).

The power law index α in terms of the nondimensional friction velocity is plotted in Fig. 3(*d*). The data have been fitted by the following relation:

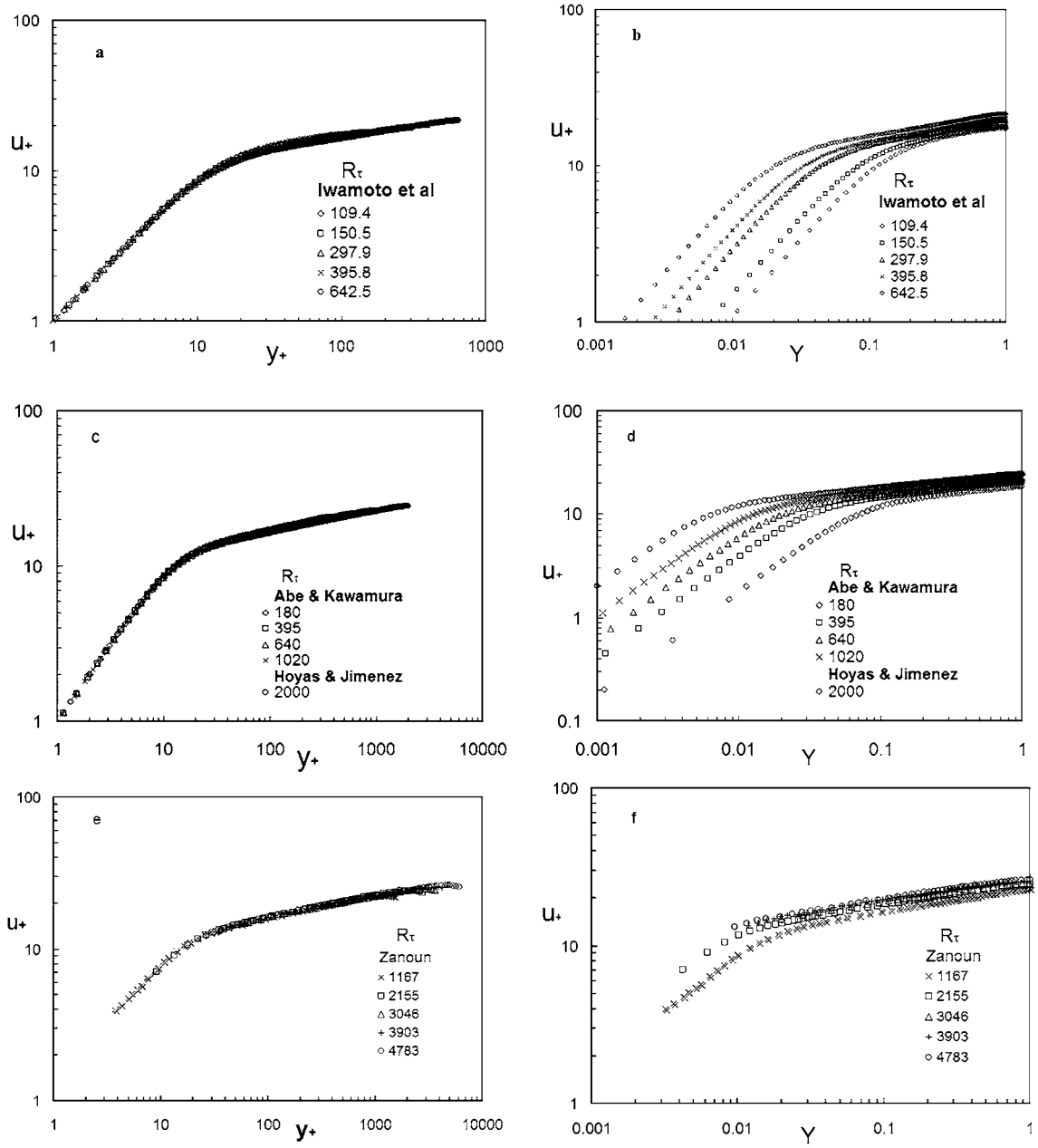

Fig. 2 ***Power law*. The velocity profiles for fully developed channel flow in the inner and outer layers' variables in the log-log plot from the DNS data of Iwamoto et al., Abe et al., and Hoyas and Jimenez, and experimental data of Zanoun for various values of Reynolds numbers**

$$\alpha = \frac{2.5\epsilon}{1 - 5.5\epsilon} \tag{67}$$

which is also in accordance with our prediction given by Eq. (20*a*). The power law prefactor C has been plotted against $1/\sqrt{\lambda}$ as shown in Fig. 3(*e*), which has been fitted by the relation

$$C = \frac{0.35}{\epsilon} + 0.1 \tag{68}$$

The data for friction factor λ have been plotted against R_τ in Fig. 3(*f*). The data have been fitted by the relation

$$\frac{1}{\sqrt{\lambda}} = 2 \log R_\tau + 1 \tag{69}$$

The friction factor power law (14) for $E=0$ becomes

$$\lambda = 8m\mathrm{Re}^{-n}, \quad n = \frac{2\alpha}{1+\alpha}, \quad m = \left(\frac{2^\alpha(1+\alpha)}{C}\right)^{2/(1+\alpha)} \tag{70}$$

where α and C may be taken from Eqs. (67) and (68). For a fixed value of $n=1/4$, the power index $\alpha=1/7$ and relation (70) yields

$$\lambda/4 = 0.07\mathrm{Re}^{-1/4} \tag{71}$$

which may be compared with the well-known empirical expression $\lambda/4=0.073\mathrm{Re}^{-1/4}$ for a channel flow proposed by Dean [4] and $\lambda/4=0.079\mathrm{Re}^{-1/4}$ for pipe flow proposed by Blasius [3] (see also Refs. [17,24].

The characteristics of surface heat-flux fluctuations have also been presented by Abe et al. [20–22], where Reynolds numbers based on the friction velocity and the channel half-width are $R_\tau = 180$, 395, 640, and 1020 and the molecular Prandtl number σ

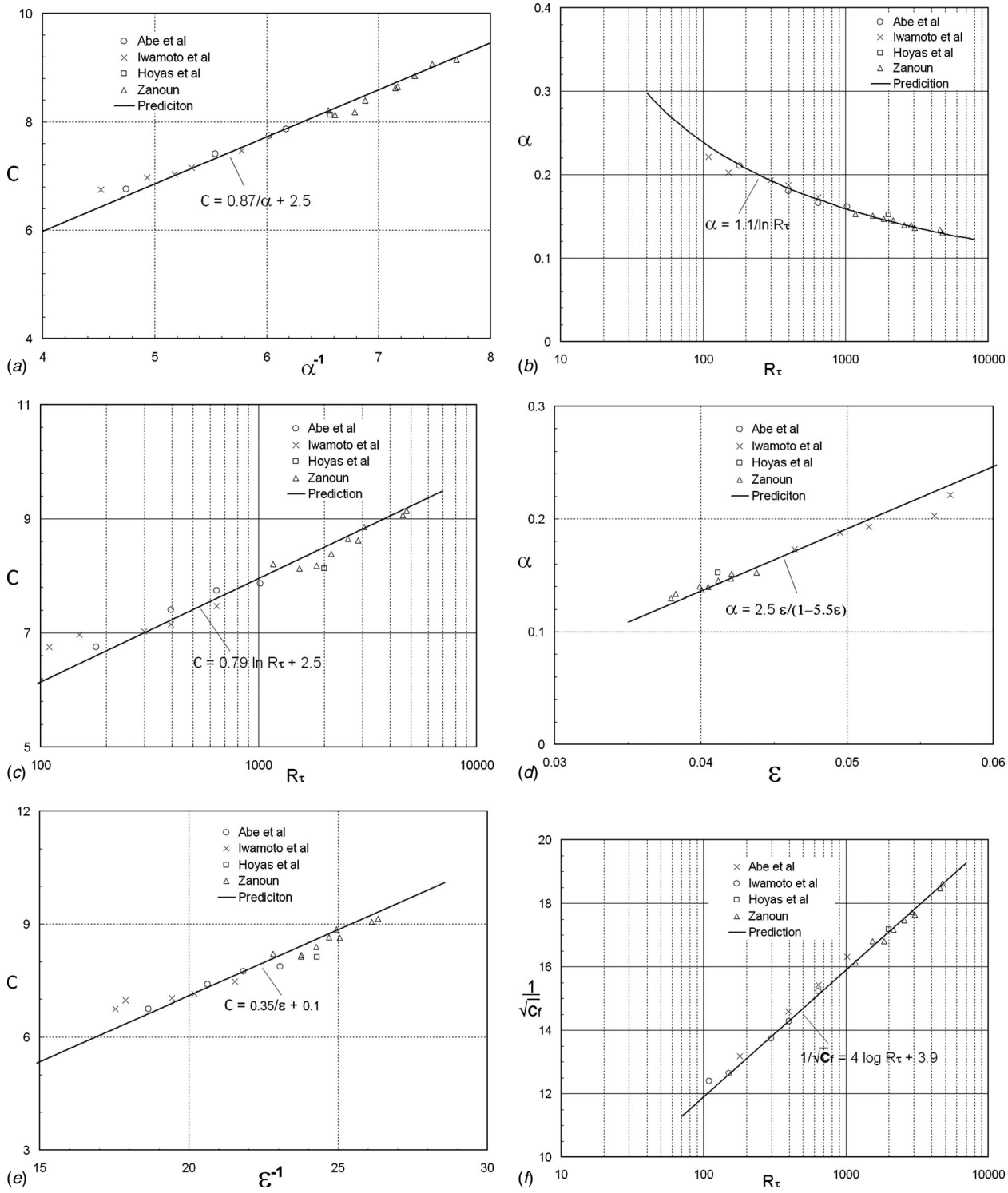

Fig. 3 The dependence of the power law constants α and C for power law velocity profile on the Reynolds numbers from the data of Iwamoto et al., Abe et al., Hoyas and Jimenez, and Zanoun

=0.71 and 0.05. The conditions that Abe et al. [20] have adopted are for the fully developed turbulent channel flow with a temperature field. It is driven by the streamwise mean pressure gradient. The temperature field is imposed by uniform heating at both walls with a constant time-averaged heat flux. All the variables are computed from the Navier–Stokes equation and energy equations, which are normalized by the friction velocity u_τ, the friction temperature $T_\tau = Q_w/\rho C_p u_\tau$, and the channel half-width d, where Q_w is the given averaged surface heat flux. The data presented are nondimensionalized by the wall variables u_τ and ν.

Log law temperature profile from the DNS data. The log law temperature profile theory in the overlap region is considered. The inner and outer temperature profiles have also a common overlap domain having a logarithmic behavior as it was in the case of the

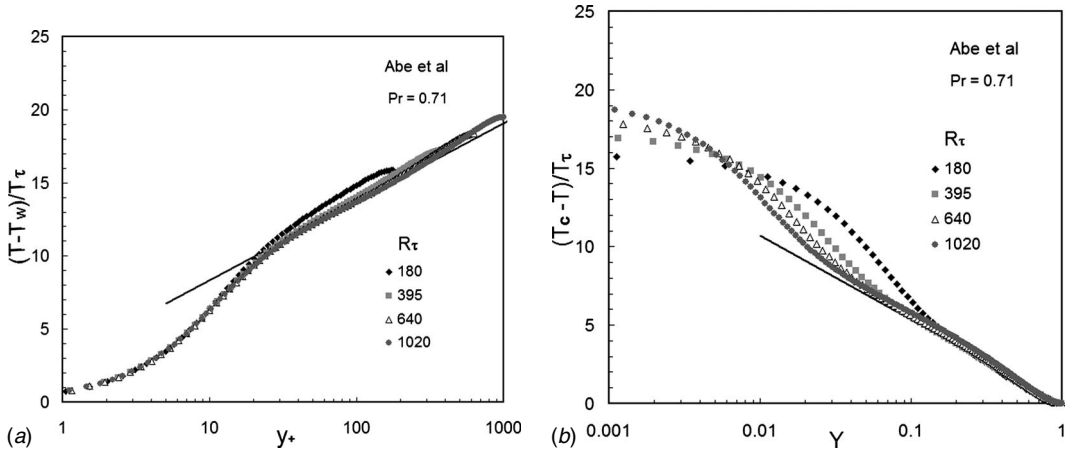

Fig. 4 ***Log law.*** **The temperature profile of the DNS data of Abe et al. for various Reynolds numbers**

velocity profile's inner and outer variables. The turbulent channel flow DNS data of the temperature distribution from Abe et al. [20] for R_τ=180, 395, and 640 are shown in Fig. 4(a) in wall variables $[(T-T_w)/T_\tau, y_+]$ on a semilog scale. The collapse of the data beyond the domain $y_+>30$ shows the log law region. The extent of this log region increases toward the outer layer as R_τ increases. For large values of y_+, the data depart from the logarithmic region due to the outer wake layer effects. The same data in the temperature defect coordinates $[(T_c-T)/T_\tau, y/\delta]$ are shown in Fig. 4(b) which shows the log law behavior in the outer region $0.1<Y<1$. However, for very small values of Y, data depart from the log region due to the influence of the wall sublayer. The prediction of the location of the Reynolds stress maxima (63) compares very well with the DNS data [20–22] (see Fig. 7 in Seena and Afzal [30]).

Power law temperature profile from the DNS data. The power law temperature profile theory has been also presented in Sec. 3. The power law index α_t and prefactor C_t are the functions of the friction Reynolds number R_τ and Prandtl number σ. The mean turbulent temperature profile data of Abe et al. [19] for R_τ=180, 395, and 640 are shown on the log-log plot in Fig. 5(a). The data show a linear region on the log-log plot indicating the existence of the power law temperature profile in the overlap domain. The collapse of the data in the domain, $y_+>30$, shows the power law region. The extent of this power law region increases toward the outer layer as the friction Reynolds number R_τ increases. The same data in the outer wall variables $[(T-T_w)/T_\tau, Y]$ are shown in Fig. 5(b). The characteristics of the power law temperature profile, the power law index α_t and prefactor C_t have been estimated for each Reynolds number.

The power law prefactor C_t is plotted against α_t^{-1}; the inverse of the power law index is shown in Fig. 6(a). The data of Abe et al. [20] for the fully developed turbulent channel flow fit to relate as follows:

$$C_t = \frac{0.82}{\alpha_t} + 1.1 \tag{72}$$

which is supported by the present prediction given by Eq. (54b). The power law index α_t against σR_τ from the DNS data of Abe et al. [20] for the fully developed turbulent channel flows is shown in Fig. 6(b). The data fit by the following relation:

$$\alpha_t = \frac{1.1}{\ln(\sigma R_\tau)} \tag{73}$$

The power law prefactor C_t from relation (54b) depends on the Peclet number ($P_\tau=\sigma R_\tau$), the product of the friction Reynolds number and the Prandtl number. The prefactor C_t data are plotted against σR_τ as shown in Fig. 6(c) leading to the following relation:

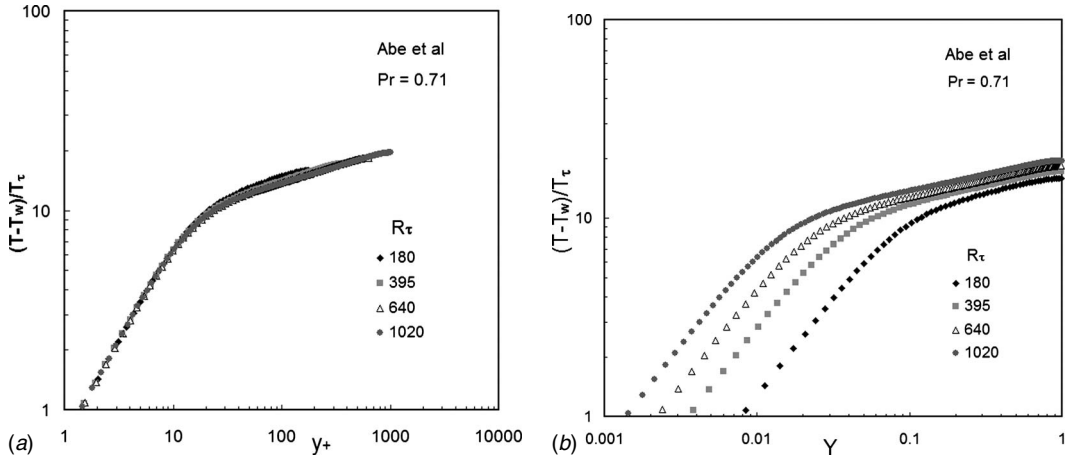

Fig. 5 ***Power law.*** **The temperature profile of the DNS data of Abe et al. for various Reynolds numbers**

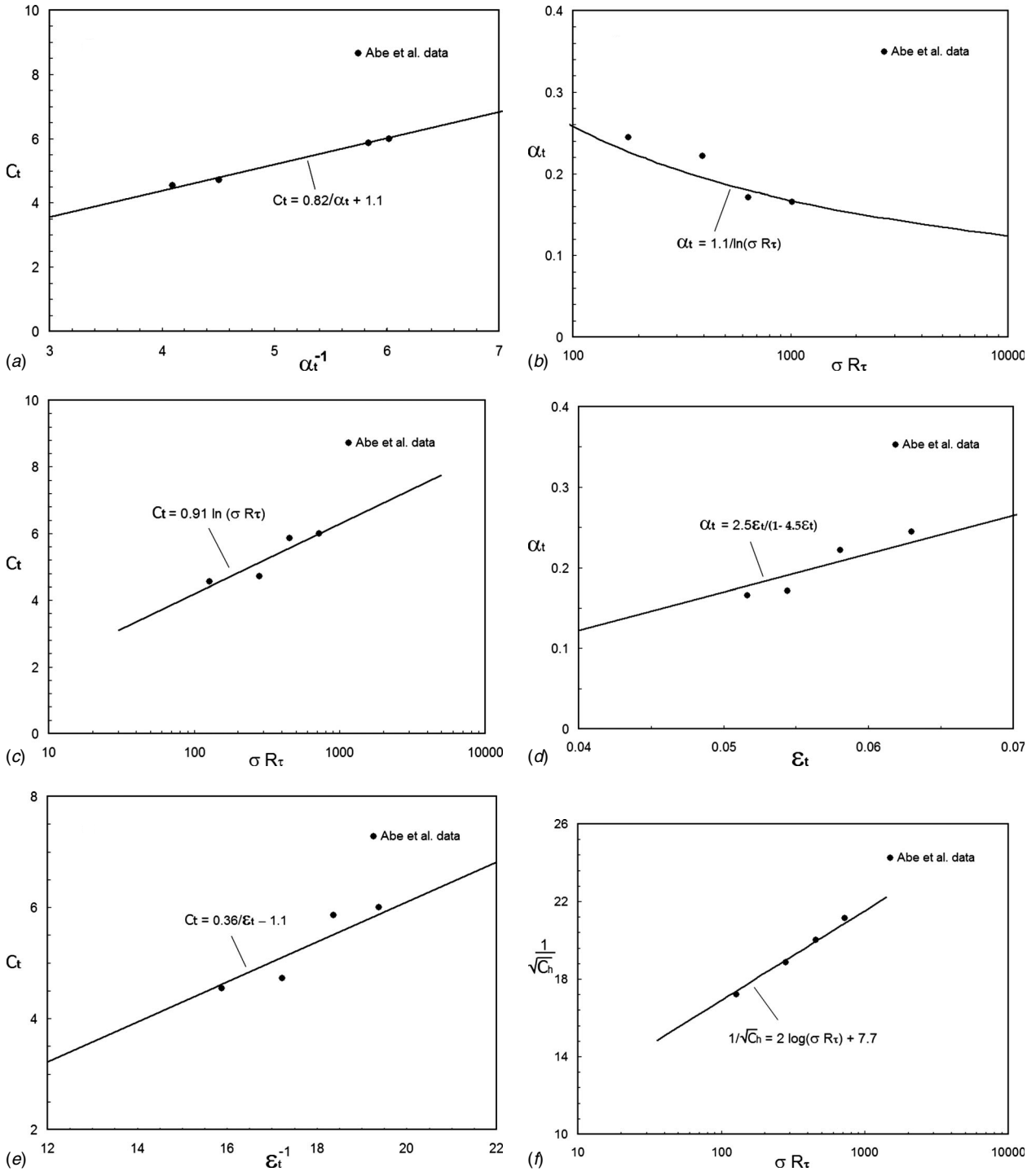

Fig. 6 The dependence of the power law constants α_t and C_t for power law temperature profile on Reynolds numbers from the data of Abe et al.

$$C_t = 0.91 \ln(\sigma R_\tau) \tag{74}$$

The power law index α_t has been expressed in terms of the non-dimensional friction temperature and is plotted in Fig. 6(*d*) The data fit to the following relation:

$$\alpha_t = \frac{2.5\epsilon_t}{1 - 4\epsilon_t} \tag{75}$$

which is also in accordance to our prediction given by Eq. (55*a*). The power law prefactor C has been plotted against $1/\sqrt{\lambda}$ and shown in Fig. 6(*e*) which fit as shown below:

$$C_t = \frac{0.35}{\epsilon_t} - 0.1 \tag{76}$$

The coefficient of heat transfer in terms of Stanton number C_h has been plotted against the product of the friction Reynolds number and Prandtl number (σR_τ) in Fig. 6(*f*). The proposed correlation is

$$\frac{1}{\sqrt{C_h}} = 2 \log(\sigma R_\tau) + 7.5 \tag{77}$$

The heat transfer power law (42) for $E=0$ becomes

$$\mathrm{St}_b = \frac{T_\tau u_\tau}{T_b u_b} = m_t \mathrm{Re}^{-(\alpha_t+\alpha)/(1+\alpha)} \tag{78}$$

$$m_t = \frac{2^{\alpha_t}(1+\alpha_t)}{C_t}\left[\frac{2^{\alpha}(1+\alpha)}{C}\right]^{(1-\alpha_t)/(1+\alpha)} \sigma^{-\alpha_t} \tag{79}$$

For $\alpha=\alpha_1=1/7$, we get the heat transfer power law that becomes $\mathrm{St}_b=m_t\mathrm{Re}^{-1/4}$, which is analogous to the relation of Dean [4] for the friction factor in a channel.

The power law temperature profile, in addition to the log law temperature profile, is also a solution in the overlap domain for very large Peclet numbers. This is not surprising as we are dealing with the open functional equation of the turbulent motion, without any closure hypothesis. The envelope of the heat transfer power law leads to the heat transfer log law. For large Peclet numbers, the power law is equivalent to the log law.

Acknowledgment

N.A. is grateful for the support of the All India Council of Technical Education, New Delhi.

References

[1] Incropera, F. P., and DeWitt, D. P., 1985, Introduction to Heat Transfer, 1st ed., Wiley, New York.
[2] Kays, W. M., and Crawford, M., 1983, Convective Heat and Mass Transfer, 3rd ed., McGraw-Hill, New York.
[3] Hager, W. H., 2003, "Blasius: A Life in Research and Education," Exp. Fluids, **14**, pp. 566–571.
[4] Dean, R. B., 1978, "Reynolds Number Dependence of Skin Friction and Other Bulk Flow Variables in Two-Dimensional Rectangular Duct Flow," ASME J. Fluids Eng., **100**, pp. 215–223.
[5] Afzal, N., 1997, "Power Law in Wall and Wake Layers of a Turbulent Boundary Layer," *Proceedings of the Seventh Asian Congress of Fluid Mechanics*, Allied, New Delhi, pp. 805–808.
[6] Schlichting, H. 1968, *Boundary Layer Theory*, McGraw-Hill, New York.
[7] Marati, N., Davoudi, J., Casciola, C. M., and Eckhardt, B., 2006, "Mean Profiles for a Passive Scalar in Wall-Bounded Flows From Symmetry Analysis," J. Turbul., 7, Article No. 61.
[8] Nikuradse, J., 1932, "Laws of Turbulent Flow in Smooth Pipes," VDI, Forschungsheft N-356, English translation NACA TTF-10, p. 359.
[9] Narasimha, R., 1996, "Different Approaches to Asymptotic Expansions of Turbulent Boundary Layer," *Asymptotic Methods for Turbulent Shear Flows at High Reynolds Numbers*, K. Gersten, ed., Kluwer, Dordrecht, pp. 5–16.
[10] Barenblatt, G. I., 1993, "Scaling Laws for Fully Developed Turbulent Shear Flows, Part I: Basic Hypothesis and Analysis," J. Fluid Mech., **248**, pp. 513–520.
[11] Barenblatt, G. I., Chorin, A. J., and Prostokishin, V. M., 1997, "Scaling Laws for Fully Developed Turbulent Flow in Pipes," Appl. Mech. Rev., **90**, pp. 413–429.
[12] Prandtl, L., 1935, "Mechanics of Fluids," *Aerodynamic Theory*, W. F. Durand, ed., Vol. 3, pp. 34–208.
[13] Afzal, N., 2001, "Power Law and Log Law Velocity Profiles in Fully Developed Turbulent Pipe Flow: Equivalent Relations at Large Reynolds Numbers," Acta Mech., **151**, pp. 171–183; 2001, "Power Law and Log Law Velocity Profiles in Fully Developed Turbulent Pipe Flow: Equivalent Relations at Large Reynolds Numbers," Acta Mech., **151**, 195–216.
[14] Afzal, N., 2005, "Scaling of Power Law Velocity Profile in Wall-Bounded Turbulent Shear Flows," *43rd AIAA Aerospace Sciences Meeting and Exhibit*, Reno, NV, Jan. 10–13, Paper No. AIAA-2005-01090.
[15] Afzal, N., 2005, "Analysis of Power Law and Log Law Velocity Profiles in Overlap Region of a Turbulent Wall Jet," Proc. R. Soc. London, Ser. A, **461**, pp. 1889–1910.
[16] Afzal, N., Seena, A., and Bushra, A., 2006, "Power Law Turbulent Velocity Profile in Transitional Rough Pipes," ASME J. Fluids Eng., **128**, pp. 548–558.
[17] Afzal, N., Seena, A., and Bushra, A., 2007, "Power Law Velocity Profile in Fully Developed Turbulent Pipe and Channel Flows," J. Hydraul. Eng., **13**(9), pp. 1080–1086.
[18] Buschmann, M. H., and Gad-el-Hal, M., 2006, "Recent developments in Scaling of Wall-Bounded Flows," Prog. Aerosp. Sci., **42**, pp. 419–467.
[19] Iwamoto, K., Suzuki, Y., and Kasagi, N., 2002, "Reynolds Number Effect on Wall Turbulence: Toward Effective Feedback Control," Int. J. Heat Fluid Flow, **23**, pp. 678–689.
[20] Abe, H., Kawamura, H., and Matsuo, Y., 2004, "Surface Heat-flux Fluctuations in a Turbulent Channel Up to R_τ=1020 With Pr=0.025 and 0.71," Int. J. Heat Fluid Flow, **25** pp. 404–419.
[21] Abe, H., and Kawamura, H., 2002, "A Study of Turbulence Thermal Structure in a Channel Flow Through DNS up to R_τ=640 With Pr=0.025 and 0.71," *Proceedings of the 9th European Turbulence Conference*, pp. 399–402.
[22] Abe, H., Kawamura, H., and Matsuo, Y., 2001, "Direct Numerical Simulation of a Fully Developed Turbulent Channel Flow With Respect to the Reynolds Number Dependence," ASME J. Fluids Eng., **123**, pp. 382–393.
[23] Hoyas, S., and Jimenez, J., 2006, "Scaling of the Velocity Fluctuations in Turbulent Channels Up to Re=2003," Phys. Fluids, **18**, 011702.
[24] Zanoun, E. S., 2003, "Answer to Some Open Questions in Wall-bounded Laminar and Turbulent Flows," Doctor-Ingeniur, thesis, University of Erlangen-Nurnberg.
[25] Afzal, N., and Narasimha, R., 1976, "Axisymmetric Turbulent Boundary Layers Along a Circular Cylinder With Constant Pressure," J. Fluid Mech., **74**, pp. 113–129.
[26] Izakson, A. A., 1937, "On Formula for the Velocity Distribution Near Walls," Tech. Phys., USSR, **4**, pp. 155–159.
[27] Millikan, C. B., 1938, "A Critical Discussion of Turbulent Flow in Channels and Circular Tubes," *Proceedings of the 5th Int. Congress Applied Mechanics*, Cambridge, J. P. den Hartog and H. Peters, eds., Wiley/Chapman and Hall, New York–London, pp. 386–392.
[28] Kolmogorov, A. N., 1991, "The Local Structure of Turbulence in Incompressible Viscous Fluid for Very Large Reynolds Numbers," Proc. R. Soc. London, Ser. A, **434**, pp. 9–13.
[29] Coles, D., 1956, "The Law of the Wake in the Turbulent Boundary Layer," J. Fluid Mech., **1**, pp. 191–226.
[30] Seena, A., and Afzal, N., 2008, "Intermediate Scaling of Turbulent Momentum and Heat Flux in a Transitional Rough Channel," ASME J. Heat Transfer, **130**(3), p. 031701.
[31] Wei, T., Fife, P., Klewicki, J., and McMurtry, P., 2005, "Scaling Heat Transfer in Fully Developed Turbulent Channel Flows," Int. J. Heat Mass Transfer, **48**, pp. 5284–5296.

Ventilation of Wind-Permeable Clothed Cylinder Subject to Periodic Swinging Motion: Modeling and Experimentation

N. Ghaddar[1]
Qatar Chair in Energy Studies Professor
Fellow ASME
Department of Mechanical Engineering,
American University of Beirut,
P.O. Box 11-0236,
Beirut 1107-2020, Lebanon
e-mail: farah@aub.edu.lb

K. Ghali
Department of Mechanical Engineering,
Beirut Arab University,
Beirut, 1107-2020, Lebanon

B. Jreije
Department of Mechanical Engineering,
American University of Beirut,
P.O. Box 11-0236,
Beirut 1107-2020, Lebanon

A theoretical and experimental study has been performed to determine the ventilation induced by swinging motion and external wind for a fabric-covered cylinder of finite length representing a limb. The estimated ventilation rates are important in determining local thermal comfort. A model is developed to estimate the external pressure distribution resulting from the relative wind around the swinging clothed cylinder. A mass balance equation of the microclimate air layer is reduced to a pressure equation assuming laminar flow in axial and angular directions and that the air layer is lumped in the radial direction. The ventilation model predicts the total renewal rate during the swinging cycle. A good agreement was found between the predicted ventilation rates at swinging frequencies between 40 rpm and 60 rpm and measured values from experiments conducted in a controlled environmental chamber (air velocity is less than 0.05 m/s) and in a low speed wind tunnel (for air speed between 2 m/s and 6 m/s) using the tracer gas method to measure the total ventilation rate induced by the swinging motion of a cylinder covered with a cotton fabric for both closed and open aperture cases. A parametric study using the current model is performed on a cotton fabric to study the effect of wind on ventilation rates for a nonmoving clothed limb at wind speeds ranging from 0.5 m/s to 8 m/s, the effect of a swinging limb in stagnant air at frequencies up to 80 rpm, and the combined effect of wind and swinging motion on the ventilation rate. For a nonmoving limb, ventilation rate increases with external wind. In the absence of wind, the ventilation rate increases with increased swinging frequency. [DOI: 10.1115/1.2944245]

Keywords: ventilation, wind-permeable fabrics, swinging motion of clothed cylinder

Introduction

Clothing microclimate ventilation is critical to the removal of sensible and latent heat from the body and consequently has a major influence on thermal comfort and dynamic insulation values of clothing ensembles. For a given ensemble, the amount of ventilation depends on wind, wearer displacement due to motion causing a wind effect, and relative motion of clothed body parts (limbs) with respect to their clothing cover. Both arms and legs swing during walking while only legs move during cycling. Different body parts are subject to different mechanisms of wind, swinging motion, and combined wind and swinging motion that stimulate ventilation at different rates. The relative importance of these mechanisms on ventilation and clothing insulation for different combinations of wind and body motion is not clear, nor are data available in literature on local ventilation rates of separate body areas and their relevance to whole body clothing microclimate ventilation. When different areas of skin have different ventilation rates, local thermal comfort evaluated by skin wittedness and comfort sensation becomes important in assessing whole body comfort. ISO-7730 [1] requires determination of clothing insulation of active persons or persons exposed to significant wind. Data on dynamic insulation have limited use since they are applicable for the specific ensembles, activity levels, and experimental conditions used in generating them. In addition, estimation of local microclimate ventilation rate through protective clothing is a critical issue in clothing design for meeting established standards on permissible exposure limits (PELs) to contaminant through skin contact.

Empirical data reported are for average whole body clothing ventilation that limits their use in understanding local body microclimate interaction with clothing and wind and in predicting body heat loss during body motion. Few studies have examined the clothing microclimate air layer ventilation and even fewer investigations dealt with the mechanism of microclimate ventilation by wind and motion. Havenith et al. [2] found that inside clothing ensemble, motion is a stronger factor in increasing the ventilation rate than the adjacent air layer. Lotens [3] had empirically derived a correlation for clothing ensemble ventilation as a function of effective wind speed and air permeability for air-permeable fabrics. Researchers have also addressed the induced ventilation through a clothed body segment due to moving limb that changes the microclimate air layer size, and ventilation due to open apertures. Previous work of Ghali et al. [4] and Ghaddar et al. [5] addressed the effect of the changing gap width induced by an oscillating body part (cylinder) within a fixed single clothing cover at uniform external environment pressure with close and open clothing apertures. The ventilation model of Ghaddar et al. [5] of the fabric-air-layer annulus was extended by Jaroudi et al. [6] for the case where the gap width varies in both the angular and axial directions due to the rotation of the limb within a clothing cylinder. Jaroudi et al. [6] model assumed uniform external pressure distribution without wind and was restricted to small swinging amplitude (the maximum swing angle is less than 5 deg) of the clothed limb. The external pressure distribution around a

[1]Corresponding author.

Contributed by the Heat Transfer Division of ASME for publication in the JOURNAL OF HEAT TRANSFER. Manuscript received May 4, 2007; final manuscript received November 29, 2007; published online July 10, 2008. Review conducted by S.A. Sherif. Paper presented at the 2007 ASME-JSME Thermal Engineering Conference and Summer Heat Transfer Conference (HT2007), Vancouver, BC, Canada, July 8–12, 2007.

clothed limb is instrumental in determining air renewal rates in the microclimate when the body part and clothing move together.

The external airflow due to wind or displaced by body motion impinges on the clothed body, and some airflows around the body, while some penetrates through the clothing. The flow around the body alters the external pressure distribution over the clothing outer surface. The flow through the fabric depends on the pressure difference between the external pressure on the clothing and the internal air layer pressure on the fabric skin side. The microclimate flow resistance depends on the microclimate layer time-space-varying size caused by the motion of the body relative to the fabric, the occurrence of local skin-clothing contact regions during motion, the presence of openings, as well as interfaces and closures between clothing system components. There is a need to develop a ventilation model from conservation laws that can take into consideration all these parameters and answer questions on the effect of wind on ventilation rates for a nonmoving clothed limb, the effect of a swinging limb in stagnant air, and the combined effect of wind and swinging motion on the ventilation.

In this work, a ventilation model will be developed to estimate the renewal flow rates for general limb motion configuration taking into consideration the periodic motion of the limbs and clothing, their geometric interaction at skin-fabric contact or no contact, open or closed clothing apertures, and in the presence of wind or no wind. The ventilation model will be validated by experiments.

Mathematical Formulation

Fabric-covered cylinders provide a convenient geometry to provide, with sufficient accuracy, the ventilation rates under different situations. Figures 1(*a*)–1(*c*) depict the schematic of the physical domain of a limb-fabric moving system where an enclosed microclimate air layer annulus of thickness $Y(x,\theta,t)$ and length L separates the outer cylindrical porous fabric boundary of radius R_f and the human limb skin of radius R_s. The domain at $x=0$ is open to the atmosphere (loose clothing openings) and at $x=L$ is closed (tight joint). The mean air layer thickness is Y_m $(=R_f-R_s)$. The angular position of the inner cylinder is donated by ϕ. The motion of a clothed swinging limb during walking is described in two phases. Starting from a concentric position of the clothed limb $(\phi=0)$, it swings at angular velocity $\dot{\phi}$ within the cylindrical fabric boundary changing the microclimate air thickness in time and space until the limb touches the fabric at $x=0$ with the contact angle ϕ_{contact} given by

$$\phi_{\text{contact}} = \tan^{-1}\frac{Y_m}{L} \tag{1}$$

and both the inner limb and the clothing boundary move together to the maximum swing angle $\phi_{\max}$ and return together to detach again $\phi=\phi_{\text{contact}}$ as the limb swings in the other direction. The no touch Phase I of the motion could be of small duration compared to the local touch Phase II duration depending on the air layer mean thickness, frequency, and swing amplitude. During phase II, the air layer thickness does not change in time and its variation in space remains the same as that reached at the end of the noncontact interval. The modeling of the ventilation rates in the air layer depends on the representation of the air layer thickness as a function of space and time during the different phases of the motion. A sinusoidal angular position ϕ can be assumed for the swinging motion of the limb at rotational speed ω related to the frequency of motion $f(\omega=2\pi ft)$. The angular position ϕ and angular velocity $\dot{\phi}$ are given by

$$\phi = \phi_{\max}\sin(\omega t) \tag{2a}$$

$$\dot{\phi} = \phi_{\max}\omega\cos(\omega t) \tag{2b}$$

During the noncontact interval (Phase I) of the motion, the air layer thickness Y at any spatial position is given by [6]

$$Y(x,\theta,t) = Y_m - (L-x)\tan\phi\cos\theta \tag{3}$$

The noncontact interval duration is constrained by the condition that

$$-\phi_{\text{contact}} \le \phi \le +\phi_{\text{contact}} \quad \text{or} \quad 0 \le Y(x=0,\theta=0 \text{ or } \pi) \le 2Y_m \tag{4}$$

A dimensionless amplitude parameter ζ can be defined at the opening $x=0$ as

$$\zeta = \frac{\tan\phi_{\max}}{\tan\phi_{\text{contact}}} \tag{5}$$

If the amplitude parameter is smaller than unity $(\zeta<1)$, then no skin-fabric contact is present and air layer thickness is calculated from Eq. (3). When $\zeta\geqslant 1$, the fabric-skin contact is present locally at $x=0$ and $\theta=0$ or π. The air layer thickness Y_{contact} during contact interval does not vary with time and is given by

$$Y_{\text{contact}}(x,\theta) = Y_m - (L-x)\tan\phi_{\text{contact}}\cos\theta, \quad \zeta \ge 1 \tag{6}$$

Air renewal in Phase I is induced by changing gap width that forces skin adjacent air in and out of the microclimate. Air renewal in Phase II is similar to the situation of a clothed cylinder subject to external wind. The relative crosswind V_∞ around the clothed limb is given by

$$V_\infty = V_w\cos\phi \pm \dot{\phi}(L-x) \tag{7}$$

where V_w is the freestream wind. Radial flow through the fabric is governed by the pressure difference between the external fabric adjacent air layer pressure and the internal microclimate pressure. The external pressure distribution around a clothed limb is instrumental in determining air renewal rates in the microclimate separating the skin and the fabric. The major assumptions in our ventilation model for low to medium permeability fabric are as follows.

(1) The external angular pressure distribution around the clothed cylinder is not influenced by the presence of the clothing cover as can be deduced from studies on flow around cylinders sheathed by clothing. Kind et al. [7] reported wind tunnel experimental measurements of static pressures on a clothed cylinder surface and on the inside surface of the sheath covering the cylinder at Reynolds numbers ranging from 55,000 to 170,000. The small quantities of air infiltrating/exfiltrating through the sheath over its upstream/downstream regions did not substantially affect the external flow pattern. Sobera et al. [8] reported similar findings for cylinders covered with low permeability fabrics and placed in cross flow at Reynolds numbers varying between 3900 and 35,000. Watanabe et al. [9] reported that the velocity distribution around the clothed cylinder was hardly influenced by clothing except for the shift of the separation point for fabric permeability of order 10^{-10} m^2.
(2) Internal airflow within the clothing microclimate is laminar. Gibson [10] reported computational fluid dynamics (CFD) simulation results that show, for a given external air velocity, the amount of air that flows around the body and the amount of air that penetrates through the clothing layer are determined by the air permeability of the clothing layer and that the flow inside the microclimate is laminar for low and medium permeability fabrics. Sobera et al. [11] reported that the flow underneath the clothing is laminar and periodic with a magnitude much smaller than the freestream velocity.
(3) The unsteadiness due to the effect of periodic swinging

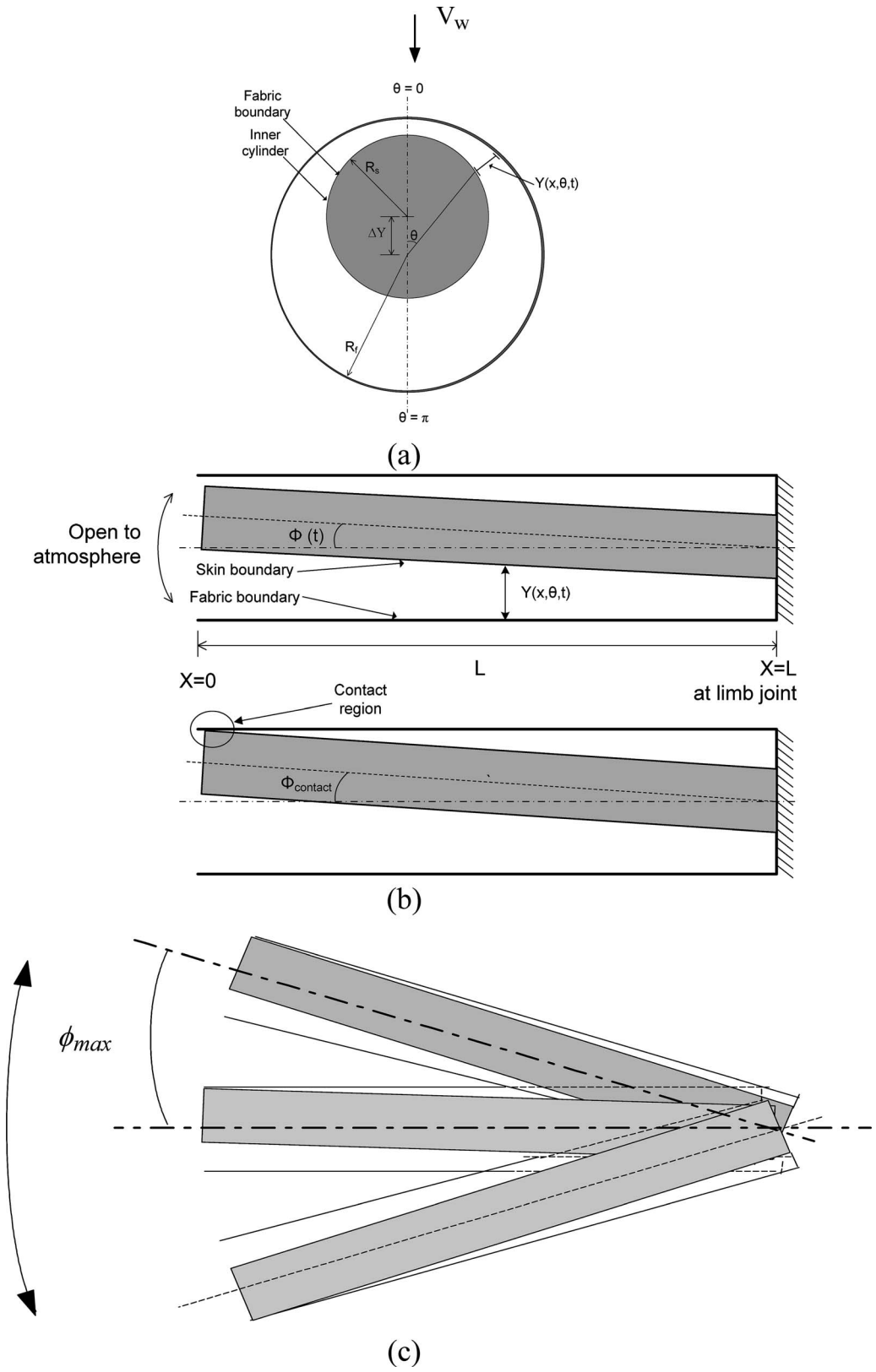

Fig. 1 Representation of the human limb motion inside the clothing cylinder showing (*a*) front view of the geometry, (*b*) side view of the geometry, and (*c*) swinging motion

motion of the cylinder with respect to the environment is negligible and the external flow can be assumed quasisteady. Iwai et al. [12] reported that at small amplitudes all related phenomena to periodic flow around a cylinder can be assumed quasisteady when flow velocity changes slowly. Guilmineau and Queutey [13] characterized peri-

odic oscillating flow over a circular cylinder in a fluid at rest by the Reynolds number, $\mathrm{Re}=V_m D/\nu$, where V_m is the maximum oscillatory velocity, and the Keulegan–Carpenter number, $\mathrm{KC}=V_m/f_e D$ where f_e is the frequency of the oscillatory flow. Sarpkaya [14] reported that at KC values below 2, depending on Re, the flow is symmetrical and attached. For values of KC between 2 and 4, the flow separates and remains attached.

The fabric considered in this study is a cotton fabric of intrinsic permeability 6.7×10^{-10} m^2. The parameter KC for walking human thigh falls in the range 1.6–2.6 and the range of Reynolds number based on the walking speed is between 10^4 and 2.5×10^5. With walking parameter range of KC and Re, it is acceptable to assume quasisteady flow. Mass balance equations of the microclimate air layer will be developed in both phases of limb motion and will be reduced to pressure equations assuming laminar flow in axial and angular directions while lumping the air layer in the radial direction.

Air Layer Mass Balance in Phase I of Limb Motion. The microclimate air layer is formulated as an incompressible lumped layer in the radial direction. During the noncontact time interval of the motion, the general air layer mass balance of Ghaddar et al. [5] is given by

$$\frac{\partial(\rho_a Y)}{\partial t}=-\dot{m}_{aY}-\frac{\partial(Y\dot{m}_{ax})}{\partial x}-\frac{\partial(Y\dot{m}_{a\theta})}{R_f\partial\theta} \tag{8a}$$

where $\dot{m}_{ax}$ is the mass flux in the axial direction in kg/m^2 s, $\dot{m}_{a\theta}$ is the mass flux in the angular direction, and $\dot{m}_{aY}$ is the radial airflow rate through the fabric given by

$$\dot{m}_{aY}=\frac{\alpha\rho_a}{\Delta P_m}(P_a-P_s) \tag{8b}$$

where α is the fabric air permeability in m^3/m^2 s, $\Delta P_m=0.1245$ kPa from standard tests on fabrics' air permeability [15], P_a is the air pressure in the microclimate trapped air layer (kPa), and P_s is the external adjacent air layer pressure (kPa). The external air pressure is assumed uniform at the environment conditions at P_∞ when no external wind is present and the radial airflow is only induced by the limb motion with respect to the fabric boundary.

The boundary conditions for the airflow are

$$\dot{m}_{ax}(x=0,\theta)=C_D\left[\frac{2\rho_a}{|P_L-P_\infty|}\right]^{1/2}[P_\infty-P_L]\quad\text{and}$$

$$\dot{m}_{ax}(x=L,\theta)=0 \tag{8c}$$

$$\dot{m}_{a\theta}(x,\theta=0)=0\quad\text{and}\quad\dot{m}_{a\theta}(x,\theta=\pi)=0 \tag{8d}$$

where Eq. (8*d*) is derived from the pressure drop at the opening by applying Bernoulli's equation from P_∞ in the far environment ($x\to-\infty$) to the opening at $x=0$, and C_D is the discharge loss coefficient at the aperture of the domain dependent on the discharge area ratio of the aperture to the air layer thickness Y. In case wind is present, the dynamic pressure term is added to P_∞ to give the environment total pressure. The key to solving for the ventilation rates during the noncontact interval of the motion cycle is to correlate the mass flow rates to the driving pressure differences in the three directions. The 3D cylinder model of Ghaddar et al. [5] is used to estimate the ventilation rates where the mass balance equation on the air layer is transformed to a scalar pressure equation that can be solved numerically to calculate the pressure at any spatial location within the air layer as a function of time. The method of solving for the pressure distribution for the case when the fabric is not in contact with the skin during the periodic motion of the inner cylinder can be found in detail in the work of Ghaddar et al. [5].

Air Layer Mass Conservation in Phase II of Limb-Clothing Motion. In this phase, both the limb and fabric move together without any change in the air layer thickness Y_{contact}. However, ventilation flow rates in the air layer are not zero due to pressure differences driven by the clothed limb motion relative to the environment air and wind if present. Assuming a Poiseuille flow model in the axial and angular directions (neglecting the fluid inertia associated with flow modulation), the mass balance yields the following pressure equation:

$$0=-\frac{\alpha(P_s(t)-P_a)}{\Delta P_m}-\frac{\partial}{\partial x}\left(\frac{Y^3}{12\mu}\frac{\partial p}{\partial x}\right)-\frac{\partial}{R_s^2\partial\theta}\left(\frac{Y^3}{12\mu}\frac{\partial p}{\partial\theta}\right) \tag{9}$$

where P_s is the external adjacent air layer pressure at the fabric surface (kPa). The same boundary conditions in Eqs. (8*c*) and (8*d*) apply to the mass balance. The external fabric pressure that drives the radial flow is assumed to be the same pressure distribution that results from a flow around a circular cylinder at flow condition V_∞. To solve the pressure equation, the time-dependent external pressure distribution around the clothed cylinder must be known as a function of angular and axial positions. A curve fit is derived from the data of Fransson et al. [16] on the pressure coefficient, $C_p=(P_s-P_\infty)/(0.5\rho_a V_\infty^2)$, distribution around a circular cylinder with suction or blowing at radial velocity ratio of $\Gamma=V_Y/V_\infty$ smaller than 6%.

Solving for the pressure distribution in the microclimate layer would provide the basis for estimating the ventilation rates for any general movement of the clothed body element and wind conditions. A finite difference method is used to discretize the pressure equation and solve for the internal pressure distribution as a function of position and time. Note that the external pressure distribution P_s in Phase I is constant and the time dependence of the microclimate pressure stems from the air layer thickness change due to the limb motion while in Phase II the microclimate pressure time dependence is due to external pressure P_s change in time.

Definition of Microclimate Ventilation Rates. The total ventilation rate is calculated as the positive flow of air into the microclimate integrated over the oscillation period (τ) per unit area of the clothed surface as follows:

$$\dot{m}_a=\frac{1}{2\pi RL\tau}\int_o^\tau\int_0^L\int_0^{2\pi}\max(0,\dot{m}_{aY})Rd\theta dxdt \tag{10a}$$

In the above integral, $\dot{m}_{aY}$ is equated to zero every time it is negative (flowing out of the microclimate). The net flow of air over one period is zero. The ventilation rate inflow to the microclimate air layer through the open aperture per unit area of clothed surface during the period of motion is calculated as

$$\dot{m}_o=\frac{1}{2\pi RL\tau}\int_0^\tau\int_0^{2\pi}\max(0,\dot{m}_{ax(x=0)})Y(\theta,x=0,t)Rd\theta dt$$

$$(\text{kg/s m}^2) \tag{10b}$$

where $\dot{m}_o$ is net flow rate through the open aperture.

The steady periodic ventilation rates can be used in the water vapor mass and energy balances of the microclimate air layer during contact and noncontact intervals to predict the associated heat loss from the limb [17–21].

Experimental Methodology

This section presents the experimental setup used for measuring the microclimate ventilation rates of a swinging limb in stagnant air and in uniform crosswind. Untreated cotton of permeability of 0.05 m^3/m^2 s was chosen as a representative of most common worn fabric. The cotton was obtained from Test fabrics Inc. (Middlesex, NJ), and is made of unmercerized cotton duck, Style No. 466 of thickness of 1 mm.

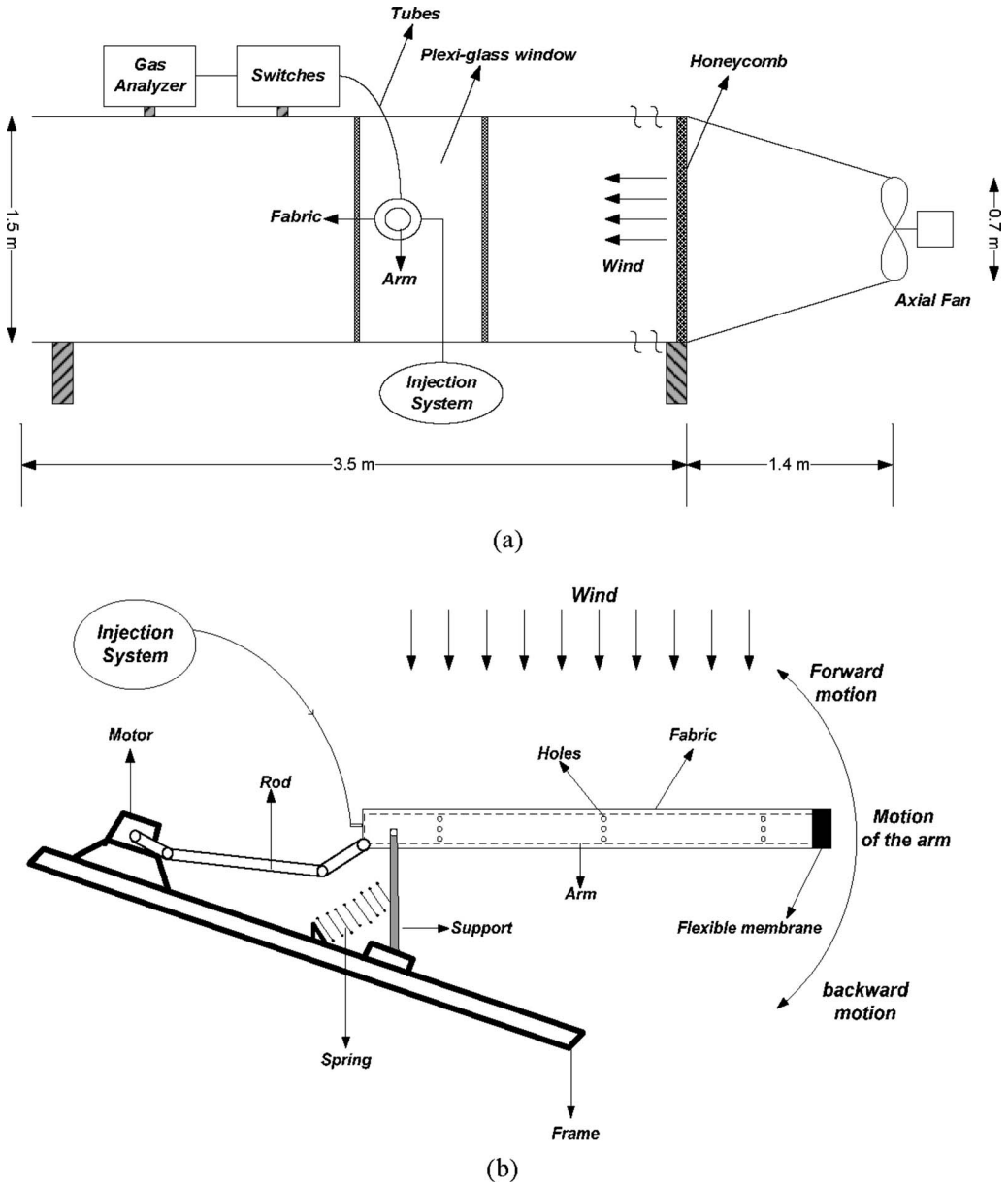

Fig. 2 A plot of (*a*) low speed wind tunnel and test section and (*b*) the swinging limb mechanism and location of measurements in a top view

The uniform crosswind experiments over the clothed swinging cylinder were conducted using a low speed wind tunnel shown in Fig. 2(*a*). The wind tunnel uses a blow type variable speed three-phase axial fan of 0.7 m diameter and peak power of 1.6 kW. The square test cross-sectional dimensions were 1.5×1.5 m^2. A Plexi-glass window was used on one side of the tunnel to observe the experiment. In order to obtain uniform velocity profile inside the tunnel, a porous metal screen was used as a flow straightener after the tunnel diffuser section. The uniform wind provided in the wind tunnel ranged from 2 m/s to 6 m/s giving a Reynolds number range from 16,000 to 40,000 based on the limb diameter. The spatial variation in the freestream velocity in the wind tunnel cross section was measured using hotwire anemometry system and was found to vary within 4% of its spatially averaged value within the cross section, and the turbulence intensity was 2–3%. The no wind experiments were performed in a climatic chamber at temperature $T_\infty = 25 \pm 0.5\,^\circ$C and relative humidity of $(50 \pm 2)\%$ [5]. Figure 2(*b*) shows a schematic of the swinging clothed limb experimental mechanism that was used in both the no-wind experiments in the climatic chamber and in the crosswind experiments in the test section of the wind tunnel. The experimental setup is placed such that the limb swings in a horizontal plane in all experiments. The swinging clothed limb setup consisted of: (i) a polyvinyl chloride (PVC) hollow inner cylinder with a diameter of 0.078 m and a length 0.6 m; (ii) an outer 0.48 m long and 0.115 m diameter cylinder made of a thin metallic screen of 2 cm open squares where the cotton fabric is wrapped around and fitted; (iii) a 12 V dc motor that drives the periodic rotational motion of the inner cylinder by means of a three-bar mechanism; (iv) a spring, which is fixed on the frame behind the rod to control the motion of the outer cylinder; (v) support platform; and (vi) flexible impermeable plastic membranes. The concentric cylinders are fixed at one end to the frame. The frequency of the inner rod oscillation ranged from 40 rpm to 80 rpm and is controlled by the speed of the motor. This is achieved by varying the voltage supply to the motor. The motion of the inner cylinder drives the motion of the outer cylinder when touch takes place at the free end and both rotate together to reach a maximum angle rotation angle of $\phi_{\max}$

=20 deg and ϕ_{contact}=2.2 deg. The free end of the outer cylinder is capped with a flexible impermeable plastic membrane to prevent air leaks from the aperture. For open aperture experiments, this membrane will be removed.

To mimic the actual swinging clothed human arm (see Figs. 1 and 2(*b*)), the spring is designed such that it controls the touch intervals of the fabric and cylinder. During forward motion of both cylinders, the outer cylinder remains in touch with the inner cylinder until the outer cylinder reaches the midhorizontal position. During the backward motion of both cylinders from the furthest position, the spring forces the outer cylinder to stay in touch with the inner cylinder at the free end until the outer cylinder is back to the midposition. The touch period fraction of the cycle (joint motion of both limb and clothing cover) is determined by recording the cylinders' motion by a high speed digital camera (100 frames/cycle) and counting the frames when both cylinders are in touch.

The microclimate ventilation rate is measured using tracer gas method for closed and open apertures. The tracer gas method is used as described by Havenith et al. [2]. The gas chosen must have a density that is close to that of air. This is to ensure that we will have no stratification. The measurements are done by radially injecting an inert gas (N_2) at a fixed rate through nozzles placed at holes drilled in the inner cylinder surface, as shown in Fig. 2(*b*). The concentration of the oxygen gas is measured in the air gap at different angular and axial locations using a standard exhaust gas analyzer (Emissions Systems INC, EMS Model 4001). Ten small diameter (5 mm) flexible tubings with end probes, to draw air samples, are positioned in two axial locations (five probes for each axial position distributed uniformly around the circumference) at $x=0.3L$ and $0.66L$ of the limb from the fixed end. The probes draw samples of air from a radial distance of 4 mm in the air layer away from the fabric outer cylinder. A switch board is designed to draw air sample for O_2 concentration measurements for different locations by switching from one tubing-probe system to the other without interfering with the airflow around the arm. The gas analyzer measurements have an accuracy of $\pm 0.05\%$ of volume of O_2 of air sample. The nitrogen gas is injected by a flow regulator that injects nitrogen into the air layer in the range 0.1–1.5 liter/min from a pressurized nitrogen vessel with precision of ± 0.01 liter/min. The standard air sample composition by volume is 79% N_2 and 21% O_2. To obtain the concentration of N_2 in the microclimate, the recorded concentration of O_2 is deducted from the 100%. The total volume flow rate renewal can be calculated from the trace gas mass flux Ψ_{tr} (m^3/s), and the measured concentrations C_a (m^3 O_2/m^3 air) and C_∞ (m^3 O_2/m^3 air) at inner and outer locations, respectively, as

$$\frac{\overline{\dot{m}_a}}{\rho_a}[C_\infty - C_a] + \psi_{\text{tr}} = 0 \tag{11}$$

The lab, where the wind tunnel experiments were performed, was well ventilated and the environmental chamber air was refreshed frequently between experiments to prevent nitrogen concentration buildup in the chamber. The actual uncertainty in the determination of the experimental ventilation mass flow rate $\overline{\dot{m}_a}$ can be found from the uncertainties in the injection rate Ψ_{tr} and measured concentrations C_a and C_∞ as

$$\Delta\overline{\dot{m}_a} = \pm \sqrt{\left[\left[\frac{\partial\overline{\dot{m}_a}}{\partial\psi_{\text{tr}}}\Delta\psi_{\text{tr}}\right]^2 + \left[\frac{\partial\overline{\dot{m}_a}}{\partial C_\infty}\Delta C_\infty\right]^2 + \left[\frac{\partial\overline{\dot{m}_a}}{\partial C_a}\Delta C_a\right]^2\right]} \tag{12}$$

Closed and open aperture experiments are conducted for 40 rpm, 60 rpm, and 80 rpm. The motion is maintained for at least 1 h before a steady injection of the N_2 through the holes of the inner cylinder was started. Steady conditions were reached after 1 h from the onset of N_2 injection. Data were recorded then every 10 min. The experiments were repeated at different N_2 injection rates to check the homogeneity of the calculated N_2 concentration inside the annulus and repeatability of the O_2 concentration measurements. A value of 0.5 liter/min was selected to conduct all the measurements. The actual uncertainty in $\Delta\overline{\dot{m}_a}$ in the range of reported experimental values of the ventilation mass flow rate (0.5–5 g/s) was found to be less than ± 0.02 g/s.

Results and Discussion

This section presents computational and experimental results, and is divided into two subsections. The first subsection is concerned with microclimate ventilation model validation with experiments and with published empirical correlations. The second is concerned with a parametric study of the separate effects of wind and swinging motion and their combined effect on ventilation of clothed limb with open and closed apertures.

Model Validation

Model Validation by Experiments. In literature, experimental data on ventilation apply for whole body ensembles. Current experimental data and model are an attempt to measure and predict ventilation for a single limb subject to swinging motion. For the covered cylinder, comparisons have been performed for open and closed aperture clothed cylinders swinging at frequencies ranging from 40 rpm to 80 rpm.

Figure 3 shows a plot of the model predictions and experimentally obtained ventilation rates for closed aperture case at different crosswind speeds as a function of the frequency domain length of 0.48 m, Y_m=0.0185 m, and $\phi_{\max}$=20 deg. Figure 4 shows a plot of the model predictions and experimentally obtained ventilation rates for the open aperture case at different crosswind speeds as a function of the frequency domain length of 0.48 m, Y_m =0.0185 m, and $\phi_{\max}$=20 deg. The agreement of the model improves significantly at higher frequencies for both open and closed aperture experiments. The mean percent error of the measurements compared with the predicted values of the model was less than 6.7% at high frequencies for both closed and open apertures. The large error at the low frequency of oscillation is due to the decrease in the homogeneity of nitrogen concentration at the different angular positions increasing the averaging error of the five readings. The microclimate flow at low frequency is laminar and is very small and the discrepancy occurs in a range that is not within typical gait where minimum walking speed reported in literature [22] was 0.9 m/s corresponding to low walking speed at swinging frequency between 55 rpm and 60 rpm depending on the stride length and number of walking steps per minute.

Model Validation With Published Empirical Correlations. Simulations are performed using our ventilation model for the case of wind 2D flow over a cylinder covered with clothing at fixed microclimate thickness and predictions of normal flow to the fabric and tangential flow around the limb are compared with the experimental data of Sobera et al. [8]. Sobera et al. [8] presented experimental results of the tangential and radial velocity components through a porous layer sheathing a cylinder subject to wind as a function of the angular coordinate θ. For $\theta < 50$ deg and $\theta > 315$ deg the radial velocity component is positive, indicating that air penetrates the outer porous cylinder in the upstream region. The tangential velocity component inside the air gap was found to have a maximal value at $\theta \approx 50$ deg. The bulk tangential velocity is nondimensionalized with respect to V_w, the Darcy number Da, and the clothing thickness ratio Ic=fabric thickness/gap thickness. Figure 5(*a*) presents a plot of the dimensionless tangential velocity components predicted by the current model and reported results of Sobera et al. [8] at R_s=0.038 m, R_f =0.0575 m, α=0.05 m/s, external wind of 1 m/s (Re=10,000), and $\text{Da}Ic = 6.2\times10^{-4}$ for the type of fabric used in our experiments. Figure 5(*b*) shows dimensionless pressure difference between the outer surface and the predicted microclimate pressure as

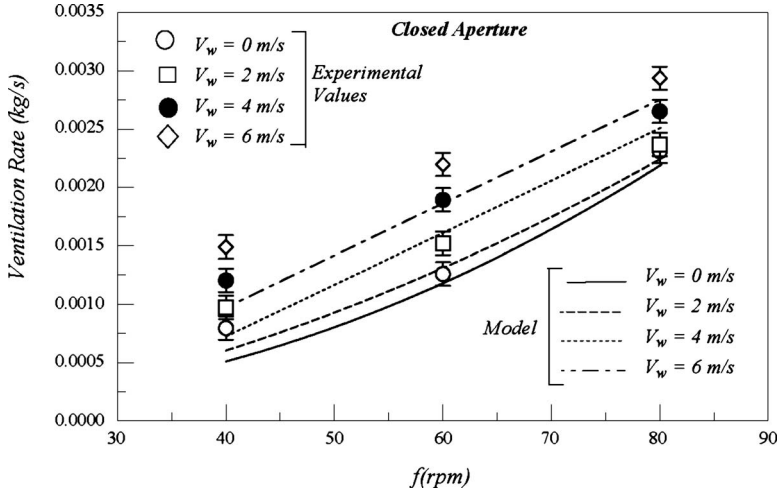

Fig. 3 A plot of the model predictions and experimentally estimated ventilation rates for closed aperture at different crosswind speeds as a function of the frequency for a domain length of 0.48 m, Y_m=0.0185 m, and ϕ_{max} =20 deg

a function of θ and the reported results of Sobera et al. [8]. The predicted microclimate pressure and tangential velocity agree well with the data of Sobera et al. [8] obtained for flow around clothed cylinders.

Effect of Wind and Swinging Motion on Ventilation. During walking, ventilation mechanism is dependent on the specific motion of the clothed body segment. Microclimate clothing ventilation in stagnant environment for open or closed apertures could be determined from uniform relative wind (walking speed) around a fixed clothed cylinder (trunk) and swinging motion of a clothed cylinder at small and large swinging angles (limbs). If walking or activity takes place in the presence of wind, then the limbs will be subjected to a combined effect of wind and swinging motions. It is of interest to recognize the dominant mechanism of ventilation at various frequencies and amplitudes of motion and wind conditions. The ventilation rate is the sum of the ventilation rate during the no-touch period (limb displacement with respect to clothing) and that during the touch period (limb and clothing move together).

Table 1 shows the percentage of the ventilation of each period for closed aperture at wind speeds of 1 m/s and 3 m/s during one cycle at R_s=0.038 m, R_f=0.0575 m, α=0.05 m/s, ϕ_{max}=20 deg, and L=0.48 m. During the no-touch period the variation in the air gap thickness creates a high difference pressure between the air gap layer and the atmosphere so the majority of the ventilation rate is found during the no-touch period because of the high pressure difference across the fabric. As the wind speed increases, the fraction of the touch period increases because higher pressure difference is created between the outer clothing surface and the microclimate surface causing higher ventilation rate during the touch interval. At low frequencies, it is obvious that the wind speed has a larger contribution to the total ventilation rate due to the low ventilation rate induced by a smaller dY/dt term.

Figures 6(a) and 6(b) show the total ventilation rates $\dot{m}_a$ and $\dot{m}_a+\dot{m}_o$ as a function of swinging frequency f at different wind speeds for (a) closed aperture and (b) open aperture, respectively,

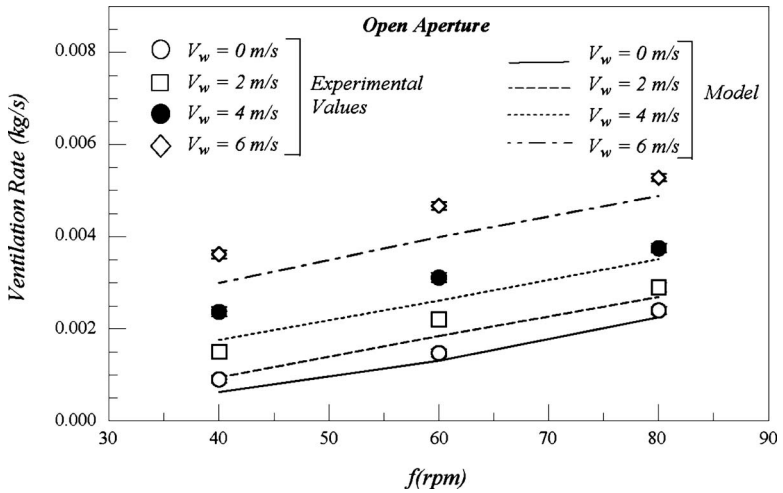

Fig. 4 A plot of the model predictions and experimentally estimated ventilation rates for open aperture at different cross wind speeds as a function of the frequency for a domain length of 0.48 m, Y_m=0.0185 m, and ϕ_{max} =20 deg

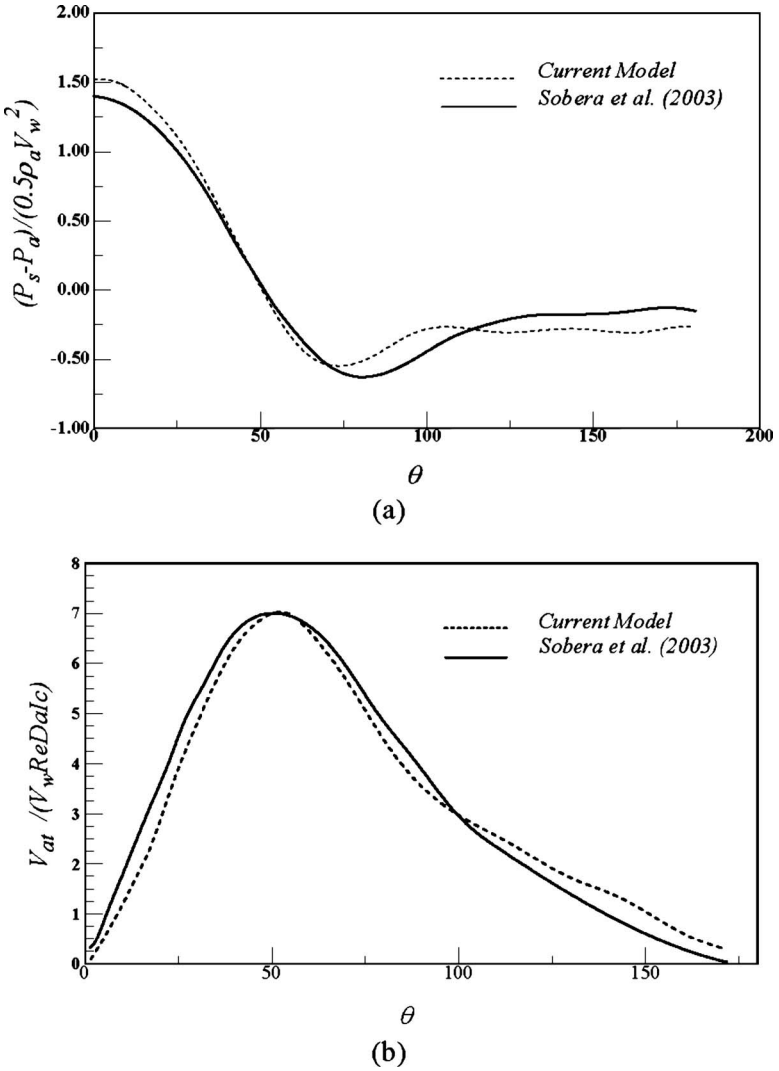

Fig. 5 A plot of the microclimate (*a*) dimensionless tangential velocity component and (*b*) dimensionless pressure difference between the outer surface and inner microclimate pressure as predicted by the current model as a function of θ and the reported results of Sobera et al. [8]

for the values of R_s=0.038 m, R_f=0.0575 m, α=0.05 m/s, $\phi_{\max}$ =20 deg, and L=0.48 m. The ventilation increases with increase in swinging frequency. For wind speeds greater than 2 m/s, a greater increase in ventilation rate is observed due to higher driving pressure difference between the outer clothing surface pressure caused by the wind and the clothing microclimate pressure. The effect of the wind speed is important at low frequencies where at f=10 rpm and wind speed of 3 m/s the ventilation rate is about five times that at wind speed of 1 m/s.

Table 1 The percentage of the ventilation of each period for closed aperture at wind speeds of 1 m/s and 3 m/s during one cycle at R_s=0.038 m, R_f=0.0575 m, α=0.05 m/s, $\phi_{\max}$=20 deg and L=0.48 m

f (rpm)	Fraction of $\dot{m}_a$ No-touch interval (%)	Fraction of $\dot{m}_a$ Touch interval (%)	$\dot{m}_a$ (kg/s m^2) During one period
	Wind at V_w=1 m/s		
80	99.16	0.84	1.55×10^{-05}
40	97.20	2.80	7.03×10^{-05}
25	91.01	8.99	2.48×10^{-04}
10	60.59	39.41	1.10×10^{-03}
	Wind at V_w=3 m/s		
80	95.13	4.87	6.50×10^{-05}
40	81.25	18.75	1.19×10^{-04}
25	52.88	47.12	2.97×10^{-04}
10	15.75	84.25	1.15×10^{-03}

The effect of the ratio of microclimate layer thickness to inner limb radius Y_m/R_s on ventilation rate at fixed clothing permeability for closed aperture is shown in Fig. 7 at V_w=1 m/s for R_s =0.038 m, R_f=0.0575 m, α=0.05 m/ for f=0 rpm, 40 rpm, and 80 rpm and L=0.48 m. The total ventilation $\dot{m}_a$ increases with increased microclimate size Y_m/R_s due to less flow resistance in the microclimate air layer angular and axial directions.

The effect of the swing amplitude for closed aperture on ventilation rate is shown in Fig. 8, where $\dot{m}_a$ is plotted against $\phi_{\max}$ for different ventilation frequencies at V_w=1 m/s. The ventilation rate decreases with increased frequency. However, at high frequency, the ventilation rate decreases with $\phi_{\max}$ until $\phi_{\max}$ =18 deg and then increases. This behavior is connected to the percentage of time the limb is in touch with the fabric with fixed gap width. At low maximum swing angle, the ventilation rate is

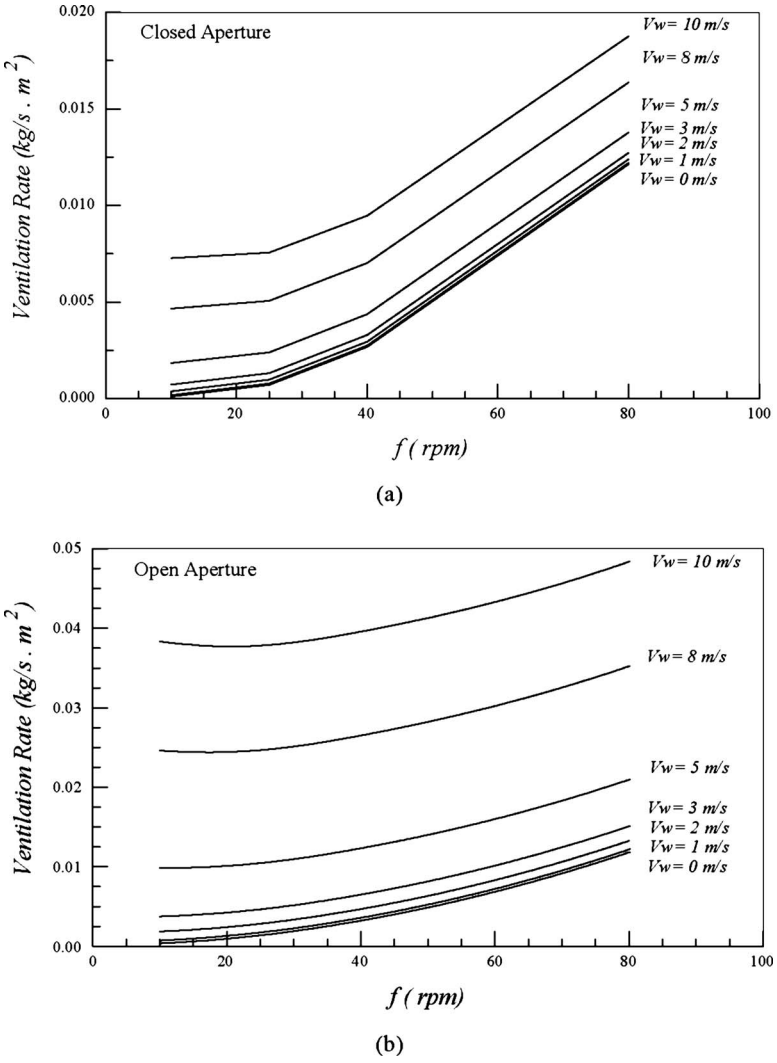

Fig. 6 A plot of ventilation rate as a function of swinging frequency f in rpm at different wind speeds for (*a*) closed aperture and (*b*) open aperture at R_s=0.038 m, R_f=0.0575 m, α=0.05 m/s, ϕ_{max}=20 deg, and L=0.48 m

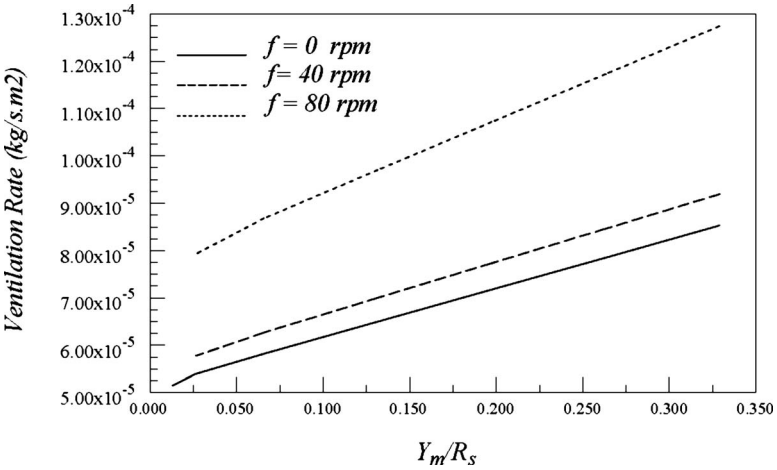

Fig. 7 The effect of the ratio of microclimate layer thickness to inner limb radius Y_m/R_s on ventilation rate for closed aperture is shown at V_w=1 m/s for R_s=0.038 m, R_f=0.0575 m, α=0.05 m/s, L=0.48 m, and f=0 rpm, 40 rpm, and 80 rpm

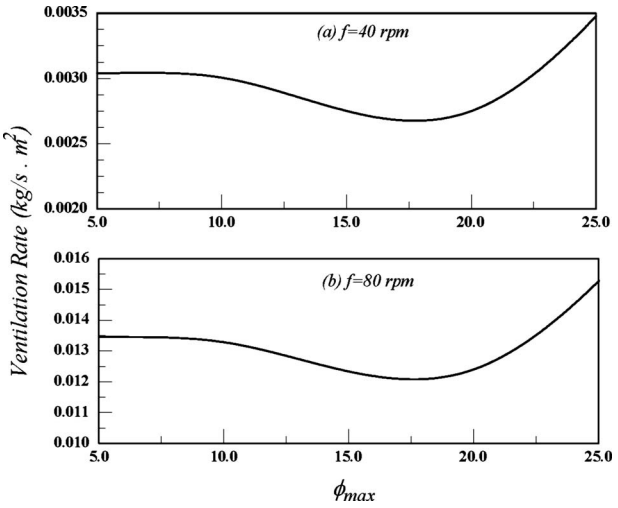

Fig. 8 A plot of $\dot{m}_a$ versus $\phi_{\max}$ at V_w=1 m/s for (*a*) *f*=40 rpm and (*b*) *f*=80 rpm

governed mainly by the rate of change of the microclimate size (dY/dt), which induces higher ventilation than during the touch interval. At high angles of swing, the amplitude of motion is high giving higher relative wind and the touch period governs the ventilation mechanism where the renewal is due to external flow around a clothed cylinder with fixed gap ($dY/dt=0$). These two opposing trends cause a minimum ventilation to occur close to $\phi_{\max}=18$ deg.

The above analysis improves our understanding of local ventilation of clothed body segments and could be a first step towards building the whole clothed body ventilation model from segments' ventilation using first principles. The whole clothed body ventilation could be predicted if appropriate connectivity boundary conditions are imposed at the clothing/segment interfaces. This will be addressed in future work.

Conclusions

A model derived from conservation laws has been developed to estimate the ventilation rates for any limb motion configuration taking into consideration the periodic motion of the limbs and clothing, their geometric interaction at skin-fabric contact or no contact for open or closed apertures, and in the presence of wind.

The ventilation rates predicted by the model on a swinging covered cylinder agreed well with experiments conducted at no wind. It is found that ventilation rate increases with the swinging frequency. For wind speeds greater than 2 m/s, the increase in the ventilation rate is substantial. The effect of the wind speed is very important at low frequencies. The ventilation rates by wind and motion are additive at low wind speeds, but deviate at higher wind speeds.

The development of the ventilation model from first conservation principles is very important to create an effective tool for designing protective clothing and predicting their thermal performance for active persons.

Acknowledgment

The financial support of the Lebanese National Council for Scientific Research and of the Qatar Chair in Energy Studies Endowment Fund is greatly acknowledged.

Nomenclature

Da = Darcy number
Ic = clothing thickness ratio=fabric thickness/gap thickness
f = frequency of oscillation of the inner cylinder in rpm
C_D = opening discharge coefficient
KC = Keulegan–Carpenter number
L = fabric length in x-direction (m)
$\dot{m}_{aY}$ = mass flow rate of air in y-direction (kg/m^2 s)
$\dot{m}_{ax}$ = mass flow rate of air in x-direction (kg/m^2 s)
$\dot{m}_{a\theta}$ = mass flow rate of air in θ-direction (kg/m^2 s)
P_a = air microclimate pressure (kPa)
P_s = external pressure on the surface of the clothed cylinder (kPa)
R_f = fabric cylinder radius (m)
R_s = skin cylinder radius (m)
Re = Reynolds number
t = time (s)
Y = instantaneous air layer thickness (m)
Y_m = mean air layer thickness (m)
Y_{contact} = air layer thickness during interval of touch (m)
V = velocity (m/s)

Greek Symbols

α = fabric air permeability (m^3/m^2 s)
ϕ = angular position of the inner cylinder with respect to the axial direction
$\phi_{\max}$ = maximum angular position
ϕ_{contact} = contact angle
Γ = radial velocity ratio of $\Gamma=V_Y/V_\infty$
ν = kinematic viscosity (m^2/s)
ω = angular frequency (rad/s)
ρ = density (Kg/m^3)
τ = period of the oscillatory motion (s)
θ = angular coordinate
μ = air viscosity (N s/m)

Subscripts

a = conditions of air in the spacing between skin and fabric
o = opening
w = external wind
∞ = environment condition

References

[1] ISO 7730:2005: Ergonomics of the thermal environment—Analytical determination and interpretation of thermal comfort using calculation of the PMV and PPD indices and local thermal comfort criteria.
[2] Havenith, G., Heus, R., and Lotens, W. A., 1990, "Clothing Ventilation, Vapor Resistance and Permeability Index: Changes Due to Posture, Movement, and Wind," Ergonomics, **33**(8), pp. 989–1005.
[3] Lotens, W., 1993, "Heat Transfer From Humans Wearing Clothing," Ph.D. thesis, TNO Institute for Perception, Soesterberg, The Netherlands.
[4] Ghali, K., Ghaddar, N., and Jaroudi, E., 2006, "Heat and Moisture Transport Through the Microclimate Air Annulus of the Clothing-Skin System Under Periodic Motion," ASME J. Heat Transfer, **128**(9), pp. 908–918.
[5] Ghaddar, N., Ghali, K., Harathani, J., and Jaroudi, E., 2005, "Ventilation Rates of Microclimate Air Annulus of the Clothing-Skin System Under Periodic Motion," Int. J. Heat Mass Transfer, **48**(15), pp. 3151–3166.
[6] Jaroudi, E., Ghaddar, N., and Ghali, K., 2006, "Heat and Moisture Transport From a Swinging Limb of a Clothed Walking Human," *Proceedings of the 13th International Heat Transfer Conference*, Australia, Aug. 17–22.
[7] Kind, R. J., Jenkins, J. M., and Seddigh, F., 1991, "Experimental Investigation of Heat Transfer Through Wind-Permeable Clothing," Cold Regions Sci. Technol., **20**, pp. 39–49.
[8] Sobera, M. P., Kleijn, C. R., Brasser, P., and Van den Akker, H. E. A., 2003, "Convective Heat and Mass Transfer to a Cylinder Sheathed by a Porous Layer," AIChE J., **49**, pp. 3018–3028.
[9] Watanabe, T., Kato, T., and Kamata, Y., 1991, "The Velocity Distribution in the Inner Flow Field Around a Clothed Cylinder," Sen'i Gakkaishi, **44**, pp. 271–275.
[10] Gibson, P. W., 1999, "Review of Numerical Modeling of Convection, Diffusion, and Phase Change in Textiles," PVP (Am. Soc. Mech. Eng.), **PVP-397**, pp. 117–126.
[11] Sobera, M. P., Kleijn, C. R., Brasser, P., and Van den Akker, H. E. A., 2006, "Subcritical Flow Past a Circular Cylinder Surrounded by a Porous Layer," Phys. Fluids, **18**, pp. 038106.
[12] Iwai, H., Mambo, T., Yamamoto, N., and Suzui, K., 2004, "Laminar Convec-

tive Heat Transfer From a Circular Cylinder Exposed to a Low Frequency Zero-Mean Velocity Oscillating Flow," Int. J. Heat Mass Transfer, **47**(8), pp. 4659–4672.
[13] Guilmineau, E., and Queutey, P., 2002, "A Numerical Simulation of Vortex Shedding From an Oscillating Circular Cylinder," J. Fluids Struct., **16**(6), pp. 773–794.
[14] Sarpkaya, T., 1986, "Forces on Circular Cylinder in Viscous Oscillatory Flow at Low Keulegan-Carpenter Numbers," J. Fluid Mech., **165**, pp. 61–71.
[15] American Society for Testing and Materials, 1983, ASTM D737-75, Standard Test Method for Air Permeability of Textile Fabrics, (IBR) approved.
[16] Fransson, J. H. M., Konieczny, P., and Alfredsson, P. H., 2004, "Flow Around a Porous Cylinder Subject to Continuous Suction or Blowing," J. Fluids Struct., **19**, pp. 1031–1048.
[17] Ghali, K., Ghaddar, N., and Jones, B., 2002, "Modelling of Heat and Moisture Transport by Periodic Ventilation of Thin Cotton Fibrous Media," Int. J. Heat Mass Transfer, **45**(18), pp. 3703–3714.
[18] Ghaddar, N., Ghali, K., and Jones, B., 2006, "Convection and Ventilation in Fabric Layers," *Thermal and Moisture Transport in Fibrous Materials*, N. Pan and P. Gibson, eds., Woodhead, Cambridge, England and CRC, Boca Raton, FL, Chap. 8, pp. 271–307.
[19] Ghali, K., Ghaddar, N., and Jones, B., 2002, "Empirical Evaluation of Convective Heat and Moisture Transport Coefficients in Porous Cotton Medium," ASME J. Heat Transfer, **124**(3), pp. 530–537.
[20] Ghaddar, N., Ghali, K., and Harathani, J., 2005, "Modulated Air Layer Heat and Moisture Transport by Ventilation and Diffusion From Clothing With Open Aperture," ASME J. Heat Transfer, **127**(3), pp. 287–297.
[21] Danielsson, U., 1993, "Convection Coefficients in Clothing Air Layers," Ph.D. thesis, The Royal Institute of Technology, Stockholm, Sweden.
[22] Emmerik, R. E. A., and Wagenaar, R. C., 1996, "Effects of Walking Velocity on Relative Phase Dynamics in the Trunk in Human Walking," J. Biomech., **29**(9), pp. 1175–1184.

Process Intensification in a "Simulated Moving-Bed" Heat Regenerator

D. S. Murthy[1]
Department of Mechanical Engineering,
Indian Institute of Technology Kanpur,
Uttar Pradesh 208 016, India

S. V. Sivakumar
Department of Chemical Engineering,
Indian Institute of Technology Kanpur,
Uttar Pradesh 208 016, India

Keshav Kant
Department of Mechanical Engineering,
Indian Institute of Technology Kanpur,
Uttar Pradesh 208 016, India

D. P. Rao
Department of Chemical Engineering,
Indian Institute of Technology Kanpur,
Uttar Pradesh 208 016, India

The solid-gas contacting for thermal storage and thermal recovery is generally carried out in fixed-bed regenerators. Compared to a fixed bed, higher thermal recovery can be achieved in a moving bed with countercurrent flow of gas and solids. However, the moving beds have not been widely used due to difficulties in solid handling. The relative movement of the bed to the gas flow can be simulated in a fixed bed by moving the inlet and outlet ports of the gas along the length of the bed. Similar simulated moving beds are already in use for adsorptive separation of liquid mixtures in chemical industries. A novel moving-port system is proposed to achieve simulated moving-bed operation in a fixed bed. We have carried out studies to evaluate the relative performance of the fixed and the simulated moving-bed heat regenerators. We have examined the feasibility of replacing a set of three blast furnaces and thermal regeneration of an adsorption bed with the simulated moving-bed regenerator. It is found that high-heat transfer intensification can be achieved. The results indicate that three blast-furnace stoves can be replaced by a simulated moving-bed regenerator of volume of about 100 times smaller than the stoves. The heat-transfer intensification is high enough to carry out thermal regeneration of the adsorption beds in a cycle time that is in the range of the pressure swing adsorption, which is favored for its faster rate of regeneration. [DOI: 10.1115/1.2927397]

Keywords: regenerator, simulated moving bed, thermal swing adsorption

1 Introduction

Process intensification is attracting attention as it is expected to bring about dramatic improvements by decreasing the equipment size or by increasing the production capacity compared to those commonly used today [1]. In the present work, a novel heat regenerator is proposed in which the thermal recovery or storage rate is one to two orders of magnitude higher than the conventional regenerator.

A vast body of literature dealing both theoretical and experimental studies on heat transfer in fixed-bed regenerators is available. Methods of solution for obtaining temperature profiles in the bed were presented based on the assumption of negligible heat conduction parallel and infinite heat conduction perpendicular to flow direction. Among them, most are based on numerical finite-difference schemes where the periodic-steady-state solution is obtained from initial guesses of the temperature profiles and successive substitution [2–7]. Analytical expressions were obtained for the temperature profiles and effectiveness of regenerative heat exchangers [8,9]. A mathematical model to describe the behavior of the long packed-bed heat regenerator accounting axial dispersion has been presented [10]. Analytical expressions were obtained for the evolving temperature front in terms of the moments of the associated Gaussian distribution. This procedure, though approximate, allows one to account for all the factors that contribute to the spreading of the temperature front due to axial dispersion of gas, film heat transfer, and conduction into the particles. The studies on experimental validation of mathematical models have been reported in Refs. [11,12]. A dynamic process model and solution technique has been developed for the hot blast stove for predicting accurately the temperature and energy content of the stoves during the thermal regenerative cycles [13,14].

Studies on heat transfer between solid and gas in moving beds have been reported in Refs. [15,16]. Analytical expressions for the fluid and solid temperature distributions and heat recovery effectiveness were presented for continuous operation for a single moving bed and two beds coupled by a fluid flow [17]. A dynamic simulation approach has been developed based on two-dimensional schematization and on time-dependent convective-conductive heat transfer [18]. This model could be used for the transient analysis of the moving-bed operation. It could be used as a useful tool in control and optimal design studies.

In a heat regenerator, heat transfer takes place between a hot gas stream and a fixed bed of cold solids and the heat is recovered from the bed by passing a cold gas stream. To make the process continuous, a two-bed configuration is generally used. When a hot gas enters an initially cold bed, a heat-transfer zone is formed and it moves along the bed from one end to the other [10,19]. Thermal equilibrium prevails on both sides of the zone; however, a small temperature difference exists between the solids and the gas within the zone (see Fig. 1). As the heat-transfer zone traverses across the bed, the solids attain the temperature of the gas. The temperature difference in the zone is dictated by the gas velocity, the heat capacities of solids, and their surface area. Because of the small temperature difference in the heat-transfer zone, the heat-transfer rate is low in fixed beds. On the other hand, if the gas velocity is high, the zone length exceeds the length of the bed and the energy storage would be less.

In a moving-bed regenerator, high temperature difference between the gas and the solids along the bed can be maintained in a manner similar to that in a counterflow shell-tube heat exchanger, by controlling the velocities of the gas and the solids. The difference in the solid and gas temperature leads to high heat-transfer

[1]Corresponding author.

Contributed by the Heat Transfer Division of ASME for publication in the JOURNAL OF HEAT TRANSFER. Manuscript received July 23, 2006; final manuscript received April 1, 2008; published online June 18, 2008. Review conducted by Anthony M. Jacobi. Paper presented at the 2004 ASME Heat Transfer/Fluids Engineering Summer Conference (HT-FED2004), Charlotte, NC, July 11–15, 2004.

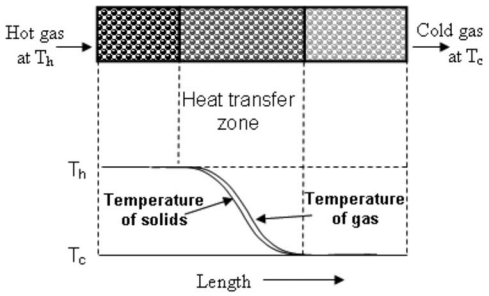

Fig. 1 Temperature front propagation of gas and solid in fixed bed

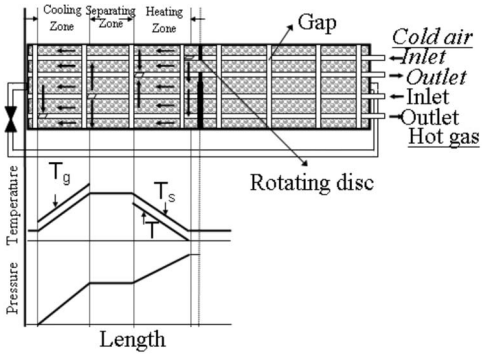

Fig. 3 SMB heat regenerator

rates. Because of the difficulties in handling the solids, the moving beds are not used at present. However, the relative movement between the solids and the gas can be simulated in a fixed bed by moving the gas inlet and outlet ports along the bed. The simulated moving bed (SMB) is already in use for the adsorptive separation processes in Chemical Industries. UOP (Des Plaines, IL) has commercialized the simulated moving-bed adsorbers for separation of liquid mixtures. In these beds, several equispaced ports are provided along the length of the bed for the injection and withdrawal of the liquids. A rotary valve periodically switches the inlet and outlet ports to achieve the simulated moving-bed operation. The use of SMB for heat exchange has not been reported in literature.

A set of three or four blast-furnace stoves is used in the iron and steel industry to exchange heat between the blast-furnace off gases and the cold air fed to the blast furnace. It appears possible to replace the stoves with a single SMB. The process of thermal regeneration of a bed saturated with a gas in the adsorptive separation of a gas mixture is similar to the heat regeneration. The saturated bed is stripped off the gas (regeneration) either by decreasing the pressure or by heating. The latter is not widely used though more economical since it is generally very slow compared to the former [20–22]. However, a SMB could permit a rapid thermal regeneration.

In this work, we have proposed a novel moving-port system to achieve a simulated moving-bed operation for heat exchange between a gas stream and a fixed bed of solids. We assessed the feasibility of replacing a set of three blast-furnace stoves with a single proposed SMB and the rapid thermal regeneration of a bed saturated with a gas.

2 Moving-Port System

Figure 2 shows a sketch of the proposed moving-port system. It consists of two closely fitted concentric tubes. The outer tube has a straight slot and the inner one has a helical slot as shown in the figure. A diamond shaped port is formed at the intersection of the two slots. On rotation of either the inner or the outer tube, the port moves continuously from one end to the other. On reaching the other end, it returns to the end abruptly from where it has started.

The moving-port system could be embedded in a fixed bed of solids to introduce a fluid stream into the bed, or withdraw a fluid stream from the bed. An appropriate gasket has to be provided between the tubes to prevent leakage of the fluid along the slot. The inner tube can be rotated using a stepper motor to move the port at a desired velocity.

3 Simulated Moving-Bed Heat Regenerator

Figure 3 shows a sketch of the proposed regenerator. It consists of a fixed bed of solids in which four moving-port systems are embedded. The cooling and heating zones are formed between the inlet and outlet ports of the hot and cold gas streams. The distance between the ports can be adjusted by rotating the inner tubes of the ports at the start of the operation. The four ports are moved at the same velocity. The pressure at the cold-air inlet is to be maintained higher than the outlet port to ensure the flow of the gas through the bed.

The pressure and temperature profiles are shown in Fig. 3. The gas pressure at the hot gas inlet is such that it is equal to the pressure at the cold-gas outlet port, so that there is no flow through the zone separating the hot and cold zones. The pressure at the hot outlet is maintained at a lower pressure than the hot inlet. For the flow of gas from one end of the bed to the other, a gas return pipeline is provided. To prevent the flow of the hot gas from the hot zone to the cold zone, the valve in the return pipeline is closed. As the zone approaches the far end of the bed, the valve in the gas line is opened and the rotating-disk valve located in the bed is closed to ensure a smooth transfer of the zones from one side of the bed to the other.

A sketch of the rotating-disk valve is shown in Fig. 4. It consists of two circular disks having holes. One of the disks can be rotated about its axis whereas the other is fixed. The passage for

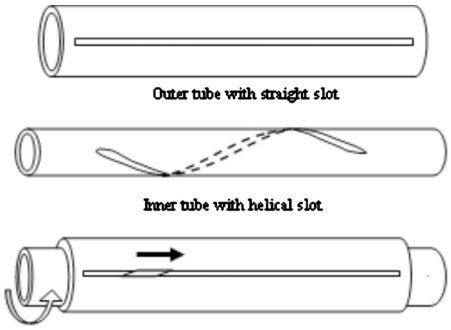

Fig. 2 Moving-port assembly

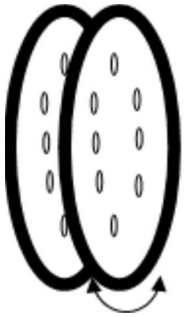

Fig. 4 Sketch of rotating-disk valve

the gas can be closed or open by partial rotation of the disk. Proper slots can be made on the rotating disk at the position of the moving-port tubes to enable it to rotate by a certain angle.

Once both the zones are transferred from one side of the rotating-disk valve to the other, the valve positions are restored to the previous settings. Thus, the heat regeneration can be achieved in a single bed. However, if the mixing of the hot and cold gases is not acceptable, two beds may be used, each embedded with two moving-port systems one each for the injection and the withdrawal of the gas.

The introduction and withdrawal of the gas could be visualized as a point source and as a sink of the gas in the bed, respectively. To attain a uniform flow in the radial direction, it takes some distance from the port. To promote a uniform velocity in the radial direction, the bed could be sectionalized using a high porosity wire-mesh packing, as shown in Fig. 3. An appropriate gap in between the sections promotes the radial flow in the gap and ensures a uniform velocity in the latter sections. In the SMB heat regenerator, the heat-transfer zone extends from the inlet to the outlet ports in both the cooling and the heating zones. A desired temperature difference at the ends can be maintained by controlling the velocity of the ports and the gas velocity. This leads to higher temperature difference between solids and gases in both sections compared to those in a fixed bed, which in turn give rise to heat-transfer intensification.

4 Modeling and Simulation

To assess the thermal performances of the proposed regenerator and the fix-bed regenerator, we have formulated mathematical models for both and carried out the computer simulation studies. The mathematical models are given below.

We have assumed that the gas velocity is uniform in the radial direction and the opening and closing valves do not cause any interruption to the steady-state operation. Furthermore, the following assumptions are made.

Heat loss from the walls is negligible. The ratio of heat flux by convection and conduction flux for the proposed SMB is 486. Therefore, we have assumed that the axial heat conduction through bed of solids is negligible. The effective thermal conductivity, used in evaluating the Pe (the Peclet number Pe $=V_s c_{ps}\rho_s/k_{\text{eff}}L$), was estimated from Ref. [23]. The containing wall of the bed is adiabatic. The gas and solids are in plug flow. Since the wall is adiabatic and the velocity is independent of the radius, the temperature would be uniform along the radius. Therefore, we assume that there would be no heat transfer in the radial direction [24].

The model for the proposed SMB is as follows. The differential energy balance for the gas phase accounting for the axial dispersion [23] is as follows:

$$G_g C_{pg}\frac{dT_g}{dx} - k_{g,\text{eff}}\frac{d^2T_g}{dx^2} = ha_s(T_s - T_g) \tag{1}$$

The boundary conditions for the gas and the solid temperature at the inlet of the heat-transfer zones considered are

$$\left.\begin{aligned} T_g &= T_{g,0} \\ T_s &= T_{s,0} \end{aligned}\right\} \quad \text{at } x = 0 \tag{2}$$

The temperature distribution within a spherical particle in the bed is determined from the differential heat conduction equation

$$\frac{\partial^2 T}{\partial r^2} + \frac{2}{r}\left(\frac{\partial T}{\partial r}\right) = \frac{C_{ps}\rho_s}{k_s}\left(\frac{\partial T}{\partial \theta}\right) \tag{3}$$

Considering that the heat-transfer zone moves with a uniform velocity, we can eliminate the time θ in terms of the zone velocity V_s and the axial distance of the bed x as $x=V_s\ \theta$ [15–17] to yield

$$\frac{\partial^2 T}{\partial r^2} + \frac{2}{r}\left(\frac{\partial T}{\partial r}\right) = \frac{V_s C_{ps}\rho_s}{k_s}\left(\frac{\partial T}{\partial x}\right) \tag{4}$$

The boundary conditions are

$$-k_s\left(\frac{\partial T}{\partial r}\right)_{r=R} = h(T_s - T_g) \tag{5a}$$

and

$$\left(\frac{\partial T}{\partial r}\right)_{r=0} = 0 \tag{5b}$$

Equations (1) and (4) along with the boundary conditions are solved using the Crank–Nicholson six-point implicit form technique as given by Ferziger [25]. The particle heat-transfer coefficient has been estimated from the correlation given by Wakao and Kaguei [23],

$$\varepsilon\frac{h}{C_{pg}G_g}\left(\frac{\mu_g C_{pg}}{k_g}\right)^{2/3} = \frac{2.876}{\text{Re}_p} + \frac{0.3023}{\text{Re}_p^{0.35}} \tag{6}$$

The gas phase pressure drop in the packed bed is estimated using the Ergun equation [26]

$$\frac{\Delta P}{L} = \frac{150V\mu}{\phi_s^2 d_p^2}\frac{(1-\varepsilon)^2}{\varepsilon^3} + \frac{1.75\rho_g V^2}{\phi_s d_p}\frac{(1-\varepsilon)}{\varepsilon^3} \tag{7}$$

The model for the fixed-bed regenerator is given below. The preliminary studies indicated that the size of the particle to be used is less than 5 mm. For the operating conditions considered here, the corresponding Bi is $0.023<0.01$. Therefore, we have considered that there is no internal temperature gradient within the particle.

The energy balance equation for the gas, accounting for axial dispersion, is

$$k_{g,\text{eff}}\frac{\partial^2 T_g}{\partial x^2} - C_{pg}\rho_g V_g\frac{\partial T_g}{\partial x} + ha_s(T_s - T_g)/\varepsilon = C_{pg}\rho_g\frac{\partial T_g}{\partial t} \tag{8}$$

The energy balance for the solid phase is

$$\rho_s C_{ps}(1-\varepsilon)\frac{\partial T_s}{\partial t} = ha_s(T_g - T_s) \tag{9}$$

The initial and boundary conditions are as follows:

At $t=0$,

$$0 \leqslant x \leqslant L, \quad T_g = T_{g0}, \quad T_s = T_{s0}$$

At $x=0$,

$$k_{g,\text{eff}}\frac{\partial T_g}{\partial x} = V_g C_{pg}\rho_g\varepsilon(T_g - T_{g0}) \quad \text{for } t > 0$$

$$x = L, \quad \frac{\partial T_g}{\partial x} = 0 \quad \text{for all } t$$

The set of coupled differential equations was solved by the method of lines. A central finite-difference technique was used to discretize over the space domain. The DASPG subroutine in the IMSL™ package was used to solve the resulting differential equations.

5 Results and Discussion

First, we have examined the feasibility of replacing the blast-furnace stoves with the proposed simulated moving-bed heat regenerator. A typical stove is 7 m in diameter and 33 m in height. Each stove goes through alternate steps of heating and cooling in a cycle referred to as "on-gas" and "on-blast" steps, respectively. The time for the on-gas step is 4.28 h and for the on-blast step, it is 2.53 h. The changes in temperatures of the off gas and the air are 1200–200°C and 90–1000°C, respectively [13,14,27,28]. We have considered that there are three blast stoves in operation at a

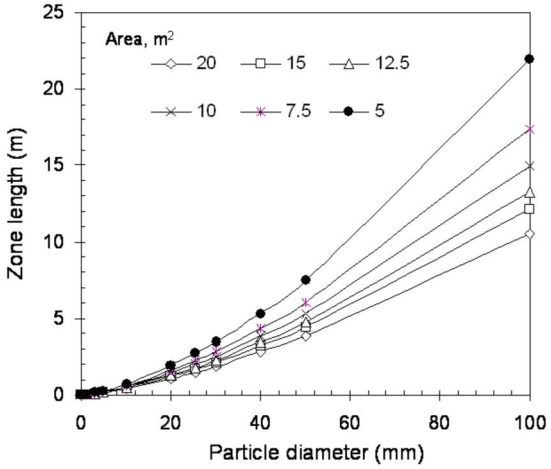

Fig. 5 Effect of particle diameter on the zone length for cooling

time, two for the heating cycle and one for the cooling cycle. The heat duty of the stoves and the other details used in the analysis are given below.

	Cooling cycle	Heating cycle
Volumetric flow rate of gas, m^3/s	:42.8	47.19
Inlet temperature, °C	:1204	40
Outlet temperature, °C	:175	1000
Density of packing material	:2000 kg/m^3	
Specific heat of packing material	:836.8 J/kg °C	
Particle diameter	:0.1–100 mm	
Area density of the bed	:36,000–36 m^2/ m^3	

Using the above parameters, we have determined the heat-transfer zone lengths of simulated moving-bed regenerators using the models presented in the previous section. The grid independency tests for the convergence of the zone length as function of spatial discretization over a wide range of grid size (from 10^{-2} to 10^{-6} m) were carried out. It has been observed that the grid size below 0.01 m has negligible effect on the results. However, we have employed a grid size of 0.001 m in all computations. The cross-sectional area beds and the particles of diameters were varied over a range of 5–20 square meter. The diameter was varied from 0.1 mm to 100 mm and the porosity of the bed was 0.4. Figures 5 and 6 present the variation of the lengths of the cooling and heating zones. It can be seen that the zone lengths

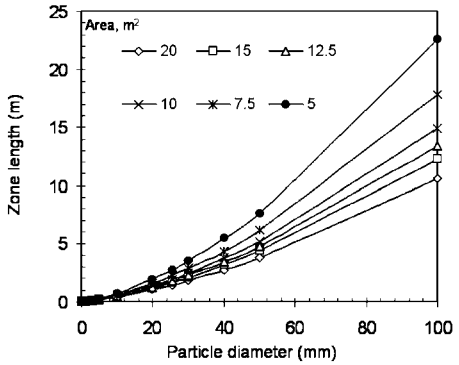

Fig. 6 Effect of particle diameter on the zone length for heating

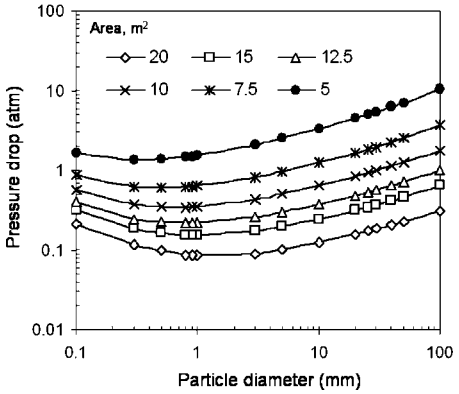

Fig. 7 Variation of pressure drop across the zone length with particle diameter for cooling

increase with the increase in particle diameter. It is evident from these figures that the zone lengths for a particle diameter decrease with increasing cross-sectional area.

The energy requirement to blow the gases through the regenerator is also an important factor besides the size of the unit. The former dictates the running cost and the latter the capital cost. The pressure drop depends on the particle diameter and cross-sectional area of the bed. The estimated pressure drops across the zone lengths are presented in Figs. 7 and 8.

The pressure drop goes through a minimum around 0.8 mm particle diameter for all cross-sectional areas of the beds. For the particle diameter of 0.8 mm, the zone lengths in both sections are in the range of 0.04–0.08 m, which is very small. The corresponding pressure drops are also the lowest. The zone volumes are about 1000 times smaller than that of the blast-furnace stoves. However, the assumption of uniform radial gas flow may not be valid for such small zone lengths. Furthermore, the cyclic variation of severe temperature gradients could pose problems in the selection of the material that could be used for the particles. For the particles of larger diameter, the zone lengths as well as the pressure drops are very high. To overcome this problem of high pressure drops, the Raschig rings (used in packed-bed distillation and absorption columns) of different diameters with different porosities were considered.

The specific area and porosity details of the Raschig rings are given in Table 1.

Figures 9 and 10 present the zone-length variation of both cooling and heating zones for different hydraulic diameters of the

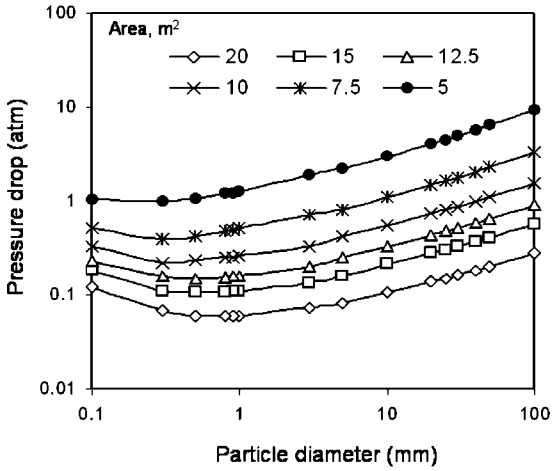

Fig. 8 Variation of pressure drop across the zone length with particle diameter for heating

Table 1 Specific area and porosity details for Raschig rings

Particle size (mm)	Sp area (m^2/m^3)	Porosity	d_h (mm)
25	202.2	0.72	14.2
15	312	0.69	8.8
10	440	0.65	5.9
6	771.9	0.62	3.2

Raschig rings and cross-sectional areas of the beds. It can be seen from the figures that zone lengths increased with increase diameter. Figure 11 shows the pressure drop data. It can be observed that the pressure drops are much smaller than that for the spherical particles. However, the zone lengths are larger for the Raschig rings as porosity is higher than for the spherical particles.

The temperature difference between the solids and the gas in SMB regenerator is shown in Figs. 12 and 13. For the case of fixed bed with 15 m^2 cross-sectional area and 10 m length, a particle size of 10 mm was considered. The gas inlet and outlet temperatures and the flow rates are the same as stated earlier. It is found that the average temperature difference between the solids and gas along the heat-transfer zone in the fixed bed is 5.2 °C. The temperature difference is nearly constant along the zone length. For the SMB, they are 76 °C and 82 °C for the cooling and heating zones, respectively.

The volume required for the SMB is 20–330 times less in comparison to the set of three stoves depending on the particle size and bed cross-sectional area. After considering the zone lengths and pressure drops, we have selected a SMB with 10 m^2 cross-sectional area filled with the Raschig rings of 10 mm diameter as an alternative to the blast-furnace stoves. For this case, the zone lengths for both heating and cooling is 0.5 m and the corresponding pressure drop is about 0.12 atm. A separation zone length of 0.5 m is provided between the cooling and heating zones and 0.25 m on either side of the zones. The port velocity in these

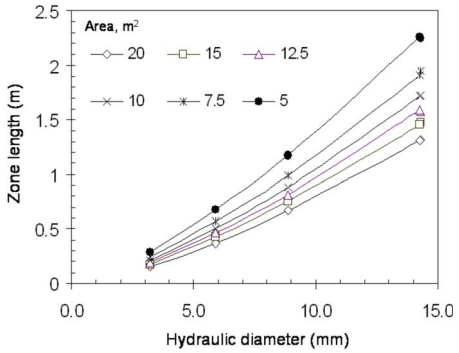

Fig. 9 Effect of hydraulic diameter on the zone length for cooling

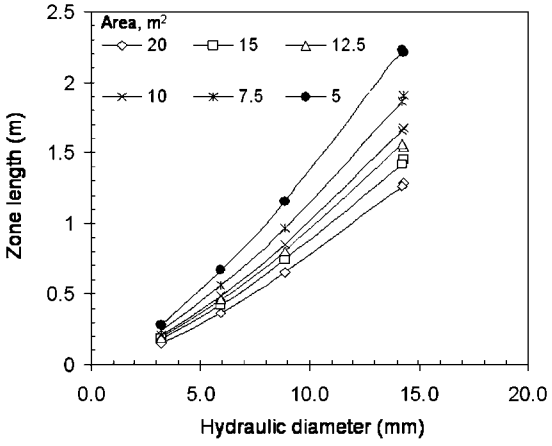

Fig. 10 Effect of hydraulic diameter on the zone length for heating

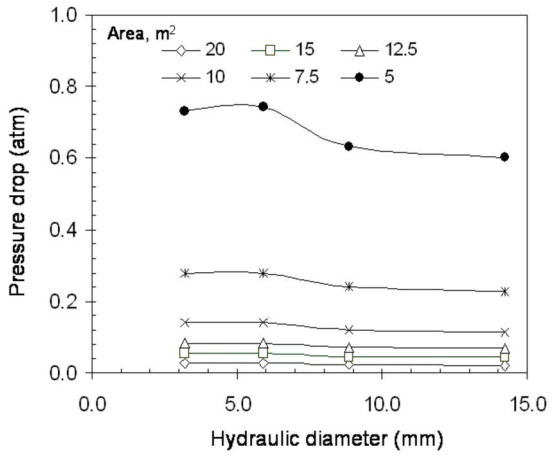

Fig. 11 Variation of pressure drop across the zone length with hydraulic diameter for cooling

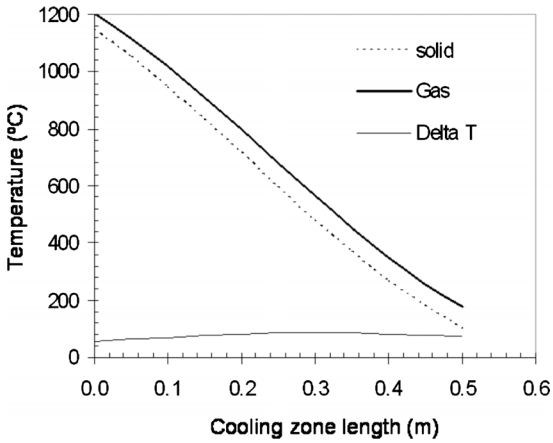

Fig. 12 Temperature profiles for gas and solid in the cooling zone

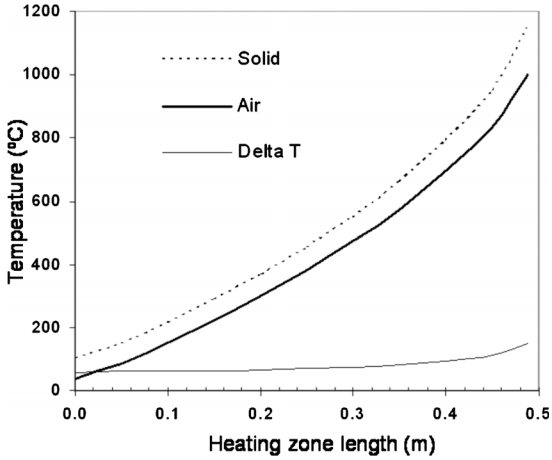

Fig. 13 Temperature profiles for gas and solid in the heating zone

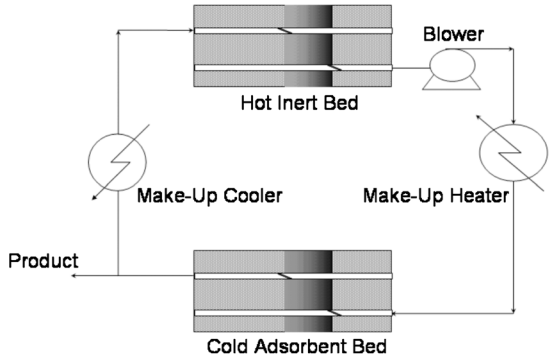

Fig. 14 Schematic of the thermal regeneration process using a SMB adsorber and an inert bed

sections is 7.8 mm/s. The total length is 4 m. Note that we have not accounted for the gaps to be provided between the sections in computing the volume reduction. The volume of the proposed SMB heat regenerator for these conditions is 95 times smaller than the blast-furnace stoves.

5.1 Thermal Regeneration of Adsorbent Bed. Adsorptive separation of a gas mixture is a cyclic process and it is accomplished using two to six fixed beds of adsorbent. The cycle consists of several steps. Each bed goes through the steps for a fixed duration of time. Figure 14 shows the schematic of heating the adsorbed bed by circulating gas through a hot inert bed [29]. Each bed is embedded with two moving-port systems. The energy in the hot inert bed is transferred to the cold bed by circulating the gas through a make-up heater and a cooler using a blower. The adsorbent bed has to be cooled back to its initial temperature. To conserve energy, the heat in the adsorbent bed is transferred back into the inert bed.

To examine the feasibility of the regeneration within a specified time, we have limited ourselves to heating of the bed. We have considered the heating step to be accomplished in 5 min. In order to assess the performance, we have computed the temperature profiles in the beds at different time intervals and pressure drops,

Table 2 Parameters used in thermal regeneration of fixed bed and SMB

Diameter of the bed: 1 m
Length of the bed: 5 m
Diameter of the particle: 2.0 mm
Bed porosity: 0.4
Specific heat capacity of adsorbent: 0.950 kJ/kg °C,
Specific heat capacity of gas: 0.876 kJ/kg °C
Density of gas: 1.2 kg/m^3
Viscosity of gas: 9.1×10^{-6} Pa s
Thermal conductivity of gas: 0.02 W/m °C
Thermal conductivity of adsorbent: 0.173 W/m °C
Thermal conductivity of inert solid: 4.67 W/m °C
Hot bed temperature: 350°C
Cold bed temperature: 50°C

Fixed Bed

	Inlet	Outlet
Gas to hot bed, °C	50	350
Gas to cold bed, °C	350	50

SMB

	Inlet	Outlet
Gas to hot bed, °C	50	330
Gas to cold bed, °C	350	70

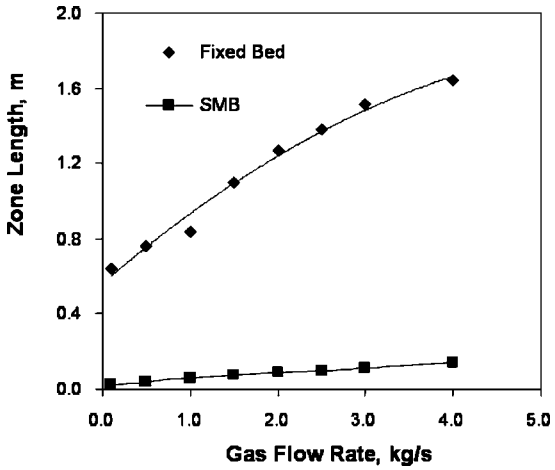

Fig. 15 Effect of gas flow rate on zone lengths in SMB and fixed beds

make-up heat, and the power requirements for circulation of the gas through the beds for a fixed bed and simulated moving bed using the parameters given in Table 2. The results are presented below.

Figure 15 presents the variation of zone lengths with the gas flow rate. It can be seen that the zone length ranged from 0.3% to 3% of the bed length for the SMB and from 15% to 35% for the fixed bed. To heat the bed in 5 min, the flow rate of the gas required is 3.3 kg/s for the fixed bed and is 3.0 kg/s for the SMB. For these flow rates, the zone length was 33.4% of the bed length for fixed bed and was only 2.2% in the SMB case. Figure 16 presents the power requirement for gas circulation. The power required is very large in the case of fixed bed, since the gas has to pass through the entire bed, whereas it is only across the zone length for the SMB.

The make-up heat has to be provided for both the fixed bed and the SMB. In the case of the fixed bed, thermal equilibrium prevails on either side of the heat-transfer zone, as shown in Fig. 1. As the zone reaches the far end of the bed, the gas temperature starts falling below 350°C. We have determined the temperature profile when the zone reaches the far end, and estimated the make-up required. Figure 17 shows the temperature profile of the gas in the fixed bed. The overshoots in the temperature profile are due to numerical oscillations. By increasing the number of grid points, the overshoots can be eliminated. However, the computational time increases by manifold. The percentage error for heat transferred in the heating step for 50 and 200 grid points is 0.019%. Therefore, we have employed 50 grid points to save on

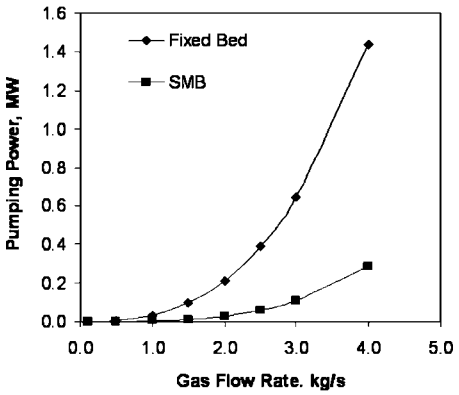

Fig. 16 Effect of gas flow rate on pumping power in SMB and fixed beds

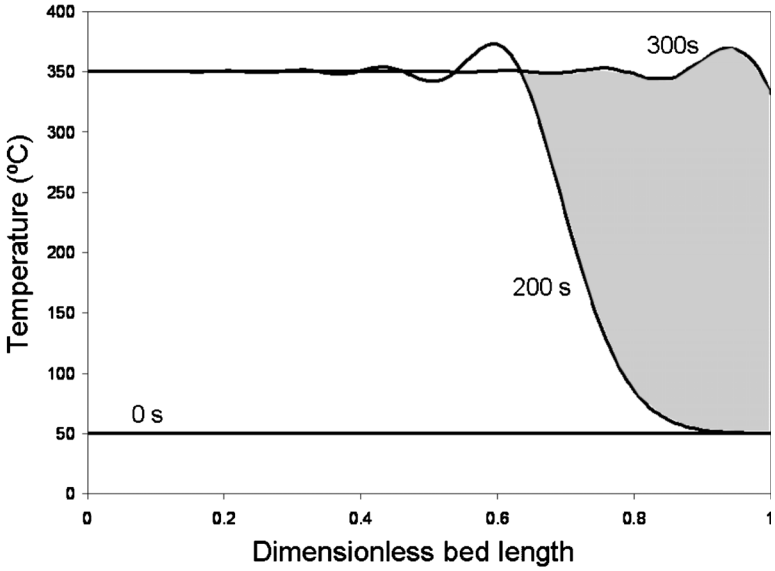

Fig. 17 Temperature profiles across the bed

computational time. From the shaded area, the make-up heat was estimated. Likewise, the gas leaving the adsorbent bed has to be cooled to be maintained at 50°C. However, in the case of SMB, make-up energies for the heating and for the cooling have to be provided throughout the regeneration step. The gas leaving the inert bed is 330°C and it has to be heated to 350°C and similarly, the gas leaving the adsorbent is at 70°C and it has to be cooled to 50°C.

The total make-up energy for heating is 189 MJ for the fixed bed and is 116 MJ for SMB in each step. The SMB has the advantage of the lower power and make-up energy requirement compared to the fixed bed. More extensive study is required to ascertain the relative performance of the fixed bed and the SMB for thermal regeneration of adsorbent beds.

6 Conclusions

We have proposed a novel simulated moving-bed heat regenerator using a fixed bed. A single SMB could replace a set of three blast-furnace stoves, and a volume reduction by a factor of 95 could be achieved with the use of SMB. The proposed SMB heat generator could be adopted for the thermal regeneration of adsorbent bed. The power requirement for gas recirculation and the make-up energy required are less with the SMB compared to the fixed bed. The study shows that a significant process intensification can be achieved using the proposed SMB.

Nomenclature

a_s = specific surface area, m^2/m^3
Bi = Biot number
C_p = specific heat, J/kg °C
d_h = hydraulic diameter, m
d_p = particle diameter, m
Fo = Fourier number
G = mass velocity, kg/m^2 s
h = particle heat-transfer coefficient, $W/m^2°C$
$k_{g,\text{eff}}$ = effective axial thermal conductivity, W/m °C
k = thermal conductivity, W/m °C
L = length of the zone, m
r = radius, m
Re_p = particle Reynolds Number, $\text{Re}_p = d_p G_g/\mu_g$
T = temperature, °C
V = superficial velocity of air, m/s
V_s = apparent solid velocity, m/s
x = distance from the outlet port, m

Greek Letters

ΔP = pressure drop, atm
ε = void fraction, dimensionless
θ = time, s
μ = dynamic viscosity, kg/m s
ρ = density, kg/m^3
ϕ = sphericity of particle, dimensionless

Subscripts

g = gas
s = solid

References

[1] Tsouris, C., and Porcelli, J. V., 2003, "Process Intensification—Has Its Time Finally Come?," Chem. Eng. Prog., **99**, pp. 50–55.
[2] Willmott, A. J., 1969, "The Regenerative Heat Exchanger Computer Representation," Int. J. Heat Mass Transfer, **12**, pp. 997–1014.
[3] Burns, A., and Willmott, A. J., 1978, "Transient Performance of Periodic Flow Regenerators," Int. J. Heat Mass Transfer, **21**, pp. 623–627.
[4] Heggs, P. A., and Foumeny, E. A., 1986, "Thermal Performance of Diabatic Cyclic Regenerators," Numer. Heat Transfer, **9**, pp. 182–199.
[5] Hill, A., and Willmott, A. J., 1987, "A Robust Method for Regenerative Heat Exchanger Calculations," Int. J. Heat Mass Transfer, **30**, pp. 241–249.
[6] Hill, A., and Willmott, A. J., 1989, "Accurate and Rapid Thermal Regenerator Calculations," Int. J. Heat Mass Transfer, **32**, pp. 465–476.
[7] Foumeny, E. A., and Pahlevanzadeh, H., 1994, "Performance Evaluation of Thermal Regenerators," Heat Recovery Syst. CHP, **14**, pp. 79–84.
[8] Klein, H., and Eigenberger, G., 2001, "Approximate Solutions for Metalic Regenerative Heat Exchangers," Int. J. Heat Mass Transfer, **44**, pp. 3553–3563.
[9] Tomeczek, J., and Wnek, M., 2006, "A Rapid Method for Counter-Flow Heat Regenerator Calculation," Int. J. Heat Mass Transfer, **49**, pp. 4194–4199.
[10] Levenspiel, O., 1983, "Design of Long Regenerators by Use of the Dispersion Model," Chem. Eng. Sci., **38**(12), pp. 20–35.
[11] Zarrinehkafsh, M. T., and Sadermeli, M., 2004, "Simulation of Fixed Bed Regenerative Heat Exchangers for Flue Gas Heat Recovery," Appl. Therm. Eng., **24**, pp. 373–382.
[12] Frigerio, S., Mehl, M., Ranzi, E., Svhweiger, D., and Schedler, J., 2007, "Improve Efficiency of Thermal Regenerators and VOCs Abatement Systems: An Experimental and Modeling Study," Exp. Therm. Fluid Sci., **31**, pp. 403–411.
[13] Muske, K. R., Howse, J. W., Hansen, G. A., and Cagliostro, D. J., 2000, "Model-Based Control of a Thermal Regenerator. Part I: Dynamic Model," Comput. Chem. Eng., **24**, pp. 2519–2531.
[14] Muske, K. R., Howse, J. W., Hansen, G. A., and Cagliostro, D. J., 2000, "Model-Based Control of a Thermal Regenerator. Part II: Control and Estimation," Comput. Chem. Eng., **24**, pp. 2507–2517.
[15] Amundson, N. R., 1956, "Solid-Fluid Interactions in Fixed and Moving Beds," Ind. Eng. Chem., **48**, pp. 26–43.
[16] William, D., and Neal, R., 1950, "Solid-Fluid Heat Exchange in Moving

Beds," Ind. Eng. Chem., **42**, pp. 1481–1488.
[17] Ssastamoinen, J. J., 2004, "Heat Exchange Between Two Coupled Moving Beds by Fluid Flow," Int. J. Heat Mass Transfer, **47**, pp. 1535–1547.
[18] Caputo, A. C., and Pelagagge, P. M., 1999, "Heat Recovery From Moving Cooling Beds: Transient Modeling by Dynamic Simulation," Appl. Therm. Eng., **19**, pp. 21–35.
[19] Handley, D., and Heggs, P. J., 1969, "The Effect of Thermal Conductivity of the Packing Material on Transient Heat Transfer in a Fixed Bed," Int. J. Heat Mass Transfer, **12**, pp. 549–570.
[20] Ruthven, D. M., Farooq, S., and Knaebel, K. S., 1994, *Pressure Swing Adsorption*, VCH, New York.
[21] Yang, R. T., 1987, *Gas Separation by Adsorption Processes*, Imperial College Press, London.
[22] Suzuki, M., 1990, *Adsorption Engineering*, Elsevier Science, Amsterdam.
[23] Wakao, N., and Kaguei, S., 1982, *Heat Transfer in Packed Beds*, Gordon and Breach Science, London.
[24] Bird, R. B., Stewart, W. E., and Lightfoot, E. N., 2002, *Transport Phenomena*, 2nd ed. Wiley, New York, p. 300.
[25] Ferziger, J. H., 1998, *Numerical Methods of Engineering Applications*, 2nd ed., Wiley, New York.
[26] McCabe, W. L., Smith, J. C., and Harriott, P., 2001, *Unit Operations of Chemical Engineering*, 6th ed., McGraw-Hill, New York.
[27] Schofield, J., Butterfield, P., and Young, P. A., 1961, "Hot Blast Stoves," J. Iron Steel Inst., London, **199**, pp. 229–240.
[28] Schofield, J., Butterfield, P., and Young, P. A., 1963, "Hot Blast Stoves: Part II," J. Iron Steel Inst., London, **201**, pp. 497–508.
[29] Rao, D. P., Sivakumar, S. V., Mandal, S., Kota, S., and Ramaprasad, B. S. G., 2005, "Novel Simulated Moving-Bed Adsorber for the Fractionation of Gas Mixtures," J. Chromatogr., A, **1069**, pp. 141–151.

Simplified Two-Dimensional Analytical Model for Friction Stir Welding Heat Transfer

Satish Perivilli[1]
Graduate Student
e-mail: svperivill21@tntech.edu

John Peddieson
Professor

Jie Cui
Associate Professor

Department of Mechanical Engineering,
Tennessee Technological University,
Cookeville, TN 38505

A two-dimensional heat transfer problem pertaining to friction stir welding is developed by converting various pin tool configurations of interest to a simplified pin only configuration by assigning an equivalent heat flux to the pin surface. Mechanical dissipation heating, responsible for the welding, is modeled by means of a thermal boundary condition at the pin surface. A series solution is developed for the temperature distributions in the workpiece (assumed to be infinite) and these distributions are analyzed at various radial and circumferential locations. It is found that the closed form solutions developed are not influenced greatly by the truncation numbers of this series. Maximum reduced temperatures pertinent to configurations available in literature are estimated from the series and one term solutions developed and compared with those observed. Furthermore, the applicability of one term solution of this series is tested for various parametric combinations based on models available in literature. It is found that the one term solution can be applied to within a reasonable range of the process governing parameters. [DOI: 10.1115/1.2927401]

Keywords: friction stir welding, mechanical dissipation heating

1 Introduction

Friction stir welding (FSW) is one of the most recent advances in the technology of welding and is oftentimes found to be more effective than conventional forms. The process begins by plunging a rotating pin tool into a workpiece until the tool's shoulder (see below) touches the workpiece. The part of the pin tool that penetrates the workpiece is referred to as the "pin" while parts of the pin tool in contact with horizontal workpiece surfaces are referred to as "shoulders." The pin tool then translates down the weld seam. The frictional heat produced by pin tool rotation combined with the associated stirring action welds materials at temperatures below their melting points, thus resulting in a superior weld quality with the absence of conventional welding defects such as oxidation, porosity, solidification, etc. Although widely used for the welding of aluminum alloys, FSW is also being used to join dissimilar metals as well.

The associated heat transfer problem is highly significant as the amount of heat generated during the process decides the quality of the weld, its mechanical properties, and distortion of the workpiece. Numerous experimental studies, ending with the development of empirical relations, have been conducted over the past few years. For example, McClure et al. [1] developed a heat transfer model, for the friction stir welding of two AA 6061-T6 plates, that takes into account plastic deformation of the weld metal and heat generation by friction at the shoulder and workpiece interface.

The mechanics of the process, related momentum transfer, and the microstructure of the resulting joint have also been investigated by various other researchers. Guerra et al. [2] investigated the flow patterns during friction stir welding by conducting experiments on bimetallic welds of aluminum copper and AA 2195-AA 6061. Murr et al. [3] compared the friction stir welding of a number of metal and alloy systems, with emphasis on the hardness profiles of friction stir welds. Sutton et al. [4] studied the microstructure of the welds with importance on grain size and microhardness variations.

In addition to the available experimental results, the advent of high speed and large memory computers has facilitated research in numerical modeling of FSW in recent years. Chao and Qi [5] developed a three-dimensional finite element model for FSW of AA 6061-T6 plates taking into account different thermal convections at the top and bottom surfaces of the workpiece, welding velocity, and a heat flux configuration. Song and Kovacevic [6] developed a heat transfer model based on an explicit central difference method and conducted an analysis with a coordinate system that moves with the tool. Colegrove and Shercliff [7] analyzed various profiled tools and investigated the effects of tool rake angle, and translational and rotational speeds on the flow field produced using FLUENT—the commercial Computational Fluid Dynamics (CFD) software that employs finite volume methods.

Ulysse [8] employed a 3D finite element model to predict the temperature and force distributions during the butt welding of two AA 7050-T7451 plates and showed that increasing the welding velocity increases the magnitude of axial and shear forces on the pin. Chen and Kovacevic [9] employed a thermomechanical model to study the various forces in FSW using finite elements. Zhu and Chao [10] investigated the nature of residual stresses in FSW using different finite element models and various materials. The structural performance of friction stir butt welded Al alloys was studied by Lomolino et al. [11]. Cho et al. [12] used a model including strain hardening to study the texture evolution and the velocity and temperature distributions in friction stir welds of stainless steel. Soundararajan et al. [13] predicted the stress development in FSW using a model with adaptive boundary conditions and mechanical tool loading to simulate FSW of two Al 6061 plates, considering a uniform value for contact conductance.

Owing to the complex nature of FSW, analytical solutions can be obtained only with the aid of significant simplifications. Although not directly related to FSW, some mathematical models that pertain to welding, in general, are available in literature. Rosenthal [14] analyzed the mathematical aspects of heat distribution during welding processes by treating the heat source sepa-

[1]Corresponding author; present address: TRAX LLC., Forest, VA 24551.

Contributed by the Heat Transfer Division of ASME for publication in the JOURNAL OF HEAT TRANSFER. Manuscript received January 17, 2007; final manuscript received March 27, 2007; published online July 3, 2008. Review conducted by Ben Q. Li.

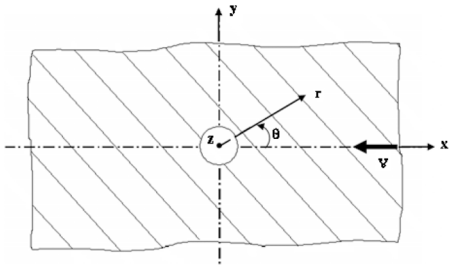

Fig. 1 Coordinate systems used for analysis

rately as a point and as a line source while assuming constant thermophysical properties of the material. The process was modeled as quasistationary and heat exchanges to the environment were neglected. Trivedi and Srinivasan [15] extended this analysis to the case of a moving cylindrical source.

In this paper, a method by which various FSW pin tool configurations can be converted to a simplified pin only configuration is discussed and used to reduce the FSW heat transfer-problem to a two-dimensional form. A methodology similar to that of Trivedi and Srinivasan [15] is employed to solve for the workpiece temperature distribution. In this approach, mechanical dissipation heating, currently thought to be responsible for most of the heating that produces the weld, is represented by a thermal boundary condition at the pin surface.

2 Governing Equations

The mechanical loads applied by the pin tool to the workpiece result in a yielded region only in the immediate vicinity of the former while most of the workpiece remains unyielded. Idealizing the localized yielded region as being coincident with the pin tool surface and treating the workpiece as rigid, the governing equation for steady heat transfer in the workpiece is given by

$$\mathbf{v} \cdot \nabla T = \alpha \nabla^2 T \tag{1}$$

where $\mathbf{v}$ is the pin tool velocity, T is the workpiece absolute temperature, and α is the workpiece thermal diffusivity (assumed to be constant).

Figure 1 introduces both a Cartesian coordinate system (x,y,z) and a cylindrical coordinate system (r,θ,z). Both of these coordinate systems are attached to the pin tool and are inertial (since the pin tool moves with a constant speed). The x axis is coincident with the bottom of the weld seam, the y axis is in the plane of the workpiece bottom, and the z axis is coincident with the pin tool centerline. The r,θ plane is coincident with the x,y plane. The pin tool is represented schematically as a circle in Fig. 1. The workpiece length and width (being much larger than the maximum pin tool radius in typical configurations) are idealized as infinite in the present analysis, as indicated in Fig. 1. Thus, from the viewpoint of the pin tool, steady conditions prevail with the workpiece moving in the negative x direction as indicated by the arrow labeled $\mathbf{v}$ in Fig. 1. For this steady problem with workpiece translational velocity v (opposite to the welding direction), Eq. (1) can be written in polar coordinates as

$$\partial_r^2 T + \partial_r T/r + \partial_\theta^2 T/r^2 + \partial_z^2 T = -P(\cos(\theta)\partial_r T - \sin(\theta)\partial_\theta T/r)/R \tag{2}$$

where

$$P = vR/\alpha \tag{3}$$

is a Peclet number.

Figure 2 depicts four FSW pin tool configurations of interest in polar cylindrical coordinates. Figure 2(*a*) represents a full penetration configuration and introduces the pin radius R, the top shoulder radius R_s, and the workpiece thickness H. Figure 2(*b*) depicts the partial penetration configuration and introduces the depth of pin penetration D. Addition of a second shoulder, of radius R_b, to the full penetration configuration results in a self-reacting configuration depicted in Fig. 2(*c*). A simplified pin only configuration, which is useful in the development of closed form solutions, is shown in Fig. 2(*d*).

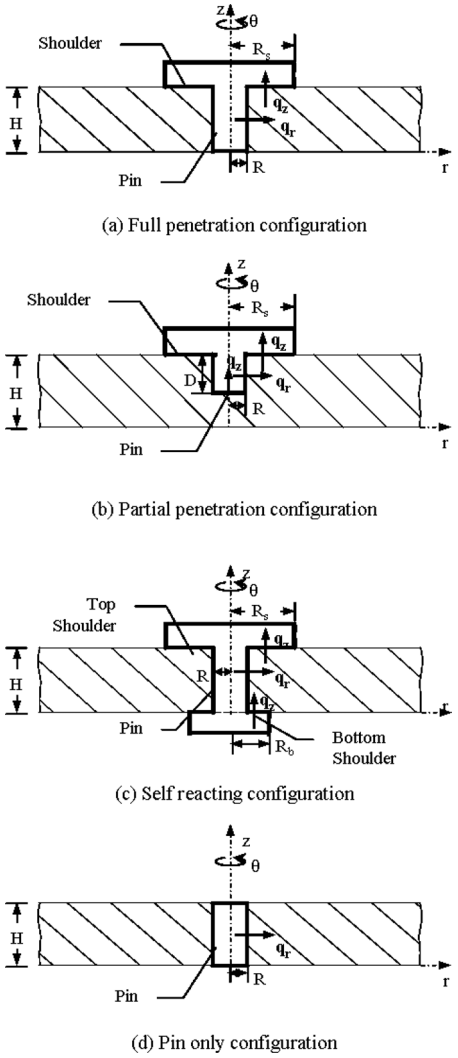

Fig. 2 Schematic of various FSW pin tool configurations ((—) pin tool; (▨) workpiece)

The arrows in Fig. 2 indicate various radial and axial heat fluxes representing mechanical dissipation heating at their respective pin tool locations. While calculating these heat fluxes, it is assumed that the mechanical power generated by the moment due to transverse shear stress (idealized at the yield value τ_0), acting on the rotating tool, is transferred to the workpiece. The power generated due to the yield stress acting on a differential area dA of the workpiece surface is given by

$$dp = \tau_0 r \Omega dA \tag{4}$$

where Ω is the angular velocity of the tool and r is the radial coordinate of a point on the surface of the pin tool. The corresponding heat flux is given by

$$q_n = dp/dA = \tau_0 r \Omega \tag{5}$$

wherein heat input to the workpiece is considered positive.

The yield stress of aluminum alloys is a function of both temperature (which varies with position) and shear rate (of which Ω would be an appropriate measure). Since FSW occurs at a constant pin tool angular velocity, the shear rate variation of the yield

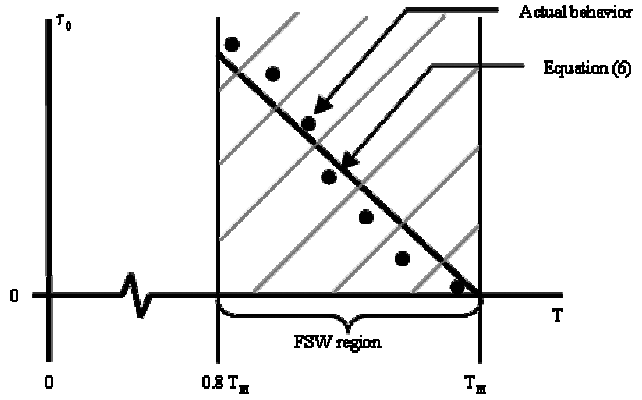

Fig. 3 Variation of actual and idealized yield stress with temperature for aluminum alloys

stress is not included in the calculations that follow. To account for all this in a way that facilitates closed form solutions, a straight line fit to yield stress versus temperature data in the FSW region,

$$\tau_0 = \tau_{0,0}(1 - T/T_M) \tag{6}$$

is used where T_M is the melting temperature and $\tau_{0,0}$ is a fitting parameter having the dimensions of stress. Equation (6) captures qualitatively both the "temperature softening" behavior exhibited by aluminum alloys at high temperatures and the vanishing of the yield stress at the melting temperature. The parameter $\tau_{0,0}$ is adjusted to create the best fit to experimental data in the FSW temperature range, as illustrated schematically in Fig. 3. Substituting Eq. (6) into Eq. (5) yields

$$q_n = \tau_{0,0}\Omega r(1 - T/T_M) \tag{7}$$

As an example, the radial heat flux associated with the cylindrical pin surfaces in Fig. 2 is defined as

$$q_r = q_r(R,\theta,z) = \tau_{0,0}\Omega R(1 - T(R,\theta,z)/T_M) \tag{8}$$

and using

$$q_r = -\kappa\partial_r T \tag{9}$$

where κ is the workpiece thermal conductivity (assumed to be constant), in Eq. (8) gives

$$\partial_r T(R,\theta,z) = -\tau_{0,0}R\Omega(1 - T(R,\theta,z)/T_M)/\kappa \tag{10}$$

as a boundary condition for the pin surfaces. Similar equations can be generated for the other tool surfaces pertinent to a configuration.

The top surface of the workpiece, not in contact with the tool surfaces, interacts with the atmosphere by means of convection heat transfer. This interaction is characterized by a heat transfer coefficient h_H and an ambient temperature T_∞. Thus, the top surface heat flux can be written as

$$q_z(r,\theta,H) = h_H(T(r,\theta,H) - T_\infty) \quad \text{for } r > R_s \tag{11}$$

and substituting

$$q_z = -\kappa\partial_z T \tag{12}$$

in Eq. (11) produces the boundary condition for the top surface as

$$\partial_z T(r,\theta,H) = h_H(T_\infty - T(r,\theta,H))/\kappa \quad \text{for } r > R_s \tag{13}$$

The bottom surface of the workpiece interacts with the backup plate in a complicated manner. Here, a simplified approach is adopted in which the backup plate is characterized by an effective constant temperature T_0 (assumed to be the same as T_∞) and the interaction by an effective convection heat transfer coefficient h_0. The heat flux at the bottom surface then becomes

$$q_z(r,\theta,0) = h_0(T_\infty - T(r,\theta,0)) \tag{14}$$

Substitution of Eq. (12) into Eq. (14) yields

$$\partial_z T(r,\theta,0) = h_0(T(r,\theta,0) - T_\infty)/\kappa \tag{15}$$

as the boundary condition for the bottom surface of the workpiece.

3 2D Approximation

To facilitate the creation of a simplified two-dimensional model of FSW heat transfer, the configurations shown in Figs. 2(*a*)–2(*c*) can be replaced with the simplified pin only configuration shown in Fig. 2(*d*) by assigning an "equivalent" heat flux to the pin's surface. This is achieved by increasing the pin surface heat flux by a correction factor, f, calculated as follows.

The heat flux on any surface of the pin tool is given by Eq. (5) and the corresponding net heat input to the workpiece from the pin tool is then

$$Q = \iint_A q_n dA \tag{16}$$

where A is the combined pin and shoulder surface areas. Substituting Eq. (5) into Eq. (16) and treating τ_0 as constant (an approximation) yield

$$Q = \tau_0\Omega \iint_A r dA \tag{17}$$

An equivalent pin surface heat flux can be defined as

$$q_r(R,\theta,z) = Q/(2\pi RH) = \tau_0\Omega \iint_A r dA/(2\pi RH) = f\tau_0 R\Omega \tag{18}$$

where

$$f = \iint_A r dA/(2\pi HR^2) \tag{19}$$

Evaluating Eq. (19) leads to

$$f = 1 + (R_s^3/R^2 - R)/(3H) \tag{20}$$

for the full penetration configuration of Fig. 2(*a*),

$$f = D/H + R_s^3/(3R^2H) \tag{21}$$

for the partial penetration configuration of Fig. 2(*b*), and

$$f = 1 + ((R_s^3 + R_b^3)/R^2 - 2R)/(3H) \tag{22}$$

for the self-reacting configuration of Fig. 2(*c*). Then, Eq. (10) is replaced with

$$\partial_r T(R,\theta,z) = -f\tau_{0,0}R\Omega(1 - T(R,\theta,z)/T_M)/\kappa \tag{23}$$

It is now possible to create a two-dimensional problem by integrating Eqs. (2) and (23) through the thickness of the workpiece. Subsequent multiplication with $1/H$ and use of Eqs. (13) and (15) yield

$$\partial_r^2\bar{T} + \partial_r\bar{T}/r + \partial_\theta^2\bar{T}/r^2 + P(\cos(\theta)\partial_r\bar{T} - \sin(\theta)\partial_\theta\bar{T}/r)/R = (h_0(T(r,\theta,0) - T_\infty) - h_H(T_\infty - T(r,\theta,H)))/(\kappa H) \tag{24}$$

and

$$\partial_r\bar{T}(R,\theta) - \bar{T}(R,\theta)/(\varepsilon R) = -T_M/(\varepsilon R) \tag{25}$$

where

$$\bar{T} = \bar{T}(r,\theta) = \int_0^H T dz/H \tag{26}$$

is the thickness averaged temperature and

$$\varepsilon = \kappa T_M/(f\tau_{0,0}\Omega R^2) \tag{27}$$

To approximate the terms multiplied by h_0 and h_H in Eq. (24), Raghulapadu [16] assumed that the heat transfer from the workpiece to the environment occurs in two stages: first from the interior at $\bar{T}$ to a surface at temperature T_s and then from this surface to the environment. If q_c and q_s represent the respective heat fluxes and h_c and h_s are the respective heat transfer coefficients associated with these processes, then equating the heat fluxes yields

$$q_c = h_c(\bar{T} - T_s) = q_s = h_s(T_s - T_\infty) \tag{28}$$

and solving Eq. (28) for T_s yields

$$T_s = (h_c\bar{T} + h_s T_\infty)/(h_c + h_s) \tag{29}$$

Identifying $T(r,\theta,H)$ with T_s and h_H with h_s in Eq. (29) yields

$$T(r,\theta,H) = (h_c\bar{T} + h_H T_\infty)/(h_c + h_H) \tag{30}$$

and, similarly, identifying $T(r,\theta,0)$ with T_s and h_0 with h_s produces

$$T(r,\theta,0) = (h_c\bar{T} + h_0 T_\infty)/(h_c + h_0) \tag{31}$$

Substituting Eqs. (30) and (31) into Eq. (24) and dropping the superposed bars from the result and Eq. (25) with the understanding that T subsequently represents the thickness averaged temperature yield

$$\partial_r^2 T + \partial_r T/r + \partial_\theta^2 T/r^2 + P(\cos(\theta)\partial_r T - \sin(\theta)\partial_\theta T/r)/R - B(T - T_\infty)/R^2 = 0 \tag{32}$$

and

$$\partial_r T(R,\theta) - T(R,\theta)/(\varepsilon R) = -T_M/(\varepsilon R) \tag{33}$$

where

$$B = (1/(1/B_H + 2/B_c) + 1/(1/B_0 + 2/B_c)) \tag{34}$$

is an effective Biot number with

$$B_H = h_H R^2/(\kappa H) \text{ and } B_0 = h_0 R^2/(\kappa H) \tag{35}$$

being the respective Biot numbers associated with the top and bottom surfaces and

$$B_c = 2h_c R^2/(\kappa H) \tag{36}$$

being a Biot number characterizing the thermal interaction between the interior and the surfaces. Based on an exact Fourier series solution, Raghulapadu [16] estimated this quantity as

$$B_c = \pi(R/H)^2 \tag{37}$$

It can be seen from Eq. (34) that B remains finite (as it should) even for infinite values of B_H and B_0. That is the reason for employing the two layer model discussed above. It should be pointed out that the two-dimensional formulation obtained above can be thought of as describing heat transfer in a moving fin.

4 2D Solution for an Infinite Workpiece

Since the dimensions of the pin tool are normally small compared to the dimensions of the workpiece, it is of interest to consider the idealization of an infinite workpiece. Here, the boundary value problem consists of Eqs. (32) and (33) and

$$T(\infty,\theta) = T_\infty \tag{38}$$

The solution process is facilitated by the substitutions

$$T = T_\infty(1 + \exp(-P\xi\cos(\theta)/2)\psi(\xi,\theta)), \quad r = R\xi \tag{39}$$

which convert Eqs. (32), (33), and (38) to the respective dimensionless differential equation

$$\partial_\xi^2\psi + \partial_\xi\psi/\xi + \partial_\theta^2\psi/\xi^2 - \lambda^2\psi = 0 \tag{40}$$

and boundary conditions

$$\partial_\xi\psi(1,\theta) - (P\cos(\theta)/2 + 1/\varepsilon)\psi(1,\theta) = -\varphi\exp(P\cos(\theta)/2)/\varepsilon,\ \psi(\infty,\theta) = 0 \tag{41}$$

where

$$\lambda = ((P/2)^2 + B)^{1/2} \tag{42}$$

and

$$\varphi = T_M/T_\infty - 1 \tag{43}$$

Substituting

$$\psi(\xi,\theta) = \sum_{n=0}^{\infty} f_n(\xi)\cos(n\theta) \tag{44}$$

into Eqs. (40) and (41) yields

$$\sum_{n=0}^{\infty}(f_n'' + f_n'/\xi - ((n/\xi)^2 + \lambda^2)f_n)\cos(n\theta) = 0 \tag{45}$$

$$\sum_{n=0}^{\infty}(f_n'(1)\cos(n\theta) - (P\cos(\theta)/2 + 1/\varepsilon)f_n(1)\cos(n\theta)) = -\varphi\exp(P\cos(\theta)/2)/\varepsilon \tag{46}$$

and

$$\sum_{n=0}^{\infty} f_n(\infty)\cos(n\theta) = 0 \tag{47}$$

Satisfaction of Eq. (45) requires that

$$f_n'' + f_n'/\xi - ((n/\xi)^2 + \lambda^2)f_n = 0 \tag{48}$$

Multiplying Eq. (46) by $\cos(m\theta)d\theta$ and integrating the result from 0 to π produce

$$f_0'(1) - (f_0(1)/\varepsilon + Pf_1(1)/4) = -\varphi C_0/\varepsilon \quad \text{for } n = 0 \tag{49}$$

$$f_1'(1) - (f_1(1)/\varepsilon + P(f_0(1) + f_1(1)/2)/2) = -\varphi C_1/\varepsilon \quad \text{for } n = 1 \tag{50}$$

$$f_n'(1) - (f_n(1)/\varepsilon + P(f_{n-1}(1) + f_{n+1}(1))/4) = -\varphi C_n/\varepsilon \quad \text{for } n = 2,3,4,\ldots,\infty \tag{51}$$

where

$$C_n = \left(\int_0^\pi \exp(P\cos(\theta)/2)\cos(n\theta)d\theta/\pi\right) \times \begin{cases} 1 & \text{for } n = 0 \\ 2 & \text{otherwise} \end{cases} \tag{52}$$

Satisfaction of Eq. (47) requires

$$f_n(\infty) = 0 \tag{53}$$

Equation (48) is a modified Bessel equation having the general solution

$$f_n(\xi) = A_n K_n(\lambda\xi) + B_n I_n(\lambda\xi) \tag{54}$$

where I_n and K_n are respective modified Bessel functions of the first and second kinds of order n, and A_n and B_n are constants. Substitution of Eq. (54) into Eq. (53) yields $B_n = 0$ and produces

$$f_n(\xi) = A_n K_n(\lambda\xi) \tag{55}$$

Substitution of Eq. (55) into Eqs. (49)–(51) yields

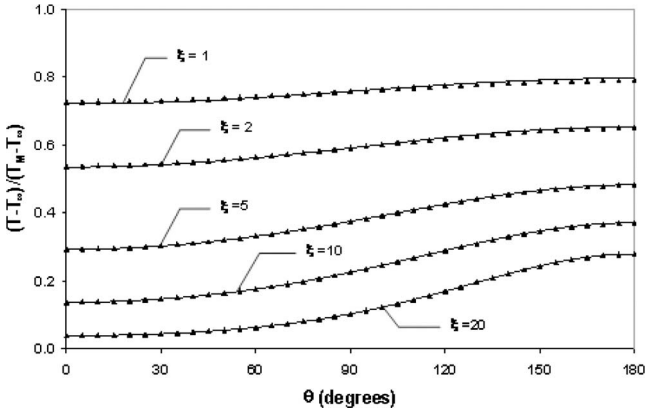

Fig. 4 Circumferential reduced temperature distribution for mechanical dissipation heating and selected summation maxima, ((—) Eq. (60) with $N=1-5$; (▲) Eq. (60) with $N=0$, $P=0.1$, $B=0$, and $\varepsilon=1$)

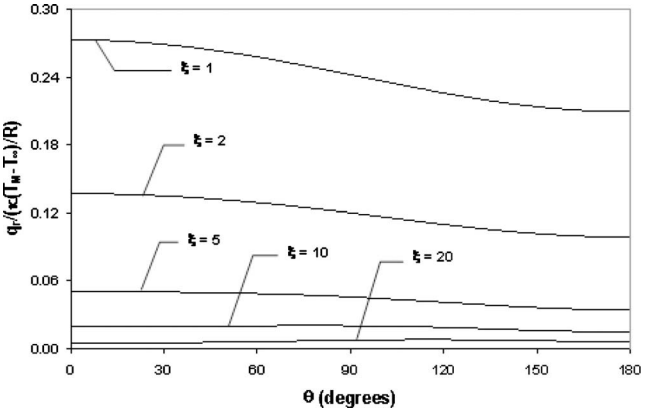

Fig. 6 Circumferential reduced radial heat flux distributions for mechanical dissipation heating ($P=0.1$, $B=0$, and $\varepsilon=1$)

$$(\lambda K_1(\lambda) + K_0(\lambda)/\varepsilon)A_0 + (PK_1(\lambda)/4)A_1 = \varphi C_0/\varepsilon \quad \text{for } n=0 \tag{56}$$

$$(PK_0(\lambda)/2)A_0 + (\lambda K_0(\lambda) + (1+1/\varepsilon)K_1(\lambda))A_1 + (PK_2(\lambda)/4)A_2 = \varphi C_1/\varepsilon \quad \text{for } n=1 \tag{57}$$

$$(PK_{n-1}(\lambda)/4)A_{n-1} + (\lambda K_{n-1}(\lambda) + (n+1/\varepsilon)K_n(\lambda))A_n + (PK_{n+1}(\lambda)/4)A_{n+1} = \varphi C_n/\varepsilon \quad \text{for } n=2,3,4,\ldots,\infty \tag{58}$$

This is an infinite set of algebraic equations to solve for the A's. Truncation to N equations produces a tridiagonal set, which can be solved without iteration or matrix inversion. Solutions must be carried out for successively larger values of N until convergence is obtained. This was accomplished by first assigning a value of zero to each A and terminating the successive solution process when each A at truncation number N differed from the corresponding A at truncation number $N-1$ by no more than 10^{-15}. This ensures both that convergence has been achieved for all A's through A_N and that all A's beyond A_N are negligible.

Once the converged A's are obtained, they can be substituted into the combination of Eqs. (39), (44), and (55) (taking truncation into account) to yield the temperature distribution. The structure of Eqs. (56)–(58) suggests the substitution

$$A_n = \varphi \hat{A}_n/\varepsilon \tag{59}$$

In terms of the $\hat{A}$'s, the corresponding temperature distribution can be written as

$$(T-T_\infty)/(T_M-T_\infty) = \exp(-Pr\cos(\theta)/(2R)) \times \sum_{n=0}^{N} \hat{A}_n K_n(\lambda r/R)\cos(n\theta)/\varepsilon \tag{60}$$

Equation (60) represents an extension of the classical quasisteady moving heat source solutions discussed by Carslaw and Jaeger [17] to a configuration pertinent to FSW.

The circumferential variation in reduced temperature for several radial positions and truncation numbers is shown in Fig. 4, for a typical parametric combination. It can be seen that the series in Eq. (60) converges rapidly with the one term truncation ($N=0$) being remarkably accurate. This one term truncation exhibits a maximum error of about 2% occurring on the pin surface. The general applicability of the one term solution will be discussed subsequently.

A corresponding reduced radial heat flux distribution can be obtained by combining Eqs. (9) and (60) to get

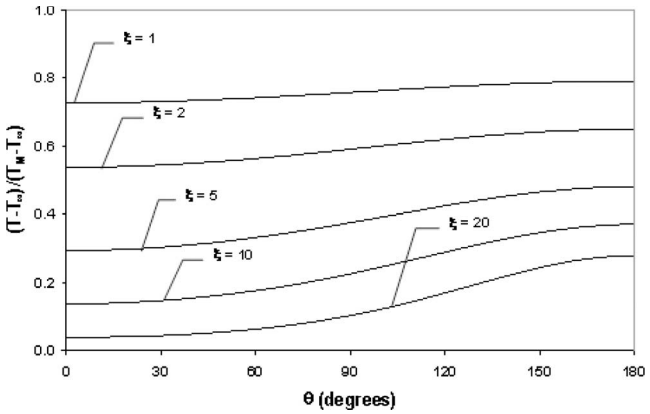

Fig. 5 Circumferential reduced temperature distributions for mechanical dissipation heating ($P=0.1$, $B=0$, and $\varepsilon=1$)

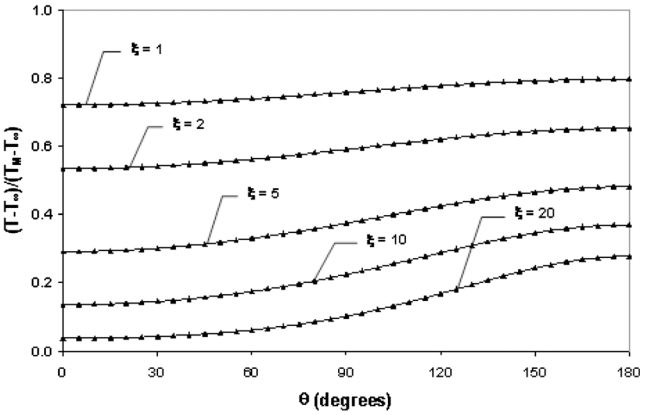

Fig. 7 Circumferential reduced temperature distributions for mechanical dissipation heating ((—) Eq. (64) and (▲) Eq. (60) with $N=0$, $P=0.1$, $B=0$, and $\varepsilon=1$)

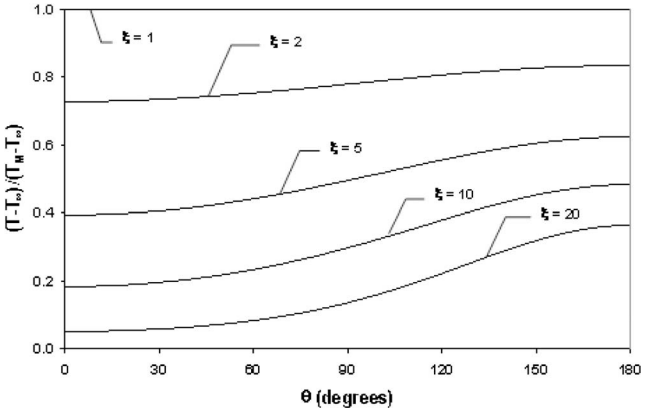

Fig. 8 Circumferential reduced temperature distributions for constant surface temperature (*P*=0.1 and *B*=0)

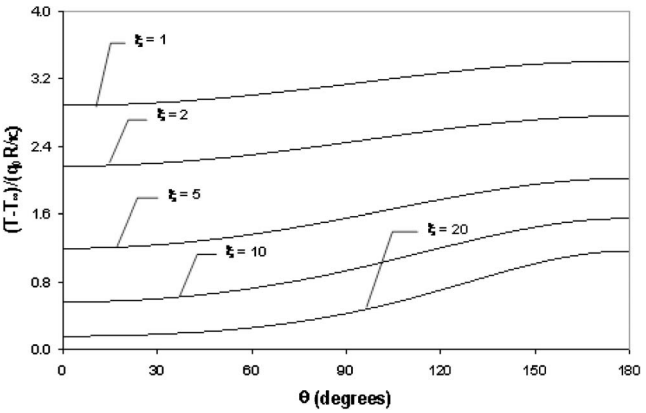

Fig. 9 Circumferential reduced temperature distributions for constant surface heat flux (*P*=0.1 and *B*=0)

$$q_r/(\kappa(T_M - T_\infty)/R) = \exp(-Pr\cos(\theta)/(2R))(\hat{A}_0(\lambda K_1(\lambda r/R) + P\cos(\theta)K_0(\lambda r/R)/2) + \sum_{n=0}^{N} \hat{A}_n(\lambda K_{n-1}(\lambda r/R) + (nR/r)K_n(\lambda r/R) + P\cos(\theta)K_n(\lambda r/R)/2)\ \cos(n\theta))/\varepsilon \quad (61)$$

Figures 5 and 6 show respective reduced temperature and radial heat flux circumferential profiles obtained for several radial positions.

For the special case of $P \ll 1$, the exponential appearing in Eq. (52) can be approximated by unity and they assume the forms

Table 1 Truncation numbers for selected Peclet numbers and three configurations (*B*=0)

	N		
P	Mechanical dissipation heating ($\varepsilon=1$)	Constant surface temperature	Constant surface heat flux
0.1	6	6	6
0.2	7	7	6
0.3	7	8	7
0.4	8	8	7
0.5	8	8	8
0.6	8	9	8
0.7	8	9	8
0.8	9	9	8
0.9	9	9	8
1.0	9	10	9

$$C_n = \begin{cases} 1 & \text{for } n = 0 \\ 0 & \text{otherwise} \end{cases} \quad (62)$$

Substituting Eq. (62) into Eqs. (56)–(58) and using Eq. (59) lead to

$$\hat{A}_n = \begin{cases} \varepsilon/(K_0(\lambda) + \varepsilon\lambda K_1(\lambda)) & \text{for } n = 0 \\ 0 & \text{otherwise} \end{cases} \quad (63)$$

Substituting Eq. (63) into Eq. (60) gives the corresponding temperature distribution

$$(T - T_\infty)/(T_M - T_\infty) = \exp(-Pr\cos(\theta)/(2R))(K_0(\lambda r/R)/(K_0(\lambda) + \varepsilon\lambda K_1(\lambda))) \quad (64)$$

Figure 7 shows the reduced temperature circumferential profiles obtained from Eq. (64). It is seen from Fig. 7 that this replicates the solution obtained from Eq. (60) by considering only the first term in the series (i.e., with $N=0$). The solution for mechanical dissipation heating contains two special cases, which are of interest. These are discussed next.

Equating ε to zero in Eq. (41) and combining the result with Eq. (39) evaluated at $\xi=1$ yield

$$T(1, \theta) = T_M \quad (65)$$

This describes the special case of a pin (cylinder) held at a constant temperature T_M, for which Eq. (60) can be shown to simplify to

Table 2 Measures of surface temperature and surface heat flux for three configurations (*B*=0)

Configuration	Quantity	max	min	av	(max−min)/av
Mechanical dissipation heating ($\varepsilon=1$)	$(T-T_\infty)/(T_M-T_\infty)$	0.7908	0.7270	0.7589	0.0841
	$q_r/(\kappa(T_M-T_\infty)/R)$	0.2730	0.2092	0.2411	0.2646
Constant surface temperature	$q_r/(\kappa(T_M-T_\infty)/R)$	0.4034	0.2346	0.3190	0.5292
Constant surface heat flux	$(T-T_\infty)/(q_0R/\kappa)$	3.4128	2.8861	3.1495	0.1672

Table 3 Maximum reduced temperatures for typical configurations involving AA 6061-T6 κ=170 N/(s K), α=69.7 mm^2/s, T_M=855.16 K, and $\tau_{0,0}$=65.12 N/mm^2

Ref.	R (mm)	R_s (mm)	D (mm)	H (mm)	V (mm/s)	Ω (1/s)	f	P	ε	$(T-T_\infty)/(T_M-T_\infty)$ Predicted Series	Predicted One term	Obs.
[5]	3.175	9.5	5.5	6.4	2.0	41.89	5.289	0.091	1.0	0.79	0.80	0.81
[6]	6.0	25.0	12.0	12.7	1.59	66.71	12.337	0.137	0.0753	0.98	1.00	0.94
[9]	3.0	12.0	6.4	6.4	2.33	52.36	10.844	0.1002	0.436	0.90	0.92	0.86
[13]	2.6	12.0	6.4	6.4	2.22	36.02	14.178	0.0828	0.6467	0.86	0.87	0.84

$$(T-T_\infty)/(T_M-T_\infty)=\exp(-Pr\cos(\theta)/(2R))\times\sum_{n=0}^{\infty}C_nK_n(\lambda r/R)/(K_n(\lambda))\cos(n\theta) \quad (66)$$

This is identical (when notational differences are taken into account) to the result presented by Trivedi and Srinivasan [15]. Figure 8 shows reduced temperature circumferential profiles based on Eq. (66) for several radial distances and a typical parametric combination.

Substituting

$$\varphi=\varepsilon q_0R/(\kappa T_\infty) \quad (67)$$

into Eq. (41) and equating ε to infinity in the result yield

$$\partial_\xi\psi(1,\theta)-P\cos(\theta)\psi(1,\theta)/2=-q_0R\exp(P\cos(\theta)/2)/(\kappa T_\infty) \quad (68)$$

This is equivalent to

$$q_r(1,\theta)=q_0 \quad (69)$$

This describes the special case of a pin (cylinder) subjected to a constant heat flux q_0, for which Eq. (60) can be shown to simplify to

$$(T-T_\infty)/(q_0R/\kappa)=\exp(-Pr\cos(\theta)/(2R))\sum_{n=0}^{N}\hat{A}_nK_n(\lambda r/R)\cos(n\theta) \quad (70)$$

with

$$\hat{A}_n=\kappa T_\infty A_n/(q_0R) \quad (71)$$

Figure 9 shows circumferential reduced temperature profiles based on Eq. (70) for several radial locations and a typical parametric combination. Comparison of Figs. 5 and 9 shows that the circumferential temperature variation at the pin surface produced by a constant surface heat flux is greater than that produced by mechanical dissipation heating.

Table 1 illustrates the effect of the Peclet number on the truncation number. For all three configurations discussed heretofore, the truncation numbers are modest. Most FSW processes are characterized by $P\ll 1$. Thus, the issue of truncation does not appear to be a constraint on the utility of the closed form solutions presented herein.

Table 2 is presented to quantify the observations mentioned previously. Comparison of the entries in the last column corresponding to the first and last lines of Table 2 indicates that the surface temperature variation produced by a constant surface heat flux is about twice as great as that produced by mechanical dissipation heating. Similarly, comparisons of the entries in the last column of Table 2 corresponding to the two middle lines show that the surface radial heat flux produced by a constant surface temperature is about twice that associated with mechanical dissipation heating. This issue is important because several FSW heat transfer models represent the heating as a specified heat source. This does not capture the fact that increasing temperature produces reduced yield stress and, thus, reduced heating. The present model is able to capture this phenomenon and suggests that a constant heat flux model may overestimate the temperature variation.

It is of interest to compare the predictions of the present simplified model with available experimental results. Table 3 presents comparisons of observed and predicted peak reduced temperatures for four typical configurations (for AA 6061-T6 FSW) discussed in previously cited literature. The material properties of AA 6061-T6, used in calculations, are given and the value of $\tau_{0,0}$ was obtained by tuning the model to predict temperatures in the FSW range. Columns 8–10 show the values of intermediate quantities calculated based on the workpiece dimensions and process parameters displayed in Columns 2–7.

Columns 11 and 12 contain respective predicted peak reduced temperatures obtained from the series solution (given by Eq. (60)) and the corresponding one term solution. Column 13 presents estimates of the maximum reduced temperatures inferred from the results discussed in each of the sources cited. Maximum temperatures were not reported and had to be estimated based on available tables and figures.

It can be seen from Table 3 that the series solution is quite accurate in predicting the peak reduced temperatures (with a maximum error of about 5% for the configuration of Chen and Kovacevic [9]). The one term solution is also acceptable (with a maximum error of about 7% for the configuration of Chen and Kovacevic [9]) but exhibits slightly greater errors overall.

5 Parametric Studies

It is of interest to investigate the sensitivity of the mechanical dissipation heating model to the values of the parameters P, ε, and B. It was found using Eqs. (3), (27), and (34)–(37) and information given in previously cited literature that respective representa-

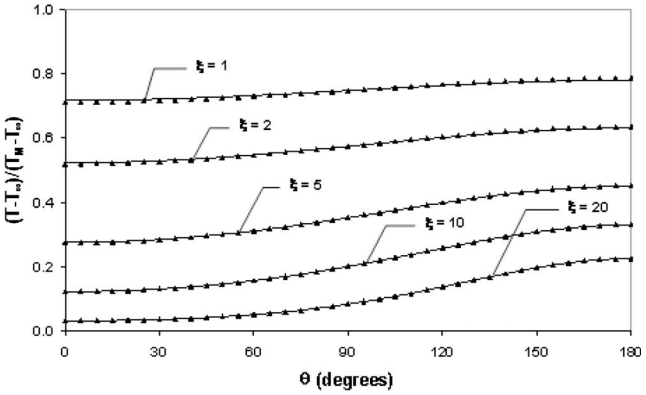

Fig. 10 Circumferential reduced temperature distributions for mechanical dissipation heating ((—) series solution and (▲) one term solution with P=0.1, B=0.001, and ε=1.0)

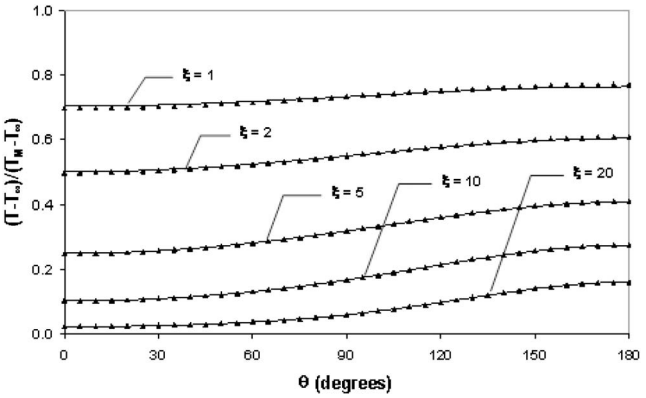

Fig. 11 Circumferential reduced temperature distributions for mechanical dissipation heating ((—) series solution and (▲) one term solution with $P=0.1$, $B=0.003$, and $\varepsilon=1.0$)

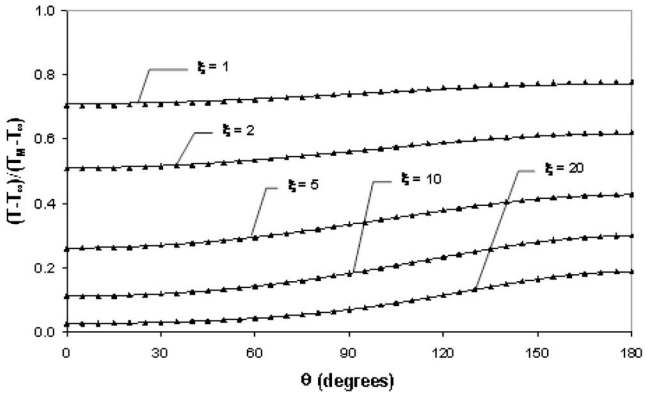

Fig. 13 Circumferential reduced temperature distributions for mechanical dissipation heating ((—) series solution and (▲) one term solution with $P=0.1$, $B=0.002$, and $\varepsilon=1.0$)

tive ranges for these parameters are [0.1, 0.6], [0.05, 1.0], and [0.0, 0.003]. In addition, it is of interest to establish the range of applicability of the one term solution described by Eq. (60), since it is a direct generalization of the classical moving line source solution. The remainder of this section presents results pertinent to these issues.

Figures 10 and 11 are representative of the sensitivity of the model to B. Comparing Figs. 10 and 11 reveals a very moderate sensitivity to the Biot number. In both simulations, the one term solution is observed to be quite accurate, exhibiting a maximum error of about 0.8% occurring at the pin surface in Fig. 10.

The sensitivity of model predictions to the value of ε is illustrated by Figs. 12 and 13. Here, the sensitivity is significant. The simulation for the smaller value of ε presented in Fig. 12 is illustrative of qualitative (as well as quantitative) inaccuracy of the one term solution for $\varepsilon \ll 1$. While the maximum quantitative inaccuracy is on the order of 5%, the one term solution is qualitatively in error by predicting temperatures in excess of the melting temperature. This, of course, is physically impossible (and, therefore, the one term solution has been terminated upon reaching the melting temperature in Fig. 12 and subsequent similar figures). The behavior for $\varepsilon \ll 1$ closely resembles that for a constant temperature pin, which the one term solution cannot capture. Figure 13 demonstrates that the accuracy of the one term solution improves with increasing ε.

Figures 14–16 illustrate the effect of varying P for a fixed combination of ε and B. Reduced temperatures corresponding to the low end of the ε range are shown in these figures. It can be seen that increasing P (increasing the welding speed) decreases the reduced temperatures. The error in the one term solution increases significantly (especially at the pin surface) with increasing Peclet number.

Similar results to those depicted in Figs. 14–16 were obtained for values of ε in the middle and high ends of the realistic range. These simulations (which are not presented graphically) confirmed the trends discussed in connection with Figs. 14–16 but showed that these trends become less pronounced as P increases. In particular, the accuracy of the one term solution was found to improve markedly as ε increases.

6 Conclusion

The three-dimensional FSW heat transfer problem was reduced to a 2D problem by averaging the governing equation and boundary conditions over the thickness of the workpiece and by replacing various pin tool configurations with a simplified pin only configuration. The workpiece was assumed to be infinite to facilitate closed form solutions. Mechanical dissipation heating was modeled as a function of the workpiece yield stress, thus implicitly treating it as a function of the material's melting temperature.

A closed form solution to the corresponding boundary value problem was obtained, which involved an infinite set of tridiagonal algebraic equations which had to be truncated and solved numerically. It was found that only a moderate number of equations had to be retained to achieve accurate results for all parametric combinations considered. A one term truncation was found to emerge from the assumption of $P \ll 1$, which represented a generalization of the classical quasistatic moving line source solution to FSW. The series solution contained the constant pin temperature and constant pin heat flux configurations as special cases. The mechanical dissipation heating solution was used to estimate peak

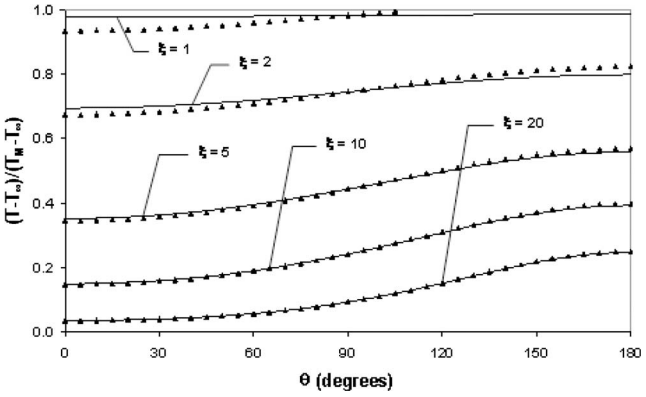

Fig. 12 Circumferential reduced temperature distributions for mechanical dissipation heating ((—) series solution and (▲) one term solution with $P=0.1$, $B=0.002$, and $\varepsilon=0.05$)

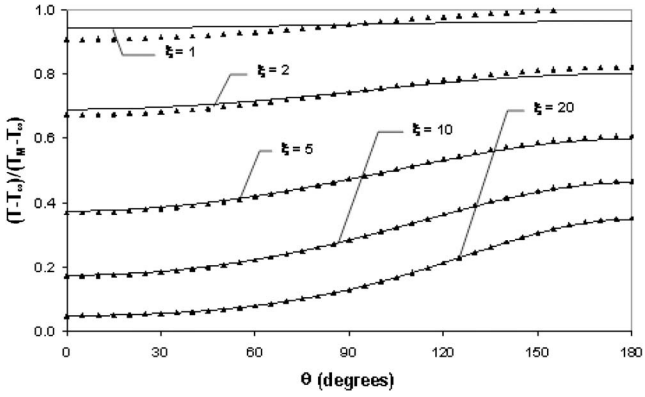

Fig. 14 Circumferential reduced temperature distributions for mechanical dissipation heating ((—) series solution and (▲) one term solution with $P=0.1$, $B=0$, and $\varepsilon=0.15$)

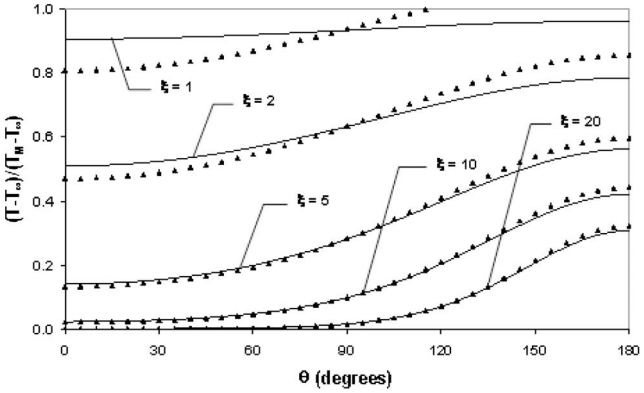

Fig. 15 Circumferential reduced temperature distributions for mechanical dissipation heating ((—) series solution and (▲) one term solution with $P=0.3$, $B=0$, and $\varepsilon=0.15$)

reduced temperatures for typical configurations available in literature and was found to predict remarkably accurate solutions for the cases considered.

A large number of simulations were carried out using the closed form solution. A selected sample of these was presented graphically for illustrative purposes. Some interesting conclusions based on these simulations are as follows.

First, the case of constant pin temperature produces a surface radial heat flux that is about twice of that associated with mechanical dissipation heating while the case of constant pin heat flux produces a pin surface temperature about twice that of mechanical dissipation heating. This suggests that care should be used when using simplified boundary conditions in FSW simulations (as has been done by several investigators who employed the constant pin heat flux model).

Second, the model appears to be considerably less sensitive to B (which characterizes external convection) than to P and ε (which, respectively, characterize the pin tool welding speed and spin rate). Increasing either of these parameters decreases the temperatures.

Third, the one term solution is most accurate for small Peclet numbers and larger ε. It is believed that this approximation, because of its simplicity and the frequent occurrence of small Peclet numbers in practice, is a useful tool for obtaining quick estimates of FSW temperature distributions.

Nomenclature

α = workpiece thermal diffusivity
B_0, B_H = Biot numbers at top and bottom workpiece surfaces

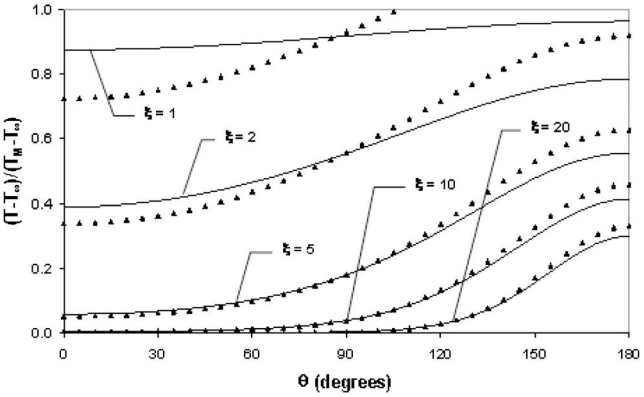

Fig. 16 Circumferential reduced temperature distributions for mechanical dissipation heating ((—) series solution and (▲) one term solution with $P=0.5$, $B=0$, and $\varepsilon=0.15$)

dA = differential area of workpiece surface
dp = power generated due to yield stress acting on dA
D = depth of pin penetration
f = area correction factor
h_0, h_H = heat transfer coefficients at top and bottom workpiece surfaces
H = workpiece thickness
κ = workpiece thermal conductivity
P = Peclet number
p = power
q_n = heat flux acting along **n**
Q = net heat input to the workpiece
(r,θ,z) = polar cylindrical coordinates of a point in the working domain
R = radius of the pin
R_b = radius of the bottom shoulder
R_s = radius of the top shoulder
τ_0 = workpiece yield stress
$\tau_{0,0}$ = a fitting parameter
T = workpiece absolute temperature (or the thickness averaged temperature)
$\bar{T}$ = thickness averaged temperature ($\bar{T}=\int_0^H T dz/H$)
T_M = workpiece melting temperature
T_∞ = ambient temperature
v = magnitude of the workpiece (tool) velocity, **v**
Ω = angular velocity of the tool
ξ = nondimensional radial coordinate ($\xi=r/R$)

References

[1] McClure, J. C., Feng, Z., Tang, T., Gould, J. E., Murr, L. E., and Guo, X., 1998, "A Thermal Model of Friction Stir Welding," *Fifth International Conference on Trends in Welding Research*, pp. 590–595.

[2] Guerra, M., Schmidt, C., McClure, J. C., Murr, L. E., and Nunes, A. C., 2003, "Flow Patterns During Friction Stir Welding," Mater. Charact., **49**, pp. 95–101.

[3] Murr, L. E., Li, Y., Tirllo, E. A., and McClure, J. C., 2000, "Fundamental Issues and Industrial Applications of Friction-Stir Welding," Mater. Technol: Adv. Perform. Mater., **15**, pp. 37–48.

[4] Sutton, M. A., Yang, B., Reynolds, A. P., and Taylor, R., 2002, "Microstructural Studies of Friction Stir Welds in 2024-T3 Aluminum," Mater. Sci. Eng., A, **323**(1–2), pp. 160–166.

[5] Chao, Y. J., and Qi, X., 1998, "Thermal and Thermo-Mechanical Modeling of Friction Stir Welding of Aluminum Alloy 6061-T6," J. Mater. Process. Manuf. Sci., **7**, pp. 215–233.

[6] Song, M., and Kovacevic, R., 2003, "Thermal Modeling of Friction Stir Welding in a Moving Coordinate System and its Validation," Int. J. Mach. Tools Manuf., **43**, pp. 605–615.

[7] Colegrove, P., and Shercliff, H., 2003, "2-dimensional CFD Modeling of Flow Round Profiled FSW Tooling," *TMS Annual Meeting, Friction Stir Welding and Processing II*, pp. 13–22.

[8] Ulysse, P., 2002, "Three-Dimensional Modeling of the Friction Stir-Welding Process," Int. J. Mach. Tools Manuf., **42**, pp. 1549–1557.

[9] Chen, C. M., and Kovacevic, R., 2004, "Thermomechanical Modelling and Force Analysis of Friction Stir Welding by the Finite Element Method," Proc. Inst. Mech. Eng., Part C: J. Mech. Eng. Sci., **218**, pp. 509–519.

[10] Zhu, X. K., and Chao, Y. J., 2004, "Numerical Simulation of TransientTemperature and Residual Stresses in Friction Stir Welding of 304L Stainless Steel," J. Mate. Process., **146**, pp. 263–272.

[11] Lomolino, S., Tovo, R., and dos Santos, J., 2005, "On the Fatigue Behavior and Design Curves of Friction Stir Butt-Welded Al Alloys," Int. J. Fatigue, **27**, pp. 305–316.

[12] Cho, J., Boyce, D. E., and Dawson, P. R., 2005, "Modeling Strain Hardening and Texture Evolution in Friction Stir Welding of Stainless Steel," Mater. Sci. Eng., A, **398**, pp. 146–163.

[13] Soundararajan, V., Zekovic, S., and Kovacevic, R., 2005, "Thermo-Mechanical Model With Adaptive Boundary Conditions for Friction Stir Welding of Al 6061," Int. J. Mach. Tools Manuf., **45**, pp. 1577–1587.

[14] Rosenthal, D., 1941, "The Mathematical Theory of Welding and Cutting," Weld. J. (Miami, FL, U.S.), **20**, pp. 220–234.

[15] Trivedi, R., and Srinivasan, S. R., 1974, "Temperature Distribution Around a Moving Cylindrical Source," ASME J. Heat Transfer, **96**, pp. 427–428.

[16] Raghulapadu, J. K., 2004, "A Rotating Plug Model of Friction Stir Welding Heat Transfer," M.S. thesis, Tennessee Technological University, Cookeville, TN.

[17] Carslaw, H. S., and Jaeger, J. C., 1947, *Conduction of Heat in Solids*, Oxford University Press, London.

Minh Do-Quang
e-mail: minh@mech.kth.se

Gustav Amberg
e-mail: gustava@mech.kth.se

Linné Flow Centre,
Department of Mechanics,
Royal Institute of Technology,
SE-811 81 Sandviken, Sweden

Claes-Ove Pettersson
Research and Development Department,
Sandvik Materials Technology,
Sweden
e-mail: claes-ove.pettersson@sandvik.com

Modeling of the Adsorption Kinetics and the Convection of Surfactants in a Weld Pool

*This paper presents a comprehensive three-dimensional, time-dependent model for simulating the adsorption kinetics and the redistribution of surfactants at the surface and in the bulk of a weld pool. A physicochemical approach that was included in this paper allows the surfactant concentration at the surface and in the bulk to depart from its thermodynamical equilibrium. The Langmuir equilibrium adsorption ratio was based on the k_{seg} coefficient of Sahoo et al. (1988, "Surface-Tension of Binary Metal—Surface-Active Solute Systems Under Conditions Relevant to Welding Metallurgy," Metall. Trans. B, **19B**, pp. 483–491) and was finally used for calculating fluid flow and heat transfer in gas tungsten arc welding of a super duplex stainless steel, SAF 2507. In this study, the authors applied the multicomponent surfactant mass transfer model to investigate the effect of the influence of sulfur and oxygen redistribution in welding of a super duplex stainless steel.* [DOI: 10.1115/1.2946476]

Keywords: surfactant, GTA welding, thermocapillary, mell flow, simulation

1 Introduction

Surface tension in liquid metals is one of the important physicochemical properties in understanding various interfacial phenomena. Moreover, it has been well established that the surface tension force (Marangoni flow) in gas tungsten arc (GTA) welding is identified as the main driving force that dominates the flow behavior in the weld pool and determines the shape and penetration of the solidified weld pool [1,2].

The surface tension of a liquid metal is considerably decreased by the adsorption of surface active elements that are known to be present in large concentrations at the surface [3,4]. Depending on the surfactant contents, the sign of surface tension coefficient $\partial\gamma/\partial T$ can be changed at a certain temperature. This change in the sign of the temperature coefficient of surface tension has significant implications in several practical systems [5].

In liquid metals, surface tension has been proven to depend considerably on the adsorption of surface-active elements such as sulfur, oxygen, and nitrogen. An early work of Szyszkowski in 1908 showed the effect of surface-active elements in liquid metals based on an empirical relation between the molality of the solution and the surface tension of the pure solvent. In 1976, Belton [6] used a combination of the Gibbs and Langmuir adsorption isotherms to develop a similar relation that described the surface tension of a liquid metal in the presence of a surface-active element. Sahoo et al. [1] included the temperature dependence of the surface tension for the pure metal in Belton's work in order to demonstrate how the temperature coefficient of surface tension changed with both temperature and composition of surface-active elements such as oxygen or sulfur. Up to now, many weld pool simulation models were based on the research of Sahoo et al. [9]. The surfactant concentration was presupposed to be constant at the equilibrium state during the simulation on those models [7–10].

In addition to the free surface tension studies, several investigators [11,12] studied the interaction between surfactant physicochemistry and fluid mechanics in a semi-infinite bubble progression model. Their researches focused on the effect of the motion at the surface at the leading end of the bubble on the redistribution of the surfactant. A steady nonequilibrium surface concentration transport equation was introduced. Winkler et al. [2] applied the physicochemical approach to the redistribution of sulfur at the surface and in the bulk for a time-dependent axisymmetric weld pool. With the inclusion of the redistribution of surfactant at the surface, the simulation results were claimed to better adapt to the experimental weld pool shapes. Recently, Winkler and Amberg [13] improved their model to include the redistribution of surfactants on a ternary Fe–S–O system of stainless steel type 304.

It has been shown that in stainless steel melts, the presence of surface-active elements such as oxygen and sulfur greatly influenced the surface tension of the alloys [5,14]. Keene et al. [14] used the levitated drop technique to study the surface tension on the Fe–S–O ternary system. Recently, Divakar et al. [15] used the sessile drop technique to measure the surface tension of liquid Fe–C–S–O alloys. Both of them agree well, and those results are used in this calculation.

In this paper, first a review of the results of the previous studies considering only sulfur redistribution is given. Furthermore, we seek to develop a more complex three-dimensional model that is capable of simulating the surfactant transport in a multicomponent system. However, in this paper, considering the relative importance of the surface-active elements in the present material and the increasing computational effort, only the Fe–S–O system is investigated.

2 Mathematical Modeling

The present mathematical model is an extension of our previous models. It was developed based on the three-dimensional, time dependent model of heat and momentum transfer [16] and extended the simple redistribution of the surfactant model on a binary system, Fe–S [17]. As in previous models we also consider the buoyancy, electromagnetic and surface tension forces, and the effect of the moving heat source. The motion of the melt is thus described by the Navier–Stokes equations by considering the liquid metal as an incompressible Boussinesq liquid,

$$\nabla \cdot \mathbf{u} = 0 \tag{1}$$

Contributed by the Heat Transfer Division of ASME for publication in the JOURNAL OF HEAT TRANSFER. Manuscript received April 16, 2007; final manuscript received March 3, 2008; published online July 9, 2008. Review conducted by Ben Q. Li.

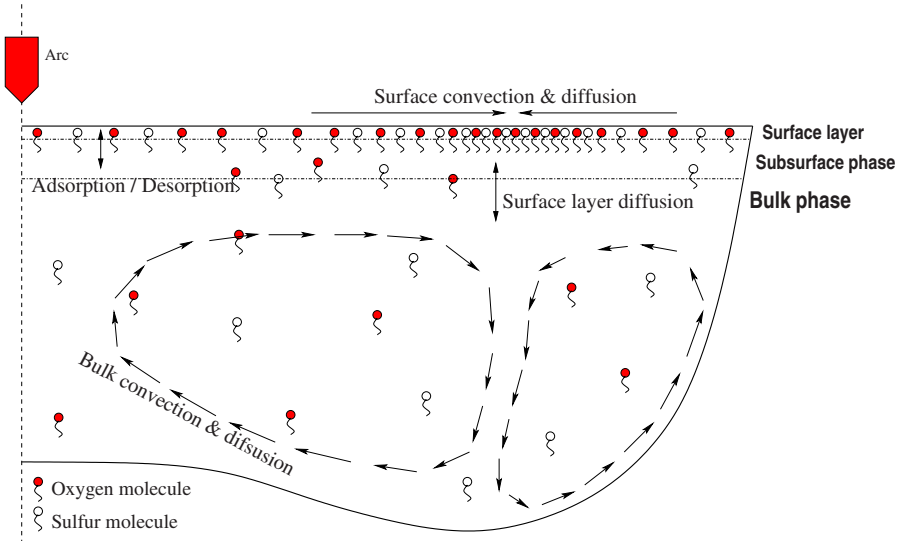

Fig. 1 Modeling multicomponent surfactant mass transfer in the weld pool

$$\frac{D\mathbf{u}}{Dt} - \frac{\partial(U_s\mathbf{u})}{\partial y} = -\frac{1}{\rho}\nabla p + \nabla\cdot(\nu((\nabla\mathbf{u}) + (\nabla\mathbf{u})^T)) + \mathbf{S} \tag{2}$$

where $\mathbf{u}$ is the fluid velocity of melt, U_s is the moving speed of arc; p is the pressure; ρ and ν are the melt density and the kinematic viscosity; $\mathbf{S}$ is the source term that includes the Lorentz force, the natural convection, etc. More details about the model for source term $\mathbf{S}$ can be found in Ref. [16]. The energy conservation is expressed as follows:

$$\frac{DT}{Dt} - \frac{\partial(U_sT)}{\partial y} = \alpha\Delta T + \frac{L^*}{\rho C_p}\left(\frac{\partial\chi}{\partial t} - \frac{\partial(U_s\chi)}{\partial y}\right) \tag{3}$$

where T is the temperature, α is the thermal diffusivity, C_p is the specific heat, L^* is the latent heat of fusion, and χ is the fraction of volume occupied by melt [18]; χ has a value of 0 in the solid region and 1 in the completely moten region. The two terms containing U_s appear as a result of the coordinate transformation [16].

At the upper surface of the workpiece, in the weld pool area, the surface tension gradient enters as a boundary condition for shear stress on the free surface (index s indicates a surface gradient operator),

$$\mu((\nabla\mathbf{u}) + (\nabla\mathbf{u})^T)\cdot\mathbf{n} = \nabla_s\gamma = \frac{\partial\gamma}{\partial T}\cdot\nabla_s T \tag{4}$$

where μ is the dynamic viscosity of the fluid and $\partial\gamma/\partial T$ is the temperature coefficient of surface tension. $\partial\gamma/\partial T$ will be computed following the Gibbs and Langmuir adsorption isotherm theory, which will be presented in the following section.

The heat input from the arc was simulated, and heat losses due to evaporation, convection, and radiation were considered. The heat flux distribution at the top was supposed to be Gaussian and could be expressed by the following equation:

$$q_{\text{Gauss}} = \frac{3Q}{\pi r_a^2}\exp\left(-\frac{3(x^2+y^2)}{r_a^2}\right) \tag{5}$$

where $Q=EI\eta$ is the total heat input, with the arc voltage E, the electric current I, and the arc efficiency η, and r_a is the effective radius of heat distribution. The evaporation heat flux was computed according to [19]

$$q_{\text{evap}} = Wh_{fg} \tag{6}$$

where q_{evap} denotes the evaporation heat flux and h_{fg} is the heat of evaporation. W is obtained by using

$$W = \exp(A_1 + \log(p_{\text{atm}}) - 0.5\log(T)) \tag{7}$$

Here A_1 is a constant varying slightly for the different species of the material to be treated and p_{atm} is the vapor pressure as obtained from [19]

$$\log(p_{\text{atm}}) = 6.121 - \frac{18.836}{T} \tag{8}$$

The radiative q_{rad} and convective q_{conv} heat losses can be calculated by using

$$q_{\text{rad}} = \sigma_b\epsilon(T^4 - T_a^4) \tag{9}$$

and

$$q_{\text{conv}} = h_c(T - T_a) \tag{10}$$

where σ_b is the Stefan–Boltzmann constant, ϵ the emissivity of steel, h_c the convection heat transfer coefficient, expressing the convective heat exchange between the top surface and the environment, and T_a the ambient temperature. The complete thermal boundary condition at the top surface then becomes

$$-k\frac{\partial T}{\partial z} = -q_{\text{Gauss}} + q_{\text{evap}} + q_{\text{rad}} + q_{\text{conv}} \tag{11}$$

Here, k is the thermal conductivity. The sidewalls and the bottom of the plate are assumed isothermal at the ambient temperature T_a=288 K due to the use of a cooled copper plate. The Neumann boundary condition $\mathbf{n}\cdot\nabla T$=0 is applied on the remaining faces of the plate: symmetry, inlet, and outlet faces.

2.1 Surfactant Mass Transfer. In order to study the surfactant phenomena at the surface of the weld pool, we used the *mixed kinetic-diffusion* model [20] where the weld pool is subdivided into three regions: the surface, the subsurface, and the bulk. The surface is supposed to be a Langmuir monolayer [21], forming a layer that is only one molecule or atomic diameter in thickness. The subsurface layer is an important aspect of kinetic models where this acts as an adsorption/desorption barrier that prevents the surfactant from adsorbing to the surface and vice versa [22]. In this model, the surfactant diffuses from the bulk to the subsurface layer by the same diffusion equation as in the bulk. However, once in the subsurface layer, the surfactant is not instantaneously adsorbed at the interface. Only those molecules that possess energy greater than a specified adsorption barrier will be able to adsorb, [12,23,24]. An illustration of the physicochemical mecha-

nisms in a weld pool can be seen in Fig. 1.

In the absence of motion, the surfactant adsorbed along the surface layer establishes an equilibrium surface concentration Γ_{eq}. The strength of the attraction of the adsorbed atom/molecule to the surface depends on the nature and the strength of the interaction between the atom and the surface. There are two types of adsorption: chemical and physical adsorption. In chemical adsorption, the atoms are strongly attracted to the surface and form chemical bonds. In physical adsorption, the atoms are weakly attracted due to van der Waals interactions.

In fact, there is a strong convection in the weld pool. With this convection, the molecules in the bulk and the surface regions are redistributed due to convection and diffusion. Viewing Fig. 1 again, there are two convective patterns in opposite directions. These appeared at the surface layer as two opposite flows. They transfer the molecules in the subsurface phase and at the surface layer toward the stagnation point and cause a higher concentration of the surfactant in that region.

The extension from a binary to a ternary system was achieved by a superposition of two binary systems [25]. Keene et al. proposed that the effects of oxygen and sulfur on the surface tension in the iron alloy are essentially additive [14]. With a strong convection present at the surface of the weld pool, a nonequilibrium surface concentration Γ develops and is determined by surface convection and diffusion for each surfactant of the species i [26] from the equation

$$\frac{\partial \Gamma_i}{\partial t} + \nabla_s \cdot (\Gamma_i \mathbf{u}_s) = \frac{1}{\mathrm{Pe}_{s,i}} \nabla_s^2 \Gamma_i + j_i^n \tag{12}$$

where ∇_s is a surface gradient operator, $\mathbf{u}_s$ is the surface velocity, $\mathrm{Pe}_{s,i} = U'L/D_s$ is the surface Péclet number, which relates surface convection rates U' to surface diffusion rates $D_{s,i}$, L is the length scale, and j_i^n is the mass flux to the surface. In the mixed kinetic-diffusion model, the bulk and the surface region are connected via the mass flux j_i^n from a sublayer, which occurs in a two-step serial process. The first step involves diffusion of surfactant from the bulk. In this case, j_i^n is provided by Fick's law

$$j_i^n = -D_{m,i}(\mathbf{n} \cdot \nabla) C_i \tag{13}$$

Here, $D_{m,i}$ is the bulk diffusion coefficient of the surfactant in the liquid material and C_i is the surfactant concentration in the bulk. The second step involves an adsorption to and desorption from the free surface. In this step, the most popular model is based on the Langmuir adsorption kinetics theory [12,24],

$$j_i^n = k_{\beta,i} C_{s,i} \Gamma_{\infty,i} \left(1 - \frac{\Gamma_i}{\Gamma_{\infty,i}}\right) - k_{\alpha,i} \Gamma_i \tag{14}$$

Here, $\Gamma_{\infty,i}$ is the upper bound on the surfactant concentration for monolayer adsorption. The adsorption rate, the first term on the right hand side, is the first order in bulk concentration that is adjacent to the surface, $C_{s,i}$. The desorption rate, the second term, is proportional to the surface concentration Γ_i. The rate coefficients k_α and k_β could be computed if the potential adsorption and desorption barrier ϵ_β and ϵ_α exists [27],

$$k_\alpha = f_\alpha(\bar{v}) \exp\left(-\frac{\epsilon_\alpha}{RT}\right) \tag{15}$$

$$k_\beta = f_\beta(\bar{v}) \exp\left(-\frac{\epsilon_\beta}{RT}\right) \tag{16}$$

where $\bar{v}$ is the mean velocity of the surfactant molecules and RT is the product of the ideal gas constant and the absolute temperature. Since the values of ϵ_α and ϵ_β are not available from experiments, we use the value of the ratio of k_α/k_β together with the condition of the adsorption rate and the desorption rate at the equilibrium state for the computation of Eq. (14) [13].

The multicomponent mass transfer equation for the surfactant in the bulk liquid is written as follows:

$$\frac{\partial C_i}{\partial t} + (\mathbf{u} \cdot \nabla) C_i = \frac{1}{\mathrm{Pe}_{m,i}} \nabla^2 C_i \tag{17}$$

where $\mathrm{Pe}_{m,i} = U'L/D_{m_i}$ is the bulk Péclet number, which relates the convection rate to the diffusion rate, $D_{m,i}$. The following boundary conditions complete the bulk transport formulation at the top surface of the weld pool. For the bottom face and the sidewall of the workpiece, the following Neumann boundary conditions are used for Eq. (17):

$$\mathbf{n} \cdot \nabla C_i = 0 \tag{18}$$

At the top surface of the weld pool, the mass flux in the surface transport equation (Eq. (12)) is given by the adsorption-desorption flux in Eq. (14). Equations (13) and (14) provide this coupling as a boundary condition on Eq. (17).

In this model, the surface concentration equation (Eq. (12)) becomes a two-dimensional equation, with Neumann boundary conditions applied at the symmetry axis and the outer upper edge of the workpiece,

$$\mathbf{n} \cdot \nabla_s \Gamma_i = 0 \tag{19}$$

2.2 Thermodynamics of Adsorption. The surface concentration, Γ, directly modifies the surface tension by the surfactant equation of state, $\gamma = f(\Gamma)$. In general, the equation of state is a nonlinear function where increasing Γ reduces γ. The most significant relation in surface thermodynamics is the Gibbs adsorption equation for the variation of surface tension γ with the temperature and with the adsorption at the surface of chemical species i [25],

$$d\gamma = -SdT - \sum_{i=1}^{n} \Gamma_i d\mu_i = -SdT - RT \sum_{i=1}^{n} \Gamma_i d(\ln C) \tag{20}$$

where S is the entropy per unit volume and μ_i is the chemical potential of chemical species i. The purpose of the ideal adsorption isotherm that is applied in a monolayer model is to relate the surfactant concentration in the bulk and the adsorbed amount at the surface. There are a number of equations that can be used, but the Langmuir isotherm equation is the most common.

As introduced by Langmuir, at the equilibrium stage, the rate of the change in Γ due to adsorption and desorption is equal. Thus, the equilibrium adsorption isotherm relating Γ_{eq} is obtained as

$$\Gamma_i = \Gamma_{\infty,i} \left(\frac{k_{L,i} C_{s,i}}{1 + k_{L,i} C_{s,i}}\right) \tag{21}$$

Here, the adsorption number $k_{L,i}$ is the Langmuir equilibrium adsorption ratio $k_{L,i} = k_{\beta,i}/k_{\alpha,i}$.

From Eqs. (21) and (20), the surface tension equation of state can be written in two equivalent ways, the Szyszkowski equation (Eq. (22)) and the Frumkin equation (Eq. (23)),

$$\gamma = \gamma_{eq} - RT \sum_{i=1}^{n} \Gamma_{\infty,i} \ln(1 + k_{L,i} C_i) \tag{22}$$

$$\gamma = \gamma_{eq} + RT \sum_{i=1}^{n} \Gamma_{\infty,i} \ln\left(1 - \frac{\Gamma_i}{\Gamma_{\infty,i}}\right) \tag{23}$$

where γ_{eq} is the surface tension of pure melt at the melting point.

Belton [6] and Belton and Hunt Medalist [28] applied the same combination of the Gibbs and Langmuir adsorption isotherms and pointed out that for the ideal adsorption and the monolayer model, the value of the adsorption coefficient for a liquid metal might be related to the surface tension through the presence of a surface-active element a_i

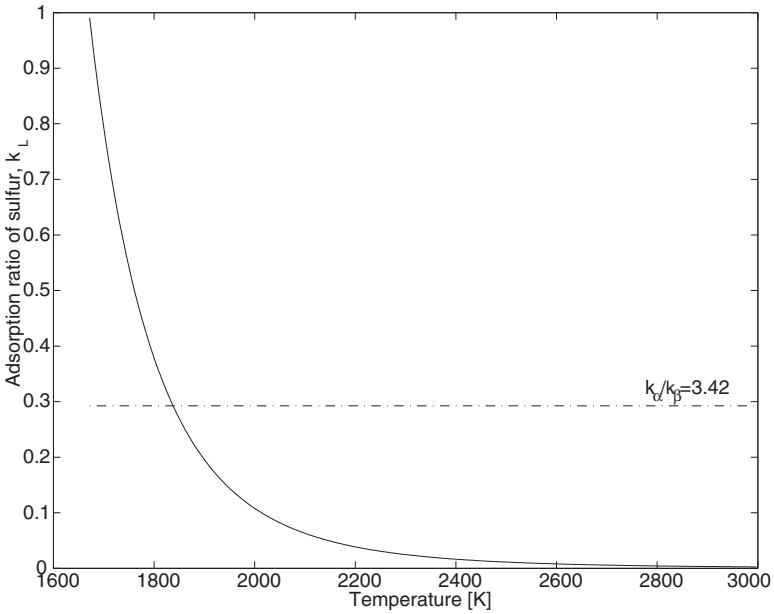

Fig. 2 The Langmuir equilibrium adsorption ratio of sulfur, $k_{L,S}$

$$\gamma = \gamma_{eq} - RT\sum_{i=1}^{n} \Gamma_{\infty,i} \ln(1 + K_{seg,i} a_i) \tag{24}$$

where the equilibrium constant for segregation K_{seg} is obtainable from Eq. (25), k_l is a constant related to the entropy of segregation, and ΔH_0 is the standard heat of adsorption,

$$K_{seg,i} = k_{l,i} \exp\left(-\frac{\Delta H_{0,i}}{RT}\right) \tag{25}$$

By comparing Eqs. (22) and (24), we could find a relation between the Langmuir equilibrium adsorption ratio $k_{L,i}$ and the equilibrium constant for segregation $K_{seg,i}$,

$$k_{L,i} = \frac{a_i}{C_i} K_{seg,i} = C_{f,i} K_{seg,i} \tag{26}$$

where $C_{f,i}$ is a factor converting from bulk concentration to mass percent, are the unit of activity element a_i. Thus, $k_{L,i}$ is now dependent on the temperature. The dependence on temperature of the Langmuir equilibrium adsorption ratio of sulfur and oxygen is shown in Figs. 2 and 3. There is also a comparison that was used in Refs. [2,17] with a constant value of the ratio of k_α/k_β (see Figs. 5 and 8).

At thermodynamic equilibrium, the surface tension equation of state with constant coefficients (A, $K_{seg,i}$) was computed from experimental data in [5]

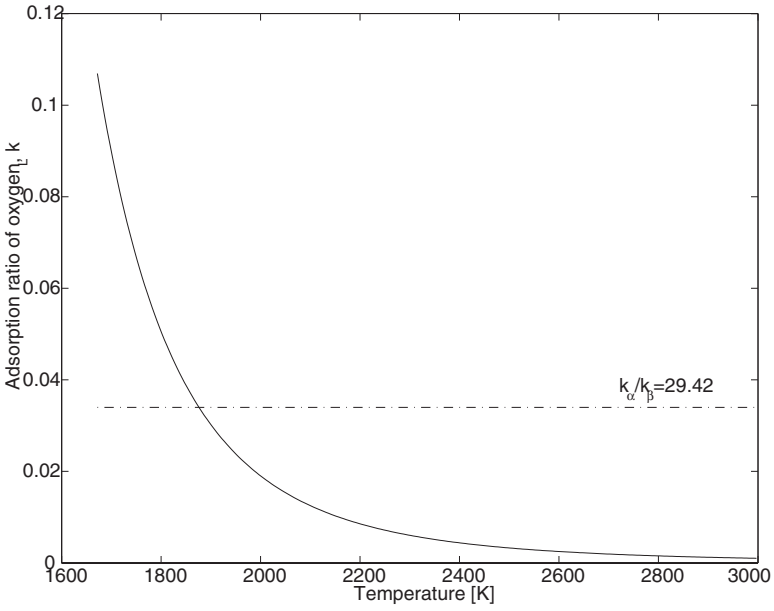

Fig. 3 The Langmuir equilibrium adsorption ratio of oxygen, $k_{L,O}$

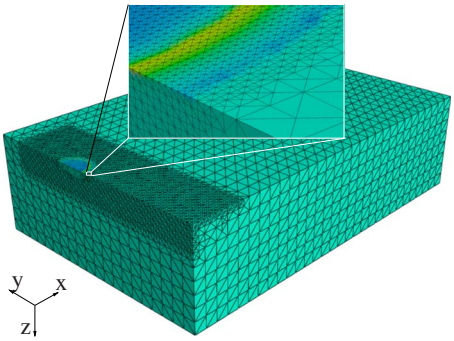

Fig. 4 An adaptive mesh

$$\gamma = \gamma_{\text{eq}} - AdT - RT\sum_{i=1}^{n} \Gamma_\infty \ln(1 + K_{\text{seg},i} a_i) \tag{27}$$

or

$$\gamma = \gamma_{\text{eq}} - AdT - RT\sum_{i=1}^{n} \Gamma_\infty \ln(1 + k_{L,i} C_i) \tag{28}$$

Here, A is the negative of $d\gamma/dT$ for pure metals.

2.3 Numerical Modeling. In the present work, an automatic generated code [29] has been used for solving the equations described in the mathematical modeling section. This code could be applied in a three-dimensional domain and for time dependent problems. Before we could solve the bulk and the surface concentration equations, the set of continuity, momentum, and energy equations need to be solved by using the numerical model that was presented in our previous work [16]. Since we have the updated values for $\mathbf{u}(x,y,z)$ and $T(x,y,z)$, the bulk concentration field $C(x,y,z)$ and the surface concentration field $\Gamma(x,y,z)$ can be calculated by solving Eqs. (17) and (12). A fully implicit method has been adopted for the bulk and surface equations. The two linearized algebraic systems are solved using a preconditioned generalized minimal residual method (GMRES). We also used a streamline-diffusion method [30] in order to increase the stability of the convective terms in Eqs. (17) and (12).

At each time step, the bulk concentration C and the surface concentration Γ in Eqs. (17) and (12) were solved using an iterative procedure. At a new time step, initial values are set to previous time step values ($\tilde{\Gamma}^k$, $\tilde{C}^k$); then the following iterative system was solved:

$$\frac{\tilde{\Gamma}^{k+1} - \Gamma^n}{\Delta t} + \nabla_s \cdot (\tilde{\Gamma}^{k+1} \mathbf{u}_s^n) = D_s \nabla_s^2 \tilde{\Gamma}^{k+1} + j_n \tag{29}$$

$$\frac{\tilde{C}^{k+1} - C^n}{\Delta t} + \nabla \cdot (\tilde{C}^{k+1} \mathbf{u}^n) = D_m \nabla^2 \tilde{C}^{k+1} \tag{30}$$

where k is the index of iteration level. Δt is the time step. Equations (29) and (30) are repeated until

$$\|\tilde{\Gamma}^{k+1} - \tilde{\Gamma}^k\| < \epsilon \quad \text{and} \quad \|\tilde{C}^{k+1} - \tilde{C}^k\| < \epsilon \tag{31}$$

During the calculations presented here, we used $\epsilon = 10^{-8}$, and the values at the new time step $n+1$ are $\Gamma^{n+1} = \tilde{\Gamma}^{k+1}$ and $C^{n+1} = \tilde{C}^{k+1}$.

In the current work, a finite element adaptive mesh refinement method has been used. An error criterion function was applied to control the mesh. The initial coarse mesh size was chosen to be $h = 2$ mm. $h = 0.5$ mm was chosen for the surface around the weld pool. This mesh size is sufficient for a smooth solution of the temperature at the top surface in order to compare with the experimental data. The error criterion function shall force the mesh at the top surface of the weld pool to be refined to the finest resolution that is allowed, $h = 0.03375$ mm. We found a mesh independent solution if the minimum mesh size was kept below $h = 0.03375$ mm. The size of this mesh is typically 200,000 nodes and 1,000,000 elements (see Fig. 4).

Table 1 Physical properties of SAF 2507 stainless steel

Physical property	Value
Density of liquid metal, ρ (kg m^{-3})	7800
Liquidus temperature, T_{liq} (K)	1672
Kinetic viscosity, ν (m^2 s^{-1})	6.81×10^{-7}
Thermal conductivity, k (W m^{-1} K^{-1})	20
Thermal diffusivity, α (m^2 s^{-1})	4.5×10^{-6}
Specific heat, C_p (J kg^{-1} K^{-1})	600
Latent heat of fusion, L^* (J kg^{-1})	256739
Electrical conductivity, σ_e (Ω^{-1} m^{-1})	7.14×10^5
Emissivity of steel, ϵ	0.7
Heat transfer coefficient, h_c (W m^{-2} K^{-1})	20
Heat of evaporation, h_{fg} (kJ kg^{-1})	6500
Constant for evaporation model, A_1	2.52
Constant in the surface tension coefficient, A (N m^{-1} K)	4.3×10^{-4}
Constant related to entropy of segregation for sulfur, $k_{l,\text{S}}$	3.18×10^{-3}
Constant related to entropy of segregation for oxygen, $k_{l,\text{O}}$	1.38×10^{-2}
Surface excess at saturation of sulfur, $\Gamma_{\infty,\text{S}}$ (mol m^{-2})	1.3×10^{-5}
Surface excess at saturation of oxygen, $\Gamma_{\infty,\text{O}}$ (mol m^{-2})	2.03×10^{-5}
Standard heat of adsorption for sulfur, ΔH_{S}^o (J mol^{-1})	$-1.66 \times 10^{+5}$
Standard heat of adsorption for oxygen, ΔH_{O}^o (J mol^{-1})	$-1.46 \times 10^{+5}$
Surface S diffusivity, $D_{s,\text{S}}$ (m^2 s^{-1})	1.7×10^{-8}
Surface O_2 diffusivity, $D_{s,\text{O}}$ (m^2 s^{-1})	2.3×10^{-9}
Bulk S diffusivity, $D_{m,\text{S}}$ (m^2 s^{-1})	3.18×10^{-8}
Bulk O_2 diffusivity, $D_{m,\text{O}}$ (m^2 s^{-1})	4.33×10^{-8}

3 Results and Discussion

In this study, simulations of GTA welding of an SAF-2507 stainless steel were carried out. The simulations of weld pools with two different moving speeds of the heat source have been done and used to compare with the experimental data. The physical properties of SAF-2507 are listed in Table 1 and the chemical compositions are listed in Table 2. The experimental setting can be found in Ref. [17]. Here, the authors present only the simulation with two different speeds ($U_s = 100$ mm min^{-1} and $U_s = 100$ mm min^{-1}) and the same welding conditions ($I = 100$ A, $U = 10.2$ V, and $\eta = 65\%$).

The weld pool shape of stainless steel is sensitive to many parameters that control the heat transfer and fluid flow in the liquid pool. Most of them are well known, and the values can be calibrated with experimental data, such as current, voltage, and weld speed. In a moving GTA weld pool, the Marangoni convection pattern on the pool surface has been widely accepted as the principal mechanism for weld shape variations in stainless steel. The results in terms of the weld pool shape depend on different quantities of minor elements, such as sulfur, oxygen, and selenium.

An overview of the numerical results for two different cases are shown in Table 3. A comparison of the experimental and previous numerical results with only sulfur as a main surfactant in the weld pool is available as well. In Fig. 5, the experimental and numerical results for the weld pool shape and fluid flow at the greatest width

Table 2 Chemical compositions of SAF-2507 (wt %)

C	N	Cr	Ni	S	Si	Mn	Cu	O
0.016	0.29	25.3	7.09	0.001	0.21	0.89	0.25	0.002

Table 3 Summary of welding results on SAF 2507 stainless steel. Welding conditions: I=100 A, U=10.2 V, and η=65%.

	U_s=100 mm min^{-1}			U_s=200 mm min^{-1}		
	Multi	Single	Expt.	Multi	Single	Expt.
Pool width (mm)	5.8	6.1	5.8	4.7	4.8	4.5
Pool depth (mm)	1.2	1.2	1.3	0.82	0.83	0.82

position of the weld pool, at y=1 mm behind the arc, are presented. The y axis is the direction of the motion of the arc, the z axis points from the surface downward and the x axis is the transverse axis. Figure 5(*B*) shows results obtained using the same model as in (Ref. [17]), only accounting for sulfur redistribution. Meanwhile, Fig. 5(*A*) shows the numerical solution of the present model. The shape of the weld pool obtained by this model showed a slightly better agreement with the experimental result than the previous one. The inward motion at the stagnant point in Fig. 5(*A*) is stronger and clearer than that in Fig. 5(*B*), which makes the periphery of the weld pool come close to the experimental shape. The new solution for the weld pool width and depth are 4.7 mm and 0.82 mm in comparison with the previous solutions of 4.8 mm and 0.83 mm and experimental results of 4.5 mm and 0.82 mm, respectively. Note that the oxygen content in this material is extremely small, 0.002 wt %, to compare with the other material type 304 stainless steel [9], where it was 0.0063 wt %. Therefore the surface tension is here rather insensitive to the oxygen surfactant. Later, by reducing the welding speed to U_s = 100 mm s^{-1}, we can see a clearer effect of the oxygen distribution on the surface tension force, Fig. 8.

In Fig. 6, the numerical results for the surface concentration at the upper surface of the workpiece were taken at different times t=1 s, 2 s, and 3 s. The arc moving speed in this case was U_s = 200 mm min^{-1}. The nominal values for sulfur and oxygen were used for the initial values of the bulk and surface concentrations. With a_S=0.001%, a_O=0.002%, the bulk concentrations at the equilibrium state were $C_{eq,S}$=2.4 mol m^{-3} and $C_{eq,O}$ = 9.6 mol m^{-3}. The surface concentration is computed using Eq. (21). Here, the Langmuir equilibrium adsorption ratio k_L is a function of temperature and is at the chosen initial stage of k_L = $k_L(T)|_{T=T_{liq}}$. Thus, the initial surface concentrations are Γ_S^0 = 9.15×10^{-6} mol m^{-2} and Γ_O^0 = 1.03×10^{-5} mol m^{-2}.

Obviously, the distribution of the surface concentration becomes asymmetric along the y-axis due to the effect of the moving heat source. The highest values occurred at the stagnant line where two counteracting motions, the inward and the outward motion, meet. The maximum value of the surface concentration at

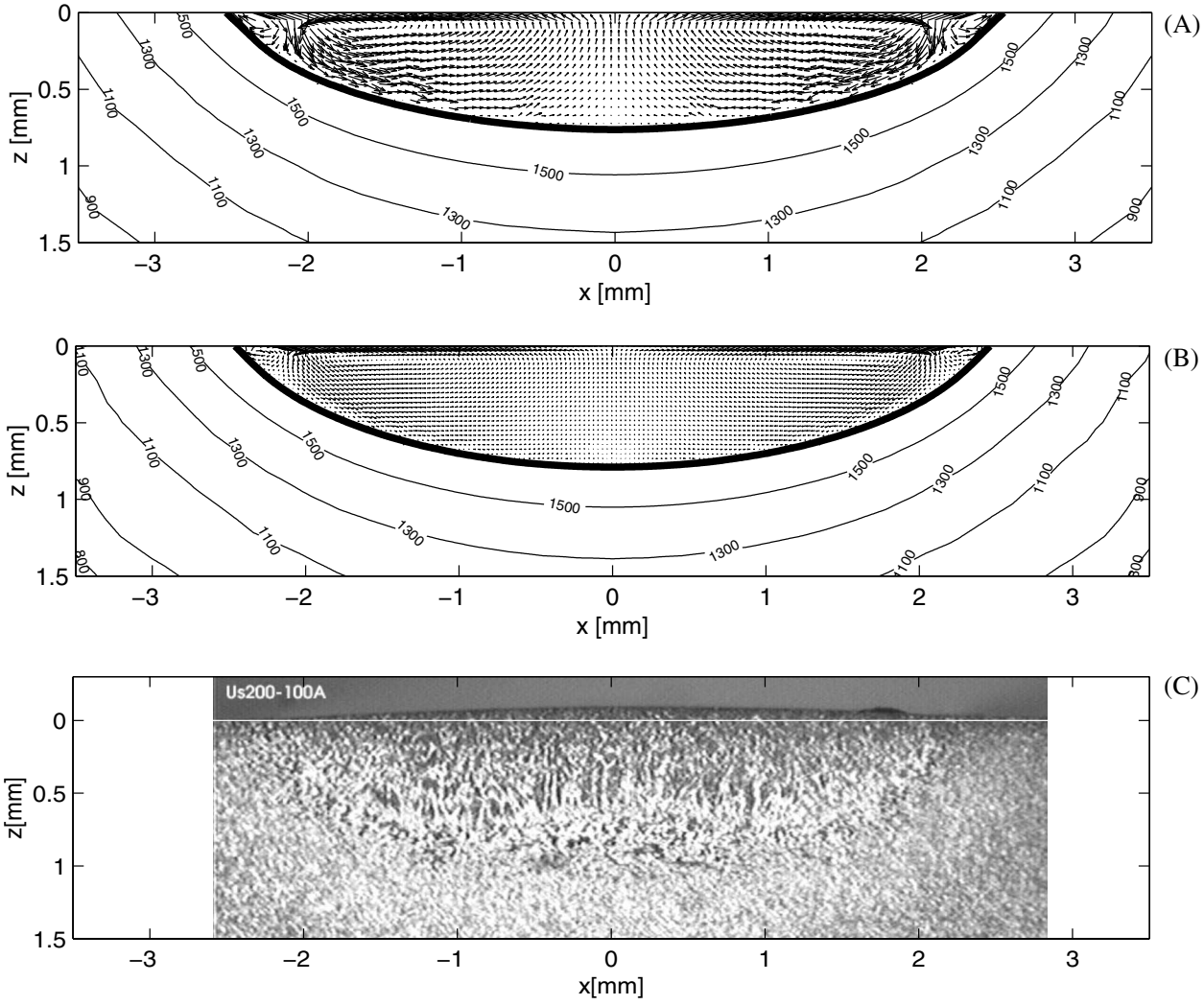

Fig. 5 The numerical and the experimental cross section of the weld pool. (*A*) Multicomponent model. (*B*) Sulfur redistribution model. (*C*) Experimental result. Welding conditions: *Us*=200 mm min^{-1}, *I*=100 A, *U*=10.2 V, and η=65%.

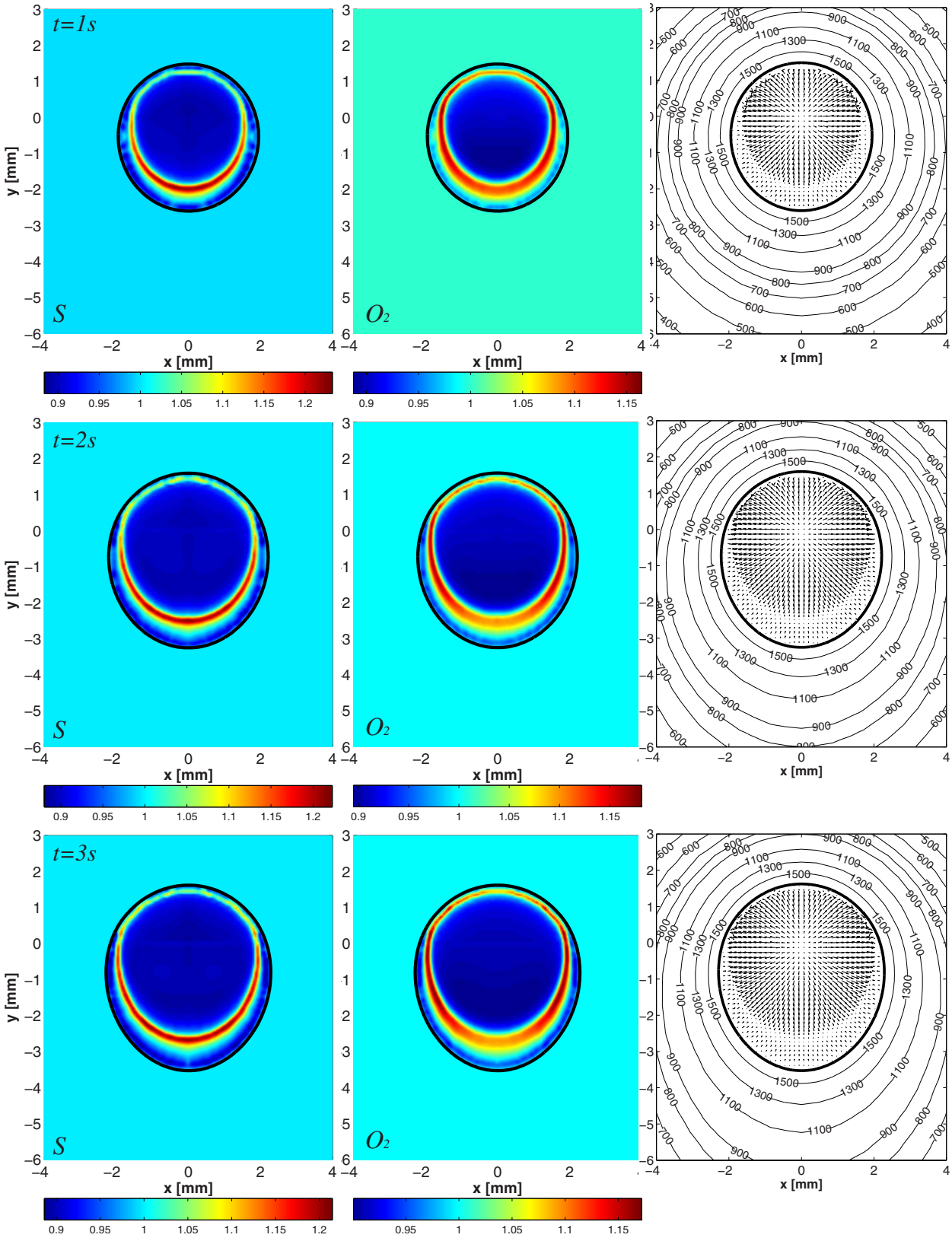

Fig. 6 The evolution of the surface concentration with the moving speed of heat source U_s=200 mm min^{-1}

these stagnant lines appears at the trailing end and could be quantified by a nondimensional value of $\tilde{\Gamma}_S^{max}$=1.217 for the sulfur concentration and $\tilde{\Gamma}_O^{max}$=1.184 for the oxygen concentration. Here, $\tilde{\Gamma}_i=\Gamma_i/\Gamma_i^0$. The temperature at this stagnant line is around 1902–1955 K. At this temperature, the sulfur activities that correspond to the surface concentration above are a_S^{max}

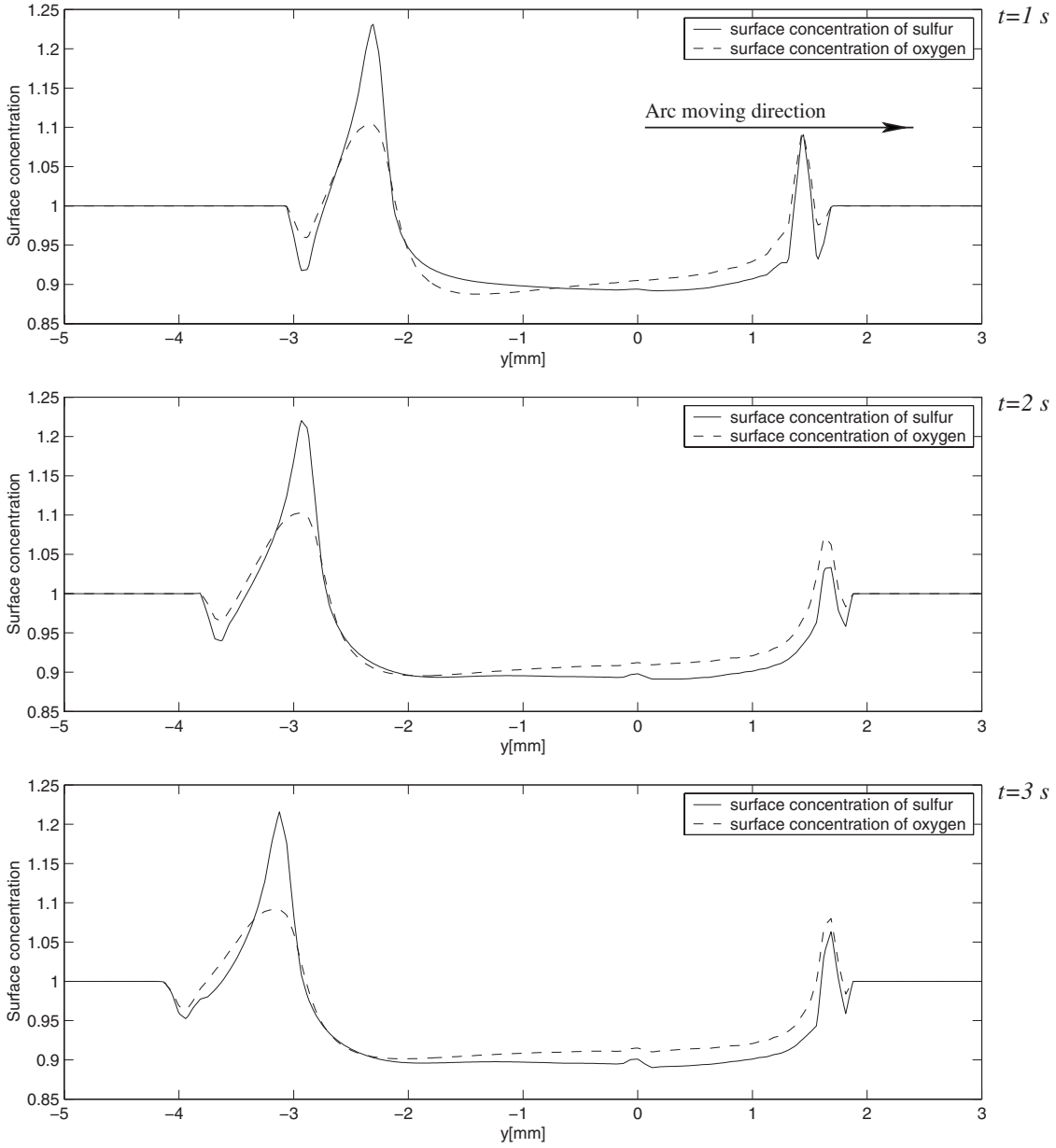

Fig. 7 The evolution of the surface concentration with the moving speed of heat source U_s=200 mm min^{-1}

=0.0013 wt % and a_O^{max}=0.0025 wt %. A profile in the y direction through the center, at the top surface of the weld pool, can be seen in Fig. 7.

In this calculation, the nondimensional Péclet numbers Pe $=U'L/D$ for the bulk concentration and the surface concentration equations were computed based on the thermocapillary velocity scale. $Pe_{m,S}=8.35\times10^6$, $Pe_{s,S}=2.12\times10^7$, $Pe_{m,O}=1.14\times10^6$, and $Pe_{s,O}=2.13\times10^8$. Here, the thermocapillary velocity scale is $U'=(\partial\gamma/\partial T)/(\Delta T/\mu)=72.32$ m s^{-1}. Note however that as is usual in thermocapillary problems, the thermocapillary velocity scale overestimates the actual maximal velocity.

The numerical results and the experimental micrograph of the weld pool with the welding speed U_s=100 mm min^{-1} are presented in Fig. 8. Similar to the result above, the new numerical result showed a better agreement with the experimental result. It is obvious that the counter-clockwise rotating vortex increased in comparison with the previous result (Fig. 8(*B*)). It was due to the additional high surface concentrations of oxygen and sulfur near the stagnation lines. The weld pool width and depth that were computed from the present model were 5.8 mm and 1.2 mm in comparison with the previous solution and experimental results of 6.1 mm and 1.2 mm, and 5.8 mm and 1.3 mm, respectively.

The surface concentration at the upper surface of the workpiece is plotted in Fig. 9. An accumulation of sulfur and oxygen molecules are observed near the stagnation line. The maximum surface concentrations after 3 s were $\tilde{\Gamma}_O^{max}=1.209$ and $\tilde{\Gamma}_S^{max}=1.187$. It corresponds to an oxygen activity of $a_O^{max}=0.0026$ wt % and a sulfur activity of $a_S^{max}=0.0012$ wt %. After 3 s of welding, we observed the steady stage solution for the shape of weld pool and also for the concentration of the surfactants at the surface.

4 Conclusions

The authors have developed a three-dimensional mathematical model considering surfactant mass transfer in a multicomponent system. The physicochemical model has been adapted to existing equations that were used in our previous studies [16,17]. This allows calculation of the fluid and heat flows and solidification

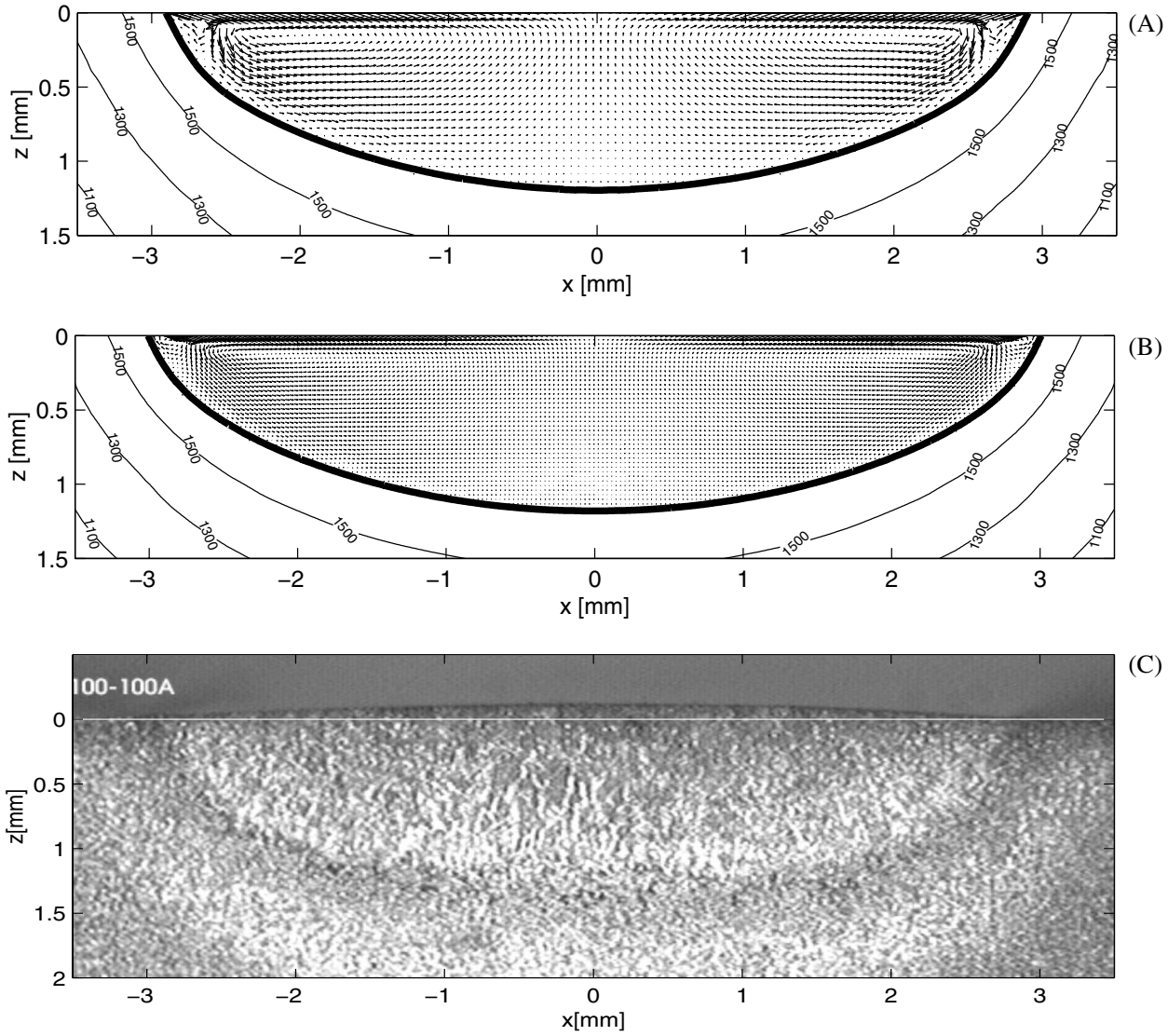

Fig. 8 The numerical and experimental cross sections of the weld pool. (*A*) Multicomponent model. (*B*) Sulfur redistribution model. (*C*) Experimental result. Welding conditions: U_s=100 mm min^{-1}, I=100 A, U=10.2 V, and η=65%.

interface to determine the weld pool shape. The surfactant redistributions at the free surface and in the bulk of the weld pool are determined by convection, diffusion, and sorption equations. In this system, sulfur and oxygen were chosen as representative surfactants. Instead of the constant Langmuir equilibrium adsorption ratio that was used in the previous model, it is now dependent on the temperature and can be computed from the experimental data of Ref. [5].

A comparison of the numerical and experimental results on GTA welding on SAF-2507 stainless steel has been presented. The weld pool shapes obtained from the simulation of welds are very well matched with the experimental weld pool shape.

Nomenclature

C = bulk concentration, mol m^{-3}
C_p = specific heat, J kg^{-1} K^{-1}
E = arc voltage, V
ΔH_0 = standard heat of adsorption
I = welding current, A
L^* = latent heat of fusion, J kg^{-1}
Pe = bulk Péclet number, dimensionless
Pe$_s$ = surface Péclet number, dimensionless
Q = total heat input
U_s = welding speed, m s^{-1}
R = gas constant
T = temperature, K
i = species of the surfactant
h_c = heat transfer coefficient
h_{fg} = heat of evaporation
k_L = Langmuir equilibrium adsorption ratio
k_l = constant related to the entropy of segregation
k_α = coefficient of the desorption rate
k_β = coefficient of the adsorption rate
p = pressure
p_{atm} = atmospheric pressure
q_{conv} = convective heat loss
q_{evap} = evaporation heat flux
q_{Gauss} = heat flux from the arc
q_{rad} = radiative heat losses
r_a = effective radius of heat distribution
$\mathbf{u}$ = velocity, m s^{-1}
$\mathbf{u}_s$ = surface velocity, m s^{-1}
α = thermal diffusivity, m^2 s^{-1}
χ = fraction of volume occupied by melt, dimensionless

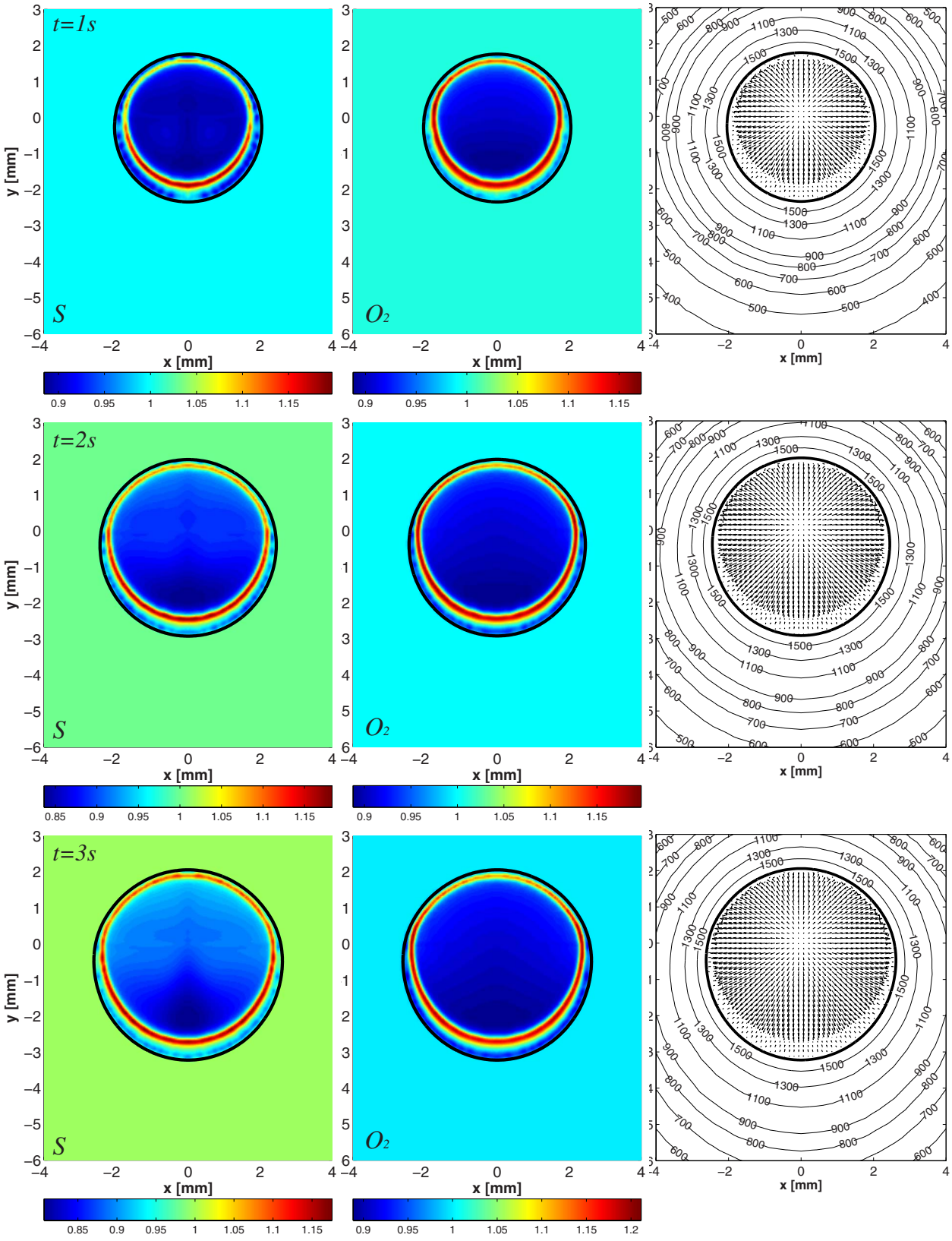

Fig. 9 The evolution of the surface concentration with the moving speed of heat source U_s=100 mm min^{-1}

η = arc efficiency
γ = surface tension, N m^{-1}
$\partial\gamma/\partial T$ = coefficient of surface tension
ν = kinematic viscosity, m^2 s^{-1}
μ = dynamic viscosity, N s m^{-2}
σ_b = Stefan–Boltzmann constant
ϵ = emissivity of steel
ϵ_α = potential desorption barrier

ϵ_β = potential adsorption barrier
Γ = surface concentration, mol m^{-2}
$\tilde{\Gamma}$ = surface concentration, dimensionless
Γ_∞ = surface concentration at saturation, mol m^{-2}
Γ_{eq} = equilibrium surface concentration, mol m^{-2}
ρ = density, kg m^{-3}

References

[1] Debroy, T., and David, S., 1995, "Physical Processes in Fusion-Welding," Rev. Mod. Phys., **67**, p. 85.
[2] Winkler, C., Amberg, G., Inoue, H., Koseki, T., and Fuji, M., 2000, "The Effect of Surfactant Redistributation on the Weld Pool Shape During GTA-Welding," Sci. Technol. Weld. Joining, **5**, p. 1.
[3] Lee, J., and Morita, K., 2002, "Evaluation of Surface Tension and Adsorption for Liquid FE-S Alloys," ISIJ Int., **42**(6), p. 588.
[4] Rosen, M., 1989, *Surfactants and Interfacial Phenomena*, 2nd ed., Wiley, New York.
[5] Sahoo, P., Debroy, T., and Mcnallan, M., 1988, "Surface-Tension of Binary Metal—Surface-Active Solute Systems Under Conditions Relevant to Welding Metallurgy," Metall. Trans. B, **19B**, pp. 483–491.
[6] Belton, G., 1976, "Langmuir Adsorption, the Gibbs Adsorption-Isotherm, and Interfacial Kinetics in Liquid-Metal Systems," Metall. Trans. B, **7B**, p. 35.
[7] Zacharia, T., David, S., Vitek, J., and Debroy, T., 1989, "Weld Pool Development During GTA and Laser-Beam Welding of Type-304, Part I—Theoretical Analysis," Weld. J. (Miami, FL, U.S.), **68**(12), p. S499.
[8] Ushio, M., and Wu, C., 1997, "Mathematical Modeling of Three-Dimensional Heat and Fluid Flow in a Moving Gas Metal Arc Weld Pool," Metall. Mater. Trans. B, **28B**, p. 509.
[9] Winkler, C., Amberg, G., Inoue, H., and Koseki, T., 1998, "A Numerical and Experimental Investigation of Qualitatively Different Weld Pool Shapes," *Mathematical Modelling of Weld Phenomena*, H. Cerjak and H. K. D. H. Bhadeshia, eds., The Institute of Materials, London, Vol. 4, pp. 37–69.
[10] DebRoy, T., 2001, "Mathematical Modeling of Fluid Flow and Heat Transfer in Fusion Welding," *Mathematical Modelling of Weld Phenomena*, H. Cerjak and H. K. D. H. Bhadeshia, eds., The Institute of Materials, London, Vol. 5, p. 1.
[11] Ginley, G., and Radke, G., 1988, "Influence of Soluble Surfactants on the Flow of Long Bubbles Through a Cylindrical Capillary," ACS Symp. Ser., **396**, p. 480.
[12] Stebe, K., and Barthés-Biesel, D., 1995, "Marangoni Effects of Adsorption-Desorption Controlled Surfactants on the Leading End of an Infinitely Long Bubble in a Capillary," J. Fluid Mech., **286**, p. 25.
[13] Winkler, C., and Amberg, G., 2005, "Multicomponent Surfactant Mass Transfer in GTA-Welding," Prog. Comput. Fluid Dyn., **5**(3–5), pp. 190–206.
[14] Keene, B., Mills, K., Bryant, J., and Hondros, E., 1982, "Effects of Interaction Between Surface Active Elements on the Surface Tension of Iron," Can. Metall. Q., **21**(4), p. 393.
[15] Divakar, M., Hajra, J., Jakobsson, A., and Seetharaman, S., 2000, "Thermodynamics of Sufarces and Adsorption in the FE-C-S-O System," Metall. Mater. Trans. B, **31B**, p. 267.
[16] Do-Quang, M., and Amberg, G., 2003, "Modelling of Time-Dependent 3D Weld Pool Flow," *Mathematical Modeling of Weld Phenomena*, H. Cerjak and H. K. D. H. Bhadeshia, eds., The Institute of Materials, London, Vol. 7, pp. 91–112.
[17] Do-Quang, M., Amberg, G., and Pettersson, C., "Experimental and Numerical Study of the Influence of Sulfur Redistributation in Welding of SAF-2507 Stainless Steel," Sci. Technol. Weld. Joining, submitted.
[18] Amberg, G., 1991, "Computation of Macrosergretation in an Iron-Carbon Cast," Int. J. Heat Mass Transfer, **34**(1), pp. 17–227.
[19] Kim, C., 1975, "Thermophysical Properties of Stainless Steels," Technical report, Argonne National Laboratory.
[20] Liggieri, L., Ravera, F., and Passerone, A., 1996, "A Diffusion-Based Approach to Mixed Adsorption Kinetics," Colloids Surf., A, **114**, p. 351.
[21] Adamson, A., and Gast, A., 1997, *Physical Chemistry of Surfaces*, Wiley, New York.
[22] Eastoe, J., and Dalton, J., 2000, "Dynamic Surface Tension and Adsorption Mechanisms of Surfactant at Air-Water Interface," Adv. Colloid Interface Sci., **85**, p. 103.
[23] Baret, J., 1968, "Kinetics of Adsorption From a Solution: Role of the Diffusion and of the Adsorption-Desorption Antagonism," J. Phys. Chem., **72**(8), p. 2755.
[24] Chen, J., and Stebe, K., 1997, "Surfactant-Induced Retardation of the Thermocapillary Migration of a Droplet," J. Fluid Mech., **340**, p. 35.
[25] Benard, J., 1983, *Adsorption on Metal Surfaces*, Elsevier Scientific, New York.
[26] Stone, H., 1990, "A Simple Derivation of the Time-Dependent Convection-Diffusion Equation for Surfactant Transport Along a Deforming Interface," Phys. Fluids A, **2**(1), p. 111.
[27] Ravera, F., Liggieri, L., and Steinchen, A., 1993, "Sorption Kinetics Considered as a Renormalized Diffusion Process," J. Colloid Interface Sci., **156**, p. 109.
[28] Belton, G., and Hunt Medalist, R., 1993, "How Fast Can We Go: The Status of Our Knowledge of the Rates of Gas-Liquid Metal Reactions," Metall. Trans. B, **24B**, p. 241.
[29] Amberg, G., Tönhardt, R., and Winkler, C., 1999, "Finite Element Simulations Using Symbolic Computing," Math. Comput. Simul., **49**, pp. 149–165.
[30] Zienkiewicz, O., and Taylor, R., 2000, *The Finite Element Method*, Vol. 3, 5th ed., Butterworth Heinemann, Oxford.

Slip Flow Heat Transfer in Annular Microchannels With Constant Heat Flux

Zhipeng Duan
e-mail: zpduan@engr.mun.ca

Y. S. Muzychka
e-mail: yuri@engr.mun.ca

Faculty of Engineering and Applied Science,
Memorial University of Newfoundland,
St. John's, NL, A1B 3X5, Canada

Microscale fluid dynamics has received intensive interest due to the emergence of microelectromechanical systems technology. When the mean free path of the gas is comparable to the channel's characteristic dimension, the continuum assumption is no longer valid and velocity slip and temperature jump may occur at the duct walls. Slip flow heat transfer in annular microchannels has been examined. The effects of velocity slip and temperature jump on the hydrodynamically and thermally fully developed heat transfer characteristics for laminar flow have been studied analytically. The analysis is carried out for both uniform wall heat flux on one wall, adiabatic on the other wall, and uniform wall heat flux on both walls. The results indicate that the slip flow Nusselt numbers are lower than those for continuum flow and decrease with an increase in Knudsen number for most practical engineering applications. The effects of Knudsen number, radius ratio, and heat flux ratio on heat transfer characteristics are discussed, respectively.
[DOI: 10.1115/1.2946474]

Keywords: slip flow, annular microchannels, heat transfer

1 Introduction

Fluid flow in microchannels has emerged as an important research area. This has been motivated by their various applications such as medical and biomedical use, computer chips, and chemical separations. The advent of microelectromechanical systems (MEMSs) has opened up a new research area where noncontinuum behavior is important. MEMSs refer to devices that have a characteristic length of less than 1 mm but greater than 1 μm, which combine electrical and mechanical components and which are fabricated using integrated circuit fabrication technologies.

Microchannels are the fundamental part of microfluidic systems. In addition to connecting different devices, microchannels are also utilized as biochemical reaction chambers, in physical particle separation, in inkjet print heads, in infrared detectors, in diode lasers, in miniature gas chromatographs, or as heat exchangers for cooling computer chips. Nominally, microchannels may be defined as channels whose characteristic dimensions are from 1 μm to 1 mm. Typical applications may involve characteristic dimensions in the range of approximately 10–200 μm. Generally, above 1 mm the flow exhibits behavior that is the same as continuum flows. The annular cross section is one useful channel shape and has potential practical applications in MEMS. Understanding the heat transfer characteristics of annular microchannel flows is very important.

The Knudsen number (Kn) relates the molecular mean free path of gas to a characteristic dimension of the duct. Knudsen number is very small for continuum flows. However, for microscale gas flows where the gas mean free path becomes comparable with the characteristic dimension of the duct, the Knudsen number may be greater than 10^{-3}. Microchannels with characteristic lengths on the order of 100 μm would produce flows inside the slip regime for gas with a typical mean free path of approximately 100 nm at standard conditions. The slip flow regime to be studied here is classified as $10^{-3} < \mathrm{Kn} < 10^{-1}$.

Contributed by the Heat Transfer Division of ASME for publication in the JOURNAL OF HEAT TRANSFER. Manuscript received March 30, 2007; final manuscript received February 15, 2008; published online July 8, 2008. Review conducted by Satish G. Kandlikar.

2 Literature Review

Rarefaction effects must be considered in gases in which the molecular mean free path is comparable to the channel's characteristic dimension. The continuum assumption is no longer valid and the gas exhibits noncontinuum effects such as velocity slip and temperature jump at the channel walls. Traditional examples of noncontinuum gas flows in channels include low-density applications such as high-altitude aircraft or vacuum technology. The recent development of microscale fluid systems has motivated great interest in this field of study. Microfluidic systems must take into account noncontinuum effects. There is strong evidence to support the use of Navier–Stokes and energy equations to model the slip flow problem, while the boundary conditions are modified by including velocity slip and temperature jump at the channel walls.

The small length scales commonly encountered in microfluidic devices suggest that rarefaction effects are important. For example, experiments conducted by Pfalher et al. [1,2], Harley et al. [3], Choi et al. [4], Arkilic et al. [5,6], Wu et al. [7], and Araki et al. [8] on the transport of gases in microchannels confirm that continuum analyses are unable to predict flow properties in microsized devices.

Arkilic et al. [5,6] investigated helium flow through microchannels. The results showed that the pressure drop over the channel length was less than the continuum flow results. The friction coefficient was only about 40% of the theoretical values. The significant reduction in the friction coefficient may be due to the slip flow regime, as according to the flow regime classification by Schaaf and Chambre [9], the flows studied by Arkilic et al. [5,6] are mostly within the slip flow regime, only bordering the transition regime near the outlet. When using the Navier–Stokes equations with a first-order slip flow boundary condition, the slip model with full tangential momentum accommodation fits the experimental data well.

Maurer et al. [10] conducted experiments for helium and nitrogen flow in 1.14 μm deep 200 μm wide shallow microchannels. Flowrate and pressure drop measurements in the slip and early transition regimes were performed for averaged Knudsen numbers extending up to 0.8 for helium and 0.6 for nitrogen. The authors

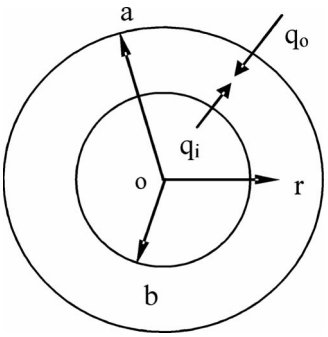

Fig. 1 A concentric circular annular duct with uniform wall heat flux

also provided estimates for second-order effects and found the upper limit of slip flow regime as the averaged Knudsen number equals 0.3 ± 0.1.

Aubert and Colin [11] studied slip flow in rectangular microchannels using the second-order boundary conditions proposed by Deissler [12]. In a later study, Colin et al. [13] presented experimental results for nitrogen and helium flows in a series of silicon rectangular microchannels. The authors proposed that the second-order slip flow model is valid for Knudsen numbers up to about 0.25.

A variety of researchers have attempted to develop second-order slip models that can be used in the transition regime. However, there are large variations in the second-order slip coefficient. The lack of a universally accepted second-order slip coefficient is a major problem in extending Navier–Stokes equations into the transition regime [14].

Slip flow heat transfer in circular tubes was investigated by Sparrow and Lin [15], Barron et al. [16], Ameel et al. [17], Larrode et al. [18], and Simek and Hadjiconstantinou [19]. Yu and Ameel [20,21] and Tunc and Bayazitoglu [22] studied slip flow heat transfer in rectangular microchannels. In these analyses both uniform wall temperature and uniform wall heat flux boundary conditions were considered. Larrode et al. [18] provided an analytical solution for thermally developing flows in a circular tube under constant wall temperature. Yu and Ameel [20,21] investigated thermally developing flows in rectangular microchannels for both constant wall temperature [20] and constant heat flux [21] conditions. Local and fully developed Nusselt numbers were obtained for hydrodynamically fully developed flow. Tunc and Bayazitoglu [22] performed an analytical study of convective heat transfer in a rectangular microchannel under constant heat flux. The flow was assumed to be fully developed both thermally and hydrodynamically. Convection heat transfer in annular macrochannels has been extensively investigated by numerical and analytical methods over the years [23]. However, no attempt has been made for solving the same problem in microchannels. With the development of microscale thermal fluid systems, there is a need to investigate slip flow heat transfer in annular microchannels.

3 Theoretical Analysis

It is necessary to first examine the velocity problem since the heat transfer analysis requires knowing velocity distributions. A schematic of the annular duct section is provided in Fig. 1. When the microchannels are long enough $(L/D_h \gg 1)$ and Reynolds number is relatively low, the momentum equation reduces to the form

$$\mu\left(\frac{d^2u}{dr^2} + \frac{1}{r}\frac{du}{dr}\right) = \frac{dp}{dx} \tag{1}$$

The velocity distribution must satisfy the slip boundary condition at the walls. The local slip velocity is proportional to the local velocity gradient normal to the wall. The corresponding slip boundary conditions are therefore

$$u = \lambda\frac{2-\sigma}{\sigma}\frac{du}{dr} \quad \text{at } r = b \tag{2}$$

$$u = -\lambda\frac{2-\sigma}{\sigma}\frac{du}{dr} \quad \text{at } r = a \tag{3}$$

where λ is the molecular mean free path. The constant σ denotes tangential momentum accommodation coefficient, which is usually between 0.87 and 1 [24]. Although the nature of the tangential momentum accommodation coefficients is still an active research problem, almost all evidence indicates that for most gas-solid interactions the coefficients are approximately 1.0. Therefore, σ may be assumed to have a value of unity. The same procedure is valid even if $\sigma \neq 1$, defining a modified Knudsen number as $\mathrm{Kn}^* = \mathrm{Kn}(2-\sigma)/\sigma$.

The characteristic length scale in the present analysis is defined as the hydraulic diameter, such that

$$\mathrm{Kn} = \frac{\lambda}{D_h} = \frac{\lambda}{2(a-b)} \tag{4}$$

A solution of these equations yields

$$u = -\frac{a^2}{4\mu}\frac{dp}{dx}\left\{1 - \frac{r^2}{a^2} + 4(1-\varepsilon)\frac{2-\sigma}{\sigma}\mathrm{Kn} - \frac{\varepsilon(1-\varepsilon^2)\left(1+4\frac{2-\sigma}{\sigma}\mathrm{Kn}\right)\left[(1-\varepsilon)\frac{2-\sigma}{\sigma}2\mathrm{Kn} - \ln\frac{r}{a}\right]}{(1-\varepsilon^2)\frac{2-\sigma}{\sigma}2\mathrm{Kn} - \varepsilon\ln\varepsilon}\right\} \tag{5}$$

The mean velocity is found by integration of Eq. (5) across the section of the duct:

$$\bar{u} = \frac{1}{A}\int udA = \frac{1}{\pi(a^2-b^2)}\int_b^a u 2\pi r dr = -\frac{a^2}{8\mu}\frac{dp}{dx}\left[1 + \varepsilon^2 + 8(\varepsilon^2 - \varepsilon + 1)\frac{2-\sigma}{\sigma}\mathrm{Kn} + \frac{\varepsilon(1-\varepsilon^2)\left(1+4\frac{2-\sigma}{\sigma}\mathrm{Kn}\right)^2}{\varepsilon\ln\varepsilon - 2(1-\varepsilon^2)\frac{2-\sigma}{\sigma}\mathrm{Kn}}\right] \tag{6}$$

where $\varepsilon = b/a$.

With the velocity solution, we may now consider the heat transfer problem.

3.1 Uniform Wall Heat Flux on the Inner Wall, Adiabatic on the Outer Wall ($q_i = q$, $q_o = 0$). The starting point of the analysis is the law of conservation of energy. For fully developed laminar flow, the energy equation takes the form

$$\rho c_p u\frac{\partial T}{\partial x} = \frac{k}{r}\frac{\partial}{\partial r}\left(r\frac{\partial T}{\partial r}\right) \tag{7}$$

For thermally fully developed flow with uniform wall heat flux, $\partial T/\partial x = dT/dx$ is a constant. From an energy balance on a length of duct dx, it follows that

$$q2\pi b dx = \rho\pi(a^2 - b^2)\bar{u}c_p dT \tag{8}$$

Solving for dT/dx and substituting into Eq. (7) gives

$$\frac{2qb}{(a^2 - b^2)}\frac{u}{\bar{u}} = \frac{k}{r}\frac{\partial}{\partial r}\left(r\frac{\partial T}{\partial r}\right) \tag{9}$$

Due to the effect of rarefaction, there is a temperature jump between the wall surface temperature T_w and the contiguous gas temperature T. The appropriate boundary conditions are

$$\frac{dT}{dr} = 0 \quad \text{at } r = a \tag{10}$$

$$T - T_w = \frac{2 - \sigma_T}{\sigma_T}\frac{2\gamma}{\gamma + 1}\frac{\lambda}{\Pr}\frac{dT}{dr} \quad \text{at } r = b \tag{11}$$

in which σ_T represents a thermal accommodation coefficient measuring the extent to which the energies of molecules impinging on a surface are affected by contact with the surface. σ_T is usually between 0.32 and 1 [24] and close to unity for typical engineering surfaces, but it may reduce to the order of 10^{-1} for especially clean surfaces. Pr and γ denote the Prandtl number and specific heat ratio, respectively. With these boundary conditions, the temperature distribution can be obtained. In order to determine the local heat transfer coefficient and Nusselt number, the bulk temperature T_b is needed and may be obtained as follows:

$$T_b = \frac{\int_b^a 2\pi r u T dr}{\int_b^a 2\pi r u dr} \tag{12}$$

After integration we can obtain the Nusselt number as

$$\mathrm{Nu}_{ii} = \frac{q_i D_h}{k(T_w - T_b)} \tag{13}$$

The solution requires several pages to show the complete Nusselt number expression. It is very space consuming and therefore must be omitted here. However, it is available from the authors upon request. In the limit of $\mathrm{Kn} \to 0$, Eq. (13) reduces to its continuum flow solution:

$$\mathrm{Nu}_{ii} = \frac{144(\varepsilon - 1)(\varepsilon^2 - 1)^2[\varepsilon^2 \ln \varepsilon - \varepsilon^2 + \ln \varepsilon + 1]^2}{[45\varepsilon^9 - 234\varepsilon^7 + 432\varepsilon^5 - 342\varepsilon^3 + 99\varepsilon + 72\varepsilon(\ln \varepsilon)^3 + (33\varepsilon^9 - 108\varepsilon^5 - 144\varepsilon^3 + 219\varepsilon)(\ln \varepsilon)^2 + (-76\varepsilon^9 + 184\varepsilon^7 + 108\varepsilon^5 - 464\varepsilon^3 + 248\varepsilon)\ln \varepsilon]} \tag{14}$$

Assuming $\sigma = 1$, $\sigma_T = 1$, $\Pr = 0.71$, $\gamma = 1.4$, we can obtain the relationship of Nu and Kn. Figure 2 shows the variation of Nusselt numbers for uniform wall heat flux on the inner wall, adiabatic on the outer wall for annular ducts, where the Nusselt number data have been normalized with the continuum flow Nusselt number. It is seen that the $\mathrm{Nu}/\mathrm{Nu}_c$ values decrease as the Knudsen number increases for the same radius ratio. The $\mathrm{Nu}/\mathrm{Nu}_c$ values also decrease with a decrease in ε for the same Kn. The fully developed Nusselt numbers for different Knudsen numbers are presented in Table 1. It is noted that Eq. (13) reduces to its corresponding continuum flow results [23] in the limit of $\mathrm{Kn} \to 0$.

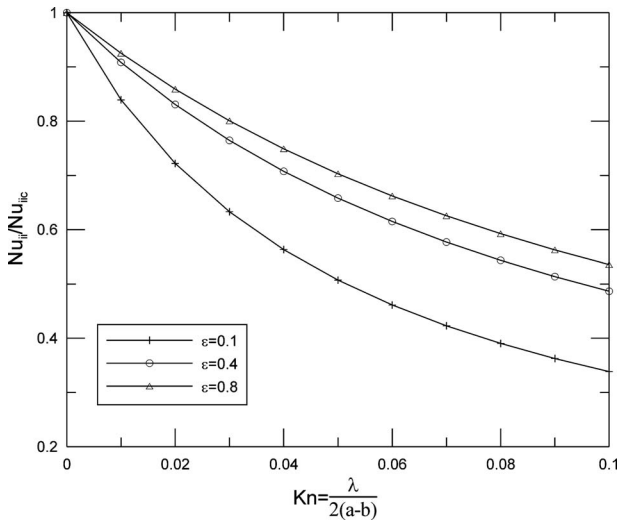

Fig. 2 Variation of Nusselt number for uniform wall heat flux on the inner wall, adiabatic on the outer wall

3.2 Uniform Wall Heat Flux on the Outer Wall, Adiabatic on the Inner Wall ($q_i = 0$, $q_o = q$). For thermally fully developed condition with uniform wall heat flux, from an energy balance on a length of duct dx,

$$q2\pi a dx = \rho\pi(a^2 - b^2)\bar{u}c_p dT \tag{15}$$

Eliminating $\partial T/\partial x$ from Eqs. (7) and (15) and rearranging

$$\frac{2qa}{(a^2 - b^2)}\frac{u}{\bar{u}} = \frac{k}{r}\frac{\partial}{\partial r}\left(r\frac{\partial T}{\partial r}\right) \tag{16}$$

Due to the effect of rarefaction, the appropriate boundary conditions are

Table 1 Fully developed Nusselt numbers Nu_{ii} case (i) for different Knudsen numbers

b/a	$\mathrm{Kn}^* = 0$	$\mathrm{Kn}^* = 0.01$	$\mathrm{Kn}^* = 0.04$	$\mathrm{Kn}^* = 0.07$	$\mathrm{Kn}^* = 0.1$
0	∞	∞	∞	∞	∞
0.001	337.04414	51.58819	14.55661	8.47398	5.97672
0.01	54.01669	28.69024	11.87604	7.48470	5.46457
0.02	32.70512	21.33320	10.39371	6.86479	5.12490
0.04	20.50925	15.38538	8.75035	6.10532	4.68769
0.05	17.81128	13.82053	8.22319	5.84363	4.53139
0.06	15.93349	12.66667	7.80261	5.62800	4.40034
0.08	13.46806	11.06362	7.16737	5.29021	4.19083
0.10	11.90578	9.99206	6.70573	5.03512	4.02914
0.15	9.68703	8.38991	5.95260	4.60069	3.74676
0.20	8.49892	7.49106	5.49354	4.32437	3.56254
0.25	7.75347	6.91204	5.18291	4.13239	3.43250
0.30	7.24115	6.50739	4.95876	3.99143	3.33602
0.40	6.58330	5.98007	4.65823	3.79954	3.20353
0.50	6.18102	5.65372	4.46803	3.67676	3.11830
0.60	5.91171	5.43397	4.33869	3.59301	3.06018
0.70	5.72036	5.27750	4.24631	3.53339	3.01894
0.80	5.57849	5.16183	4.17839	3.49089	2.98868
0.90	5.46988	5.10665	4.12284	3.45118	2.95475

$$\frac{dT}{dr} = 0 \quad \text{at } r = b \tag{17}$$

$$T - T_w = -\frac{2-\sigma_T}{\sigma_T}\frac{2\gamma}{\gamma+1}\frac{\lambda}{\mathrm{Pr}}\frac{dT}{dr} \quad \text{at } r = a \tag{18}$$

With these boundary conditions, the temperature distribution can be obtained in the same manner as the previous case.

After integration the bulk temperature T_b using Eq. (12) we can obtain the Nusselt number as

$$\mathrm{Nu}_{oo} = \frac{q_o D_h}{k(T_w - T_b)} \tag{19}$$

As before the solution requires several pages to show the complete Nusselt number expression. In the limit of $\mathrm{Kn} \to 0$, Eq. (19) reduces to its continuum flow solution:

$$\mathrm{Nu}_{oo} = \frac{144(\varepsilon-1)(\varepsilon^2-1)^2[\varepsilon^2\ln\varepsilon - \varepsilon^2 + \ln\varepsilon + 1]^2}{[-99\varepsilon^8 + 342\varepsilon^6 - 432\varepsilon^4 + 234\varepsilon^2 - 45 + 72\varepsilon^8(\ln\varepsilon)^3 + (-219\varepsilon^8 + 144\varepsilon^6 + 108\varepsilon^4 - 33)(\ln\varepsilon)^2 + (248\varepsilon^8 - 464\varepsilon^6 + 108\varepsilon^4 + 184\varepsilon^2 - 76)\ln\varepsilon]} \tag{20}$$

Moreover, the limit of Eq. (19) that corresponds to a circular tube for $\varepsilon \to 0$ is

$$\mathrm{Nu}_{oo} = \frac{q_o D_h}{k(T_w - T_b)} = \frac{48}{\dfrac{11 + 128\dfrac{2-\sigma}{\sigma}\mathrm{Kn} + 384\left(\dfrac{2-\sigma}{\sigma}\mathrm{Kn}\right)^2}{\left(1 + 8\dfrac{2-\sigma}{\sigma}\mathrm{Kn}\right)^2} + 48\dfrac{2-\sigma_T}{\sigma_T}\dfrac{2\gamma}{\gamma+1}\dfrac{\mathrm{Kn}}{\mathrm{Pr}}} \tag{21}$$

Assuming $\sigma=1$, $\sigma_T=1$, $\mathrm{Pr}=0.71$, $\gamma=1.4$, we can get the relationship of Nu and Kn. Figure 3 shows the variation of Nusselt numbers for uniform wall heat flux on the outer wall, adiabatic on the inner wall for annular ducts. It is seen that the $\mathrm{Nu}/\mathrm{Nu}_c$ values decrease as the Knudsen number increases for the same radius ratio. The $\mathrm{Nu}/\mathrm{Nu}_c$ values increase with a decrease in ε for the same Kn. The fully developed Nusselt numbers for different Knudsen numbers are demonstrated in Table 2. It is seen that Eq. (19) reduces to its corresponding continuum flow results [23] in the limit of $\mathrm{Kn} \to 0$.

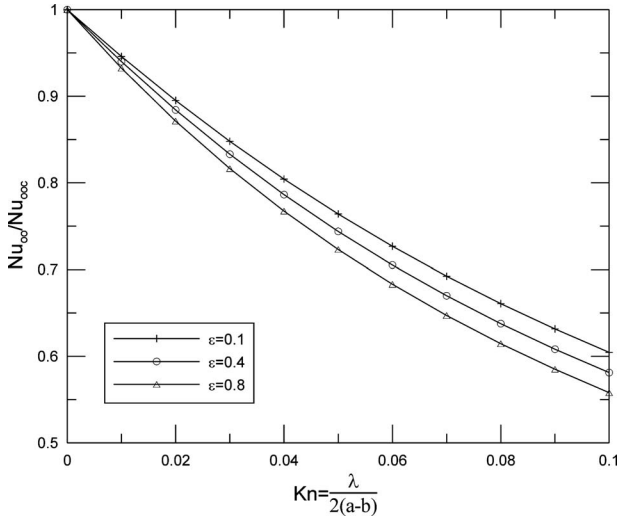

Fig. 3 Variation of Nusselt number for uniform wall heat flux on the outer wall, adiabatic on the inner wall

3.3 Uniform Wall Heat Flux on Both Walls ($q_i \neq 0$, $q_o \neq 0$).

The corresponding boundary conditions are

$$-k\frac{\partial T}{\partial r} = q_i, \quad r = b \tag{22}$$

$$k\frac{\partial T}{\partial r} = q_o, \quad r = a \tag{23}$$

As the boundary conditions are nonhomogeneous, solutions for these boundary conditions can be obtained by the principle of superposition once the solutions for each boundary condition are derived. Consider the problem as two components (1 and 2): Problem 1

$$\rho c_p u\frac{\partial T_1}{\partial x} = \frac{k}{r}\frac{\partial}{\partial r}\left(r\frac{\partial T_1}{\partial r}\right) \tag{24}$$

The boundary conditions are

$$-k\frac{\partial T_1}{\partial r} = q_i, \quad r = b \tag{25}$$

Table 2 Fully developed Nusselt numbers Nu_{oo} case (ii) for different Knudsen numbers

b/a	$\mathrm{Kn}^*=0$	$\mathrm{Kn}^*=0.01$	$\mathrm{Kn}^*=0.04$	$\mathrm{Kn}^*=0.07$	$\mathrm{Kn}^*=0.1$
0	4.36364	4.22916	3.76201	3.31123	2.92359
0.001	4.58657	4.27301	3.76998	3.31379	2.92445
0.01	4.69234	4.41098	3.81332	3.32884	2.92923
0.02	4.73424	4.46555	3.83847	3.33786	2.93144
0.04	4.77803	4.51708	3.86441	3.34621	2.93172
0.05	4.79198	4.53214	3.87177	3.34796	2.93083
0.06	4.80323	4.54373	3.87711	3.34882	2.92957
0.08	4.82070	4.56063	3.88403	3.34887	2.92642
0.10	4.83421	4.57269	3.88802	3.34770	2.92290
0.15	4.86026	4.59354	3.89256	3.34296	2.91414
0.20	4.88259	4.60981	3.89496	3.33840	2.90669
0.25	4.90475	4.62560	3.89787	3.33524	2.90100
0.30	4.92801	4.64233	3.90215	3.33379	2.89707
0.40	4.97917	4.68022	3.91551	3.33583	2.89394
0.50	5.03653	4.72413	3.93480	3.34352	2.89597
0.60	5.09922	4.77322	3.95897	3.35566	2.90194
0.70	5.16618	4.82649	3.98695	3.37121	2.91092
0.80	5.23654	4.88378	4.01949	3.38944	2.92227
0.90	5.30955	4.94356	4.05602	3.40928	2.93510

$$\frac{\partial T_1}{\partial r} = 0, \quad r = a \tag{26}$$

Problem 2

$$\rho c_p u \frac{\partial T_2}{\partial x} = \frac{k}{r}\frac{\partial}{\partial r}\left(r\frac{\partial T_2}{\partial r}\right) \tag{27}$$

The boundary conditions are

$$\frac{\partial T_2}{\partial r} = 0, \quad r = b \tag{28}$$

$$k\frac{\partial T_2}{\partial r} = q_o, \quad r = a \tag{29}$$

Due to the effect of rarefaction, there is a temperature jump between the wall surface temperature T_w and the contiguous gas temperature T. In mathematical terms, the boundary conditions are as follows:

$$T_1 - T_{wi1} = \frac{2-\sigma_T}{\sigma_T}\frac{2\gamma}{\gamma+1}\frac{\lambda}{\mathrm{Pr}}\frac{dT_1}{dr} \quad \text{at } r = b \tag{30}$$

$$T_2 - T_{wi2} = \frac{2-\sigma_T}{\sigma_T}\frac{2\gamma}{\gamma+1}\frac{\lambda}{\mathrm{Pr}}\frac{dT_2}{dr} \quad \text{at } r = b \tag{31}$$

$$T_1 - T_{wo1} = -\frac{2-\sigma_T}{\sigma_T}\frac{2\gamma}{\gamma+1}\frac{\lambda}{\mathrm{Pr}}\frac{dT_1}{dr} \quad \text{at } r = a \tag{32}$$

$$T_2 - T_{wo2} = -\frac{2-\sigma_T}{\sigma_T}\frac{2\gamma}{\gamma+1}\frac{\lambda}{\mathrm{Pr}}\frac{dT_2}{dr} \quad \text{at } r = a \tag{33}$$

applying the principle of superposition

$$T = T_1 + T_2 \tag{34}$$

$$T_b = T_{b1} + T_{b2} \tag{35}$$

$$T_{wi} = T_{wi1} + T_{wi2} \tag{36}$$

$$T_{wo} = T_{wo1} + T_{wo2} \tag{37}$$

The solutions of Problems 1 and 2 have been correspondingly obtained from the above cases ((i) and (ii)); therefore superposition of these solutions is the solution of the original problem. Nu_i and Nu_o are evaluated at the inner and outer walls, respectively. For convenience, we may define two parameters ε_i, ε_o,

$$\varepsilon_i = \frac{T_{wi1} - T_{b1}}{T_{wi1} + T_{wi2} - T_{b1} - T_{b2}} \tag{38}$$

$$\mathrm{Nu}_i = \frac{q_i D_h}{k(T_{wi} - T_b)} = \mathrm{Nu}_{ii}\varepsilon_i \tag{39}$$

$$\varepsilon_o = \frac{T_{wo2} - T_{b2}}{T_{wo1} + T_{wo2} - T_{b1} - T_{b2}} \tag{40}$$

$$\mathrm{Nu}_o = \frac{q_o D_h}{k(T_{wo} - T_b)} = \mathrm{Nu}_{oo}\varepsilon_o \tag{41}$$

The solutions for the Nu_i and Nu_o are quite involved. The program MAPLE was used to assist in the computation. It is extremely space consuming and therefore must be omitted here. However, they are available from the authors upon request.

Moreover, when $q_i = q_o$, the limit of Eqs. (39) and (41) that corresponds to a parallel-plate channel for $\varepsilon \to 1$ is

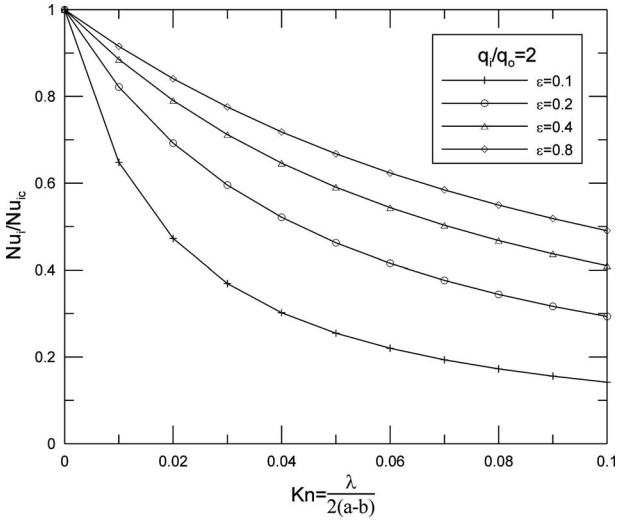

Fig. 4 Variation of Nu_i for uniform wall heat flux on both walls

$$\mathrm{Nu}_i = \mathrm{Nu}_o = \frac{qD_h}{k(T_w - T_b)} = \frac{140}{\dfrac{17 + 336\dfrac{2-\sigma}{\sigma}\mathrm{Kn} + 1680\left(\dfrac{2-\sigma}{\sigma}\mathrm{Kn}\right)^2}{\left(1 + 12\dfrac{2-\sigma}{\sigma}\mathrm{Kn}\right)^2} + 140\dfrac{2-\sigma_T}{\sigma_T}\dfrac{2\gamma}{\gamma+1}\dfrac{\mathrm{Kn}}{\mathrm{Pr}}} \tag{42}$$

Assuming $\sigma = 1$, $\sigma_T = 1$, $\mathrm{Pr} = 0.71$, $\gamma = 1.4$, we can obtain the relationship of Nu and Kn. Figure 4 shows the variation of Nu_i for uniform wall heat flux on both walls for annular ducts. It is seen that the $\mathrm{Nu}_i/\mathrm{Nu}_{ic}$ values decrease as the Knudsen number increases for the same ε and q_i/q_o. The $\mathrm{Nu}_i/\mathrm{Nu}_{ic}$ values increase with an increase in ε for the same Kn and q_i/q_o. Figure 5 demonstrates the effects of q_i/q_o for Nu_i for uniform wall heat flux on both walls for annular ducts. The $\mathrm{Nu}_i/\mathrm{Nu}_{ic}$ values increase with an increase in q_i/q_o for the same Kn and ε.

Figure 6 shows the variation of Nu_o for uniform wall heat flux on both walls for annular ducts. It is seen that the $\mathrm{Nu}_o/\mathrm{Nu}_{oc}$

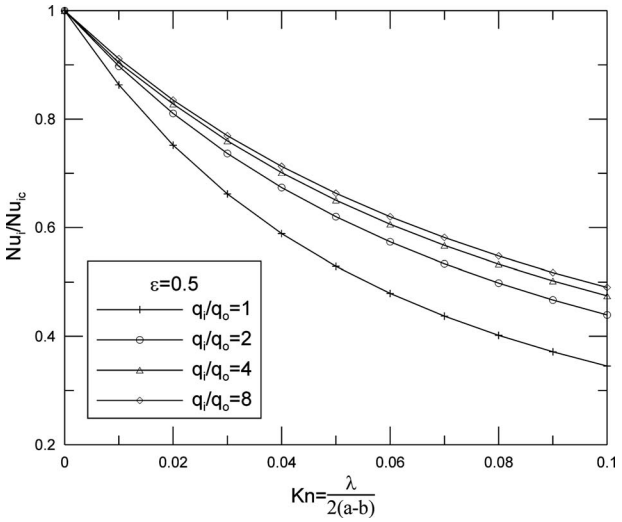

Fig. 5 Effects of q_i/q_o for Nu_i for uniform wall heat flux on both walls

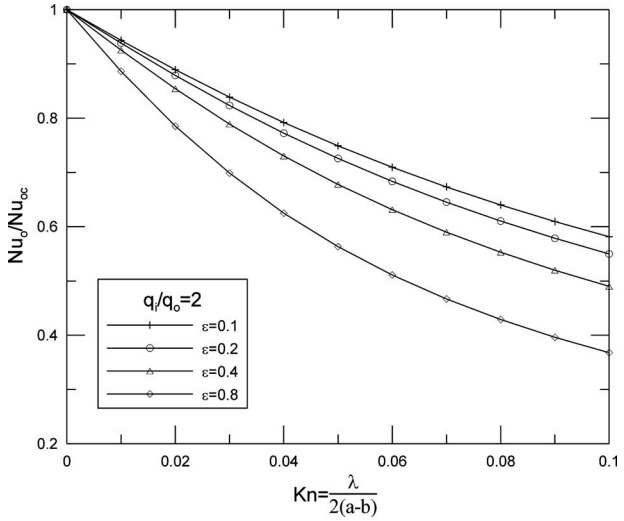

Fig. 6 Variation of Nu_o for uniform wall heat flux on both walls

values decrease as the Knudsen number increases for the same ε and q_i/q_o. The Nu_o/Nu_{oc} values increase with a decrease in ε for the same Kn and q_i/q_o. Figure 7 illustrates the effects of q_i/q_o for Nu_o for uniform wall heat flux on both walls for annular ducts. The Nu_o/Nu_{oc} values decrease with an increase in q_i/q_o for the same Kn and ε.

Now, we consider two special cases of specified constant wall heat fluxes in order to compare with the available continuum flow results in the open literature [23]. Two special cases of specified constant wall heat fluxes are (A) constant and equal axial heat fluxes specified on both walls such that at any axial location the peripheral wall temperatures are constant but different at the inner and outer walls; (B) constant but different wall heat fluxes specified on both walls such that at any axial location the peripheral wall temperatures at the inner and outer walls are constant and equal. Note that the heat flux is specified as positive if the heat transfer is from the wall to the fluid. The fully developed Nusselt numbers for both these cases are presented in Tables 3–6. A negative Nusselt number means that heat transfer takes place from the fluid to the wall. An infinite Nusselt number at the inner wall

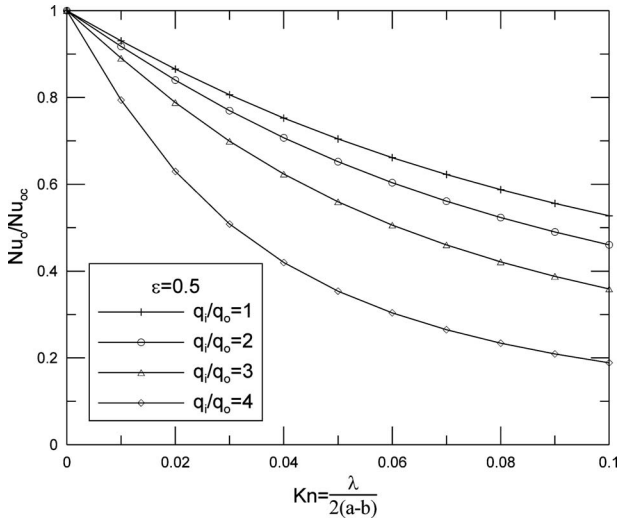

Fig. 7 Effects of q_i/q_o for Nu_o for uniform wall heat flux on both walls

Table 3 Fully developed Nusselt numbers at the inner walls Nu_i case (iii-A) for different Kn

b/a	Kn*=0	Kn*=0.01	Kn*=0.04	Kn*=0.07	Kn*=0.1
0	0	0	0	0	0
0.0001	−7.222	−7.775	−12.753	−36.118	43.424
0.001	−7.507	−8.045	−13.262	−40.165	38.867
0.01	−8.912	−9.826	−17.639	−133.195	23.535
0.02	−10.270	−11.593	−23.670	161.919	17.945
0.04	−13.269	−15.695	−48.714	36.963	13.153
0.05	−15.055	−18.300	−85.684	28.059	11.847
0.06	−17.128	−21.500	−270.336	23.046	10.871
0.08	−22.569	−30.941	97.476	17.540	9.494
0.10	−31.036	−49.601	44.947	14.545	8.558
0.15	−128.740	228.507	21.509	10.804	7.129
0.20	88.712	42.656	15.302	8.999	6.307
0.25	37.359	25.680	12.394	7.922	5.765
0.30	25.166	19.267	10.695	7.201	5.378
0.40	16.555	13.786	8.779	6.290	4.860
0.50	13.111	11.316	7.720	5.734	4.525
0.60	11.248	9.905	7.045	5.358	4.291
0.70	10.077	8.989	6.576	5.087	4.118
0.80	9.272	8.348	6.229	4.881	3.984
0.90	8.684	7.867	5.960	4.716	3.875
1.00	8.235	7.501	5.755	4.590	3.791

means $T_{wi}=T_b$ only and does not mean infinite heat flux. It is noted that Eqs. (39) and (41) reduce to its corresponding continuum flow results [23] in the limit of $Kn \to 0$.

4 Results and Discussion

Due to the temperature jump boundary condition, the bulk gas temperature of slip flow is lower than the gas temperature of continuum flow. The temperature jump is equivalent to a thermal contact resistance between the wall and gas, while the slip velocity acts to decrease the thermal contact resistance. The velocity slip and temperature jump bring about opposite effects on the temperature difference between the gas and the wall; the velocity slip tends to decrease the temperature difference between the gas and the wall, while the temperature jump tends to increase the difference. It is clear that the effects of velocity slip would tend to increase the Nusselt number, while the temperature jump would act to decrease the Nusselt number.

Larrode et al. [18] studied slip flow heat transfer in circular tubes and Yu and Ameel [20,21] investigated slip flow heat transfer in rectangular microchannels. They proposed that heat transfer could be increased or decreased compared to continuum flow conditions depending on β and Knudsen number, where β is defined as

$$\beta = \frac{\dfrac{2-\sigma_T}{\sigma_T}\dfrac{2\gamma}{\gamma+1}\dfrac{1}{\mathrm{Pr}}}{\dfrac{2-\sigma}{\sigma}} \tag{43}$$

and includes all of the parameters associated with the gas and wall interaction.

Actually, only when β and Knudsen number are very small (such as $\beta<0.3$ for parallel plates and $\beta<0.8$ for circular tubes) does it appear possible for the effects of velocity slip to win out over the opposite effects of the temperature jump and thus make a Nusselt number greater than the continuum flow value. In other words, when the tangential momentum accommodation coefficient is significantly smaller than thermal accommodation coefficient, the Nusselt number will be greater than the continuum flow value. However, for practical engineering applications, it is extremely difficult to realize and heat transfer is always reduced when slip flow occurs.

Table 4 Fully developed Nusselt numbers at the inner walls Nu_i case (iii-B) for different Kn

b/a	Kn*=0	Kn*=0.01	Kn*=0.04	Kn*=0.07	Kn*=0.1	q_i/q_o
0	∞	∞	∞	∞	∞	∞
0.0001	4051.526	59.989	15.159	8.675	6.077	847.448
0.001	563.701	55.171	14.829	8.565	6.021	114.141
0.01	91.097	37.065	13.144	7.970	5.718	17.348
0.02	55.320	29.525	12.094	7.573	5.509	10.236
0.04	34.772	22.595	10.804	7.054	5.230	6.206
0.05	30.209	20.627	10.357	6.866	5.127	5.319
0.06	27.026	19.131	9.988	6.706	5.038	4.703
0.08	22.833	16.988	9.406	6.447	4.893	3.893
0.10	20.162	15.505	8.962	6.243	4.777	3.379
0.15	16.334	13.204	8.196	5.878	4.567	2.642
0.20	14.253	11.853	7.696	5.630	4.421	2.240
0.25	12.924	10.953	7.338	5.448	4.314	1.981
0.30	11.993	10.302	7.067	5.307	4.229	1.798
0.40	10.764	9.418	6.680	5.102	4.106	1.551
0.50	9.979	8.837	6.413	4.957	4.018	1.389
0.60	9.429	8.423	6.216	4.849	3.951	1.272
0.70	9.020	8.111	6.064	4.764	3.899	1.182
0.80	8.701	7.864	5.941	4.695	3.856	1.110
0.90	8.446	7.665	5.850	4.638	3.820	1.050
1.00	8.235	7.501	5.755	4.590	3.791	1.000

Table 5 Fully developed Nusselt numbers at the outer walls Nu_o case (iii-A) for different Kn

b/a	Kn*=0	Kn*=0.01	Kn*=0.04	Kn*=0.07	Kn*=0.1
0	4.364	4.229	3.762	3.311	2.924
0.0001	4.526	4.235	3.763	3.312	2.924
0.001	4.589	4.276	3.772	3.315	2.926
0.01	4.721	4.438	3.834	3.345	2.941
0.02	4.792	4.519	3.880	3.369	2.956
0.04	4.894	4.625	3.947	3.409	2.980
0.05	4.937	4.666	3.974	3.426	2.991
0.06	4.977	4.705	4.000	3.442	3.001
0.08	5.052	4.774	4.047	3.472	3.021
0.10	5.122	4.839	4.090	3.500	3.040
0.15	5.288	4.988	4.190	3.566	3.085
0.20	5.449	5.130	4.284	3.630	3.129
0.25	5.608	5.270	4.377	3.692	3.172
0.30	5.767	5.409	4.468	3.753	3.215
0.40	6.089	5.689	4.649	3.875	3.300
0.50	6.419	5.973	4.831	3.995	3.385
0.60	6.759	6.263	5.013	4.115	3.468
0.70	7.109	6.561	5.197	4.235	3.550
0.80	7.472	6.864	5.380	4.354	3.632
0.90	7.847	7.188	5.571	4.472	3.712
1.00	8.235	7.501	5.755	4.590	3.791

Table 6 Fully developed Nusselt numbers at the outer walls Nu_o case (iii-B) for different Kn

b/a	Kn*=0	Kn*=0.01	Kn*=0.04	Kn*=0.07	Kn*=0.1	q_i/q_o
0	4.364	4.229	3.762	3.311	2.924	∞
0.0001	4.781	4.468	3.945	3.450	3.030	847.448
0.001	4.939	4.595	4.019	3.503	3.070	114.141
0.01	5.251	4.926	4.205	3.624	3.154	17.348
0.02	5.404	5.084	4.307	3.690	3.199	10.236
0.04	5.603	5.279	4.438	3.775	3.257	6.206
0.05	5.679	5.351	4.488	3.807	3.279	5.319
0.06	5.747	5.415	4.531	3.836	3.298	4.703
0.08	5.865	5.523	4.604	3.884	3.331	3.893
0.10	5.967	5.616	4.666	3.924	3.359	3.379
0.15	6.182	5.807	4.790	4.005	3.413	2.642
0.20	6.363	5.966	4.891	4.070	3.456	2.240
0.25	6.524	6.104	4.976	4.124	3.492	1.981
0.30	6.672	6.230	5.052	4.171	3.524	1.798
0.40	6.941	6.455	5.185	4.253	3.577	1.551
0.50	7.185	6.657	5.300	4.323	3.622	1.389
0.60	7.414	6.844	5.405	4.386	3.662	1.272
0.70	7.631	7.020	5.501	4.442	3.698	1.182
0.80	7.840	7.185	5.591	4.495	3.731	1.110
0.90	8.040	7.348	5.676	4.545	3.762	1.050
1.00	8.235	7.501	5.755	4.590	3.791	1.000

For small β, the velocity slip dominates and heat transfer is enhanced. At large β, the temperature jump dominates and heat transfer is weakened. When the temperature jump at the wall is neglected (β=0), in other words, only the velocity slip at the wall is considered, the Nusselt number increases with an increase in Knudsen numbers. The same results were found by several researchers [16,17,19–21]. Ignoring temperature jump will lead to significant overprediction of heat transfer.

5 Conclusion

This paper investigated slip flow heat transfer in annular microchannels with constant heat flux under hydrodynamically and thermally fully developed condition. The analysis is carried out for both uniform wall heat flux on one wall, adiabatic on the other wall, and uniform wall heat flux on both walls. The results indicate that the slip flow Nusselt numbers are lower than those for continuum flow and decrease with an increase in Knudsen number for most practical engineering applications. Only when β are very small is it possible for the effects of velocity slip to override the opposite effects of the temperature jump and thus make a Nusselt number greater than the continuum flow value. The effects of Knudsen number, radius ratio, and heat flux ratio on heat transfer characteristics are discussed, respectively.

Acknowledgment

The authors acknowledge the support of the Natural Sciences and Engineering Research Council of Canada (NSERC).

Nomenclature

A = flow area, m^2
a = outer radius of a concentric annular duct, m
b = inner radius of a concentric annular duct, m
c_p = specific heat at constant pressure, J/kg °C
D_h = hydraulic diameter, $=4A/P$

h = local fully developed heat transfer coefficient, $W/m^2\,°C$
Kn = Knudsen number, $=\lambda/D_h$
Kn* = modified Knudsen number, $=Kn(2-\sigma)/\sigma$
k = thermal conductivity, W/m °C
L = channel length, m
Nu = fully developed Nusselt number
Nu_c = fully developed Nusselt number for continuum flow
P = perimeter, m
Pr = Prandtl number, $\mu c_p/k$
p = pressure, N/m^2
q_i = inner wall heat flux per unit area, W/m^2
q_o = outer wall heat flux per unit area, W/m^2
r = radical coordinate, m
T = temperature, K
T_w = wall temperature, K
T_b = bulk temperature, K
u = velocity, m/s
$\bar{u}$ = average velocity, m/s
x = axial coordinates, m

Greek Symbols

β = dimensionless variable
γ = ratio of specific heats
ε = dimensionless radius ratio, $=b/a$
λ = molecular mean free path, m
μ = dynamic viscosity, $N\,s/m^2$
ν = kinematic viscosity, m^2/s
ρ = gas density, kg/m^3
σ = tangential momentum accommodation coefficient
σ_T = thermal accommodation coefficient

Subscripts

c = continuum
i = inner walls
o = outer walls

References

[1] Pfahler, J., Harley, J., Bau, H., and Zemel, J. N., 1991, "Gas and Liquid Flow in Small Channels," *Micromechanical Sensors, Actuators, and Systems*, DSC-Vol. **32**, ASME, New York, pp. 49–58.

[2] Pfahler, J., Harley, J., Bau, H., and Zemel, J. N., 1990, "Gas and Liquid Transport in Small Channels," *Micromechanical Sensors, Actuators, and Systems*, DSC-Vol. **19**, ASME, New York, pp. 149–157.

[3] Harley, J., Huang, Y., Bau, H., and Zemel, J. N., 1995, "Gas Flows in Micro-Channels," J. Fluid Mech., **284**, pp. 257–274.

[4] Choi, S. B., Barron, R. F., and Warrington, R. O., 1991, "Fluid Flow and Heat Transfer in Microtubes," *Micromechanical Sensors, Actuators, and Systems*, DSC-Vol. **32**, ASME, New York, pp. 123–134.

[5] Arkilic, E. B., Breuer, K. S., and Schmidt, M. A., 1994, "Gaseous Flow in Microchannels," *Application of Microfabrication to Fluid Mechanics*, Vol. FED-197, ASME, New York, pp. 57–66.

[6] Arkilic, E. B., Breuer, K. S., and Schmidt, M. A., 1997, "Gaseous Slip Flow in Long Microchannels," J. Microelectromech. Syst., **6**(2), pp. 167–178.

[7] Wu, S., Mai, J., Zohar, Y., Tai, Y. C., and Ho, C. M., 1998, "A Suspended Microchannel With Integrated Temperature Sensors for High Pressure Flow Studies," *Proceedings of IEEE Workshop on Micro Electro Mechanical Systems*, Heidelberg, Germany, pp. 87–92.

[8] Araki, T., Kim, M. S., Hiroshi, I., and Suzuki, K., 2000, "An Experimental Investigation of Gaseous Flow Characteristics in Microchannels," *Proceedings of International Conference on Heat Transfer and Transport Phenomena in Microscale*, G. P. Celata, ed., Begell House, New York, pp. 155–161.

[9] Schaaf, S. A., and Chambre, P. L., 1958, *Flow of Rarefied Gases*, Princeton University Press, Princeton, NJ.

[10] Maurer, J., Tabeling, P., Joseph, P., and Willaime, H., 2003, "Second-Order Slip Laws in Microchannels for Helium and Nitrogen," Phys. Fluids, **15**, pp. 2613–2621.

[11] Aubert, C., and Colin, S., 2001, "High-Order Boundary Conditions for Gaseous Flows in Rectangular Microducts," Microscale Thermophys. Eng., **5**, pp. 41–54.

[12] Deissler, R. G., 1964, "An Analysis of Second-Order Slip Flow and Temperature-Jump Boundary Conditions for Rarefied Gases," Int. J. Heat Mass Transfer, **7**, pp. 681–694.

[13] Colin, S., Lalonde, P., and Caen, R., 2004, "Validation of a Second-Order Slip Flow Model in Rectangular Microchannels," Heat Transfer Eng., **25**, pp. 23–30.

[14] Barber, R. W., and Emerson, D. R., 2006, "Challenges in Modeling Gas-Phase Flow in Microchannels: from Slip to Transition," Heat Transfer Eng., **27**, pp. 3–12.

[15] Sparrow, E. M., and Lin, S. H., 1962, "Laminar Heat Transfer in Tubes Under Slip Flow Conditions," ASME J. Heat Transfer, **84**, pp. 363–369.

[16] Barron, R. F., Wang, X. M., Ameel, T. A., and Warrington, R. O., 1997, "The Graetz Problem Extended to Slip Flow," Int. J. Heat Mass Transfer, **40**(8), pp. 1817–1823.

[17] Ameel, T. A., Barron, R. F., Wang, X. M., and Warrington, R. O., 1997, "Laminar Forced Convection in a Circular Tube With Constant Heat Flux and Slip Flow," Microscale Thermophys. Eng., **1**(4), pp. 303–320.

[18] Larrode, F. E., Housiadas, C., and Drossinos, Y., 2000, "Slip Flow Heat Transfer in Circular Tubes," Int. J. Heat Mass Transfer, **43**, pp. 2669–2680.

[19] Simek, O., and Hadjiconstantinou, N. G., 2001, "Slip Flow Constant-Wall-Temperature Nusselt Number in Circular Tubes in the Presence of Axial Heat Conduction," *Proceedings of ASME International Mechanical Engineering Congress and Exposition*, New York, Paper No. IMECE2001/HTD-24106.

[20] Yu, S. P., and Ameel, T. A., 2001, "Slip Flow Heat Transfer in Rectangular Microchannels," Int. J. Heat Mass Transfer, **44**(22), pp. 4225–4234.

[21] Yu, S. P., and Ameel, T. A., 2002, "Slip Flow Convection in Isoflux Rectangular Microchannels," ASME J. Heat Transfer, **124**, pp. 346–355.

[22] Tunc, G., and Bayazitoglu, Y., 2002, "Heat Transfer in Rectangular Microchannels," Int. J. Heat Mass Transfer, **45**(4), pp. 765–773.

[23] Shah, R. K., and London, A. L., 1978, *Laminar Flow Forced Convection in Ducts*, Academic, New York, Chap. 12, pp. 291 and 295.

[24] Rohsenow, W. M., and Choi, H. Y., 1961, *Heat, Mass, and Momentum Transfer*, Prentice-Hall, Englewood Cliffs, NJ, Chap. 11.

Thin Film Phonon Heat Conduction by the Dispersion Lattice Boltzmann Method

Rodrigo A. Escobar
Departamento de Ingeniería Mecánica y Metalúrgica,
Pontificia Universidad Católica de Chile,
Vicuña Mackenna 4860, Macul
Santiago, Chile
e-mail: rescobar@ing.puc.cl

Cristina H. Amon[1]
Raymond Lane Distinguished Professor
ASME Life Fellow
Mechanical Engineering Department,
Carnegie Mellon University,
Pittsburgh, PA 15213
e-mail: camon@cmu.edu
e-mail: cristina.amon@utoronto.ca

Numerical simulations of time-dependent thermal energy transport in semiconductor thin films are performed using the lattice Boltzmann method applied to phonon transport. The discrete lattice Boltzmann Method is derived from the continuous Boltzmann transport equation assuming nonlinear, frequency-dependent phonon dispersion for acoustic and optical phonons. Results indicate that the heat conduction in silicon thin films displays a transition from diffusive to ballistic energy transport as the characteristic length of the system becomes comparable to the phonon mean free path and that the thermal energy transport process is characterized by the propagation of multiple superimposed phonon waves. The methodology is used to characterize the time-dependent temperature profiles inside films of decreasing thickness. Thickness-dependent thermal conductivity values are computed based on steady-state temperature distributions obtained from the numerical models. It is found that reducing feature size into the subcontinuum regime decreases thermal conductivity when compared to bulk values, at a higher rate than what was displayed by the Debye-based gray lattice Boltzmann method. [DOI: 10.1115/1.2944249]

Keywords: conduction, phonon, lattice Boltzmann, thermal conductivity

Introduction

The past decades have seen the development of advanced integrated circuit fabrication techniques that allow increasingly higher numbers of individual components to be built within microchips. As the characteristic lengths of individual components of electronic devices are reduced, following the trend dictated by Moore's law, the ability to model thermal energy transport effects in those devices has turned out to be increasingly important. At such small length scales (currently in the order of tens of nanometers), the continuum media assumption breaks down, and it is therefore necessary to consider the physics of energy transport at a more fundamental level than what is done in macroscale, which basically implies taking into account the different energy carriers associated with specific materials. In crystalline semiconductor solids, materials of great interest to the microelectronics industry, the main energy carriers are phonons, which are quantized lattice vibrations. Thermal modeling of electronic devices has traditionally been based on the Fourier equation of heat conduction, which is valid only when the characteristic length of the device is larger than the phonon mean free path by at least one and desirably more orders of magnitude and when the time scale of the process is much longer than the phonon relaxation time. It is now well established that a conventional analysis of heat transport based on Fourier's equation leads to erroneous results when the mean free path of the heat carriers becomes comparable to or larger than the characteristic length of the domain of interest [1]. In addition, the Fourier equation assumes an instantaneous heat propagation, which leads to significant errors in the thermal predictions as the time scale of interest becomes comparable to or smaller than the relaxation time of the heat carriers [2]. Current transistor technology, for example, is yielding devices with channel lengths within the 90 nm technology node, and even smaller transistors (65 nm technology node) are in development phase as of 2005 [3]. It is clear from this that phonon transport in submicron semiconductor structures is likely to be within the subcontinuum regime and also that more accurate and consistent models for phonon transport are therefore needed in order to accurately model the thermal response of such devices.

For short time scales, on the order of the phonon relaxation time and length scales much larger than the phonon mean free path, the Cattaneo equation is developed from the Boltzmann transport equation (BTE). However, both the Cattaneo and Fourier equations are special limiting cases of the BTE, and as such, they either lack accuracy or require extensive computational efforts. Additionally, it is beyond their ability to simulate a multilength and multitime scale phenomenon as required for a successful thermal simulation of microelectronic devices.

The BTE with the single relaxation time approximation can be used to accurately simulate energy transport in the subcontinuum regime, as long as the particle assumption for the heat carriers is valid, that is, whenever the time scale is longer than the collision time characteristic of a scattering event and when the characteristic length is larger than the phonon wavelength, λ. However, when the characteristic length of the system is on the order of λ, we can no longer assume a particle nature for phonons and will have to resort to performing a molecular dynamics analysis of the problem. Moreover, extensive computational effort is required to solve the BTE since it involves multiple variables descriptive for space, time, and momentum or velocity space.

Based on this, we consider the transport of thermal energy in microelectronic components a very important subject of study, for which an existing adequate theoretical background coming from the solid-state physics is available, and allows describing its fundamentals. In what follows, we will first describe the lattice Boltzmann method (LBM) applied to heat conduction in crystalline semiconductor solids, introducing the use of nonlinear phonon dispersion. Then, a discussion on thermal conductivity and phonon relaxation times will be presented. Following this, results will be presented for both thin film heat conduction and size-dependent thermal conductivity.

[1]Present address: Faculty of Applied Science and Engineering, 35 St. George Street, Room 170, Toronto, ON M5S 1A4, Canada.

Contributed by the Heat Transfer Division of ASME for publication in the JOURNAL OF HEAT TRANSFER. Manuscript received May 16, 2007; final manuscript received December 7, 2007; published online July 10, 2008. Review conducted by Jayathi Murthy. Paper presented at the 2007 ASME-JSME Thermal Engineering Conference and Summer Heat Transfer Conference (HT2007), Vancouver, BC, Canada, July 8–12, 2007.

Dispersion Lattice Boltzmann Method for Phonon Transport

The LBM is a discrete development of the BTE, which can be used to simulate energy transport problems within the applicability range of the BTE. Recent efforts in LBM implementation have been based on the Debye model, resulting in what has been called the gray LBM. The gray LBM [4–7] considers a linear dispersion relation, from which only a single frequency-independent phonon propagation speed can be computed. However, it is widely known that phonon dispersion relations in crystalline semiconductors are nonlinear and that different phonon polarizations exist for multiatomic crystalline structures, such as silicon. The nonlinear dispersion relations translate into frequency-dependent phonon parameters, such as propagation speed, energy density, mean free path, and relaxation time. It is, therefore, desirable to consider nonlinear dispersion in order to accurately predict phonon transport in crystalline semiconductors.

The dispersion model is an attempt to avoid simplified models and assumptions such as the Einstein, Debye, and semigray [8] models since all of them restrict the full use of the nonlinear dispersion relations in one way or another. This model considers all phonon polarizations and modes, without restricting the contributions of any of them, and allows the BTE to govern the physics of the energy transport process without simplifying assumptions. Starting with the dispersion relations, the dispersion model first discretizes the frequency spectrum by dividing it in a number of frequency bands, each one exhibiting a particular phonon propagation speed. Simultaneously, a lattice Boltzmann kinetic equation (LBKE) is solved for each discrete frequency band at each discrete time step. Total energy density is found by a proper integration of the frequency-dependent energy density, and the physics of phonon transport in each frequency band is coupled to all other bands via a common lattice temperature and an appropriate expression for the frequency-dependent relaxation times.

Phonon propagation speed, density of state, energy density, and heat capacity are computed as functions of phonon polarization and frequency. We use the dispersion relations presented by Dolling [9] for silicon in the (100) direction, which, having a diatomic crystal structure, displays both acoustic and optical, longitudinal and transverse phonon polarizations. There are two degenerate transverse modes for both acoustic and optical polarizations (denoted as TA and TO), and one longitudinal mode per phonon branch (denoted as LA and LO). The phonon propagation speed can be computed from the dispersion relations as the first derivative of phonon frequency with respect to phonon wave number [10]. From this, it was found that LA phonons propagate with the fastest speeds ranging from almost 9000 m/s to slightly above 5000 m/s. Transverse acoustic phonons are slower, but they exhibit a greater range of speeds, from about 7000 m/s to almost zero. Traditionally, optical phonons have been considered too slow to effectively contribute to thermal transport, and therefore, several approaches model them by entirely neglecting the propagation speed on the grounds that it is sufficiently close to zero (as in the Einstein, semigray, and Narumanchi [11] models). However, as we have found, longitudinal optical phonons have a propagation speed ranging from 4000 m/s to almost zero, which is comparable to the propagation speed of acoustic phonons, both LA and TA. It was found that TO phonons also posses a range of propagation speeds from about 1200 m/s to almost zero, although it could be argued that these speeds are negligible when compared to the fastest propagating modes of LA phonons. It is our intent to solve simultaneous BTEs for all phonon polarization modes, which, in our view, is a more fundamental approach than those previously described. Eliminating the common assumption of zero propagation speed for optical phonons allows us to consider a more accurate physical modeling of the phonon transport process.

The phonon energy density can be computed from an adequate manipulation of the phonon dispersion relations. The energy density for a polarization p can be written as the frequency integral of the product between Planck's constant, phonon frequency, phonon distribution function, and phonon density of states as

$$e_p = \int_{\Delta\omega_p} \hbar\omega_p f D(\omega)_p d\omega_p \tag{1}$$

Here, the phonon distribution function is given by the solution of the BTE with appropriate boundary conditions. Under equilibrium conditions, the phonon distribution function is given by the Bose–Einstein equilibrium distribution,

$$f^0 = \frac{1}{e^{(\hbar\omega/k_B T)} - 1} \tag{2}$$

The total phonon energy density, which is a function of temperature, can be computed as the sum of the contributions from all phonon branches, or

$$e_T = \sum_p e_p = e_{\mathrm{LA}} + 2e_{\mathrm{TA}} + e_{\mathrm{LO}} + 2e_{\mathrm{TO}} \tag{3}$$

The next step in the setup of the dispersion model is the discretization of the frequency spectrum for all phonon branches and modes. This essentially means that the continuous dispersion relation is divided into discrete frequency bands of prescribed bandwidth $\Delta\omega$. The total number of frequency bands for each phonon branch and mode is determined by the accuracy of the solution, in a way similar to how spatial meshes are refined until a mesh-independent solution is achieved. It is important to note that since every phonon branch and mode has a different frequency range, the discretization of each frequency spectrum will likely have different bandwidths. Once the frequency spectrum is discretized and each discrete frequency band is determined, a band-averaged phonon propagation speed is found by using

$$\nu_{\Delta\omega} = \frac{1}{\Delta\omega}\int_{\Delta\omega} \nu(\omega) d\omega \tag{4}$$

which applies to each frequency band for all phonon branches and modes. One important consequence of discretizing the frequency spectrum is that it directly affects the LBM site-to-site transport restriction. Since this restriction relates the length of the site-to-site distance (also known as lattice distance) to the magnitude of the discrete time step, or $\Delta x = c_i \Delta t$, we observe that for different discrete propagation speeds we will either have different lattice spacings or different time step magnitudes. In our approach, the time step is fixed to a sufficiently small value compared to the phonon relaxation time, thus allowing acceptable temporal accuracy for all frequency bands. As a consequence, the lattice spacing for each band is different and given by the site-to-site transport restriction. Therefore, another main characteristic of the dispersion LBM is that it solves simultaneous LBKEs for each discrete frequency bands, each one having its own spatial discretization. The numerical integration necessary to find the phonon energy density at a given position within the spatial domain requires the use of an interpolation scheme every time step since the lattice sites for different discrete frequency bands do not necessarily coincide at the same location. In consequence, there will be as many different spatial discretizations as frequency bands times the number of phonon branches and modes. After performing spatial refinement studies, results are independent of frequency spectrum discretization when using 51 frequency bands for each phonon branch and mode.

Derivation of the LBKE. The LBKE for the dispersion model can be directly derived from a BTE form, under the relaxation time approximation, expressed in terms of the phonon distribution As mentioned, all relevant phonon parameters are frequency dependent. The derivation that follows applies to a single frequency band, but it is at the same time valid for any and all frequency

bands in the discretized frequency spectrum. We start from the BTE expressed in a phonon distribution function form, which is

$$\frac{\partial f}{\partial t} + \mathbf{v} \cdot \nabla f = \frac{f^0 - f}{\tau} \tag{5}$$

where f is the phonon distribution function, f^0 is the equilibrium phonon distribution function, $\mathbf{v}$ the frequency-dependent phonon propagation speed, and τ is the frequency-dependent phonon relaxation time. The first derivatives of the phonon distribution function with respect to time and space can be discretized as

$$\frac{\partial f}{\partial t} = \frac{f(x,t+\Delta t) - f(x,t)}{\Delta t} \tag{6}$$

$$\frac{\partial f}{\partial x} = \frac{f(x+\Delta x,t+\Delta t) - f(x,t+\Delta t)}{\Delta x} \tag{7}$$

Introducing the directionality subscript i in order to account for phonon propagation in a discrete lattice direction, then denoting the frequency-dependent discrete phonon propagation speed along the discrete direction i as c_i, and substituting Eqs. (6) and (7) into the BTE expression given by Eq. (5), we obtain

$$\frac{f_i(x,t+\Delta t) - f_i(x,t)}{\Delta t} + c_i \frac{f_i(x+\Delta x,t+\Delta t) - f_i(x,t+\Delta t)}{\Delta x} = \frac{f_i^0(x,t) - f_i(x,t)}{\tau} \tag{8}$$

From the site-to-site transport restriction, we select a time step/lattice spacing relation given by $\Delta x = c_i \Delta t$, where Δt is fixed and both Δx and c_i are frequency dependent and thus have specific values for each discrete frequency band. This leads to the expression

$$f_i(x+\Delta x,t+\Delta t) - f_i(x,t) = \frac{\Delta t}{\tau}(f_i^0(x,t) - f_i(x,t)) \tag{9}$$

Rearranging this equation and defining a weight factor $W_i = \Delta t/\tau$, where Δt is the time step, we can write the LBKE that governs the scattering and propagation of phonons in the lattice as

$$f_i(x + c_i\Delta t, t+\Delta t) = (1 - W_i) f_i(x,t) + W_i f_i^0(x,t) \tag{10}$$

The total phonon distribution function is the sum of discrete phonon distributions along all discrete lattice directions D,

$$f(x,t) = \sum_{i=1}^{D} f_i(x,t) \tag{11}$$

The equilibrium phonon distribution function in this case is computed directly from the Bose–Einstein distribution, where the frequency value is given by the band-averaged frequency of each frequency band, and the temperature is the total lattice temperature, the computation of which is described in the next section.

For multidimensional structures, the methodology is similar. In 2D problems, a particular D2Q9 lattice is used and an LBKE (as in Eq. (10)) is solved for every frequency band at each time step. A numerical interpolation is then used to compute phonon distribution functions. Then, Eq. (1) is used to compute the phonon energy density at the point of interest, from which a temperature can be computed as explained in previous sections. Again, interpolation is used to compute phonon equilibrium distribution functions in the lattice sites corresponding to the spatial discretization for each frequency band. Reference [12] can be consulted for details regarding an application of LBM to 2D structures.

Boundary Conditions: Prescribed Temperature Level. The Dirichlet boundary condition (corresponding to a constant prescribed temperature level, which can also be a function of space and time) uses the Bose–Einstein distribution to find the phonon distribution function corresponding to the desired temperature level. In this expression, thermodynamic equilibrium is assumed at the boundary and, therefore, all the discrete phonon distribution functions along any discrete lattice direction have the same value and are given by

$$f_i = \frac{1}{D} \frac{1}{e^{(\hbar\omega_j/k_B T)} - 1} \tag{12}$$

where $\hbar$ is Planck's constant divided by 2π, k_B the Boltzmann constant, T the lattice temperature, the subscript i the discrete lattice propagation direction of interest, the subscript j the band-averaged frequency for the jth discrete frequency band, and D the total number of discrete propagation directions in the lattice. A detailed algorithm for the dispersion LBM has been presented elsewhere [13].

On Thermal Conductivity Computations. When considering a gray phonon transport model [5–7], the phonon mean free path, relaxation time, heat capacity, and thermal conductivity can be related by means of the kinetic theory of gases formula given by

$$k = \tfrac{1}{3} C v \Lambda \tag{13}$$

where C is the heat capacity, v is the phonon propagation speed, and Λ is the phonon mean free path. Normally, bulk values for both the thermal conductivity and heat capacity are found in the literature for a range of temperatures, and the phonon propagation speed can be easily computed from the application of the Debye assumption. This makes the computation of the phonon mean free path relatively straightforward and, as a result, a Knudsen number is well defined and unique for a given system. In contrast, the dispersion LBM considers the thermal conductivity to be the sum of contributions from all phonon branches, contributions that are defined as integrals over the frequency spectrum as

$$k = \sum_p \int_\omega C_\omega v_\omega^2 \tau_\omega d\omega \tag{14}$$

where ω is the phonon frequency, C_ω is the frequency-dependent heat capacity, v_ω is the frequency-dependent phonon propagation speed, τ_ω is the frequency-dependent phonon relaxation time, and p indicates the different phonon branches. In this case, no straightforward mathematical relation for τ_ω exists, and thus, it cannot be extracted from Eq. (14). Instead, phonon relaxation must be previously known in order to compute the value of thermal conductivity. The problem is then to find suitable phonon relaxation time expressions that can allow us to compute an accurate prediction of bulk thermal conductivity.

Traditionally, researchers have tried to predict phonon relaxation times by considering the different types of scattering events to which phonons are subject. Phonon scattering events can be divided into two categories: elastic scattering by lattice imperfections, where the incident phonon energy or frequencies are not changed, and inelastic scattering by phonon-phonon collisions. Effective phonon relaxation time values are obtained from a combination of all known phonon scattering mechanisms. This effective relaxation time can be computed by assuming that the scattering processes are independent and do not interact with each other. This assumption, although not exactly exact for inelastic scattering, can be implemented by using the Matthiessen rule.

Expressions for each type of phonon relaxation time or scattering rate can be found in several sources from the literature. For example, Callaway [14] developed his analysis based on the Debye model. This analysis does not distinguish between longitudinal and transverse polarizations and only gives good agreement with experimental data at temperatures below and around the temperature at the maximum value of thermal conductivity, but not at higher temperatures. Holland [15] extended the work of Callaway by incorporating the contributions of longitudinal and transverse phonons and using different forms for the phonon relaxation times, which result in better agreement with experimental data

than what Callaway's approach was able to obtain. However, in the Callaway and Holland models, there is no analytical method for predicting the values of the arbitrary constants used, and therefore closure of the model depends on fitting these parameters to previously existing experimental data. It has been argued [16,17] that the successful fits of experimental data in these models result from the application of proper arbitrary fitting constants and not from an accurate physics model. Moreover, this approach is only suitable for materials whose thermal properties are known. If that is the case, the experimental thermal conductivity values can be used to validate the scattering rate models (again by proper fitting of constants). Unfortunately this approach cannot be utilized for materials of unknown thermal properties since then there would be no way of properly adjusting the fitting constants.

Another shortcoming of the Debye-derived methods [14,15,18,19] results from neglecting the contribution of optical phonons. Both longitudinal and transverse optical phonons are confined to a narrow range on the frequency spectrum. This has led to the simplification presented in the Einstein model, in which both modes are collapsed into a linear dispersion curve of constant frequency. Optical modes have been modeled as to display slow propagation speeds, and at first, the Einstein model (which assigns them zero speed, that is, purely capacitive properties) seemed to be appropriate, especially in view of the extensive computational efforts required to solve a BTE that considers nonlinear dispersion for all acoustic and optical modes. However, assigning them zero propagation speed results in neglecting their contribution to the thermal conductivity, and thus, all Debye-based models focus only on relaxation time expressions for acoustic phonons. This has led to relaxation times for optical phonons receiving limited attention in the literature [20–22], and as a result there is a significant lack of anharmonic scattering expressions that could readily be used. Recently, researchers have begun to question the accuracy of this approach, and there is increasing evidence that the contribution of optical phonons to the thermal conductivity is not negligible [23–25]. Additionally, the self-heating process of silicon-on-insulator (SOI) transistors is heavily affected by optical phonon confinement within a hotspot region, and as a result, accurate relaxation time expressions for optical phonons are of critical importance in modeling the heat transport in these regions of microelectronic components [26]. Even recent research that incorporates optical phonons only does so by assuming that they are of a purely capacitive mode and assigning them zero propagation speed [8].

It is therefore clear that most approaches fail to account for the true dispersive nature of the phonon frequency spectrum. As a result, full BTE expressions for optical phonons have not been solved simultaneously to acoustic modes, and adequate expressions for the optical mode relaxation time are still lacking. This work in part addresses these issues, trying to present a novel approach to thin film heat conduction and thermal conductivity prediction by developing a model that incorporates all phonon modes in order to solve simultaneous BTE's, in addition to considering the multiple length scale nature of the problem.

Analytical Prediction of Bulk Thermal Conductivity. As has been discussed, the only information needed to successfully simulate the thermal behavior of a crystalline structure with the LBM are adequate analytical expressions or numerical data for the dispersion relations (from which the phonon propagation speed is derived) and for the phonon relaxation times. The latter still lacking, we have resorted to compute them by implementing three-phonon interactions following the model by Han and Klemens [22]. This approach has been demonstrated to recover the bulk value of thermal conductivity for silicon [11] and seems to be adequate for our needs. However, this analysis, based on perturbation theory, relies on the assumption of low temperatures ($T < 100$ K) and, thus, is expected to fail at higher temperatures. Moreover, one valid alternative available is that of Sinha and Goodson [27], which presents mean free path data for bulk silicon at room temperature. In our opinion, the lack of adequate phonon relaxation time expressions is going to hinder the accuracy of our LBM method until more reliable expressions are developed. Additional details on the Han and Klemens (HK) model can be found in the literature [11,22,28]. In the model, the frequency spectrum is discretized in equal-width frequency bands, whose interaction with each other are constrained by energy and momentum conservation rules. A two-step process characterizes energy exchange between frequency bands: first, a normal process between low-wave-vector phonons and intermediate-wave-vector phonons, and then an Umklapp process between the intermediate phonons and those at the Brillouin zone. It has been argued [22,28] that important three-phonon interactions are of the types: $T+L \leftrightarrow L$, $L+T \leftrightarrow L$, and $L+L \leftrightarrow L$. Interactions with optical modes ($T+L \leftrightarrow O$, $L+T \leftrightarrow O$, and $L+L \leftrightarrow O$) are *N* processes and cannot be included in the thermal conductivity computation. For simplicity, Narumanchi et al. [8,11] collapsed all optical modes into a single frequency band of constant frequency and zero propagation speed. Due to the intensive nature of the computational effort required to obtain frequency-dependent optical mode relaxation times, a hybrid model is proposed here: acoustic mode relaxation times are obtained from the HK [22] model, and optical mode relaxation times are those presented by Sinha and Goodson [27].

Table 1 Analytical predictions for thermal conductivity of bulk silicon

Model	HK, BS	HK, no BS	Hybrid
k (W/m K)	123	160	153
% error	16.4	7.8	3.3

In the HK [22] model, inverse relaxation times for a specific process have the general form

$$\frac{1}{\tau_{ij}} = \frac{a\gamma^2\hbar}{3\pi\rho\nu_{\mathrm{ph}}^b\nu_g^c}\omega_i\omega_j\omega_k R_c^2\left(\frac{1}{e^{\hbar\omega_j/k_BT}-1} - \frac{1}{e^{\hbar\omega_k/k_BT}-1}\right) \quad (15)$$

where τ_{ij} is the relaxation time that accounts for energy exchange between the bands i and j of frequency ω_i and ω_j, ω_k is the intermediate phonon frequency that completes the three-phonon interaction, v_g is the phonon group velocity at ω_j, and v_{ph} is the phase velocity of the i mode. The effective relaxation time for a discrete frequency band centered on ωi is found as the combination of all phonon scattering processes in a Mathiessen sense as

$$\frac{1}{\tau_{\mathrm{eff},\omega_i}} = \sum_i \frac{1}{\tau_{ij}} \quad (16)$$

We have compared the HK model to a *hybrid* model based on Han and Klemens [22] for acoustic modes, plus the addition of optical mode relaxation time data extracted from Sinha and Goodson [27]. The influence of phonon-boundary scattering in the model was tested. The bulk silicon phonon mean free path data presented in Ref. [27] is available only at room temperature, and thus the prediction of thermal conductivity with this model is possible only at room temperature. As seen in Table 1, the hybrid model seems to better predict the bulk thermal conductivity model at room temperature, displaying a percentage error of only 3.3% when compared to the experimental data of Ho et al. [29]. As a consequence, the hybrid model is adopted as the most accurate relaxation time model available for use with the dispersion LBM.

Results

In what follows, we first present time-dependent temperature profiles depicting the transition from diffusive to ballistic phonon transport in silicon thin films of decreasing thickness, obtained with the dispersion LBM. The effects of including nonlinear phonon dispersion as compared to the existing gray LBM are discussed, as well as the influence that ballistic phonon transport has

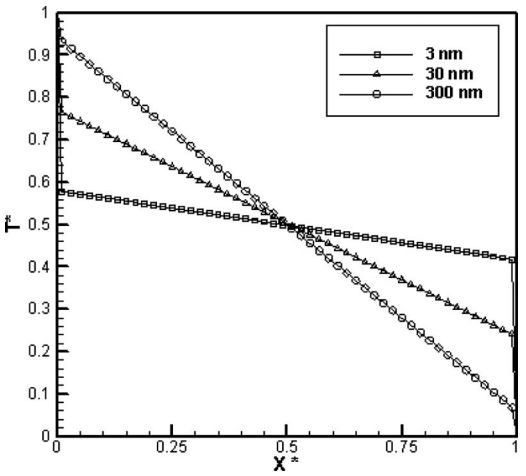

Fig. 1 Dimensionless steady-state temperature distributions along a one-dimensional film over different film thicknesses

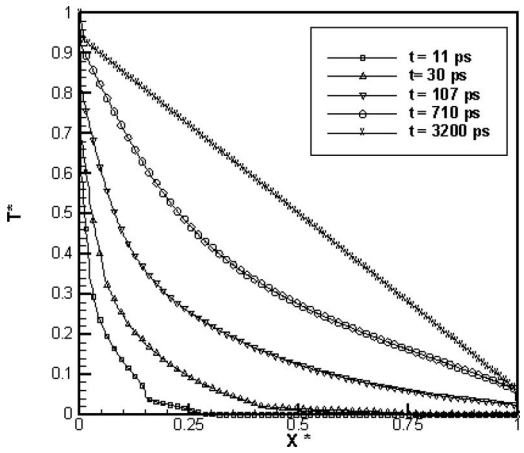

Fig. 2 Transient temperature profile inside a 300 nm thin film

on the thin film thermal conductivity. Thus, from here on we refer specifically to the gray LBM results presented by Escobar et al. [6]. Finally, the predictions for thickness-dependent thermal conductivity obtained with both the gray and dispersion LBMs are presented and discussed in an effort to elucidate the effect of considering nonlinear phonon dispersion in the LBM.

Transition to Ballistic Transport in Thin Films. In this section we present results for silicon thin film heating. The physical situation is that of a film of variable thickness, subject to imposed temperature conditions at each boundary. Unlike the gray LBM [6], where the Knudsen number is defined as the ratio between the characteristic length scale and the phonon mean free path, the dispersion model exhibits a complication arising from its frequency-dependent nature: the frequency spectrum discretization and the frequency-dependent phonon mean free path combine and result in a frequency-dependent Knudsen number, which has different values for each frequency band. Therefore, we present results in this section as a function of film thickness rather than Knudsen number.

A film of thickness d is considered and modeled as a one-dimensional domain of length d. The initial temperature of the film is taken to be T_1. At time $t=0$, the right boundary of the film is kept at T_1 while the left boundary is set at a higher temperature T_2. In the LBM simulation, grid refinements are conducted until the solution is no longer dependent on the lattice distance. As a general rule, grid independence and numerical stability are ensured for lattice spacing shorter than the phonon mean free path, with a useful rule of thumb indicating that lattice spacing of one-third of the phonon mean free path gives an optimal combination of accuracy and relatively reduced computational expense.

Steady-state dimensionless temperature distributions in the thin film are shown in Fig. 1 for films with thicknesses between 3 nm and 300 nm. Here, the dimensionless length is $X^*=x/d$, where x is the distance measured from the high temperature boundary, and the dimensionless temperature is $T^*=(T-T_1)/(T_2-T_1)$.

The dispersion LBM simulation of films thicker than 1000 nm was found to be unfeasible due to the extremely high computational cost. The simulations for this work were performed in computational platforms consisting of Intel Xeon processors running at 2.20 GHz, with 8 Gb of random access memory (RAM). The system's configuration allowed us to simulate films thinner than 1000 nm. Similar to what was found by using the gray model, decreasing film thickness translates into increasing temperature slip at the boundaries, which is in agreement with results previously reported in the literature [2,5,6,8].

The transient dimensionless temperature profiles in a 300 nm thin film are shown in Fig. 2. Although there is some similarity with gray LBM results that fall within the diffusive regime, in this case a wave behavior can be seen at short times ($t=11$ ps and $t=30$ ps), to be later dampened into a temperature profile that resembles diffusive transport ($t>30$ ps). However, the temperature slip at the boundaries is a clear indication that this case falls within the transitional regime. At steady-state conditions, the temperature profile displays a linear drop inside the film, with temperature slip conditions at each boundary.

Decreasing the film thickness by an order of magnitude results in a 30 nm thin film, whose transient dimensionless temperature profiles are shown in Fig. 3. Marked differences exist with gray LBM results. In this case, the temperature profile is composed of a combination of traveling phonon energy waves, as opposed to the single propagating wave of the gray LBM. At short times ($t=3.47$ ps), it can be seen that the faster acoustic phonons have propagated inside the film and are about to reach the cold boundary, while the slower but more energetic optical phonons have only begun to leave the hot boundary. Characteristic temperature slip conditions are seen in the hot boundary. As time advances, all acoustic phonon waves have already reached the cold boundary, and only the slow optical phonon waves still propagate ($t=37.6$ ps). Finally, steady-state conditions are achieved, the temperature profile displays slip conditions at both boundaries and a linear drop inside the thin film.

Figure 4 shows the transient dimensionless temperature profiles in a 3 nm thin film, which is considered to be the lower limit at which an LBM can be applied; the film thickness is on the order

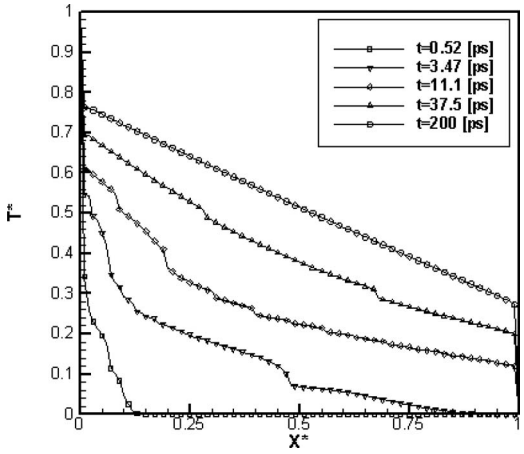

Fig. 3 Transient temperature evolution inside a 30 nm thin film

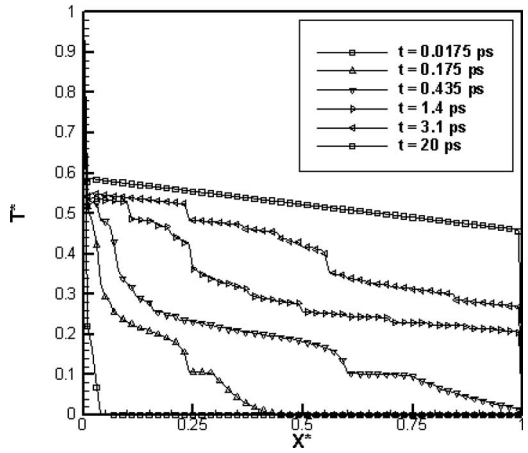

Fig. 4 Transient temperature evolution inside a 3 nm thin film

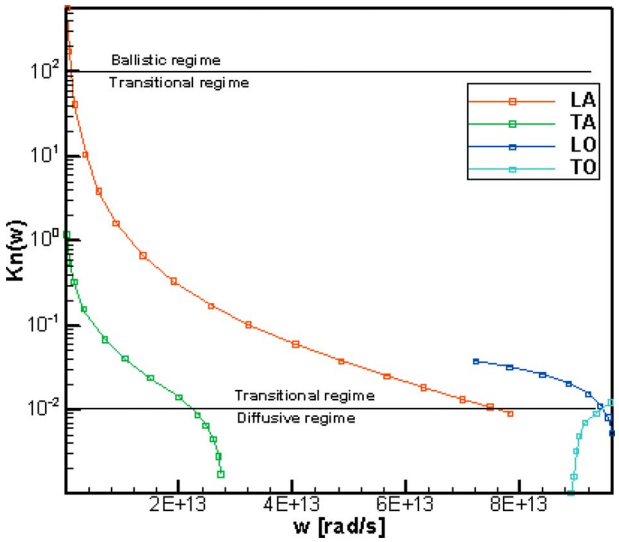

Fig. 5 Frequency-dependent Kn for a film of thickness of 1000 nm

of phonon wavelengths and, therefore, a molecular approach is needed to perform thermal analysis below this thickness. Marked differences exist with gray LBM results. In this case, the temperature profile is composed of a combination of traveling phonon energy waves, as opposed to the single propagating wave of the gray LBM. At short times (t=0.175 ps), it is clearly seen that faster acoustic phonons have propagated inside the film and are about to hit the cold boundary, while slower but energetic optical phonons have only begun to leave the hot boundary. Characteristic temperature slip conditions are seen in the hot boundary. As time advances, all acoustic phonon waves have already reached the cold boundary, and only slow optical phonon waves propagate (t=3.1 ps). Finally, steady-state conditions are achieved and the temperature profile displays slip conditions at the boundaries and a linear drop inside the thin film.

The temperature slip condition can be explained by observing that constant temperature levels at the boundaries have the net effect of enforcing an emission of phonons with an energy density corresponding to the imposed boundary temperature. As the frequency-dependent band Knudsen number for a given frequency band approaches a value that situates the frequency band within the subcontinuum regime, the phonons traveling toward the boundary have a significantly different energy density than that of the phonons emitted from the boundary, therefore resulting in an abrupt change in energy density, which displays itself as the temperature slip at the boundaries. The magnitude of the temperature slip at the boundary is proportional to the Knudsen number, being zero in the limit of a vanishing Knudsen number, as occurs for a purely diffusive regime, characteristic of Fourier conduction. Thus, in the context of the dispersion model, each frequency band displays a temperature slip whose magnitude is given by the band Knudsen number and thus represents a band thermal resistance. The total thermal resistance of the superimposed temperature slip conditions is to be given by the final temperature profile and the magnitude of the boundary temperature slip.

One interesting characteristic of the dispersion LBM model, a fundamental difference with the gray LBM, is the coexistence of different transport regimes for a given film thickness. Here, we define a frequency-dependent band Knudsen number as $\mathrm{Kn}(\omega)=\Lambda(\omega)/d$, where $\Lambda(\omega)$ is the frequency-dependent phonon mean free path and d the film thickness. The diffusive regime is defined for a very small or vanishing Knudsen number, which can be arbitrarily expressed as $\mathrm{Kn}(\omega)<0.01$, with the other limit being the purely ballistic regime, defined as $\mathrm{Kn}(\omega)>100$. To illustrate this point, Fig. 5 depicts the band Knudsen number for all phonon branches in a film of 1000 nm thickness, as a function of phonon frequency. The figure normalizes the phonon mean free path data for silicon presented in Fig. 13 from Ref. [27] by dividing it with the film thickness of 1000 nm.

It is observed that only the lowest-frequency LA bands, which happen to propagate at the fastest speeds of the phonon system, are located at a Knudsen number range that characterize them as being within the purely ballistic regime. Higher-frequency LA bands are mostly located within the transitional regime, except for the bands the with highest frequency, which are located at Knudsen numbers characteristic of the diffusive regime. TA and LO branches have both a band Knudsen number range within the transitional and diffusive regimes, while most TO bands are well within the diffusive regime. The implications of this behavior are twofold: First, at a film thickness that in the gray LBM could be located close to the diffusive regime, the dispersion model presents results that are shifted toward the transitional regime. Second, the transition to ballistic regime is likely to be a process that occurs at a wider range of film thicknesses due to the order-of-magnitude differences in band Knudsen number range for all branches. This basically implies that energy transport in a film of a given arbitrary thickness is likely to display characteristics of at least two, if not all three, of the transport regimes.

Validation of the Dispersion LBM. The task of performing dispersion LBM simulations within the diffusive regime is indeed formidable. The multiple LBKEs that need to be simultaneously solved, each having its own lattice spacing, make the task of reaching the diffusive regime a most difficult enterprise. Considering the required computational effort, a direct validation of the dispersion LBM in the diffusive regime, by comparing with Fourier diffusion solutions, is not feasible under the current structure of the dispersion LBM code. The first resulting recommendation is to avoid the use of LBM, in any of its forms (gray and dispersion), for the simulation of diffusive regime problems. For this, traditional techniques based on discretization of the Fourier heat conduction equation are more efficient, which limits the use of LBM-based techniques to the transitional and ballistic regimes. The second recommendation is to embark in a revision and modification of the current code in order to make it more efficient and able to simulate a broader range of length and time scales. Incorporating parallel computing capabilities to the LBM code is part of the author's ongoing work.

Thickness-Dependent Thermal Conductivity. As we have seen, the analytical model used for selecting the appropriate expressions of phonon mean free path for the dispersion LBM was able to recover the thermal conductivity value for bulk silicon

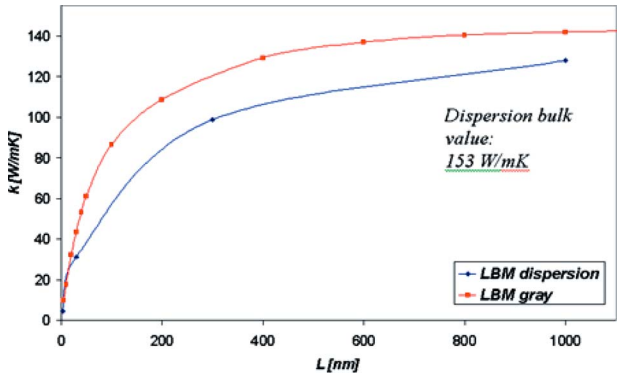

Fig. 6 Thermal conductivity as a function of film thickness

with an acceptable accuracy. To further analyze the dispersion LBM capabilities, this section presents results for thermal conductivity as a function of film thickness of the one-dimensional model based on the steady-state temperature distribution displayed in the previous section. To compute the effective size-dependent thermal conductivity, it is necessary to first know the heat flux being transported across the film and the magnitude of the temperature slip.

The heat flux can be computed by using a general expression of heat flux, applying it to each discrete frequency band for all phonon modes and then adding their contributions, as given by

$$q_{\mathrm{LBM}} = \sum_{p} \int_{\Delta\omega_p} v_i \hbar \omega f D(\omega) d\omega \tag{17}$$

The bulk value of thermal conductivity is known from Eq. (14) and Table 1. This value is used in Eq. (18) to find the frequency-dependent effective thermal conductivity, and the total effective thermal conductivity is computed as the sum of all frequency-dependent contributions of all phonon modes,

$$k_{\mathrm{effective}}(\omega) = \frac{k_{\mathrm{bulk}}}{1 + 2C\mathrm{Kn}(\omega)} \tag{18}$$

where C corresponds to a geometric parameter that takes into account the magnitude of the boundary temperature slip [30].

Figure 6 depicts a comparison between out-of-plane effective thermal conductivity predictions by the gray and dispersion LBMs. As can bee seen, the gray LBM predicts an effective thermal conductivity value that remains close to the bulk value of 148 W/(m K) down to a film thickness of 1000 nm. Further decreases in the film thickness cause a slight decrease of the effective thermal conductivity down to a film thickness of approximately 400 nm. For films thinner than 400 nm, the decrease on thermal conductivity is more pronounced and the gray LBM eventually predicts an effective thermal conductivity value of zero for a film of vanishing thickness. This behavior is consistent with the gray LBM formulation, in which the transition to ballistic transport is a function of a single parameter, the Knudsen number. Subcontinuum effects start to influence the energy transport process at Knudsen numbers of about Kn=0.1, corresponding to a film thickness of 410 nm. The transition to ballistic transport occurs between Kn=0.1 (for film thickness of d=410 nm) and Kn =10 (for film thickness of d=4.1 nm), a phenomenon that is manifested by the reduction of effective thermal conductivity value.

Following what was expressed in previous sections, the analytical dispersion model gives a bulk thermal conductivity value of 153 W/m, which compares well with the value predicted by the gray LBM, 145 W/m K, and is in good agreement with the experimental value of 148 W/m K. As we have mentioned, reaching the diffusive regime with the dispersion LBM would involve the simulation of films with thickness in the order of millimeters, which does not compare well with the actual capabilities of the LBM code, as the limit for feasible simulations was found to be about 1000 nm. Thus, we are prevented from reaching a purely diffusive regime and have instead computed effective thermal conductivity values for film thickness below 1000 nm.

As seen in Fig. 6, the thickness-dependent effective thermal conductivity predicted by the dispersion LBM is consistently lower than that predicted by the gray LBM. The dispersion model predicts an earlier shift from the diffusive transport regime to the transitional regime, a situation that arises from phonon frequency bands clearly residing in the transitional transport region (Fig. 5), this, even for a film thickness that the gray model had characterized as being very close to the diffusive regime. Further reducing the film thickness results in more phonon frequency bands being located within the transitional regime, and as a result, the general trend is for the dispersion LBM to predict values of effective thermal conductivity lower than the gray LBM. As for the physical mechanism that results in the effective thermal conductivity being lower than the bulk value, this is thought to be due to strong phonon-boundary scattering, where phonons traveling to and from the prescribed temperature boundaries are forced to suddenly change their energy density, which induces the boundary temperature slip conditions observed in Figs. 1–4. Although it is somewhat difficult to validate the results for our 1D model, in the limit of large length scales the dispersion LBM is able to recover the bulk value of thermal conductivity, and in the size effect regime they compare well to those presented in Refs. [16,17,22–25,28].

Conclusions

The dispersion LBM is used to study the transition to ballistic transport in silicon films of varying thickness. It is found that the solution for the temperature distribution inside thin films corresponds to the superposition of multiple phonon propagating waves, each of them traveling at a characteristic frequency-dependent propagation speed given by the dispersion relation of each phonon mode. Transition to ballistic transport is not fully achieved for films of thickness as low as 3 nm, a consequence of most frequency bands being located within the transitional regime even for that reduced thickness. On the other extreme of large length scales, it is found that simulating the transition to diffusive transport is unfeasible due to the large domain sizes required, which are in the order of millimeters. This is again a result of most frequency bands residing within the transitional regime for film thickness deemed within the diffusive regime by the gray LBM. As a consequence, the thickness-dependent effective thermal conductivity values predicted by the dispersion LBM are consistently lower than those predicted by the gray LBM for the same film thickness. The dispersion LBM, which includes the effects of nonlinear dispersion relations for all phonon branches, is considered to be more accurate than the gray LBM due to the improved phonon physics inherently captured by the model, which allows the simulation of multiple discrete phonon frequency bands and the explicit treatment of optical phonons without simplifying assumptions. This is a considerable improvement from the Debye-based gray LBM, which only considers a single phonon mode with a constant propagation speed and is therefore unable to capture the behavior of phonon modes characterized by propagation speeds different from the one defined by the Debye model.

Acknowledgment

The authors gratefully acknowledge support from the National Science Foundation Grant No. CTS-0103082, the ICES Pennsylvania Infrastructure Technology Alliance (PITA) Program sponsored by the Commonwealth of Pennsylvania's Department of Community and Economic Development, the Pontificia Universidad Católica de Chile, and the Chilean Fondo Nacional de Ciencia y Tecnología (FONDECYT), through Grant Nos. 1050087 and 11030620.

References

[1] Flik, M., Choi, B., and Goodson, K., 1992, "Heat Transfer Regimes in Microstructures," ASME J. Heat Transfer, **114**, pp. 666–674.

[2] Majumdar, A., 1993, "Microscale Heat Conduction in Dielectric Thin Films," ASME J. Heat Transfer, **115**, pp. 7–16.

[3] International Technology Roadmap for Semiconductors, ITRS 20053 update (http://public.itrs.net/).

[4] Succi, S., 2001, *The Lattice-Boltzmann Equation for Fluid Dynamics and Beyond*, Clarendon Press, Oxford, UK.

[5] Zhang, W., and Fisher, T. S., 2002, "Application of the Lattice-Boltzmann Method to Sub-Continuum Heat Conduction," ASME Paper No. IMECE2002-32122.

[6] Escobar, R. A., Ghai, S. S., Jhon, M. S., and Amon, C. H., 2006, "Multi-Length and Time Scale Thermal Transport Using the Lattice Boltzmann Method With Application to Electronics Cooling," Int. J. Heat Mass Transfer, **49**, pp. 97–107.

[7] Ghai, S. S., Kim, W. T., Escobar, R. A., Amon, C. H., and Jhon, M. S., 2005, "A Novel Heat Transfer Model and Its Application to Information Storage Systems," J. Appl. Phys., **97**, p. 10P703.

[8] Narumanchi, S., Murthy, J., and Amon, C., 2005, "Comparison of Different Phonon Transport Models for Predicting Heat Conduction in Silicon-on-Insulator Transistors," ASME J. Heat Transfer, **127**, pp. 713–723.

[9] Dolling, G., 1963, "Lattice Vibrations in Crystals With the Diamond Structure," *Symposium on Inelastic Scattering of Neutrons in Solids and Liquids*, IAEA, Vienna, pp. 37–48.

[10] Tien, C. L., Majumdar, A., and Gerner, F. M., 1998, *Microscale Heat Conduction*, Taylor & Francis, Washington, D.C..

[11] Narumanchi, S. V., Murthy, J. Y., and Amon, C. H., 2003, "Simulation of Unsteady Small Heat Source Effects in Sub-Micron Heat Conduction," ASME J. Heat Transfer, **125**, pp. 896–903.

[12] Escobar, R. A., 2005, "Lattice Boltzmann Modeling of Phonon Transport in Silicon Films," Ph.D. thesis, Department of Mechanical Engineering, Carnegie Mellon University.

[13] Callaway, J., 1959, "Model for Lattice Thermal Conductivity at Low Temperatures," Phys. Rev., **113**, pp. 1046–1051.

[14] Holland, M. G., 1963, "Analysis of Lattice Thermal Conductivity," Phys. Rev., **132**(6), pp. 2461–2471.

[15] McGaughey, A. J. H., and Kaviany, M., 2004, "Quantitative Validation of the Boltzmann Transport Equation Phonon Thermal Conductivity Model Under the Single-Mode Relaxation Time Approximation," Phys. Rev. B, **69**, p. 094303.

[16] McGaughey, A. J. H., Chung, J. D., and Kaviany, M., 2003, "Integration of Molecular Dynamics Simulations and Boltzmann Transport Equation in Phonon Thermal Conductivity Analysis," ASME Paper No. IMECE2003-41899.

[17] Tiwari, M. D., and Agrawal, Bal K., 1971, "Analysis of the Lattice Thermal Conductivity of Germanium," Phys. Rev. B, **4**, pp. 3527–3532.

[18] Sood, K. C., and Roy, M. K., 1993, "Longitudinal Phonons and HighTemperature Heat Conduction in Germanium," J. Phys.: Condens. Matter, **5**, pp. 301–312.

[19] Klemens, P. G., 1958, "Thermal Conductivity and Lattice Vibrational Modes," *Solid State Physics*, F. Seitz and D. Thurnbull, eds., Academic Press, New York, pp. 1–98.

[20] Klemens, P. G., 1969, "Theory of Thermal Conductivity of Solids," *Thermal Conductivity*, R. P. Tye, ed., Academic, London, pp. 1–68.

[21] Han, Y.-J., and Klemens, P. G., 1993, "Anharmonic Thermal Resistivity of Dielectric Crystals at Low Temperatures," Phys. Rev. B, **48**, pp. 6033–6042.

[22] Chung, J. D., McGaughey, A. J. H., and Kaviany, M., 2004, "Role of Phonon Dispersion in Lattice Thermal Conductivity Analysis," ASME J. Heat Transfer, **126**, pp. 376–380.

[23] McGaughey, A. J. H., and Kaviany, M., 2004, "Thermal Conductivity Decomposition and Analysis Using Molecular Dynamics Simulations. Part I. Lennard-Jones Argon," Int. J. Heat Mass Transfer, **47**, pp. 1783–1798.

[24] McGaughey, A. J. H., and Kaviany, M., 2004, "Thermal Conductivity Decomposition and Analysis Using Molecular Dynamics Simulations. Part II. Complex Silica Crystals," Int. J. Heat Mass Transfer, **47**, pp. 1799–1816.

[25] Pop, E., Sinha, S., and Goodson, K. E., 2003, "Detailed Phonon Generation Simulations Via the Monte Carlo Method," ASME Paper No. HT2003-47312.

[26] Sinha, S., and Goodson, K., 2005, "Review: Multiscale Thermal Modeling in Nanoelectronics," Int. J. Multiscale Comp. Eng., **3**(1), pp. 107–133.

[27] Narumanchi, S. V. J., Murthy, J. Y., and Amon, C. H., 2003, "Simulations of Heat Conduction in Sub-Micron Silicon-on-Insulator Transistors Accounting for Phonon Dispersion and Polarization," ASME Paper No. IMECE2003-42447.

[28] Ho, C., Powell, R., and Liley, P., 1972, "Thermal Conductivity of the Elements," J. Phys. Chem. Ref. Data, **1**, pp. 279–421.

[29] Escobar, R., Smith, B., and Amon, C., 2006, "Lattice Boltzmann Modeling of Subcontinuum Energy Transport in Crystalline and Amorphous Microelectronics Devices," ASME J. Electron. Packag., **128**, pp. 115–124.

[30] Escobar, R., and Amon, C. H., 2007, "Influence of Phonon Dispersion on Transient Thermal Response of Silicon-on-Insulator Transistors Under Self-Heating Conditions," ASME J. Heat Transfer, **129**(7), pp. 790–797.

Experimental Study of Heat Conduction in Aqueous Suspensions of Aluminum Oxide Nanoparticles

Y. Sungtaek Ju[1]
e-mail: just@seas.ucla.edu

Jichul Kim

Ming-Tsung Hung

Mechanical and Aerospace Engineering Department,
University of California,
Los Angeles, CA 90095

We report measurements of the thermal conductivity of aqueous suspensions of aluminum oxide nanoparticles with nominal diameters of 20 nm, 30 nm, and 45 nm and at volume concentrations up to 10%. Potential complications in the pulsed transient hot-wire technique for characterizing nanofluids are examined, which motivate the development of a microhot strip setup with a small thermal time constant. The average particle size is monitored for samples subjected to different durations of sonication and the thermal conductivity is determined at two different temperatures for each of the samples. The present data do not reveal any anomalous enhancement in the thermal conductivity previously reported for comparable nanofluids. The concentration dependence of the thermal conductivity can be explained using the conventional effective medium model with a physically reasonable set of parameters. [DOI: 10.1115/1.2945886]

Keywords: nanofluid, thermal conductivity, transient hot wire technique

Introduction

Enhanced heat transfer in colloids of nanoparticles, often referred to as nanofluids, has received a lot of attention lately. Several experimental studies reported that the thermal conductivity of nanofluids is considerably higher than that of base liquids [1–3]. Such outstanding properties would make nanofluids attractive for various thermal applications.

Many studies attempted to identify mechanisms responsible for the anomalous improvement in the thermal conductivity of nanofluids. Wang et al. [4] and later Keblinski et al. [3] pointed out that loosely packed aggregates of nanoparticles can occupy larger "effective" volumes than individual particles that make up the aggregates. Theoretical prediction based on the nominal particle concentration may therefore significantly underestimate the thermal conductivity. Prasher et al. [5] extended the model of Wang et al. [4] and suggested that the thermal conductivity reaches a peak when the average number of particles in a single aggregate is approximately 8. Another recent model [6] proposed that the abnormal increase in thermal conductivity could be explained by the presence of chainlike agglomerates, which are more effective than spherical particles in enhancing the thermal conductivity.

A different class of models, although still a subject of heated debate, attributes the enhancement to microconvection associated with Brownian motions of nanoparticles. Semi-empirical models proposed by Prasher et al. [7], Chon et al. [8], and others, for example, could capture both the temperature and particle size dependence of the thermal conductivity. These models were also deemed consistent with the observation of Krishnamurthy et al. [9], who reported drastic enhancement in the mass diffusivity of a molecular dye in colloids of aluminum oxide nanoparticles.

Several recent studies employed new experimental techniques to investigate heat conduction in nanofluids, motivated in part by the recognition that experimental studies had not quite kept pace with theoretical studies. Most early experimental studies used established thermal conductivity measurement techniques [10], such as a steady-state method, a temperature oscillation method, and several variations of transient hot-wire methods. More recent studies employed an optical beam-deflection technique [11], a thermal lensing method [12], and a forced Rayleigh scattering method [13].

Quite surprisingly, the results of many recent experimental studies deviate considerably from those of earlier studies. Putnam et al. [11], for example, observed no appreciable enhancement in the thermal conductivity of colloids of Au nanoparticles. This is in stark contrast to the work of Patel et al. [14], who reported considerable increase in the thermal conductivity of similarly prepared colloids at concentrations well below 1%. Strong temperature dependence reported in early studies also could not always be reproduced.

It is not clear whether such large discrepancy is due to subtle but critical differences among nanofluid samples or due to experimental errors. In the vast majority of early studies, the size of particles/aggregates in nanofluids was not directly measured. Basic information on nanoparticles was also often missing in many previous articles. We believe that there remains a critical need for further systematic experimental studies to achieve meaningful progress in understanding heat transport phenomena in nanofluids.

In the present article, we report our effort in accurate measurements of the thermal conductivity of aqueous suspensions of aluminum oxide nanoparticles, for which the anomalous thermal conductivity enhancement have been best documented [5,8,10]. We examine potential complications in the pulsed transient hot-wire technique, which motivate us to develop a microhot strip setup that has a microsample chamber with a small thermal time constant. Aluminum oxide nanoparticles of three different nominal diameters (20 nm, 30 nm, and 45 nm) are used to prepare three sets of different nanofluids. The particle/aggregate size and the thermal conductivity of these nanofluids are measured and reported as a function of sonication time or temperature.

[1]Corresponding author.

Contributed by the Heat Transfer Division for publication in the JOURNAL OF HEAT TRANSFER. Manuscript received June 6, 2007; final manuscript received January 3, 2008; published online July 10, 2008. Review conducted by Peter Vadasz. Paper presented at the 2007 ASME-JSME Thermal Engineering Conference and Summer Heat Transfer Conference (HT2007), Vancouver, BC, Canada, July 8–12, 2007.

Potential Complications in Pulsed Transient Hot-Wire Measurements

The pulsed transient hot-wire technique and its variations, such as the transient hot strip technique [15], have been widely used to measure the thermal conductivity of liquids. These techniques are deemed advantageous because they can significantly reduce measurement time and minimize error due to natural convection.

In analyzing raw data from pulsed transient hot-wire measurements, one assumes that the sample is initially in thermal equilibrium with the surrounding. Significant errors can result when this condition is not satisfied. This is an important concern for nanofluids. Preparation of nanofluids often requires prolonged sonication, which can lead to substantial temperature rise in the sample. Given the finite kinetics of particle agglomeration, however, one may find it necessary to perform thermal conductivity measurements right after sonication is completed. It is also often necessary to perform repeated measurements and average their results by applying multiple successive heating pulses. These requirements can lead to two different types of potential errors, one caused by the overall cooling of a liquid sample during measurements and the other caused by temperature inhomogeneity created by successive heating pulses.

Error Due to Overall Sample Cooling. To have a first-order assessment of the first type of error, we measure the thermal conductivity of pure water as a function of time elapsed after sonication. A glass beaker of diameter 32 mm is filled with 15 ml of de-ionized water. After 1 h of sonication, the beaker is removed from the sonicator for thermal conductivity measurements. We use a custom-made macroscale hot wire made of a Pt wire of length 1.5 cm and a diameter of 25 μm. The wire and voltage probes are encapsulated in a 25 μm thick Kapton layer.

A 2 s long current pulse is applied to the hot wire and the resulting temperature rise is obtained by monitoring its electrical resistance. To extract the thermal conductivity, the temporal temperature profile is analyzed using numerical solutions to the transient three-dimensional heat conduction equation. Our simulation code is based on the well-established finite volume method. The thermal resistance of the Kapton layer, including the associated thermal boundary resistance, is considered an adjustable parameter in our simulations. In addition to a grid and time step independence study, we validate our data analysis procedure by confirming that our experimental data agree with literature values [16] for various solids and liquids, including quartz, fused silica, water, methanol, and glycerin/water mixture, to within 2%.

Figure 1 shows the thermal conductivity data and the wire temperature as a function of elapsed time after sonication. The wire temperature may serve as an approximate measure of the liquid temperature around the hot wire. The thermal conductivity decreases over time until it reaches an approximately constant value about 50 min after the start of the experiment. The dotted line shows the literature value [16] at each measured wire temperature, which initially deviates substantially from the measured data. The pulsed transient hot-wire technique overestimates the thermal conductivity when the sample cools down during measurements. Note that even a few degrees of temperature variations can lead to appreciable errors in the measured thermal conductivity.

Error Due to Preceding Heating Pulses. The second type of error can be significant even when a sample is in equilibrium with the surrounding at the beginning of an experiment. Repeated measurements are often necessary to reduce random errors. Each application of a heating pulse, however, disturbs the temperature field within the sample and hence subsequent measurements. An important parameter is therefore time interval between successive heating pulses.

To have a first-order assessment of the second type of error, we measure the thermal conductivity of a pure water sample that is originally in thermal equilibrium with the ambient at 23°C. The experimental setup and data analysis procedures are the same as before. We apply N heating pulses, each separated from the preceding one by a fixed time interval. By analyzing the resulting N temperature profiles, we can extract N different values of the thermal conductivity. We then repeat a similar experiment using a different time interval between heating pulses.

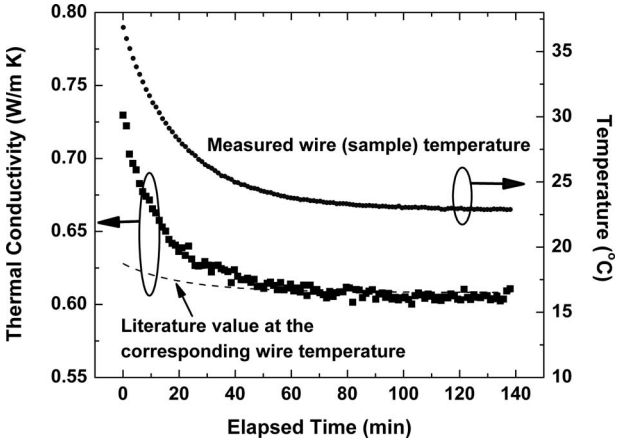

Fig. 1 The time evolution of the thermal conductivity of a sonicated water sample and the wire temperature obtained from our macroscale hot-wire setup. The literature value of the thermal conductivity at each wire temperature is shown as the dashed line.

Figure 2 shows the average value of the thermal conductivity obtained for $N=20$ as a function of time interval between successive heating pulses. In our macroscale hot-wire setup, the pulsed transient hot-wire technique overestimates the thermal conductivity by as much as 8% when there is only 5 s delay between pulses.

Microhot Strip Setup

Our experimental observation in the previous section motivates us to develop a new setup (Fig. 3) consisting of a microhot strip and a microchamber with a small thermal time constant. Such a setup allows us to perform accurate measurements without the need for a prolonged thermal equilibration step.

A thin metal film heater of width 20 μm, length 1 mm, and thickness 200 nm is fabricated on a glass slide using standard microfabrication techniques. A block made of polydimethylsiloxane (PDMS) is then bonded to the glass slide to form a sealed cylindrical chamber. The chamber can hold approximately 120 μl of a sample liquid. The device is immersed in a temperature-

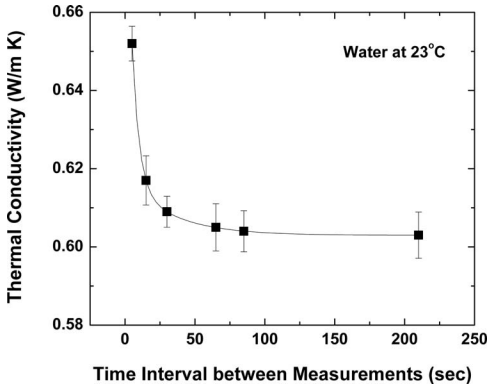

Fig. 2 The thermal conductivity of water measured using the macroscale hot-wire setup as a function of time interval between successive heating pulses

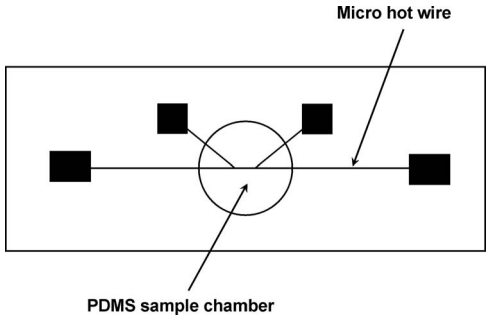

Fig. 3 Schematic of the microhot-wire device

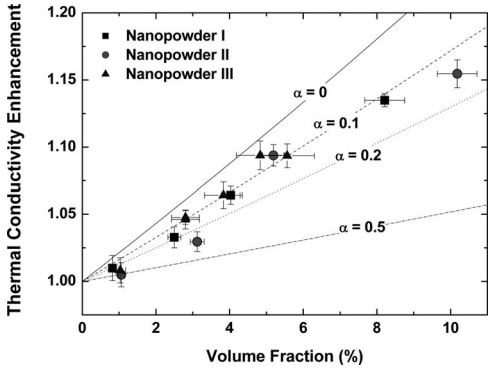

Fig. 4 The ratio between the thermal conductivity of the nanofluids and that of pure water at 23°C. The lines are the predictions of the effective medium model.

controlled water bath during the thermal conductivity measurements. The temperature stability of the water bath is 0.01°C.

During each measurement, a heating pulse of duration approximately 1 s is applied to the microstrip and the resulting temperature rise is measured using a precision voltmeter with a time resolution of 1 ms. We again use numerical simulations to analyze data from our microhot strip and extract the thermal conductivity of the liquid sample. The thermal conductivity of the glass slide is measured using the microstrip in the absence of a liquid sample, which agrees with the value obtained separately using the three-omega technique. The setup is further validated by comparing our data to literature values for water from room temperature to 70°C.

We note that our data analysis assumes that the continuum heat diffusion model is valid. In analyzing the temperature versus time data obtained for both pure water samples and our nanofluid samples, we do not observe any anomalous behavior. We alert the reader, however, that previous theoretical studies [17] suggested the possibility of a transient lag effect due to solid-fluid interactions. Further studies are necessary to examine the potential time dependence of the effective thermal conductivity of nanofluids at much shorter time scales.

Nanofluid Sample Preparation

Nanofluids used in the present study are prepared by dispersing commercially available Al_2O_3 nanopowders in water. Three nominally spherical Al_2O_3 nanoparticles with different specific surface areas (SSAs) are used. Details of the nanoparticles are provided in Table 1.

Each type of nanoparticles is mixed into filtered de-ionized water using an ultrasonic agitator to produce nanofluids of nominal particle volume concentrations up to 10%. We measure both the volume and weight of each nanofluid using a graduated cylinder of resolution 0.1 ml and an analytic balance, respectively, to independently determine the particle volume and mass concentrations. The effective particle densities determined after 1 h of sonication are 3.7×10^3 kg/m^3, 3.6×10^3 kg/m^3, and 3.5×10^3 kg/m^3 for Nanopowders I, II, and III, respectively. These densities are consistent with the values reported by the manufacturers to within 10%, suggesting that our nanofluid samples do not contain agglomerates with significant amount of trapped air.

Nanofluid Thermal Conductivity Data

Figure 4 shows the ratio between the thermal conductivity of the nanofluids and that of pure water at 23°C as a function of the *measured* volume concentration. The thermal conductivity increases approximately linearly with particle volume concentration. The enhancement observed is similar for all three types of nanofluids.

We used the conventional effective medium model as presented by Nan et al. [18] to analyze the thermal conductivity data:

$$\frac{k}{k_m}=\frac{1+2\alpha+2k_m/k_p+2f[1-\alpha-k_m/k_p]}{1+2\alpha+2k_m/k_p-f[1-\alpha-k_m/k_p]} \quad (1)$$

Here, k, k_p, and k_m are the thermal conductivity of the nanofluid, nanoparticles, and water, respectively. The parameter $\alpha=2R_{bd}k_m/d$ reflects the impact of the thermal boundary resistance R_{bd} between nanoparticles of diameter d and the base liquid.

The thermal conductivity of aluminum oxide nanoparticles can be very different from that of bulk aluminum oxide due to voids, defects, or the size effect on phonon transport. We use a semiphe-

Table 1 Aluminum oxide nanoparticles used to synthesize three types of nanofluids in the present study. The information was supplied by the manufacturers.

Nanofluid sample	Nanopowder I	Nanopowder II	Nanopowder III
Manufacturer	Nanophase Technologies Corporation	Nanotechnologies Inc.	Shandong Zhongshun Sci & Tech Development Co., Ltd
Nanoparticle designation	NanoTek® Aluminum Oxide (Product 0115)	Aluminum oxide (Alumina) nanopowder	Aluminum oxide (α-Al_2O_3)
Purity	99.95%,	100%	99.9%
Average particle size (APS)*	45 nm	30 nm	20 nm
Specific surface area (SSA)	35 m^2/g (BET)	50 m^2/g	65 m^2/g
Appearance	White powder	White powder	White powder
Nominal density	3.6 g/cm^3	3.9 g/cm^3	3.5–3.9 g/cm^3
Morphology	Spherical	Spherical	Spherical
Crystal phase	Delta: Gamma=70:30	Gamma	Alpha
Manufacturing technique	Physical vapor synthesis (PVS)	Pulsed plasma process	N/A

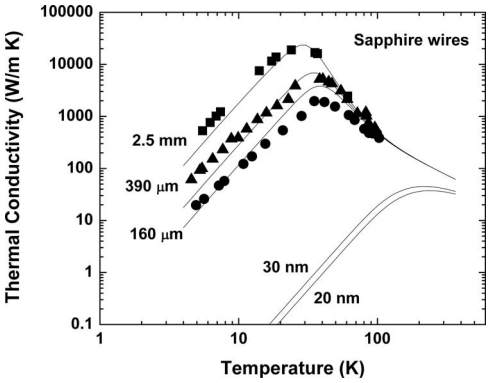

Fig. 5 Callaway's model prediction for the thermal conductivity of sapphire wires and alumina nanostructures

nomenological model of Callaway for the phonon thermal conductivity [19] to estimate the size effect on the thermal conductivity of nanoparticles.

We first obtain model parameters for sapphire, which is modeled as an isotropic Debye solid, using the previously reported thermal conductivity of sapphire fibers [20]. The model is then used to predict the thermal conductivity of nanostructures of dimensions 20 nm and 30 nm, as illustrated in Fig. 5. The predicted thermal conductivities are approximately 36 W/m K and 41 W/m K at room temperature, which are comparable to that of bulk sintered aluminum oxide samples. Since some of the nanoparticles used in the present study are γ or δ phase Al_2O_3 and may contain defects, the thermal conductivity of the nanoparticles can be smaller even in the absence of a strong size effect. The thermal conductivity of plasma sprayed γ-Al_2O_3 films, for example, was reported to be as low as 5 W/m K. A lower bound to the thermal conductivity of alumina nanoparticles may be estimated from the thermal conductivity of highly disordered AlO_x films ($\sim$1.6 W/m K) with density comparable to that of γ-Al_2O_3.

Included in Fig. 4 are prediction from the effective medium model using a particle thermal conductivity k_p of 5 W/m K and four different values of the boundary resistance parameter α (0, 0.1, 0.2, and 0.5). Our data from all three types of nanofluids can be explained with parameter α=0.1, which is equivalent to having R_{bd} of approximately 1×10^{-8} m^2 K/W for particles with d =130 nm (see next section). This thermal boundary resistance is comparable to the resistance determined for Au-water interface [21].

Characterization of Nanoparticle Size

The size of nanoparticles is often determined from the SSA or using transmission electron microscopy (TEM) images. These measurements, however, can be performed only for dry nanoparticles and may not represent the true size of particles or their aggregates as they exist in nanofluids.

We perform dynamic light scattering (DLS) measurements using a commercial instrument (N4 Plus, Beckman Coulter, Inc.) to estimate the size of Al_2O_3 nanoparticles as suspended in their carrier liquids. The DLS technique monitors the Brownian motion of particles dispersed in a liquid by illuminating the sample with a laser beam and detecting the scattered light. If the particles in a solution are homogeneous, the autocorrelation function of the scattered-light intensity is a single decaying exponential:

$$G(\tau) \propto \exp(-2\tau/\Gamma)$$

The inverse of the time constant Γ is equal to DK^2, where D is the Brownian diffusivity of the particles and K is defined as

Table 2 DLS measurements of aqueous solutions containing standard latex beads

Known bead size	Size determined by DLS (nm)	Volume fraction determined by DLS
50 nm	42.4 ± 8.1	100%
Mixture of 50 nm/200 nm	44.2 ± 2.9	80.1%
	177.9 ± 19.9	19.9%

$$K = \frac{4\pi n}{\lambda}\sin\left(\frac{\theta}{2}\right)$$

Here, n is the refractive index of the liquid, λ is the wavelength of the laser, and θ is the angle of scattering intensity measurement. By fitting the measured autocorrelation function with the model, one can determine the Brownian diffusivity D of the particles, which is in turn a function of the particle size:

$$D = \frac{k_B T}{3\pi\eta d}$$

Here, k_B is the Boltzmann constant, T is the temperature, and η is the liquid viscosity.

Since the particle concentrations of our nanofluids are too high for light scattering measurements, we dilute our samples by about 1000-folds right before each measurement. All measurements are conducted at the ambient temperature 25°C by letting each sample reach thermal equilibrium.

To assess the accuracy of our particle size measurements, we prepare two reference solutions containing latex beads of known diameters: one solution with 50 nm beads and the other with a mixture (80:20) of 50 nm and 200 nm beads. The data shown in Table 2 are within 10–20% of the known diameters for both solutions, demonstrating that the DLS technique can provide reasonably accurate measurements of the size of nanoparticles.

Sonication Time Dependence

A previous work [22] reported that the thermal conductivity of nanofluids of Fe showed strong dependence on sonication time. This observation has been rationalized using the hypothesis that better particle dispersion and hence enhanced particle Brownian motion lead to increase in the nanofluid thermal conductivity. To examine this hypothesis further, we determine the thermal conductivity and average particle size of our aluminum oxide nanofluids as a function of sonication time.

Cleanroom-grade de-ionized water is filtered right before nanofluid preparation using a 0.2 μm pore filter. A dynamic scattering measurement on the filtered water does not detect any foreign particles. We then prepare two stock solutions of nanofluids at 5% volume concentration by suspending precise amounts of Nanopowder II in the water. In one of the stock solutions, 0.5 vol. % of Tween-80 surfactant is added to further improve particle dispersion.

Both samples are vigorously stirred using an ultrasonic agitator (UP100H, Dr. Hielsher, GmbH) for up to 12 h. A small amount of sample is removed from the stock solutions every 3 h to measure the thermal conductivity and average particle size. The pH stays nearly constant at 5.3 for both stock solutions, which is comparable to the value reported in an earlier study [5]. The thermal conductivity is measured at 25°C and then 50°C using the microhot strip setup described earlier.

Figures 6 and 7 show our experimental results. The measured particle size decreases slightly after 3 h of sonication but remains constant thereafter to within our experimental uncertainty. The measured values are considerably larger than the nominal particle

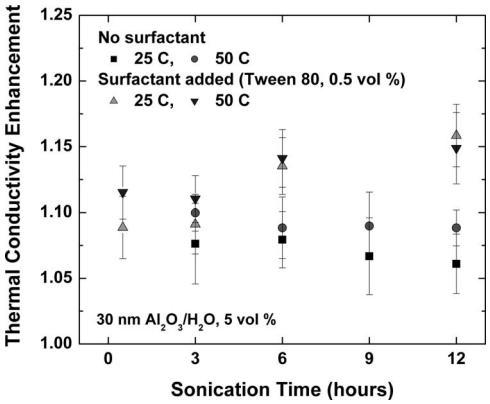

Fig. 6 Sonication time and temperature dependence of the thermal conductivity of the nanofluids prepared with Nanopowder II

size reported by the manufacturer but are comparable to the value (~120 nm) reported by Waite et al. [23] for solutions of γ-alumina nanopowders immediately after sample preparation. These alumina powders had a nominal average diameter of 13 nm in the dry state and were manufactured by the flame hydrolysis of $AlCl_3$. Our dynamic scattering measurements of commercially available colloids of aluminum oxide nanoparticles (nominal particle diameter <20 nm, Sigma Aldrich Inc.) also yield a comparable particle/aggregate size.

For the solution prepared without any surfactant, the thermal conductivity enhancement is less than 10%, both at 25°C and 50°C. No significant change in thermal conductivity is observed even after 12 h of sonication. The thermal conductivity of the nanofluid prepared with the surfactant does increase appreciably after 6 h of sonication. One might be tempted to attribute this to improved particle dispersion. DLS measurements, however, show that no significant change in particle size can be observed even after 12 h of sonication.

This observed increase in thermal conductivity after prolonged sonication may be an experimental artifact. Continuous bombardment of nanoparticles on the sonicator tip generates an appreciable amount of metal debris. The problem is more severe for the second nanofluid sample because we used a higher sonication power. Indeed, the density of the second nanofluid stock solution is found to increase from 1.123 g/ml to 1.155 g/ml, which is equivalent to almost 25% increase in particle volume concentration.

Both the experimental data on particle aggregation by Waite et al. [23] and our experimental data on the thermal conductivity

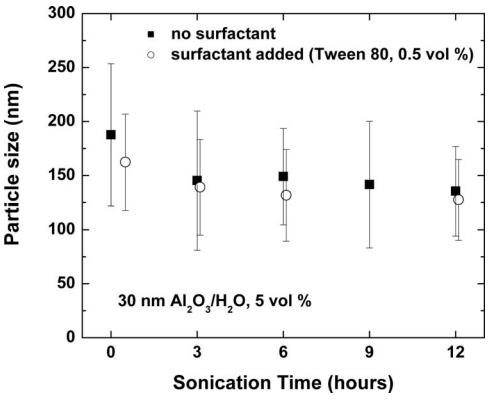

Fig. 7 Sonication time dependence of the particle size in the nanofluids prepared using Nanopowder II

disagree with some of previous data [5,8,24]. Chon et al. [8] observed that the thermal conductivity of aluminum oxide nanofluids increases rapidly with decreasing nominal particle size and increasing temperature. Prasher et al. [5] also reported significant temperature dependence and predicted a peak in the thermal conductivity enhancement for nanofluids with alumina particles of diameter below 20 nm. Our data, however, are consistent with other recent studies, most of them employing optical techniques [11–13].

Since we use an independent electrical measurement technique in our study, any discrepancy with the earlier studies may not be due to experimental errors but perhaps due to subtle but important differences in nanopowders or nanofluid preparation procedures that result in drastic difference in the size or shape of suspended particles/aggregates.

Summary and Conclusion

We perform a systematic experimental study of heat conduction in aqueous suspensions of aluminum oxide nanoparticles at volume concentrations up to 10%. We develop a microhot strip setup to reduce experimental errors resulting from spatial or temporal temperature inhomogeneity within a liquid sample. The volume concentration dependence of the thermal conductivity does not show any anomalous behavior and can be explained using the effective medium model with a physically reasonable set of parameters.

The average particle size and the thermal conductivity are measured as a function of sample sonication time. The size of particles/aggregates in our nanofluid samples is much greater than the nominal particle size reported by the manufacturers and does not change appreciably with sonication time up to 12 h.

Our data do not reveal any anomalous enhancement in the thermal conductivity or strong temperature dependence reported in other previous studies. The discrepancy may reflect subtle differences in nanopowders or nanofluid preparation procedures that result in drastic difference in the size or shape of suspended particles/aggregates. Our work highlights the need for sample exchanges and cross-validation experiments to advance science and engineering of enhanced heat transfer in nanofluids.

Acknowledgment

We would like to thank Shandong Zhongshun Sci & Tech Development Co., Ltd. for providing us with one of the nanopowder samples. Our experimental work was also made possible in part by work sponsored by the National Science Foundation through Grant No. CTS-0422789.

Nomenclature

d = nanoparticle diameter, m
D = Brownian diffusivity, m^2/s
k = thermal conductivity of nanofluids, W/m K
k_B = Boltzmann constant, J/K
k_p = thermal conductivity of nanoparticles, W/m K
k_m = thermal conductivity of a base liquid, W/m K
n = refractive index
R_{bd} = thermal boundary resistance, m^2 K/W
T = temperature, K
α = thermal boundary resistance parameter ($=2R_{bd}k_m/d$)
Γ = time constant for light scattering measurements, s
η = liquid viscosity, Pa s
λ = wavelength of the laser, m
θ = angle for light scattering measurements

References

[1] Eastman, J. A., Choi, S. U. S., Li, S., Yu, W., and Thompson, L. J., 2001, "Anomalously Increased Effective Thermal Conductivities of Ethylene Glycol-

Based Nanofluids Containing Copper Nanoparticles," Appl. Phys. Lett., **78**(6), pp. 718–720.
[2] Eastman, J. A., Phillpot, S. R., Choi, S. U. S., and Keblinski, P., 2004, "Thermal Transport in Nanofluids," Annu. Rev. Mater. Res., **34**, pp. 219–246.
[3] Keblinski, P., Eastman, J. A., and Cahill, D. G., 2005, "Nanofluids for Thermal Transport," Mater. Today, **8**(36), pp. 36–44.
[4] Wang, B.-X., Zhou, L.-P., and Peng, X.-F., 2003, "A Fractal Model for Predicting the Effective Thermal Conductivity of Liquid With Suspension of Nanoparticles," Int. J. Heat Mass Transfer, **46**, pp. 2665–2672.
[5] Prasher, R., Phelan, P. E., and Bhattacharya, P., 2006, "Effect of Aggregation Kinetics on the Thermal Conductivity of Nanoscale Colloidal Solutions (Nanofluid)," Nano Lett., **6**(7), pp. 1529–1534.
[6] Prasher, R., Evans, W., Meakin, P., Fish, J., Phelan, P., and Keblinski, P., 2006, "Effect of Aggregation on Thermal Conduction in Colloidal Nanofluids," Appl. Phys. Lett., **89**, 143119.
[7] Prasher, R., Bhattacharya, P., and Phelan, P. E., 2005, "Thermal Conductivity of Nanoscale Colloidal Solutions (Nanofluids)," Phys. Rev. Lett., **94**, 025901.
[8] Chon, C. H., Kihm, K. D., Lee, S. P., and Choi, S. U. S., 2005, "Empirical Correlation Finding the Role of Temperature and Particle Size for Nanofluid (Al_2O_3) Thermal Conductivity Enhancement," Appl. Phys. Lett., **87**, 153107.
[9] Krishnamurthy, S., Bhattacharya, P., Phelan, P. E., and Prasher, R. S., 2006, "Enhanced Mass Transport in Nanofluids," Nano Lett., **6**(3), pp. 419–423.
[10] Li, C. H., and Peterson, G. P., 2006, "Experimental Investigation of Temperature and Volume Fraction Variations on the Effective Thermal Conductivity of Nanoparticle Suspensions (Nanofluids)," J. Appl. Phys., **99**, 084314.
[11] Putnam, S. A., Cahill, D. G., and Braun, P. V., Ge, Z., and Shimmin, R. G., 2006, "Thermal Conductivity of Nanoparticle Suspensions," J. Appl. Phys., **99**(8), 084308.
[12] Rusconi, R., Rodari, E., and Piazza, R., 2006, "Optical Measurements of the Thermal Properties of Nanofluids," Appl. Phys. Lett., **89**, 261916.
[13] Venerus, D. C., Kabadi, M. S., Lee, S., and Perez-Luna, V., 2006, "Study of Thermal Transport in Nanoparticle Suspension Using Forced Rayleigh Scattering," J. Appl. Phys., **100**, 094310.
[14] Patel, H. E., Das, S. K., Sundararajan, T., Nair, A. S., George, B., and Pradeep, T., 2003, "Thermal Conductivities of Naked and Monolayer Protected Metal Nanoparticle Based Nanofluids: Manifestation of Anomalous Enhancement and Chemical Effects," Appl. Phys. Lett., **83**(14), 2931–2933.
[15] Gustafsson, S. E., Karawacki, E., and Chohan, M. A., 1986, "Thermal Transport Studies of Electrically Conducting Materials Using the Transient Hot-Strip Technique," J. Phys. D, **19**(5), pp. 727–735.
[16] Incropera, R. P., DeWitt, D. P., Bergman, T. L., and Lavine, A. S., 2007, *Introduction to Heat Transfer*, 5th ed., Wiley, New York.
[17] Vadasz, P., 2006, "Heat Conduction in Nanofluid Suspensions," ASME J. Heat Transfer, **128**(5), pp. 465–477.
[18] Nan, C.-W., Birringer, R., Clarke, D. R., and Gleiter, H., 1997, "Effective Thermal Conductivity of Particulate Composites With Interfacial Thermal Resistance," J. Appl. Phys., **81**(10), pp. 6692–6699.
[19] Hung, M.-T., Choi, O., Guo, Z., Hahn, H. T., and Ju, Y. S., 2006, "Heat Transport in Graphite Nanoplatelet (GNP)-Reinforced Polymeric Nanocomposites and Aluminum Oxide Nanofluids," Proceedings of the 9th AIAA/ASME Joint Thermophysics and Heat Transfer Conference, San Francisco, CA, Jun. 5–8, Paper No. AIAA 2006-3112.
[20] Tomaru, T., Suzuki, T., Uchiyama, T., Yamamoto, A., Shintomi, T., Taylor, C. T., Yamamoto, K., Miyoki, S., Ohashi, M., and Kuroda, K., 2002, "Maximum Heat Transfer Along a Sapphire Suspension Fiber for a Cryogenic Interferometric Gravitational Wave Detector," Phys. Lett. A, **301**, pp. 215–219.
[21] Ju, Y. S., 2005, "Impact of Nonequilibrium Between Electrons and Phonons on Heat Transfer in Metallic Nanoparticles Suspended in Dielectric Media," ASME J. Heat Transfer, **127**(12), pp. 1400–1402.
[22] Hong, T.-K., Yang, H.-S., and Choi, C. J., 2005, "Study of the Enhanced Thermal Conductivity of Fe Nanofluids," J. Appl. Phys., **97**, 064311.
[23] Waite, T. D., Cleaver, J. K., and Beattie, J. K., 2001, "Aggregation Kinetics and Fractal Structure of γ-Alumina Assemblages," J. Clim., **241**, pp. 333–339.
[24] Das, S. K., Putra, N., Thiesen, P., and Roetzel, W., 2003, "Temperature Dependence of Thermal Conductivity Enhancement for Nanofluids," ASME J. Heat Transfer, **125**(4), pp. 567–574.

The Solid-State Neck Growth Mechanisms in Low Energy Laser Sintering of Gold Nanoparticles: A Molecular Dynamics Simulation Study

Heng Pan

Seung H. Ko

Costas P. Grigoropoulos[1]
e-mail: cgrigoro@me.berkeley.edu

Laser Thermal Laboratory,
Department of Mechanical Engineering,
University of California-Berkeley,
Berkeley, CA 94720-1740

Molecular dynamics (MD) simulations were employed to investigate the mechanism and kinetics of the solid-state sintering of two crystalline gold nanoparticles (4.4–10.0 nm) induced by low energy laser heating. At low temperature (300 K), sintering can occur between two bare nanoparticles by elastic and plastic deformation driven by strong local potential gradients. This initial neck growth occurs very fast (<150 ps), and is therefore essentially insensitive to laser irradiation. This paper focuses on the subsequent longer time scale intermediate neck growth process induced by laser heating. The classical diffusion based neck growth model is modified to predict the time resolved neck growth during continuous heating with the diffusion coefficients and surface tension extracted from MD simulation. The diffusion model underestimates the neck growth rate for smaller particles (5.4 nm) while satisfactory agreement is obtained for larger particles (10 nm). The deviation is due to the ultrafine size effect for particles below 10 nm. Various possible mechanisms were identified and discussed. [DOI: 10.1115/1.2943303]

Keywords: nanoparticles, sintering, laser, molecular dynamics simulation, neck growth

1 Introduction

Recent interest in fabricating flexible electronics has spurred extensive research related to delivering and defining both active and passive materials in a cost effective and precise manner. The printing of nanoparticles followed by low temperature thermal treatment has shown substantial promise in ultralow-cost electronic fabrication [1]. Employing laser radiation to selectively sinter nanoparticles and define micron, even submicron features has demonstrated advantages in terms of meeting performance and cost requirements [2,3]. Previous research efforts on laser patterning of nanoparticles in microfabrication as well as envisioned future research in nanoparticle based nanofabrication have sparked great interest in understanding the associated fundamental phenomena, such as nanoscale phase change, sintering, or coalescence transformation induced by laser irradiation, as needed for realizing low resistance Ohmic nanocontacts [4].

In this study, molecular dynamics (MD) is employed to study the fundamental physics involved in nanoparticle sintering by continuous laser heating. There are a variety of sintering or coalescence models, such as the conventional neck growth model, either based on diffusion [5–7] or viscous flow [8] and the K-F type model [9,10]. In the conventional model, the detailed necking profile is tracked and diffusion mechanisms need to be identified. In the K-F type model, which is widely used in the aerosol research community, a simple linear relation between excess surface area and neck growth rate is used [10] instead of tracking the detailed necking profile. The K-F model can be applied to viscous flow or solid diffusion based process requiring no identification of the diffusion mechanisms is needed. Most of these models are applied to isothermal sintering process with a few exceptions [11], where temperature variation due to the heat exchange with the surrounding environment is considered.

Investigations have focused on the applicability of the macroscopic sintering model to the nanoscale phenomenon. New mechanisms emerge in nanoscale sintering, such as elastic/plastic deformation and dislocation [12,13]. Existing facets could slow down the curvature driven diffusion [14]. It is also argued that the linear relation for diffusion is no longer valid for nanoscale sintering since the thermodynamic driving force stemming from chemical potential gradients is very large for particles below 100 nm [15]. Moreover, in nanoscale sintering, interatomic attraction becomes very important inducing accelerated necking growth. This "force-driven" diffusion needs to be distinguished from standard "random walk" ones and treated differently [13]. There have been efforts to model the nanoscale phenomenon by modifying the bulk physical properties to account for ultrafine size effects: Xing [16] improved the coalescence time prediction by using depressed melting temperature and Arcidiacono [17] applied a similar approach to obtain reasonable predictions of the neck growth for ultrafine nanoparticles. Clearly, more work is needed to reach quantitative evaluation of the usefulness of the conventional neck growth mode that ignores all ultrafine size effects. It should be noted the physical parameters needed for the analytical model need to be extracted directly from MD simulation, whereas the confined size effects on the physical properties can be fully taken into account without using modifications of bulk properties, therefore avoiding respective errors.

In summary, this paper applied MD simulations to study the sintering of gold nanoparticles by continuous heating. A conventional neck growth model was modified and adopted for continuous heating. The physical properties were extracted from simulation directly. MD simulation was employed to cover a wide size

[1] http://www.me.berkeley.edu/ltl/ltl.html

Contributed by the Heat Transfer Division of ASME for publication in the JOURNAL OF HEAT TRANSFER. Manuscript received July 5, 2007; final manuscript received October 11, 2007; published online July 11, 2008. Review conducted by Cholik Chan.

range (4.4–10 nm) and longer simulation time (~10 ns), enabling the evaluation of the applicability of the conventional models over correspondingly wider size range.

2 Modeling Methods

2.1 Molecular Dynamics Simulation. To track the sintering process, an atomistic simulation approach using classical MD was employed. In this study, the glue potential for gold developed by Ref. [18] was adopted since it was found to yield an accurate description of bulk, defect, and surface properties of gold. In the glue model, the potential energy of a system of N atoms consists of a sum of pair potentials and a many-body glue energy:

$$V = \frac{1}{2}\sum_{ij} \phi(r_{ij}) + \sum_{i} U(n_i) \tag{1}$$

where r_{ij} is the distance between two atoms, $\phi(r_{ij})$ is a standard two-body potential, and $U(n_i)$ is the energy associated with the coordination n_i of the atom i. The parameters are reconstructed empirically to reproduce the experimental values of gold over a wide range of thermodynamic conditions. The details of the model and related parameters are given in Ref. [18].

A parallel MD simulation program has been developed that can currently handle up to 150,000 atoms for the study of relatively long time scale events (~10 ns), such as sintering, at a reasonable computational time. Atom trajectories were determined by integrating the classical equations of motion using the velocity form of the VERLET algorithm with rescaling of atomic velocities to achieve temperature control. Time steps of 3.0 fs were typically used and the atom neighbor list was updated every time step. Single gold nanoparticles of various sizes (2633, 5053, and 31077 atoms) were prepared at different temperatures. The target temperature was obtained by rescaling every 200 time steps. The rescaling was applied for 10^4 time steps, after which, up to 10^5 time steps were allowed to achieve full equilibrium before property sampling was conducted.

To simulate the sintering process, two identical particles were first brought into contact at a center-to-center distance of $2R$ +0.5 nm at ~300 K. The initial neck growth was allowed to complete without laser irradiation. After the initial neck growth, the particle pairs were subjected to continuous laser heating. The heating rate is in the range of 0.89×10^{11}–2.20×10^{11} K/s simulating the heating by a continuous laser with laser intensity around 10^{10} W/m^2. No heat loss to the environment was considered in the present study. To mimic the laser heating, the kinetic energy of the system was increased by a fixed amount at each step by rescaling the velocities, so the total energy increases linearly in time.

The structural change was monitored during sintering via calculating bond order parameters (BOPs). Four BOPs were used together to identify the structure accurately. The values of these BOPs for fcc, hcp, and amorphous structures and the detailed description of the BOP can be found in Ref. [19].

2.2 Analytical Neck Growth Model. The model is essentially the one presented by Johnson [6] modified for continuous heating. The geometrical configuration and symbols of the sintering particles that follow Johnson [6] are shown in Fig. 1. Each particle is represented by a sphere with radius a. ρ is the radius of the neck surface, α is a measure of the grain-boundary groove angle, c is the distance of the center of the particle to the symmetry plane, δ is the extent of the overlapping of the two spheres, and A_V is the surface area of the neck. The value of c gives an indirect measure with respect to the mechanisms at work. Its value will only decrease from its initial value if material is moved between the particles by grain-boundary or volume diffusion. It is also assumed that a is unchanged during the sintering. This geometry is valid only until $x=a$. At that value, the system assumes a "pill" shape. This is sufficient for modeling the necking growth, but cannot follow the system all the way to complete coalescence.

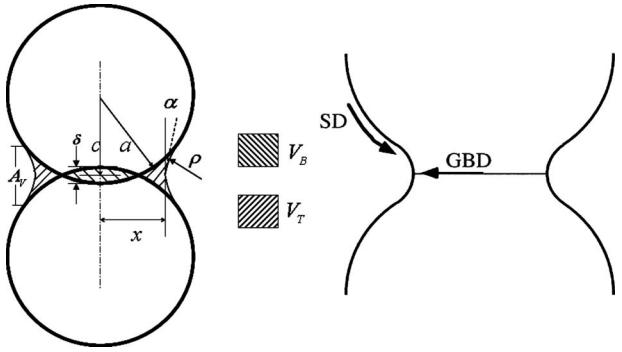

Fig. 1 Sintering geometry and atom movement pathways for different sintering mechanisms

With a few additional geometrical parameters defined as follows, $y=a-c/a$, $X=x/a$, $R=\rho/a$, and $\theta=\sin^{-1}(a-ya+\rho\sin\alpha/a+\rho)$, the exact equations for the geometrical parameters can be written as [6]

$$\rho = \frac{a(y^2-2y+X^2)}{2(1-(1-y)\sin\alpha - X\cos\alpha)} \tag{2}$$

$$A_V = 4\pi\rho[(\theta-\alpha)(a+\rho)\cos\theta - \rho(\sin\theta-\sin\alpha)] \tag{3}$$

$$X = (1+R)\cos\theta - R\cos\alpha \tag{4}$$

The total volume of the material that has moved into the neck, defined as V_T, will be the sum of the volume of overlap of the original sphere V_B and the volume of material arriving from the sphere surface V_S. The schematic of V_B and V_T are shown in Fig. 1. Thus,

$$V_T = V_B + V_S \tag{5}$$

By geometry reasoning,

$$V_T = 2\pi a^3R^2(1+R)[2(\sin\theta-\sin\alpha) - \cos\theta(\sin\theta\cos\theta+\theta - \sin\alpha\cos\alpha-\alpha) - \sin\theta(\sin^2\theta-\sin^2\alpha\alpha)]$$

$$V_B = \left(\frac{2\pi a^3y^2}{3}\right)(3-y) \tag{6}$$

In order to evaluate V_B and V_S, the mechanisms of the neck growth needs to be identified. It is known for nanosize particle sintering that only grain-boundary and surface diffusion mechanisms are in effects [20]. Therefore, let J_{GBD} and J_{SD} represent the material flux, then

$$\frac{dV_S}{dt} = \Omega J_{\mathrm{SD}} \tag{7}$$

$$\frac{dV_B}{dt} = \Omega J_{\mathrm{GBD}} \tag{8}$$

where Ω is the molar volume. The individual flux can be calculated from the equations derived by Johnson [6]. By expressing the flux in terms of stress gradients rather than concentration gradients and assuming that the stress distribution is a function of radial position along the grain boundary, the grain-boundary flux can be written by

$$J_{\mathrm{GBD}} = \frac{8\pi\gamma bD_B(x+\rho\cos\alpha)}{kTx\rho} \tag{9}$$

The surface diffusion flux can be written as a function of concentration using Fick's equation. The variation of the concentration of vacancies due to the surface curvature can be expressed in terms

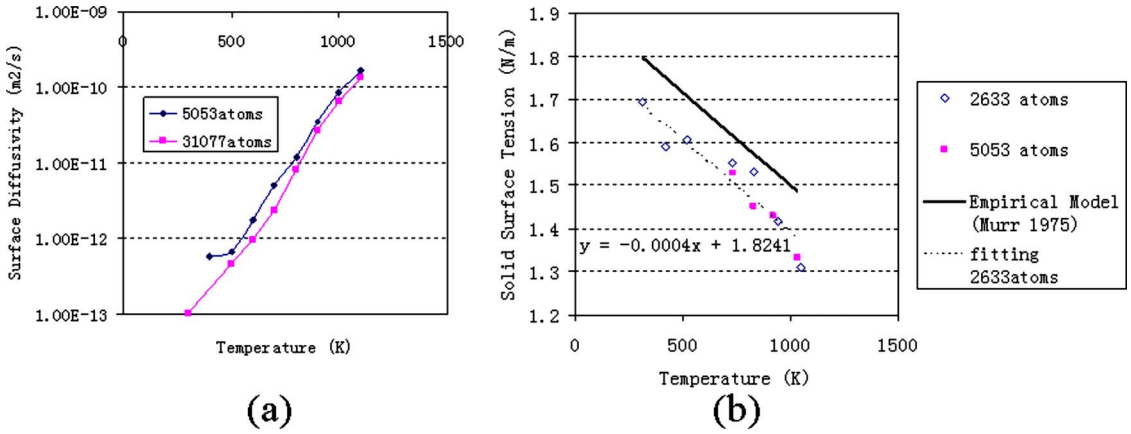

Fig. 2 Extracted diffusion coefficients (*a*) and surface tension (*b*) from MD simulation

of geometrical parameters. Therefore, the surface diffusion flux can be written by

$$J_{\mathrm{SD}} = \frac{2\pi\gamma\Omega^{1/3}D_S(X + 2XR - R\cos\alpha)}{akTR^2} \tag{10}$$

where D_B and D_S are the diffusion coefficients for grain boundary and surface, respectively, b is the thickness of the region of enhanced diffusion at the grain boundary, k is the Boltzmann constant, T is the temperature, and γ is the surface tension.

The temperature of the particle subjected to laser irradiation can be calculated by assuming uniform temperature inside the particle and neglecting the temperature increase due to the reduction of surface area:

$$\frac{dT}{dt} = \frac{IA_{\mathrm{cross}}\kappa}{CV_P} \tag{11}$$

where I is the laser intensity, A_{cross} is the cross section area of the particle, C is the specific heat, V_P is the particle volume, and κ is the absorption efficiency, which is determined from predetermined heating rate.

The implementation of the above model is described as the following. Equation (11) is used to calculate the temperature at any instant of time. The rate equations for the neck volume (Eqs. (7) and (8)) were integrated numerically with respect to time to update the neck volume based on the flux equations ((9) and (10)). At each time step, the simultaneous nonlinear equations (Eqs. (2)–(6)) governing the geometry were solved using a Powell–Hydrid algorithm in MATLAB to obtain the new necking profile. An initial temperature and neck volume were specified to begin the computation.

3 Results and Discussion

3.1 Extracting Physical Properties From MD Simulations. The self-diffusion coefficient D is calculated from the slope of the atomic mean-square displacement (MSD):

$$\mathrm{MSD} = \frac{1}{N}\sum_{i=1}^{N}[r_i(t) - r_i(0)]^2 \tag{12}$$

$$D = \frac{1}{6}\frac{d}{dt}(\mathrm{MSD}) \tag{13}$$

where N is the number of atoms sampled and r is the position of each atom. For the present study, D is evaluated for surface atoms. The extracted surface diffusivities for different particle sizes are plotted in Fig. 2(*a*). It is interesting to note that smaller particles have higher diffusivities, qualitatively in agreement with empirical consideration of size effects on diffusivity [16]. For the present study, grain-boundary diffusivity D_B is estimated to be same as of surface diffusivity D_S [21].

The surface tension is computed using the mechanical approach reported by Thompson [22].

$$\gamma = \left(-\frac{(p_L - p_G)^2}{8}\int_0^\infty r^3\frac{dP_N(r)}{dr}dr\right)^{1/3} \tag{14}$$

where p_G is the gas pressure outside the particle, which is neglected, p_L is the pressure inside the particle, and P_N is the normal component of the pressure to the spherical surface. It is worthy mentioning that the term $(r/2)(dP_N(r)/dr)$ in this equation stems from the mechanical arguments [22] that relate surface tension γ to $P_N(r) - P_T(r)$, where the tangential component of the pressure P_T can be related to P_N by $P_T(r) = P_N(r) + (r/2)(dP_N(r)/dr)$. The p_L and P_N were obtained following the procedures described in Ref. [22]. Since the pressure outside the particle is neglected, then the upper bound in the integration in Eq. (14) is actually a particle radius. It should be pointed out that Eq. (14) is valid for gas-liquid interface. This liquid droplet model is applied to solid nanoparticles in this paper as an approximation. The validity of this approximation is based on a recent publication [23] where the calculated surface stresses for silver nanoparticles (similar size as the particles considered in this paper) are close to the theoretical values of surface energies. The calculated surface tension is plotted in Fig. 2(*b*) along with an empirical model from Murr [24]. A reasonable agreement was found except that the extracted values are lower than the empirical bulk data, which might be due to the small size effects [22].

3.2 MD Results. Owing to their ultrafine size, sintering can occur between the two bare nanoparticles at low temperature without laser irradiation. The qualitative features of the sintering of two nanoparticles (2633 atoms, 2.2 nm radius) at 300 K are clearly seen in Fig. 3(*a*), where the neck width is plotted against time. The sintering consists of two phases, i.e., a very fast neck growth within 10 ps wherein the neck grows to about 1.2 nm, followed by a slower process that increases the neck radius to about 1.5 nm within 150 ps. It is clear that the first fast neck growth is due to the elastic deformation. According to Zhu [12], the upper limit of the contact radius due to the elastic deformation of two 2.4 nm Cu nanoparticles is 0.84 nm. This value is on the same order of the neck width observed after the first neck growth. The slow growth after the elastic deformation is due to the movement of the atoms near the void that is driven very strongly toward the void by very high atomic potential gradients where two surfaces of rapid curvature form a sharp cusp on contact [13].

The resulting dumb-bell shape particle pair is then subjected to laser irradiation. The evolution of the radius of gyration along the

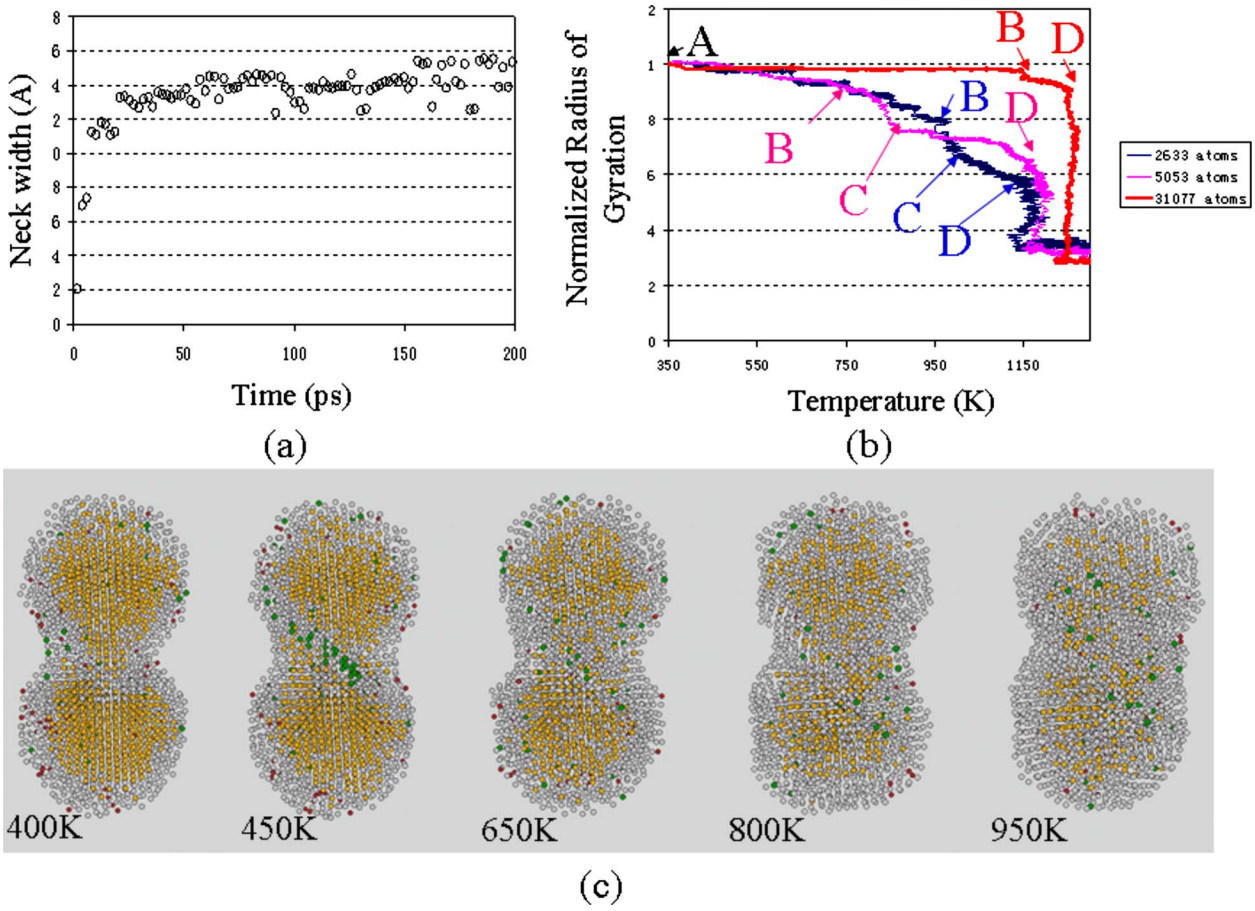

Fig. 3 Initial neck growth with respect to time (*a*), the temperature dependence of the radius of gyration. The transitions points are labeled as *B*, *C*, *D* for each size particle. The blue, purple, and red labels and curves represent 2633-, 5053-, and 3,1077-atom particles, respectively (*b*). and configurations of the 2633-atom particle pair at different temperature, with atoms colored according to their local structure (*c*).

interparticle axis of the particle pair is plotted against temperature for different particle sizes in Fig. 3(*b*). For each size particle, there are two obvious drops of the gyration radius, labeled as *B* and *D*. It is obvious that for both cases the turning point *D*, marking the full coalescence, is due to melting. For the 2633-atom particles, the evolution toward equilibrium shape is continuous at high temperature (after *B*) and more steplike at low temperature (before *B*), indicating that at high temperatures atoms continuously move to their final positions, whereas an additional discontinuous mechanism is operative at low temperatures. One possible mechanism is the presence of facets, which persist or rearrange during coalescence in a discontinuous manner [14]. Another more likely mechanism is due to the plastic deformation induced by a large number of small "sliding" events of atomic planes at the grain boundaries or dislocations within the grains [25]. To provide insight into the atom movements, a vector field showing the atom trajectory is shown in Fig. 4(*a*). Each vector connects the positions of an atom before and after the shape transition. The atom trajectory between *A* and *B* reveals that one particle is almost uniformly sliding in one direction and the other moves in another direction and that most of the sliding deformation occurs near the grain boundary. To better understand this sliding mechanism, crystalline structure of atoms was identified via determining the BOPs. Atoms in local fcc order are considered to be inside the crystalline grain and colored as yellow; atoms in local hcp order are classified as stacking faults and colored as green. All other atoms are considered as belonging to the grain boundaries or amorphous layers, colored as gray, shown in Fig. 3(*c*). It is seen that crystalline structure is formed in the necking region after the initial rapid neck growth at low temperature (400 K). At the beginning of the heating process, a dislocation at the necking region is developed indicated by a plane of stacking faults (hcp). During the heating, instead of increasing the hcp atoms, the grain-boundary (amorphous) atoms keep growing at the necking region suggesting that grain-boundary sliding could be responsible for most of the steplike transformations up to the turning point *B*.

For particles consisting of 5053 atoms, the quick drops at *B* and *D* can still be distinguished. However, unlike the case for 2633-atom particles, the steplike drop before *B* is absent. The reason could be that larger size particles can pile up dislocations in the interior, rendering the dislocation mechanism less important [13]. Meanwhile, with a lower fraction of atoms assigned to grain boundaries, the grain-boundary sliding becomes less possible [25]. Instead, the atom trajectory reveals that grain-boundary diffusion is the dominant mechanism at this point, as shown in Fig. 4(*b*), where atoms migrate along the boundary between the two particles. To study the mechanism of the observed drop at point *B*, the atom motion trajectory between *B* and *C* is also plotted in Fig. 4(*c*). It can be seen that a large portion of atoms move from the center region to the neck region. Contrary to what one might expect, the movement as observed through the atomic motion is not symmetric. Evidently, the neck grows by surface diffusion on the "top" of the particle, while interior atoms move down to fill in the neck at the "bottom," developing a flow pattern similar to the reported by Zachariah [26] in a simulation of coalescence of two 580-atom particles. It appears that coalescence takes place via both a surface and a grain-boundary mechanism. However, unlike

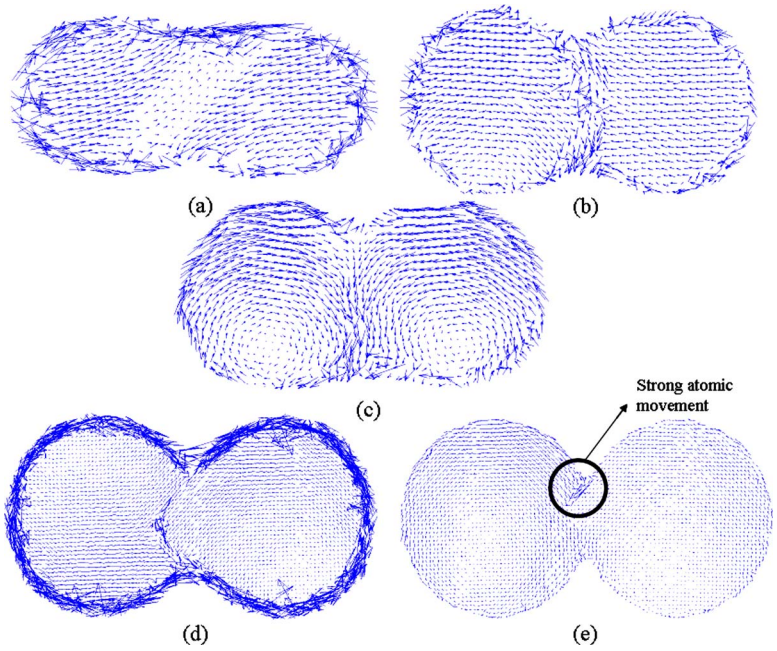

Fig. 4 Motion of atoms during the transition from *A* to *B* for 2633 atoms (*a*), from *A* to *B* (*b*), and *B* to *C* (*c*) for 5053-atom particle; figures subtitled (*d*) and (*e*) represent the motion of atoms for 31,077-atom particles during the transition between the two points indicated by arrows in Fig. 5(*c*) and in Fig. 5(*d*), respectively

the conventional grain-boundary diffusion where atoms migrate along a very thin grain-boundary layer [6], a large portion of atoms outside the grain-boundary layer also participate in the movement. The flow pattern resembles a viscous flow type motion. The deviation from normal diffusion could be attributed to the failure of linear diffusion kinetic law in the presence of the large driving force for these nanoscale dimensions [15]. This can also be attributed to the accumulation of amorphous layer. Calculations of the fraction of atomic structure composition reveals that at point *B*, around 78% of the atoms are amorphous. It is known that viscous flow is a very important mechanism for amorphous materials [27]. The accumulation of amorphous layer enabling rapid viscous flow driven by surface curvature to reduce surface energy could be another possible reason for the drop at point *B*. Wang [28] also reported a premelting transformation accompanying a structural change from fcc to hcp. It was suggested in his paper [28] that it is the building up of an amorphous layer during the heating process that drives the premelting transformation where planes of atoms slide against each other, thus transforming fcc atoms into hcp and vice versa. The transformation in the present study can be due to a similar mechanism, except that no structural change is found, which could also be attributed to the exceptionally high fraction of amorphous atoms. Lastly, it needs to be pointed out that for such small particles, surface energy tends to be very important, therefore resulting in a surface tension driven atomic migration that might be faster than normal force free diffusion migration. To quantitatively understand the difference in neck growth rate, MD results will be compared to analytical predicting in the next section. Starting from *C*, the evolution slows down due to the so-called "sphereication" process. This process is driven by curvature induced surface diffusion. This process continues until *D* where melting occurs and the cluster collapses into a sphere.

For larger particle (31077 atom), it can be noted that the transition points (*B* and *D*) approach each other [28]. As a consequence, the transition point *B* is less apparent and occurs very close to *D*. Correspondingly, the reduction of the radius of gyration is completed almost entirely by the melting transition for the large particles with the heating rate considered. As will be pointed out in Sec. 3.3, grain-boundary and surface diffusions are the major mechanisms for neck growth before reaching melting for this size of particle. To summarize, the major contributing solid-state neck growth mechanisms during laser heating for different particle sizes are listed in Table 1.

3.3 Comparison With Neck Growth Model. The time resolved neck growth during the heating predicted by the modified neck growth model for solid-state diffusion is plotted along with the MD simulation results for 5.4 nm (5053 atoms) and 10 nm (31,077 atoms) particles subjected to different heating rates. It can be found that the analytical modeling always underestimates the growth rate for 5.4 nm particles when the neck growth undergoes through the intermediate transition (point *B*, indicated in Figs. 3 and 5). The possible causes for this departure have been discussed in the previous section. On the contrary, satisfactory agreement can be found for 31,077-atom (10 nm) particles. In Fig. 5(*c*), the solid-state neck growth model reasonably predicts the neck radius, indicating that surface diffusion and grain-boundary diffusion are mostly responsible for the neck growth. Correspondingly, Fig. 4(*d*) showing the atomic trajectory between the two arrows, as described in Fig. 5(*c*), clearly indicates that very active atomic movement can only occur at the surface and along grain boundary in agreement with the analysis. The agreement in Fig. 5(*d*) is less

Table 1 Summarized major neck growth mechanisms during laser sintering for different particle sizes

Size	Major solid-state neck growth mechanisms during laser heating
2633 atoms	Grain-boundary slidings/dislocations; surface diffusion
5053 atoms	Grain-boundary diffusion; surface diffusion; viscous flow
31,077 atoms	Grain-boundary diffusion; surface diffusion

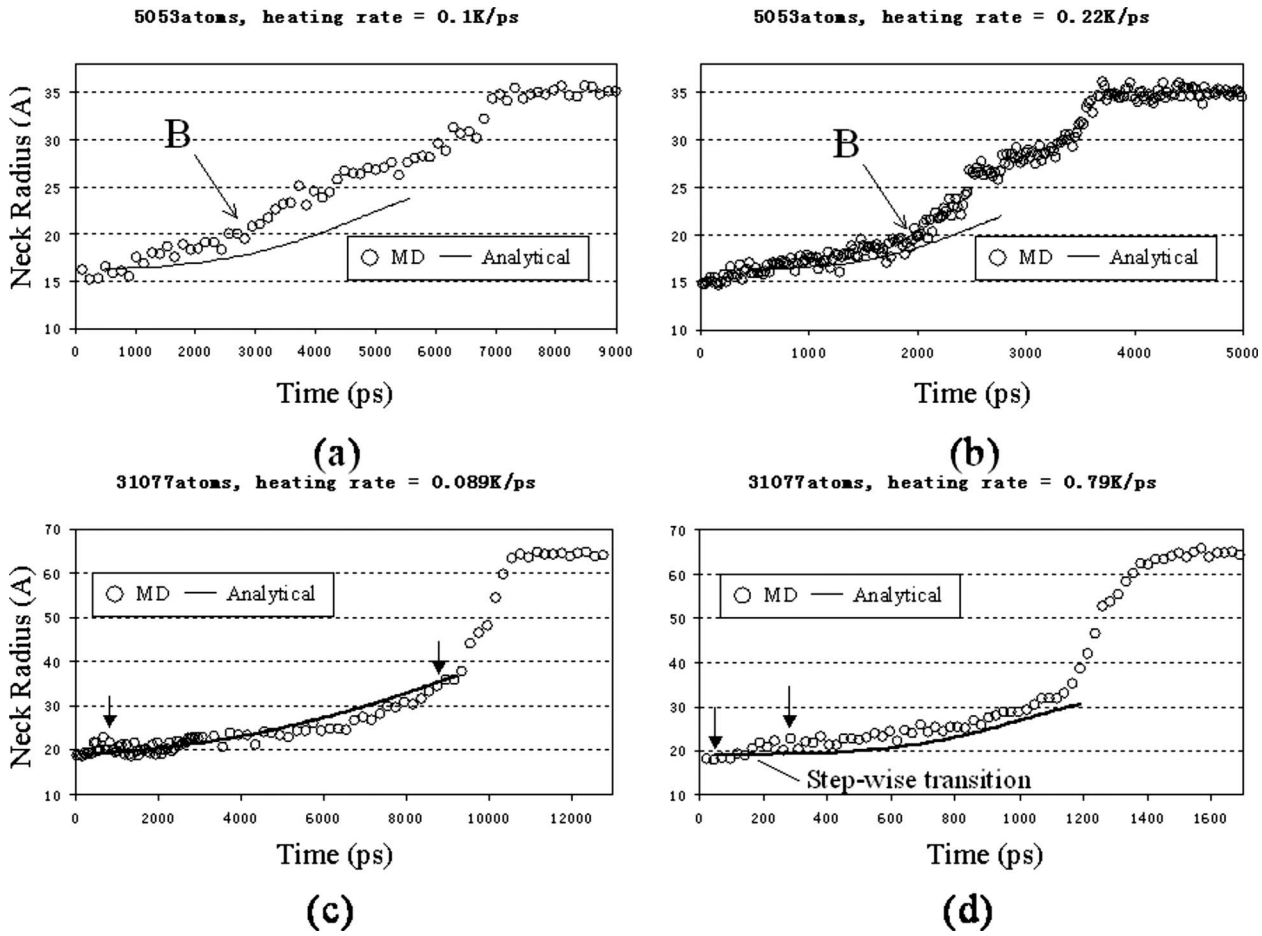

Fig. 5 The comparison between analytical model and MD simulations for 5053 atoms (*a*) and (*b*) and 31,066 atoms (*c*) and (*d*). The solid line is the analytical model and circle is the MD simulations.

satisfactory mostly due to the stepwise neck growth indicated in the figure. Similarly, to provide an insight into this stepwise transition, the atomic trajectory between the arrows as indicated in Fig. 5(*d*) is plotted in Fig. 4(*e*). It can be seen that the major contributions of atomic movements originate from the contact line of the neck surface. The radius of the neck surface is very small and therefore a deviation of neck growth rate can be expected as explained by Pan [15] and Zeng [13].

It should be pointed out that in the current study, only the solid-state diffusion driven neck growth within the entire sintering and coalescence process has been discussed using the analytical model. The temperature range covered so far is below the equilibrium melting temperature. The remaining of the neck growth process and the completion of the coalescence require the particle temperature to approach or even exceed melting temperature, where especially higher neck growth rate is expected as described in Fig. 5 for the final stage in the process. It is believed that the final stage can be described by K-F model [10] with given precise values of viscosity (as a function of temperature). Evaluation of the viscosity using the MD simulation to complete the description of the coalescence is still under investigation.

4 Conclusions

MD simulation was applied to study the solid diffusion necking growth of gold nanoparticles induced by laser heating. A classical neck growth model was modified to enable prediction of the neck growth during the continuous heating process. With the assistance of MD simulation, the detailed neck growth mechanisms were identified and analyzed for different particle sizes. Satisfactory agreement between analytical neck growth model and MD simulation was found only for large particles (10 nm). The small grain size effects for particle below 10 nm are the major causes for the failure of the conventional model.

Acknowledgment

Financial support to the University of California, Berkeley by the U.S. National Science Foundation under Grant Nos. CTS-0417563 and CMMI-0700827 is gratefully acknowledged.

References

[1] Ko, S. H., Pan, H., Grigoropoulos, C. P., Luscombe, C. K., Frechet, J. M.J., and Poulikakos, D., 2007, "Air Stable High Resolution Organic Transistors by Selective Laser Sintering of Ink-Jet Printed Metal Nanoparticles," Appl. Phys. Lett., **90**, 141103.
[2] Ko, S. H., Pan, H., Grigoropoulos, C. P., Luscombe, C. K., Fréchet, J. M. J., and Poulikakos, D., 2007, "All-Inkjet-Printed Flexible Electronics Fabrication on a Polymer Substrate by Low-Temperature High-Resolution Selective Laser Sintering of Metal Nanoparticles," Nanotechnology, **18**(34), 345202.
[3] Ko, S. H., Chung, J., Pan, H., Grigoropoulos, C. P., and Poulikakos, D., 2007, "Fabrication of Multiplayer Passive and Active Electric Components on Polymer Using Inkjet Printing and Low Temperature Laser Processing," Sens. Actuators, A, **134**(1), pp. 161–168.
[4] Kim, S. J., and Jang, D., 2005, "Laser-Induced Nanowelding of Gold Nanoparticles," Appl. Phys. Lett., **86**, 033112.
[5] Kuczinski, G. C., 1949, "Self-Diffusion in Sintering of Metallic Particles," Trans. Am. Inst. Min., Metall. Pet. Eng., **185**, pp. 169–178.
[6] Johnson, D. L., 1968, "New Method of Obtaining Volume, Grain-Boundary, and Surface Diffusion Coefficients From Sintering Data," J. Appl. Phys., **40**(1), pp. 192–200.
[7] Nichols, F. A., and Mullins, W. W., 1965, "Morphological Changes of a Surface of Revolution Due to Capillarity-Induced Surface Diffusion," J. Appl. Phys., **36**(6), pp. 1826–1835.
[8] Frenkel, J., 1945, "Viscous Flow of Crystalline Bodies Under the Action of Surface Tension," J. Phys. (USSR), **4**(5), pp. 385–391.

[9] Koch, W., and Friedlander, S. K., 1990, "The Effect of Particle Coalescence of the Surface Area of a Coagulating Aerosol." J. Colloid Interface Sci., **140**(2), pp. 419–427.
[10] Friendlander, S. K., and Wu, M. K., 1994, "Linear Rate Law for the Decay of the Excess Surface Area of a Coalescing Solid Particle," Phys. Rev. B, **49**(5), pp. 3622–3624.
[11] Lehtinen, K. E., and Zachariah, M., 2002, "Energy Accumulation in Nanoparticle Collision and Coalescence Processes," J. Aerosol Sci., **33**, pp. 357–368.
[12] Zhu, H., and Averback, R. S., 1996, "Sintering Processes of Two Nanoparticles: A Study of Molecular-Dynamics Simulations," Philos. Mag. Lett., **73**(1), pp. 27–33.
[13] Zeng, P., Zajac, S., Clapp, P. C., and Rifkin, J. A., 1998, "Nanoparticle Sintering Simulation," Mater. Sci. Eng., A, **252**, pp. 301–306.
[14] Combe, N., Jensen, P., and Pimpinelli, A., 2000, "Changing Shapes in the Nanoworld," Phys. Rev. Lett., **85**(1), pp. 110–113.
[15] Pan, J., 2004, "Solid-State Diffusion Under a Large Driving Force and the Sintering of Nanosized Particles," Philos. Mag. Lett., **84**(5), pp. 303–310.
[16] Xing, Y., and Rosner, D., 1999, "Prediction of Spherule Size in Gas Phase Nanoparticle Synthesis," J. Nanopart. Res., **1**, pp. 277–291.
[17] Arcidiacono, S., Bieri, N. R., Poulikakos, D., and Grigoropoulos, C. P., 2004, "On the Coalescence of Gold Nanoparticles," Int. J. Multiphase Flow, **30**, pp. 979–994.
[18] Ercolessi, F., Parrinello, M., and Tosatti, E., 1998, "Simulation of Gold in the Glue Model," Philos. Mag. A, **58**(1), pp. 213–226.
[19] Steinhardt, P. J., Nelson, D. R., and Ronchetti, M., 1993, "Bond-Orientational Order in Liquids and Glasses," Phys. Rev. B, **28**(2), pp. 784–805.
[20] Zhang, W., and Gladwell, I., 1998, "Sintering of Two Particles by Surface and Grain Boundary Diffusion—A Three-Dimensional Model and a Numerical Study," Comput. Mater. Sci., **12**, pp. 84–104.
[21] Saitoh, K., and Kitagawa, H., 1999, "Molecular Dynamics Study of Surface Effects on Atomic Migration Near Aluminum Grain Boundary," Comput. Mater. Sci., **14**, pp. 13–18.
[22] Thompson, S. M., Gubbins, K. E., Walton, J. P. R. B, Chantry, R. A. R., and Rowlinson, J. S., 1984, "A Molecular Dynamics Study of Liquid Drops," J. Chem. Phys., **81**(1), pp. 530–542.
[23] Medasani, B., Park, Y. H., and Vasiliev, I., 2007, "Theoretical Study of the Surface Energy, Stress, and Lattice Contributing of Silver Nanoparticles," Phys. Rev. B, **75**, p. 235436.
[24] Murr, L. E., 1975, *Interfacial Phenomena in Metals and Alloy*, Addison-Wesley, Reading, MA.
[25] Schiotz, J., Tolla, F. D. D., and Jacobsen, K. W., 1998, "Softening of Nanocrystalline Metals at Very Small Grain Sizes," Nature (London), **391**(5), pp. 561–563.
[26] Zachariah, M., and Carrier, M., 1999, "Molecular Dynamics Computation of Gas-Phase Nanoparticle Sintering: A Comparison With Phenomenological Models," J. Aerosol Sci., **30**(9), pp. 1139–1151.
[27] Exner, H., 1979, "Principles of Single Phase Sintering," Reviews on Powder Metallurgy and Physical Ceramics, **1**, pp. 7–251.
[28] Wang, Y., and Dellago, C., 2003, "Structural and Morphological Transitions in Gold Nanorods: A Computer Simulation Study," J. Phys. Chem. B, **107**, pp. 9214–9219.

Patterns of Double-Diffusive Natural Convection With Opposing Buoyancy Forces: Comparative Study in Asymmetric Trapezoidal and Equivalent Rectangular Enclosures

E. Papanicolaou[1]
e-mail: elpapa@ipta.demokritos.gr

V. Belessiotis
e-mail: beles@ipta.demokritos.gr

"Demokritos" National Center for Scientific Research,
Solar and other Energy Systems Laboratory,
Aghia Paraskevi,
Attiki 15310, Greece

The patterns arising from instabilities of double-diffusive natural convection due to vertical temperature T and solute concentration c gradients in confined enclosures are investigated numerically with the finite-volume method, for mixtures with Lewis numbers Le both $Le<1$ (e.g., air-water vapor) and $Le>1$. The problem originated from the need to gain better understanding of the transport phenomena encountered in greenhouse-type solar stills. Therefore, an asymmetric, composite trapezoidal geometry is here the original geometry of interest, for which no studies of stability phenomena are available in the literature. However, this is first related to the simpler and more familiar rectangular geometry having the same aspect ratio A equal to 0.3165, a value lying in a range for which available results are also limited, particularly for air-based mixtures. The case of opposing buoyancy forces is studied in particular (buoyancy ratios $N<0$), at values $N=-1$, -0.5 and $N=-0.1$, for which a wide spectrum of phenomena is present. The thermal Rayleigh number Ra is varied from the onset of convection up to values where transition from steady to unsteady convective flow is encountered. For $Le=0.86$ in the rectangular enclosure, a series of supercritical, pitchfork steady bifurcations (primary and secondary) is obtained, starting at $Ra\approx 13{,}250$, with flow fields with three, four, and five cells, whereas in the trapezoidal enclosure the supercritical bifurcation is always with two cells. For higher values of Ra ($Ra\geq 165{,}000$), oscillatory phenomena make their appearance for all branches, with their onset differing between branches. The oscillations exhibit initially a simple periodic pattern, which subsequently evolves into a more complex one, with changes in the structure of the respective flow fields. For $Le=2$ and 5, subcritical branches are also encountered and the onset of convection is in most cases periodic oscillatory (overstability). This behavior manifests itself in the form of standing, traveling and modulated waves (SWs, TWs and MWs, respectively) and with an increase of Ra there is a transition from oscillatory to steady convection, either directly or, most often, through an intermediate range of Ra with aperiodic oscillations. In the trapezoidal enclosure, oscillations at onset of convection appear only for $N=-1$ in the form of traveling waves (TWs), succeeded by aperiodic and then steady convection, while for $N=-0.5$ and -0.1, the bifurcations are transcritical, comprising a supercritical branch with two flow cells originating at $Ra=0$ and a subcritical branch with either two or four cells.
[DOI: 10.1115/1.2944241]

Keywords: double diffusion, enclosures, bifurcations, trapezoidal

1 Introduction

Double-diffusive convection, arising from the combined action of two fields described by variables with two different diffusivity coefficients, for instance, temperature and solute concentration, is characterized by dynamics that are far more complex than convection driven by temperature differences alone. Since more diffusing components may be present, the more general term "multicomponent convection" has also been introduced [1]. Several fields of application may be listed as relevant to double-diffusive convection, among others, astrophysics, metallurgy and materials science, geophysics, geology, etc. [1]. Particularly interesting is the case whereby the action of one field counteracts the action of the other. N expresses the ratio of the corresponding buoyancy forces [2], so that assisting buoyancy forces arise for $N>0$ and opposing ones for $N<0$. The latter case has been identified by several researchers as a model problem for the study of bifurcations in the solution of the differential equations that describe the system.

Generally, available analytical and numerical studies have so far considered two-dimensional configurations and may be classified in terms of the direction of the imposed gradients (vertical or horizontal) and the extent of the fluid domain in the second direc-

[1]Corresponding author.

Contributed by the Heat Transfer Division for publication in the JOURNAL OF HEAT TRANSFER. Manuscript received July 16, 2007; final manuscript received November 9, 2007; published online July 14, 2008. Review conducted by Gautam Biswas.

tion (infinite or bounded by rigid walls). In most cases, infinite layers or very large aspect-ratio enclosures have been considered, using periodic lateral boundary conditions. Among the most representative such studies in configurations involving vertical gradients are those by Huppert and Moore [3], Da Costa et al. [4], Deane et al. [5], Moore et al. [6], and Moore and Weiss [7]. Linear and nonlinear stability theories have been considered for infinite layers with stress-free boundaries and various Prandtl and Lewis numbers. For fixed Pr, Le, and solutal Rayleigh number, Huppert and Moore [3] identified six transition points by increasing the thermal Rayleigh number, first from the conductive solution to simple periodic oscillations, which later evolved first into more complex ones, then into aperiodic ones, and eventually into steady (monotonic) convection. Da Costa et al. [4] and Moore et al. [6] studied the oscillatory patterns in more details, investigating their spatial and temporal symmetric or nonsymmetric features, while Deane et al. [5] based their investigation in the classification of the oscillatory patterns into traveling, standing, and modulated waves and the conditions under which each of these are stable. Moore and Weiss [7] studied the interactions between modes characterized by a different number of rolls, in the presence of Hopf, pitchfork, and transcritical bifurcations.

More recently, studies such as those by Mamou et al. [8] and Ouriemi et al. [9] have considered vertical gradients of heat and solute in low-to-medium-aspect-ratio enclosures bounded by rigid walls, the former study also investigating the square cavity. Mamou et al. [8] obtained numerical solutions using the finite-element method in enclosures with stress-free and nonslip horizontal boundaries. They also used Galerkin and finite-element method for linear stability analysis, along with weak nonlinear perturbation theory and the parallel-flow approximation for shallow enclosures with Neumann boundary conditions on the horizontal walls. The latter approach was also employed by Ouriemi et al. [9] to obtain analytical solutions in shallow cavities, considering also small angles of inclination and the Soret effect, accompanied by numerical solutions using the finite-volume method.

Bifurcation phenomena for opposing buoyancy forces with horizontal gradients in cavities have been studied numerically, among others, by Xin et al. [10] and Bergeon et al. [11]. In the former study, the configurations were an infinite vertical layer and closed rectangular cavities, including the square one. Transcritical bifurcations were found in the square cavity, whereas in the infinite layer, alternating pitchfork and transcritical bifurcations were obtained with increasing aspect ratio. Bergeon et al. [11] also considered aspect ratios equal to 1 or higher, up to infinity, for different angles of inclination and presented bifurcation diagrams, where pitchfork (primary and secondary) and transcritical bifurcations were identified and the symmetry characteristics of the arising patterns were examined.

The oscillatory onset of convection from the conducting state, characteristic of double diffusive and not common in pure thermal convection, has also been confirmed and visualized in experiments by many investigators, most commonly with respect to the onset of TWs in water-alcohol or water-ethanol binary mixtures [12,13]. Others focused on the transition from TWs to stationary convection [14–16], while presenting evidence of modulated waves as well [14]. More insights into the development and properties of the experimentally observed TWs were presented in the analytical study by Linz et al. [17], which considered impermeable sidewalls.

The motivation for the present study arose from the need to complete the investigation originally undertaken by the authors in order to study the problem of natural convective flow and heat/mass transfer in greenhouse-type solar stills [18,19]. This flow is driven by the differences in the values of temperature and concentration between the saline water in the basin (T_b and c_b, respectively) and the glass cover (T_t and c_t), i.e., $\Delta T = T_b - T_t$ and $\Delta c = c_b - c_t$, and takes place inside an enclosure of an asymmetric trapezoidal geometry. The above investigations considered many

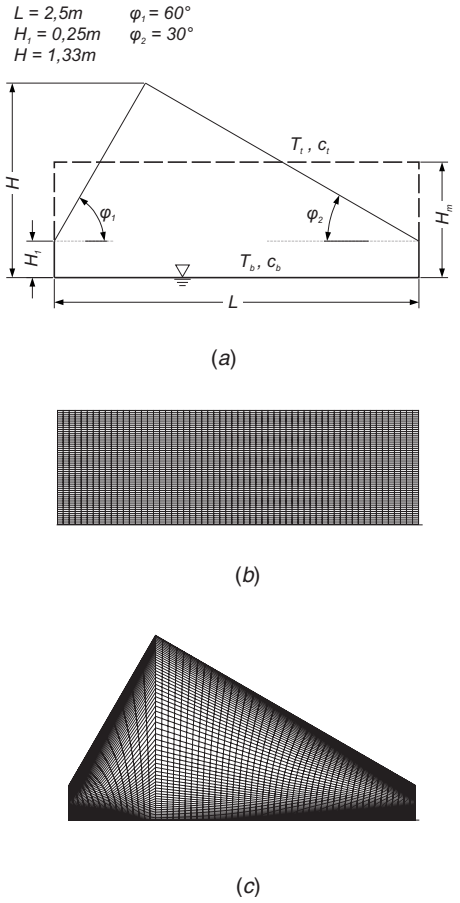

Fig. 1 (*a*) Original asymmetric trapezoidal geometry [18,19] and equivalent rectangular geometry. Computational grid for (*b*) equivalent rectangular and (*c*) original trapezoidal enclosures.

aspects of the problem, by covering both the laminar and the turbulent flow regimes, first in the pure thermal-buoyancy case [18] and then for double-diffusive convection, with both assisting and opposing buoyancy forces [19]. When an air-vapor mixture is considered, the coefficient β^* is positive [2], as is also β; therefore N is positive when ΔT and Δc are both of the same sign and negative in the opposite case. However, opposing buoyancies may appear during the morning hours, when a temperature inversion develops with the cover exhibiting higher temperature than the water in the basin.

The unsteadiness that was observed in the laminar-flow simulations in the form of periodic oscillations and the nonuniqueness of steady flow patterns encountered led the authors to explore the features of the instabilities that may be encountered in such configurations for air-based mixtures, extending the range of values of the governing parameters, particularly N, Le, and Ra. Given the fact that such phenomena have not been adequately analyzed in the literature for confined rectangular configurations, and the need to relate to a simpler geometry, the present work focuses first on a rectangular geometry, which is taken as the reference and is equivalent to the actual trapezoidal geometry in the sense that they have a suitably defined, common aspect ratio and the same cross-sectional area. With the understanding that these are exactly the criteria that define here the term *equivalent rectangular geometry*, its construction from the original trapezoidal geometry of a solar still is depicted in Fig. 1(*a*) (dashed line). As a characteristic length, a mean height H_m of the composite trapezoidal cross section is selected. As may be easily inferred, the cross-sectional areas of both shapes of interest are equal. Finally, even though the

air-water vapor mixture is the original fluid of interest ($Le<1$), the study extended itself to a wider range of mixtures with higher Lewis numbers ($Le>1$), still using air as the base fluid (solvent). Such configurations relate also to problems of flow and heat transfer in attic spaces of buildings [20] and to triangular geometries in general, which are known to exhibit their own bifurcation characteristics and are of current interest [21,22]. To limit the scope of this work, for fluid mixtures with $Le>1$, the range of Rayleigh numbers is limited to values up to the onset of oscillatory behavior that emanates from the steady convective solutions. That is, this behavior is not being considered in detail for $Le>1$, but only the oscillatory behavior at the onset of convection.

2 Mathematical Model

2.1 General Description. The mathematical model employed for the numerical computation of the flow, temperature, and concentration fields using the finite-volume method is based on the stream function ψ and vorticity ω. This approach offers advantages in two-dimensional natural convection problems, particularly when the pressure, which with this approach is eliminated from the system of equations, is not of interest. In the rectangular geometry, a formulation of the equations in a Cartesian coordinate system would have been sufficient. However, here the same version of the code as in the trapezoidal geometry (Papanicolaou et al. [18]) is used, so that the solution in both cases is obtained on a generalized, curvilinear coordinate system (ξ, η) after a suitable transformation of the space derivatives.

The equations are first written in a Cartesian coordinate system, nondimensionalized with the width L for the space coordinates, as this is a more convenient length to use in the trapezoidal geometry, while the dimensionless Cartesian velocity components are used to describe the flow field, along with Ψ and Ω. The Boussinesq approximation is used and the Soret and Dufour effects are neglected. The thermal Rayleigh number is denoted simply by Ra, or by either Ra_H and Ra_m, respectively when it is based on the height H of the rectangular or the mean height of the trapezoidal enclosure H_m, which are equal. Besides, by using the ratio N as an independent parameter, the concentration Rayleigh number Ra_c need not be further referenced in what follows.

3 Model Equations: Boundary Conditions

The computational grids used for each geometry are shown on Figs. 1(*b*) and 1(*c*). For these grids, the equations need to be transformed from the Cartesian system (X,Y) to a generalized, curvilinear system (ξ, η) so that the following system of equations is obtained.

In *stream function equation,*

$$\frac{B_{11}}{\mathbf{J}^2}\frac{\partial^2\Psi}{\partial\xi^2}+\frac{B_{22}}{\mathbf{J}^2}\frac{\partial^2\Psi}{\partial\eta^2}+2\frac{B_{12}}{\mathbf{J}^2}\frac{\partial^2\Psi}{\partial\xi\partial\eta}+P\frac{\partial\Psi}{\partial\xi}+Q\frac{\partial\Psi}{\partial\eta}=-\Omega \quad (1)$$

In *generalized transport equation,*

$$\mathbf{J}\frac{\partial\phi}{\partial\tau}+\frac{\partial}{\partial\xi}\left[U_1\phi-\Gamma_\phi\frac{B_{11}}{\mathbf{J}}\frac{\partial\phi}{\partial\xi}\right]+\frac{\partial}{\partial\eta}\left[U_2\phi-\Gamma_\phi\frac{B_{22}}{\mathbf{J}}\frac{\partial\phi}{\partial\eta}\right]=\frac{\partial}{\partial\xi}\left(\Gamma_\phi\frac{B_{12}}{\mathbf{J}}\frac{\partial\phi}{\partial\eta}\right)+\frac{\partial}{\partial\eta}\left(\Gamma_\phi\frac{B_{21}}{\mathbf{J}}\frac{\partial\phi}{\partial\xi}\right)+\mathbf{J}S_\phi \quad (2)$$

where ϕ represents the variables Ω, θ, and C and $\mathbf{J}$ is the determinant of the coordinate transformation matrix $\mathbf{J}=\det(\partial x_i/\partial\xi_j)$. The diffusion coefficients Γ_ϕ and source terms S_ϕ are defined in Table 1. The velocities U_1, U_2 are equal to $U_1=\beta^{11}U+\beta^{21}V$, $U_2=\beta^{12}U+\beta^{22}V$, and the dimensionless temperature and concentration are $\theta=(T-T_t)/\Delta T, C=(c-c_t)/\Delta c$. For the metric factors β^{ij}, B_{ij} and the control functions P, Q, the reader is referred to Refs. [18,19]. The boundary conditions are those of no-slip ($U=V=\Psi=0$) on the solid walls, whereas $\theta=C=1$ along the bottom and $\theta=C=0$ along the top horizontal surface, respectively. The vertical sidewalls are taken as adiabatic, both with respect to heat and to mass transfer.

Table 1 Diffusion coefficients Γ_ϕ and source terms S_ϕ for variable ϕ in the generic transport equation, Eq. (2).

ϕ	Γ_ϕ	S_ϕ
Ω	Pr	$-\mathrm{Ra}_L\ \mathrm{Pr}\left(\frac{1}{\mathbf{J}}\right)\left[\left(\beta^{21}\frac{\partial\theta}{\partial\xi}+\beta^{22}\frac{\partial\theta}{\partial\eta}\right)+N\left(\beta^{21}\frac{\partial C}{\partial\xi}+\beta^{22}\frac{\partial C}{\partial\eta}\right)\right]$
θ	1	0
C	1/Le	0

4 Numerical Scheme

The finite-volume method is used, along with an unsteady numerical procedure since the objective is to study the oscillatory phenomena that are expected, either at the onset of convection or at large values of Ra. More details about the numerical approach and its validation may be found in previous studies by Papanicolaou et al. [18,19]. Here, it is briefly mentioned that the alternating direction implicit (ADI) method is used to advance Eq. (2) in time and the successive over-relaxation (SOR) for Eq. (2), the latter method using a nine-point stencil since additional terms appear in the tranformed Poisson equation compared to the Cartesian case. The convective terms in Eq. (2) are discretized using the high-order HLPA scheme. The computer code was validated in a series of selected test cases for which experimental, benchmark numerical or analytical solutions were available, both for laminar and turbulent flows including double-diffusion problems and trapezoidal geometries (Papanicolaou et al. [18,19]). A nonuniform 61×61 grid was found adequate for grid-indepenedent results as will be demonstrated below, with a maximum allowable time step of $\Delta\tau=2\times10^{-6}$ in the rectangular and 10^{-6} in the trapezoidal geometry. The effect of the grid dimensions on the results is presented in later sections.

5 Results and Discussion

5.1 Model Parameters. Based on the angles and the actual dimensions of the composite trapezoidal geometry (Fig. 1(*a*)), the mean height H_m is found equal to $0.79125m$, so that a rectangular cavity of aspect ratio $A=H_m/L=0.3165$ arises. The first system in this investigation is the air-vapor mixture, for which the Schmidt number is equal to $Sc=\nu/D=0.60$, and, thus, the Lewis number, obtained for $Pr=\nu/\alpha=0.7$, is equal to $Le=Sc/Pr=0.86$ [2]. For this mixture, the previous investigation in the trapezoidal geometry [19] considering $N=-1$ as the base value for the case of opposing buoyancy forces found that steady laminar flow prevailing at low Ra exhibits a periodic oscillatory behavior at values $Ra_L=Ra_m/A^3\geq4.5\times10^6$ ($Ra_m\approx142{,}670$). Therefore, the present study starts by still taking $N=-1$ as the base value for both geometries but, as will become obvious from what follows, it is necessary for the investigation to start at much lower values of Ra, since the phenomena in the laminar, steady-flow region also present significant interest.

5.2 Rectangular Geometry. In this case, the study by Mamou et al. [8], using linear and nonlinear stability analyses and for the case when the imposed concentration gradient has a stabilizing effect ($Ra_c<0$) and the temperature gradient a destabilizing one ($Ra>0$), obtained solutions both for an infinite horizontal layer and for confined enclosures, with rigid sidewalls. Ouriemi et al. [9] using a similar analysis presented results for slightly inclined cavities also, with or without the Soret effect. Both studies have distinguished between two major ranges of Lewis number values, namely, $Le<1$ and $Le>1$. In the former case, the transition from the rest state to convection is always of supercritical

nature, whereas, in the latter case, subcritical transition is also possible and generally the preferred mode. Therefore, in the analysis that follows values of Le that lie within both these regions are selected. On the other hand, an important parameter is the buoyancy ratio N, which is first assigned the base value used in Ref. [19], $N=-1$, but then additional values in the range $-1 < N < 0$ are also examined.

Le<1: Low-to-Intermediate Ra_H. By selecting either the rest state or the pure diffusive solution as the initial condition, a total of six pitchfork bifurcation branches of steady-flow solutions were identified, consisting of three pairs of equivalent solutions and these are all shown in Fig. 2. Bifurcation diagrams are here shown in terms of the midpoint stream function (Fig. 2(*a*)) along with the respective flow- and temperature-field patterns (concentrations fields, not differing much from the respective temperature fields, are omitted for the sake of brevity) and the horizontal velocity component at a selected point on the left half of the enclosure (Fig. 2(*b*)). The branches are identified by the number of cells in the flow field and letters *a* and *b* that indicate their location in the velocity diagram (positive or negative values of velocity). The pure diffusion (trivial) solution with zero flow was obtained below the value $Ra_H=13{,}250$, where the first steady-state convective solutions made their appearance, characterized by three recirculating cells. The nonsymmetric appearance in Fig. 2(*a*) is due to the fact that the branches are numerically obtained from discrete points, and the inherent features of the numerical code make it biased toward one or the other of two equivalent branches (a or b). In addition, even though all bifurcations are supercritical pitchfork, only branches 3a and 3b appear to originate from the trivial solution (zero amplitude of Ψ, V). These branches are stable at zero amplitude, whereas 4a and 5a–b are not, a point which will be further clarified below.

At the value $Ra_H=20{,}000$, the equivalent solution with three cells but with the opposite sense of rotation (branch 3b) first appeared, whereas branch 4a made its first appearance at $Ra_H \approx 27{,}550$ and 4b was more difficult to obtain, first appearing at $Ra_H \approx 52{,}700$. At a slightly higher value of Ra_H, $Ra_H \approx 53{,}000$, branch 5b with five recirculating cells, exhibiting central symmetry, first appeared, while branch 5a even though setting in much later, at $Ra_H \approx 65{,}000$, was the preferred mode for a wider range of values thereupon (at least for up to $Ra_H \approx 90{,}000$). The mean Nusselt number, divided by the conduction value, is also plotted in terms of Ra_H in Fig. 2(*c*), where it may be observed that its value decreases with an increase in the number of cells.

Le<1: High Ra_H. All six branches already described exhibited an oscillatory behavior with an increase in the Rayleigh number, after undergoing a Hopf bifurcation. Each mode exhibits its own patterns and the phenomena are quite diverse. The evolution to the oscillatory regime is generally accompanied by changes in the shape and size of the cells of Fig. 2(*a*), a fact that, for instance, in the case of branches 3a and 3b, is responsible for the change in the slope of the Ψ_{mid} curves in Fig. 2(*a*) at high Ra_H. In all cases, the inner cells are squeezed as the outer ones grow inwards and a gradual inclination of the cells with respect to the vertical develops. The odd-numbered patterns of cells always maintain central symmetry in this process, while the four-cell mode maintains vertical symmetry.

At their onset, the oscillations are characterized by a simple periodic, sinusoidal form and manifest themselves in the form of a swaying motion about the original vertical cell axis. With a further increase in Ra_H, the phenomena become more complex, as more frequencies appear. These phenomena set in earlier for branches 5a and 5b (at $Ra_H \approx 165{,}000$, Figs. 3(*a*) and 3(*b*), whereas for the remaining four branches these appear at $Ra_H \approx 215{,}000$. The onset of oscillatory phenomena for branches 4a and 4b is accompanied by a doubling of the number of cells (Fig. 3(*c*)), while the oscillations manifest themselves again with the swaying motion described above. The oscillation of the cells for branches 3a and 3b are about their vertical axis, starting at $Ra_H \approx 215{,}000$ and becoming quite complex already at $Ra_H \approx 220{,}000$ with a significant increase in the period of oscillations (Fig. 3(*d*)). The structure of the flow field exhibits drastic variations, always, however, maintaining central symmetry.

Le>1, N=−1. Here, the values Le=2 and Le=5 are selected, which cover a wide range of fluid mixtures with air as the solvent [2] and, for each of these, the value of N is first set at $N=-1$ and then successively reduced to $N=-0.5$ and $N=-0.1$. In this range of values of Le, subcritical convection and oscillatory flow (overstability) are expected, with the oscillations typically manifesting themselves as either standing wave (SW) or TW [5]. Which of the two modes will prevail depends, apart from physical parameters such as Le, N, and the Rayleigh number, on whether an unbounded domain or one bounded by rigid walls is considered.

For $N=-1$ and Le=2, convection is indeed found to set in in an oscillatory fashion, and more specifically in the form of SWs. This occurs first at $Ra_H=25{,}000$, whereas for $Ra_H<25{,}000$ the pure diffusion solution is obtained with zero flow. First, a SW flow pattern with three cells, having a fixed location in space and reversing their sense of rotation periodically, sets in, whereas at $Ra_H=40{,}000$, a SW regime with two cells is established (three- and two-cell modes, respectively). When starting from a quiescent state, the oscillations take longer times to reach saturation for the three-cell mode compared to the two-cell mode (dimensionless times of 1.2 and 0.55, respectively), as may be seen in Fig. 4(*a*). In Figs. 4(*b*) and 4(*c*), the two limiting states of the oscillating flow field within a cycle for each mode are shown after saturation has been attained. The three-cell mode persists up to $Ra_H=34{,}000$, whereas above that value and up to $Ra_H=39{,}000$ a competition between the two modes occurs, evidenced by flow patterns with alternating three- and two-cell modes.

Upon increasing the Rayleigh number, more complex oscillatory patterns appear, still with two major cells. The number of cells changes at a value of Rayleigh equal to $Ra_H=70{,}000$, with the complex periodic pattern still persisting for up to $Ra_H=90{,}000$, followed by a wide range of values of Ra_H where the oscillations become chaotic, a behavior which was called chaotic waves (CWs) by Deane et al. [5]. At around $Ra_H=180{,}000$, the flow stabilizes to an almost steady convective, centrosymmetric pattern with three cells, a state for which the term stationary overturning convection (SOC) has prevailed over the past decades [16,17]. This pattern exhibits hysteresis, since by reducing the Rayleigh number starting from the solution at $Ra_H=180{,}000$ the almost steady behavior is obtained also at $Ra_H=170{,}000$ and first at $Ra_H=160{,}000$ the flow returns to the CW regime described earlier. On the other hand, moving upwards by increasing the value of Ra_H, the steady behavior was found to persist for up to $Ra_H=280{,}000$, the highest value considered here.

The onset of convection is similar at the higher value of Le, Le=5 and still at $N=-1$, with zero flow obtained for $Ra_H<11{,}000$ and SW oscillatory patterns with three and two cells obtained in the range $Ra_H \approx 11{,}000-18{,}000$, succeeded by a more irregular pattern thereupon. These are obtained by initializing the computations from the solution at the immediate lower Ra_H. If, however, initialization is made from the quiescent state, a regular TW pattern now appears at $Ra_H=25{,}000$, characterized by a single frequency, as may be seen in Fig. 5. Since the horizontal extent is equal to 1 (dimensionless), the speed of the wave (or phase velocity) may be computed as the inverse of the period of the TW and the calculated value is shown in Fig. 5.

Similar results in the form of TWs are obtained for Ra_H up to $Ra_H \approx 29{,}000$. At Ra=30,000, however, the state obtained is an aperiodic-oscillatory one, persisting for a wide range of Ra_H above that value and succeeded by a SOC pattern first at $Ra_H=70{,}000$. At this Ra_H, it was possible to obtain both three- and four-cell modes, the former one by initializing with the quiescent state, while the latter one by starting the computations from the diffusion solution, respectively. All these steady and oscillatory branches obtained for $N=-1$ at Le=5, are depicted in Fig. 6(*a*) in

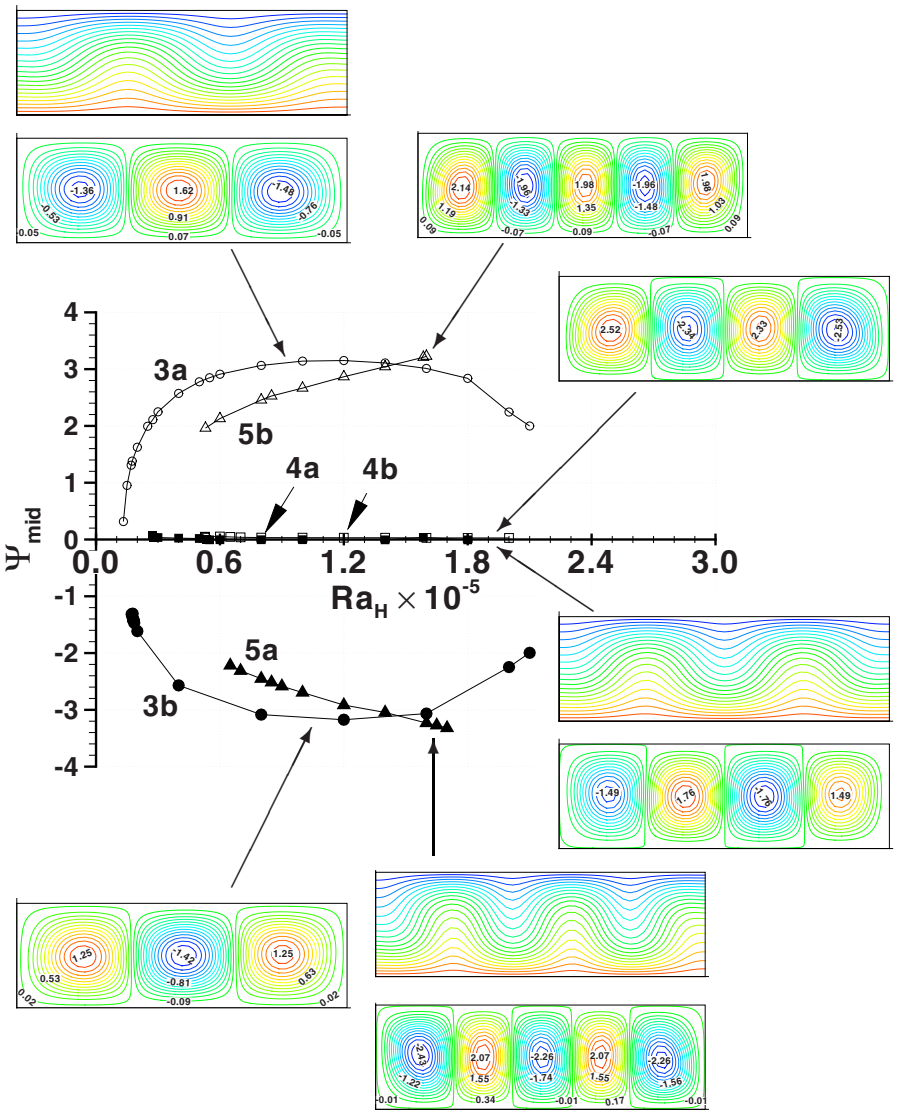

(*a*)

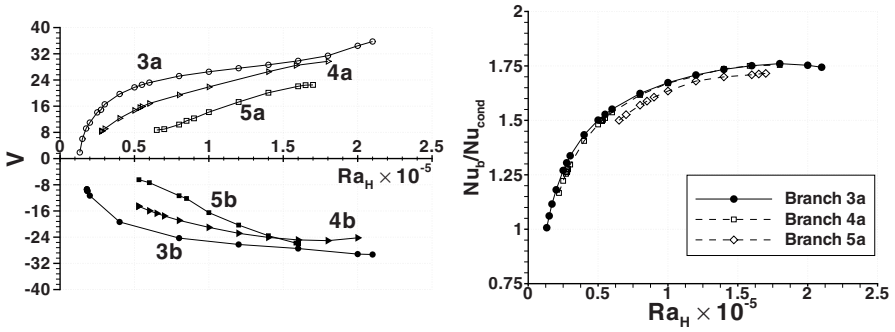

(*b*) (*c*)

Fig. 2 Bifurcation diagrams of the solutions and corresponding flow-temperature field patterns for the rectangular cavity at Le=0.86, *N*=−1: (*a*) stream function at the cavity center; (*b*) horizontal velocity component at point (0.207, 0.102); (*c*) mean Nusselt number normalized by the conduction value

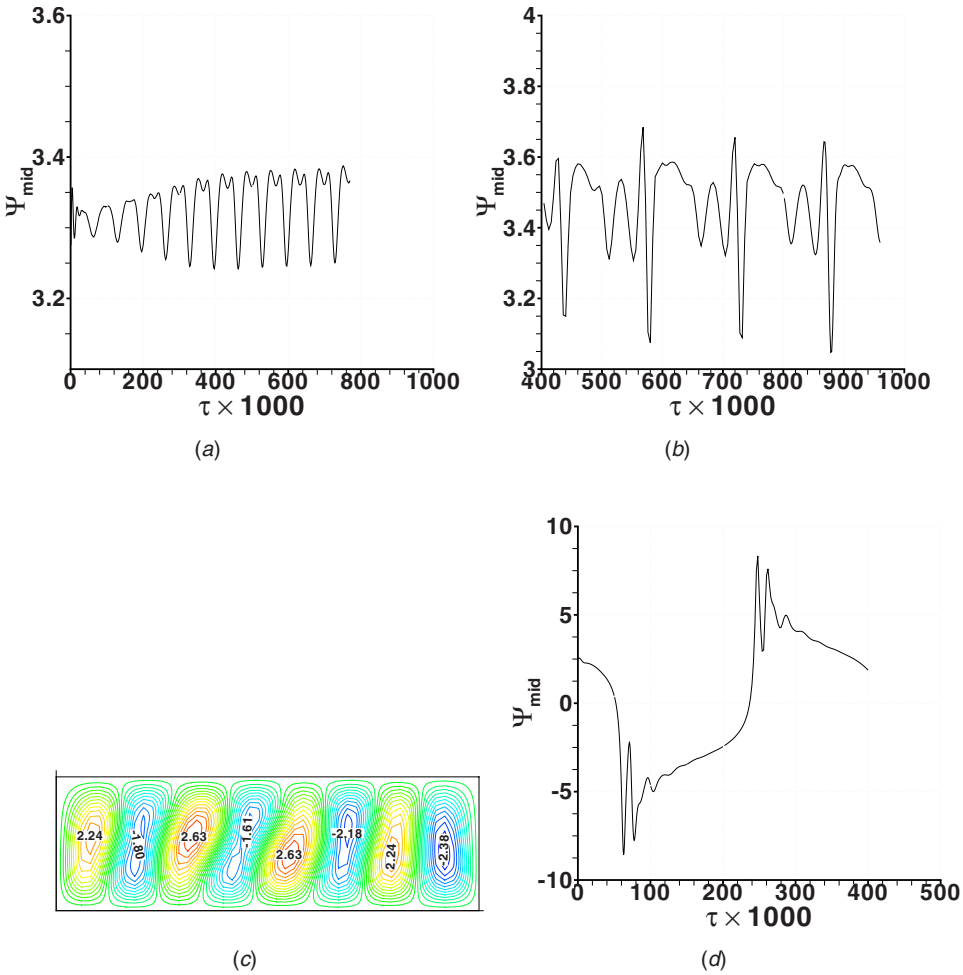

Fig. 3 Oscillatory patterns of the stream function in the rectangular enclosure for Le=0.86, $N=-1$: midpoint value (Ψ_{mid}) for the five-cell branch at (*a*) $Ra_H=170,000$; (*b*) $Ra_H=180,000$; (*c*) instantaneous flow field evolving from the four-cell branch at $Ra_H=220,000$; (*d*) temporal variation of Ψ_{mid} for the three-cell branch at $Ra_H=220,000$

terms of Ψ_{max}, with $Ra^0=Ra/Ra_1^{sup}$ (where Ra_1^{sup} is defined below, after Eq. (3)) and using mean values for the oscillatory cases. Both three- and four-cell steady branches revert to the aperiodic-oscillatory state upon reducing Ra_H (dashed line), the former already at 40,000, whereas the latter at 30,000, after first going through a new mode of low-frequency and amplitude, periodic oscillations at $Ra_H=35,000$.

$Le>1$, $-1<N<0$. Reducing now the buoyancy factor to $N=-0.5$, first at Le=2, the behavior of the system changes significantly. Now the overstability sets in at $Ra_H=6500$ ($Ra^0=3.46$) and the arising oscillatory state is limited to within a narrow range of values (up to $Ra_H=7250$). The main pattern is that of single-frequency periodic SW, with three cells. Contrary to the findings for $N=-1$, the SW regime is directly succeeded by SOC as soon as Ra_H attains the value of 7300 and, even though at lower values of Ra_H the three-cell mode is the preferred one, at higher values a steady, four-cell mode now arises (Fig. 6(*b*)). This may be sustained for up to $Ra_H=9000$ ($Ra^0=4.79$) upon reducing Ra_H, reverting to the three-cell mode at $Ra_H=8000$. Proceeding backwards along the three-cell branch, a hysteresis is observed, since steady flow persists up to a saddle node, estimated at $Ra_H \approx 6500$.

For the same value of the buoyancy parameter, $N=-0.5$, and for Le=5, some new phenomena have been observed. As for $N=-1$, SW and TW patterns are both obtained, for up to $Ra_H=4800$. However, at $Ra_H=5000$, a new, MW pattern makes its appearance (Fig. 6(*c*)) and persists for up to $Ra_H=5400$. A TW pattern also sets in, with translating motion from right to left and limited within the left half of the enclosure, for up to $Ra_H=6500$, followed by SOC with three flow cells at $Ra_H=6600$ and a four-cell mode at $Ra_H=20,000$, maintained down to $Ra_H=7000$ upon reducing the Rayleigh number. Then, interestingly enough, at $Ra_H=6500$, a new asymmetric, steady-flow pattern establishes, with two main cells shifted to the right of the enclosure (about 2/3 of its length), leaving the remaining 1/3 at a very low flow intensity, as shown in Fig. 6(*d*). On the other hand, by reducing Ra, the three-cell mode reverts to the MW pattern described earlier, at $Ra_H=5000$.

At the smallest value of N considered, $N=-0.1$, first at Le=2, a new sequence of states is obtained, since overstability is not found for any value of Ra_H, while, on the other hand, the steady convection obtained is supercritical, with a critical value of $Ra_{sup} \approx 2300$, that is, at 1.225 times the critical value for thermal buoyancy alone. Still at $N=-0.1$ and for Le=5, zero flow is obtained for $Ra<2800$, whereas oscillatory flow (SW) with three cells is obtained only within a narrow range of Ra, Ra=2800–2900. Steady flow with three and four cells is obtained above these values, the former mode exhibiting hysteresis and the latter reverting to the three-cell mode by decreasing Ra.

Comparison With Stability Analysis: Literature Results. First, considering the $Le<1$ results, from the stability analysis of Mamou et al. [8] and Ouriemi et al. [9], the critical values for each

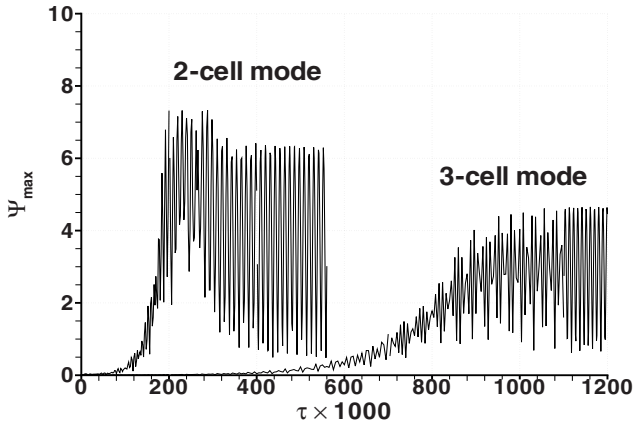

(*a*)

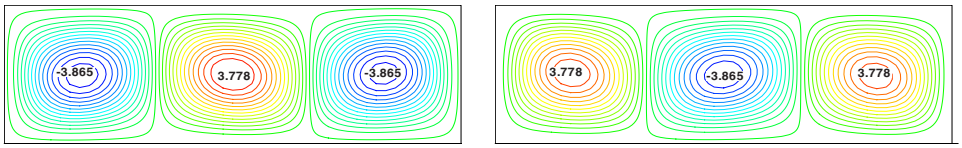

(*b*)

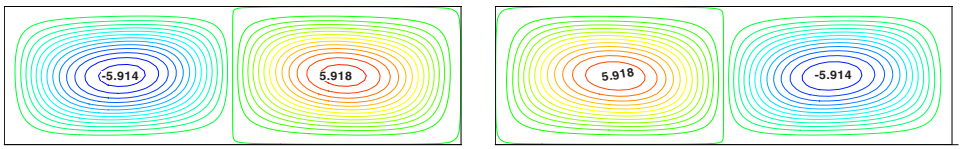

(*c*)

Fig. 4 Oscillatory onset of convection in the form of standing waves in the rectangular enclosure at Le=2, *N*=−1: (*a*) time history of Ψ_{max} for three- and two-cell modes, Ra_H=27,500 and Ra_H=40,000, respectively. Streamlines for (*b*) the three-cell and (*c*) the two-cell modes at the two limiting states of maximum amplitude within a cycle of oscillations at the saturated state.

successive supercritical bifurcation i obtained by linear stability analysis may here be written as

$$Ra_{cr,i} = \frac{1}{1 + N\text{Le}} Ra_i^{sup} \tag{3}$$

where Ra_i^{sup} are the critical values of the RB problem for the same geometry. For a finite aspect-ratio cavity, bounded by rigid sidewalls, Jackson and Winters [23] have obtained the first two eigenvalues of the RB problem as a function of the aspect ratio and from that study and for the present aspect ratio $A=3.16$, it may be found by interpolation that $Ra_1^{sup}=1878$ and $Ra_2^{sup}=2042$, corresponding to three- and four-cell modes, respectively. By virtue of Eq. (3), $Ra_{cr,1}=13{,}146$ and $Ra_{cr,2}=14{,}294$ are obtained for the respective critical values of the double-diffusion problem. The first one lies exactly in the range found here numerically (13,000-13,250). The delayed onset of the four-cell mode based on the critical Ra values may be interpreted in view of the effect of sidewall boundaries and the competition between modes in the RB problem, which was analyzed, among others, by Metzener [24]. In the present case, above the value of $Ra_{cr,2}=14{,}294$ both the three- and the four-cell modes are possible according to the linear stability analysis, and the nonlinear effects are the ones that determine the preferred mode, so that the three-cell mode continues to be the preferred one up to $Ra_H=27{,}550$.

Similar phenomena have been discussed in the RB problem in porous media by Riley and Winters [25] and in the analysis of the Eckhaus instability by Tuckerman and Barkley [26]. They distinguished between primary and secondary bifurcations, the former emanating from trivial solutions (eg., zero flow) while the latter from branches of primary bifurcations. Based on their analysis, it can be claimed that here branches 3a,b are the primary bifurcations, whereas at $Ra_{s,2} \approx 22{,}000$, there is a secondary bifurcation stabilizing the four-cell mode, which is necessarily unstable at its onset [26] and, thus, in the interval $Ra_{cr,2}$ and $Ra_{s,2}$. As for branches 5*a* and 5*b*, these may also be viewed as competing with the four-cell branches at higher Ra_H, whereby the four-cell mode is the preferred one for $Ra_H < 65{,}000$ and the five-cell mode for $Ra_H \geq 65{,}000$, even though the latter may be obtained already at $Ra_H=52{,}700$. Hysteresis is also present in the exchange between the four- and the five-cell modes.

Proceeding now to the Le>1 results, the critical values for supercritical convection may again be found from Eq. (3). This here is the case only for $N=-0.1$, Le=2, where a value of $Ra^{sup}=2347$ is computed. This is in very close agreement to the numerical result, which located the supercritical bifurcation point between La=2300 and 2400. As far as the critical value for oversta-

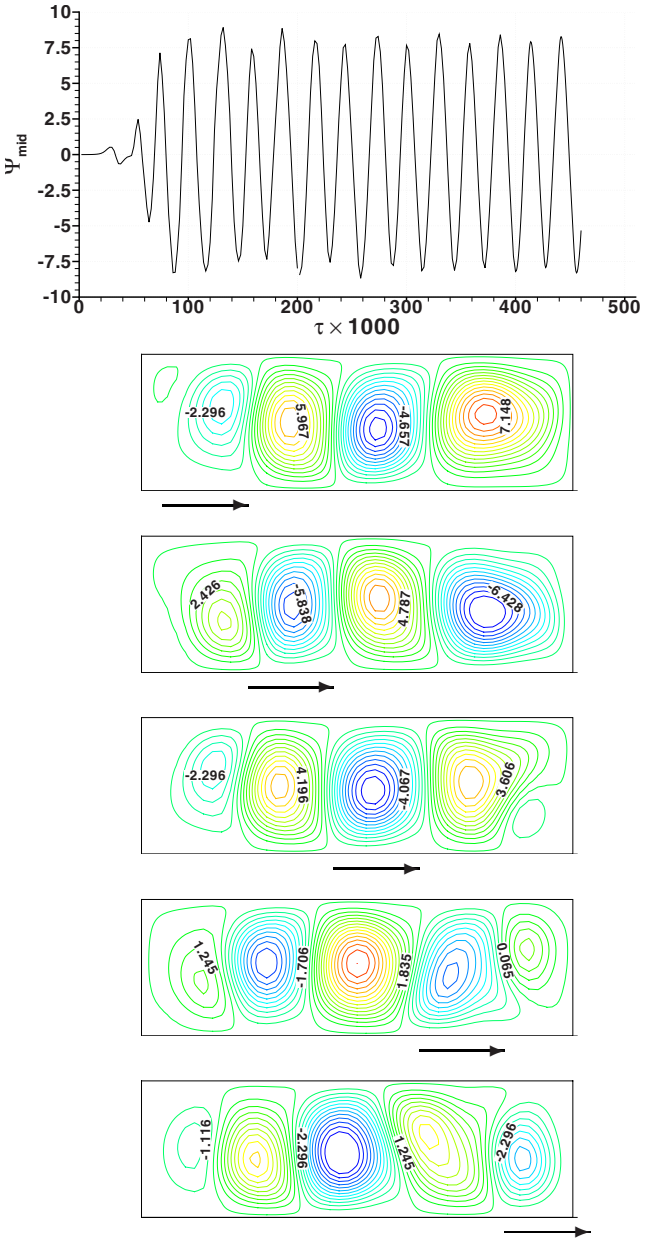

Fig. 5 TW pattern in the flow field for the rectangular enclosure with Le=5, $N=-1$ and $Ra_H=25,000$. Time history of midpoint stream function and streamlines at five different instants over a single period are shown (dimensionless wave speed =35.461).

bility, critical values have been presented by Dean et al. [5], for an infinite layer with stress-free horizontal boundaries and by Mamou et al. [8] for various types of boundary conditions, using linear stability analysis and an approximate approach. In the present notation, the expression for the critical value can be written as

$$\mathrm{Ra}_{\mathrm{cr}}^{\mathrm{over}} = \frac{b}{1 - aN\mathrm{Le}}\mathrm{Ra}_i^{\mathrm{sup}} \tag{4}$$

where $a=-(1+\sigma_i \mathrm{Pr}\ \mathrm{Le})/(\mathrm{Le}^2(1+\sigma_i \mathrm{Pr}))$, $b=(\mathrm{Le}+1)(1+\sigma_i \mathrm{Pr}\ \mathrm{Le})/(\sigma_i \mathrm{Pr}\ \mathrm{Le}^2)$, and σ_i is a parameter that depends on the aspect ratio of the enclosure and the boundary conditions and refers to the ith eigenvalue of the RB problem. Based on the data of Mamou et al. [8], for the present aspect ratio and rigid-rigid horizontal boundaries with Dirichlet boundary conditions, $\sigma_1 \approx 2$ for the first (three-cell) mode is obtained. Therefore, the critical values for oscillations obtained for Le=2 are 18,351, 6328 at $N=-1$ and -0.5, respectively, whereas no oscillatory onset of convection is found possible at $N=-0.1$. The latter finding was indeed confirmed by the numerical results, whereas the onset of oscillations was numerically predicted at values of Ra, equal to 25,000 and 6500 for $N=-1$ and -0.5, respectively. The latter value is in good agreement, while the former is found higher. The same trend is also observed for Le=5, whereby for $N=-1$, -0.5, and -0.1 from Eq. (4) the values 7727, 3863, and 2759 are computed, while numerically the oscillations first appear at 11,000, 4200, and 2800, respectively. Again, the agreement is good at the lower absolute values of N but significantly delayed for $N=-1$. This might be attributed to the particular case being more sensitive to the effect of aspect ratio and sidewall boundary conditions, which may not be adequately taken into account in the linear stability analysis. For the same reason, the authors could also not confirm numerically the critical values for the onset of subcritical convection $\mathrm{Ra}_{\mathrm{cr}}^{\mathrm{sub}}$ obtained by a weak nonlinear analysis [8].

5.3 Trapezoidal Geometry

Pure Thermal Convection (N=0). Due to the nonsymmetric nature of the present geometry, pitchfork bifurcations, which are symmetry breaking bifurcations, are not expected, unlike the rectangular enclosure case. Indeed, results obtained for $N=0$, here only briefly discussed due to lack of space, confirmed the presence of a transcritical bifurcation, comprising a supercritical branch with two cells (Fig. 7(*a*)) and a subcritical branch with four cells (Fig. 7(*b*)). It was found that the critical value for supercritical convection is $\mathrm{Ra}^{\mathrm{sup}}=0$, i.e., motion starts as soon as $\Delta T>0$. This can be justified, since in the trapezoidal enclosure case ΔT may not be viewed as applied entirely in the vertical direction, but also as producing a horizontal differential-heating effect, known to induce convective motion already as soon as ΔT exceeds zero. In order to define Ra^0 therefore in the trapezoidal case, the critical value $\mathrm{Ra}^{\mathrm{sup}}$ for the onset of convection in the rectangular enclosure is still considered in what follows. The subcritical branch was first obtained numerically for $\mathrm{Ra}_m=30,000$, and traced backwards to a saddle-node point at $\mathrm{Ra}_m \approx 13,750$. At $\mathrm{Ra}_m=31,705$, ($\mathrm{Ra}_L=10^6$) the supercritical branch exhibited already the first periodic oscillations, an indication of a Hopf bifurcation taking place. It is worth mentioning that this configuration with $N=0$ has also been studied in the fully turbulent regime by Papanicolaou et al. [18].

Double-Diffusive Convection, Le<1. The case with Le=0.86 and $N=-1$ was considered, extending essentially the results of Papanicolaou and Belessiotis [19] to lower Rayleigh numbers, covering now the range from the onset of convection to the threshold of unsteadiness of the steady branches. It was found that convection at its onset is of supercritical form, with a critical number $\mathrm{Ra}^{\mathrm{sup}} \approx 8000$. The main flow pattern consists of two major cells, as shown in Figs. 7(*c*) and 7(*d*). It is interesting to observe that the cell occupying the left section is clockwise (cw) rotating for $N=-1$ but counterclockwise (ccw) rotating for $N=0$, when both cases were initialized from the quiescent state.

For $N=-1$ at $\mathrm{Ra}_m=20,000$, the cw rotating cell to the left dominates, both in size and strength of recirculation; however, at higher values ($\mathrm{Ra}_m=95,114$ or $\mathrm{Ra}_L=3\times10^6$) the ccw rotating cell increases in strength and size and pushes the cw rotating cell to the left, giving it a more skewed appearance (Fig. 7(*d*)). Gradually, a small third cell develops just below the top edge of the cavity and is responsible for the periodic-oscillatory behavior that follows and sets in at $\mathrm{Ra}_m=126,818$ ($\mathrm{Ra}_L=4.5\times10^6$). This phenomenon has already been discussed in a previous study [19]. Figure 7(*e*) illustrates the form of the supercritical convective branch in terms of the maximum stream function value $\Psi_{\max}$ and compared to the same quantities for $N=0$. No steady modes with a number of cells greater than 2 were found for this set of parameters.

Double-Diffusive Convection, Le>1. Given the variety of

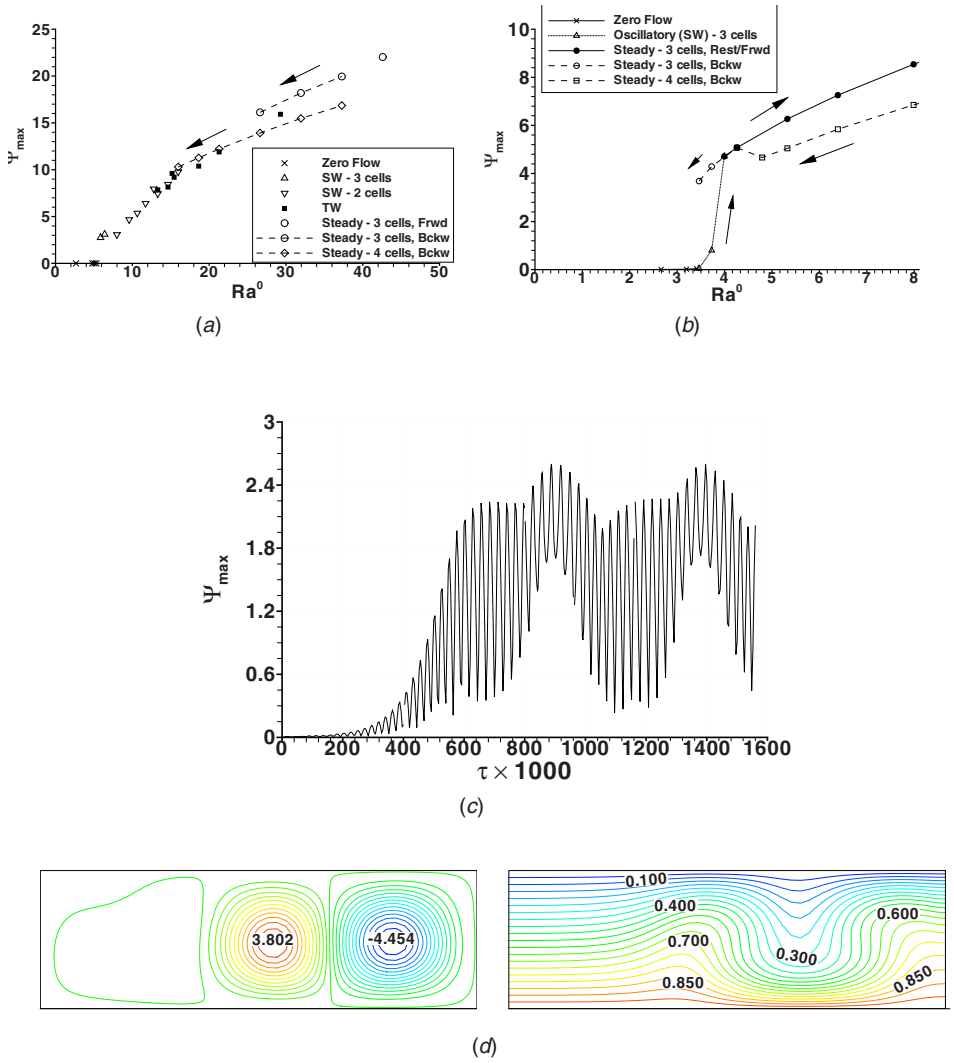

Fig. 6 Bifurcation diagrams for the rectangular enclosure at (*a*) Le=5, *N*=−1; (*b*) Le=2, *N*=−0.5. Special patterns encountered only for Le=5, *N*=−0.5: (*c*) MWs (Ra_H=5000) and (*d*) asymmetric steady solutions (streamlines and isotherms) at Ra_H=6500.

states that were found to develop in the rectangular cavity for Le>1 by varying the value of *N*, as already outlined in the preceding sections, the corresponding phenomena were now investigated in the trapezoidal geometry. As before, first the value of Le=2 with *N*=−1 was considered. Convection does not start until Ra_m=35,000, where it sets in in a periodic-oscillatory fashion as indicated in the plot of the midpoint value of the stream function in Fig. 8(*a*). This periodic behavior, which is represented by a subcritical branch, was found to persist for up to Ra_m=50,000. Similar to the phenomena observed in the case of the rectangular geometry with the same parametric values Le and *N*, the periodic-oscillatory regime is succeeded by a long rage of Ra values where the oscillations are aperiodic. For the present set of parameters, this range was found to extend from Ra_m=60,000 to 10,0000. At Ra_m=120,000 SOC is obtained, as may be seen in Fig. 8(*b*). The flow- and temperature-field patterns for this case are also shown in Fig. 8. As may be observed, this pattern is significantly different than the steady-flow pattern for the value Le=0.86 in Figs. 7(*c*) and 7(*d*). In the SOC state, hysteresis has been observed, as this pattern was sustained for up to Ra_m=95,114 ($Ra_L=3\times10^6$) by reducing the Rayleigh number, and reverted to the aperiodic-oscillatory pattern at Ra_m=90,000.

Quite similar phenomena have been observed for the higher Lewis number, Le=5, still at *N*=−1, with only the critical values being different. More specifically, periodic-oscillatory convection was first observed at Ra_m=13,000, with zero flow at lower values, and persisted for up to Ra_m=20,000, being succeeded by aperiodic convection for $25{,}000 \leqslant Ra_m \leqslant 37{,}000$ and SOC at Ra_m=40,000. Here, the hysteresis effect was more prolonged as Ra was reduced, the SOC pattern being sustained for up to Ra_m=20,000 and reverting to the aperiodic oscillatory state thereafter. All branches obtained for *N*=−1 are depicted in Figs. 9(*a*) and 9(*b*), both for Le=2 and Le=5, where the maximum stream function is plotted as a function of Ra^0, using time-averaged values for the oscillatory cases.

In order to check the effect of the computational grid on the results, various dimensions have been considered, starting with level 1 (31×31), then successively multiplying the number of nodes by factors of 2, 3 and 4. In terms of the frequency of oscillations for the periodic solutions, a comparison has shown that its value is relatively grid insensitive for the chosen dimensions. Particularly from Level 2, which is the base grid, upwards the values lie very close to one another (within 1.4%). The effect of grid size on the steady solutions is presented below.

The periodic-oscillatory patterns for one selected set of parameters (*N*=−1 and Le=5) are shown in Fig. 10 for Ra_m=20,000. Even though it is more difficult to perceive this compared to the rectangular-enclosure case, the oscillations have the form of TWs,

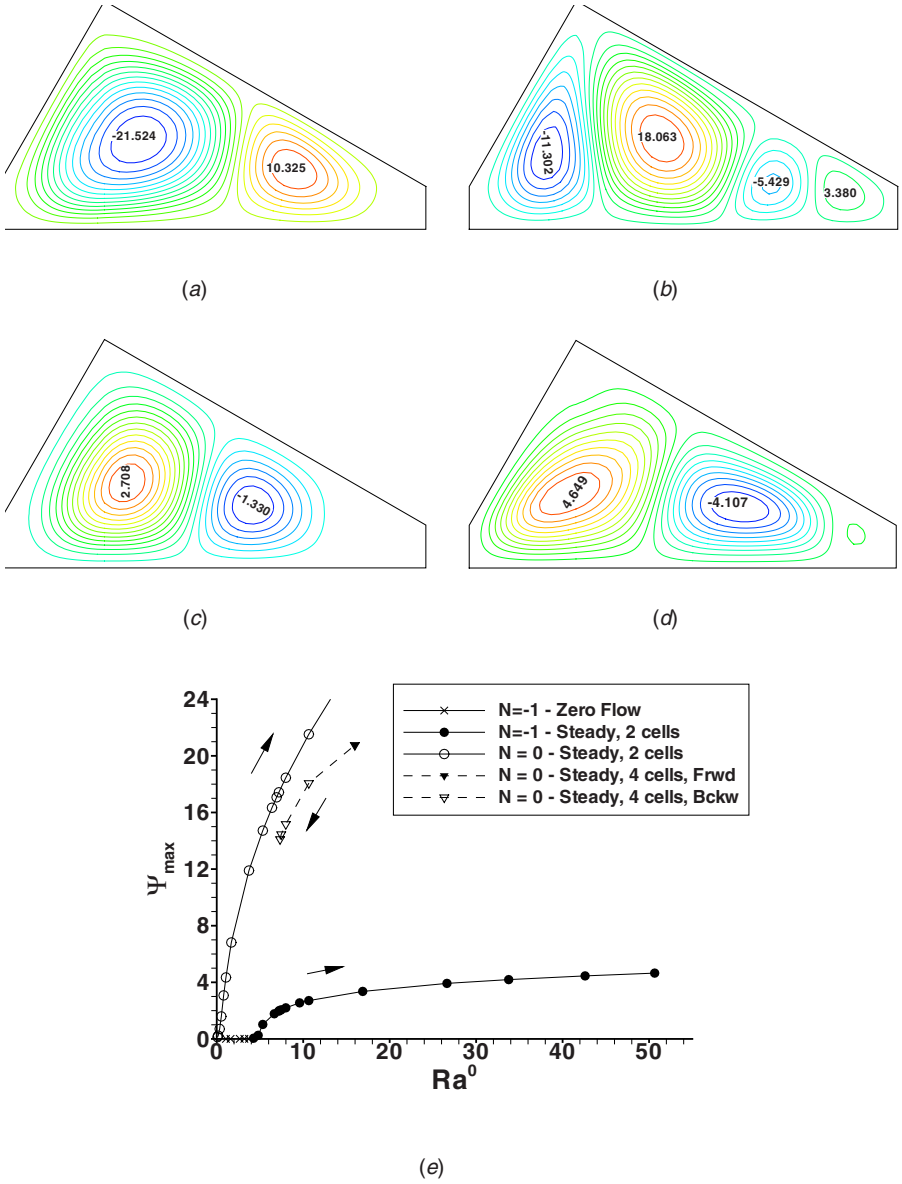

Fig. 7 Flow patterns in the trapezoidal enclosure computed for (*a*) $N=0$, $Ra_m=20,000$ (supercritical); (*b*) $N=0$, $Ra_m=20,000$ (subcritical); (*c*) Le=0.86, $N=-1$, $Ra_m=20,000$; (*d*) Le=0.86, $N=-1$, $Ra_m=95114$; (*e*) corresponding bifurcation diagram in terms of Ψ_{max}

since the maxima of the stream function are not shown to have a fixed location in space but move horizontally from left to right (Fig. 10), as does the characteristic plumelike shape in the temperature field. Another evidence for this is the fact that the oscillations develop much faster than the long times required by SWs (e.g., Fig. 4) and the times needed to reach the final saturated state are much shorter. The path length for the horizontal movement is now shorter than in the rectangular case, since the long inclined surface inhibits the further horizontal translation of cells. With the same reasoning as in the rectangular case (Fig. 5), a dimensionless wave speed may be calculated as the inverse of the period of the TW and its value is shown in Fig. 10.

At the lower values of N, $N=-0.5$ and $N=-0.1$, and for both Le=2 and Le=5, the phenomena observed exhibit similarities since transcritical bifurcations with even-numbered cell patterns are obtained. The supercritical branch is characterized by a a flow field with two main cells and originates at $Ra^{sup}=0$. The subcritical branch is, in general, a four-cell branch, first being captured at relatively high Rayleigh numbers ($Ra_m=30,000$ or higher) and reverting to the two-cell branch when traced backwards by reducing Ra_m. This situation, along with the corresponding flow and temperature fields, is depicted in Fig. 11 for Le=2, using full (open) symbols for forward (backard) movement along the steady branches unless otherwise specified. The only case where no four-cell branch was observed was for Le=5 and $N=-0.5$, where instead the supercritical branch with $Ra^{sup}=0$ transitioned to a two-cell subcritical branch at $Ra_m=3100$ upon increasing Ra_m, after going through a periodic oscillatory state, which was found to be stable only around $Ra_m=3000$ (Fig. 12(*a*)). The Nusselt number diagram for these branches is also shown in Fig. 12(*b*) where it may be observed that the subcritical branch is characterized by a much higher heat transfer rate compared to the supercritical branch, for which there is only a slight deviation from the conduction value.

Some additional aspects of the results for Le=2 and $N=-0.5$ are shown in Fig. 13. An interesting observation in the flow field is that for the supercritical two-cell branch shown in Fig. 11, if

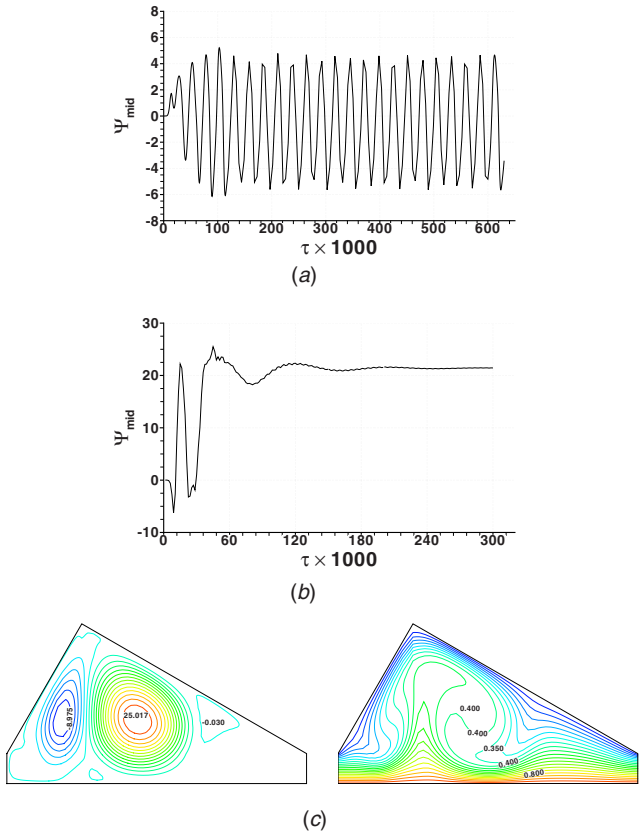

Fig. 8 Oscillatory and steady flow in the trapezoidal enclosure with Le=2, *N*=−1. Midpoint stream function history is shown at (*a*) Ra_H=35,000 and (*b*) Ra_H=120,000, along with streamlines and isotherms (*c*) for case (*b*).

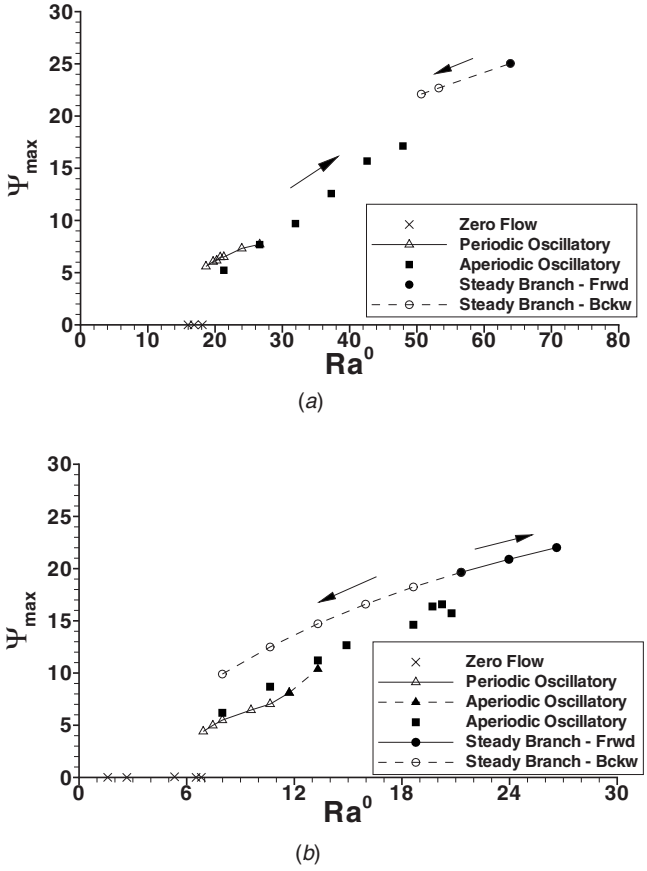

Fig. 9 Oscillatory and steady branches of the flow in the trapezoidal enclosure with *N*=−1 and (*a*) Le=2; (*b*) Le=5

one takes the ratio of Ψ_{max} for the ccw-to the cw-rotating cell it is observed that this has an almost fixed value, roughly equal to 1.57 at small Ra_m, then switching into another constant value of approximately 1.91 at larger values (Fig. 13(*a*)). This is accompanied by a growth in the size of the ccw-rotating cell, pushing the

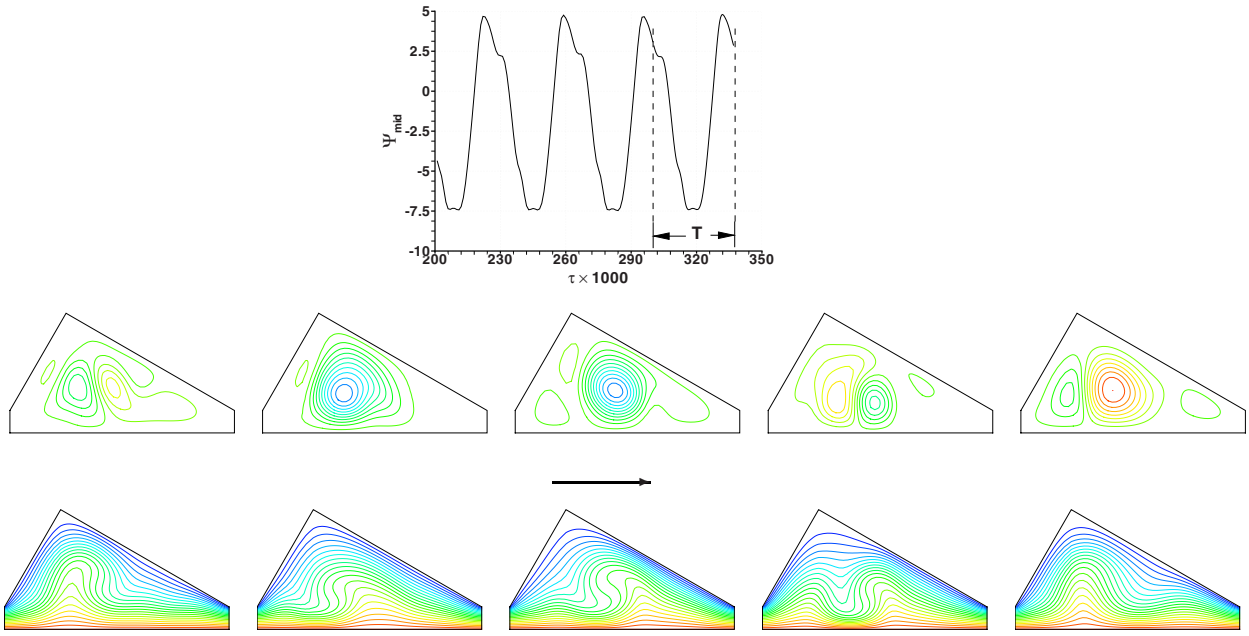

Fig. 10 Oscillatory flow- and temperature-field patterns in the trapezoidal enclosure for Le=5, *N*=−1, Ra_m=20,000 within one period *T*. Streamlines values are from −10.933 to 6.875, isotherms from 0 to 1 (21 values). Dimensionless wave speed=27.310.

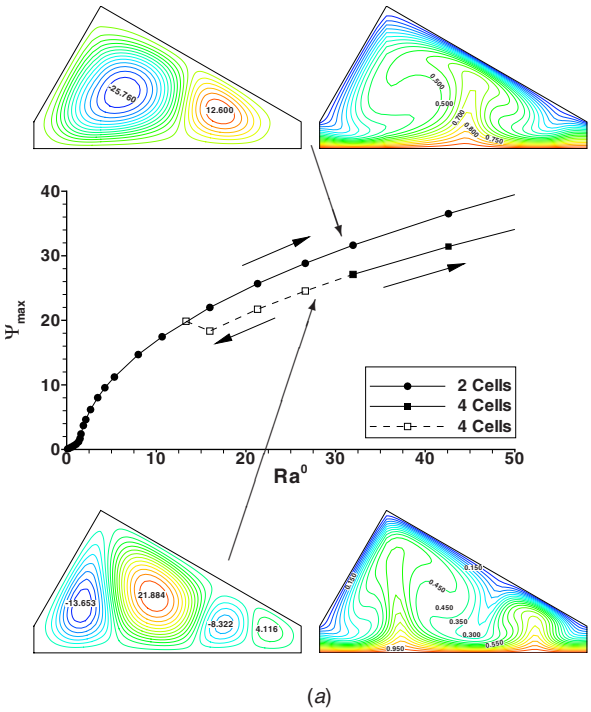

(*a*)

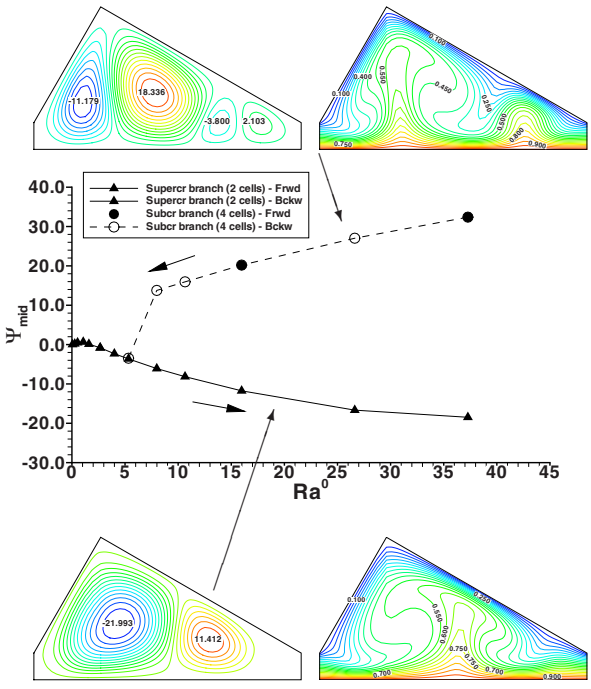

(*b*)

Fig. 11 Branches of solutions for the trapezoidal cavity with Le=2 and *N*=−0.5 (*a*) and *N*=−0.1 (*b*). One diagram for the maximum (*a*) and one for the midpoint stream function (*b*) are shown for each case (the others having a similar form), along with respective streamlines and isotherms for each branch at Ra_m=30,000 ($Ra^0 \approx 16$).

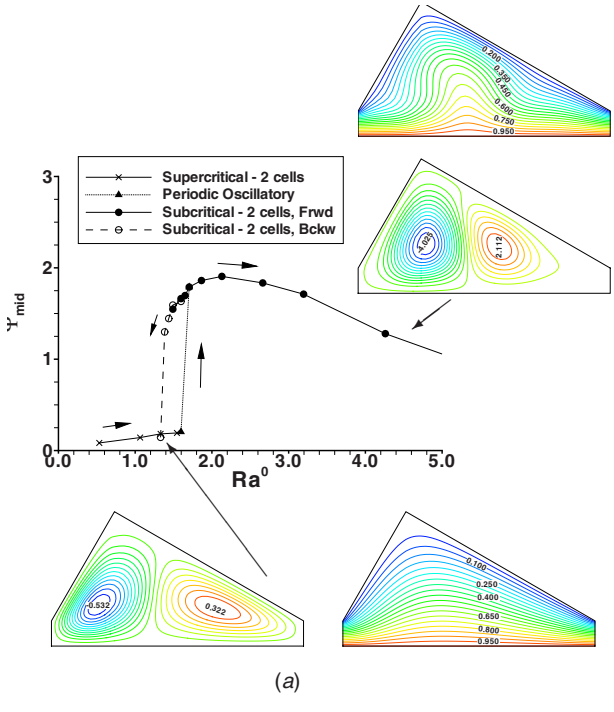

(*a*)

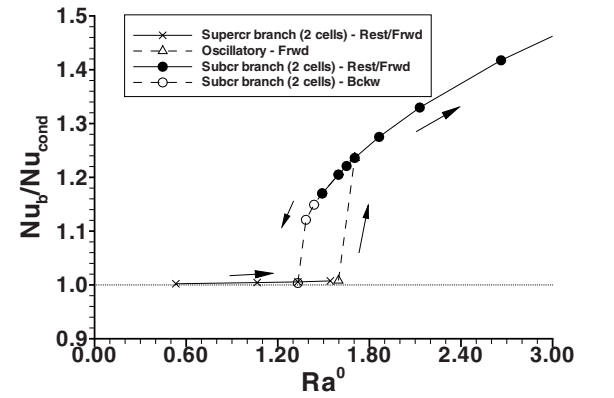

(*b*)

Fig. 12 Bifurcation diagrams for the trapezoidal cavity with Le=5, *N*=−0.5: (*a*) stream function at the cavity center, along with contour lines of stream function and temperature at Ra_m =2900 (supercritical branch) and Ra_m=3000 (subcritical branch); (*b*) mean Nusselt number, normalized with the conduction value

second cell further to the right. In Fig. 13(*b*), the Nusselt number Nu_b averaged along the bottom surface and normalized by dividing with the conduction value (Nu_{cond}) is plotted also for this case and it may be observed that the four-cell mode has higher values than the two-cell mode at the same values of Ra_m. This was always found to be the case for all parametric values where the two modes coexist, whereas in the rectangular enclosure the three-cell mode exhibited generally higher values of Nu_b than the four-cell mode (Fig. 2(*c*)). Finally, the effect of the grid dimensions is demonstrated for computations for the four-cell mode at the highest Rayleigh number considered for this case, Ra_m=120,000. As may be observed in Figs. 13(*c*) and 13(*d*), the grid with dimensions 61×61 (base grid) produces results both for Ψ_{max} and Nusselt number, which are within 1% compared to the 121×121 grid while it requires much less computational effort.

Table 2 summarizes the results obtained for both geometries for Le>1, providing a comparative overview of all modes obtained along with the corresponding ranges of Ra.

6 Conclusions

The double-diffusive natural convection with vertical driving temperature and concentration gradients has been studied numerically inside a composite trapezoidal and an equivalent rectangular

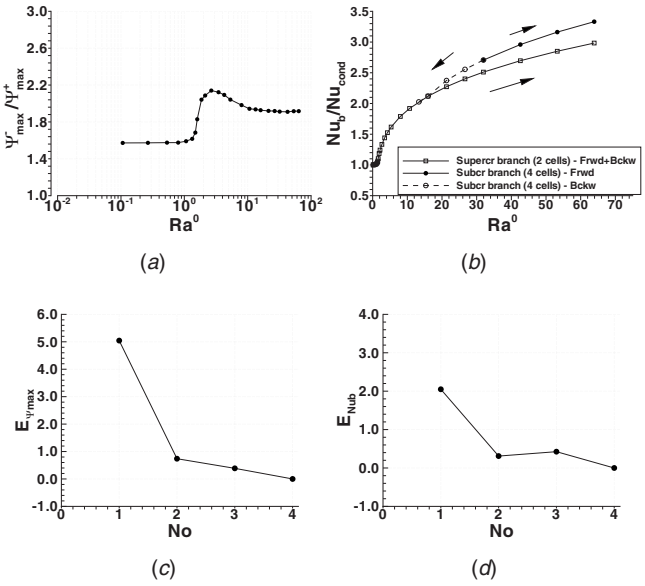

Fig. 13 Results for the trapezoidal enclosure with Le=2 and *N*=−0.5: (*a*) Cell-strength diagram for the supercritical two-cell branch, (*b*) bifurcation diagrams of the normalized Nusselt number at the bottom (heated) surface, ((*c*) and (*d*)) effect of grid dimensions on Ψ_{max} and Nusselt number (percent error) (1=31×31, 2=61×61 (base grid), 3=91×91, 4=121×121)

enclosure both of aspect ratio 0.3165 (height/width). Opposing buoyancy forces were considered ($N<0$) with Lewis numbers $\mathrm{Le}<1$ corresponding to the system air/water vapor and other air-based mixtures with $\mathrm{Le}>1$. In the former case, the onset of convection in the rectangular geometry is always of supercritical nature, with a multiplicity of steady solutions with flow fields of three, four, and five flow cells. These correspond to primary and secondary pitchfork bifurcations. A transition into a periodic, oscillatory behavior at higher Rayleigh numbers has been observed. In the trapezoidal geometry the onset of convection is supercritical with two flow cells, whereas transition to oscillatory flow at high Ra takes place. For $\mathrm{Le}>1$, overstability at onset of convection in the rectangular enclosure is observed at buoyancy ratio $N=-1$, originally in the form of SWs, but then TWs or MWs at higher Ra have been observed, suceeded first by aperiodic oscillations then changing into steady convection. At lower values of N, the SW is the preferred mode of oscillations and supercritical onset of convection is also possible. In the trapezoidal enclosure case, TWs are the prevailing mode in the oscillatory onset of convection at high values of N, whereas steady, transcritical bifurcations are present at lower values of N, with the supercritical branch originating at $\mathrm{Ra}=0$. Only an even number of flow cells (two or four) have appeared in the flow field, with the subcritical branch characterized by four cells in most cases.

The diversity of expected steady and oscillatory states should be taken into account in the numerical simulation of natural convection problems in relevant practical applications involving mixtures (such as solar stills), whereby a critical issue is also the type of initial conditions used to start the computations. Besides, inclined boundaries and asymmetry lead to significantly different stability behaviors for enclosures of the same aspect ratio and cross-sectional area.

Nomenclature

A = dimensionless average height (or aspect ratio) of the enclosure $A=H_m/L$
c = solute concentration (kg solute/kg mixture)
C = dimensionless concentration $C=(c-c_t)/\Delta c$
D = mass diffusivity for solute (m^2/s)
g = magnitude of the gravitational acceleration (m/s^2)
H = maximum vertical height of the enclosure (m)
H_1 = height of the vertical side walls of the enclosure (m)
H_m = average height of the enclosure $H_m=0.5(H+H_1)$ (m)

Table 2 Summary of results for both geometries considered: ranges of Ra_m for each regime obtained for Le>1 at the various values of *N*

	Rectangular enclosure			Trapezoidal enclosure		
N	−1	−0.5	−0.1	−1	−0.5	−0.1
			Le=2			
Zero flow	<25,000	<6500	<2400	<35,000	—	—
Periodic oscil. (SW)	25,000–90,000 (three and two cells)	6700–7250 (three cells)	—	—	—	—
Periodic oscil. (TW)	—	—	—	35,000–50,000	—	—
Aperiodic oscil.	100,000–170,000	—	—	60,000–100,000	—	—
Steady, two cells	—	—	—	⩾95,000 (SOC)	⩾0 (Supercr.)	⩾0 (Supercr.)
Steady, three cells	⩾170,000 (SOC)	⩾6500 (SOC)	⩾2400 (Supercr.)	—	—	—
Steady, four cells	—	⩾9000 (Subcr.)	⩾3000 (Subcr.)	—	⩾30,000 (Subcr.)	⩾15,000 (Subcr.)
			Le=5			
Zero flow	<11,000	<4200	<2800	⩽12,800	—	—
Periodic oscil. (SW)	11,000–24,000 (three and two cells)	4200–4800 (three cells)	2800–2900 (three cells)	—	—	—
Periodic oscil. (TW or MW)	25,000–29,000 (TW)	5000–5400 (MW)	—	13,000–20,000 (TW)	3000 (TW)	—
Aperiodic oscil.	30,000–60,000	—	—	22,000–39,000	—	—
Steady, two cells	—	6500 (Asymm.)	—	15,000–50,000 (SOC)	⩾0 (Supercr.) ⩾2600 (Subcr.)	⩾0 (Supercr.)
Steady, three cells	⩾50,000 (SOC)	⩾5300 (SOC)	⩾2550 (SOC)	—	—	—
Steady, four cells	⩾40,000 (SOC)	⩾7000 (Subcr.)	⩾4000 (Subcr.)	—	—	⩾15,000 (Subcr.)

$\mathbf{J}$ = Jacobian of the coordinate transformation matrix $\mathbf{J}=\det(\partial x_i/\partial \xi_j)$

L = length of base of the enclosure (m)

Le = Lewis number $\mathrm{Le}=\alpha/D=\mathrm{Sc}/\mathrm{Pr}$

N = ratio of buoyancy forces $N=\beta^*\Delta c/\beta\Delta T=\mathrm{Ra}_c/\mathrm{Ra}_L$

Nu = Nusselt number averaged over a surface $\mathrm{Nu}=\int_0^1 \mathrm{Nu}_s ds$

Nu_s = local Nusselt number varying along a surface $\mathrm{Nu}_s=(\partial\theta/\partial n)_w$

Pr = Prandtl number of fluid $\mathrm{Pr}=\nu/\alpha$

Ra_c = concentration(solutal) Rayleigh number based on the enclosure base $\mathrm{Ra}_c=g\beta^*\Delta cL^3/\nu\alpha^2$

Ra_L = thermal Rayleigh number based on the enclosure base $\mathrm{Ra}_L=g\beta\Delta TL^3/\nu\alpha$

Ra_m = thermal Rayleigh number based on the average height H_m of the enclosure $\mathrm{Ra}_m=g\beta\Delta TH_m^3/\nu\alpha=A^3\mathrm{Ra}_L$

Sc = Schmidt number $\mathrm{Sc}=\nu/D$

t = physical time (s)

T = local temperature (K)

x,y = vertical and horizontal Cartesian coordinate distance respectively (m)

X,Y (or X_i) = dimensionless vertical and horizontal Cartesian coordinate distance, respectively, $X=x/L$, $Y=y/L$

u,v = vertical and horizontal Cartesian velocity components, respectively (m/s)

U,V = dimensionless Cartesian velocity components $(U,V)=(u/(\alpha/L),v/(\alpha/L))$

Greek Symbols

α = thermal diffusivity of air (m^2/s)

β = volumetric coefficient of thermal expansion $\beta\equiv-(1/\rho)(\partial\rho/\partial T)_p$ (K^{-1})

β^* = volumetric coefficient of expansion with concentration $\beta^*\equiv-(1/\rho)(\partial\rho/\partial c)_p$ (kg^{-1})

Δc = vertical concentration difference $\Delta c=c_b-c_t$

ΔT = vertical temperature difference $\Delta T=T_b-T_t$

θ = dimensionless temperature $\theta=(T-T_t)/\Delta T$

ξ, η (or ξ_j) = coordinates in the curvilinear (transformed system)

ν = kinematic viscosity of air (m^2/s)

τ = dimensionless time $\tau=t/(L^2/\alpha)$

Ψ = dimensionless stream function $U=-\partial\Psi/\partial Y$, $V=\partial\Psi/\partial X$

Ω = dimensionless vorticity $\Omega=\partial V/\partial X-\partial U/\partial Y$

Subscripts

b = value of a variable at the bottom boundary

t = value of a variable at the top boundary

[2]It should be noted that here Ra_c is defined using the thermal diffusivity α practice, which has been adopted by several authors [1,3], while others use the mass diffusivity for solute D instead.

References

[1] Turner, J. S., 1985, "Multicomponent Convection," Annu. Rev. Fluid Mech., **17**, pp. 11–44.

[2] Gebhardt, B., Jaluria, Y., Mahajan, R. L., and Sammakia, B., 1988, *Buoyancy-Induced Flows and Transport*, Hemisphere, Washington.

[3] Huppert, H. E., and Moore, D. R., 1976, "Nonlinear Double-Diffusive Convection," J. Fluid Mech., **78**, pp. 821–854.

[4] Da Costa, L. N., Knobloch, E., and Weiss, N. O., 1981, "Oscillations in Double-Diffusive Convection," J. Fluid Mech., **109**, pp. 25–43.

[5] Deane, A. E., Knobloch, E., and Toomre, J., 1987, "Traveling Waves and Chaos in Thermosolutal Convection," Phys. Rev. A, **36**(6), pp. 2862–2869.

[6] Moore, D. R., Weiss, N. O., and Wilkins, J. M., 1991, "Asymmetric Oscillations in Thermosolutal Convection," J. Fluid Mech., **233**, pp. 561–585.

[7] Moore, D. R., and Weiss, N. O., 2000, "Resonant Interactions in Thermosolutal Convection," Proc. R. Soc. London, Ser. A, **456**, pp. 39–62.

[8] Mamou, M., Vasseur, P., and Hasnaoui, M., 2001, "On Numerical Stability Analysis of Double-Diffusive Convection in Confined Enclosures," J. Fluid Mech., **433**, pp. 209–250.

[9] Ouriemi, M., Vasseur, P., and Bahloul, A., 2005, "Natural Convection of a Binary Fluid in a Slightly Inclined Shallow Cavity," Numer. Heat Transfer, Part A, **48**(6), pp. 547–565.

[10] Xin, S., Le Quéré, P., and Tuckerman, L. S., 1998, "Bifurcation Analysis of Double-Diffusive Convection With Opposing Horizontal Thermal and Solutal Gradients," Phys. Fluids, **10**(4), pp. 850–858.

[11] Bergeon, A., Ghorayeb, K., and Mojtabi, A., 1999, "Double Diffusive Instability in an Inclined Cavity," Phys. Fluids, **11**(3), pp. 549–559.

[12] Walden, R. W., Kolodner, P., Passner, A., and Surko, C. M., 1985, "Traveling Waves and Chaos in Convection in Binary Fluid Mixtures," Phys. Rev. Lett., **55**(5), pp. 496–499.

[13] Moses, E., and Steinberg, V., 1986, "Flow Patterns and Nonlinear Behavior of Traveling Waves in a Convective Binary Fluid," Phys. Rev. A, **34**(1), pp. 693–697.

[14] Lhost, O., and Platten, J. K., 1988, "Transitions Between Steady States, Traveling Waves, and Modulated Waves in the System Water-Isopropanol Heated From Below," Phys. Rev. A, **38**(6), pp. 3147–3150.

[15] Lhost, O., and Platten, J. K., 1989, "Experimental Study of the Transition From Nonlinear Traveling Waves to Steady Overturning Convection in Binary Mixtures," Phys. Rev. A, **40**(8), pp. 4552–4557.

[16] Ohlsen, D. R., Yamamoto, S. Y., Surko, C. M., and Kolodner, P., 1990, "Transition From Traveling-Wave to Stationary Convection in Fluid Mixtures," Phys. Rev. Lett., **65**,(12–17), pp. 1431–1434.

[17] Linz, S. J., Lücke, M., Müeller, H. W., and Niederländer, J., 1988, "Convection in Binary Fluid Mixtures: Traveling Waves and Lateral Currents," Phys. Rev. A, **38**(11), pp. 5727–5742.

[18] Papanicolaou, E., Voropoulos, K., and Belessiotis, V., 2002, "Natural Convective Heat Transfer in an Asymmetric Greenhouse-Type Solar Still-Effect of Angle of Inclination," Numer. Heat Transfer, Part A, **42**(8), pp. 855–880.

[19] Papanicolaou, E., and Belessiotis, V., 2005, "Double-Diffusive Natural Convection in an Asymmetric Trapezoidal Enclosure: Unsteady Behavior in the Laminar- and the Turbulent-Flow Regime," Int. J. Heat Mass Transfer, **48**(1), pp. 191–209.

[20] Ridouane, E. H., Campo, A., and Hasnaoui, M., 2006, "Benefits Derivable From Connecting the Bottom and Top Walls of Attic Enclosures With Insulated Vertical Side Walls," Numer. Heat Transfer, Part A, **49**(2), pp. 175–193.

[21] Holtzman, G. A., Hill, R. W., and Ball, K. S., 2000, "Laminar Natural Convection in Isosceles Triangular Enclosures Heated From Below and Symmetrically Cooled From Above," ASME J. Heat Transfer, **122**(3), pp. 485–491.

[22] Ridouane, E. H., and Campo, A., 2006, "Formation of a Pitchfork Bifurcation in Thermal Convection Flow Inside an Isosceles Triangular Cavity," Phys. Fluids, **18**(7), 074102.

[23] Jackson, C. P., and Winters, K. H., 1984, "A finite-Element Study of the BÉnard Problem Using Parameter-Stepping and Bifurcation Search," Int. J. Numer. Methods Fluids, **4**(2), pp. 127–145.

[24] Metzener, P., 1986, "The Effect of Rigid Sidewalls on Nonlinear Two-Dimensional BÉnard Convection," Phys. Fluids, **29**(5), pp. 1373–1377.

[25] Riley, D. S., and Winters, K. H., 1989, "Modal Exchange Mechanisms in Lapwood Convection," J. Fluid Mech., **204**, pp. 325–358.

[26] Tuckerman, L. S., and Barkley, D., 1990, "Bifurcation Analysis of the Eckhaus Instability," Physica D, **46**(1), pp. 57–86.

Vertical Free Convective Boundary-Layer Flow in a Bidisperse Porous Medium

D. A. S. Rees
Department of Mechanical Engineering,
University of Bath,
Bath BA2 7AY, UK

D. A. Nield
Department of Engineering Science,
University of Auckland,
Private Bag 92019,
Auckland 1142, New Zealand

A. V. Kuznetsov
Department of Mechanical and Aerospace Engineering,
North Carolina State University,
Campus Box 7910,
Raleigh, NC 27695-7910

In this article, we study the effect of adopting a two-temperature and two-velocity model, appropriate to a bidisperse porous medium (BDPM), on the classical Cheng–Minkowycz study of vertical free convection boundary-layer flow in a porous medium. It is shown that the boundary-layer equations can be expressed in terms of three parameters: a modified volume fraction, a modified thermal conductivity ratio, and a third parameter incorporating both thermal and BDPM properties. A numerical simulation of the developing boundary layer is guided by a near-leading-edge analysis and supplemented by a far-field analysis. The study is completed by a presentation of numerical simulations of the elliptic equations in order to determine how the adoption of the BDPM model affects the thermal fields in the close vicinity of the origin. [DOI: 10.1115/1.2943304]

Keywords: bidisperse porous medium, free convection, numerical simulation, asymptotic analysis

1 Introduction

A bidisperse porous medium (BDPM, see Fig. 1), as informally defined by Chen et al. [1,2], is composed of clusters of large particles that are agglomerations of small particles. Thus, there are macropores between the clusters and micropores within them. Applications are found in bidisperse adsorbent or bidisperse capillary wicks in a heat pipe. Since the bidisperse wick structure significantly increases the area available for liquid film evaporation, it has been proposed for use in the evaporator of heat pipes.

A BDPM may thus be looked at as a standard porous medium in which the solid phase is replaced by another porous medium, whose temperature may be denoted by T_p if local thermal equilibrium (LTE) is assumed within each cluster. We can then talk about the f-phase (the macropores) and the p-phase (the remainder of the structure). An alternative way of looking at the structure is to regard it as a porous medium in which fractures or tunnels have been introduced. One can then think of the f-phase as being a "fracture phase" and the p-phase as being a "porous phase."

The Darcy model for the steady-state momentum transfer in a BDPM is represented by the following pair of coupled equations for the Darcy velocities $\mathbf{v}^*_f$ and $\mathbf{v}^*_p$, where the asterisks denote dimensional variables,

$$\mathbf{G} = \left(\frac{\mu}{K_f}\right)\mathbf{v}^*_f + \zeta(\mathbf{v}^*_f - \mathbf{v}^*_p) \tag{1a}$$

$$\mathbf{G} = \left(\frac{\mu}{K_p}\right)\mathbf{v}^*_p + \zeta(\mathbf{v}^*_p - \mathbf{v}^*_f) \tag{1b}$$

Here, $\mathbf{G}$ is the negative of the applied pressure gradient, μ is the fluid viscosity, K_f and K_p are the permeabilities of the two phases, and ζ is the coefficient for momentum transfer between the two phases.

These equations were applied by Nield and Kuznetsov [3,4] to forced convection in a channel and by Nield and Kuznetsov [5] to the Horton–Rogers–Lapwood problem (the paradigmatic problem for natural convection in an enclosed region). These studies were reviewed by Nield and Kuznetsov [6].

In this article, we apply the two-velocity two-temperature formulation to a problem that is paradigmatic for external natural convection in a porous medium, namely, the problem of convection past a vertical plate, a problem first considered by Cheng and Minkowycz [7]. The problem leads naturally to a boundary-layer formulation. We are guided by a study of Rees and Pop [8]. These authors used a model incorporating two temperatures (local thermal nonequilibrium (LTNE)) but a single velocity. Related work is presented in Mohamad [9], Rees and Pop [10], and Haddad et al. [11,12]. For the more general aspects of convection in a porous medium past a vertical plate, the reader is referred to the survey by Nield and Bejan [13]. A preliminary report on this topic was presented by Nield and Kuznetsov [14].

2 Analysis

We consider steady two-dimensional flow in a BDPM induced by a vertical heated plate held at the constant temperature T_w and embedded in the BDPM with ambient temperature T_∞. The equations of continuity (expressing conservation of mass) for the velocity components in the two phases are

$$\frac{\partial u_f^*}{\partial x^*} + \frac{\partial v_f^*}{\partial y^*} = 0 \tag{2a}$$

$$\frac{\partial u_p^*}{\partial x^*} + \frac{\partial v_p^*}{\partial y^*} = 0 \tag{2b}$$

We note that in the traditional Darcy formulation, the pressure is an intrinsic quantity, i.e., it is the pressure in the fluid. We recognize that in a BDPM, the fluid occupies all of the f-phase and a fraction of the p-phase. We denote the volume fraction of the f-phase by ϕ (something that in a regular porous medium would be called the porosity) and the porosity in the p-phase by ε. Thus, $1-\phi$ is the volume fraction of the p-phase, and the volume fraction of the BDPM occupied by the fluid is $\phi+(1-\phi)\varepsilon$. The volume average of the temperature over the fluid is

$$T_F^* = \frac{\phi T_f^* + (1-\phi)\varepsilon T_p^*}{\phi + (1-\phi)\varepsilon} \tag{3}$$

Contributed by the Heat Transfer Division of ASME for publication in the JOURNAL OF HEAT TRANSFER. Manuscript received June 14, 2007; final manuscript received October 24, 2007; published online July 11, 2008. Review conducted by Jamal Seyed-Yagoobi.

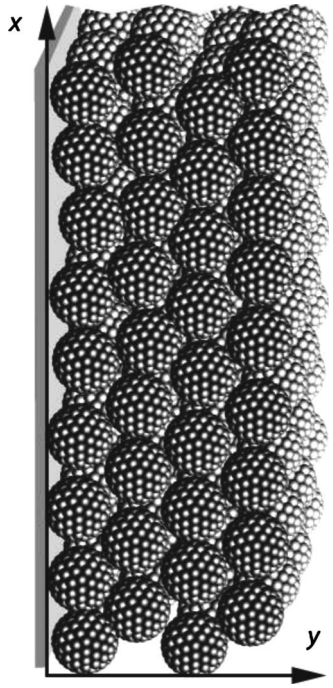

Fig. 1 Sketch of a BDPM adjacent to a vertical plate

The drag force (per unit volume) balances the gradient of the excess pressure over hydrostatic. Our basic hypothesis is that in a BDPM, the drag is increased by an amount $\zeta(\mathbf{v}_f^* - \mathbf{v}_p^*)$ for the f-phase and decreased by the same amount for the p-phase. Accordingly, we write the momentum equations as

$$\frac{\partial p^*}{\partial x^*} = -\frac{\mu}{K_f} u_f^* - \zeta(u_f^* - u_p^*) + \rho_F \hat{g}\hat{\beta}(T_F^* - T_\infty) \tag{4a}$$

$$\frac{\partial p^*}{\partial x^*} = -\frac{\mu}{K_p} u_p^* - \zeta(u_p^* - u_f^*) + \rho_F \hat{g}\hat{\beta}(T_F^* - T_\infty) \tag{4b}$$

$$\frac{\partial p^*}{\partial y^*} = -\frac{\mu}{K_f} v_f^* - \zeta(v_f^* - v_p^*) \tag{4c}$$

$$\frac{\partial p^*}{\partial y^*} = -\frac{\mu}{K_p} v_p^* - \zeta(v_p^* - v_f^*) \tag{4d}$$

Here, ρ_F is the density of the fluid, $\hat{\beta}$ is the volumetric thermal expansion coefficient of the fluid, and $\hat{g}$ is the gravitational acceleration. In writing Eqs. (4a) and (4b), we have recognized that variations of pressure due to buoyancy are intrinsic (rather than volume averaged) quantities, and so the usual procedure of averaging over a representative elementary volume is not necessarily appropriate. In the case of buoyancy, the solid and thermal conductivities are not involved, and so it is reasonable to treat the thermal aspect of buoyancy in a special way. It was found in Ref. [5] that a coherent mathematical representation required that the buoyancy terms in Eqs. (4a) and (4b) be the same.

The thermal energy equations are taken as

$$\phi(\rho c)_f \mathbf{v}_f^* \cdot \nabla T_f^* = \phi k_f \nabla^2 T_f^* + h(T_p^* - T_f^*) \tag{5a}$$

$$(1-\phi)(\rho c)_p \mathbf{v}_p^* \cdot \nabla T_p^* = (1-\phi) k_p \nabla^2 T_p^* + h(T_f^* - T_p^*) \tag{5b}$$

Here, c denotes the specific heat at constant pressure, k denotes the thermal conductivity, and h is an interphase heat transfer coefficient (incorporating the specific area). The precise definition of k_p is not important for our present purpose. It could be estimated by the weighted average, taken over the p-phase, of the fluid and solid conductivities.

It should be noted that since the velocity in the p-phase will generally be small in comparison to that in the macropores, it is a good approximation to assume thermal equilibrium within the p-phase. We assume homogeneity on the global scale. For further discussion on LTE, the reader is referred to Rees et al. [15].

We introduce dimensionless variables as follows:

$$(x^*, y^*) = d(\hat{x}, \hat{y}), \quad p^* = \frac{k_f \mu}{(\rho c)_f K_f} p \tag{6}$$

$$(u_f^*, v_f^*) = \frac{\phi k_f}{(\rho c)_f d}(\hat{u}_f, \hat{v}_f), \quad (u_p^*, v_p^*) = \frac{(1-\phi)k_p}{(\rho c)_p d}(\hat{u}_p, \hat{v}_p) \tag{7}$$

$$T_f^* = (T_w - T_\infty)\theta_f + T_\infty, \quad T_p^* = (T_w - T_\infty)\theta_p + T_\infty \tag{8}$$

We also introduce the stream functions $\hat{\psi}_f$ and $\hat{\psi}_p$ defined so that

$$\hat{u}_f = \frac{\partial \hat{\psi}_f}{\partial \hat{y}}, \quad \hat{v}_f = -\frac{\partial \hat{\psi}_f}{\partial \hat{x}}, \quad \hat{u}_p = \frac{\partial \hat{\psi}_p}{\partial \hat{y}}, \quad \hat{v}_p = -\frac{\partial \hat{\psi}_p}{\partial \hat{x}} \tag{9}$$

(We use the sign convention in Rees and Pop [8] rather than that in Nield and Kuznetsov [5].) We define a Rayleigh number R based on properties in the f-phase by

$$R = \frac{\rho_F \hat{g}\hat{\beta}(T_w - T_\infty) K_f d}{\mu \phi k_f / (\rho c)_f} \tag{10}$$

Elimination of the pressure from Eqs. (4a)–(4d) then leads to

$$(1+\sigma_f)\nabla^2 \hat{\psi}_f - \beta\sigma_f \nabla^2 \hat{\psi}_p = R\frac{\partial \theta_F}{\partial \hat{y}} \tag{11a}$$

$$-\sigma_f \nabla^2 \hat{\psi}_f + \beta\left(\frac{1}{K_r} + \sigma_f\right)\nabla^2 \hat{\psi}_p = R\frac{\partial \theta_F}{\partial \hat{y}} \tag{11b}$$

where

$$\frac{\partial \theta_F}{\partial \hat{y}} = \frac{\varphi \dfrac{\partial \theta_f}{\partial \hat{y}} + (1-\phi)\varepsilon \dfrac{\partial \theta_p}{\partial \hat{y}}}{\phi + (1-\phi)\varepsilon} \tag{12}$$

Here, we have introduced the dimensionless parameters

$$\sigma_f = \frac{\zeta K_f}{\mu}, \quad \beta = \frac{(1-\phi)k_p(\rho c)_f}{\phi k_f (\rho c)_p} \tag{13}$$

Thus, σ_f is an interphase momentum transfer parameter, while β is a modified thermal diffusivity ratio. Also, the thermal energy equations ((5a) and (5b)) become

$$\nabla^2 \theta_f = \hat{h}(\theta_f - \theta_p) + \frac{\partial \hat{\psi}_f}{\partial \hat{y}}\frac{\partial \theta_f}{\partial \hat{x}} - \frac{\partial \hat{\psi}_f}{\partial \hat{x}}\frac{\partial \theta_f}{\partial \hat{y}} \tag{14a}$$

$$\nabla^2 \theta_p = \gamma\hat{h}(\theta_p - \theta_f) + \frac{\partial \hat{\psi}_p}{\partial \hat{y}}\frac{\partial \theta_p}{\partial \hat{x}} - \frac{\partial \hat{\psi}_p}{\partial \hat{x}}\frac{\partial \theta_p}{\partial \hat{y}} \tag{14b}$$

where

$$\gamma = \frac{\phi k_f}{(1-\phi)k_p}, \quad \hat{h} = \frac{hd^2}{\phi k_f} \tag{15}$$

Thus, γ is a modified thermal conductivity ratio and $\hat{h}$ is an interphase heat transfer parameter.

Next, we introduce the boundary-layer scaling,

$$\hat{x} = x, \quad \hat{y} = R^{-1/2} y, \quad \hat{\psi}_f = R^{1/2}\psi_f, \quad \hat{\psi}_p = R^{1/2}\psi_p \tag{16}$$

and the shorthand notation

$$\tau = \frac{\phi}{\phi + (1-\phi)\varepsilon}, \quad K_r = \frac{K_p}{K_f} \tag{17}$$

Then, we get

$$(1+\sigma_f)\frac{\partial^2 \hat{\psi}_f}{\partial y^2} - \beta\sigma_f \frac{\partial^2 \hat{\psi}_p}{\partial y^2} = \tau\frac{\partial \theta_f}{\partial y} + (1-\tau)\frac{\partial \theta_p}{\partial y} \tag{18a}$$

$$-\sigma_f \frac{\partial^2 \hat{\psi}_f}{\partial y^2} + \beta\left(\frac{1}{K_r} + \sigma_f\right)\frac{\partial^2 \hat{\psi}_p}{\partial y^2} = \tau\frac{\partial \theta_f}{\partial y} + (1-\tau)\frac{\partial \theta_p}{\partial y} \tag{18b}$$

$$\frac{\partial^2 \theta_f}{\partial y^2} = H(\theta_f - \theta_p) + \frac{\partial \psi_f}{\partial y}\frac{\partial \theta_f}{\partial x} - \frac{\partial \psi_f}{\partial x}\frac{\partial \theta_f}{\partial y} \tag{18c}$$

$$\frac{\partial^2 \theta_p}{\partial y^2} = \gamma H(\theta_p - \theta_f) + \frac{\partial \psi_p}{\partial y}\frac{\partial \theta_p}{\partial x} - \frac{\partial \psi_p}{\partial x}\frac{\partial \theta_p}{\partial y} \tag{18d}$$

where

$$H = \hat{h}/R \tag{19}$$

The appropriate boundary conditions are

$$\psi_f = 0, \quad \psi_p = 0, \quad \theta_f = 1, \quad \theta_p = 1 \quad \text{at } y = 0 \tag{20a}$$

$$\frac{\partial \psi_f}{\partial y}, \ \frac{\partial \psi_p}{\partial y}, \ \theta_f, \theta_p \to 0 \quad \text{as } y \to \infty \tag{20b}$$

These boundary conditions allow Eqs. (18*a*) and (18*b*) to be integrated once to yield

$$(1+\sigma_f)\frac{\partial \hat{\psi}_f}{\partial y} - \beta\sigma_f \frac{\partial \hat{\psi}_p}{\partial y} = \tau\theta_f + (1-\tau)\theta_p \tag{21a}$$

$$-\sigma_f \frac{\partial \hat{\psi}_f}{\partial y} + \beta\left(\frac{1}{K_r} + \sigma_f\right)\frac{\partial \hat{\psi}_p}{\partial y} = \tau\theta_f + (1-\tau)\theta_p \tag{21b}$$

We now introduce the usual boundary-layer transformation appropriate to the Cheng–Minkowycz problem:

$$\psi_f = x^{1/2} f(x,\eta), \quad \psi_p = x^{1/2} g(x,\eta) \tag{22a}$$

$$\theta_f = \theta_f(x,\eta), \quad \theta_p = \theta_p(x,\eta) \tag{22b}$$

where

$$\eta = \frac{y}{x^{1/2}} \tag{23}$$

One then has the system

$$(1+\sigma_f)f' - \beta\sigma_f g' = \tau\theta_f + (1-\tau)\theta_p \tag{24a}$$

$$-\sigma_f f' + \beta\left(\frac{1}{K_r} + \sigma_f\right)g' = \tau\theta_f + (1-\tau)\theta_p \tag{24b}$$

$$\theta_f'' + \tfrac{1}{2} f\theta_f' = Hx(\theta_f - \theta_p) + x(f'\theta_{fx} - \theta_f' f_x) \tag{24c}$$

$$\theta_p'' + \tfrac{1}{2} g\theta_p' = \gamma Hx(\theta_p - \theta_f) + x(g'\theta_{px} - \theta_p' g_x) \tag{24d}$$

subject to the boundary conditions

$$f = 0, \quad g = 0, \quad \theta_f = 1, \quad \theta_p = 1 \quad \text{at } \eta = 0 \tag{24e}$$

$$\theta_f, \theta_p \to 0 \quad \text{as } \eta \to \infty \tag{24f}$$

It is worth noting that the boundary conditions (24*f*), together with Eqs. (24*a*) and (24*b*), imply that $f', g' \to 0$ as $\eta \to \infty$. In these equations, the primes denote derivatives with respect to η and the x-subscripts denote derivatives with respect to x.

Equations (24*a*)–(24*d*) contain six parameters. Before we proceed further, we demonstrate that the number of parameters can be reduced to 3. The transformation

$$f(\eta) = C_f F(\eta) \tag{25a}$$

$$g(\eta) = C_p G(\eta) \tag{25b}$$

where

$$C_f = \frac{1 + 2K_r\sigma_f}{1 + \sigma_f + K_r\sigma_f} = \frac{\mu + 2\zeta K_p}{\mu + \zeta K_f + \zeta K_p} \tag{26a}$$

$$C_p = \frac{K_r + 2K_r\sigma_f}{\beta(1 + \sigma_f + K_r\sigma_f)} = \frac{\phi}{1-\phi}\left(\frac{K_p}{K_f}\right)\left(\frac{k_f/(\rho c)_f}{k_p/(\rho c)_p}\right)C_f \tag{26b}$$

reduces Eqs. (24*a*), (24*b*), and (24*e*) to the form

$$F' = \tau\theta_f + (1-\tau)\theta_p \tag{27a}$$

$$G' = \tau\theta_f + (1-\tau)\theta_p \tag{27b}$$

$$F = 0, \quad G = 0, \quad \theta_f = 1, \quad \theta_p = 1 \quad \text{at } \eta = 0 \tag{27c}$$

From Eqs. (27*a*) and (27*b*), $F - G$ has zero derivative everywhere, and by Eq. (27*c*) has zero value at $\eta = 0$, and so $F - G$ is identically zero; that is, $F \equiv G$. Using this fact, Eqs. (24*c*) and (24*d*) then reduce to

$$\theta_f'' + \frac{C_f}{2} F\theta_f' = Hx(\theta_f - \theta_p) + C_f x(F'\theta_{fx} - \theta_f' F_x) \tag{27d}$$

$$\theta_p'' + \frac{C_p}{2} F\theta_p' = \gamma Hx(\theta_p - \theta_f) + C_p x(F'\theta_{px} - \theta_p' F_x) \tag{27e}$$

We now introduce

$$A = (C_f^{\,2} + C_p^{\,2})^{1/2} \tag{28a}$$

$$\delta = \tan^{-1}(C_p/C_f) = \tan^{-1}\left(\frac{\phi}{1-\phi}\left(\frac{K_p}{K_f}\right)\left(\frac{k_f/(\rho c)_f}{k_p/(\rho c)_p}\right)\right) \tag{28b}$$

so that

$$C_f = A\cos\delta \tag{28c}$$

$$C_p = A\sin\delta \tag{28d}$$

and rescale so that

$$F(\eta) = \tilde{F}(\tilde{\eta})/A \tag{29a}$$

$$\eta = \tilde{\eta}/A \tag{29b}$$

At the same time, one can then eliminate the parameter H by using the transformation

$$\xi = Hx \tag{30}$$

to get the set of differential equations

$$\tilde{F}' = \tau\theta_f + (1-\tau)\theta_p \tag{31a}$$

$$\theta_f'' + \frac{\cos\delta}{2}\tilde{F}\theta_f' = \xi(\theta_f - \theta_p) + \cos\delta\,\xi(\tilde{F}'\theta_{f\xi} - \theta_f'\tilde{F}_\xi) \tag{31b}$$

$$\theta_p'' + \frac{\sin\delta}{2}\tilde{F}\theta_p' = \gamma\xi(\theta_p - \theta_f) + \sin\delta\,\xi(\tilde{F}'\theta_{p\xi} - \theta_p'\tilde{F}_\xi) \tag{31c}$$

The primes now denote derivatives with respect to $\tilde{\eta}$. These differential equations are subject to the boundary conditions,

$$\tilde{F} = 0, \quad \theta_f = 1, \quad \theta_p = 1 \quad \text{at } \xi = 0 \tag{31d}$$

$$\theta_f, \theta_p \to 0 \quad \text{as } \xi \to \infty \tag{31e}$$

We observe that we now have just three parameters, τ, γ, and δ, as defined by Eqs. (17), (15), and (28*b*), respectively, representing a volume fraction, a modified thermal conductivity ratio, and a

combination of thermal and BDPM parameters. The dependent variables are a single stream function and two temperatures.

3 Analysis Near the Leading Edge

We now perform an expansion in powers of ξ to third order starting from equations Eq. (31*a*)–(31*c*). Accordingly, we make the expansion

$$(\tilde{F},\theta_f,\theta_p)=(\tilde{F}_0,\theta_{f0},\theta_{p0})+\xi(\tilde{F}_1,\theta_{f1},\theta_{p1})+\xi^2(\tilde{F}_2,\theta_{f2},\theta_{p2})+\xi^3(\tilde{F}_3,\theta_{f3},\theta_{p3})+\ldots \tag{32}$$

and obtain the equations

$$\tilde{F}_n{}'=\tau\theta_{fn}+(1-\tau)\theta_{pn}\quad \text{for } n=0,1,2,3 \tag{33a}$$

$$\theta_{f0}''+\frac{\cos\delta}{2}\tilde{F}_0\theta_{f0}'=0 \tag{33b}$$

$$\theta_{f1}''+\frac{\cos\delta}{2}(\tilde{F}_0\theta_{f1}'+\tilde{F}_1\theta_{f0}')=\theta_{f0}-\theta_{p0}+\cos\delta[\tilde{F}_0'\theta_{f1}-\theta_{f0}'\tilde{F}_1] \tag{33c}$$

$$\theta_{f2}''+\frac{\cos\delta}{2}(\tilde{F}_0\theta_{f2}'+\tilde{F}_1\theta_{f1}'+\tilde{F}_2\theta_{f0}')=\theta_{f1}-\theta_{p1}+\cos\delta[2(\tilde{F}_0'\theta_{f2}-\theta_{f0}'\tilde{F}_2)+(\tilde{F}_1'\theta_{f1}-\theta_{f1}'\tilde{F}_1)] \tag{33d}$$

$$\theta_{f3}''+\frac{\cos\delta}{2}(\tilde{F}_0\theta_{f3}'+\tilde{F}_1\theta_{f2}'+\tilde{F}_2\theta_{f1}'+\tilde{F}_3\theta_{f0}')=\theta_{f2}-\theta_{p2}+\cos\delta[3(\tilde{F}_0'\theta_{f3}-\theta_{f0}'\tilde{F}_3)+2(\tilde{F}_1'\theta_{f2}-\theta_{f1}'\tilde{F}_2)+(\tilde{F}_2'\theta_{f1}-\theta_{f2}'\tilde{F}_1)] \tag{33e}$$

together with similar equations for θ_p.

In particular, the zero-order system is

$$\tilde{F}'=\tau\theta_{f0}+(1-\tau)\theta_{p0} \tag{34a}$$

$$\theta_{f0}''+\frac{\cos\delta}{2}\tilde{F}\theta_{f0}'=0 \tag{34b}$$

$$\theta_{p0}''+\frac{\sin\delta}{2}\tilde{F}\theta_{p0}'=0 \tag{34c}$$

$$\tilde{F}=0,\quad \theta_{f0}=1,\quad \theta_{p0}=1\quad \text{at } x=0 \tag{34d}$$

$$\theta_{f0},\theta_{p0}\to 0\quad \text{as } x\to\infty \tag{34e}$$

For the regular (monodisperse) porous medium (the case $\sigma_f=0$, $K_r=0$, $\tau=1$, that is, for $\delta=0$, $\tau=1$) the system of equations reduces to

$$f_0'=\theta_0 \tag{35a}$$

$$\theta_{f0}''+\tfrac{1}{2}f_0\theta_{f0}'=0 \tag{35b}$$

$$\theta_{f0}=1 \tag{35c}$$

the solution of which was presented by Cheng and Minkowycz [7]. The chief features of interest are that

$$f_0\to 1.61613\quad \text{as } \eta\to\infty \tag{36a}$$

$$\theta_0'(0)=-0.44378 \tag{36b}$$

and θ_0 becomes exponentially small as $\eta\to\infty$. The numerical values are those obtained by Rees and Pop [8].

4 Analysis Far From the Leading Edge

We consider the situation when x (and therefore ξ) is asymptotically large. We expand $\tilde{F}$, θ_f, and θ_p in the form

$$(\tilde{F},\theta_f,\theta_p)=(\tilde{F}^{(0)},\theta_f^{(0)},\theta_p^{(0)})+\xi^{-1}(\tilde{F}^{(1)},\theta_f^{(1)},\theta_p^{(1)})+\ldots \tag{37}$$

Substitution into Eqs. (31*a*)–(31*c*) gives at leading order

$$\theta_f^{(0)}-\theta_p^{(0)}=0 \tag{38}$$

and hence $\theta_f^{(0)}=\theta_p^{(0)}\equiv\theta^{(0)}$, say.

Using this result, at the next order, one has

$$F_\eta^{(0)}=\theta^{(0)} \tag{39a}$$

$$\theta_{\eta\eta}^{(0)}+\frac{\cos\delta}{2}\tilde{F}^{(0)}\theta_\eta^{(0)}=\theta_f^{(1)}-\theta_p^{(1)} \tag{39b}$$

$$\theta_{\eta\eta}^{(0)}+\frac{\sin\delta}{2}\tilde{F}^{(0)}\theta_\eta^{(0)}=\gamma(\theta_p^{(1)}-\theta_f^{(1)}) \tag{39c}$$

A linear combination of the last two equations then gives

$$\theta_{\eta\eta}^{(0)}+\frac{\Gamma}{2}\tilde{F}^{(0)}\theta_\eta^{(0)}=0 \tag{39d}$$

where

$$\Gamma=\frac{\gamma\cos\delta+\sin\delta}{\gamma+1} \tag{40}$$

Then the transformation

$$\tilde{\zeta}=\Gamma^{1/2}\eta,\quad \hat{F}^{(0)}(\tilde{\zeta})=\Gamma^{1/2}\tilde{F}^{(0)}(\eta) \tag{41}$$

gives

$$\hat{F}_{\tilde{\zeta}}^{(0)}=\theta^{(0)} \tag{42a}$$

$$\theta_{\tilde{\zeta}\tilde{\zeta}}^{(0)}+\frac{1}{2}\hat{F}^{(0)}\theta_{\tilde{\zeta}}^{(0)}=0 \tag{42b}$$

The boundary conditions for this set of differential equations are

$$\hat{F}^{(0)}=0,\quad \theta^{(0)}=1\quad \text{at } \tilde{\zeta}=0 \tag{42c}$$

$$\theta^{(0)}\to 0\quad \text{as } \tilde{\zeta}\to\infty \tag{42d}$$

Thus, again, we have the system studied by Cheng and Minkowycz [7].

At the next order of asymptotic approximation, one has a homogenous linear system of differential equations and boundary conditions for $\theta_f^{(1)}$ and $\theta_p^{(1)}$, which admits an eigensolution of arbitrary magnitude. This means that we have an insoluble system of equations at $O(\xi^{-1})$. One could, in principle, proceed further by introducing $\xi^{-1}\ln\xi$ terms, as was done by Rees and Pop [8], but we judged that in the present case there would be little gain in doing so since the $\xi^{-1}\ln\xi$ and ξ^{-1} terms can only be differentiated in terms of their magnitude at exceptionally large values of ξ.

5 Numerical Solutions

Three different numerical schemes were used to obtain the results displayed in Figs. 2–6. First, a standard fourth order Runge–Kutta scheme was used together with a multiple shooting strategy to solve the small-ξ equations given in Eqs. (34*a*)–(34*e*). We found that $\eta_{\max}=10$ is sufficient to contain the boundary layer for the leading order terms, F_0, θ_{f0}, and θ_{p0}. However, when four terms are taken, it is essential to take $\eta_{\max}$ to be at least 25, although $\eta_{\max}=40$ was used with 400 uniformly spaced intervals. We define Q_f and Q_p to be the derivatives of the temperature fields at the surface:

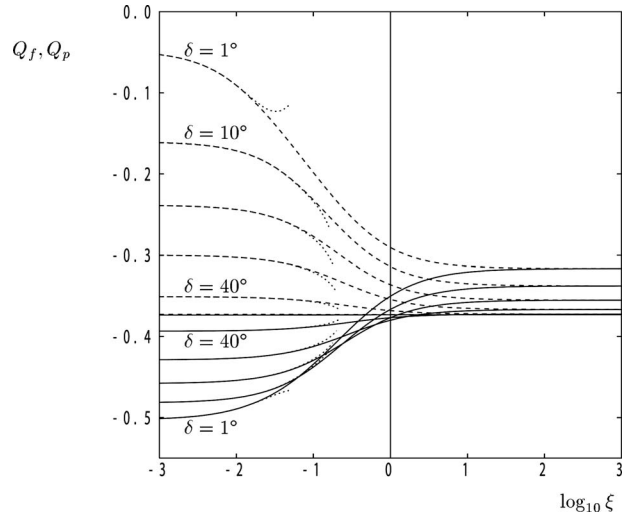

Fig. 2 Variation of Q_f (continuous lines) and Q_p (long dashes) with ξ for τ=0.5 and γ=1, where δ takes the values of 1 deg, 10 deg, 20 deg, 30 deg, 40 deg, and 44.9 deg. Also shown are the four-term small-ξ expansions (dotted lines).

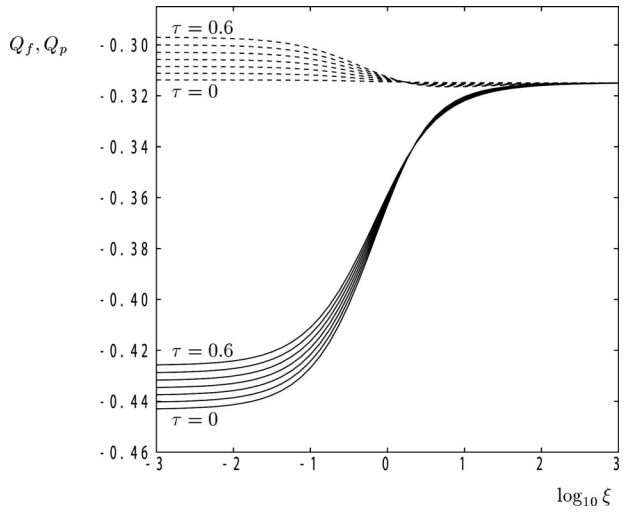

Fig. 4 Variation of Q_f (continuous lines) and Q_p (long dashes) with ξ for $\gamma=10^{-2}$ and δ=30 deg, where τ takes the values of 0.0, 0.1, 0.2, 0.3, 0.4, 0.5, and 0.6

$$Q_f = \left.\frac{\partial\theta_f}{\partial\eta}\right|_{\eta=0} \quad \text{and} \quad Q_p = \left.\frac{\partial\theta_p}{\partial\eta}\right|_{\eta=0} \tag{43}$$

and these are plotted in Figs. 2–4.

Second, the parabolic system of equations given by Eqs. (31*a*)–(31*c*) was solved using the Keller-box method. The governing equations were rewritten in first order form in η, discretized using central differences in both η and ξ, and the resulting nonlinear difference equations were solved using a multidimensional Newton–Raphson scheme. The details of the block-Thomas algorithm, which is used for this purpose is now quite standard. For these simulations, we used $\eta_{\max}=25$ with 500 uniformly spaced intervals. Although this method is formally of second order accuracy, the solutions obtained at $\xi=0$ are precisely the same as those obtained for F_0, θ_{f0}, and θ_{p0} to four significant figures. We used a nonuniform grid in the ξ-direction, which was formed by using a uniform grid in $\log_{10}\xi$ for all points except for at $\xi=0$.

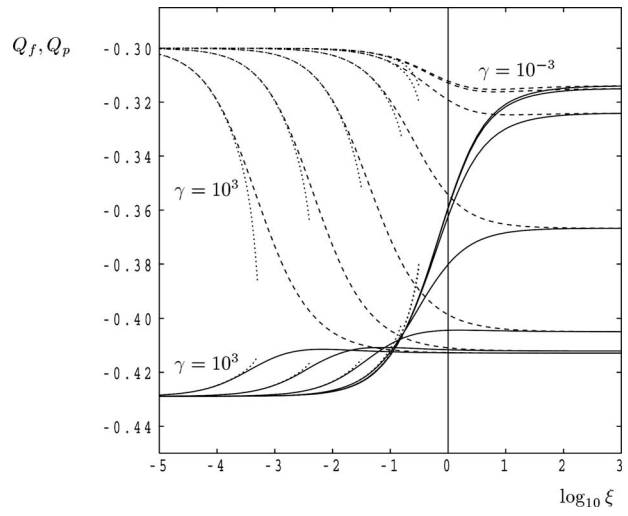

Fig. 3 Variation of Q_f (continuous lines) and Q_p (long dashes) with ξ for τ=0.5 and δ=30 deg, where γ takes the values of 10^{-2}, 10^{-1}, 1, 10, 10^2, and 10^3. Also shown are the four-term small-ξ expansions (dotted lines).

Third, the full elliptic system given by Eqs. (11*a*), (11*b*), (14*a*), and (14*b*) was solved using an implicit time-stepping code. Rees and Bassom [16] considered the flow induced by a uniformly hot semi-infinite surface bounding an otherwise cold monodisperse porous medium subject to LTE, and found that the full steady elliptic equations reduce to ordinary differential form when written in parabolic coordinates, and when the porous medium is taken to occupy the semi-infinite region $y \geq 0$. Thus, parabolic coordinates offer a computationally efficient means for solving the governing equations for complicated cases, such as the stability analysis of Rees [17] and the study of LTNE effects by Rees [18]. In both these cases, time stepping was undertaken using a backward difference in time with second order central differences in space. The fully implicit scheme also employed coordinate stretching to increase the efficiency of the code, and the solution at each time step was obtained using the full multigrid methodology with V-cycling; further details may be found in Rees [17].

The parabolic coordinate system we used is given by the transformation

$$X = (\bar{\xi}^2 - \bar{\eta}^2)/4, \quad Y = \bar{\xi}\bar{\eta}/2 \tag{44}$$

following the transformation of Eq. (18) by

$$\Psi = R^{1/2}\psi, \quad X = R^{-1/2}x, \quad Y = R^{-1/2}y \tag{45}$$

to obtain

$$\frac{\partial^2\Psi}{\partial\bar{\xi}^2} + \frac{\partial^2\Psi}{\partial\bar{\eta}^2} = \tau\left[\frac{\bar{\xi}}{2}\frac{\partial\theta_f}{\partial\bar{\eta}} + \frac{\bar{\eta}}{2}\frac{\partial\theta_f}{\partial\bar{\xi}}\right] + (1-\tau)\left[\frac{\bar{\xi}}{2}\frac{\partial\theta_p}{\partial\bar{\eta}} + \frac{\bar{\eta}}{2}\frac{\partial\theta_p}{\partial\bar{\xi}}\right] \tag{46a}$$

$$\frac{(\bar{\xi}^2+\bar{\eta}^2)}{4}\left[\frac{\partial\theta_f}{\partial t} + H\cos\delta(\theta_f - \theta_p)\right] = \frac{\partial^2\theta_f}{\partial\bar{\xi}^2} + \frac{\partial^2\theta_f}{\partial\bar{\eta}^2} + \cos\delta\left[\frac{\partial\Psi}{\partial\bar{\xi}}\frac{\partial\theta_f}{\partial\bar{\eta}} - \frac{\partial\Psi}{\partial\bar{\eta}}\frac{\partial\theta_f}{\partial\bar{\xi}}\right] \tag{46b}$$

$$\frac{(\bar{\xi}^2+\bar{\eta}^2)}{4}\left[\frac{\partial\theta_p}{\partial t} + H\gamma\sin\delta(\theta_p - \theta_f)\right] = \frac{\partial^2\theta_p}{\partial\bar{\xi}^2} + \frac{\partial^2\theta_p}{\partial\bar{\eta}^2} + \sin\delta\left[\frac{\partial\Psi}{\partial\bar{\xi}}\frac{\partial\theta_p}{\partial\bar{\eta}} - \frac{\partial\Psi}{\partial\bar{\eta}}\frac{\partial\theta_p}{\partial\bar{\xi}}\right] \tag{46c}$$

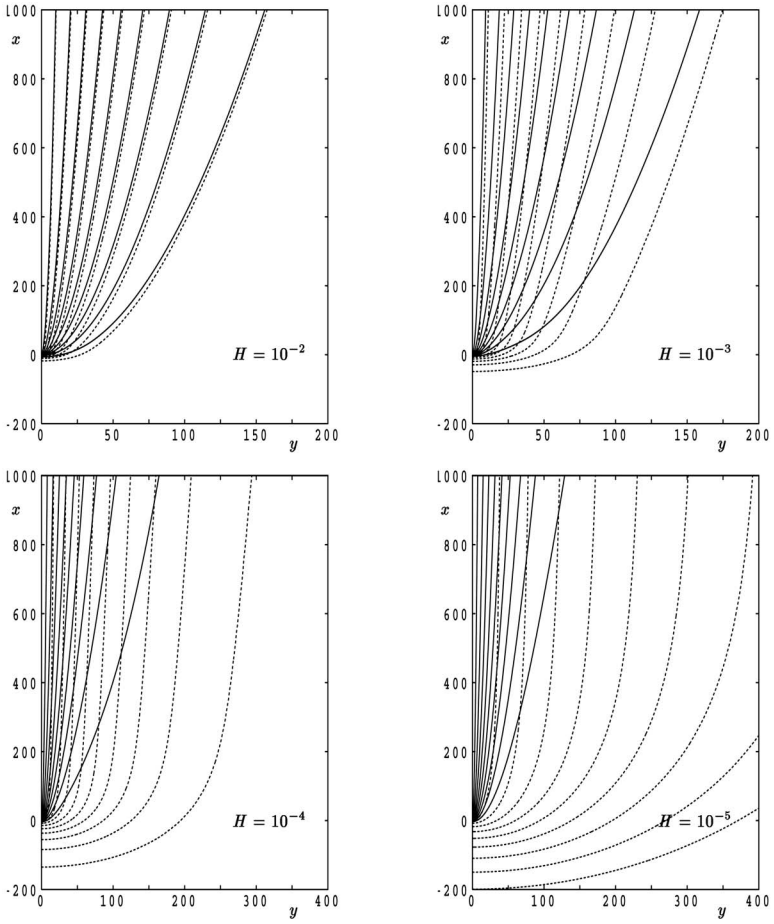

Fig. 5 Isotherms for both the fluid phase (continuous lines) and solid phase (dashed lines) for γ=1.0, τ=1, δ=0 for various values of *H*

We note that when x is large (and therefore $\bar{\xi}$ is large), the coordinate $\bar{\eta}$ is almost identical to the boundary-layer coordinate, η. In our simulations, we also employed an exponential coordinate stretching in both the $\bar{\xi}$ and $\bar{\eta}$ directions. In particular, we took $\bar{\eta}=e^{\hat{\eta}}-1$, where $\hat{\eta}_{\max}$ was taken to be 3.5. This means that $\bar{\eta}_{\max} \approx 31.16$, which is in excess of the value, 25, which we deemed earlier to be the minimum that could be used. We employed 128 grid points in the $\bar{\xi}$ direction and 64 in the $\bar{\eta}$ direction.

6 Results and Discussion

Figures 2–4 show how the surface rates of heat transfer, Q_f and Q_p, vary with ξ for various combinations of the governing parameters, γ, δ, and τ. These figures show the results of the parabolic simulations, while comparisons to the four-term small-ξ expansion are shown in Figs. 2 and 3 only.

Figure 2 concentrates on the values $\tau=0.5$ and $\gamma=1$ and depicts how the heat transfer characteristics change with the value of δ, where we note (i) that $\delta=0$ corresponds to a monodisperse system where the p-phase is solid (and therefore we should also have $\tau=1$) and (ii) that $\delta=45$ deg corresponds to a situation where the two phases act identically.

In all cases (except for $\delta=45$ deg), the porous medium is subject to strong LTNE between the phases near the leading edge. The mathematical reason for this is that the boundary layer equations for the respective phases are decoupled at leading order, while the physical reason is the asymmetry between the phases, in general, where advection is much stronger in the fluid phase. As ξ increases, the source/sink terms become more effective and this results in the gradual approach to LTE. The detailed numerical results show that LTE is established later as δ reduces toward zero; this is because of the decreasing amount of advection in the p-phase in that limit.

The effect of varying γ is shown in Fig. 3 for the case where $\tau=0.5$ and $\delta=30$ deg. Here, we have taken γ in the range from 10^{-3} to 10^{3}. Given that γ multiplies the source/sink terms in the θ_p equation, it is not a surprise to see that LTE is established very early (i.e., at small values of ξ) when γ is large, but is delayed considerably when γ is small. We can also see that the range of validity of the small-ξ expansion depends very strongly on the value of γ, unlike the situation shown in Fig. 2.

When τ is allowed to vary, we are allowing the relative magnitudes of the buoyancy forces corresponding to the two phases to change. When $\gamma=10^{-2}$ and $\delta=30$ deg, the curves shown in Fig. 4 indicate that there is a little change in the detailed evolution of the rate of heat transfer with ξ. This is not unexpected, because τ is a volume fraction independent of any thermal property. At any chosen value of ξ, the corresponding set of curves for larger values of γ are found to vary even less than those shown in Fig. 4.

Table 1 shows how the large-ξ asymptotic analysis given in Sec. 5 compares to the parabolic simulations at $\xi=10^{5}$ for one typical parameter set. This table shows that the leading order solutions are reproduced exceptionally well by the parabolic simulations.

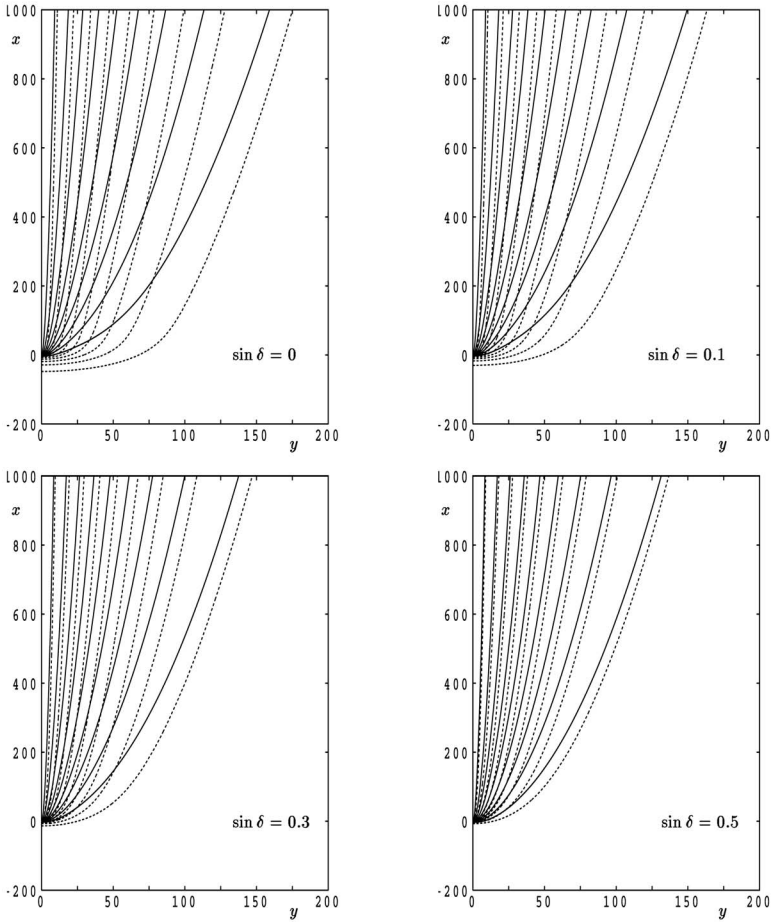

Fig. 6 Isotherms for both the fluid phase (continuous lines) and solid phase (dashed lines) for γ=1.0, τ=0.8, H=0.001 for various values of δ

The above discussion centered on situations where the boundary-layer approximation is valid, and therefore streamwise diffusion has been neglected. Thus, the small-ξ analysis is, strictly speaking, valid only while the boundary-layer approximation remains valid. We therefore turn our attention to the detailed convection, which takes place near to the leading edge of the heated surface. Figures 5 and 6 depict the isotherms for both phases for a variety of cases within this elliptic regime.

Figure 5 shows how the magnitude of H affects the thermal fields when γ=1, τ=1, and δ=0 deg. For relatively large values of H, which, in the present context means values that are greater than 0.01, the two phases are almost in LTE even in the region near the leading edge. However, as H decreases, the p-phase is affected decreasingly by the fluid movement in the f-phase, and therefore the temperature field in the p-phase is able to conduct with decreasing hindrance. Conversely, as the f-phase is increasingly isolated from the p-phase, the thickness of its boundary layer decreases as H decreases.

Figure 6 indicates how variations in δ affect the thermal fields when H=0.001, γ=1, and τ=0.8. When δ=0, we recover a situation with fairly strong LTNE because H is fairly small. However, the fact that γ=1 means that, once again, the phases satisfy identical energy equations when δ=45 deg and they will then be in global LTE. This figure shows the approach to LTE as δ varies from zero toward 45 deg.

Finally, we mention that variations in τ yield almost no discernable change in the isotherms; this is in accord with Fig. 4.

Table 1 Comparison of the large-ξ asymptotic solutions [see Eqs. (41), (42*a*), and (42*b*)] with the values obtained using the parabolic solver at ξ=10^5 (with δ=30 deg and τ=0.5). At least four significant figures of accuracy are attained.

γ	$f(\infty)$	$\theta'(0)$	$1.61613/\Gamma^{1/2}$	$-0.44378\Gamma^{1/2}$
0.001	2.284701	−0.313899	2.28472	−0.31391
0.01	2.277300	−0.314920	2.27731	−0.31494
0.1	2.213098	−0.324057	2.21310	−0.32407
1	1.955555	−0.366739	1.95552	−0.36676
10	1.771048	−0.404950	1.77100	−0.40497
100	1.740335	−0.412096	1.74029	−0.41212
1000	1.737057	−0.412874	1.73701	−0.41290

7 Concluding Remarks

If one wishes to generalize the interphase coupling in the BDPM model by replacing Eqs. (1*a*) and (1*b*) by

$$\mathbf{G} = \left(\frac{\mu}{K_f}\right)\mathbf{v}^*_f + \zeta(\mathbf{v}^*_f - b\mathbf{v}^*_p) \tag{47a}$$

$$\mathbf{G} = \left(\frac{\mu}{K_p}\right)\mathbf{v}^*_p + \zeta(c\mathbf{v}^*_p - d\mathbf{v}^*_f) \tag{47b}$$

then our previous analysis carries through but now Eqs. (26*a*) and (26*b*) are replaced by

$$C_f = \frac{1 + (b + c)K_r\sigma_f}{1 + (1 + cK_r)\sigma_f + (c - bd)K_r\sigma_f^2} \tag{48a}$$

$$C_p = \frac{K_r + (1 + d)K_r\sigma_f}{\beta[1 + (1 + cK_r)\sigma_f + (c - bd)K_r\sigma_f^2]} \tag{48b}$$

As a consequence, one then has

$$\delta = \tan^{-1}\left\{\frac{K_r}{\beta}\left[\frac{1 + (1 + d)\sigma_f}{1 + (b + c)K_r\sigma_f}\right]\right\} \tag{49}$$

rather than this expression with $b=c=d=1$, but everything else is the same. For small values of σ_f and K_r, the angle δ changes little with variation of b, c, and d. In this respect, our BDPM model is robust.

It appears that the number of parameters in the analysis cannot be reduced beyond 3. This reinforces our belief that the BDPM system is a distinctive system that is well worth studying.

Our present interest is largely in the way the BDPM situation differs from the LTNE model for a regular porous medium. It now appears that the latter is the nongeneric case, one that requires an asymptotic analysis involving the matching of inner and outer solutions, occasioned by fact that the solid-phase temperature in a regular medium decays relatively slowly with distance normal to the boundary wall.

We conclude with some remarks about the status of our model, which is radically new and in some respects tentative. As far as we are aware, the only published works on the model are our papers [3–5,14]. In formulating this model, we aimed for the simplest possible model that would capture the main physical phenomena, such as velocity dispersion, in a BDPM. No attempt at derivation by volume averaging has yet been made, and to the best of our knowledge, no suitable experimental correlations for a BDPM are available. We hope that our work will stimulate relevant experimental and theoretical investigations. Our interphase momentum transfer parameter is currently a parameter to be determined by subsequent experiment. Brinkman effects can be treated by adding the usual Brinkman term, as in Refs. [3–5]. (These are necessary if information about wall friction is desired.) The effect of Forchheimer drag (and quadratic advective inertial terms) is a topic for further investigation.

Nomenclature

c = specific heat at constant pressure
d = characteristic length scale
$\mathbf{G}$ = negative of the applied pressure gradient
$\hat{g}$ = gravitational acceleration
h = interphase heat transfer coefficient (incorporating the specific area)
$\hat{h}$ = dimensionless interphase heat transfer parameter, $hd^2/\phi k_f$
H = $\hat{h}/R$
k = thermal conductivity
K = permeability
K_r = permeability ratio, K_p/K_f
p^* = pressure
R = Rayleigh number, $\rho_F g\hat{\beta}(T_w - T_\infty)K_f d/[\mu\phi k_f/(\rho c)_f]$
T^* = temperature
T_F^* = volume average temperature defined in Eq. (3)
T_w = wall temperature
T_∞ = ambient temperature
u^* = x-component of velocity
v^* = y-component of velocity
$\mathbf{v}^*$ = filtration velocity, (u^*, v^*)
x^* = vertical coordinate
y^* = horizontal coordinate

Greek Symbols

β = modified thermal capacity ratio, $(1-\phi)k_p(\rho c)_f/[\phi k_f(\rho c)_p]$
$\hat{\beta}$ = volumetric thermal expansion coefficient of the fluid
γ = modified thermal conductivity ratio, $\phi k_f/[(1-\phi)k_p]$
Γ = parameter defined in Eq. (40)
δ = parameter defined in Eq. (28b)
ε = porosity within the p-phase
ζ = coefficient for momentum transfer between the two phases
η = boundary-layer parameter defined in Eq. (23)
$\tilde{\eta}$ = modified boundary-layer parameter defined in Eq. (29b)
θ = dimensionless temperature defined in Eq. (8)
μ = fluid viscosity
ξ = parameter defined in Eq. (30)
ρ = density
ρ_F = density of the fluid
σ_f = f-phase momentum transfer parameter, $\zeta K_f/\mu$
τ = $\phi/[\phi+(1-\phi)\varepsilon]$
ϕ = volume fraction of the f-phase

Subscripts

f = fracture phase (macropores)
p = porous phase (micropores)

Superscript

$*$ = dimensional variable

References

[1] Chen, Z. Q., Cheng, P., and Hsu, C. T., 2000, "A Theoretical and Experimental Study on Stagnant Thermal Conductivity of Bi-Dispersed Porous Media," Int. Commun. Heat Mass Transfer, **27**, pp. 601–610.

[2] Chen, Z. Q., Cheng, P., and Zhao, T. S., 2000, "An Experimental Study of Two Phase Flow and Boiling Heat Transfer in Bi-Disperse Porous Channels," Int. Commun. Heat Mass Transfer, **27**, pp. 293–302.

[3] Nield, D. A., and Kuznetsov, A. V., 2004, "Forced Convection in a Bi-Disperse Porous Medium Channel: A Conjugate Problem,"Int. J. Heat Mass Transfer, **47**, pp. 5375–5380.

[4] Nield, D. A., and Kuznetsov, A. V., 2005, "A Two-Velocity Two-Temperature Model for a Bi-Dispersed Porous Medium: Forced Convection in a Channel," Transp. Porous Media, **59**, pp. 325–339.

[5] Nield, D. A., and Kuznetsov, A. V., 2006, "The Onset of Convection in a Bidisperse Porous Medium," Int. J. Heat Mass Transfer, **49**, pp. 3068–3074.

[6] Nield, D. A., and Kuznetsov, A. V., 2005, "Heat Transfer in Bidisperse Porous Media," *Transport Phenomena in Porous Media III*, D. B. Ingham and I. Pop, eds., Elsevier, Oxford, Chap 2.

[7] Cheng, P., and Minkowycz, W. J., 1977, "Free Convection About a Vertical Plate Imbedded in a Porous Medium With Application to Heat Transfer From a Dyke," J. Geophys. Res., **82**, pp. 2040–2044.

[8] Rees, D. A. S., and Pop, I., 2000, "Vertical Free Convective Boundary-Layer Flow in a Porous Medium Using a Thermal Nonequilibrium Model," J. Porous Media, **3**, pp. 31–44.

[9] Mohamad, A. A., 2001, "Natural Convection From a Vertical Plate in a Saturated Porous Medium: Non-Equilibrium Theory," J. Porous Media, **4**, pp. 181–186.

[10] Rees, D. A. S., and Pop, I., 2002, "Comments on 'Natural Convection from a Vertical Plate in a Saturated Porous Medium: Non-Equilibrium Theory' by A. A. Mohamad," J. Porous Media, **5**, pp. 225–227.

[11] Haddad, O. M., Al-Nimr, M. A., and Al-Khateeb, A. N., 2004, "Validation of the Thermal Equilibrium Assumption in Natural Convection From a Vertical Plate Embedded in a Porous Medium: Non-Darcian Model," Int. J. Heat Mass Transfer, **74**, pp. 2037–2042.

[12] Haddad, O. M., Al-Nimr, M. A., and Al-Khateeb, A. N., 2004, "Validity of the Local Thermal Equilibrium Assumption in Natural Convection From a Vertical Plate Embedded in a Porous Medium," J. Porous Media, **8**, pp. 85–95.

[13] Nield, D. A., and Bejan, A., 2006, *Convection in Porous Media*, 3rd ed., Springer, New York.

[14] Nield, D. A., and Kuznetsov, A. V., 2008, "Natural Convection About a Vertical Plate Embedded in a Bidisperse Porous Medium," Int. J. Heat Mass Transfer, **51**, pp. 1658–1664.
[15] Rees, D. A. S., Bassom, A. P., and Siddheswar, P. G., 2008, "Local Thermal Non-Equilibrium Effects Arising From the Injection of a Hot Fluid Into a Porous Medium," J. Fluid Mech., **594**, pp. 379–398.
[16] Rees, D. A. S., and Bassom, A. P., 1991, "Some Exact Solutions for Free Convective Flows Over Heated Semi-Infinite Surfaces in Porous Media," Int. J. Heat Mass Transfer, **34**, pp. 1564–1567.
[17] Rees, D. A. S., 1993, "Nonlinear Wave Stability of Vertical Thermal Boundary Layer Flow in a Porous Medium," ZAMP, **44**, pp. 306–313.
[18] Rees, D. A. S., 2003, "Vertical Free Convective Boundary-Layer Flow in a Porous Medium Using a Thermal Nonequilibrium Model: Elliptical Effects," ZAMP, **54**, pp. 437–448.

Artificial Neural Networks (ANNs): A New Paradigm for Thermal Science and Engineering

Kwang-Tzu Yang
Life Fellow ASME
Department of Aerospace and Mechanical Engineering,
University of Notre Dame,
Notre Dame, IN 46556
e-mail: kwang-tzu.yang.1@nd.edu

The use of artificial neural network (ANN), as one of the artificial intelligence methodologies, in a variety of real-world applications has been around for some time. However, the application of ANN to thermal science and engineering is still relatively new, but is receiving ever-increasing attention in recent published literature. Such attention is due essentially to special requirement and needs of the field of thermal science and engineering in terms of its increasing complexity and the recognition that it is not always feasible to deal with many critical problems in this field by the use of traditional analysis. The purpose of the present review is to point out the recent advances in ANN and its successes in dealing with a variety of important thermal problems. Some current ANN shortcomings, the development of recent advances in ANN-based hybrid analysis, and its future prospects will also be indicated. [DOI: 10.1115/1.2944238]

Keywords: artificial neural networks, artificial intelligence, heat exchangers, dynamic system modeling, adaptive control

Introduction

In the past nearly three decades, we have been witnessing an overwhelming ground swelling in the development of computer-based algorithms in a group known as soft computing. This development has been driven by increasingly broader applications, which are difficult to deal with by conventional approaches, particularly those in engineering. Since such algorithms in soft computing are mostly based on simplistic models of human intelligence and evolutionary experience, they are also broadly known as artificial intelligence (AI) methodologies. They generally have the characteristics of very simple computational steps, often accompanied by a very large number of repeated computational cycles. This is very much in contrast to hard computing, which generally deals with numerical solutions to differential equations based on hard science, such as conservation laws and the like. Examples of soft-computing methodologies include artificial neural networks (ANNs), optima search algorithms such as genetic algorithm (GA) and genetic programming (GP), fuzzy-logic control, expert systems, data mining, and others. It is interesting to note that all these methodologies are based on very different natural human-related phenomena. Each of them has received in-depth development in the recent past in specific targeted applications. One important area of soft computing is in problems of thermal science and engineering. Up to the very recent past, these problems have largely been treated by traditional hard-computing approaches, along with experiments carried out for the purpose of validating the analysis or for performance correlations. However, there is a clear indication that thermal problems are becoming increasingly more complex and that the need for modeling single steady phenomena is rapidly migrating to the need for dealing with dynamics, system performance, optimization, and control. Unfortunately, the traditional approaches are simply not robust enough to handle such increased complexity, and new methodologies are definitely needed for this purpose.

As given in a recent review [1], several of the AI methodologies have shown very promising results to deal with just the type of complexity mentioned above. However, their applications to thermal problems are still rather tentative. Among the various soft-computing methodologies, only the ANN analysis and fuzzy-logic control have seen some sustained interest in recent years. Even then, studies in fuzzy-logic control have almost all concentrated in HVAC applications, primarily due to the fuzzy constraint related to human comfort. ANNs, on the other hand, have addressed a much wider application based on thermal applications to date and are specifically addressed in the present review. The purpose of this paper is to present the basic ANN methodology, its attributes and shortcomings, and implemental issues, and then to be followed by different groupings of thermal problems that have been treated by the ANN analysis and their corresponding results. Also discussed are ANN-based hybrid methodologies with other AI analyses to achieve more promising results not possible with the ANN analysis alone. Finally, some future prospects of ANN applications related to emerging critical thermal problems will also be presented. It is hoped that the present review of the ANN methodology and applications will enable us to appropriately call the ANN methodology a new paradigm for thermal problem studies and will thus encourage many more thermal engineers and practitioners to seriously consider ANN for treating future critical thermal problems, which are difficult to treat by traditional means.

Artificial Neural Network (ANN) Analysis

Despite the apparent popularity of fuzzy-logic control in the relatively narrow HVAC applications (see examples in Refs. [2–4]), ANNs are now unquestionably the leading soft-computing methodology for the general thermal problems. There are several significant reasons for this. First of all, it has a powerful ability to recognize accurately the inherent relationship between any set of input and output without a physical model, and yet the ANN results do account for all the physics relating the output to the input. This ability is essentially independent of the complexity of the underlying relation such as nonlinearity, multiple variables and parameters, and noisy and uncertain input and output data. This essential ability is known as pattern recognition as the result of learning. Secondly, the methodology is inherently fault tolerant, due to the large number of processing units in the network undergoing massive parallel data processing. Thirdly, its learning ability also gives the methodology the ability to adapt to changes in the parameters. This ability enables the ANN to deal with time-

Contributed by the Heat Transfer Division of ASME for publication in the JOURNAL OF HEAT TRANSFER. Manuscript received August 21, 2007; final manuscript received October 10, 2007; published online July 9, 2008. Review conducted by Yogesh Jaluria.

dependent dynamic modeling and adaptive control by means of neurocontrollers. This ability significantly enables thermal engineers to delve into system analysis and control, a complexity which simply cannot be treated by any traditional analysis at the present time. Finally, the basic ANN methodology has much flexibility to incorporating elements of other soft-computing methodologies such as fuzzy logic and GA, for example, to further improve its capability to deal with additional complexity in thermal problems.

On the other hand, despite these capabilities of the basic ANN methodology, it must be pointed out that input-output data sets must be available in the learning process to train the neural networks. Even though this requirement seems to be a serious shortcoming of the ANN analysis, it is, however, not really the case. The reality is the existence and availability of a large amount of experimental data sets for various thermal phenomena and device performances accumulated over a long time. They are mostly in the form of heat-transfer correlations. Such available data sets are the perfect vehicle for use with the ANN analysis. Furthermore, experimental data for thermal problems will always be available, in general, as they normally are required to validate theoretical models and analysis. In addition, experimental data obtained under specific dynamic conditions can also be used to train dynamic ANNs. Furthermore, the neural network can be trained in real time when the experimental data are being obtained at the same time, a feature useful in the development of dynamic adaptive-control schemes. Here again, the complexity of the problem under consideration is not an issue. In the next section, the ANN analysis in its basic methodology will be described, along with the discussion of the various issues of implementation. Examples of thermal problems with increasing complexity that have been treated by the ANN analysis with promising results are then shown and discussed.

Artificial Neural Network (ANN) Methodology

The description that follows is essentially that of Schalkoff [5]. The structure and function of the ANN attempt to mimic that of the biological neural network. The most popular fully interconnected ANN consists of a large number of processing units known as nodes or artificial neurons, organized in layers. There are, in general, three groups of node layers, namely, the input layer, one or more hidden layers, and an output layer, each of which is occupied by a number of nodes. All the nodes of each hidden layer are connected to all nodes of the previous and following layers by means of internode synaptic connectors or simply connectors. Each of the connectors, which mimic the biological neural synapsis, is characterized by a synaptic weight. The nodes of the input layer are used to designate the parameter space for the problem under consideration, while the output-layer nodes correspond to the unknowns of the problem under consideration. The parameters in the input layer need not to be all independent, and this is also true in the output layer.

At each hidden-layer node, the node input consists of a sum of all the node outputs from the nodes in the previous layer modified by the individual interconnector weights and a local node bias, which represents the propensity of the combined input to trigger a response at the node. It is thus clear that the weights are simply weighting functions that determine the relative importance of the signals from all the nodes in the previous layer. At each hidden node, the node output is determined by an activation function, which plays the role to determine whether the particular node is to activate ("fire") or not. It is thus seen that by the connector and node operations, information, which starts at the input layer, moves forward toward the output layer. Such a network is known as a fully connected feed-forward network.

When the information reaches the output layer, errors can be determined by comparing the calculated feed-forward data with the experimental output data to determine the error at each of the output node. These errors are then used to adjust all the node biases and connector weights in the entire network to minimize the errors by means of a learning or training procedure. The most popular training procedure for fully connected feed-forward networks is known as the supervised backpropagation learning scheme [5,6] where the weights and biases are adjusted layer by layer from the output layer toward the input layer. The whole process of feeding forward with backward learning is then repeated until a satisfactory error level is reached or become stationary.

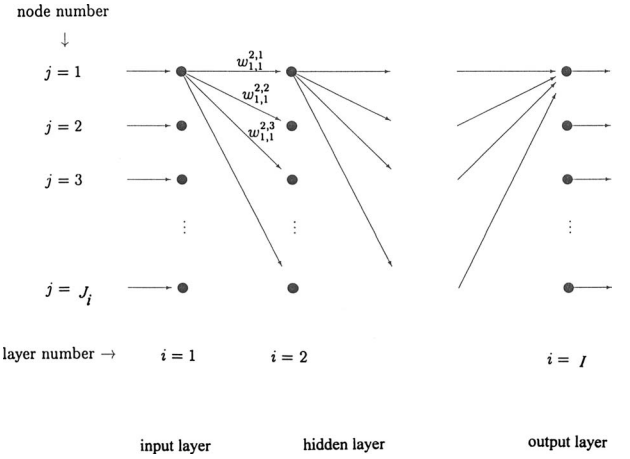

Fig. 1 Schematic of a fully connected multilayer ANN

The step-by-step ANN methodology just qualitatively described is now presented. Figure 1 shows the structure or configuration of such a network, consisting of the input, hidden, and output layers with node and layer designations, where i refers to the layer number with $i=1$ for the input layer and $i=I$ for the output layer, I being the total number of layers. Similarly, j is the node number in any layer, counting from the top in Fig. 1. Since the node numbers are likely to vary from layer to layer, the maximum j value is designated by J_i, depending on the layer number, and J_I is thus the number of unknowns in the output layer. As a result, each node is designated by (i,j). A somewhat different designation is used for all the connectors, since there are two nodes involved. The node on the left is designated by subscripts, while the right node in the forward direction is designated by superscripts. For instance, the synaptic weight $w_{1,1}^{2,3}$ refers to the connector from Node (1,1) to Node (2,3), and so on. In addition, symbols are also needed to deal with the nodal input and output at each node. Firstly, the nodal input to Node (i,j) is written as

$$x_{i,j} = \theta_{i,j} + \sum_{k=1}^{J_{i-1}} w_{i-1,k}^{i,j} y_{i-1,k} \tag{1}$$

where $\theta_{i,j}$ is the nodal bias at (i,j), and $y_{i-1,k}$ is the nodal output at $(i-1,k)$ at the previous layer. This equation clearly indicates that each signal coming from the previous layer is tampered by the weight in the same connector before they are added, and also finally modified by the local node bias, to form the input to the local node (i,j). It is thus seen that the weights and biases perform significant roles in influencing the node operation, and that the information to be processed represents the combined influence of all nodes from the previous layer. The node output, $y_{i,j}$, is then driven by the input, $x_{i,j}$, through the activation function or sometimes known as the threshold function

$$y_{i,j} = \phi_{i,j}(x_{i,j}) \tag{2}$$

which plays the same role of the biological neuron, as to whether it should fire or not on the basis of the strength of the input signal. When the input signal is weak, the artificial neuron simply produces a small output. On the other hand, when the input signal

exceeds a certain threshold, the artificial neuron fires and then sends a strong signal to all the connectors and then to all the nodes in the next layer. Several relevant activation functions have been proposed in the past [5,6], including the step function, the logistic sigmoid function, the hyperbolic tangent, the Gaussian, the wavelet, and others. One interesting practice is that the activation function may be changed from one hidden layer to another. However, the one that is the most popular and preferred is the continuous version of the step function, known as the logistic sigmoid function, which possesses continuous derivatives to avoid computational difficulties. It is also highly nonlinear, a behavior that could prove to be beneficiary in dealing with highly nonlinear input-output relations. It is generally written as

$$\begin{aligned} \phi_{i,j}(\xi) &= (1 + e^{-\xi/c})^{-1}, \quad i > 1 \\ &= \xi, \quad i = 1 \end{aligned} \tag{3}$$

where the constant c determines the steepness of the function. Finally, it is noted that the node output $y_{i,j}$ represented by the sigmoid function always lies between 0 and 1 for all $x_{i,j}$. Therefore, from a computational point of view, it is desirable to normalize the network input and output data with the largest and smallest of each of the data sets used in the ANN analysis.

As already mentioned, the most critical step in the ANN methodology is the learning or training process in which the errors determined at the output layer are successively reduced by systematically adjusting the weights and biases throughout the network, eventually to a level low enough to satisfy the user. Among the several available training algorithms, the most commonly used in the multilayer fully connected ANN is the feed-forward backpropagation training procedure based on a steepest-gradient error-correction process. The reader is referred to Haykin [6] for other available routines. In the usual thermal problems treated by the ANN analysis, the training data are based on experiments with the matched input-output data sets. The inputs represent the problem parameters, while the outputs are the desired unknowns. Each single experiment with the corresponding input-output data is called a run. For a given chosen network architecture of layers and nodes, the very first step in the training process is to assign initial values to all the synaptic weights and biases in the network. The values may be either positive or negative, and in general practice, are taken to be less than unity in absolute values. The second step is to complete all the node input and output calculations based on Eqs. (1)–(3) for all the layers. When $i=I$, the values of $y_{I,j}$ are then the network output data based on the given input data from that run. The backpropagation procedure then starts with an error function quantified by

$$\delta_{I,j} = (t_{I,j} - y_{I,j}) y_{I,j} (1 - y_{I,j}) \tag{4}$$

where $t_{I,j}$ is the normalized output target for the j-node of the last output layer, and this equation is simply a finite-difference approximation of the derivative of the sigmoid function. Once all $\delta_{I,j}$ are calculated, the computation then moves back to the previous layer $I-1$. Since the target outputs for this layer do not exist, a surrogate error is utilized and calculated instead for the hidden layer $I-1$, as given by

$$\delta_{I-1,k} = y_{I-1,k}(1 - y_{I-1,k}) \sum_{j=1}^{J_I} \delta_{I,j} w_{I-1,k}^{I,j} \tag{5}$$

These similar calculations are then continued from layer to layer in the backward direction until Layer 2. After all the errors $\delta_{i,j}$ are known, the changes in the weights and biases can then be determined by the generalized delta rule [7]

$$\Delta w_{i-1,k}^{i,j} = \lambda \delta_{i,j} y_{i-1,k} \tag{6}$$

$$\Delta \theta_{i,j} = \lambda \delta_{i,j} \tag{7}$$

for all $i<\mathrm{I}$, from which all the adjustments in the weights and biases can be determined. The quantity λ is known as the learning rate that is used to scale down the degree of change made to the connectors and nodes. The larger the learning (or training) rate, the faster the network will learn, but there is a chance that the ANN may not reach the desired outcome due to oscillatory error behaviors. Its value is normally determined by numerical experimentation, and a commonly arrived value is in the range 0.4–0.5. In some practice to further modulate the error-correction rates, a momentum term is added to Eqs. (6) and (7) characterized by a momentum rate based on the old weight and bias changes in the previous learning iteration [7].

A cycle of training consists of computing a new set of weights and biases successively for all the experimental runs in the training data. The calculations are then repeated over many cycles while recording an overall error quantity for a specific run within each cycle, given by

$$E_r = \frac{1}{2} \sum_{j=1}^{J_I} (t_{I,j} - y_{I,j})^2 \tag{8}$$

After a cycle of the experimental runs is completed, a maximum or average cycle error can be determined. It is important to note that the weights and biases are continually updated throughout the runs and cycles. The training is terminated when the last cycle error falls below a prescribed threshold or becomes stationary. The final sets of weights and biases can then be used for prediction purposes, and the corresponding ANN becomes a model of the input-output relation of the thermal problem. However, it is noted that there is also another completely different unsupervised training procedure [6] based on a stochastic searching methodology, also known as self-organizing maps. In most cases, this methodology is used to deal with problems with a large number of outputs, generally not suitable for thermal problems.

It is now clear that the overall ANN analysis involves just a few deterministic and algebraic steps repeated many times on the computer, while keep tab on the propagation of cycle errors in the training process. On the other hand, the methodology does involve a relatively large number of free parameters and choices. They include the number of hidden layers, the number of nodes in each layer, the initial weights and biases, the learning rate, the minimum number of training data sets, and sometimes also the choice of input parameters. All these do have a material effect on the ANN results. While literature does provide some semirational suggestions and recommendations [5,8,9], past experience and numerical trials and experimentation still represent the best guides. As pointed out by Yang [1] and Zeng [9], studies are being pursued currently to provide a more rational basis for some of the choices. Several guidelines may be of some interest. Despite the simple computational steps, overall effort is still an important issue, and does depend on the total number of nodes in the network, as a large number of nodes also tend to slow down the training process. The general idea is to seek a number of hidden layers and a number of nodes in each hidden layer as low as possible, but still permit efficient flow of information from the input layer to the output layer. In a new thermal problem, there are likely more input (parameter) nodes than output nodes. One reasonable practice is that the first hidden layer should have the same number of nodes as that in the input layer, and this number decreases toward the output layer, and the number of hidden layers depends on problem complexity. One flexibility in the ANN methodology is that both numbers of the hidden layer and the corresponding nodes can be increased at will from training cycle to training cycle, if the cycle errors do not decrease as expected. On the other hand, it must be cautioned that too many nodes may suffer the same fate as using polynomial curve-fitting schemes by collocation at specific data points, thus creating large errors in attempting interpolation between successive data points. One interesting

strategy regarding the node-number issue is suggested by Kramin [10] by first training a large network, which can then be reduced in size, and by removing those nodes, which do not significantly affect the training result. There is another suggestion based on a reversed strategy by adding nodes systematically as training proceeds [11]. These practices suggest that the network architecture, relative to the node number, can be freely modified throughout a single training cycle. A more rational procedure of optimizing the ANN architecture based on evolutionary programming is also available [12], as will be discussed separately in a later section. The issue of assigning initial weights and biases is always difficult in a new application. Without past information or data, the current practice is simply to generate a set of initial data from a random number generator of bounded numbers. A more rational, but complex method is that suggested by Lehtokangas et al. [13] based on an orthogonal least-squares algorithm. The choice of the training rate λ has not been rationally studied so far, and at the same time, the only guide is by numerical experimentation. As mentioned previously, a value somewhere between 0.4 and 0.5 can be used as a starting point, and reasonable results can be expected. Finally, the sigmoid activation function, as already pointed out, is a surrogate for a step function with continuous derivatives, thus avoiding possible computational difficulties. However, it also possesses asymptotic limits of [0,1], and may cause difficulties when these limits are approached. Therefore, the usual practice is to normalize all physical variables in an arbitrarily restricted range such as [0.15,0.85] to limit the computational efforts. Finally, there is another common and recommended practice in the way that the experimental data sets are utilized for training. Since the ANN is to be trained to recognize the input-output relations, which are generally somewhat noisy and do contain experimental uncertainties, it is desirable to include as many training data sets as possible. However, it is also important to set aside about one-quarter of the entire data sets to serve as testing data sets to evaluate the accuracy of the ANN results.

Artificial Neural Network (ANN) Applications to Thermal Problems

The application of ANN analysis to thermal problems has not had a long history. It is fair to say that such applications so far have only been largely exploratory and tentative, despite the fact that results have been uniformly promising in all cases. Only more recently, there is increasing interest in the use of ANN analysis for thermal- and energy-related applications, for three reasons. One reason is common to all fields of engineering, in that the underlying technical knowledge starts to lag behind what is needed in the ever-increasing complexity of the field of application. There is a constant push for analysis based on new paradigms to meet the demand. This is certainly the case in thermal engineering problems. The ANN analysis as a new paradigm represents an excellent candidate for this purpose. The second reason is the very nature of thermal problems, which involve a multitude of fundamental disciplines, their interactions, and likely complex geometry. The traditional approach and associated numerical analysis are so far only capable of treating a small segment of problems required in current critical applications. It is therefore understandable that experiments have played such an important role in the development of thermal science and engineering. Much of the raw experimental data still exist today. On the other hand, these experimental data have been correlated with dimensionless groups and are treated as physical models for performance prediction and design. As will be discussed later, there is a fundamental inadequacy in these correlated results, which has only been realized recently. On the other hand, such existing database and other experimental data to follow can be strategically used to develop excellent ANN-based thermal models. The third and last reason for the increased interest in the ANN analysis is the significant recent advances in the development of the ANN methodology itself. Such advances and further continued demonstration of the attainable excellent results are attracting an increasing number of thermal engineers to apply the ANN analysis to critical and challenging thermal problems.

Three broad categories of thermal problems have been successfully treated by the new ANN paradigm, despite the tentative nature of the applications in all these categories. For the reasons just cited, many more such problems with increasing complexity are expected to be similarly treated in the near future. The first category deals with steady behaviors of complex thermal phenomena and performance of complex thermal devices. In these cases, there is high complexity in interacting fluid-flow and heat-transfer processes along with the effect of complex geometry. Much of the current knowledge is based on heat-transfer correlations and unsatisfactory approximate theories. The ANN analysis can be applied to obtain ANN-based models, which are significantly more accurate than the traditional correlated models. The second category deals with time-dependent dynamic thermal phenomena and the corresponding thermal devices. Unfortunately, traditional approaches are almost powerless in developing viable dynamic models for such thermal problems, mainly due to the effect of added thermal masses for applications under dynamic conditions. The development of accurate ANN-based dynamic models requires, in addition to appropriate dynamic experimental data, only simple extensions of the basic ANN methodology. An additional advantage is that, as will be shown in more detail later, it is possible to use recurrent networks to train the network adaptively in real time, so that the dynamic model is being established as the physical dynamic process is evolving. The last category deals with even more complex dynamic thermal systems, which require robust control to ensure the proper dynamic performance of the systems. In such systems, it is also necessary to have the ability for real-time adaptive control to meet all the performances requirement when parameters undergo unknown changes. It will be shown later that this control capability can indeed be developed and experimentally verified by using the ANN analysis with real-time online adaptive training of a neurocontroller.

In the following sections, specific examples of ANN-analyzed thermal problems in the above-mentioned application categories will be given, along with some details of the associated ANNs and the results. These examples will also be supplemented with additional cited references.

ANN Applications in Steady Thermal Problems

Of all the steady thermal problems, one of the most important critical applications deals with heat exchangers and their performance with a great variety of geometry and operational conditions. Even for the simplest heat exchangers, only tentative large-scale CFD-based analysis has been attempted to predict their performance. The common practice, however, is to develop approximate theoretical models based on the use of overall coefficients of heat transfer made of individual heat-transfer coefficients for each fluid obtained from correlations with experimental data in terms of dimensionless numbers [14]. Simplifying assumptions are made, in general, as a part of the approximate model, such as, among others, constancy of the correlated coefficients and thermophysical properties, and greatly simplified geometrical parameters. As a result, it is not uncommon to find that the resulting heat-transfer rates do not predict well the actual heat-transfer performance of the heat exchangers under consideration. Despite the availability of large-scale computing analysis, there is still no real viable alternative in recent times, if not for the new paradigm of the ANN-based analysis. As will be shown in the following few examples, the ANN analysis provides a very accurate paradigm for modeling the heat exchanger performance, which does not use any simplifying and artificial assumptions, but still capture all the physical effects that relate the input physical parameters to the heat exchanger performance [1].

Among the very first applications of the ANN methodology to thermal problems is understandably the analysis of experimental

convective heat-transfer data [15,16] and to the performance and design of fin-tube heat exchangers [17,18]. In the studies of Refs. [15–17], the attention is given to the use of the standard coefficients of heat transfer, while the ANN applied in Ref. [18] is directed toward the experimental heat-transfer rates directly. As will be pointed out later, the use of coefficient of heat transfer is also subjected to uncertainty, including the physical effects not accounted for in the correlations, such as fluid-flow nonuniformity and maldistribution, variable properties and the use of reference temperature, and nonuniform temperature differences. The study in Ref. [18] essentially bypasses these uncertainties by going directly to the all-important heat-transfer rate so that all effects are included in the input (parameter space)–output (heat-transfer rate) relation, leaving only the uncertainties associated with the experimental measurements. This issue is of critical importance for thermal engineering and applications. If the new paradigm of using the ANN analysis can be demonstrated that it produces much more accurate models relating any input-output data sets, even just for the steady thermal problems, that would suggest that all past correlations could be upgraded for much improved performance prediction and better design of the associated thermal devices. The net result would have a very large economic benefit to the industry involved. On the other hand, thermal engineers doing the ANN analysis still would have to have the physical insight to determine the proper input parameters to use, before the ANN analysis can be successful.

The early ANN applications in thermal problems were mostly exploratory, tentative, and with a narrow focus. In order to explore the full potential of the ANN paradigm, there is a need to carry out systematic studies to assess the viability of the ANN analysis in thermal problems with increasing complexity. For this purpose, we have undertaken a series of ANN studies in our own laboratory in the recent past in all three application groups including carrying out the needed detailed experiments to provide the training and testing data. Several such studies under steady-state conditions will now be shown, along with the ANN results. Whenever possible, pertinent additional literature will be cited to give a broader picture of the new ANN-based paradigm.

We have chosen the fin-tube compact heat exchangers [1,19,20] as the thermal devices for our ANN studies. They are very commonly used in many diverse thermal applications and detailed raw experimental data for some of them are also available for training and testing purposes. In addition, it is simple to carry out our own experiments under well-controlled conditions in our own laboratory, when needed, to support our overall ANN development studies. Another important reason for taking the fin-tube compact heat exchangers as our thermal devices is that they are geometrically complex so that their specific effects could be properly accounted for in the ANN analysis.

Our first set of ANN studies deals with three different heat exchangers used in very different applications with increasing geometrical complexity, which are shown in Fig. 2, all operating under steady conditions. The ANN modeling results can then be compared with those of the traditional least-squares power-law correlations and those directly from the experiments. The first heat exchanger in Fig. 2(*a*) is a simple single-row air-water finned coil for air-heating applications. Careful steady-state experiments were carried out in an open wind tunnel to measure the air-side and water-side terminal temperatures and the two flow rates with error bands within 0.7% in the measured heat-transfer rates from detailed uncertainty analysis [18]. The final 259 sets of test data were correlated by the traditional dimensionless numbers using the least-squares regression analysis [19–21]. Such correlations are known not to be unique due to the uncertainty caused by the unknown tube-wall temperatures, which were not measured in the experiments. The predicted rate of heat transfer by this correlation for the set of test data has an error band of $\pm 10\%$, generally considered quite good. However, this measured heat-transfer error band obviously cannot all be attributed to the measurement errors alone. In fact, it can be traced to the deficiencies associated with the specific correlations. The physics in the flow and heat-transfer phenomena are known to be very complex, and as already noted before, some of the physics, such as flow mal-distribution and geometric complexity, are definitely not accounted for in the correlations, and hence some accuracy is lost.

Now we will see if the ANN analysis will provide a better model for the same data sets. This ANN analysis is based on the methodology detailed in the last section, 197 data sets out of the total 259 tests were used for training the ANN, while the rest were used to test the ANN predictions. For the ANN analysis, there were four input nodes in the input layer, corresponding to the normalized air and water flow rates, and the air and water inlet temperatures, and a single output node for the physical heat-transfer rate in the output layer. It is important to note that all inputs to the ANN are real physical quantities and, in particular, no property values are needed. The network configuration designation is usually given by numerals referring to the nodes in the successive layers. Some details of the ANN analysis are now given. For the case of the 4-5-2-1-1 configuration, for example, training was carried out to 200,000 cycles, each covering one complete sequence of feed-forward and backward propagation for all the training data sets. The mean-square errors in the maximum and average errors within each cycle could then be calculated, as shown in Fig. 3. It is seen that the maximum error asymptoted at about 150,000 cycles after undergoing a local minimum, while the corresponding average error reached its minimum at about 100,000 cycles. In either case, the error levels were quite small. In another configuration of 4-2-1, a similar training based on the same training data sets was carried out. The predicted heat-transfer rate from the ANN analysis was based on the final set of adjusted weights and biases, as shown in Table 1. These final values illustrate quite typically those in usual ANN applications. In the current study, 14 different ANN configurations, as shown in Table 2, were utilized to show their relative error and standard deviation sensitivities for the 62 test data sets, where the quantity $\mathbf{R}$ is the mean value of the ratios of the experimental heat-transfer rate to that of the ANN predictions, indicating the average accuracy of the predictions, and σ is the standard deviation of the heat-transfer ratios from their mean, which is an indication of the degree of scatter of the ANN predictions. It is seen that the network configuration with $\mathbf{R}$ closest to unity is 4-1-1-1, while the network 4-5-5-1 is the one with the smallest σ. It does seem that the criterion on σ is a more important one, since the 4-5-5-1 network has errors still confined to a range less than $\pm 3.7\%$ for all testing data sets, even though most of the scatter still lies in the range less than $\pm 0.7\%$. Of particular interest is that the error band in the test heat-transfer rate prediction from the ANN analysis is now in the range of measurement uncertainties of the experimental data, and thus signifies that most of the significant physics in the heat-transfer process of the test heat exchanger is accounted for by the ANN results, thus attesting to the excellent functional pattern-recognition ability of the ANN methodology. A more striking demonstration of the ANN results for the 4-5-5-1 network is the parity plot of the comparison between the ANN results and that from the traditional least-squares correlation analysis, as clearly shown in Fig. 4.

If the ANN approach is to be a viable one to deal with steady thermal problems with different degrees of complexity, it should also be capable to treat heat exchangers with greater geometrical complexity and also with operating conditions that involve more difficult physics. The compact multirow, multicolumn, fin-tube heat exchanger shown in Fig. 2(*b*) for air-cooling purposes utilizing chilled water flowing inside the tubes seems to satisfy these conditions. This heat exchanger was studied in great detail by extensive careful experimental measurements and correlations in terms of the Colburn *j*-factors by McQuiston [22,23]. Since the chilled water temperature could cause the air temperature to fall below its dew point, condensation would occur on the fin surfaces,

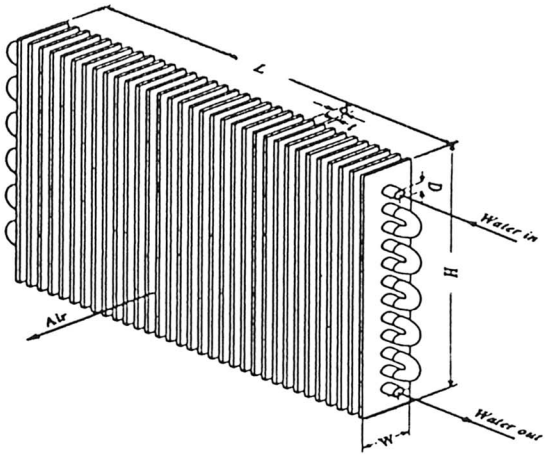

(a) Single-row fin-tube heat exchanger

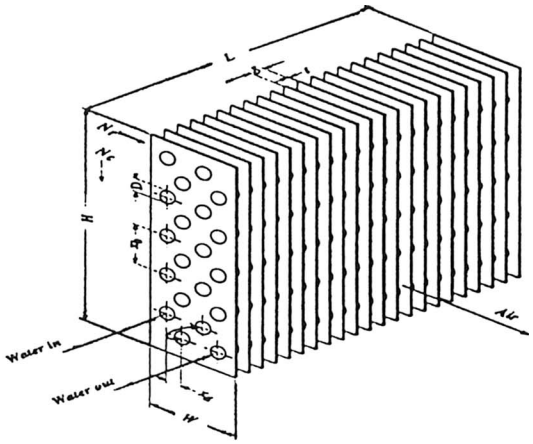

(b) Multi-row multi-column fin-tube heat exchanger

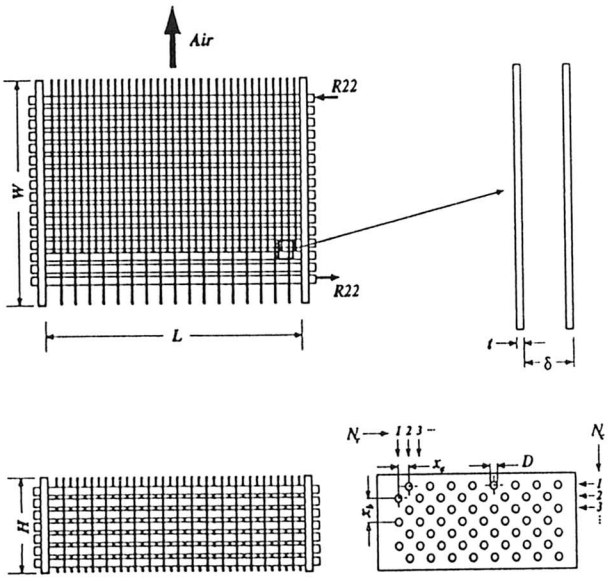

(c) Compact fin-tube heat exchanger with air and R-22 as fluids

Fig. 2 Fin-tube heat exchangers as thermal systems

and the data collected contained all three different fin-surface conditions, namely, dry surface, surface with dropwise condensation, and surface with film condensation. Dropwise and film condensation cases were differentiated by purely subjective visualization. Also because of the condensation phenomena, the film spacing became an added important parameter, and was also treated as an input parameter. In addition, on the water side only high Reynolds-number turbulent-flow conditions were considered so that the two coefficients of heat transfer could be conveniently decoupled. The experimental data were correlated for the air-side heat- and mass-transfer coefficients in the form of the Colburn j-factors under different surface conditions. The dry surface data were later recorrelated by Gray and Webb [24] to improve the correlation accuracy. Also, these correlations were more recently further significantly improved, based on the same functional form for the j-factors as those used originally by McQuiston [23] by seeking global minimum error conditions [25]. In Ref. [25], an ANN analysis was also carried out to assess its accuracy as a model to compare with that of the correlations. Several network configurations were tried with the best results given by a fully connected feed-forward network of 5-5-3-3 and using the back-propagation learning algorithm given in the last section, as shown in Fig. 5. It is seen that the five input nodes correspond to the air-inlet, dry-bulb and wet-bulb temperatures, the chilled water inlet temperature, the airflow Reynolds number, and the fin spacing. The three output nodes correspond to those of j_s for the sensible heat transfer, j_t, for the total heat transfer, and Q for the total heat-transfer rate. The j-factors were used only so that the results could be directly compared to that of the original correlation results of McQuiston [23]. Of the total 327 experimental data sets reported, 91 sets were associated with the dry-surface conditions, while 117 and 119 sets were related to dropwise and film condensations, respectively. These data sets were utilized to train separate ANNs. Also, the entire 327 data sets were also used to train another single ANN. The purpose here was to determine whether the ANNs trained with separate data sets involving different physics would perform better than the ANN trained with the complete data

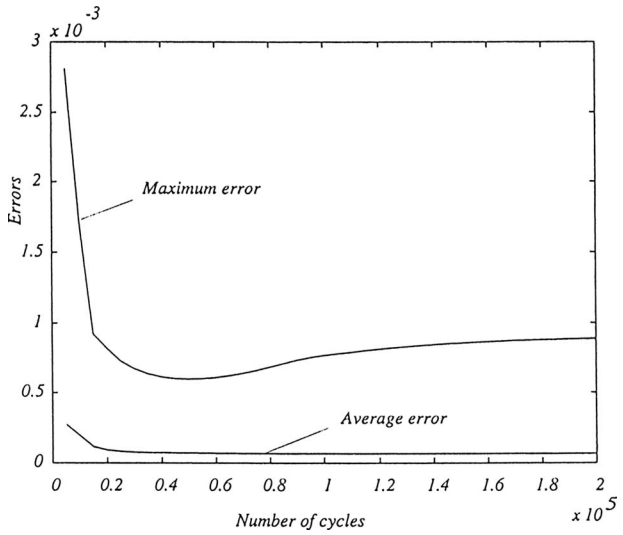

Fig. 3 Training errors for 4-5-2-1-1 ANN for heat exchanger in Fig. 2(*a*)

set. Every training process was based conservatively on 800,000 training cycles. The results in the rms percentage deviations of the four ANNs from those of the experiments are shown in Table 3, including those of the original correlations of McQuiston [23] and the improved dry-surface correlation of Gray and Webb [24]. It is of interest to note that in the total heat transfer, being a physical quantity, the ANN recognized its correct relation with the physical input data, and that such a low level of error in the total heat transfer is again close to the expected experimental uncertainties. Similar results can also be seen for the other two surface conditions. In addition, the ANNs give better predictions for dry surfaces than those for wet surfaces, as the physics involved in the latter surfaces is certainly more complex. On the other hand, when the ANNs are trained with the entire data sets by disregarding the surface conditions, all deviations tend to increase, as the ANN attempted to negotiate, with more difficulty, with the different physics involved. However, even in this case, the predicted total heat-transfer rate, which is the ultimate unknown in practice, had deviation bounds only of the order of $\pm 2.7\%$. The parity plots of all heat-transfer rates from the ANN results and the respective experimental data are shown in Figs. 6–8, and the accuracy of the ANN results is seen to be truly remarkable [25]. Before discussing the study of the heat exchanger in Fig. 2(*c*) in another ANN application, it is of interest to mention here another significant use of the ANN methodology for the discovery of new knowledge. The analysis of the humid air just described provides an example of this capability in combination with an AI clustering algorithm [1,26] By prescribing three clusters, the algorithm divided the entire data set into three clusters, which, interestingly, correspond to the data for the three surface conditions. Therefore, subjective visual information is really not needed for the prediction of detailed performance of this heat exchanger. Since this is an example where the ANN analysis is used in conjunction with another AI algorithm, it will be revisited later in a section on hybrid algorithms involving ANN.

Table 1 Typical synaptic weights and biases for ANN configuration of 4-2-1 associated with ANN analysis of heat exchanger in Fig. 2(*a*)

i	j	k	l	$w_{i,j}^{k,l}$	i	j	$\theta_{i,j}$
1	1	2	1	−8.744	2	1	−1.574
1	1	2	2	0.401	2	2	−2.474
1	2	2	1	1.321	3	1	−1.848
1	2	2	2	1.120			
1	3	2	1	0.772			
1	3	2	2	1.356			
1	4	2	1	−0.303			
1	4	2	2	−0.223			
2	1	3	1	−7.741			
2	2	3	1	8.576			

Table 2 Comparison of relative mean heat-transfer rates and the corresponding standard of deviation by different ANN configurations for heat exchanger in Fig. 2(*a*)

Configuration	R	σ
4-1-1	1.02373	0.266
4-2-1	0.98732	0.084
4-5-1	0.99796	0.018
4-1-1-1	1.00065	0.265
4-2-1-1	0.96579	0.089
4-5-1-1	1.00075	0.035
4-5-2-1	1.00400	0.018
4-5-5-1	1.00288	0.015
4-1-1-1-1	0.95743	0.258
4-5-1-1-1	0.99481	0.032
4-5-2-1-1	1.00212	0.018
4-5-5-1-1	1.00214	0.016
4-5-5-2-1	1.00397	0.019
4-5-5-5-1	1.00147	0.022

$$R = \frac{1}{N_p}\Sigma_{r=1}^{N_p} R_r, \qquad \sigma = \sqrt{\frac{1}{N_p}\Sigma_{r=1}^{N_p}(R_r - R)^2}$$

Now we mention another example involving a very complex, multirow, multicolumn, fin-tube heat exchanger used as an evaporator in a refrigeration application, again under steady operating conditions. The heat exchanger geometry is shown in Fig. 2(*c*). The Refrigerant R-22 flowed inside the tubes, while air was again flowing through the air passages. The extreme geometric complexity was in the finned passages with decreasing finned spacing of airflow to limit the possibility of air-passage blockage due to frost formation. In addition, the refrigerant underwent boiling evaporation inside the tubes [27]. This is one instance that only 38 sets of data were experimentally obtained covering a large number of parameters. An ANN analysis was attempted to see how far the training with very limited data could be pursued to a reasonable conclusion. To accommodate all the free parameters involved, an ANN was chosen with a fully connected network configuration of 11-11-6-1, as shown in Fig. 9. There were seven geometrical ratios and four operating parameters in the input layer and one single output node for the total heat-transfer rate. It is understandable that all 38 data sets were used in the training. The ANN prediction of the total rate of heat transfer against the available data is shown in Fig. 10 in the form of a parity plot. It is easily noted that the accuracy of the results is remarkable. The rms error of the percentage difference between the predictions and measurements is less than $\pm 1.5\%$, again of the same order as the estimated experimental uncertainties. However, it is unrealistic to expect that this one example would have general validity. In fact, it is known and expected that errors from the ANN analysis would increase as the number of training data sets decreases, and also that the ANN analysis would be expected to perform poorly if it tries to predict results outside the domain of the training data set [28]. However, if the empty domain is small, then the ANN predictions would not suffer much. This may indeed be the case for the refrigeration coil just considered since in ANN applications for dealing with real-world complex thermal problems, there is always a tendency to limit experimental data sets suitable for training. Therefore, the limited data issue discussed here is an important one. Fortunately, ANN-based error-estimate methodologies are available to determine the relative importance of each

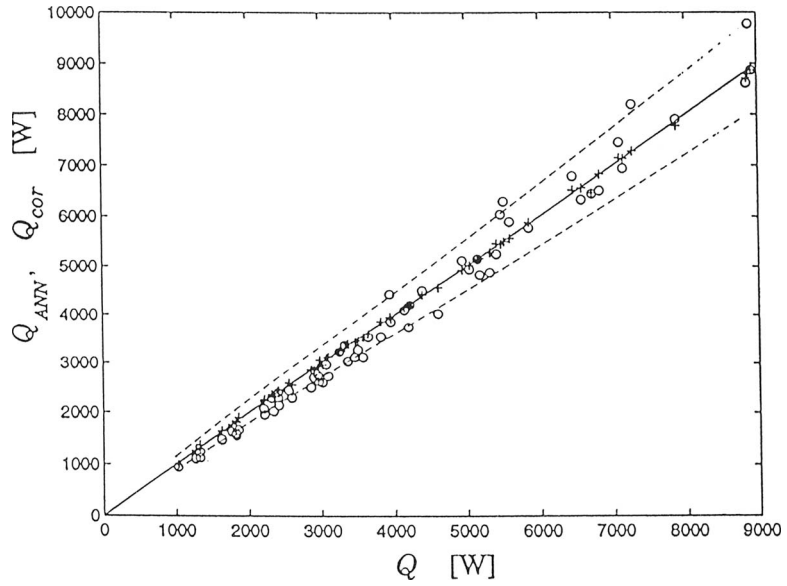

Fig. 4 Comparison of ANN and correlation predictions of heat transfer for heat exchanger in Fig. 2(*a*), O correlations, +ANN, dotted lines representing ±10% deviations

data point in the limited data set. A good example is the one based on statistical cross validation to determine the domain where additional measurements are needed [27,28].

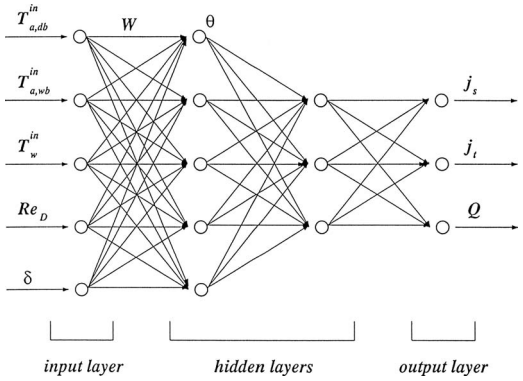

Fig. 5 A 5-5-3-3 neural network for the analysis of heat exchanger of Fig. 2(*b*)

Table 3 Comparison of percentage errors in predictions between the ANN and standard power-law correlations for ANN analysis of heat exchanger in Fig. 2(*b*)

Surface	Method	j_s	j_t	Q_t
Dry	McQuiston	14.57	14.57	6.07
	Gray and Webb	11.62	11.62	4.95
	ANN	1.002	1.002	0.928
Dropwise	McQuiston	8.50	7.55	—
	Gray and Webb	—	—	—
	ANN	3.32	3.87	1.446
Filmwise	McQuiston	9.01	14.98	—
	Gray and Webb	—	—	—
	ANN	2.58	3.15	1.960
Combined	ANN	4.58	5.05	2.69

While compact fin-tube heat exchangers and their performance are representative examples of complex thermal devices and phenomena for ANN analysis, there are other steady thermal problems that have also received recent attention in applying the ANN analysis. A brief review of such applications will be given here. First of all, it would be appropriate to cite recent reviews of specific areas of steady-state ANN applications. Specific examples with either significant thermal applications or extended ANN analysis will then be shown and discussed. The broad-based early review of Sen and Yang [8] has already been noted earlier. There are also two additional reviews dealing with energy systems [29] and multiphase flows with and without heat transfer [30].

The review of Kalogirou [29] includes a brief background of ANN and a brief account of the basic ANN methodology, and describes several classes of energy-related problems, which were successfully treated by applying the described basic ANN methodology. They include, among others, solar energy systems for modeling the heating-up response and design of a steam-generating plant, for the estimation of a parabolic trough-collector intercept factor and local concentration ratio, and the determination of hourly solar irradiance dependent on astronomical, and

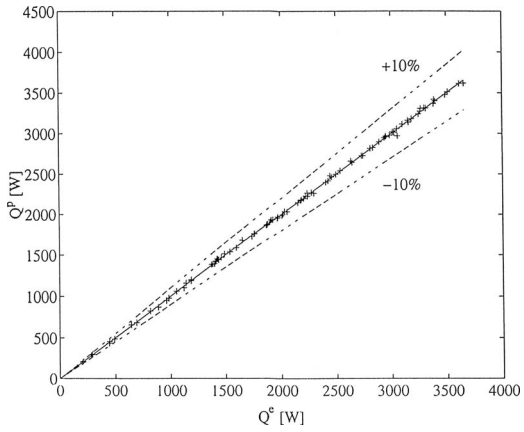

Fig. 6 Experimental versus ANN-predicted total heat transfer for the heat exchanger in Fig. 2(*b*) under dry-surface conditions

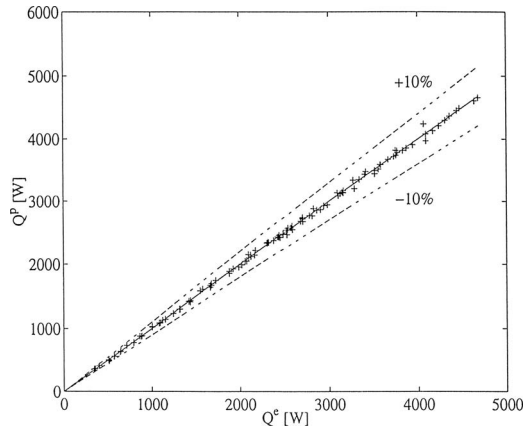

Fig. 7 Experimental versus ANN-predicted total heat transfer for the heat exchanger in Fig. 2(*b*) under dropwise condensation conditions

meteorological-climatic data. Also described are ANN applications in HVAC systems for determining building thermal loads and their prediction, for controlling the temperature in operating buses based on the ambient temperature, number of passengers, and time of day, and also applications in combustion phenomena including turbulent combustion modeling and waste incineration processes. Several additional applications mentioned include forecasting and prediction in energy management practices and prediction of frost buildup in evaporator coils for designing efficient defrosting practices. While in all these energy-related applications using the ANN analysis, excellent results were the norm [29], the success of each application clearly still depends on the choice of the input parameters, the availability of training data sets, and computational experimentation to determine the optimum configuration of the network and other free parameters in the basic methodology.

Another review of significant ANN applications to thermal problems has been more recently given by Sen and Yang [30] in the specific area of multiphase system with and without heat transfer. The difficulty of theoretically modeling such problems by standard traditional approaches is well known, and available approximate models have been based only on detailed experiments and their data correlations. It is generally recognized that despite the availability of large accumulation of good experimental data, the correlations have been rather tentative and uncertain, and in many cases led to predictions with substantial errors compared to the experimental results. It is therefore not surprising to find the

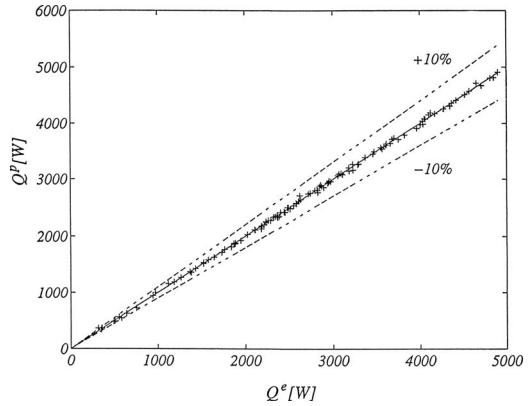

Fig. 8 Experimental versus ANN-predicted total heat transfer for the heat exchanger in Fig. 2(*b*) under film condensation conditions

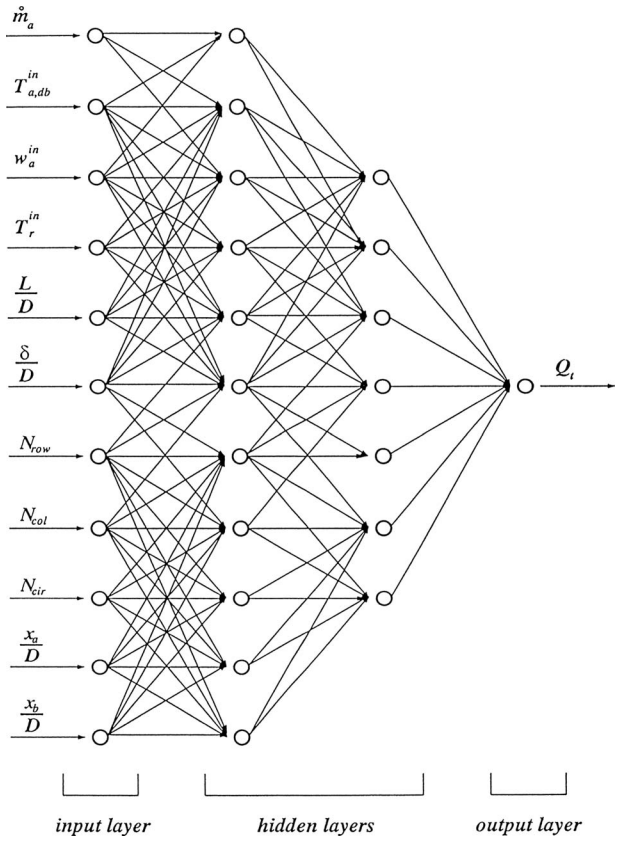

Fig. 9 Configuration of an 11-11-7-1 neural network for the evaporator heat exchanger in Fig. 2(*c*)

rising development of ANN-based models of such multiphase systems, in view of its essential capability of recognition of complex patterns and the availability of good experimental databases. The review in Ref. [30] identified seven specific areas of ANN applications, which will now be briefly discussed in terms of their application significance and appropriate modifications of the basic ANN methodology to improve the model development. At the outset, it is pertinent to mention that because of the complexity in multiphase systems and the flexibility in the ANN methodology, it is natural to combine it with additional algorithms to effect better or more optimum results. More discussions on this issue will be made in a later section on ANN-based hybrid algorithms.

The first area mentioned in Ref. [30] deals with the phenomena of two-phase flow in pipes. Two-phase gas-liquid flows are among

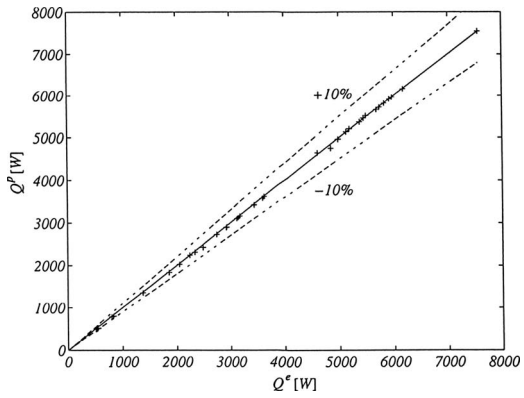

Fig. 10 Experimental versus ANN-predicted total heat transfer for the heat exchanger in Fig. 2(*c*) under limited data

the most complex and difficult phenomena in heat transfer, characterized by interfacial interactions and relative movement between the phases. The case with a single component is even more complex. In view of applications such as thermohydraulics in nuclear reactors, petroleum processing, and biomedical processes, predictive models based on traditional correlations are only valid for distinct flow regimes such as bubbly, slug, churn, annular, and stratified flows. Therefore, such correlation models cannot be used unless the specific flow regime is first identified. For two-component, two-phase flows (air-water, for instance) in pipes, the nonintrusive impedance measurements of the area-averaged void fractions give different signal characteristics for different flow regimes. These data are then used to train the ANN. In one study [31], because of the relationship between the impedance signal and the specific flow regime is not crisp, the ANN output was placed in series with a fuzzy-logic classifier to determine the likely flow regime. The three-layer 2-12-6 ANN adopted is also of some general interest. The two inputs are the diagonal and neighboring impedances, and the six-node output layer consists of two nodes identical to those in the input layer for identification purposes, one each providing the standard deviations of the diagonal and neighboring impedances, and the last two nodes are related to the media of the inputs. The training data consisted of 200 data points for each of the four flow regimes. Additional data points were used for testing the ANN predictions. In a subsequent study of the same problem [32], two freestanding ANNs were used for flow-regime identification. One is again a three-layer connected configuration, but with only one single output node, which is the flow-regime indicator. The input layer had four nodes consisting of the mean and standard deviations of the diagonal and neighboring impedance data, and the hidden layer had 12 nodes. The second ANN is based on a self-organized (unsupervised) neural network with two layers only to cluster the two input data into four categories corresponding to the four flow regimes. Both studies [31,32] produced good results in the flow-regime identification. These examples also show the flexibility and possible modification of the basic ANN methodology. The same review also mentioned another ANN flow-regime identification study dealing with oil-gas-water multiphase flow in a horizontal pipe [33]. The instantaneous differential-pressure signals from the flow were measured with a piezoresistance pressure transducer with very fast response. The signals were preprocessed and denoised by a wavelet methodology to give characteristic vectors of various flow regimes, which were then used as inputs to the ANN to classify the flow regimes. The analysis was used to just identify three flow regimes, namely, stratified flow, intermittent flow, and annular flow. The input layer had nine nodes characterizing the preprocessed signals, and the output had three nodes with (1,0,0) for stratified flow, (0,1,0) for intermittent flow, and (0,0,1) for annular flow. The lone hidden layer had five nodes. A nonlinear least-squares algorithm was used to improve the learning speed and overall training efficiency. A total of 200 data sets were used for training, while additional 95 sets were for testing. The results show that the flow-identification accuracy was 95% for the stratified flow and 92% for both intermittent and annular flows.

As reviewed in Ref. [30], the second specific area of multiphase thermal systems treated by the ANN analysis deals with two-phase flow with heat transfer, as characterized by the added complexity due to temperature differences. The ANN application to predict the critical heat flux in round vertical-tube flow of water under low pressure and oscillating flow conditions for either natural or forced circulations was carried out in a more recent study by Su et al. [34]. A fully connected 7-10-1 ANN with the standard feed-forward algorithm was chosen, but using a hyperbolic-tangent activation function, representing a slight variation of the basic methodology. The training process was aided by the use of both optimized learning and momentum rates. The inputs included pressure, mean mass flow rate, relative amplitude, inlet subcooling, oscillation period, and geometrical ratio of the heated length to tube diameter. One additional input node was a numeral unity, providing a threshold to nodes in the next layer. This example thus illustrates another slight modification to the standard algorithm. The ten-node hidden layer also included a unity node for the same purpose. The single-node output layer was a dimensionless ratio of the critical heat flux with oscillation to that without oscillation given by the test data. The study utilized two separate trained networks: one with natural and the other for forced circulation data sets. It was demonstrated that the average parity ratios of the training sets were well within 10%, while the average error of the testing data was on the order of 1.0%, again comparable to the experimental uncertainties.

The third topic area reviewed in Ref. [30] deals with even more complex phenomena of multiphase flow and heat transfer in such specialized systems as bubble columns, packed towers, fluidized beds, and heat transfer and flow in fluid-particle two-phase systems. In each of the problem areas, ANNs were utilized to develop predictive models for heat and mass transfer because of the nonlinear mapping capabilities of the ANNs. Examples of these applications will concentrate on the different algorithmic aspects of the ANNs used, as deviated from the standard methodology. The first example treats the correlation of heat-transfer rate fluctuations in 3D bubble columns with quantitative dynamic behavior of bubble and liquid motions [35]. The ANN was trained with a three-layer configuration by the time-series data of local heat transfer from hot-wire measurements. The ANN analysis was that of the standard methodology. Usually, the choice of inputs depends on the physical insights. However, when the phenomena are very complex as in bubble columns, the input parameters might not be obvious. Here in numerical experimentation, the number of input-layer nodes was varied from 2 to 8, and the middle hidden layer from 5 to 50. The trials, together with the single output node for the local time-averaged heat-transfer rate of the liquid phase during a given time period, were used in the training process to determine the optimum number of nodes of the first two layers. These trials resulted in an optimum number of nodes of the first two layers and a 6-10-1 configuration. About one-half of the hot-wire data in the time series in a 20 cm column at gas velocities of 2.3 cm/s, 6.2 cm/s, and 9.0 cm/s were selected as the ANN training data sets, while the remaining data of the 20 cm, 40 cm, and 80 cm columns, measured at the same position over the whole range of gas velocities, were used for testing. The ANN prediction results for all three-column sizes showed that the parity errors between the predicted and measured coefficients of heat transfer were within 20%, while the average error was less than 3%. One interesting result is that none of the measured data for the larger column sizes were used in the training data set, indicating that the relation between the local heat transfer and dynamic liquid and bubble motions was independent of the column size. The result clearly demonstrates that the ANN analysis in this instance is capable of generating new knowledge.

A last example in this third topic area deals with the infiltration of nonaqueous phase liquid (NAPL) through a vertical, homogeneous, soil column initially saturated with water, as studied by Morshed and Powers [36]. An ANN analysis was utilized to develop an appropriate model for the elevation and volume of NAPL. One novelty in this study was that the training and testing data sets were generated by a theoretical model. These data sets were preprocessed by dimensional analysis to identify dimensionless terms associated with the input-output relations. Numerical experiments were carried out to determine the optimum number of nodes in the middle hidden layer in a 4-5-10 configuration. A hyperbolic-tangent activity function was used for the hidden layer and a linear activation function was used for the output layer. One-half of the total 410 data sets were used for training, while the rest of the data sets were used for testing. The results showed that for the training data set, the regression coefficient had an average of 0.989 (1.0 for perfect match). For the testing set, the same coefficient ranged from 0.962 to 1.0, which indicated a great

success of the ANN model. In the parity comparison, 195 of the 205 data points fell within the range of 10% of the experimental values.

The fourth topic reviewed in Ref. [30] treats heat transfer in evaporators and boiling heat transfer in liquid mixtures. One example has already been given earlier in Ref. [27] dealing with very limited data for a Freon evaporator, and hence will not be repeated here. The more recent study of Kelleher et al. [37] attempted to predict nucleate pool boiling heat transfer from a vertical tube bank with and without fins on the tubes in Refrigerant R-114 with various amounts of oil present by utilizing the ANN analysis. In practice, such oil is present due to carryover of lubricant oil from the compressor. Different sets of test data served as training and testing data. The input layer of the three-layer fully connected ANN configuration consisted of four nodes, representing the temperature over saturation, number of active tubes, mass percent of oil in the test refrigerant, and whether the tubes were finned or staggered. The output layer had a single node related to the boiling heat flux. Entirely satisfactory ANN predictions realized with parity errors again approach the uncertainties of the experimental data. Another is the study of Liu et al. [38], which deals with boiling heat-transfer enhancement using organic additives. The primary objective was to evaluate and predict the boiling heat flux as a function of the addictive molecular structure. The ANN model was trained with 30 additives and tested additional 11 additives used in the testing samples. The molecular structure of any additive was represented by four parameters in the ANN input, and the single output was the relative increase in the boiling heat flux at the same temperature difference with the additive. There were two hidden layers, for each of which the number of nodes was allowed to vary between 1 and 14. Numerical experimentation revealed that the optimized number of nodes for the first and second hidden layers were 3 and 6, respectively. Another deviation from the common practice was that the hyperbolic-tangent activation function was applied to the nodes in the first hidden layer, the sigmoid function for nodes in the second hidden layer, and a linear function for nodes in the output layer. Good results were obtained, showing 100% parity accuracy for the training data sets and over 90% for the testing cases. Analysis of the results showed that the molecular weights of the additives and the polar groups had the greatest effects on the boiling heat-transfer enhancement. This gives another example of the knowledge discovery ability of the ANN analysis.

Furthermore, industrial thermal processes are generally very complex and involve the interactions of different components. The performance of the entire process is difficult to model, which is, however, needed for performance prediction and control. Only possible information must necessarily come from direct experiments. This is indeed a natural situation for the ANN analysis. Since some individual processes also involve multiphase phenomena, their ANN analysis and results were also covered in the recent review [30], which included an example of the simulation of heat transfer during spray cooling in conjunction with predicting cooling times in metal processing [39]. The hear-transfer data were obtained experimentally for a range of pressure ratios for surface temperatures up to 800°C. In this study, a commercial neural network code was used, but it also included a GA with a statistical estimator to assure the relevance of the inputs to the ANN. Two separate models were created from the code: a spray characterization model and a heat-transfer model. In the characterization model, the ANN had five input nodes corresponding to air pressure, water pressure, air and water flow rates, and nozzle height. The lone output node is denoted water mass flux. In the heat-transfer model, there were three inputs of time, surface temperature, and the water mass flux together with a coefficient of heat transfer as the only output. While the first ANN yielded good results compared to the experimental data, the second ANN produced unsatisfactory results, suggesting that the relevant experimental data should definitely be improved. This case shows the feasibility of using strategically more than one ANN in series to simplify the network structures and also suggests the possibility of the presence of faulty or inaccurate experiments. Basically, the same physical problem was treated with the ANN analysis by Ward et al. [40], using a single four-layer network with air and water pressures and the surface temperatures as the inputs, and the coefficient of heat transfer as the lone output, and there were two hidden layers, each with eight nodes to start with. One novelty here was that the errors in the output layer were used to adjust the network configuration and the activation functions until the overall root-mean-square error became acceptably low. This is another example where the network parameters, including the configuration, are allowed to systematically vary until satisfactory results are obtained. This same reference also discussed several other ANN-based analyses of industrial processes such as prediction of pollutant emissions from pulverized coal combustion, modeling of chemical vapor deposition [41], and performance prediction of a stoker-fired boiler [42].

The very last area of multiphase processes reviewed in Ref. [30]. is that involved in the thermal processing of food. It is known that first-principles thermal-processing models for food are difficult to develop and essentially nonexistent, and the primary reason is due to the lack of adequate constitutive relations and the corresponding thermophysical properties. However, the critical need for such models for process optimization and control, process design, and scaling-up processes is quite self-evident. Experimental data, however, are amply available to provide the only processing information for food production, in general. Therefore, it is only natural to inquire if good modeling results can also be realized by using the ANN analysis. The study carried out by Mittal and Zhang [43] should give an indication of this prospect. It dealt with the prediction of freezing times for food products, and treated food products of arbitrary shape. Therefore, it is not really surprising to find that the training data were derived from a theoretical model such as the one developed by Pham [44]. The ANN adopted was the commercially available code know as WARDNETS, and had ten input nodes of product thickness, width, length, surface convective coefficient of heat transfer, thermal conductivity of frozen product, product density, specific heat of unfrozen product, moisture content of product, initial product temperature, and the ambient temperature. The network configuration is that of 10-40-40-40-1, where the lone output was the freezing time. Different activation functions such as Gaussian, Gaussian complement, and hyperbolic tangent were all tried to determine the best choice. Similarly, the learning and momentum rates were also arbitrarily chosen at first to determine the best learning performance. A total of 44,351 data sets were generated from the theoretical model, from which 60% of the data sets, randomly chosen, were used for training and the rest for testing. The ANN results showed that for more than 83% of the test data sets, the parity error was less than 5%, while the average parity error was only 3.54%, but the maximum error was still as high as 86%. Also, an attempt was made to compare the ANN prediction with some 150 data points of experiment, and it was found that in 87% of these cases, the parity error was less than 10%.

For steady-state thermal problems, there are still many other individual efforts in exploring the applications of the basic ANN analysis for purpose of model development and functional identification. For the interested reader, the following references may offer a glimpse of additional thermal problems that have been successfully treated by the ANN methodology: thermal placement in power electronics [45], thermodynamic properties [46], thermal imaging processing [47], delay-time determination in HVAC systems [48], inverse radiation heat transfer for design and control [49], and subcooled water critical heat flux [50].

ANN Applications in Dynamic Thermal Problems

In thermal engineering, one of the most neglected areas of research is the modeling of dynamic behaviors of thermal devices

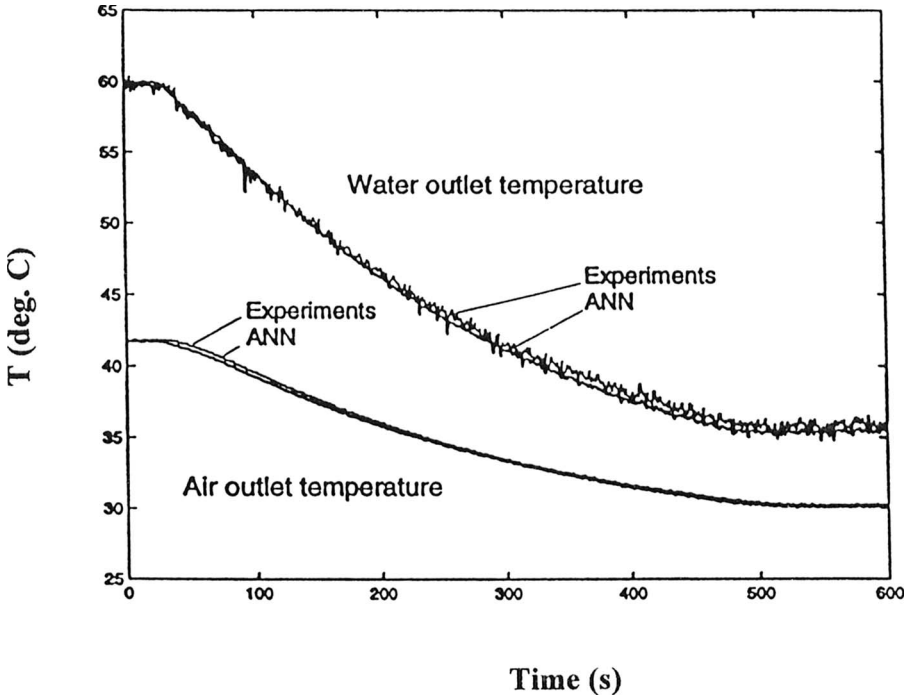

Fig. 11 Dynamic prediction by ANN for sudden cooling

and systems. All such devices in real applications operate in dynamic conditions in responding to changes in the operating parameters and boundary conditions. In addition, the performance of one device is also affected by other devices and components that are directly or indirectly connected to it, due to the thermal masses involved. Therefore, we do need dynamic models for their performance under dynamic conditions. Furthermore, there is even a more critical role for such dynamic models. As applications become more complex, especially those involved in thermal systems and processes with multitude and interconnected thermal devices, it becomes amply clear that such systems and processes must meet a certain performance requirement. One viable solution is to develop robust and adaptive control schemes and implement them to satisfy such requirement. The popular proportional-integral-derivative (PID) controllers are simply not robust enough, since in typical complex thermal problems nonlinear behaviors are the norm. Many known control schemes that are robust, stable, adaptive, and optimal all require dynamic plant models for their implementation. Here lies, then, another reason for the need for dynamic models. It has been known that traditional analysis cannot be depended on developing dynamic models even for simple thermal devices. On the other hand, it now appears that the ANN-based paradigm, with the dynamic training data obtained either online or offline, offers a real viable solution [12].

The central scheme in the dynamic modeling by ANN is the addition of time as a variable for both training and prediction. One equivalent, but more efficient method of training is to provide the variables at time t as inputs, and the values of the same variables at $t+\Delta t$ as the outputs, and also keep the incremental variables small so that simple ANN configurations can be used. The training is successively carried out to cover the entire time period of a single experimental run. Such a network where the input and output change their places is generally known as a recurrent network [51–54]. As an illustration, a series of tests dealing with the dynamic heating and cooling of air by the same single-row fin-tube heat exchanger shown in Fig. 2(*a*), used previously under static conditions, was carried out to obtain the dynamic data on the outlet temperatures of both air and water flows, by varying the water inlet temperatures in small incremental steps while keeping the other variables such as the flow rates of both fluids and the inlet air temperature all constant [8]. More specifically, the water inlet temperature was varied in increments of 5.56°C from 32.2°C up to 65.6°C. These data were then used to train the ANNs for dynamic applications, using a simple 3-5-2 network. The three input nodes corresponded to the inlet and outlet water temperatures and the air outlet temperature at time t, and the two output nodes corresponded to the air and water outlet temperatures at the next time instant. For testing the ANN predictions, three additional experiments were performed. In the first testing experiments, the system was first brought up to a steady temperature of 60°C, and the heater was then set at 37.8°C. The resulting sudden decrease of the air-water outlet temperatures is shown in Fig. 11. The ANN predictions were excellent and the slight oscillations in the measured water outlet temperatures were due to local flow turbulence. In the second testing experiments, the water inlet temperature was ramped manually and the results are shown in Fig. 12. The ANN result was equally excellent. In the third testing experiments, we designed a system to see if the ANN analysis could predict the system behavior when an input variable was different from the one in the training data. In this case, the changes in the air and water outlet temperatures were measured when the airflow rate was first increased to a value greater than the one used in the training data, and then decreased to a lower value. It may be of interest to note that this collective deviation from that of the training data could also be interpreted as a source of noise that could indeed exist in real applications. The results are shown in Fig. 13, and the predictions are not as good. However, it is still remarkable that the ANN analysis still predicts the correct overall trends with rather small errors. It is noted, however, that all these three examples specifically deal with training and testing of first-order problems, in that the training only requires one single time step between the input and output. In general problems, it is conceivable that a higher-order training may be needed due to system complexity. However, as demonstrated by Diaz et al. [52], it is rarely necessary to train the network with data from two previous time steps, as long as the chosen time step is reasonably small. Also in the examples shown in this section,

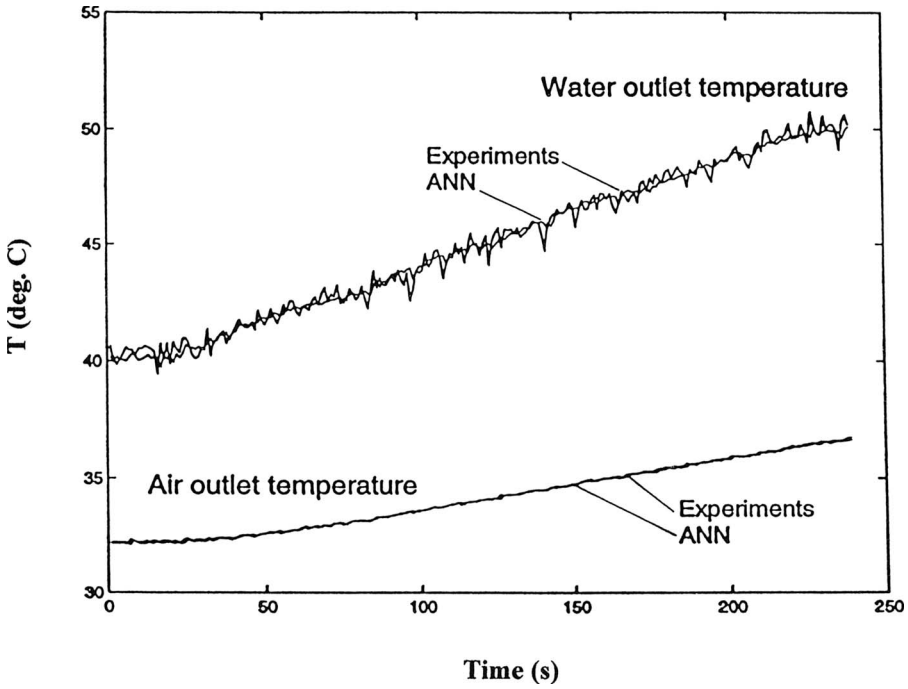

Fig. 12 Dynamic prediction by ANN for ramped heating

the training is carried out offline, meaning that the training of the network is carried out independently from the testing cases. However, in many thermal applications, operating conditions are either uncertain or unknown. In such cases, the training must be carried out adaptively in that the training is done online, and continuing as the new operating data become available. This obviously important feature of the ANN analysis is critical in the development of desirable control schemes for complex thermal systems and processes, as will be demonstrated in the next section.

ANN Applications in Dynamic Thermal Control

As already mentioned before, dynamic thermal control represents the key to achieve optimum performance of complex thermal systems. As the thermal systems become even more complex in time, as universally expected in real applications to come, the need for optimal dynamic control also becomes increasingly more critical. A common practice is to use feedback control involving a system (plant) model, in conjunction with a standard PID control-

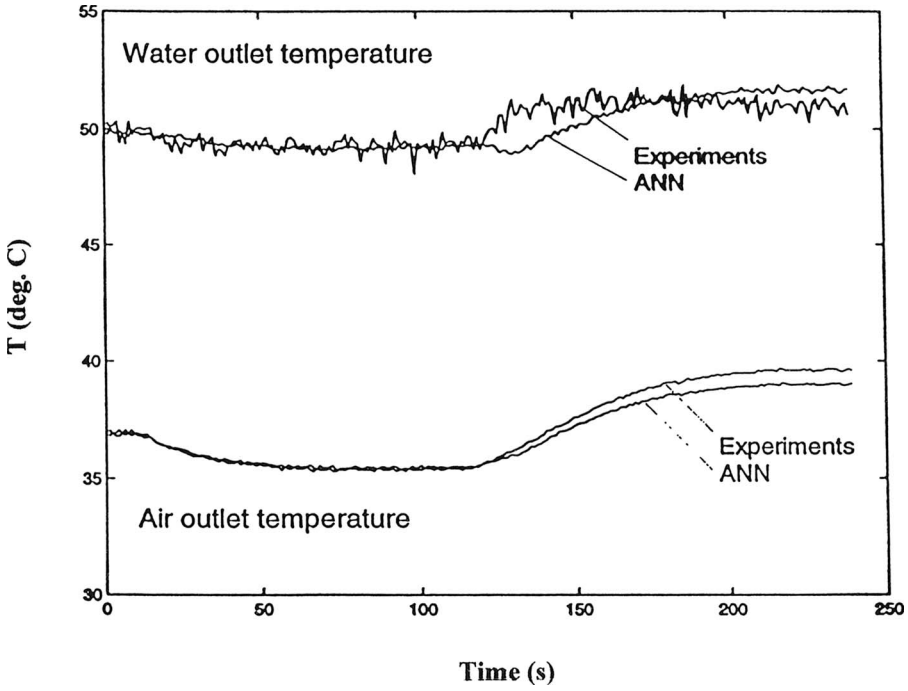

Fig. 13 Dynamic prediction by ANN for changes in the airflow rates

ler. Such control, unfortunately, requires constant manual supervision to achieve, if at all, optimality. Many dynamic control strategies [8] have been proposed to alleviate the shortcomings with the PID controller, with or without a plant model. On the other hand, there are many advantages to use plant models based on ANNs, and among them is the fact that an inverse ANN model, which is nothing but the model with the input and output switched, can serve as a controller or a neurocontroller [55–58]. This ANN characteristic opens up many possible ways to develop innovative control strategies for complex thermal system applications. To quote just a few examples, we find them in the use of recurrent networks [59–61], control of heat exchanger performance [51,52,62], HVAC control [59,60,63,64], and thermal process control [40,65–67]. The specific purpose of these ANN control strategies is to ensure the system performance to satisfy certain prescribed requirements known as performance targets, such as stabilization after occurrence of disturbance, prescribed temperature bounds, minimum system energy consumption, and the like. The ultimate goals are that the desired control strategies and their implementation should be robust and generic, adaptive for automatic accommodation to changes in operational parameters, optimal for satisfying performance requirement under all expected operating conditions, and in real time for quick implementation of the control strategies. Another basic requirement is to ensure controllability at all times. It should be noted at the outset the current development of dynamic adaptive control strategies based on ANN for most complex thermal systems is still in the exploratory stage, and the emphasis is largely placed on developing desirable controllers for simple thermal systems such as individual thermal devices to ensure meeting their performance requirement. As it will be shown, such strategies are essentially available at the present time. However, as the number of controlled variables increases, the design of the corresponding control strategies also becomes increasingly complex, and this is the area where research studies would likely be concentrated in the future [67,68].

For the purpose of the present review, it is appropriate to illustrate the present state of the development of neurocontroller strategies and their performance by means of examples, based on studies in our own laboratory, along with some commentary on some of the ANN applications. In general, even in a simple single input–single output (SISO) control system, there are two basic issues in implementing an ANN-based control strategy. One is the decision of the basic control scheme, nonadaptive (conventional) or adaptive, and the other is to determine how the ANN, as a neurocontroller, is trained. The difference between the conventional and adaptive control schemes is that the former reacts to disturbances acting upon the controlled variables, while the latter disturbances acting upon the parameters of the process [69]. Adaptive control consists of automatically adjusting in real time the parameters of the controller, the weights and biases of the neurocontroller in this case, so that a desired level of performance of the control system is achieved when the process parameters being controlled are unknown or vary with time. Training of neurocontroller can be either offline or online. The type of training shown previously to develop the three dynamic models in Figs. 11–13 is a typical example of offline training. The other uses a neurocontroller that adapts to the changing conditions of the system [63]. Thermal devices and their networks are systems that are subject to variations in their behaviors in time. An example is the problem of fouling, which presents a change in the operational behaviors of thermal systems. Consequently, a neurocontroller designed and built for such systems will have to adapt itself to the new operational conditions, or otherwise the control action will be biased. Many operating thermal devises and systems also have inherent unique complexity and nonlinearity. For instance, the system to be controlled not only includes the thermal device itself, but also its associated hardware such as piping, pumps or fans, heaters or coolers, and also instrumental hardware. Furthermore,

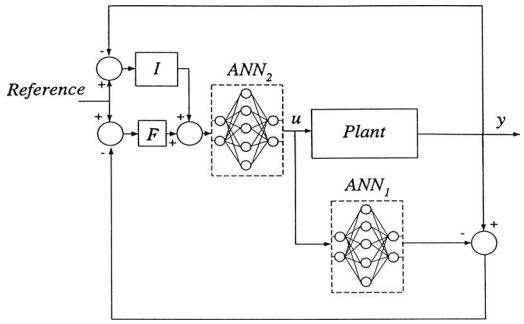

Fig. 14 General IMC structure with integral control

there is always unavoidable delay between what happens at the thermal device and at the measurement station at some distance away, where the control signal is generated. Such delay may also vary with the changing operating conditions. Fortunately, the neurocontrollers are very well suited for these difficult tasks, as they can be taught by adaptive training to learn the responses of the system at any given time instant.

The example to be used here to demonstrate a viable neurocontroller-based control strategy and its verification by means of experiments again deals with the single-row water-to-air heat exchanger used in our earlier ANN studies, as shown in Fig. 2(*a*). In the experiments, the terminal air and water temperatures were measured by thermocouples. The airflow in the open wind tunnel was controlled by a variable-speed drive that could be operated either manually or automatically from a PC. The airspeed could be controlled within a certain range and was measured by a pitot tube located upstream of the heat exchanger. The calibration of the airflow measurements was performed using average air velocities based on ASHRAE test codes. A single point temperature measurement was used upstream of the heat exchanger and five thermocouples connected in parallel were used to obtain the outlet air temperature. Information about the four terminal temperatures of air and water flows, the water mass flow, and the airspeed, and the time instant were sent to the PC that also served as a controller. The inlet water temperature was varied by a heater with a PID-controlled electric resistance, and the water mass flow rate was changed by an electronic valve so the percentage of valve opening could be controlled as desired from the PC. The data acquisition board used could obtain up to 16 different channels of data simultaneously. LABVIEW was used to acquire and send data to the experimental system and a program written in C interfaced with it to perform the desired control function. Other details of the experiments and data acquisition can be found in Refs. [52,69]. Here the thermal system was confined to a SISO system to control the air outlet temperature, and for ease of experimentation the airflow rate was taken as the control variable with all other variables fixed.

There are several control schemes that use ANN as the dynamic controller of a physical system [55]. It is noted that in an earlier study, an attempt was made to implement a neurocontroller-based control scheme in which the training of the controller was carried out completely offline [52,70]. However, since such schemes do not include adaptive capability, it has only limited applications, and the reader is referred to Refs. [55,69] for details. The emphasis here is placed on the adaptive-training capability, while the ANN performs its control functions such as minimizing the target error, maintaining the stability of the changing neurocontroller, and satisfying some other optimal conditions that may be imposed on the system control. In addition, the adaptive neurocontroller scheme is developed within the framework of the internal model control (IMC) [55,61,71], because of its good characteristics of adaptation, robustness, and stability. The idea behind the IMC, shown schematically in Fig. 14, is to have an ANN plant model of the heat exchanger system, designated as ANN_1, in parallel with

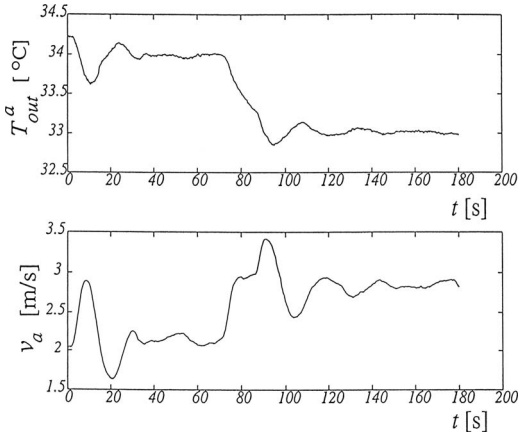

Fig. 15 Sudden change of the set point in the air-outlet temperature under IMC-based adaptive neurocontrol

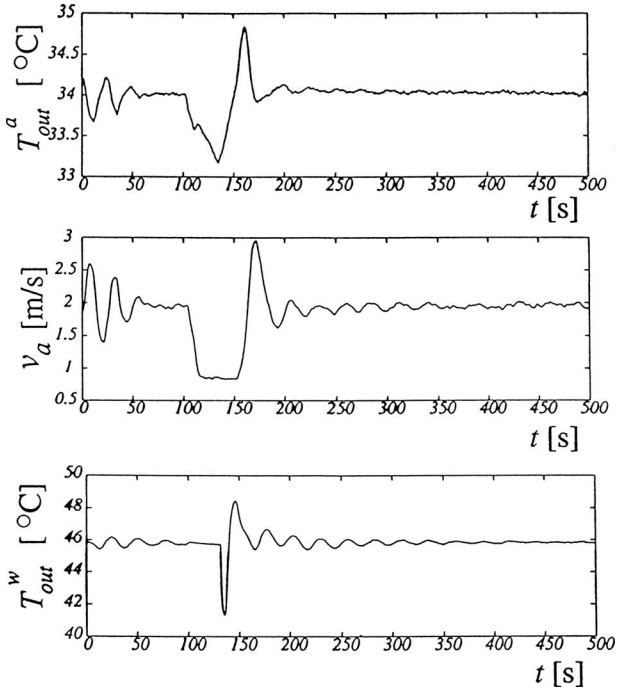

Fig. 16 Response to water-side disturbance by water-flow disruption under IMC-based adaptive neurocontrol

the real system. The difference between the output of the real system and the model is used as the feedback for the neurocontroller, ANN_2, located in the forward path of the control scheme. The ANN_1 is first trained to learn the dynamics of the plant. ANN_2 is then trained to learn the inverse dynamics to be a nonlinear controller. In the adaptive-control experiments, the two neuronets were trained with information of the exit air temperature and the airspeed, while the inlet air and water temperatures and the water flow rates are kept constant. The data are normally obtained by making measurements of the system subjected to small increments in the set point. The Filter F and the Integral controller I would help the system to reach the actual set-point temperature even with the noise embedded in the measurements [52]. Adaptation, as described earlier, consists of automatically adjusting in real time the parameters of the neurocontroller so that a desired level of control performance can be achieved, when the parameters being controlled were unknown or changing with time [55,69]. The adaptation is done by carrying out single training cycles until the performance criteria are satisfied [72]. The effects of different time constants of various components in the system do require a backup control function that can usually be provided by a PID controller until the ANNs adapt to any new operating condition of the plant.

It is also important to note that under the adaptive control mode when the neurocontroller is trained online with new incoming data, one objective is to minimize the target error between the output and the prediction. In doing so, the neurocontroller being trained may produce a dynamic unstable behavior, and therefore the stability of the controller must be continually monitored at all times during training. Such a process to maintain stability has also been developed, as given in Ref. [70]. At the same time, when the ANN parameters with respect to the target error also ensure stability, it is also possible to simultaneously consider other optimal criteria, such as minimizing the plant energy consumption and driving the system to an operating point to satisfy all three desired criteria. Other functions need to be optimized can be treated the same way.

Five sets of experiments were carried out on the same single-row fin-coil heat exchanger to verify the validity of the IMC-based neurocontroller strategy. These are individually discussed in the following and it will be shown that satisfactory performance of the neurocontroller was reached in all cases [69]. The first experiment corresponded to a sudden change in the set point of the outlet air temperature, with the result shown in Fig. 15. The top curve shows the time variation of the outlet air temperature, and the bottom curve shows the needed time-dependent control variable in the airspeed. The experiment consisted of turning on the controller at an outlet temperature close to 34 °C, while maintaining a constant water flow rate of 2.71×10^{-4} m^3/s. When the adaptation criteria, i.e., stability and target error, were not matched, the controller started the adaptation process to let a PID controller keep the physical plant as close as possible to the set-point temperature until the adaptation criteria were satisfied. It is seen in Fig. 15 that, during the first 30 s in the test, the controller was indeed adapting, and then it stabilized the plant at the desired set-point temperature. At $t=70$ s, the set point was suddenly changed to 33 °C. The controller detected an abrupt change in the target error and started another adaptation process. During this period, the PID controller took over again and tried to keep the system close to the new set point. At about $t=90$ s, the neurocontroller regained control of the system and stabilized it at the new set point. It is interesting to observe that the airspeed increased by about 50%.

The second test dealt with the case of water-side disturbance, caused by shutting off the water flow for a specified period of time. As shown in Fig. 16 of the experimental result, the neurocontroller was first turned on and adapted until the adaptation criteria were satisfied. The initial oscillations were mainly due to the action of the PID controller while the neurocontroller adapted. It then kept the system close to the same 34 °C for the air outlet temperature. At $t=100$ s, the disturbance was applied for a period of 30 s. The neurocontroller worked until $t=110$ s, at which point it handed the control action to the PID while it underwent a second adaptation. At t=130 s, the water flow resumed. In the mean time, the PID tried to keep up with the reference temperature by reducing the airspeed to a minimum, but was unable to maintain the outlet air temperature without the water flow. The adaptation of the neurocontroller was complete around $t=170$ s, after which it took over the control action. Figure 16 also showed the water outlet temperature during the same period. Between 100 s and 130 s, there was no water flow so that the water outlet temperature remained the same. When the water flow resumed, the cold water that remained in the heat exchanger flowed past the thermocouple, and was followed by hot water that was stagnant in the heater. The resulting blip in the water outlet temperature could be seen in the figure. The temperature oscillations were due to portions of cold

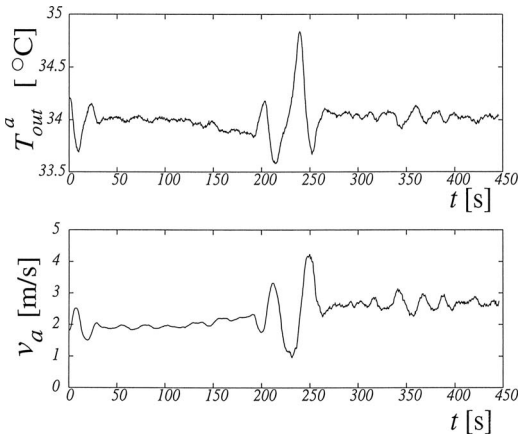

Fig. 17 Response to air-side disturbance with gradual reduction of air-inlet area under IMC-based adaptive neurocontrol

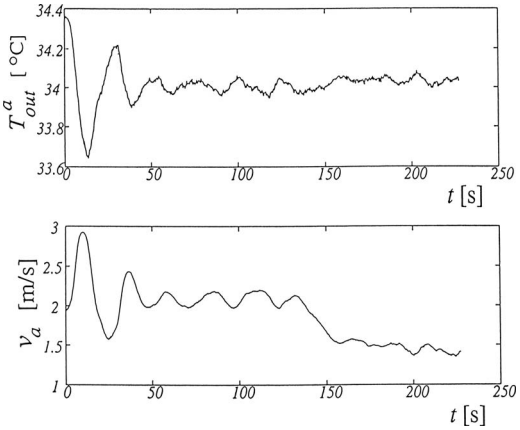

Fig. 19 Energy minimization routine to reduce both flow rates while maintaining set temperature as an added ability of the neurocontroller

and hot water repeatedly passing the thermocouple while circulating within the closed loop. It is also seen that the airspeed has a similar oscillatory behavior.

The third experiment was the most critical for the neurocontroller by reducing the air inlet area of the open wind tunnel, thus representing a structural change in the heat exchanger thermal system. Two separate subexperiments were performed; one by reducing the cross-sectional area gradually and the other suddenly. Figure 17 shows the measured results for the first case with gradual air-inlet area reduction. In the first 30 s, the system was under PID control, and the neurocontroller gained the control at the 30 s mark. From 100 s to 220 s, the air inlet area was blocked gradually to only one-half of the original area. During this period, the neurocontroller increased the airspeed to maintain the system at 34 °C. There was a point at about 190 s when the ANN model was not able to characterize the system and a new adaptation began, and continued until about 260 s. After it had learned, the new relation between the output air temperature and the airspeed took over the control action to stabilize the system. It is observed in Fig. 17 that there were some oscillations of the temperature between 330 s and 350 s marks, but the outlet air temperature finally settled down to the original set point.

An even more critical test is the same as that of the first air-side disturbance test, except with one-half of the inlet air area suddenly blocked. The results are shown in Fig. 18. At first, the outlet air temperature was close to the original set point. For the first 50 s, the controller adapted until it learned the system behavior and kept the temperature stable at the original value. At 150 s, half of the air inlet area was blocked suddenly, and the controller adapted until it learned the characteristics of the new system. It is seen in Fig. 18 that the airspeed increased approximately 50%. Finally, at about the 240 s mark, the neurocontroller regained its control of the plant and stabilized the system at the original set point.

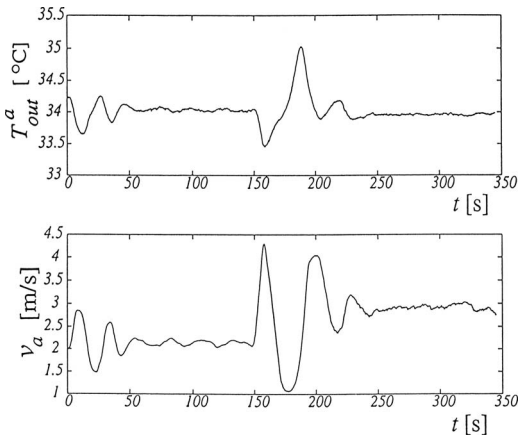

Fig. 18 Response to air-side disturbance with sudden reduction of air-inlet area under IMC-based adaptive neurocontrol

The next and the last experiment is not a demonstration to show the feasibility of the IMC-based neurocontroller, but to illustrate an important new capability of this controller. In addition to the desired control to achieve the accuracy, adaptation, and stability of this control strategy, this neurocontroller is also able to handle any optimal condition or conditions that may be imposed on the control by the system operation. In this last experiment, it was also deemed desirable to minimize the energy consumption in the thermal system, though any other optimal condition can be similarly treated. It was first determined that from exploratory experiments, it was found that the electric heater was the thermal component that consumed the most energy, and that the lower water and airflow rates would lead to lower use of the thermal energy. From these exploratory experiments, the energy for each sampled measurements would give the direction of decreasing energy use. The controller would then drive the system in this direction. However, if the controller senses that the system is behaving in an opposite way, it will then adapt to the new desirable characteristics of the system. The implementation of this capability is done as follows. In addition to the two adaptation criteria for the weights and biases of the ANNs, i.e., low target error and stable operation, a third is added representing minimizing of energy consumption. When the two basic adaptation criteria are satisfied, the training based on the third adaptation criterion is then turned on. The result of this experiment is given in Fig. 19, showing the lower airspeed after the last training is turned on, thus implying lower water flow rates, while the set-point temperature is still maintained.

While the IMC-based neurocontroller strategy is seen to satisfy all nonlinear dynamic control requirements as demonstrated by the above experimental tests, this demonstration has been limited to SISO systems. In principle, this is not a limitation of the adaptive neurocontroller strategy. However, it is true that for general multiple-input and multiple-output (MIMO) systems, the corresponding control strategy does become very complex, and as already pointed out, it represents a very fruitful area of research for ANN-based applications. Also, it may be important to point out that an even newer research paradigm based on broad-based artificial intelligence (AI) methodologies may be needed to develop new strategies for dealing with very large scale and very complex thermal systems that require versatile scalability to reduce system complexity to manageable levels. A small step in this direction is

already emerging, and it is based on the development of integrated hybrid AI methodologies, as discussed in the next section.

Hybrid ANN Methodologies

As it is generally known, the ANN methodology is one of the most successful AI methodologies or soft-computing algorithms that have found applications in thermal problems and systems [1,8]. However, there are other (AI) algorithms that are also very successful in this regard. Good examples include evolutionary algorithms (GA and GP), clustering analysis, fuzzy-logic systems and control, expert systems, data mining, virtual memory, and others. Their applications deal with many tasks such as pattern recognition, decision making, system control, information processing, natural languages, symbolic mathematics, speech recognition, artificial vision, and robotics. One interesting characteristic of these methodologies is that they are mostly complementary rather than competitive, and it is often somewhat advantageous to deploy them in combination than exclusively to achieve higher levels of utility, efficiency, and performance in applications in thermal problems and systems. As discussed earlier regarding the implementation issues in the basic ANN analysis, there are free parameters and steps in the nodal calculations that need to be determined, as well as in the learning algorithm that could be modified or optimized. Even though all of these determinations can be ascertained in given applications by numerical experiments, it is nevertheless not a very efficient process. This is where all the other soft-computing and AI methodologies can be called upon to improve the basic ANN analysis as additional subroutines. Conversely, it is also plausible that the ANN itself can be considered as subroutines to be inserted into the other AL methodologies to improve their own performance.

As all the major (AI) methodologies, including the ANN, are still under active development, the progress in developing hybrid algorithms understandably has not yet been very robust, However, it is appropriate here to cite just a few examples of these ANN-based hybrids to illustrate where we are now and also suggest areas for further studies. Genetic algorithms (Gas), as an evolutionary algorithm [1,73], is a rather popular search engine to find various optima in conjunction with ANN and ANN fuzzy-logic applications. Vonk et al. [74], for instance, proposed a methodology to automatically generate configuration based on evolutionary computation such as GA. Kaminski et al. [75] studied the thermal deterioration processes by combined ANN and GA analysis. Oliveira and Sousa [39] utilized GA with a statistical estimator to determine the relevance of complex input parameters for ANN applications. Tarca et al. [76] adopted an integrated GA-ANN strategy for modeling important multiphase flow characteristics. Clustering, as already demonstrated, involves pattern recognition of subgroups within a large database [25,77–80], and can be used for knowledge generation as well as to determine the relevant input parameters similar to that in Ref. [39]. Also, it is of great interest to note a major emerging hybrid AI methodology known as neuro-fuzzy or fuzzy-neuro system, which has been shown to be very successful in dealing with pattern recognition of noisy and fuzzy sets of data. Two texts with somewhat different emphases are those of Jany et al. [81] dealing with the computational methodology and Brown and Harris [82] with adaptive modeling and control. These hybrid algorithms have also been used for several individual applications, such as the GA-based neuro-fuzzy system for temperature control [83], development of a fuzzy-neural module for home comfort in buses [84], prediction of critical heat flux using fuzzy theory and ANN [85], and the study using an ANN module in series with a fuzzy-logic module [31] for flow-regime identification in two-phase flows, as already mentioned in the section on ANN-based steady thermal problems.

The current status of ANN-based hybrid algorithms is definitely gaining popularity as they are capable of dealing with increasingly more complex thermal phenomena and problems. It is definitely expected that, as fundamental research on AI methodology including the ones on ANN, we will see many fruitful developments of hybrid algorithms to address thermal problems that are difficult to handle at the present time.

Future Prospects for ANN Methodologies

From the present brief review, it is seen that ANN methodologies and the corresponding new paradigm represent a promising way to approach and solve difficult thermal problems. Shortcomings such as the need for reliable experimental data and uncertain choice of free parameters in the basic ANN methodology do exist, but their effects are expected to be reduced in time as results of more basic studies on the methodology become available. Much of that is on going right now. On the other hand, with the ever-present noisy, imperfect, and uncertain information in real-world applications, it is perfectly logical to suspect that ANN alone may not provide the whole answers to complicated problems, but also rely on combined solutions from the AI universe. This movement is now already under way, and thermal engineers must be prepared to participate and lead, if the thermal science and engineering discipline continues to flourish. A good example is that now it is well within reach to treat very complex thermal systems in scalable design and control such as large thermal plants with highly interconnected subsystems involving multitude of thermal devices, by means of dynamic agent-based control with the full implement of all the major AI methodologies [86–88].

Conclusions

The present paper gives a brief review of the current status of applying the new artificial neural network (ANN) paradigm to difficult and complex thermal problems that cannot be readily solved by traditional approaches. In addition to the description of the basic ANN methodology and their possible variations, examples are given in terms of three major areas of ANN applications, namely, steady thermal problems, dynamic thermal modeling, and adaptive thermal control. Attributes of the ANN results are shown in terms of accuracy and flexibility in its use, and also their computational and experimental validations. Also discussed are hybrid algorithms in which the ANN plays a major role, along with other associated AI methodologies, for improved performance in the applications. Finally, some broad future prospects are also indicated.

Acknowledgment

The author is grateful to the late Mr. D. R. Dorini for supporting much of the studies mentioned in the review in Hydronics Laboratory. He would particularly thank his colleague and collaborator, Professor M. Sen, for his engineering and mathematical insight and the enthusiasm for AI. He also would like to thank his friend and colleague, R. L. McClain, for his support of our undertakings. In addition, he wishes to acknowledge the significant contributions of former students X. W. Zhao, G. Diaz, A. Pacheco-Vega, and W. H. Cai.

Nomenclature

c = steepness factor
D = tube diameter, m
E_r = error function in each run
F = filter
H = height of heat exchanger, m
I = total layer number
i = layer number
i,j = node designation
J_I = number of nodes in the output layer
J_i = maximum value of j in Layer i
j = node number in each layer
j_s = sensible heat Colburn j-factor
j_t = total heat Colburn j-factor
m = mass rate of flow, kg/s

N_{cir} = number of circuits in heat exchanger
N_{col} = number of columns in heat exchanger
N_{row} = number of rows in heat exchanger
Q = total rate of heat transfer
Q_{ANN} = Q based on ANN prediction
Q_{cor} = Q based on correlation
$\mathbf{R}$ = mean value of the ratios of experimental heat-transfer rate to that of ANN prediction
Re = Reynolds number
s = seconds
T = temperature, °C
t = time, s
t = tube sheet thickness, m
$t_{I,j}$ = target value at the output layer node
v = air velocity, m/s
W = width of the heat exchanger, m
w = synaptic weight
x = node input
x_∂ = lateral tube spacing, m
x_b = vertical tube spacing, m
y = node output
Δ = increment
δ = fin spacing, m
$\delta_{i,j}$ = node error
$\theta_{i,j}$ = node bias
λ = learning rate
ξ = activation function variable
σ = standard deviation
$\phi_{i,j}$ = node activation function

Subscripts and Superscripts

a = air side
db = dry bulb
out = outlet
r = refrigerant
wb = wet bulb

References

[1] Yang, K. T., 2007, "Role of Artificial Intelligence (AI) in Thermal Sciences and Engineering," ASME Paper No. HT-2007-32042.
[2] Kolokotsa, D., Tsiavos, D., Stavrakakis, G. S., Kalaitzakis, K., and Antonidakis, E., 2001, "Advanced Fuzzy Logic Controllers Design and Evaluation for Building Occupants Thermal-Visual Comfort and Indoor Air Quality Satisfaction," Energy Build., **33**(6), pp. 531–543.
[3] Westphalen, D., Roth, K. W., and Brodrick, J., 2003, "Fuzzy Logic for Controls," ASHRAE J., **45**(6), pp. 31–47.
[4] Calvino, F., Gennusa, M. L., Rizzo, G., and Scaceianoce, G., 2004, "The Control of Indoor Thermal Comfort Conditioning: Introducing a Fuzzy Adaptive Controller," Energy Build., **36**(2), pp. 97–102.
[5] Schalkoff, R., 1997, *Artificial Neural Networks*, McGraw-Hill, New York.
[6] Haykin, S., 1999, *Neural Networks, A Comprehensive Foundation*, 2nd ed., Prentice-Hall, Englewood Cliffs, NJ.
[7] Rumelhary, D. E., Hinton, D. E., and Williams, R. J., 1986, "Learning Internal Representations by Error Propagation," *Parallel Distributed Processing: Exploration in the Microstructure of Cognition*, Vol. 1, MIT, Cambridge, MA.
[8] Sen, M., and Yang, K. T., 2000, "Applications of Artificial Neural Networks and Genetic Algorithms in Thermal Engineering," *CRC Handbook of Thermal Engineering*, F. Kreith, ed., CRC, Boca Raton, FL, pp. 4-620–4-661.
[9] Zeng, P., 1998, "Neural Computing in Mechanics," Appl. Mech. Rev., **51**(2), pp. 173–197.
[10] Kramin, E. D., 1990, "Simple Procedure for Pruning Back Propagation-Trained Neural Networks," IEEE Trans. Neural Netw., **1**(2), pp. 239–242.
[11] Gagarin, N., Flood, I., and Albrecht, P., 1994, "Computing Track Attributes With Artificial Neural Networks," J. Comput. Civ. Eng., **8**(2), pp. 179–200.
[12] Angeline, P. J., Saunder, G. M., and Pollack, J. B., 1994, "Complete Introduction of Recurrent Neural Networks," *Proceedings of the Third Annual Conference on Evolutionary Programming*, A. V. Sebald and L. J. Fogel, eds., World Scientific, Singapore, pp. 1–8.
[13] Lehtokangas, M., Saarinen, J., and Kaski, K., 1995, "Initializing Weights of a Multilayer Perceptron Network by Using the Orthogonal Least Square Algorithm," Neural Comput., **7**, pp. 982–999.
[14] Shah, R. K., and Ball, K. J., 2000, "Heat Exchangers," *CRC Handbook of Thermal Engineering*, F. Kreith, ed., CRC, Boca Raton, FL, pp. 4-50–4-113.
[15] Thibault, J., and Grandjean, B. P. A., 1991, "Neural Network Methodology for Heat Transfer Data Analysis," Int. J. Heat Mass Transfer, **34**(8), pp. 2063–2070.
[16] Jambunathan, K., Hartle, S. L., Ashforth-Frost, S., and Fontama, V. N., 1996, "Evaluating Convective Heat Transfer Coefficients Using Neural Networks," Int. J. Heat Mass Transfer, **39**(11), pp. 1241–1256.
[17] Lavric, D., LaVric, V., Muntean, O., and Danciu, E., 1994, "Auto-Organizing Algorithm for Design of Fin Heat Exchangers," Rev. Roum. Chim., **39**(11), pp. 1241–1256.
[18] Zhao, X., Sen, M., Yang, K. T., and McClain, R. L., 1995, "An Artificial Neural Network Model of a Heat Exchanger," Symposium on Thermal Science Engineering in Honor of Chancellor Chang-Lin Tien, pp. 83–88.
[19] Shah, R. K., 1985, "Compact Heat Exchangers," *Handbook of Heat Transfer Applications*, 2nd ed., W. M. Rohsenow, J. P. Hartnett, and E. N. Garnic, eds., McGraw-Hill, New York, NY, pp. 4-174–4-312.
[20] Shah, R. K., Kraus, A. D., and Metzger, D., eds., 1990, *Compact Heat Exchangers*, Hemisphere, New York.
[21] Diaz, G., Sen, M., Yang, K. T., and McClain, R. L., 1999, "Simulation of Heat Exchanger Performance by Artificial Neural Networks," HVAC&R Res., **5**(3), pp. 195–208.
[22] McQuiston, F. C., 1978a, "Heat, Mass and Momentum Transfer Data for Five Plate-Fin-Tube Heat Transfer Surfaces," ASHRAE Trans., **84**, pp. 266–293.
[23] McQuiston, F. C., 1978b, "Correlation of Heat, Mass, and Momentum Transport Coefficients for Plate-Fin-Tube Heat Transfer Surfaces With Staggered Tubes," ASHRAE Trans., **84**, pp. 294–309.
[24] Gray, D. L., and Webb, R. L., 1986, "Heat Transfer and Friction Correlations for Plate Finned-Tube Heat Exchanger Having Plate Fins," *Proceedings of the Eighth International Heat Transfer Conference*, Vol. 6, pp. 2745–2750.
[25] Pacheco-Vega, A., Diaz, G., Sen, M., Yang, K. T., and McClain, R. L., 2001, "Heat Rate Predictions in Humid Air-Water Heat Exchanger Using Correlations and Neural Networks," ASME J. Heat Transfer, **123**, pp. 348–354.
[26] Theodoridis, S., and Kontroumbas, K., 1999, *Pattern Recognition*, Academic, New York.
[27] Pacheco-Vega, A., Sen, M., Yang, K. T., and McClain, R. L., 2001, "Neural Network Analysis of Fin-Tube Refrigerating Heat Exchanger With Limited Experimental Data," Int. J. Heat Mass Transfer, **44**, pp. 763–770.
[28] Niyogi, P., and Girosi, F., 1999, "Generalization Bounds for Function Approximation From Scattered Noisy Data," Adv. Comput. Math., **10**(1), pp. 51–80.
[29] Kalogirou, S. A., 1999, "Applications of Artificial Neural Network in Energy Systems—A Review," Energy Convers. Manage., **40**, pp. 1073–1087.
[30] Sen, M., and Yang, K. T., 2003, "A Review of Multiphase Flow and Heat Transfer With Artificial Neural Networks," ASME Paper No. IMECE 2003 41761.
[31] Tsoukalas, L. H., Ishii, M., and Mi, Y., 1997, "A Neurofuzzy Methodology for Impedance-Based Multiphase Flow Identification," Eng. Applic. Artif. Intell., **10**(6), pp. 545–555.
[32] Mi, Y., Ishii, M., and Tsoukalas, L. H., 1998, "Vertical Two-Phase Flow Identification Using Advanced Instrumentation and Neural Networks," Nucl. Eng. Des., **184**(2–3), pp. 409–420.
[33] Wu, H. J., Zhou, F. D., and Wu, Y. Y., 2001, "Intelligent Identification System of Flow Regime of Oil-Gas-Water Multiphase Flow," Int. J. Multiphase Flow, **27**(3), pp. 459–475.
[34] Su, G., Morita, K., Fukuda, K., Pidduck, M., Dounan, J., and Miettinen, J., 2003, "Analysis of the Critical Heat Flux in Round Vertical Tubes Under Low Pressure and Flowoscillation Conditions—Applications of Artificial Neural Network," Nucl. Eng. Des., **230**, pp. 17–35.
[35] Tsutsumi, A., Chen, W., Hasegawa, T., and Otawara, K., 2001, "Neural Networks for Prediction of the Dynamic Heat Transfer Rate in Bubble Columns," Ind. Eng. Chem. Res., **40**(23), pp. 5358–5361.
[36] Morshed, J., and Powers, S. E., 2000, "Regression and Dimensional Analysis for Modeling Two-Phase Flow," Transp. Porous Media, **38**(1–2), pp. 205–221.
[37] Kelleher, M. D., Cronley, T. J., Yang, K. T., and Sen, M., 2001, "Using Artificial Neural Networks to Develop a Predictive Method From Complex Experimental Heat Transfer Data," ASME Paper No. IMECE 2001/HTD-24285.
[38] Liu, T., Sun, X., Li, X., and Wang, H., 2002, "Neural Network Analysis of Boiling Heat Transfer Enhancement Using Additives," Int. J. Heat Mass Transfer, **45**(25), pp. 5083–5089.
[39] Oliveira, M. S. A., and Sousa, A. C. M., 2001, "Neural Network Analysis of Experimental Data for Air/Water Spray Cooling," J. Mater. Process. Technol., **113**(1–3), pp. 439–453.
[40] Ward, J., Wilcox, S. J., Tan, O. H., Tan, C. K., Payne, R. J., and Garwood, D. R., 2001, "Simulation of a Range of Thermal Systems by Artificial Neural Networks," ASME Paper No. IMECE2001/HTD-24284.
[41] Wang, X. A., and Mahajan, R. L., 1995, "CVD Epitaxial Deposition in a Vertical Barrel Reactor: Process Modelling and Optimization Using Neural Network Models," J. Electrochem. Soc., **142**(9), pp. 3123–3132.
[42] Chong, A. Z. S., Wilcox, S. J., and Ward, J., 2000, "Application of a Neural Network Based Controller on an Industrial Chain-Grate, Stoker-Fired Boiler," J. Inst. Energy, **73**, pp. 208–214.
[43] Mittal, G. S., and Zhang, J., 2000, "Prediction of Freezing Time for Food Products Using a Neural Network," Food Res. Int., **33**(7), pp. 557–562.
[44] Pham, Q. T., 1986, "Simplified Equation for Predicting the Freezing Time of Food Stuffs," J. Food Technol., **21**, pp. 209–219.
[45] Kos, A., 1993, "Approach to Thermal Placement in Power Electronics Using Neural Networks," *Proceedings of the IEEE International Symposium on Circuits Systems*, Vol. 4, pp. 2427–2430.
[46] Normandin, A., Grandjean, B. P. A., and Thibault, J., 1993, "PVT Data Analysis Using Neural Network Models," Ind. Eng. Chem. Res., **32**(5), pp. 970–975.
[47] Naka, M., Imai, T., Shida, T., Sato, M., Ito, R., and Akamine, I., 1993, "Ther-

mal Image Processing Using Neural Network," *Proceedings of the International Joint Conference on Neurak Networks*, Nagoya Japan, Part 3, Vol. 3, pp. 2065–2068.
[48] Huang, S.-H., and Nelson, R. M., 1994, "Delay Time Determination Using an Artificial Neural Network," ASHRAE Trans., **100**(1), pp. 831–840.
[49] Erturk, H., Ezekoye, A., and Howell, J. R., 2002, "The Use of Inverse Formulation in Design and Control of Transient Radiation Systems," Proceedings of the International Heat Transfer Conference, Grenoble, France, pp. 729–734.
[50] Mazzola, A., 1997, "Integrating Artificial Neural Networks and Empirical Correlations for the Prediction Water-Cooled Critical Heat Flux," Rev. Gen. Therm., **36**(11), pp. 799–806.
[51] Ayoubi, M., 1997, "Dynamic Multi-Layer Perceptron: An Application to the Nonlinear Identification and Predictive Control of a Heat Exchanger," *Applied Neural Adaptive Control Technology*, J. Kalkkuhl, K. J. Hunt, R. Zbikowski, and A. Dzielinski, eds., World Scientific, Singapore, pp. 205–230.
[52] Diaz, G., Sen, M., Yang, K. T., and McClain, R. L., 2001, "Dynamic Prediction and Control of Heat Exchangers Using Artificial Neural Networks," Int. J. Heat Mass Transfer, **44**, pp. 1671–1679.
[53] Kuroe, Y., and Kimura, I., 1995, "Modeling of Unsteady Heat Conduction Field by Using Composite Recurrent Neural Networks," *Proceedings of the IEEE International Conference Neural Networks*, Part 1, Vol. 1, pp. 323–328.
[54] Kreider, J. F., Sharbaro, D., Zbikowski, R., and Gawthrop, P. L., 1992, "Building Energy Use Prediction and System Identification Using Recurrent Neural Networks," J. Sol. Energy Eng., **117**(3), pp. 161–166.
[55] Hunt, K. J., Sharbaro, D., Zbikowski, R., and Gawthrop, P. L., 1992, "Neural Networks for Control Systems—A Survey," Automation, **28**(6), pp. 1083–1112.
[56] Warwick, K., Irwin, G. W., and Hunt, K. J., 1992, *Neural Networks for Control and Systems*, Short Run, Exeter, UK.
[57] Alessandri, A., Verona, F. B., Parisini, T., and Torrini, A., 1994, "Neural Approximations for the Optimal Control of Heating Systems," *Proceedings of Conference on Control Applications*, Vol. 3, pp. 1613–1618.
[58] Narendra, K., and Mukhopadhyay, S., 1996, "Intelligent Control Using Neural Networks," *Intelligent Control Systems, Theory and Applications*, M. Gupta and N. Sinha, eds., IEEE, New York, pp. 151–186.
[59] Jeannette, E., Assawamartbunlue, P., Curtiss, P., and Kreider, J. F., 1998, "Experimental Results of a Predictive Neural Network HVAC Controller," ASHRAE Trans., **104**(2), pp. 6.
[60] Curtiss, P. S., Kreider, J. F., and Brandemuehl, M. J., 1993, "Artificial Neural Networks Proof of Concept for Local and Global Control of Commercial Building HVAC Systems," Proceedings of ASME International Solar Energy Conference, pp. 429–443.
[61] Nahas, E. P., Henson, M. A., and Seborg, D. E., 1992, "Nonlinear Internal Method Control Strategy for Neural Network Models," Comput. Chem. Eng., **16**(12), pp. 1039–1057.
[62] Bittanti, S., and Piroddi, L., 1997, "Nonlinear Identification and Control of a Heat Exchanger: A Neural Network Approach," J. Franklin Inst., **334B**(1), pp. 135–153.
[63] Ding, Y., and Wong, K. V., 1990, "Control of a Simulated Dual-Temperature Hydronic System Using Neural Network Approach," ASHRAE Trans., **96**(2), pp. 727–732.
[64] Dounis, A. L., Santamouris, M. J., and Lefas, C. C., 1992, "Implementation of Artificial Intelligence Techniques in Thermal Comfort Control for Passive Solar Buildings," Energy Convers. Manage., **33**(3), pp. 175–182.
[65] Mahajan, R. L., and Wang, X. A., 1993, "Neural Network Models for Thermally Based Microelectronic Manufacturing Processes," J. Electrochem. Soc., **140**(8), pp. 2287–2293.
[66] Marwah, M., Li, Y., and Mahajan, R. L., 1996, "Integrated Neural Network Modeling for Electronic Manufacturing," J. Electron. Manuf., **6**(2), pp. 79–91.
[67] Carriere, A., Cela, A., and Hamam, Y., 1994, "Neural Network-Based Adaptive Control of a Nonlinear System: Application to a Thermal Process," *Proceedings of the IEEE Conference on Systems, Man, and Cybernetics*, Vol. 2, pp. 1133–1138.
[68] Lalot, S., and Lecoeuche, S., 2001, "Online Identification of Circulation Electrical Heaters as MISO Systems Using Artificial Neural Networks," *Proceedings of NHTC'01, 35th NHTC*, Anaheim, CA, Paper No. NHTC 2001-20153.
[69] Diaz, G., Sen, M., Yang, K. T., and McClain, R. L., 2001, "Adaptive Neural Control of Heat Exchangers," ASME J. Heat Transfer, **123**, pp. 585–591.
[70] Diaz, G., Sen, M., Yang, K. T., and McClain, R. L., 2004, "Stabilization of Thermal Neurocontrollers," Appl. Artif. Intell., **18**(5), pp. 447–466.
[71] Abe, N., Seki, K., and Kanoh, M., 1994, "Internal Model Control for Single Tubular Heat Exchanger System," *Proceedings of the International Conference on Industrial Electronics, Control, and Instrumentation*, Vol. 2, pp. 1165–1170.
[72] Diaz, G., Sen, M., Yang, K. T., and McClain, R. L., 2001, "On-Line Training of Artificial Neural Networks for Control of a Heat Exchanger Test Facility," *Proceedings of ASME NHTC'01, 35th NHTC*, Anaheim, CA, Paper No. NHTC2001-20054.
[73] Michell, M., 1997, *An Introduction to Genetic Algorithm*, MIT, Cambridge, MA.
[74] Vonk, E., Jain, L. C., and Johnson, R. P., 1997, *Automatic Generation of Neural Architecture Using Evolutionary Computation*, World Scientific, Singapore.
[75] Kaminski, W., Strumillo, P., and Tomczak, E., 1996, "Genetic Algorithms and Artificial Neural Networks for Description of Thermal Deterioration Processes," Drying Technol., **14**(9), pp. 2117–2133.
[76] Tarca, L. A., Grandjean, B. P. A., and Larachi, F., 2002, "Integrated Genetic Algorithm-Artificial Neural Network Strategy for Modeling Important Multiphase Flow Characteristics," Ind. Eng. Chem. Res., **41**(10), pp. 2543–2551.
[77] Kaufman, L., and Rousseeuw, P. J., 1990, *Finding Groups in Data: An Introduction to Cluster Analysis*, Wiley, New York.
[78] Anderberg, M. R., 1973, *Cluster Analysis for Applications*, Academic, New York.
[79] Jain, A. K., Murty, M. N., and Flynn, P. J., 1999, "Data Clustering: A Review," ACM Comput. Surv., **31**(3), pp. 264–323.
[80] Jain, A. K., Duin, R. P. W., and Mao, I. C., 2000, "Statistical Pattern Recognition: A Review," IEEE Trans. Pattern Anal. Mach. Intell., **22**(1), pp. 4–37.
[81] Jang, J.-S. R., Sun, C.-T., and Mizutain, E., 1997, *Neuro-Fuzzy and Soft Computing*, Prentice-Hall, Englewood Cliffs, NJ.
[82] Brown, M., and Harris, C., 1994, *Neurofuzzy Adaptive Modeling and Control*, Prentice-Hall, Englewood Cliffs, NJ.
[83] Lin, C. J., 2004, "A GA-Based Neural Fuzzy System for Temperature Control," Fuzzy Sets Syst., **143**(2), pp. 311–333.
[84] Kah, A. H., San, Q. Y., Guan, S. C., Kiat, W. C., and Koh, Y. C., 1995, "Smart Air-Conditioning System Using Multilayer Perceptron Neural Network With a Modular Approach," *Proceedings of the IEEE International Conference on ICNN '95*, Perth, Australia, Vol. 5, pp. 2314–2319.
[85] Moon, S. K., and Chang, S. H., 1994, "Classification and Prediction of the Critical Heat Flux Using Fuzzy Theory and Artificial Neural Networks," Nucl. Eng. Des., **150**(1), pp. 151–161.
[86] Khosla, R., and Dillon, T., 1997, *Engineering Intelligent Hybrid Multi-Agent Systems*, Kluwer, Dordrecht.
[87] So, A. T., and Chan, W. L., 1999, *Intelligent Building Systems*, Kluwer, Dordrecht.
[88] Yang, K. T., and Sen, M., 2002, "Agent Networks for Intelligent Dynamic Control of Complex Hydronic Building Systems—Part 1: Framework for Agent Network Development," Int. J. Arch. Sci., **3**(1), pp. 43–50.

Logarithmic Expansions for Reynolds Shear Stress and Reynolds Heat Flux in a Turbulent Channel Flow

Abu Seena
Department of Mechanical Engineering,
Korea Advanced Institute of Science and Technology,
Daejeon 305-701, Korea

A. Bushra
Department of Civil Engineering,
University of Nebraska-Lincoln,
Omaha, NE 68182-0178

Noor Afzal
Faculty of Engineering,
Aligarh Muslim University,
Aligarh 202002, India

*The heat and fluid flow in a fully developed turbulent channel flow have been investigated. The closure model of Reynolds shear stress and Reynolds heat flux as a function of a series of logarithmic functions in the mesolayer variable have been adopted. The interaction between inner and outer layers in the mesolayer (intermediate layer) arising from the balance of viscous effect, pressure gradient and Reynolds shear stress (containing the maxima of Reynolds shear stress) was first proposed by Afzal (1982, "Fully Developed Turbulent Flow in a Pipe: An Intermediate Layer," Arch. Appl. Mech., **53**, 355–377). The unknown constants in the closure models for Reynolds shear stress and Reynolds heat flux have been estimated from the prescribed boundary conditions near the axis and surface of channel. The predictions are compared with the DNS data Iwamoto et al. and Abe et al. for Reynolds shear stress and velocity profile and Abe et al. data of Reynolds heat flux and temperature profile. The limitations of the closure models are presented.* [DOI: 10.1115/1.2944240]

Keywords: Reynolds heat flux closure model, thermal mesolayer, temperature profile

1 Introduction

Recently, Sreenivasan and Bershadskii [1] while considering the mean velocity distribution near the peak of the Reynolds shear stress also attempted to extend the buffer layer by proposing a Reynolds stress closure model, and the same was also published in Sreenivasan and Bershadskii [2]. Earlier, the Reynolds stress closure model was proposed by Panton [3–5], but he did not use the very long and complicated expression for the velocity distribution (see Eq. (11), Panton [3]). In a fully developed turbulent pipe or channel flow, Afzal [6] proposed a mesolayer theory in the mesolayer variable $\eta = y_+/\sqrt{R_\tau}$ and predicted the Reynolds shear stress as

$$\tau_+ = 1 - R_\tau^{-1/2}\left(\eta + \frac{J(\eta)}{\eta}\right) \tag{1}$$

where $J(\eta) = A_o + (A_i - A_o)\exp(-m\eta)$, $J = A_i$ for $\eta \to 0$, $J = A_o$ for $\eta \to \infty$, and m is a constant related to log laws in a mesolayer velocity profile. The velocity profile solution [7] is a composite relation

$$\frac{U_c - u}{u_\tau} = (A_i - A_o)E_1(m\eta) - A_o \ln Y + \Pi A_o[2 - W(Y)] \tag{2}$$

where $E_1(x) = \int_x^\infty t^{-1}e^{-t}dt$ is the exponential integral and [7] adopted $m = 1$. This is a generalization of Coles wall-wake profile (with wake function $W(Y)$) with s contribution from the buffer layer near the wall. Afzal [6] from relation (1) for the traditionl two layer theory $A_i = A_0 = 1/k$ predicted the maximum of Reynolds shear stress as

$$y_{+m} = \sqrt{\frac{R_\tau}{k}}, \quad \tau_{+m} = 1 - \frac{2}{\sqrt{kR_\tau}} \tag{3}$$

Sreenivasan and Bershadskii [1,2] adopted a closure model in a series of square of the logarithmic expansion in the variable y_+/y_{+m}, involving $y_{+m} = \beta\sqrt{R_\tau}$, the maxima of Reynolds shear stress in the mesolayer (or the intermediate layer in between inner and outer layers). The unknown constant, $\gamma_1, \ldots$, in Reynolds shear stress expansion was regarded as independent of Reynolds number at least for high enough $R_\tau \to \infty$. As shown in the present work it is not appropriate but rather incorrect.

The basic work of Afzal [6–9] on mesolayer has not been cited in Sreenivasan and Bershadskii [1,2] even though their expansion of Reynolds shear stress is associated with the mesolayer variable (Afzal [6]) rather than the wall layer (with variable y_+). Earlier, Sahay [10] (dissertation Director Sreenivasan), in his Ph.D. thesis, on p. 13, stated: "Afzal (1982) attempted to put the three-layer scheme on a firmer theoretical basis. For the study of the mean momentum equation, under various limiting processes, he identified that the intermediate limit process, $y_+ = O(R_\tau^{-1/2})$ and $R_\tau \to \infty$ leads to a non-trivial dominant balance among all the terms of the equation. Using the asymptotic expansions in three layers, followed by asymptotic matching, he arrives at the same result* as Long and Cheng (1981). It is appropriate to mention here that when we came up with idea of investigating the mean momentum equation under the various limiting process we were unaware of Afzal's paper." The text "same result" marked by * in this comment [10] mentioned above is not correct because the work of Afzal [7] proposed a rational mesolayer theory, showing that the mesolayer theory of Long and Chen [11] is untenable (see also Afzal [7–9]). Moreover, in the Second Asian Congress of Fluid Mechanics in Beijing during 1983, Afzal [12] contributed a three-layer theory of turbulent boundary layer on a flat plate, where Sreenivasan [13] also contributed a paper on the fine scale of turbulence in boundary layers. Further, in subsequent papers Sreenivasan and Sahay [14], Sahay and Sreenivasan [15], McKeon and Sreenivasan [16], and previous papers by Sreenivasan [17,18], while describing the turbulent flow scales and the structure, considered the mesolayer but unduly ignored the rational mesolayer theory of Afzal [6–9,12]. Moreover, Sreenivasan et al. [18] (page 198, lines 26–27) stated that "Mixed scaling consists of the geometric mean on the inner and outer scales has also been proposed (Johansson and Alferdsson [19]"), duing 1982. This statement of Sreeinivasan [18] attributing the mixed scaling to the work of Johansson and Alferdsson [19] is not correct as these authors have not even talked about the mixed scaling or the mesolayer in the work [19]. Sreenivasan [18] cited Long and Chen [11] at an inappropriate place and ignored the citation of the intermediate layer theory of Afzal [6–9]. Further, Sreenivasan [17] during the year 1987 while proposing a critical layer (equivalent to the mesolayer [11] / intermediate layer [6–9]) has neither cited the mesolayer of Long and Chen [11] nor intermediate layer of Afzal [6–9]. In fact, Afzal [6] in 1982 published a rational three layer theory for turbulent pipe and channel flows (see also Afzal [7–9]).

Antonia et al. [20], Tsuji [21], Guala et al. [22], and Balakumar and Adrian [23] adopted the mesolayer relation $y^+_{\max} = 2R_\tau^{1/2}$ from

Contributed by the Heat Transfer Division of ASME for publication in the JOURNAL OF HEAT TRANSFER. Manuscript received June 5, 2007; final manuscript received November 9, 2007; published online July 10, 2008. Review conducted by Yogesh Jaluria.

Refs. [14,15,18] instead of the earlier mesolayer relation $y^+_{max} = 1.85R_\tau^{1/2}$ proposed by Afzal [7] and analogous relation by Long and Chen [11]. The prediction of the Reynolds shear stress maxima by relation (4) was first proposed by Afzal [7,10], but Panton [3–5] incorrectly attributed these relations to himself. Zanoun [24] also incorrectly attributed these relations to Panton [3]. Wei et al. [25] and Klewicki et al. [26,27] and Fife et al. [28], while displaying the Reynolds shear stress data, adopted the mesolayer variables of Afzal [7] but did not cite the first original work by Afzal [7,10,11]. The interaction between inner and outer layers in the mesolayer (intermediate layer) from balance of viscous effect, pressure gradient and Reynolds shear stress containing the maxima of Reynolds shear stress was first proposed by Afzal [6–8]. In the recent work, Morrison [31,32], Panton [4,5] and others [19–30,33] have failed to note that the work of Afzal [6–8] preceded to other cited authors [14–30,33] by 5 to 25 years. In fact, Figs. 8 and 9 in Afzal [6] show Laufer's pipe data and Fig. 3 in Afzal [8] the Klebanoff boundary layer data in the mesolayer variables, as well as the comparison of data with mesolayer predictions [6,8]. The inner time scale $T_i = \nu/u_\tau^2$, outer time $T_o = \delta/u_\tau$, and mesolayer scale T_m is the geometric mean of inner and outer time scales $T_m = \sqrt{T_i T_o} = \sqrt{\nu\delta/u_\tau^3} = \delta_m/u_\tau$. The period of the frequency of occurences of burst scales with mesolayer was simulaneouly proposed by Afzal [9] and Alferdsson and Johansson [34], while attributing the mesolayer length to Afzal [8], but the later work by Shah and Antonia [35], Osterlund et al. [36], and Nagano and Houra [37], have not cited the first original work by Afzal [6–9].

In the present work, the series of logarithmic functions for Reynolds shear stress in Reynolds mean momentum equation and another series of logarithmic functions for Reynolds heat flux for Reynolds energy equation have been investigated in the fully developed turbulent channel flow at large Reynolds numbers. The limitations of logarithmic expansions for Reynolds shear stress and the Reynolds heat flux have been investigated.

2 Momentum Transfer in a Turbulent Channel Flow

The Reynolds equation in a fully developed turbulent channel flow in traditional wall variables $y_+ = yu_\tau/\nu$, $u_+ = u/u_\tau$, and $\tau_+ = \tau/(\rho u_\tau^2)$ becomes

$$\frac{du_+}{dy_+} + \tau_+ = 1 - \epsilon y_+ \tag{4}$$

where $\epsilon = R_\tau^{-1}$. The maxima of Reynolds shear stress occurs at $\eta_m = \beta$ and $\tau_{+m} \equiv h = 1 - \sqrt{\epsilon}\chi$, where β and χ are constants of order unity (Afzal [6]). The logarithmic expansion for the Reynolds shear stress τ_+ around the maximum value in mesolayer variables may be taken as

$$\tau_+ = h[1 - \gamma_1[\ln(\eta/\beta)]^2 \cdots + \cdots] \tag{5}$$

where $\gamma_1, \ldots$ and h are functions of Reynolds number. The integration of the momentum equation (Eq. (4)) gives the velocity profile, and in mesolayer variable η it yields

$$\left[\frac{u_+}{\eta} + \frac{\eta}{2}\right]\frac{1}{\sqrt{R_\tau}} = p_0 + p_1\left[\ln\left(\frac{\eta}{e\beta}\right)\right]^2 \tag{6}$$

$$p_0 = 1 - h + h\gamma_1 \tag{7a}$$

$$p_1 = h\gamma_1 \tag{7b}$$

$$\gamma_1^{-1} = [\ln(\alpha\sqrt{R_\tau}/\beta)]^2 \tag{7c}$$

In the work of Sreenivasan and Bershadskii [1,2] the unknown constant $\gamma_1, \ldots$ in Reynolds shear stress expansion (Eq. (5)) was regarded as independent of Reynolds number at least for high enough $R_\tau \to \infty$. Moreover, Sreenivasan and Bershadskii [1,2] adopted the data of Iwamoto et al. [38] and McKeon [39], but the values of constant γ_1 from data have not been stated. As shown in present work it is not appropriate but rather incorrect. On the Reynolds shear stress closure model (Eq. (5)) we impose a boundary condition near the axis of the channel $y_+ = \alpha R_\tau$ and $\eta = \alpha\sqrt{R_\tau}$, where $\alpha \sim 1$ the Reynolds shear stress $\tau_+ = 0$, and Eq. (5) yields

$$\gamma_1^{-1} = \ln(\sqrt{\alpha R_\tau}/\beta)]^2 \tag{8}$$

which again shows that γ_1 is a function of Reynolds number.

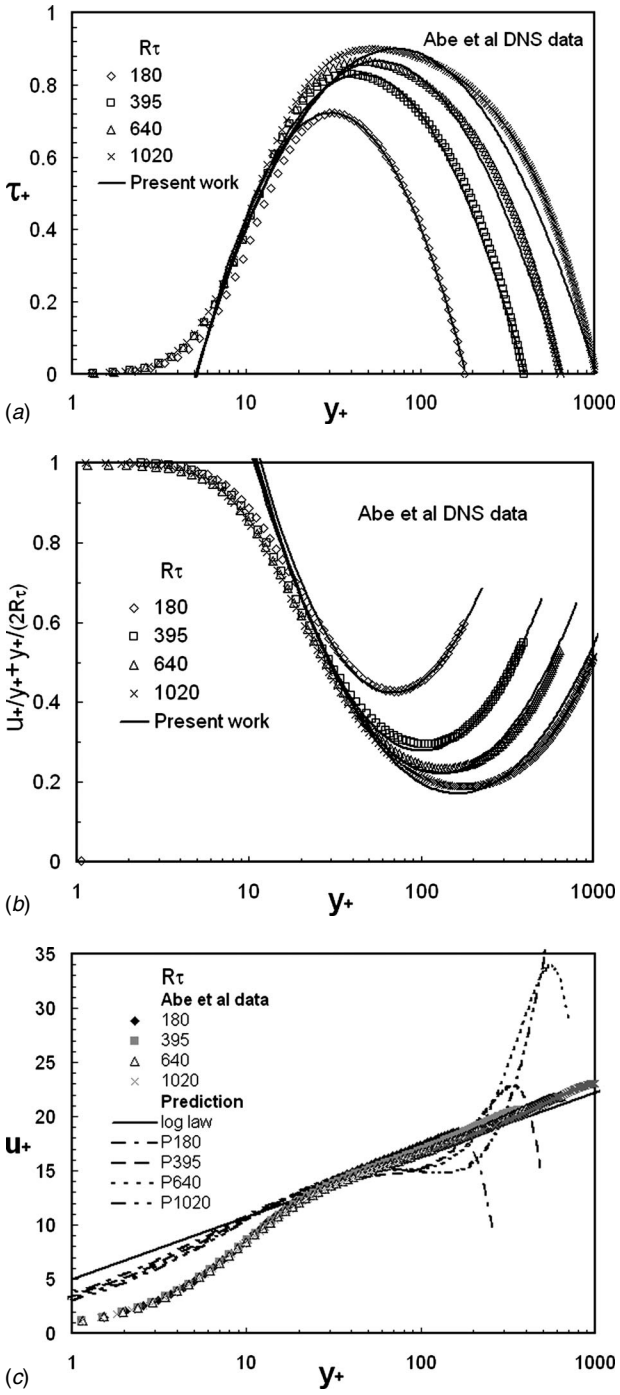

Fig. 1 Comparison of the DNS data of Abe et al. for four Reynolds numbers with the present work. (*a*) Reynolds shear stress τ_+ versus y_+. (*b*) Velocity distribution $u_+/y_+ + y_+/(2R_\tau)$ versus y_+. (*c*) Velocity distribution u_+ versus y_+.

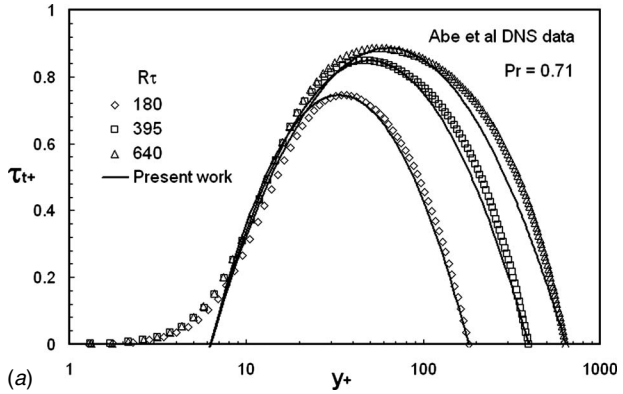

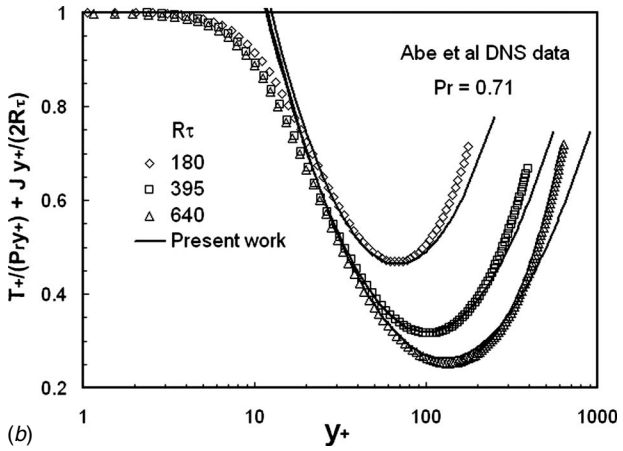

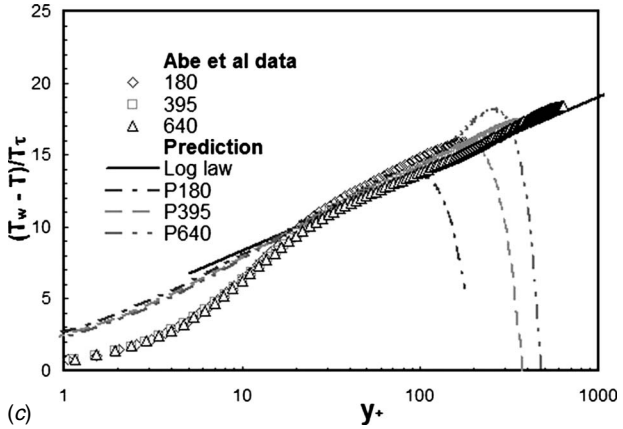

Fig. 2 Comparison of the DNS data of Abe et al. for three Reynolds numbers with the present work. (*a*) Reynolds heat flux τ_{t+} versus y_+. (*b*) Temperature distribution $T_+/(\mathrm{Pr}y_+)+y_+J/(2R_\tau)$ versus y_+. (*c*) Temperature distribution T_+ versus y_+.

3 Heat Transfer in a Turbulent Channel Flow

The thermal Reynolds equation of temperature profile in a fully developed channel flow is [40–42]

$$\frac{1}{\mathrm{Pr}}\frac{dT_+}{dy_+}+\tau_{t+}=1-R_\tau^{-1}\frac{u_\tau}{U_b}\int_0^{y_+}u_+dy_+ \tag{9}$$

In terms of temperature $T_+=(T-T_w)/T_\tau$, Reynolds heat flux $\tau_t=\tau_t/(\rho C_p u_\tau T_\tau)$ and $y_+=yu_\tau/\nu$

$$\frac{\nu}{\mathrm{Pr}}\frac{\partial^2 T}{\partial y^2}+\frac{\partial \tau_t}{\rho \partial y}=u\frac{\partial T}{\partial x} \tag{10}$$

Here $T(y)$ is the temperature, y is the normal coordinate, $\tau_t=-\rho C_p\langle v't'\rangle$ is the appropriate thermal Reynolds stress, Pr is molecular Prandtl number, $T_\tau=q_w/(\rho C_p u_\tau)$ is the friction temperature, and q_w is the wall heat flux.

The Reynolds heat flux logarithmic expansion, in analogy with Eq. (8), becomes

$$\tau_{t+}=h_t[1-\gamma_{t1}[\ln(\eta/\beta_t)]^2\cdots+\cdots] \tag{11}$$

The maxima of Reynolds heat flux occurs at (Seena and Afzal [40]) $\eta_{tm+}=\beta_t$ and $\tau_{tm+}=h_t$. The fist two terms in Eq. (11) are considered, where $\tau_+=0$ at $\eta=\alpha_t\sqrt{R_\tau}$ near the axis of the channel and $\eta=\beta_t^2/(\alpha_t\sqrt{R_\tau})$ near the wall yields $\gamma_{t1}^{-1}=\ln(\sqrt{\alpha_t R_\tau}/\beta_t)]^2$, which again shows that γ_1 is a function of Reynolds number.

The temperature distribution based on relation (10), after integration of the energy (Eq. (10)) gives

$$\frac{T_+}{\mathrm{Pr}y_+}+\frac{y_+}{2R_\tau}K(y_+)=g_t(y_+) \tag{12}$$

$$g_t(y_+)=p_{t0}+p_{t1}\left[\ln\left(\frac{y_+}{ey_{tm+}}\right)\right]^2$$

$$p_{t0}=1-h_t+h_t\gamma_{t1},\quad p_{t1}=h_t\gamma_{t1} \tag{13}$$

$$K(y_+)=2\frac{u_\tau}{U_b}y_+^{-1}\int_0^{y_+}\int_0^{y_+}u_+dy_+dy_+$$

The integrals in the function $K(y_+)$ have been estimated from velocity distribution (Eq. (6)) to obtain

$$K(y_+)=\frac{u_\tau}{U_b}\left[-\frac{y_+^3}{24R_\tau}+\frac{y_+^2}{6}\left\{p_0+p_1\left(\left(\ln\frac{\eta}{ce\beta}\right)^2+d\right)\right\}\right] \tag{14}$$

$$c=\exp\left(\frac{1}{2}+\frac{\sqrt{e}}{3}\right) \tag{15a}$$

$$d=\frac{e}{9}+\frac{1}{4} \tag{15b}$$

The above relations for temperature profile in mesolayer variables become

$$\left[\frac{T_+}{\mathrm{Pr}\eta}+\frac{\eta}{2}K(\eta)\right]\frac{1}{\sqrt{R_\tau}}=p_{t0}+p_{t1}\left[\ln\left(\frac{\eta}{e\beta}\right)\right]^2 \tag{16}$$

4 Results and Discussion

The Reynolds shear stress and velocity profile from DNS data of Abe et al. [41,42] for four friction Reynolds numbers $R_\tau=180$, 395, 640, and 1020 are plotted and shown in Figs. 1(*a*)–1(*c*). The Reynolds shear stress prediction from relation (20) is shown in Fig 1(*a*). The predictions agree very well with DNS data in the entire domain, little above the sublayer ($y_+>8$). The velocity distribution data of Iwamoto et al. [38] in the variables $[u_+/y_+ +y_+/(2R_\tau), y_+]$ are shown in Fig. 1(*b*), and our prediction (Eq. (10)) (as solid lines) where the data are in good agreement for all values little above the sublayer ($y_+>8$). The velocity profile data shown in Fig. 1(*c*) in terms of the traditional wall variables (u_+, y_+) are compared with classical log law,

$$u_+=k^{-1}\ln y_+ + B \tag{17}$$

where $k=0.4$ and $B=5$. The prediction (Eq. (6)) in the sublayer $y_+<15$ overestimates the values, and toward the outer region it departs from the classical log law (Eq. (17)) as well as the DNS data, which are somehow not been observed in Fig. 1(*b*). In Iwa-

moto et al. [38] the DNS data of Reynolds shear stress and velocity profile for five friction Reynolds numbers R_τ=109.4, 150.5, 297.9, 395.8, and 642.5 have behaviors analogous to those in Figs. 1(*a*)–1(*c*), and no additional comment is needed.

The Reynolds heat flux and temperature from the DNS data of Abe et al. [41,42] for four friction Reynolds numbers, R_τ=180, 395, 640, and 1020, are shown in Figs. 2(*a*)–2(*c*). The Reynolds heat flux prediction from relation (20) is shown in Fig. 2(*a*). The predictions agree very well with DNS data in the entire domain, little above the sublayer ($y_+ > 8$). The temperature profile data of Abe et al. are in terms of the variables $[T_+/(\mathrm{Pr}y_+) + y_+J/(2R_\tau), y_+]$. Our prediction (Eq. (14)) (as solid lines) is shown in (Fig. 2(*b*)), and the data are in good agreement above the sublayer ($y_+ > 8$). The temperature profile data shown in Fig. 2(*c*) in terms of the traditional wall variables (T_+, y_+) are compared with classical log law,

$$T_+ = k_t^{-1} \ln y_+ + B_t \tag{18}$$

where k_t=0.43 and B_t=3. The prediction (Eq. (16)) in the sublayer $y_+ < 15$ overestimates the values, and toward the outer region it departs from the classical log law (Eq. (18)) as well as the DNS data, which are somehow not been observed in Fig. 2(*b*).

Note added in proof: Lundgren [43] has not also cited the mesolayer scale theory proposed by Afzal [6–8,44,45] that preceded by 20–25 years. Further, if mean velocity vector in work of Afzal [5–9,12] and Afzal and Bush [44] are replaced by instantaneous velocity vector, we get the results of Lungren [43] for instantaneous velocity vector.

Acknowledgment

N.A. is grateful for the support of All India Council of Technical Education, New Delhi.

References

[1] Sreenivasan, K. R., and Bershadskii, A., 2006, "The Mean Velocity Distribution Near the Peak of the Reynolds Shear Stress, Extending Also to the Buffer Region," *IUTAM Symposium on One Hundred Years of Boundary Layer Research*, G. E. A. Meier and K. R. Sreenivasan, eds., Springer, Dordrecht, The Netherlands.

[2] Sreenivasan, K. R., and Bershadskii, A., 2006, "Finite-Reynolds-Number Effects in Turbulence Using Logarithmic Expansions," J. Fluid Mech., **554**, pp. 477–498.

[3] Panton, R. L., 1997, "A Reynolds Stress Function for Wall Layers," ASME J. Fluids Eng., **119**, pp. 325–330.

[4] Panton, R. L., 2005, "Review of Wall Turbulence as Described by Composite Expansions," Appl. Mech. Rev., **58**, pp. 1–40.

[5] Panton, R. L., 2007, "Composite Asymptotic Expansions and Scaling Wall Turbulence," Philos. Trans. R. Soc. London, Ser. A, **365**, pp. 733–754.

[6] Afzal, N., 1982, "Fully Developed Turbulent Flow in a Pipe: An Intermediate Layer," Arch. Appl. Mech., **53**, pp. 355–377.

[7] Afzal, N., 1984, "The Mesolayer Theory of Turbulent Flows," AIAA J., **22**, pp. 437–439.

[8] Afzal, N., 1982, "A Sub-Boundary Layer With a Two Dimensional Turbulent Boundary Layer," Journal de Mecanique Theorique et Appliquee, **1**, pp. 963–973.

[9] Afzal, N., 1984, "Period Between Bursting in Turbulent Shear Flow: Intermediate Scaling," Curr. Sci., **53**(12), pp. 640–642.

[10] Sahay, A., 1997, "The Mean Velocity and the Reynolds Shear Stress in Turbulent Pipe and Channel Flows," Ph.D. thesis, Yale University.

[11] Long, R. R., and Chen, T. C., 1981, "Experimental Evidence of the Existence of the Mesolayer in Turbulent Systems," J. Fluid Mech., **105**, pp. 19–59.

[12] Afzal, N., 1983, "Three Layer Theory of Turbulent Boundary Layer on a Flat Plate," *Proceedings of the Second Asian Congress of Fluid Mechanics*, Science, Beijing, pp. 316–321.

[13] Sreenivasan, K. R., 1983, "Characteristics of Fine Scale of Turbulence in Boundary Layers," *Proceedings of the Second Asian Congress of Fluid Mechanics*, Science, Beijing, pp. 84–90.

[14] Sreenivasan, K. R., and Sahay, A., 1997, "The Persistence of Viscous Effects in the Overlap Region, and the Mean Velocity in Turbulent Pipe and Channel Fows," *Self Sustaining Mechanisms of Wall Turbulence*, R. Panton, ed. WIT, Bath, UK.

[15] Sahay, A., and Sreenivasan, K. R., 1999, "The Wall-Normal Position in Pipe and Channel Flows at Which Viscous and Turbulent Shear Stresses Are Equal," Phys. Fluids, **11**(10), pp. 3186–3188.

[16] McKeon, B. J., and Sreenivasan, K. R., 2007, "Introduction: Scaling and Structure in High Reynolds Number Wall-Bounded Flows," Philos. Trans. R. Soc. London, Ser. A, **365**, pp. 635–646.

[17] Sreenivasan, K. R., 1987, "A Unified View of the Origin and Morphology of the Turbulent Boundary Layer Structure," *Turbulence Management and Relaminarisation*, H. W. Liepmann and R. Narasimha, eds., Springer-Verlag, New York, p. 37–61.

[18] Sreenivasan, K. R., 1989, "The Turbulent Boundary Layer," *Frontiers in Experimental Fluid Mechanics*, M. Gad-el-Hak, ed., Springer-Verlag, Berlin, pp. 159–209.

[19] Johansson, A. V., and Alferdsson, P. H., 1982, "On the Structure of Turbulent Channel Flow," J. Fluid Mech., **121**, pp. 295–314.

[20] Antonia, R. A., Teitel, M., Kim, J., and Browne, L. W. B., 1992, "Low Reynolds-Number Effects in a Fully Developed Turbulent Channel Flow," J. Fluid Mech., **236**, p. 579–605.

[21] Tsuji, Y., 1999, "Peak Position of Dissipation Spectrum in Turbulent Boundary Layers," Phys. Rev. E, **59**, pp. 7235–7238.

[22] Guala, M., Hommema, S. E., and Adrian, R. J., 2006, "Large-Scale and Very Large Scale Motions in Turbulent Pipe Flow," J. Fluid Mech., **554**, pp. 521–542.

[23] Balakumar, B. J., and Adrian, R. J., 2007, "Large- and Very-Large Scale Motions in Channel and Boundary Layer Flows," Philos. Trans. R. Soc. London, Ser. A, **365**, pp. 665–681.

[24] Zanoun, E. S., 2003, "Answer to Some Open Questions in Wall-Bounded Laminar and Turbulent Flows," Doctor-Ingeniur, University of Erlangen-Nurnberg.

[25] Wei, T., McMurtry, P., Klewicki, J., and Fife, P., 2005, "Mesoscaling of the Reynolds Shear Stress in Turbulent Channel and Pipe Flows," AIAA J., **43**(11), pp. 2350–2353.

[26] Klewicki, J. C., Fife, P., Wei, T., and McMurtry, P. A., 2006, "Overview of a Methodology for Scaling the Indeterminate Equations of Wall Turbulence," AIAA J., **44**(11), pp. 2475–2481, see also AIAA Paper No. 2005-4671.

[27] Klewicki, J., Fife, P., and Wei, T., 2007, "A Physical Model of the Turbulent Boundary Layer Consonant with Mean Momentum Balance Structure," Philos. Trans. R. Soc. London, Ser. A, **365**, 823–839.

[28] Fife, P., Klewicki, J., McMurtry, P., and Wei, T., 2005, "Multiscaling in the Presence of Indeterminacy: Wall-Induced Turbulence," Multiscale Model. Simul., **4**(3), pp. 936–959.

[29] Wei, T., Fife, P., Klewicki, J., and McMurtry, P., 2005, "Scaling Heat Transfer in Fully Developed Turbulent Channel Flows," Int. J. Heat Mass Transfer, **48**, pp. 5284–5296.

[30] Phuong, M. L., and Papavassiliou, D. V.2008, "On the Scaling of Heat Transfer Using Thermal Flux Gradients for Fully Developed Turbulent Channel and Couette Flows," Int. Commun. Heat Mass Transfer, **35**, pp. 404–412.

[31] Morrison, J. F., McKeon, B. J., Jiang, W., and Smith, A. J., 2004, "Scaling of the Streamwise Velocity Component in Turbulent Pipe Flow," J. Fluid Mech., **508**, pp. 88–131.

[32] Morrison, J. F., 2007, "The Interaction Between Inner and Outer Regions of Turbulent Wall-Bounded Flow," Philos. Trans. R. Soc. London, Ser. A, **365**, pp. 683–698.

[33] Wosnik, M., Castillo, L., and George, W. K., 2000, "A Theory for Turbulent Pipe and Channel Flows," J. Fluid Mech., **421**, pp. 115–145.

[34] Alferdsson, P. H., and Johansson, A. V., 1984, "Time Scales in Turbulent Channel Flow," Phys. Fluids, **27**, pp. 1974–1981.

[35] Shah, D. A., and Antonia, R. A., 1989, "Scaling of Bursting Period in Turbulent Boundary Layer and Duct Flows," Phys. Fluids A, **1**(2), pp. 318–325.

[36] Osterlund, J. M., Lindgren, B., and Johansson, A. V., 2003, "Flow Structure in Zero Pressure Gradient Turbulent Boundary Layer at High Reynolds Numbers," Eur. J. Mech. B/Fluids, **22**, pp. 379–370.

[37] Nagano, Y., and Houra, T., 2004, "Scaling of Near Wall Structures in Turbulent Boundary Layers Subjected to Adverse Pressure Gradient," *Reynolds Number Scaling in Turbulent Flow, IUTAM Symposium*, Kluwer Academic, Dordrecht, pp. 291–296.

[38] Iwamoto, K., Suzuki, Y., and Kasagi, N., 2002, "Reynolds Number Effect on Wall Turbulence: Toward Effective Feedback Control," Int. J. Heat Fluid Flow, **23**, pp. 678–689.

[39] McKeon, B. J., 2003, "High Reynolds Number Turbulent Pipe Flow," Ph.D. thesis, Princeton University.

[40] Seena, A., and Afzal, N., 2008, "Intermediate Scaling of Turbulent Momentum and Heat Transfer in a Transitional Rough Channel," ASME J. Heat Transfer, **130**, p. 031701.

[41] Abe, H., Kawamura, H., and Matsuo, Y., 2004, "Surface Heat-Flux Fluctuations in a Turbulent Channel up to R_τ=1020 With Pr=0.025 and 0.71," Int. J. Heat Fluid Flow, **25**, pp. 404–419.

[42] Abe, H., Kawamura, H., and Matsuo, Y., 2001, "Direct Numerical Simulation of a Fully Developed Turbulent Channel Flow With Respect to the Reynolds Number Dependence," ASME J. Fluids Eng., **123**, pp. 382–393.

[43] Lundgren, T. S., 2007, "Asymptotic Analysis of the Constant Pressure Turbulent Boundary Layer," Phys. Fluids, **19**, p. 055105.

[44] Afzal, N., and Bush, W. B., 1985, "A Three Layer Asymptotic Analysis of Turbulent Channel Flows," Proc. Indian Acad. Sci., Sect. A, **94**, pp. 135–148.

[45] Afzal, N., 1983, "Analysis of a Turbulent Boundary Layer Subjected to a Strong Adverse Pressure Gradient," Int. J. Eng. Sci., **21**, pp. 563–576.

Laminar Forced Convection for Flow Across a Cylinder With Longitudinal Fins of Finite Thickness

S. C. Haldar[1]
e-mail: schaldar@rediffmail.com

G. S. Kochhar

K. Manohar

Department of Mechanical and Manufacturing Engineering,
Faculty of Engineering,
University of the West Indies,
St. Augustine, Trinidad, Trinidad and Tobago

Conjugate numerical solution of laminar forced convection for cross-flow over a cylinder with external longitudinal fins of finite thickness has been carried out. The rate of heat transfer from the fins increases and that from the free area of the cylinder marginally decreases with an increase in thickness, length, and number of fins. The rate of heat transfer from the fins alone is usually much higher than that from the cylinder surface. As a consequence, the net result of these two opposing effects is an increase in the total heat transfer over that of the smooth cylinder, the amount increasing with an increase in thickness, length, and number of fins but with diminishing returns. The fins are more effective at high Re values than at low ones. [DOI: 10.1115/1.2946477]

Keywords: forced convection, longitudinal fin, cross flow, finned cylinder

1 Introduction

Forced convection across a smooth cylinder is a very old topic and has been investigated extensively due to its wide range of applications. Morgan [1] listed 150 experimental studies and 29 published correlations based on experimental and theoretical results conducted prior to 1975. He reported wide discrepancies amongst the results and possible reasons for them. He also proposed a correlation of the form $\mathrm{Nu}=C\mathrm{Re}^n$ with seven pairs of values for the constants C and n to cover a range of Reynolds numbers from 10^{-4} to 2×10^5. These correlations have been recommended by Rohsenhow et al. [2]. In order to enhance the rate of heat transfer from the cylinder, fins of uniform thickness are attached to it, most commonly in longitudinal or angular orientations. Depending on the applications, the fins may be fixed on the inner or the outer surfaces of a cylinder. In the case of annular fins of uniform thickness attached to the outer surface of the circular cylinder, each fin surface is parallel to one of the planes of a three-dimensional cylindrical polar coordinate system and this eases the discretization of the physical domain for a numerical solution. However, this is not so for the longitudinal fins of uniform thickness fixed onto a circular cylinder. The articles on convection from a horizontal cylinder with longitudinal fins, which the authors could locate, are by Rustum and Soliman [3], by Chai and Patankar [4] dealing with internal fins, and by Abu-Hijleh [5–10], Haldar [11], and Haldar et al. [12] dealing with external fins. Only three of these [7,8,10] pertain to forced convection across a horizontal cylinder with external longitudinal fins, the topic of the present article. All the articles cited above except that of Haldar et al. [12] suffer from two major drawbacks, the assumption of an isothermal fin at the base temperature and a negligible fin thickness. In order to take advantage of the fin surfaces coinciding with the radial coordinate direction of cylindrical polar coordinates, the fin thickness was neglected. When the fin thickness is assumed to be zero, the temperature variation along the fins cannot be determined numerically and this necessitates the assumption of a uniform fin temperature at the base value. The present investigation reveals that as the fin thickness reduces, the deviation from isothermality increases. Thus the two assumptions, isothermal fins at the base temperature and negligible fin thicknesses, are not compatible. With the inclusion of fin thickness, the results now depend on two additional parameters, the fin thickness itself and the fin thermal conductivity.

2 Problem Description

The schematic of the problem is presented in Fig. 1 along with the coordinate directions and the respective velocity components. The problem is symmetric about the vertical diameter, the upper and lower segments of which correspond to $\theta=0$ deg and 180 deg, respectively. The fluid flows crosswise to the cylinder with an undisturbed velocity U_∞^* and temperature T_∞^* in the direction, as shown in the figure. The fins are rectangular, having thickness t^* and length L^*, and are positioned at an equal angular spacing around the cylinder. The cylinder surface was deemed isothermal at a temperature higher than the freestream value. The base of each fin was considered at the temperature of the cylinder surface.

3 Describing Equations and Boundary Conditions

For the fins, only the conduction equation needs to be solved and this is

$$\frac{\partial^2 T}{\partial x^2}+\frac{\partial^2 T}{\partial y^2}=0 \tag{1}$$

For the fluid region, the flow equations in vorticity-stream-function formulation were solved and these are

$$u\frac{\partial\Omega}{\partial r}+\frac{v}{r}\frac{\partial\Omega}{\partial\theta}=\frac{2}{\mathrm{Re}}\nabla^2\Omega \tag{2}$$

$$u=\frac{1}{r}\frac{\partial\psi}{\partial\theta}\ \text{and}\ v=-\frac{\partial\psi}{\partial r} \tag{3}$$

$$\nabla^2\psi=-\Omega \tag{4}$$

The conservation of energy in the fluid region in dimensionless variables takes the form

$$u\frac{\partial T}{\partial r}+\frac{v}{r}\frac{\partial T}{\partial\theta}=\frac{2}{\mathrm{Re\,Pr}}\nabla^2 T \tag{5}$$

where

$$\nabla^2=\frac{\partial^2}{\partial r^2}+\frac{1}{r}\frac{\partial}{\partial r}+\frac{1}{r^2}\frac{\partial}{\partial\theta^2}$$

Advantage was taken of the symmetry about the vertical diameter, and the equations were solved in one-half of the physical domain. A pseudocylinder of a diameter large enough not to influence the results was considered as one of the boundaries to facilitate the computation. The conditions to be satisfied on all the boundaries of the fluid region are given next.

[1]Corresponding author.

Contributed by the Heat Transfer Division of ASME for publication in the JOURNAL OF HEAT TRANSFER. Manuscript received June 1, 2007; final manuscript received February 15, 2008; published online July 10, 2008. Review conducted by Louis C. Burmeister.

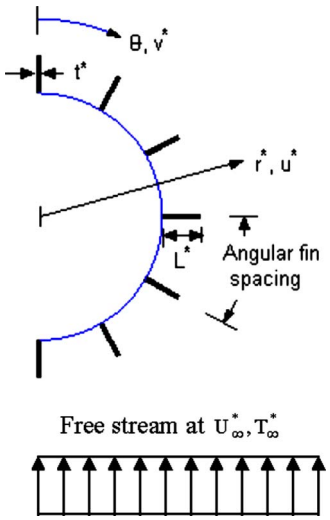

Fig. 1 Schematic of the physical problem

Cylinder.

$$\psi = 0, \quad \Omega = -\frac{\partial^2 \psi}{\partial r^2}, \quad \text{and } T = 1$$

Fin surfaces. $\psi=0$ at all the exposed fin surfaces. The upper and lower surfaces of each fin were assumed to coincide with the constant θ-line passing through the center of the respective fins for the purpose of determining the vorticity. Accordingly, $\Omega = -(1/r^2)(\partial^2\psi/\partial\theta^2)$ at the upper surface, $\Omega=(1/r^2)(\partial^2\psi/\partial\theta^2)$ at the lower surface, and $\Omega=-\partial^2\psi/\partial r^2$ at the tip of each fin.

The continuity of heat flux at either side, solid and fluid, of the three exposed surfaces of each fin was the condition for the temperature.

Symmetry lines at $\theta=0$ *and* π. $\psi=0$ with $\partial^2\psi/\partial\theta^2=0$ as the additional condition. Symmetry about θ demands $v=0$ and $\partial u/\partial\theta=0$, resulting to $\Omega=0$. Also, symmetry requires $\partial T/\partial\theta=0$.

Outer pseudocylinder. $\Psi=r_o \sin\theta$ and $\Omega=0$. For temperature, the conditions are $T=0$ if u is negative (inflow) and $\partial T/\partial r=0$ if u is positive (outflow).

4 Numerical Method

The governing dimensionless equations were solved by a finite difference technique based on control volume discretization over nonstaggered grids. The equations were discretized following the third-order accurate QUICK scheme [13] with central differencing for the wall adjacent control volumes.

A grid refinement study was undertaken with various pairs of radial and angular grid spacings in order to arrive at values that produced grid-independent results. Initially, radial spacing was gradually reduced and the angular spacing was kept fixed. This exercise yielded a radial spacing of 0.01 up to the fin tip plus 0.2, and 0.1 farther away as sufficient. The angular spacing was then varied and a uniform value of 1 deg was found to produce results with acceptable accuracy. Each fin was discretized by a maximum of 200 equally spaced nodes along the length and 20 along its thickness.

Equation (2) was solved for Ω, Eq. (4) for ψ, and Eq. (3) for the velocity components u and v from ψ until the values converged. Now, with the known velocity field, Eq. (1) for each of the fins and Eq. (5) for the fluid region were solved simultaneously together with the imposition of heat flux continuity at each fin surface exposed to the fluid until convergence was achieved.

The global convergence of the flow and temperature was deemed to have been achieved when the differences of vorticity and temperature values at each grid point between two consecutive iteration cycles were less than 0.001% and 0.000001%, respectively.

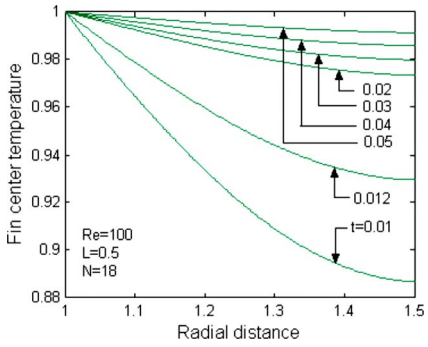

Fig. 2 Effect of the fin thickness on the temperature of the fin at 40 deg

The formation of a recirculation zone at the rear of the cylinder at high Re necessitated locating the outer pseudocylinder beyond about 15 times the radius of the cylinder, measured from the center.

5 Results and Discussions

The results were first generated for the case of a smooth cylinder for Re from 10^{-4} to 500, and the Nusselt numbers obtained were found to agree very well with those of Morgan [1] except at very low Re. This validates the numerical code as well as the choice of grids. For the case of a finned cylinder, the rate of heat transfer depends on the number, length, thickness, and thermal conductivity of the fins, and also on the Reynolds number. In order to reduce the number of variables, solutions were performed for a fixed value of the ratio of fin to air thermal conductivity of 2000. Results were generated for $0 \leqslant N \leqslant 18$ equally spaced over the entire (360 deg) cylinder, $0.1 \leqslant L \leqslant 0.5$, $0.01 \leqslant t \leqslant 0.05$, and for three values of Re (1, 10, and 100). The fluid around the cylinder was chosen as air by specifying a Pr value of 0.7.

5.1 Effect of Fin Parameters *L*, *N*, and *t*. The rate of heat transfer from a finned cylinder consists of two components; one from the uncovered part of the cylinder surface, $Q_{\text{cyl}}=\Sigma_{\text{cyl}} -(\partial T/\partial r)dA$, and the other from the three exposed surfaces of each fin, $Q_{\text{fin}}=\Sigma_{\text{fins}}-(\partial T/\partial n)dA$, where n represents normal to the respective surface and A represents the area. The sum of these two provides the total rate of heat transfer. Both these components are influenced by the various fin parameters, viz., thickness, length, number, thermal conductivity of fins, Reynolds number.

From the fin base, heat is conducted to the fin and then convected from its three surfaces to the surrounding fluid. With increasing fin thickness, the base area linearly increases while the increase in exposed fin surface area is negligible. This necessitates an increase in fin temperature with thickness to satisfy the equality between the rate of heat transfer to the fin at the base and that from the fin to the fluid. The increase in fin temperature with thickness reduces the temperature gradient at the fin base for a fixed cylinder surface temperature, which may be noted at $r=1$, as shown in Fig. 2. The net result of the two opposing effects, increasing the base area and decreasing the temperature gradient, is an increase in heat transfer from the fins with thickness, as shown in Fig. 3. As expected, the contribution from the fins increases when the cylinder is provided with more fins of the same thickness (Fig. 3).

An increase in fin temperature due to an increase in thickness (Fig. 3) causes the air temperature adjacent to the cylinder to rise and causes a consequent reduction of temperature gradient at the cylinder surface. Additionally, the free cylinder area marginally

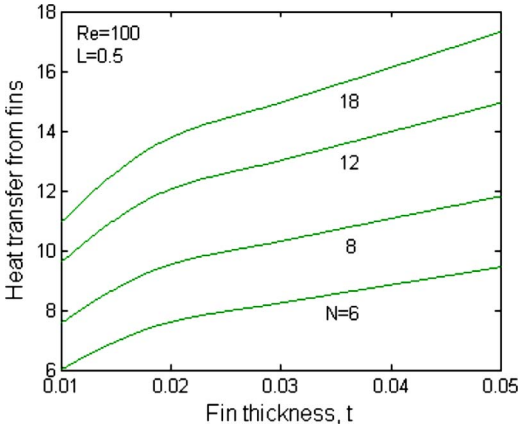

Fig. 3 Variation of heat transfer from the fins with thickness and number of fins

reduces with increasing fin thickness. On account of these two, the rate of heat transfer from the free area of the cylinder marginally decreases with increasing thickness (Fig. 4). The relatively sharp reduction between dimensionless thicknesses 0.01 and 0.02 is due to a large increase in fin temperature within that range (Fig. 2). Another important observation from Fig. 4 is that of reduction of heat transfer from the cylinder surface with more fins of the same thickness.

The total dimensionless heat transfer may be obtained by adding the contribution of the fins (Fig. 3) and the cylinder surface (Fig. 4). The profiles of the total heat transfer with fin thickness are similar to those of Fig. 3 since the contribution by the fins is much greater than that by the cylinder surface.

5.2 Effect of Reynolds Number, Re. The results presented in Figs. 2–4 are for Re=100. In order to investigate the effects of the Reynolds number, the total dimensionless heat transfer from a finned cylinder has been plotted in Fig. 5 as a function of fin length for 18 fins of thickness 0.05, and in Fig. 6 as a function of the number of fins for a fin length of 0.5 and a thickness of 0.05. The intercepts on the y-axis are the total heat transfer values at the respective Re for the case of a smooth cylinder. The rate of heat transfer increases over its value for the smooth cylinder with increase in number as well as length of fins but with diminishing returns. The rate of heat transfer from a cylinder with 18 fins of length 0.5 and thickness 0.05 is about 1.58 times of that of the smooth cylinder at Re=1, while it is about 1.98 times at Re=10, and about 2.30 times at Re=100.

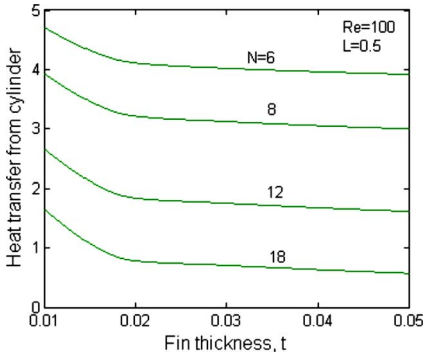

Fig. 4 Heat transfer from the uncovered part of the cylinder with thickness and number of fins

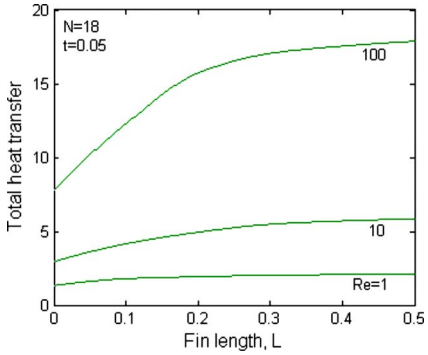

Fig. 5 Total heat transfer with fin length at different Re

Nomenclature

d^* = cylinder diameter, m; $d=d^*/r_c^*=2$
k_a^* = thermal conductivity of air, W m^{-1} K^{-1}.
L^* = fin length, m; $L=L^*/r_c^*$
N = number of fins over the entire cylinder
Pr = Prandtl number
Q_{cyl}^* = rate of heat transfer from the cylinder surface, W; $Q_{\text{cyl}}=Q_{\text{cyl}}^*/k_a^* r_c^*(T_c^*-T_\infty^*)$
Q_{fin}^* = rate of heat transfer from the fins, W; $Q_{\text{fin}}=Q_{\text{fin}}^*/k_a^* r_c^*(T_c^*-T_\infty^*)$
r^* = radial distance, m; $r=r^*/r_c^*$
r_c^* = cylinder radius, m; $r_c=1$
r_o^* = radius of the outer pseudocylinder, m; $r_o=r_o^*/r_c^*$
Re = Reynolds number, $\text{Re}=U_\infty^* d^*/\vartheta^*$
T^* = temperature, K; $T=(T^*-T_\infty^*)/(T_c^*-T_\infty^*)$
T_c^* = cylinder surface temperature, K; $T_c=(T_c^*-T_\infty^*)/(T_c^*-T_\infty^*)=1$
T_∞^* = freestream temperature, K; $T_\infty=(T_\infty^*-T_\infty^*)/(T_c^*-T_\infty^*)=0$
t^* = fin thickness, m; $t=t^*/r_c^*$
U_∞^* = freestream velocity, m s^{-1}; $U_\infty=1$
u^* = radial velocity, m s^{-1}; $u=u^*/U_\infty^*$
v^* = angular velocity, m s^{-1}; $v=v^*/U_\infty^*$
x^* = coordinate distance along the fin length, m; Eq. (1); $x=x^*/r_c^*$
y^* = coordinate distance along the fin thickness, m; Eq. (1); $y=y^*/r_c^*$

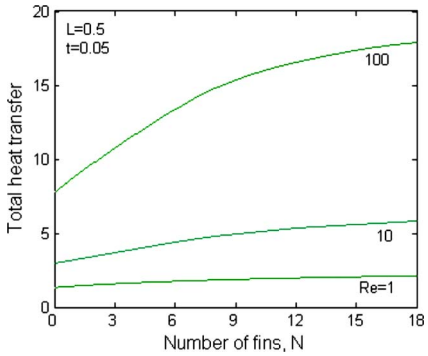

Fig. 6 Total heat transfer with number of fins at different Re

Greek Symbols

ϑ^* = kinematic viscosity, $m^2\,s^{-1}$

θ = angular coordinate

ψ^* = stream function, $m^2 s^{-1}$; $\psi = \psi^*/\vartheta^*$

Ω^* = vorticity about the z-axis, s^{-1}; $\Omega = \Omega^*/(\vartheta^*/r_c^{*2})$

Superscript

$*$ = dimensional quantity

References

[1] Morgan, V. T., 1975, "The Overall Convective Heat Transfer From Smooth Circular Cylinders," Adv. Heat Transfer, **11**, pp. 199–264.

[2] Rohsenhow, W. M., Hartnett, J. P., and Cho, Y. I., 1998, "Forced Convection, External Flows," *Handbook of Heat Transfer*, 3rd ed., McGraw-Hill, New York, Chap. 6.

[3] Rustum, I. M., and Soliman, H. M., 1990, "Numerical Analysis of Laminar Mixed Convection in Horizontal Internally Finned Tubes," Int. J. Heat Mass Transfer, **33**(7), pp. 1485–1496.

[4] Chai, J. C., and Patankar, S. V., 1993, "Laminar Natural Convection in Internally Finned Horizontal Annuli," Numer. Heat Transfer, Part A, **24**, pp. 67–87.

[5] Abu-Hijleh, B., 2003, "Optimization of Natural Convection Heat Transfer From a Cylinder With High Conductivity Fins," Numer. Heat Transfer, Part A, **43**, pp. 65–82.

[6] Abu-Hijleh, B., 2003, "Natural Convection Heat Transfer From a Cylinder With High Conductivity Permeable Fins," ASME J. Heat Transfer, **125**, pp. 282–288.

[7] Abu-Hijleh, B., 2003, "Enhanced Forced Convection Heat Transfer From a Cylinder Using Permeable Fins," ASME J. Heat Transfer, **125**, pp. 804–811.

[8] Abu-Hijleh, B., 2003, "Numerical Simulation of Forced Convection Heat Transfer From a Cylinder With High Conductivity Radial Fins in Cross-Flow," Int. J. Therm. Sci., **42**, pp. 741–748.

[9] Abu-Hijleh, B., 2004, "Mixed Convection From a Cylinder With Highly Conductive Fins in Cross-Flow," Heat Transfer Eng., **25**(6), pp. 33–44.

[10] Abu-Hijleh, B., 2005, "Fin Placement for Optimal Forced Convection Heat Transfer From a Cylinder in Cross-Flow," Int. J. Numer. Methods Heat Fluid Flow, **15**(3), pp. 277–295.

[11] Haldar, S. C., 2004, "Laminar Free Convection Around a Horizontal Cylinder With External Longitudinal Fins," Heat Transfer Eng., **25**(6), pp. 45–53.

[12] Haldar, S. C., Manohar, K., Kochhar, G. S., and Sahoo, R. K., 2007, "Numerical Study of Laminar Free Convection About a Horizontal Cylinder With Longitudinal Fins of Finite Thickness," Int. J. Therm. Sci., **46**, pp. 692–698.

[13] Leonard, B. P., 2000, "Bounded Higher-Order Upwind Multidimensional Finite-Volume Convection-Diffusion Algorithms," *Advances in Numerical Heat Transfer*, Vol. 1, W. J. Minkowycz and E. M. Sparrow, eds., Taylor & Francis, London.

Extreme Plane Wall Midplane Temperatures Due to Sequential Heating and Cooling

T. L. Bergman
Department of Mechanical Engineering,
University of Connecticut,
191 Auditorium Road, Unit 3139,
Storrs, CT 06269
e-mail: tberg@engr.uconn.edu

The thermal response of a one-dimensional plane wall to sequential heating and cooling is considered. Of interest is the thermal response at the midplane of the wall in terms of the extreme temperatures that evolve after heating subsides. Correlations are generated to estimate the extreme temperatures and the times at which they occur. [DOI: 10.1115/1.2945879]

Keywords: transient conduction, sequential heating and cooling

Introduction

The thermal response of objects can often be estimated by employing one-dimensional analyses. The most familiar analytical solutions are for sudden heating or cooling at the boundary(ies) of the domain and the evolution of temperatures to some steady state [1–5].

In applications ranging from food processing to nondestructive testing [6–11], an object is often *sequentially* heated then cooled, with similar initial and steady-state temperatures. The thermal response of regions internal to the object is of interest, and this response may not be obvious. For sequential heating and cooling, maximum internal temperatures can occur long after surface cooling begins.

Problem Description

Consider a plane wall of width $2L$ and initial temperature, T_i. Heating (Phase 1) is associated with $T_{\infty,h}$ and h_h, while cooling (Phase 2) is induced by $T_{\infty,c}$ and h_c. The initial and final wall temperatures are identical, $T_{\infty,c}=T_i$. Boundary conditions applied at $x=\pm L$ are identical, leading to symmetric temperature distributions about the wall centerline, $x=0$. Assuming constant properties, the governing equation for the temperature distribution is

$$\frac{\partial^2\theta}{\partial x^{*2}}=\frac{\partial\theta}{\partial \mathrm{Fo}} \tag{1}$$

where $\theta=(T-T_\infty)/(T_i-T_\infty)$ and the initial and boundary conditions for Phase 1 are

$$\theta(x^*,0)=1 \tag{2a}$$

$$\left.\frac{\partial\theta}{\partial x^*}\right|_{x^*=0}=0 \tag{2b}$$

$$\left.\frac{\partial\theta}{\partial x^*}\right|_{x^*=1}=-\mathrm{Bi}_1\theta(1,\mathrm{Fo}) \tag{2c}$$

Here, $\mathrm{Bi}_1\equiv h_hL/k$ and Fo_1 is the duration of Phase 1. For Phase 2, the boundary conditions are

$$\left.\frac{\partial\theta}{\partial x^*}\right|_{x^*=0}=0 \tag{3a}$$

$$\left.\frac{\partial\theta}{\partial x^*}\right|_{x^*=1}=-\mathrm{Bi}_2(\theta(1,\mathrm{Fo})-1) \tag{3b}$$

where $\mathrm{Bi}_2\equiv h_cL/k$ and the initial condition for Phase 2 is the temperature distribution at Fo_1.

Results

Equations (1), (2*a*)–(2*c*), (3*a*), and (3*b*) were solved numerically for $0.05<\mathrm{Fo}_1<\infty$ using a 1D finite-volume method [12]. An implicit formulation was employed with $\Delta x^*=0.05$ and time steps of $\Delta\mathrm{Fo}=0.001\mathrm{Fo}_1$. The simulations were verified by comparing predictions of $\theta(x^*=0,\mathrm{Fo}_1)$ with exact solutions for Phase 1 [12]. Agreement to within three digits was noted in all cases reported here.

Thermal Response. A typical response ($\mathrm{Bi}_1=10$, $\mathrm{Bi}_2=1$, $\mathrm{Fo}_1=0.1$) is shown in Fig. 1. Increasing physical temperatures in Phase 1 correspond to decreasing values of θ. Temperatures at the midplane ($x^*=0$), quarter-thickness ($x^*\approx0.5$), and surface ($x^*=1$) of the wall reveal that the surface thermal response is quick (θ decreases rapidly) compared to internal regions. At the onset of Phase 2, $\theta(x^*=1)$ increases rapidly (the physical temperature decreases rapidly) relative to the interior regions. The midplane θ continues to drop as thermal energy propagates inward from regions that are distant from the surface and the *extreme* midplane temperature, $\theta_{\min}$, occurs at $\mathrm{Fo}_2\approx0.37$. The maximum change in θ_o from its initial value ($1-\theta_o(0,\mathrm{Fo}_2)=0.212$) is six times greater than that at $\mathrm{Fo}_1(1-\theta_o(0,\mathrm{Fo}_1)=0.033)$. Hence, the continued heating of internal regions during Phase 2 can be significant.

Simulations and Correlations. About 300 simulations were performed for $0.01\leqslant\mathrm{Bi}_1\leqslant1000$, $0\leqslant\mathrm{Bi}_2\leqslant1000$, and $0\leqslant\mathrm{Fo}_1\leqslant\infty$, covering a broad range of heating and cooling conditions and heating durations. Recall that (i) *exact* infinite series solutions exist for $\mathrm{Fo}\leqslant\mathrm{Fo}_1$ and (ii) *approximate* (single-term) solutions yield acceptable results for $\mathrm{Fo}\geqslant0.2$ [12]. Also, an approximate solution for the steady-state midplane temperature exists for applications of (iii) *adiabatic* boundary conditions during Phase 2 and is

$$\theta_{\min,a}=\frac{\sin\zeta_1}{\zeta_1}C_1\exp(-\zeta_1^2\mathrm{Fo}_1) \tag{4}$$

where $\zeta_1\tan\zeta_1=\mathrm{Bi}_1$ and $C_1=4\sin\zeta_1/[2\zeta_1+\sin(2\zeta_1)]$. In the following discussion, these three solutions are termed exact, approximate, and adiabatic.

Values of $\theta_{\min}$ are shown in Fig. 2. Figure 2(*a*) is for gentle heating ($\mathrm{Bi}_1=0.1$) with lumped-capacitance behavior evident in Phase 1; $\theta_{\min}$ exists at $\mathrm{Fo}\approx\mathrm{Fo}_1$. For more robust heating ($\mathrm{Bi}_1=1$; Fig. 2(*b*)), $\theta_{\min}$ exhibits sensitivity to cooling conditions (Bi_2); numerical predictions associated with $\mathrm{Bi}_2=0.01$, 0.1, 1, 10, and 100 are shown as data points. Results for $\mathrm{Bi}_2=1000$ are nearly identical to those for $\mathrm{Bi}_2=100$ and therefore correspond to $\mathrm{Bi}_2\rightarrow\infty$ (constant temperature boundaries during Phase 2) and are labeled "CST." For any Fo_1, all values of $\theta_{\min}$ lie between the adiabatic and CST results, as expected. For example, heating must

Contributed by the Heat Transfer Division of ASME for publication in the JOURNAL OF HEAT TRANSFER. Manuscript received August 31, 2007; final manuscript received December 26, 2007; published online July 14, 2008. Review conducted by A. Haji-Sheikh.

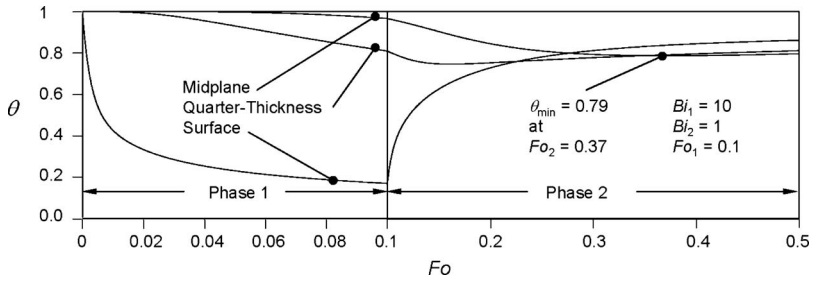

Fig. 1 Typical thermal response for sequential heating and cooling

occur for $Fo_{1,a}=0.92$ to achieve $\theta_{min}=0.5$ if adiabatic conditions are applied at Fo_1. Alternatively, heating until $Fo_{1,e}=1.09$ is necessary to achieve the same value of θ_{min} at Fo_1, as noted from the exact results. For CST conditions, $Fo_{1,CST}=1.03$ would be required.

For more intense heating (Fig. 2(*c*)), θ_{min} becomes more sensitive to wall cooling. Now, to achieve $\theta_{min}=0.5$, $Fo_{1,a}=0.27$, $Fo_{1,e}=0.45$, and $Fo_{1,CST}=0.39$. For $Bi_1=100$ (Fig. 2(*d*)) cooling conditions become even more influential, with $Fo_{1,a}=0.20$, $Fo_{1,e}=0.39$, and $Fo_{1,CST}=0.32$ needed for $\theta_{min}=0.5$. For $Bi_1>100$, the surface temperature during heating approaches $T_{\infty,h}$, and the limiting case results for $Bi_1=\rightarrow\infty$ (not shown) are nearly identical to those for $Bi_1=100$.

As evident in Fig. 2, θ_{min} exhibits an exponential decay with time. The curve fits of Table 1 were generated based on approximately 200 simulations and may be used to estimate θ_{min}.

The time at which θ_{min} is reached may also be important. Values of Fo_2 were found for $0.1\leqslant Bi_1\leqslant 1000$ and $0.01\leqslant Bi_2\leqslant 1000$. Some results for $Bi_2=0.01$, 1, and 100 are shown in Fig. 3. For robust cooling, $Fo_2\rightarrow Fo_1$, as expected. Gentle cooling ($Bi_2=0.01$) leads to large lag times with $Fo_2\gg Fo_1$. The Fo_2 dependence on Bi_1 is weak compared to Bi_2, as shown for $Fo_1=1$, $Bi_2=0.01$. The data points at this location correspond to $Bi_1=0.4$, 1, 4, 10, 40, and 100, yielding Fo_2 values of 1.53, 1.51, 1.47, 1.43, 1.41, and 1.41, respectively. Hence, a wide range of Bi_1 is represented by this cluster of data, with Fo_2 changing by less than 10% as Bi_1 spans the range from lumped capacitance to CST behavior in Phase 1. The curve fits of Table 2 were generated by analyzing approximately 200 simulations in the range of $0.1\leqslant\theta_{min}\leqslant 0.9$.

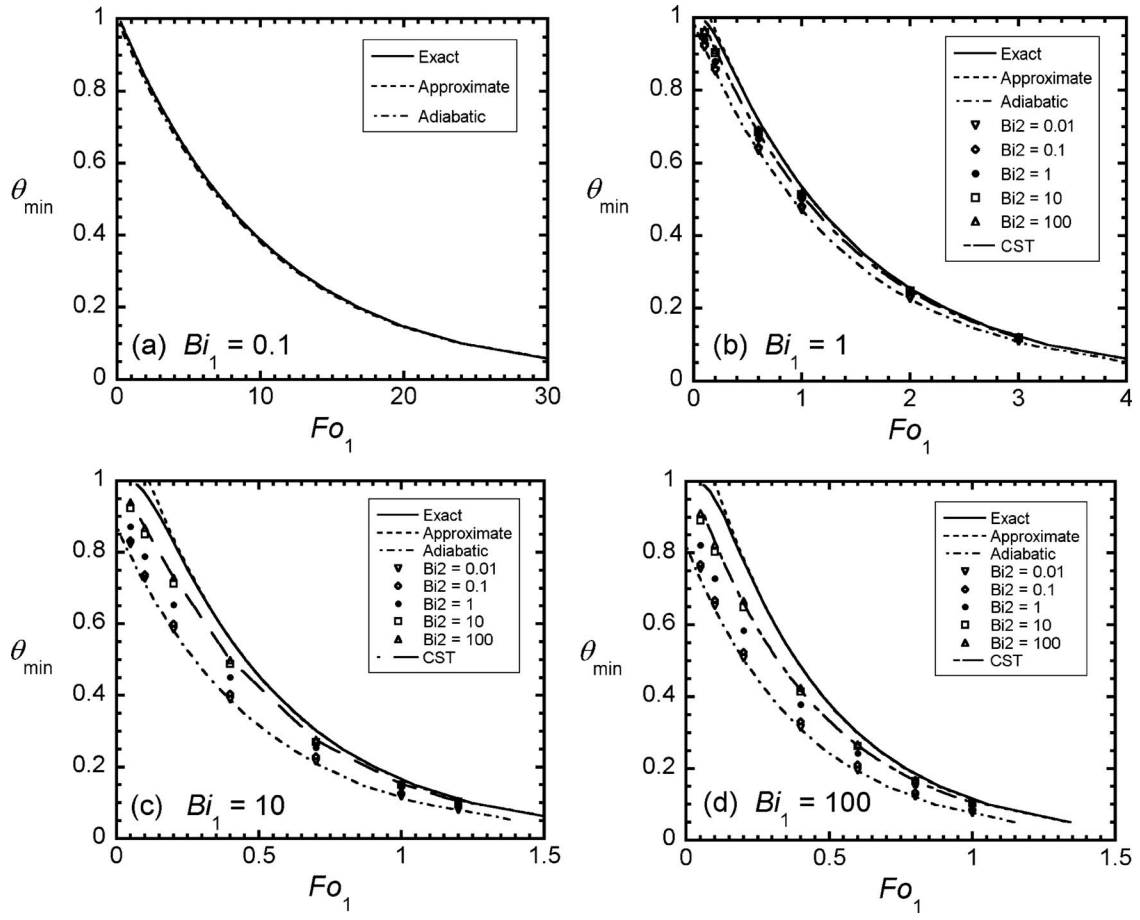

Fig. 2 Extreme midplane temperatures that develop in response to various heating and cooling conditions and durations: (*a*) $Bi_1=0.1$, (*b*) $Bi_1=1$, (*c*) $Bi_1=10$, (*d*) $Bi_1=100$

Table 1 Curve fits of the form $\theta_{min}=ae^{(-bFo_1)}$. Valid for $0.1\lesssim\theta_{min}\lesssim0.9$ and $Fo_1\geq0.05$.

Bi_1	Bi_2	a	b	χ^2	Comment
0.1	All Bi_2	1.0059	0.09627	—	Based on the average of the exact, approximate, and adiabatic responses.
0.4	0	0.99648	0.35155	1	Or use Eq. (4)
	0.01	0.99598	0.34915	1.000	
	0.1	1.0027	0.34714	1.000	
	1	1.0217	0.34824	0.9999	
	10	1.0350	0.34959	0.9999	
	100	1.0384	0.34986	0.9999	
	1000	1.0307	0.34990	0.9999	
1	0	0.98589	0.74005	1	Or use Eq. (4)
	0.01	0.98686	0.73395	1.000	
	0.1	0.99215	0.72175	1.000	
	1	1.0196	0.71851	0.9998	
	10	1.0468	0.72295	0.9998	
	100	1.0539	0.72387	0.9998	
	1000	1.0549	0.72410	0.9998	
4	0	0.92635	1.5985	1	Or use Eq. (4)
	0.01	0.92348	1.5758	0.9999	
	0.1	0.93187	1.5276	0.9999	
	1	1.0009	1.5177	0.9999	
	10	1.0751	1.5443	0.9998	
	100	1.0945	1.5506	0.9998	
	1000	1.0968	1.5508	0.9998	
10	0	0.8745	2.0414	1	Or use Eq. (4)
	0.01	0.8759	2.0007	0.9999	
	0.1	0.88483	1.9261	0.9999	
	1	0.95546	1.8945	1.0000	
	10	1.0423	1.9273	0.9999	
	100	1.0665	1.9371	0.9998	
	1000	1.0908	1.9680	0.9999	
40	0	0.82877	2.3459	1	Or use Eq. (4)
	0.01	0.82736	2.3065	0.9999	
	0.1	0.83754	2.2094	0.9999	
	1	0.92656	2.1750	0.9999	
	10	1.0331	2.2267	0.9999	
	100	1.0617	2.2393	0.9999	
	1000	1.0654	2.2409	0.9998	
100	0	0.81833	2.4193	1	Or use Eq. (4)
	0.01	0.83200	2.4007	0.9996	
	0.1	0.84188	2.2968	0.9996	
	1	0.91741	2.2344	1.0000	
	10	1.0135	2.2721	0.9998	
	100	1.0402	2.2824	0.9998	
	1000	1.0443	2.2871	0.9998	
1000	0	0.82861	2.4918	1	Or use Eq. (4)
	0.01	0.81490	2.4282	0.9999	
	0.1	0.82528	2.3211	0.9999	
	1	0.91143	2.2685	0.9999	
	10	1.0169	2.3175	0.9998	
	100	1.0460	2.3316	0.9998	
	1000	1.0495	2.3327	0.9998	

4 Discussion

As an example, consider a plane wall characterized by $Bi_1=6$ and $Bi_2=0.3$. A value of $\theta_{min}=0.4$ is desired. How long must heating last, and when is θ_{min} attained?

From Table 1, constants for $Bi_1=6$, $Bi_2=0.3$ may be found, yielding $a=0.93165$ (0.92410), $b=1.6566$ (1.6783), and $Fo_1=0.51$ (0.50) when the Bi_1 (Bi_2) entries are iterated first. From Table 2 with $Fo_1=0.51$, $Bi_1=6$, and $Bi_2=0.3$, Fo_2 is in the range of $0.62\leq Fo_2\leq0.88$. As a check, $Fo_1=0.51$ (0.50) was specified in the computer program, yielding $\theta_{min}=0.391$ (0.398) at $Fo_2=0.742$ (0.740). Hence, the values of θ_{min} are in good agreement, and the predicted value of Fo_2 is bracketed by values generated with Table 2.

From the practical perspective, *if* θ_{min} is assumed to occur at Fo_1, underprediction of θ_{min} will result. In the context of defining a heat treatment process, proper accounting of internal heating during Phase 2 will reduce the specified value of Fo_1, increasing productivity and decreasing energy consumption. Obviously, the

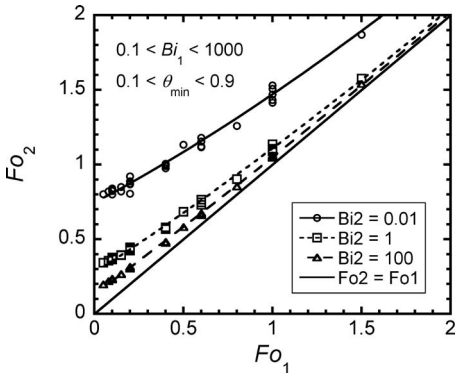

Fig. 3 Time at which the extreme midplane temperature occurs under various heating and cooling conditions and durations

results presented here are also valid for sequential cooling and heating operations.

Nomenclature

a, b, c = constants
Bi = Biot number, hL/k
Fo = Fourier number, $\alpha t/L^2$
h = convection heat transfer coefficient, $W/m^2 K$
k = thermal conductivity, W/m K
L = plane wall half-width, m
t = time, s
T = temperature, K
x = through-plane coordinate direction, m
x^* = dimensionless x location, x/L
α = thermal diffusivity, m^2/s
χ^2 = chi-square error
θ = dimensionless temperature, $(T-T_\infty)/(T_i-T_\infty)$

Table 2 Curve fits of the form $Fo_2 = a + bFo_1 + cFo_1^2$. Valid for $0.1 \leq \theta_{min} \leq 0.9$ and $0.05 \leq Fo_1 \leq 3$

Bi_2	a	b	c	χ^2
0.01	0.70296	0.79486	0.020453	0.998
0.1	0.46274	0.81319	0.020039	0.999
1	0.24773	0.88160	0.013497	0.999
10	0.13908	0.93395	0.0076446	0.999
100	0.11808	0.94356	0.0065436	0.999
1000	0.11836	0.93961	0.0070374	0.999

Subscripts

a = adiabatic
c = cooling
CST = constant surface temperature
e = exact
h = heating
i = initial
min = minimum
o = midplane location
1,2 = first or second phase of heating
∞ = ambient

References

[1] Carslaw, H. S., and Jaeger, J. C., 1986, *Conduction of Heat in Solids*, 2nd ed., Oxford University Press, London.
[2] Schneider, P. J., 1957, *Conduction Heat Transfer*, Addison-Wesley, Reading, MA.
[3] Kakac, S., and Yener, Y., 1993, *Heat Conduction*, Taylor & Francis, Washington, D.C.
[4] Poulikakos, D., 1994, *Conduction Heat Transfer*, Prentice-Hall, Englewood Cliffs, NJ.
[5] Gebhart, B., 1993, *Heat Conduction and Mass Diffusion*, McGraw-Hill, New York.
[6] Jin, Z. Q., and Liu, J. P., 2006 "Rapid Thermal Processing of Magnetic Materials," J. Phys. D, **39**, pp. R227–R244.
[7] Xie, L. F., Watanabe, H., and Mihori, T., 1997, "An Inverse Method for Achieving Correct Heat Sterilization of Conduction-Heated Food With Come-Up Heating," J. Japanese Society for Food Science and Technology, **7**, pp. 470–476.
[8] Bellara, S. R., McFarlane, C. M., Thomas, C. R., and Fryer, P. J., 2000, "The Growth of *Esherichia coli* in a Food Simulant During Conduction Cooling: Combining Engineering and Microbiological Modelling," Chem. Eng. Sci., **55**, pp. 6085–6095.
[9] Fu, Y. F., Wong, Y. L., Poon, C. S., and Tang, C. A., 2007, "Numerical Tests of Thermal Cracking Induced by Temperature Gradient in Cement-Based Composites Under Thermal Loads," Cem. Concr. Compos., **29**, pp. 103–116.
[10] Liu, L., and Kardomateas, G. A., 2006, "Thermal Buckling of a Fire-Damaged Composite Column Exposed to Heat Flux," AIAA J., **44**, pp. 2024–2033.
[11] Wang, C., Tang, G. C., Wang, B., Zevallos, M., and Alfano, R. R., 2006, "Detection of Subsurface Defects Using a Hybrid Heating and Cooling Imaging Technique," Appl. Phys. Lett., **88**, p. 194101.
[12] Incropera, F. P., DeWitt, D. P., Bergman, T. L., and Lavine, A. S., 2007, *Fundamentals of Heat and Mass Transfer*, Wiley, New York.

The Effect of a Transition Layer Between a Fluid and a Porous Medium: Forced Convection in a Channel

A. V. Kuznetsov
Department of Mechanical and Aerospace Engineering,
North Carolina State University,
Campus Box 7910,
Raleigh, NC 27695-7910
e-mail: avkuznet@eos.ncsu.edu

D. A. Nield
Department of Engineering Science,
University of Auckland,
Private Bag 92019,
Auckland 1142, New Zealand
e-mail: d.nield@auckland.ac.nz

Flow in a three-layer channel is modeled analytically. The channel consists of a transition layer sandwiched between a porous medium and a fluid clear of solid material. Within the transition layer, the reciprocal of the permeability varies linearly across the channel. The Brinkman model is used for the momentum equations for the porous medium layer and the transition layer. The velocity profile is obtained in closed form in terms of Airy, exponential, and polynomial functions and this is employed to find analytically the Nusselt number for fully developed forced convection with boundaries subject to uniform and constant heat flux. [DOI: 10.1115/1.2945905]

Keywords: transition layer, forced convection, channel, porous medium

1 Introduction

Recent developments in the requirement of cooling of electronic equipment have led to an increased interest in forced convection in a porous medium partly or wholly occupying a channel (see, for example, Nield and Bejan [1]). There is currently a divergence of opinion on the best way to model flow in a fluid adjacent to a porous medium. One way is to employ a single domain model with a momentum equation of Brinkman type for the porous medium subdomain and with the Navier–Stokes equation (the same equation but with the Darcy drag term omitted, and perhaps with a different viscosity) for the fluid subdomain. At the interface, four matching conditions are employed, namely, the continuity of tangential velocity (Darcy seepage velocity in the porous medium), normal velocity, tangential stress, and normal stress. The fact that the expression for the stress that is valid in the fluid is not also valid in the porous medium is often ignored. In other words, a jump in tangential stress and normal stress computed from the usual velocity shear is ignored. The method of averaging over a representative elementary volume gives expressions for the stress jump but these involve empirical coefficients that are not easily determined.

A second way is to employ a two-domain model, with a Darcy momentum equation for the porous medium and with a single boundary condition replacing the tangential velocity and tangential stress pair. This boundary condition involves the Beavers–Joseph boundary condition, something that is usually treated as an empirical parameter.

A third way was introduced by Nield and Kuznetsov [2]. This is essentially a three-domain model. They studied unidirectional flow in a parallel-plate channel consisting of three layers, with a transition layer sandwiched between a porous medium and a fluid clear of solid material. They assumed that within the transition layer, the reciprocal of the permeability varies linearly across the channel and matches with the outer layers in a continuous fashion. They used the Brinkman model for the momentum equations for the porous medium layer and the transition layer. They pointed out that because there is no jump in permeability at either interface, there are expected to be negligible jumps of tangential stress at those interfaces. They obtained expressions for the velocity profile in each of the three layers in closed form. In the case of the transition layer, Airy functions were involved.

Nield and Kuznetsov [2] were primarily interested in how the overall volume flux and the fluid interface friction coefficient calculated on their model compared to those from the two-domain model employing the Beavers–Joseph boundary condition. In the present paper, the focus is on heat transfer. The case of fully developed convection in a channel with boundary walls held at uniform constant heat flux is studied.

2 Analysis

We consider a parallel-plate channel with unidirectional flow in the x-direction, and a triple layer with permeability distribution in the transverse direction as follows.
In Region 1,

$$1/K = 0 \quad \text{for } 0 < y^* < \xi H \tag{1a}$$

In Region 2,

$$\frac{1}{K} = \frac{y^* - \xi H}{K_0(\eta - \xi)H} \quad \text{for } \xi H < y^* < \eta H \tag{1b}$$

In Region 3,

$$K = K_0 \quad \text{for } \eta H < y^* < H \tag{1c}$$

Here, the asterisks denote the dimensional variables and H is the channel width.

Thus, Region 1 is a fluid clear of solid material; Region 3 is a porous medium with constant permeability, while Region 2 is a transition layer with a linear distribution of the reciprocal of the permeability, with continuity of permeability at the interface boundaries. We suppose that there is a uniform and constant negative pressure gradient G throughout the triple layer domain and that the Brinkman model is employed in each porous medium layer. Then the momentum equations for the respective regions are as follows:

$$\mu \frac{d^2 {u_1}^*}{dy^{*2}} + G = 0 \quad \text{for } 0 < y^* < \xi H \tag{2a}$$

$$\mu_{e2} \frac{d^2 {u_2}^*}{dy^{*2}} - \frac{\mu}{K_2} {u_2}^* + G = 0 \quad \text{for } \xi H < y^* < \eta H \tag{2b}$$

$$\mu_{e3} \frac{d^2 {u_3}^*}{dy^{*2}} - \frac{\mu}{K_3} {u_3}^* + G = 0 \quad \text{for } \eta H < y^* < H \tag{2c}$$

Here, μ is the fluid viscosity while μ_{e2} and μ_{e3} are the effective viscosities. Dimensionless variables are now defined by

$$y = \frac{y^*}{H} \tag{3a}$$

Contributed by the Heat Transfer Division of ASME for publication in the JOURNAL OF HEAT TRANSFER. Manuscript received November 19, 2007; final manuscript received February 11, 2008; published online July 14, 2008. Review conducted by Peter Vadasz.

$$u = \frac{\mu u^*}{GH^2} \tag{3b}$$

and a Darcy number Da together with viscosity ratios M_2 and M_3 are defined by

$$\mathrm{Da} = \frac{K_0}{H^2} \tag{4a}$$

$$M_2 = \frac{\mu_{e2}}{\mu} \tag{4b}$$

$$M_3 = \frac{\mu_{e3}}{\mu} \tag{4c}$$

Equations (2*a*)–(2*c*) become

$$\frac{d^2u_1}{dy^2} + 1 = 0 \quad \text{for } 0 < y < \xi \tag{5a}$$

$$M_2\frac{d^2u_2}{dy^2} - \frac{1}{\mathrm{Da}}\left(\frac{y-\xi}{\eta-\xi}\right)u_2 + 1 = 0 \quad \text{for } \xi < y < \eta \tag{5b}$$

$$M_3\frac{d^2u_3}{dy^2} - \frac{u_3}{\mathrm{Da}} + 1 = 0 \quad \text{for } \eta < y < 1 \tag{5c}$$

These equations must be solved subject to the boundary and matching conditions

$$u_1 = 0 \quad \text{at } y = 0 \tag{6a}$$

$$u_1 = u_2 \tag{6b}$$

and

$$\frac{du_1}{dy} = \frac{du_2}{dy} \quad \text{at } y = \xi \tag{6c}$$

$$u_2 = u_3 \tag{6d}$$

and

$$\frac{du_2}{dy} = \frac{du_3}{dy} \quad \text{at } y = \eta \tag{6e}$$

$$u_3 = 0 \quad \text{at } y = 1 \tag{6f}$$

We now introduce the shorthand notation,

$$\lambda_2 = \frac{1}{[M_2\mathrm{Da}(\eta-\xi)]^{1/3}} \tag{7a}$$

$$\lambda_3 = \frac{1}{(M_3\mathrm{Da})^{1/2}} \tag{7b}$$

We also introduce a transformed transverse variable

$$\tilde{y} = \lambda_2(y - \xi) \tag{8}$$

and write $u_2(y) \equiv U_2(\tilde{y})$. Equations (5*a*)–(5*c*) become

$$\frac{d^2u_1}{dy^2} + 1 = 0 \quad \text{for } 0 < y < \xi \tag{9a}$$

$$\frac{d^2U_2}{d\tilde{y}^2} - \tilde{y}U_2 + \frac{1}{\lambda_2{}^2M_2} = 0 \quad \text{for } 0 < \tilde{y} < \lambda_2(\eta - \xi) \tag{9b}$$

$$\frac{d^2u_3}{dy^2} - \lambda_3{}^2u_3 + \frac{1}{M_3} = 0 \quad \text{for } \eta < y < 1 \tag{9c}$$

The general solutions of these equations are

$$u_1 = c_1y + d_1 - \frac{y^2}{2} \tag{10a}$$

$$U_2 = c_2\,\mathrm{Ai}(\tilde{y}) + d_2\,\mathrm{Bi}(\tilde{y}) + \frac{\pi}{M_2\lambda_2{}^2}\mathrm{Ni}(\tilde{y}) \tag{10b}$$

and so

$$u_2 = c_2\,\mathrm{Ai}(\lambda_2(y-\xi)) + d_2\,\mathrm{Bi}(\lambda_2(y-\xi)) + \frac{\pi}{M_2\lambda_2{}^2}\mathrm{Ni}(\lambda_2(y-\xi)) \tag{10b′}$$

$$u_3 = c_3\exp(\lambda_3y) + d_3\exp(-\lambda_3y) + \frac{1}{M_3\lambda_3{}^2} \tag{10c}$$

Here, $\mathrm{Ni}(x)$ is the function introduced by Nield and Kuznetsov [2] and defined by

$$\mathrm{Ni}(x) = \mathrm{Ai}(x)\int_0^x \mathrm{Bi}(t)dt - \mathrm{Bi}(x)\int_0^x \mathrm{Ai}(t)dt \tag{11}$$

and so having the useful property that $\mathrm{Ni}(0) = \mathrm{Ni}'(0) = 0$. The function $\mathrm{Ni}(x)$ is related to the Scorer function $\mathrm{Gi}(x)$ (see, for example, Vallée and Soares [3]) by

$$\mathrm{Ni}(x) = \mathrm{Gi}(x) - \mathrm{Bi}(x)\int_0^\infty \mathrm{Ai}(t)dt = \mathrm{Gi}(x) - \mathrm{Bi}(x)/3 \tag{12}$$

Substitution of Eqs. (10*a*)–(10*c*) in Eqs. (6*a*)–(6*f*) yields the matrix equation

$$\mathbf{Mx} = \mathbf{c} \tag{13}$$

where

$$\mathbf{M} = \begin{bmatrix} 0 & 1 & 0 & 0 & 0 & 0 \\ \xi & 1 & \dfrac{-\mathrm{Ai}(0)}{\mathrm{Ai}[\lambda_2(\eta-\xi)]} & \dfrac{-\mathrm{Bi}(0)}{\mathrm{Bi}[\lambda_2(\eta-\xi)]} & 0 & 0 \\ 1 & 0 & \dfrac{-\lambda_2\mathrm{Ai}'(0)}{\mathrm{Ai}[\lambda_2(\eta-\xi)]} & \dfrac{-\lambda_2\mathrm{Bi}'(0)}{\mathrm{Bi}[\lambda_2(\eta-\xi)]} & 0 & 0 \\ 0 & 0 & 1 & 1 & -\exp[-\lambda_3(1-\eta)] & -\exp[\lambda_3(1-\eta)] \\ 0 & 0 & \dfrac{\lambda_2\mathrm{Ai}'[\lambda_2(\eta-\xi)]}{\mathrm{Ai}[\lambda_2(\eta-\xi)]} & \dfrac{\lambda_2\mathrm{Bi}'[\lambda_2(\eta-\xi)]}{\mathrm{Bi}[\lambda_2(\eta-\xi)]} & -\lambda_3\exp[-\lambda_3(1-\eta)] & \lambda_3\exp[\lambda_3(1-\eta)] \\ 0 & 0 & 0 & 0 & 1 & 1 \end{bmatrix} \tag{14}$$

$$\mathbf{x} = \begin{bmatrix} c_1 \\ d_1 \\ \hat{c}_2 \\ \hat{d}_2 \\ \hat{c}_3 \\ \hat{d}_3 \end{bmatrix} \tag{15}$$

$$\mathbf{c} = \begin{bmatrix} 0 \\ \xi^2/2 \\ \xi \\ \dfrac{1}{M_3\lambda_3{}^2} - \dfrac{\pi}{M_2\lambda_2{}^2}\mathrm{Ni}[\lambda_2(\eta-\xi)] \\ -\dfrac{\pi}{M_2\lambda_2}\mathrm{Ni}'[\lambda_2(\eta-\xi)] \\ -1/M_3\lambda_3{}^2 \end{bmatrix} \tag{16}$$

In writing Eq. (16), we have used the fact that $\mathrm{Ni}(0)=\mathrm{Ni}'(0)=0$. Also, in order to produce a better conditioned matrix, we have introduced the scaling

$$\hat{c}_2 = c_2\mathrm{Ai}[\lambda_2(\eta-\xi)], \quad \hat{d}_2 = d_2\mathrm{Bi}[\lambda_2(\eta-\xi)], \quad \hat{c}_3 = c_3 e^{\lambda_3}$$
$$\hat{d}_3 = d_3 e^{-\lambda_3} \tag{17}$$

A quantity of interest is the dimensionless mean velocity $\bar{u}$ defined by

$$\bar{u} = \int_0^\xi u_1 dy + \int_\xi^\eta u_2 dy + \int_\eta^1 u_3 dy \tag{18}$$

One finds that

$$\begin{aligned}\bar{u} &= \int_0^\xi u_1 dy + \lambda_2{}^{-1}\int_0^{\lambda_2(\eta-\xi)} U_2 d\bar{y} + \int_\eta^1 u_3 dy \\ &= \frac{1}{2}c_1\xi^2 + d_1\xi - \frac{1}{6}\xi^3 + \frac{c_2}{\lambda_2}\int_0^{\lambda_2(\eta-\xi)} \mathrm{Ai}(t)dt + \frac{d_2}{\lambda_2}\int_0^{\lambda_2(\eta-\xi)} \mathrm{Bi}(t)dt \\ &\quad + \frac{\pi}{M_2\lambda_2{}^3}\int_0^{\lambda_2(\eta-\xi)} \mathrm{Ni}(t)dt + \frac{c_3}{\lambda_3}(\exp(\lambda_3) - \exp(\lambda_3\eta)) \\ &\quad - \frac{d_3}{\lambda_3}(\exp(-\lambda_3) - \exp(-\lambda_3\eta)) + \frac{1-\eta}{M_3\lambda_3{}^2}.\end{aligned} \tag{19}$$

We wrote a FORTRAN code to solve Eq. (13) to obtain the elements in Eq. (15) and then substitute into Eqs. (10*a*)–(10*c*) to obtain the velocity profile and the mean velocity.

For the case of symmetric constant heat flux boundary conditions, one finds that the thermal energy equation leads to (compare Eq. (4.120), with different notation, in Ref. [1])

$$\frac{d^2\hat{T}_i}{dy^2} = -\beta_i\hat{u}_i(y), \quad i = 1,2,3 \tag{20}$$

Here, $\hat{u}_i = u_i/\bar{u}$ and $\hat{T}_i = (T^* - T_w)/(T_m - T_w)$ and for shorthand we have written

$$\beta_i = \frac{2\mathrm{Nu}}{\tilde{k}_i} \tag{21}$$

Here, $\tilde{k}_i = k_i/\bar{k}$, where $\bar{k}$ is the mean value of k given by

$$\bar{k} = \xi k_1 + (\eta-\xi)k_2 + (1-\eta)k_3 \tag{22}$$

where k_i is the conductivity of the ith layer and the Nusselt number Nu is defined in terms of the channel width H (rather than the hydraulic diameter) by

$$\mathrm{Nu} = \frac{Hq''}{\bar{k}(T_w{}^* - T_m{}^*)} \tag{23}$$

where

$$\begin{aligned}T_m{}^* &= \frac{1}{H\bar{u}^*}\int_0^H u^*T^*dy^* \\ &= \frac{1}{H\bar{u}^*}\left[\int_0^{\xi H} u_1{}^*T_1{}^*dy^* + \int_{\xi H}^{\eta H} u_2{}^*T_2{}^*dy^* + \int_{\eta H}^H u_3{}^*T_3{}^*dy^*\right]\end{aligned} \tag{24}$$

$$\bar{u}^* = \frac{1}{H}\int_0^H u^*dy^* = \frac{1}{H}\left[\int_0^{\xi H} u_1^*dy^* + \int_{\xi H}^{\eta H} u_2^*dy^* + \int_{\eta H}^H u_3^*dy^*\right] \tag{25}$$

Since we do not have a closed form expression for the indefinite integral of $\mathrm{Ni}(x)$, we proceed as follows. We write

$$\begin{aligned}&\hat{T}_1|_{y=0} = T_{10}, \quad \left.\frac{d\hat{T}_1}{dy}\right|_{y=0} = T'_{10} \\ &\hat{T}_2|_{y=\xi} = T_{2\xi}, \quad \left.\frac{d\hat{T}_2}{dy}\right|_{y=\xi} = T'_{2\xi} \\ &\hat{T}_3|_{y=\eta} = T_{3\eta}, \quad \left.\frac{d\hat{T}_3}{dy}\right|_{y=\eta} = T'_{3\eta}\end{aligned} \tag{26}$$

The temperature profile functions are

$$\hat{T}_1(y) = T_{10} + yT'_{10} - \beta_1\int_0^y\left[\int_0^\tau \hat{u}_1(t)dt\right]d\tau \tag{27a}$$

$$\hat{T}_2(y) = T_{2\xi} + (y-\xi)T'_{2\xi} - \beta_2\int_\xi^y\left[\int_\xi^\tau \hat{u}_2(t)dt\right]d\tau \tag{27b}$$

$$\hat{T}_3(y) = T_{3\eta} + (y-\eta)T'_{3\eta} - \beta_3\int_\eta^y\left[\int_\eta^\tau \hat{u}_3(t)dt\right]d\tau \tag{27c}$$

The temperature gradient functions are

$$\frac{d\hat{T}_1}{dy} = T'_{10} - \beta_1\int_0^y \hat{u}_1(t)dt \tag{28a}$$

$$\frac{d\hat{T}_2}{dy} = T'_{2\xi} - \beta_2\int_\xi^y \hat{u}_2(t)dt \tag{28b}$$

$$\frac{d\hat{T}_3}{dy} = T'_{3\eta} - \beta_3\int_\eta^y \hat{u}_3(t)dt \tag{28c}$$

The boundary conditions are

$$\hat{T}_1 = 0 \text{ at } y = 0 \tag{29a}$$

$$\hat{T}_1|_{y=\xi} = \hat{T}_2|_{y=\xi} \tag{29b}$$

$$\tilde{k}_1 \left.\frac{d\hat{T}_1}{dy}\right|_{y=\xi} = \tilde{k}_2 \left.\frac{d\hat{T}_2}{dy}\right|_{y=\xi} \tag{29c}$$

$$\hat{T}_2|_{y=\eta} = \hat{T}_3|_{y=\eta} \tag{29d}$$

$$\tilde{k}_2 \left.\frac{d\hat{T}_2}{dy}\right|_{y=\eta} = \tilde{k}_3 \left.\frac{d\hat{T}_3}{dy}\right|_{y=\eta} \tag{29e}$$

$$\hat{T}_3 = 0 \text{ at } y = 1 \tag{29f}$$

These lead to the equation

$$\mathbf{N}\mathbf{y} = \mathbf{d} \tag{30}$$

where

$$\mathbf{N} = \begin{bmatrix} 1 & 0 & 0 & 0 & 0 & 0 \\ 1 & \xi & -1 & 0 & 0 & 0 \\ 0 & \tilde{k}_1 & 0 & -\tilde{k}_2 & 0 & 0 \\ 0 & 0 & 1 & \eta-\xi & -1 & 0 \\ 0 & 0 & 0 & \tilde{k}_2 & 0 & -\tilde{k}_3 \\ 0 & 0 & 0 & 0 & 1 & 1-\eta \end{bmatrix} \tag{31}$$

$$\mathbf{y} = \begin{bmatrix} T_{10} \\ T'_{10} \\ T_{2\xi} \\ T'_{2\xi} \\ T_{3\eta} \\ T'_{3\eta} \end{bmatrix} \tag{32}$$

$$\mathbf{d} = \begin{bmatrix} 0 \\ \beta_1 \int_0^\xi \left[\int_0^\tau \hat{u}_1(t)dt \right] d\tau \\ \tilde{k}_1 \beta_1 \int_0^\xi \hat{u}_1(t)dt \\ \beta_2 \int_\xi^\eta \left[\int_\xi^\tau \hat{u}_2(t)dt \right] d\tau \\ \tilde{k}_2 \beta_2 \int_\xi^\eta \hat{u}_2(t)dt \\ \beta_3 \int_\eta^1 \left[\int_\eta^\tau \hat{u}_3(t)dt \right] d\tau \end{bmatrix}$$

$$= 2\mathrm{Nu} \begin{bmatrix} 0 \\ \tilde{k}_1^{-1} \int_0^\xi \left[\int_0^\tau \hat{u}_1(t)dt \right] d\tau \\ \int_0^\xi \hat{u}_1(t)dt \\ \tilde{k}_2^{-1} \int_\xi^\eta \left[\int_\xi^\tau \hat{u}_2(t)dt \right] d\tau \\ \int_\xi^\eta \hat{u}_2(t)dt \\ \tilde{k}_3^{-1} \int_\eta^1 \left[\int_\eta^\tau \hat{u}_3(t)dt \right] d\tau \end{bmatrix} \tag{33}$$

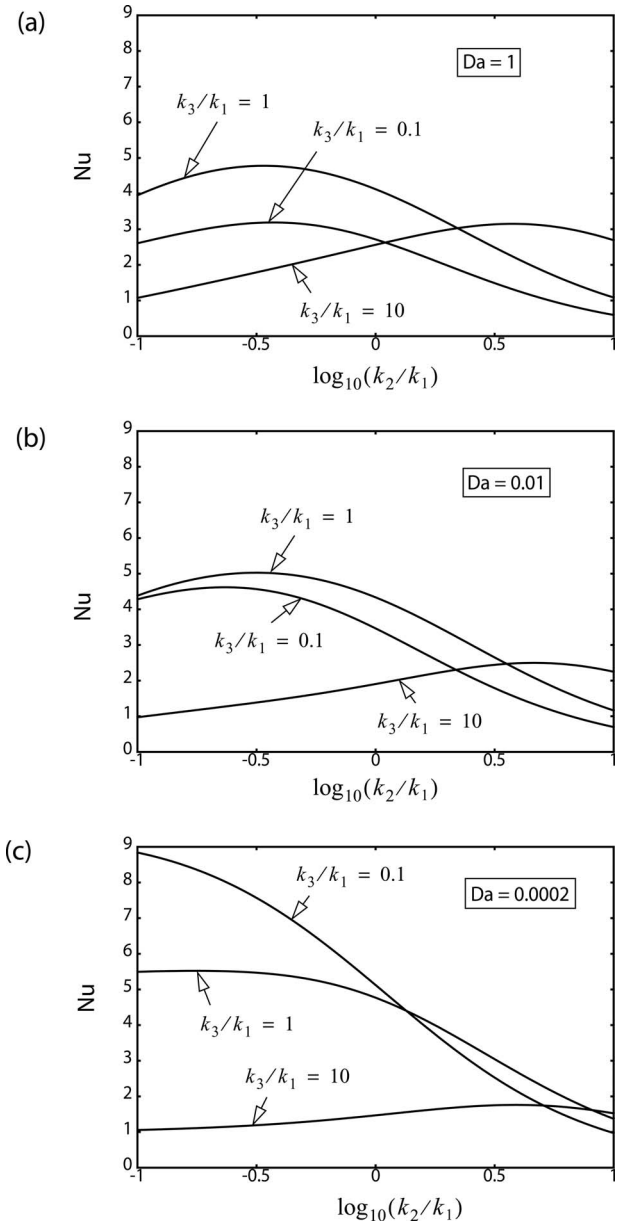

Fig. 1 Plots of the Nusselt number as a function of conductivity ratios for various values of the Darcy number (*a*) Da=1, (*b*) Da=0.01, and (*c*) Da=0.0002, for a fat transition layer (ξ=1/3, η=2/3)

Solution of Eq. (30) for **y** and substitution into Eqs. (27*a*)–(27*c*) followed by substitution into the integral consistency identity

$$\int_0^\xi \hat{u}_1\hat{T}_1 dy + \int_\xi^\eta \hat{u}_2\hat{T}_2 dy + \int_\eta^1 \hat{u}_3\hat{T}_3 dy = 1 \tag{34}$$

gives an equation for Nu. We wrote a FORTRAN code to implement this procedure.

3 Results and Discussion

Our analysis involves a large number of parameters and we present results for some representative values only. We select the value unity for each of the viscosity ratios M_2 and M_3. We concentrate on the cases of a "fat transition layer" (ξ=1/3, η=2/3) and a "thin transition layer" (ξ=0.49, η=0.51), and for each of these layers treat the subcases of Da=1.0, Da=0.01, and Da =0.0002, the smallest value for which we could compute. The

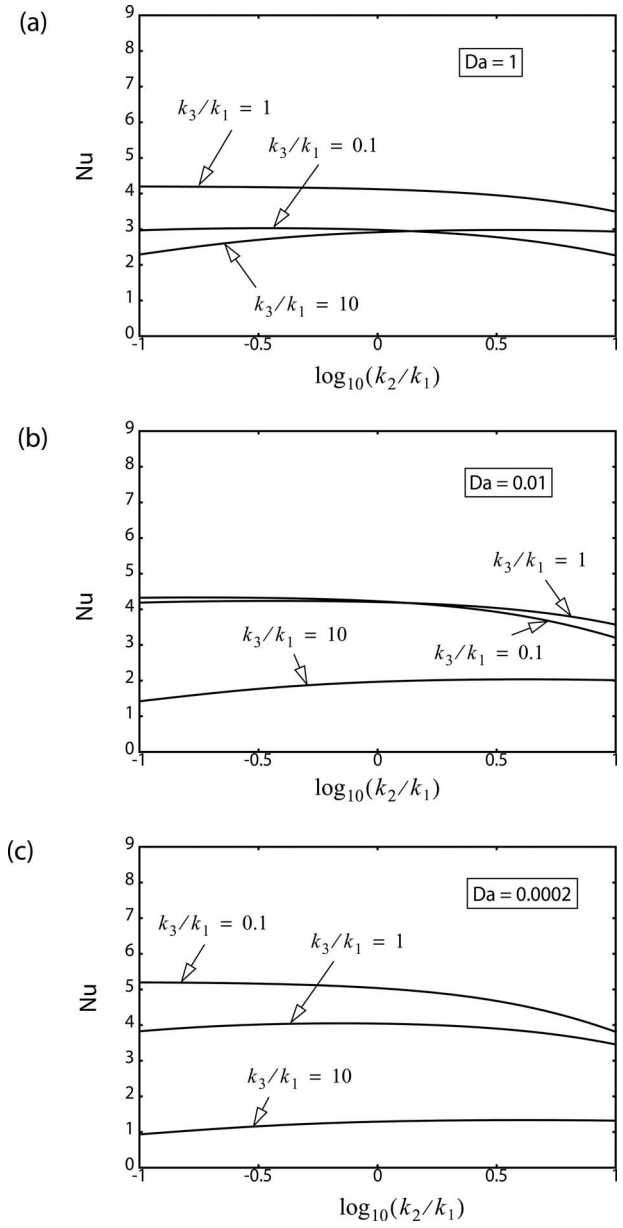

Fig. 2 Plots of the Nusselt number as a function of conductivity ratios for various values of the Darcy number (*a*) Da=1, (*b*) Da=0.01, and (*c*) Da=0.0002, for a thin transition layer (ξ=0.49, η=0.51)

limitation on the computation is related to the fact that in the limit as $\xi \to 0$, $\eta \to 1$, $\mathrm{Da} \to 0$ the problem becomes singular; the velocity profile approaches a $1/y$ dependence and the mean velocity tends to infinity.

Values of the Nusselt number for various values of the other parameters are plotted in Figs. 1 and 2. The case Da=1 approximates that for a layer of a fluid clear of solid material. Thus, the plots for that case show the effect of heterogeneity of thermal conductivity more or less independently of the hydrodynamic effect. As expected, the value for the homogeneous situation ($k_1 = k_2 = k_3$), namely, 4.123, is close to the well known value 70/17 =4.118 for the clear fluid case. The plotted curves have maxima, illustrating the fact that deviation away from homogeneity generally leads to a reduction in the value of Nu. Also, as expected, we see that the amount of reduction for a fat layer is greater than that for a thin layer.

We also see that when Da becomes small, the effect of conductivity heterogeneity becomes accentuated. When k_1 is less than both k_2 and k_3 (the case of relatively low conductivity fluid) the value of Nu can exceed 70/17 by a substantial amount.

As expected, the curves plotted in Fig. 2 are flat. For a thin transition layer, the value of k_2 is not important.

4 Conclusion

We have modeled analytically flow in a channel consisting of a transition layer sandwiched between a porous medium and a fluid clear of solid material, using the Brinkman model and assuming that within the transition layer the reciprocal of the permeability varies linearly across the channel. The Nusselt number has been obtained for the case where the walls are subject to uniform constant heat flux.

Nomenclature

- Da = Darcy number, K_0/H^2
- G = applied pressure gradient
- H = channel width
- K = permeability
- K_0 = reference permeability defined in Eqs. (1*a*)–(1*c*)
- k = thermal conductivity
- $\bar{k}$ = mean value of k
- $\tilde{k}_i$ = $k_i/\bar{k}$, where k_i is the value of k in layer i (i =1,2,3)
- M_2 = viscosity ratio in Region 2, μ_{e2}/μ
- M_3 = viscosity ratio in Region 3, μ_{e3}/μ
- Nu = Nusselt number
- u = dimensionless filtration velocity, $\mu u^*/GH^2$
- u^* = filtration velocity
- $\bar{u}$ = dimensionless mean velocity defined in Eq. (19)
- y = dimensionless transverse coordinate, y^*/H
- y^* = transverse coordinate

Greek Symbols

- β = parameter defined by Eq. (21)
- η = position of the interface between Regions 2 and 3
- λ_2, λ_3 = parameters defined in Eqs. (7*a*) and (7*b*)
- μ = fluid viscosity
- μ_{e2} = effective viscosity in Region 2
- μ_{e3} = effective viscosity in Region 3
- ξ = position of the interface between Regions 1 and 2

References

[1] Nield, D. A., and Bejan, A., 2006, *Convection in Porous Media*, 3rd ed., Springer, New York.

[2] Nield, D. A., and Kuznetsov, A. V., 2007, "The Effect of a Transition Layer Between a Fluid and a Porous Medium: Shear Flow in a Channel," Transp. Porous Media, submitted.

[3] Vallée, O., and Soares, M., 2004, *Airy Functions and Applications to Physics*, World Scientific, London.